**The Thesis Committee for Alexander Sebastian MacDonald Urquhart**
**Certifies that this is the approved version of the following thesis:**

# Structural controls on $CO_2$ leakage and diagenesis in a natural long-term carbon sequestration analogue: Little Grand Wash fault, Utah

**APPROVED BY**
**SUPERVISING COMMITTEE:**

**Supervisor:**

Peter Eichhubl

**Co-Supervisor:**

Tip Meckel

**Co-Supervisor:**

Stephen E. Laubach

Peter B. Flemings

Marc A. Hesse

Scott W. Tinker

# Structural controls on $CO_2$ leakage and diagenesis in a natural long-term carbon sequestration analogue: Little Grand Wash fault, Utah

**by**

**Alexander Sebastian MacDonald Urquhart, BA**

**Thesis**

Presented to the Faculty of the Graduate School of
The University of Texas at Austin
in Partial Fulfillment
of the Requirements
for the Degree of

**Master of Science in Geological Sciences**

**The University of Texas at Austin**
**August 2011**

# Acknowledgements

Peter Eichhubl devoted countless hours to teaching me how to undertake a large research project. To my immense benefit he took constant interest in my progress, never losing track of me between his many projects. He was available even late in the evenings to have long discussions about my work, which I greatly appreciate, even if they were sometimes very long. I am enduringly grateful to him for abiding and patiently correcting my often haphazard and flailing approach to research, for pushing me to use all the tools and resources available, and for teaching me to eschew the TLA and its beguiling cousins.

I am grateful to everyone on my committee for giving me their time and their excellent expert advice. Steve Laubach encouraged a more comprehensive approach to the thesis process by exhorting us to improve all aspects of our writing. He also maintained the lab's spirits with reading parties, cactus golf and other questionable diversions. Tip Meckel showed me what it's like to live in wonder of science, notably through water droplets on the window of an airplane. Scott Tinker, Peter Flemings and Marc Hesse provided detailed feedback that dramatically improved the quality of this project.

My field and laboratory research were supported by generous funds from the GDL Foundation and the Geology Foundation of the Jackson School of Geosciences. The project is performed as part of the Center for Frontiers of Subsurface Energy Security at UT Austin, an Energy Frontier Research Center funded by the U.S. Department of Energy, Office of Science, Office of Basic Energy Sciences, under Award Number DE-SC0001114.

I am endlessly indebted to Philip Guerrero, for making sure I didn't accidentally drop out, making sure I was fed at least one day a month, maintaining an apparently

infinite patience with late forms, and always cheerfully helping me work through the System, even if I deserved no such help; and to Nicole Evans, for her help time and time again in navigating the vicissitudes of administrative shuffling and a desperate office crunch.

Many thanks to Greg Thompson, for readily preparing one batch of thin sections after another, for sharing his expertise and for advising me how to proceed with difficult sample preparations; Kitty Milliken, for patiently teaching me to use roomfuls of equipment, and for trusting me to enter those rooms alone; Glen Baum, for his help, on short notice and with a heavy schedule, in acquiring porosity and permeability data for many of my samples and for taking the time to review my description of those processes; Donggao Zhao, for teaching me how to use an array of expensive and delicate machinery, and for his availability and support when those machines didn't work the way I wanted them to work; Jiemin Lu for his help in sample preparation and the daunting task of interpreting X-ray diffraction results; and Jay Santillan, for making his expertise available to smooth over the cavernous gaps in my geochemical understanding.

If I finished this project, it was only for the support of friends near and afield—those who drove me to work by their ceaseless nagging, and those who gave respite by talking of other things or introducing me to squash and the culinary art of bird preparation.

The constant Connor Cobean was a fearless, peerless assistant in the field and an unwavering source of good humor under the lash of wind, rain and snow—a friend whose company dramatically improved my mood, work ethic and final product.

Tekla Harms inspired my delight in geology and encouraged me to consider graduate school, for which I am more grateful than she can know.

And of course I thank my parents—for passing on a love and wonder of the natural world, for showing me the meaning of the word *sublime*, for letting me fill their house with rocks, for tolerating my inconsistencies, and for everything else.

# Abstract

## Structural controls on $CO_2$ leakage and diagenesis in a natural long-term carbon sequestration analogue: Little Grand Wash fault, Utah

Alexander Sebastian MacDonald Urquhart, M.S.Geo.Sci
The University of Texas at Austin, 2011

Supervisor: Peter Eichhubl
Co-supervisors: Tip Meckel and Stephen E. Laubach

The Little Grand Wash normal fault near Green River, eastern Utah, hosts a series of naturally occurring $CO_2$ seeps in the form of active and extinct $CO_2$-charged springs distributed along the fault zone. I have studied the association of fault structure with $CO_2$-related alteration as an analogue for the long-term (1,000- to 10,000-year) effects of leakage through faults in $CO_2$ sequestration reservoirs. Structure and alteration in a portion of the Little Grand Wash fault zone were mapped at a 1:700 scale in order to determine the association of faulting with $CO_2$-related diagenesis. I combined structural and diagenetic mapping were combined with laboratory analyses of mineralogical, isotopic and textural changes in order to assess controls on the migration of $CO_2$ traveling up the fault and its effects on the fault itself.

The fault zone is 200 m wide at its widest and contains 4–5 major subparallel fault segments that form multiple soft- and hard-linked relay ramps. The area includes a travertine

deposit and related sandstone alteration: outcrop-visible coloration, porosity-occluding calcite cement and veins occasionally so abundant that they obliterate the rock fabric. Structural mapping shows that the travertine is located at an intersection of major fault segments constituting the hard link of a 450-meter-long relay ramp. Sandstone alteration is confirmed to be related to the $CO_2$ seep by mapping its distribution, which shows a decrease in concentration away from the travertine, and by the unique isotopic signature of calcite cement near the travertine. At distances greater than 25 m from the travertine intense alteration disappears, though scattered fault-subparallel veins and patchy, burial-related calcite cement remain. Intense alteration is limited to major fault overlaps and does not permeate the fault zone along its entire length, nor does it extend outside the zone. This indicates that rising $CO_2$-laden fluids do not flow uniformly through the entire fault zone, but that vertical flow is channeled at fault intersections.

In thin section, porosity near the travertine has been extensively or completely occluded by calcite cement. Permeability in some conduit samples is less than 1 mD, three or four orders of magnitude lower than sandstone away from the travertine. In active $CO_2$ conduits, such reduction in porosity and permeability would occlude the preferred flow conduit and ultimately restrict upward flow of $CO_2$-charged water.

X-ray diffraction detects small amounts of goethite and hematite and a decrease in chlorite-smectite in altered conduit sandstones. Calcite is abundant, but many authigenic minerals predicted by geochemical models of $CO_2$ influx into sandstone reservoirs are not observed, including kaolinite, aragonite, dolomite, siderite, ankerite or dawsonite. This difference between observed and predicted mineral occurrence likely results from differences in mineral kinetics between natural and laboratory systems.

Prediction of leakage risk based on fault geometry improves the ability to assess the suitability of potential carbon sequestration reservoirs, many of which will be faulted. The point seep nature of leakage through a fault zone limits the amount of $CO_2$ that can escape over time and also enables targeted surface monitoring for $CO_2$ escape into the atmosphere—both critical for ensuring the effectiveness of injection projects and earning the trust necessary for carbon sequestration to gain public acceptance. The point seep nature of leakage also accelerates the rate at which conduits may seal through mineralization, since precipitation from a large volume of fluid is focused in a narrow conduit. The presence of multiple fossil and active seep locations along the Little Grand Wash fault, active at different times in the geologic past, indicates that cementation may be effective in sealing single conduits but that fault systems with complex geometry such as Little Grand Wash may continue to leak for a long period of time.

# Table of Contents

# List of Tables

## List of Figures

# 1. INTRODUCTION

## 1.1 Background

Carbon sequestration, also known as carbon capture and storage, is a promising technological approach to the challenge of reducing anthropogenic $CO_2$ emissions in order to mitigate climate change (Hepple and Benson, 2003, 2005). If successful and widely implemented, the process can help reduce the greenhouse gas effect by preventing a large amount of $CO_2$ from entering the atmosphere. Because it employs formation-scale storage reservoirs and targets stationary sources that produce 13–14 $GtCO_2$ per year (60% of annual worldwide $CO_2$ emissions) (IPCC, 2005), sequestration can potentially store vast volumes of $CO_2$. Identified possible $CO_2$ storage reservoirs include saline aquifers, coal seams and hydrocarbon reservoirs. These have an estimated capacity of roughly 1,150–3,650 $GtCO_2$ in North America (NETL, 2007) and 1,675–11,100 $GtCO_2$ globally (IPCC, 2005). In the United States, 95% of the 500 largest point source $CO_2$ producers are located within 50 miles of one of these potential injection reservoirs (Dooley et al., 2006).

For carbon storage to successfully mitigate climate change, injected $CO_2$ must remain sequestered for long periods of time. The tolerance for leakage is low: Storage reservoirs will need to be better than 99% efficient on an annual basis for up to 1,000 years (Hepple and Benson, 2003, 2005) or cumulative leakage will render storage ineffective. This standard permits a maximum leakage rate of 0.10–0.01% per year in order to stabilize atmospheric concentrations of $CO_2$ at 350–450 ppmv, assuming sequestration of 1–15 $GtCO_2$ per year for 300 years (Dooley and Wise, 2003a, 2003b; Hepple and Benson, 2003, 2005). In addition, the Environmental Protection Agency's permitting process for $CO_2$ injection requires applicants to show that injection will not have a major environmental impact or pollute underground sources of drinking water (Osborne, 2002; EPA, 2010). This means an injection reservoir must prevent $CO_2$-rich fluids from leaking into overlying aquifers, as such movement could contaminate drinking water supplies by introduction of saline brines, trace metals, carcinogens such as arsenic, and other dissolved solids (Gale, 2004; Siirila et al., 2010). Finally, because $CO_2$ gas is colorless, odorless and heavier than air, it can, under rare circumstances, collect undetected at the surface in potentially lethal pools (Gale and Davison, 2004; Gouveia et al., 2005; Bogen et al., 2006; Holloway et al., 2007). It is therefore critical, both for public safety and for the general acceptance of sequestration, that a reservoir does not leak substantial volumes of $CO_2$.

Mineral trapping—the sequestration of $CO_2$ via mineral precipitation in a reservoir—has been proposed as an effective long-term mode of storage (Gunter et al., 1993; Xu et al., 2005; Zerai et al., 2006), but some researchers have shown that this may be insufficient, sequestering only 1–24% of a $CO_2$ charge even over tens of millions of years (Johnson and Nitao, 2002; White et al., 2005; Wilkinson et al., 2009b; Lu et al., 2011). This means physical trapping of the remaining volume remains critical for effective storage. Many potential sequestration reservoirs will inevitably be faulted, and faults may act as concentrated paths for vertical fluid flow through a seal, into overlying permeable strata and aquifers, and even up to the surface (e.g., Forster and Smith, 1988; Knipe, 1993; Curewitz and Karson, 1997; Allis et al., 2001; Anderson and Fairley, 2008; Siirila et al., 2010). The low tolerance for leakage means that easy migration paths for escaping fluids could compromise the suitability of a prospective reservoir. Assessment of potential injection reservoirs, which is mandated by the Environmental Protection Agency (2010), will therefore require comprehensive characterization of the role faults might play in the distribution and migration of $CO_2$: Will they facilitate leakage to the surface or overlying aquifers? If so, will enough $CO_2$ escape to render the injection project ineffective or potentially dangerous? Even a proportionally insignificant trickle could present an unacceptable hazard if it were to pool at the surface. Alternately, the leakage paths could be sealed off by mineralization resulting from the presence of $CO_2$-rich fluids (Johnson and Nitao, 2002; Baines and Worden, 2004; Frima et al., 2005; Burnside et al., 2007). Self-sealing faults would make the reservoir more secure by using the injected fluids to find and close off possible escape paths, but some research indicates that such a process cannot necessarily be relied upon to contain a leaking system (Knipe, 1993; Yielding et al., 1997; Heath et al., 2009).

If faults have the potential to be sealed off, it is important to understand how and where they will seal and where they might leak, in order to facilitate leakage detection. Because $CO_2$ does not flow uniformly out of a fault zone, there is some concern about reliable long-term methods of leakage detection (Heath et al., 2003; Allis et al., 2005; Heath et al., 2009). Detection efforts must be intelligently designed with regard to the mode of escape. If gas escape occurs only at scattered points throughout a long and wide fault zone, uninformed placement of detection stations will be ineffective. Even detectors placed in a wide grid may fail to detect a leak, as $CO_2$ gas disperses quickly in the atmosphere with even a gentle breeze and may be undetectable as near as 100 m away (Gouveia et al., 2005; Gouveia and Friedmann, 2006). Additional understanding of how escape vectors intersect the surface could therefore be used to determine locations where a dense network of detectors is advisable as a means of targeted monitoring for leaking gas (Caine et al., 1996; Heath et al., 2009).

Modeling and experimental attempts to predict where faults will leak are limited by a lack of data and the slow reaction speed of realistic experiments, or, alternately, the accelerated time frames required to obtain results (Pearce et al., 1996; Baines and Worden, 2004; White et al., 2005; Kampman et al., 2009). Modelers face a tradeoff between including in their simulations the complexities of physical and chemical processes or greatly simplifying their models in order to approach large-scale long-term problems (Childs et al., 1996; Celia and Nordbotten, 2009; Dockrill and Shipton, 2010), and it has been shown that modeled chemical reactions do not always match actual reactions (Wilkinson et al., 2009b). Attempts to study flow dynamics and $CO_2$-related reservoir evolution in the subsurface are constrained by the limits of core sampling and seismic detection to identify flow-altering features such as fractures and grain dissolution (Rotevatn et al., 2007; Nightingale et al., 2009). A different and complementary approach to improving our ability to characterize potential injection reservoirs and making informed decisions about the placement of gas detection stations is to look at faulted, outcrop-exposed natural $CO_2$ systems as analogues for long-term reservoir behavior after $CO_2$ injection. Studying these systems will hone our understanding of how faults act as fluid escape paths, and how $CO_2$-rich water will in turn affect transmissibility through these paths.

The Little Grand Wash fault is a normal fault in eastern Utah (Figure 1) that is transmitting $CO_2$ from deep (2.6 km) Paleozoic strata to the surface (Wilkinson et al., 2009a), where up to 30 tons per day are expelled from springs within the fault zone (Baer and Rigby, 1978; Gouveia et al., 2005; Gouveia and Friedmann, 2006; Burton et al., 2008). Leakage does not occur uniformly throughout the fault zone, but rather at only a few points throughout the entire length and breadth of the fault (Figure 2). The natural presence, distribution and long history of these $CO_2$-charged springs makes Little Grand Wash an opportunity to study the controls, effects and implications of long-term $CO_2$-rich fluid flow through sandstones in a structurally complex fault zone.

Figure 1: The Little Grand Wash fault zone is located on the Colorado Plateau in eastern Utah, down dip from the San Rafael Swell.

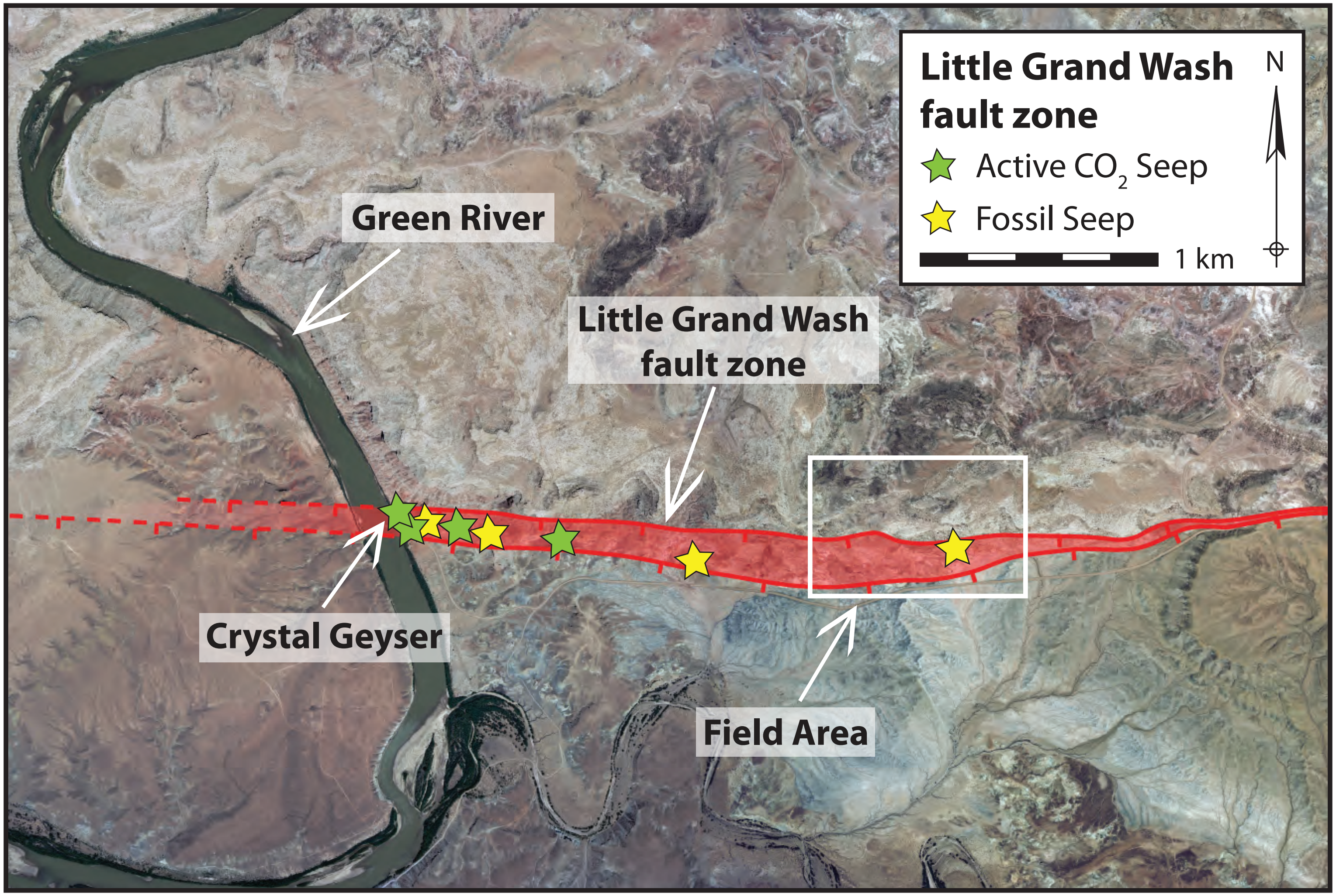

Figure 2: A segment of the Little Grand Wash fault; travertine deposits represent active and inactive $CO_2$-charged springs. The study area is at the widest point of the fault zone, with a fossil travertine deposit as its focal point.

## 1.2 Goals

There is a need for fault characterization in potential $CO_2$ injection reservoirs (Dockrill and Shipton, 2009). This study attempts to determine how structure causes leakage and where leakage will occur along faults such as Little Grand Wash, which do not leak uniformly. Are such leaks problematic for carbon sequestration? Do they present major and persistent escape paths for $CO_2$, or do they seal off sufficiently to make potential injection reservoirs viable for $CO_2$ storage? What is the nature of $CO_2$-related alteration within a fault zone, and what are the structural controls on that alteration? Fluids often migrate along faults, which may in part explain the presence of $CO_2$ seeps in the Little Grand Wash fault zone, but the distribution and size of these seeps indicate a more complex scenario than simple fault transport to the surface. The following complementary objectives build on each other in order to address these questions:

- Map at 1:700 scale the minor fault segments and internal structure of the Little Grand Wash fault zone;
- record the nature of alteration and map its distribution in the Little Grand Wash fault zone and surrounding area;
- make a petrographic comparison of altered and unaltered samples from inside and outside the fault zone and determine what is and what is not $CO_2$-related diagenesis (lithologic alteration such as mineral precipitation and dissolution) using an assortment of analytical techniques;
- look for a spatial relationship between the internal structure of the fault zone and $CO_2$-related diagenesis in the fault zone as an indication of a structural control on leakage;

- combine field observations and laboratory analyses, including porosity and permeability measurements of altered samples, to characterize the likely effects of $CO_2$-related alteration on fluid flow through a fault zone;
- use this characterization to draw implications for the advisability, consequences and practicalities of injecting $CO_2$ into faulted reservoirs.

## 1.3 Geologic Setting

### 1.3.1 LITTLE GRAND WASH FAULT

The Little Grand Wash fault is located on the Colorado Plateau in eastern Utah, approximately 6.5 km south of the town of Green River (Figure 1). It is an east-west-striking normal fault dipping to the south with a maximum throw of 260–290 m (McKnight, 1940; Dockrill and Shipton, 2010). The fault is roughly 61 km long and cuts a north-plunging open anticline (Campbell and Baer, 1978; Doelling, 2002). The broad area of interest for this study is only about 3 km long (Figure 2), and is located at roughly the hinge of the anticline. The fault zone is up to 200 m wide and contains a complex series of south-dipping subparallel fault segments. These segments vary in length from a couple meters to several hundred meters. Hecker (1993) mentioned that the collapse of deep salt-cored structures produced some Quaternary fault activity in this region, and Shipton et al. (2004) reported relationships between travertine and the Little Grand Wash fault consistent with recent fault activity. No evidence of recent movement was observed during field work for this project, however.

### 1.3.2 SPRINGS AND SOURCES

Eight to ten active and fossil $CO_2$ seeps are distributed along the Little Grand Wash fault (Figure 2). The $CO_2$ rises from depth both in aqueous solution and as a separate free phase (Heath, 2004; Allis et al., 2005; Kampman et al., 2009); as the water ascends to the surface, the aqueous solution degasses $CO_2$ due to the decrease in pressure and the comparatively low atmospheric $P_{CO2}$ (Pearson et al., 1978; Heath, 2004). The origin of the water and the $CO_2$ emitted from these springs is a matter of debate. Carbon dioxide can be produced by solution of subsurface carbonate rocks (Farmer, 1965) and by acidic ground water reacting with a clastic aquifer, but Campbell et al. (1978) noted that that abundance of

$CO_2$ in the Green River area is too great to result from these processes. The most comprehensive studies (Heath, 2004; Wilkinson et al., 2009a) used extensive isotopic and dissolved-solid analysis to postulate dual sources for both the water and $CO_2$. The water has low salinity and is predominantly (80–90%) of meteoric origin, rising from the Navajo aquifer, which is recharged at the nearby San Rafael Swell (Baer and Rigby, 1978; Campbell and Baer, 1978; Hood and Patterson, 1982; Heath et al., 2009; Wilkinson et al., 2009a); the remaining 10–20% of water is a brine ascending from the deeper, sub-Paradox Salt Paleozoic aquifer. Unlike many of the natural $CO_2$ reservoirs found in the Colorado Plateau, which are the result of mantle degassing (Pearce et al., 1996; Gilfillan et al., 2008), most (80–99%) of the $CO_2$ erupting in the Little Grand Wash fault is of crustal origin (Heath, 2004; Heath et al., 2009; Wilkinson et al., 2009a). It is inorganic and primarily a product of either thermal metamorphism of carbonates or clay-carbonate reactions (silicate hydrolysis and carbonate dissolution) that occurred in the Paleozoic aquifer during burial of the Colorado Plateau (Farmer, 1965; Mayo et al., 1991; Heath et al., 2002; Heath, 2004; Heath et al., 2009). The remaining portion (1–20%) of $CO_2$ is from mantle degassing. Though the Navajo aquifer supplies the majority of water, it is ruled out as a $CO_2$ contributor because the $CO_2$ is not of biological origin and the Navajo has no other processes that would form a significant volume of $CO_2$ gas.

In the Little Grand Wash fault, the most conspicuous $CO_2$ seep is Crystal Geyser, a cold-water geyser driven by rising free-phase $CO_2$ and $CO_2$ degassing from aqueous solution (Figure 3) (Waltham, 2001; Heath et al., 2009). The geyser erupts once or twice a day at predictable intervals and emits 150–360 $kgCO_2$ per minute during those eruptions (Baer and Rigby, 1978; Gouveia et al., 2005; Gouveia and Friedmann, 2006). The geyser was created in 1935 when the Glen Ruby #1-X State well was spudded into an old travertine deposit on the east bank of Green River (McKnight, 1940; Powell, 1961; Baer and Rigby, 1978). At present

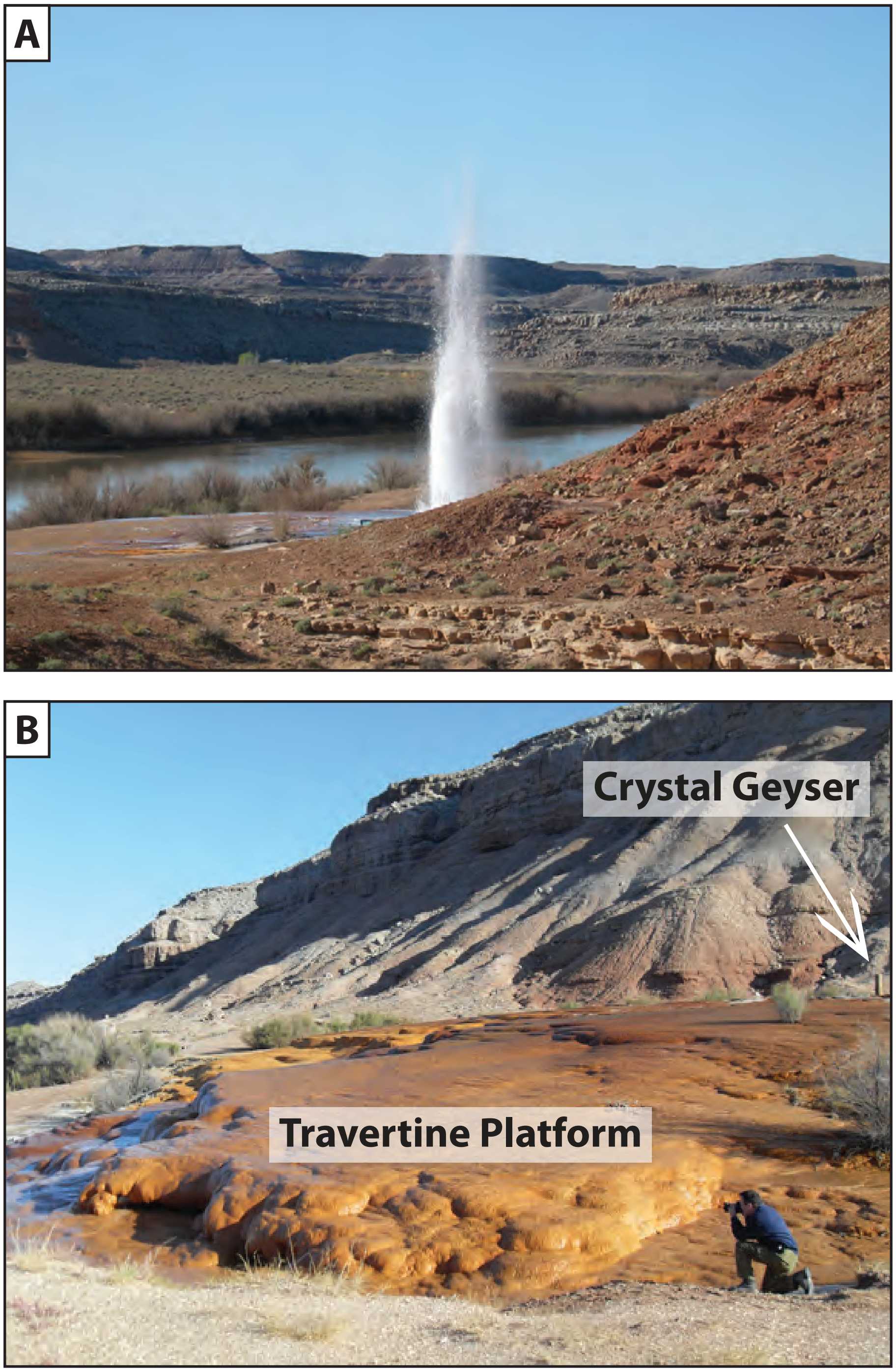

Figure 3: **A:** Crystal Geyser is a cold-water geyser driven by $CO_2$ rising through the Little Grand Wash fault zone. **B:** The geyser discharges $CO_2$-rich water, which deposits fresh travertine as it flows into Green River (out of view to the left); photograph taken facing north.

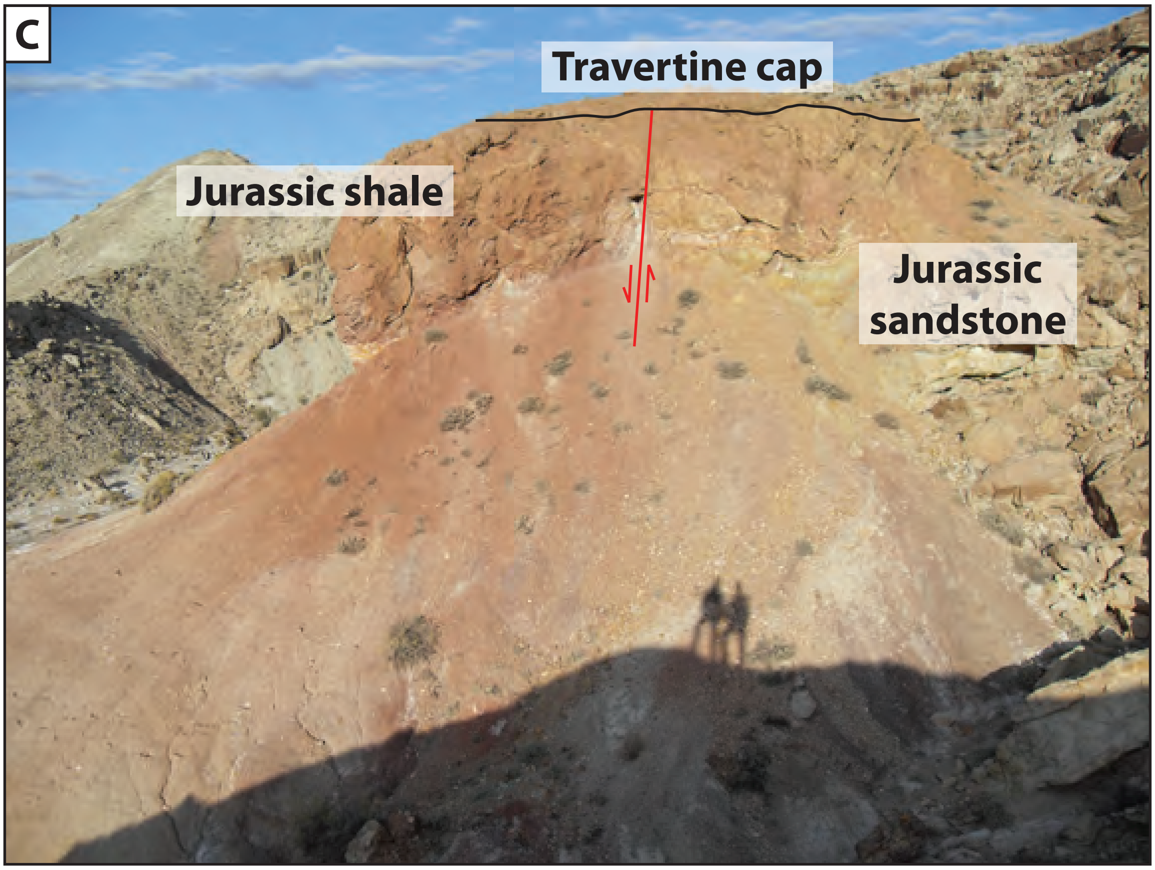

Figure 3: **C:** The travertine deposit in the map area lies on a juxtaposition of Jurassic Salt Wash sandstone with Jurassic Brushy Basin shale.

a new 50–60-m travertine platform is forming underneath Crystal Geyser (Figure 3). The travertine precipitates as $CO_2$ degasses from the discharging spring water (see Appendix A for an explanation of this process). Little Grand Wash fault has 8–10 of these travertine deposits distributed along strike (Figure 2). All of them are located within the fault zone, indicating that the water and gas discharging from these springs are using the fault as a migration path to the surface. Some springs, such as Crystal Geyser, are actively precipitating travertine; other inactive $CO_2$ seeps are marked by "fossil" travertine deposits but are no longer transmitting water (Doelling, 1994). Uranium-series dating on the travertines shows that this $CO_2$-laden water has been leaking from various springs throughout the fault for as much as 113 ka (Burnside et al., 2009; Burnside, 2010). The process appears to have proceeded discontinuously throughout the entire period, as scattered springs were formed and flowed for up to 10 ka before shutting down.

The focus area for this study is a section of the fault zone 2 km east of Crystal Geyser (Figure 2). The map area is about 990 m east-to-west and 690 m north-to-south. The focal point of the map area is a fossil travertine platform deposited on top of Jurassic shale and sandstone (Figure 3). The area surrounding the platform is considerably incised, indicating that the travertine forms an erosion-resistant cap. The deposit is in a topographically low area (Figure 4), flanked by a 35-meter-tall steep ledgy slope (part of the 40-m fault scarp) and about 100 m below the highest point in the map area.

### 1.3.3 STRATIGRAPHY AND DEPOSITIONAL SETTING

The area and topography around Green River and Little Grand Wash fault are dominated by thick shale formations. In the map area, the fault itself stands out in relief in large part because it juxtaposes resistant ledge-forming sandstones against soft shales. The

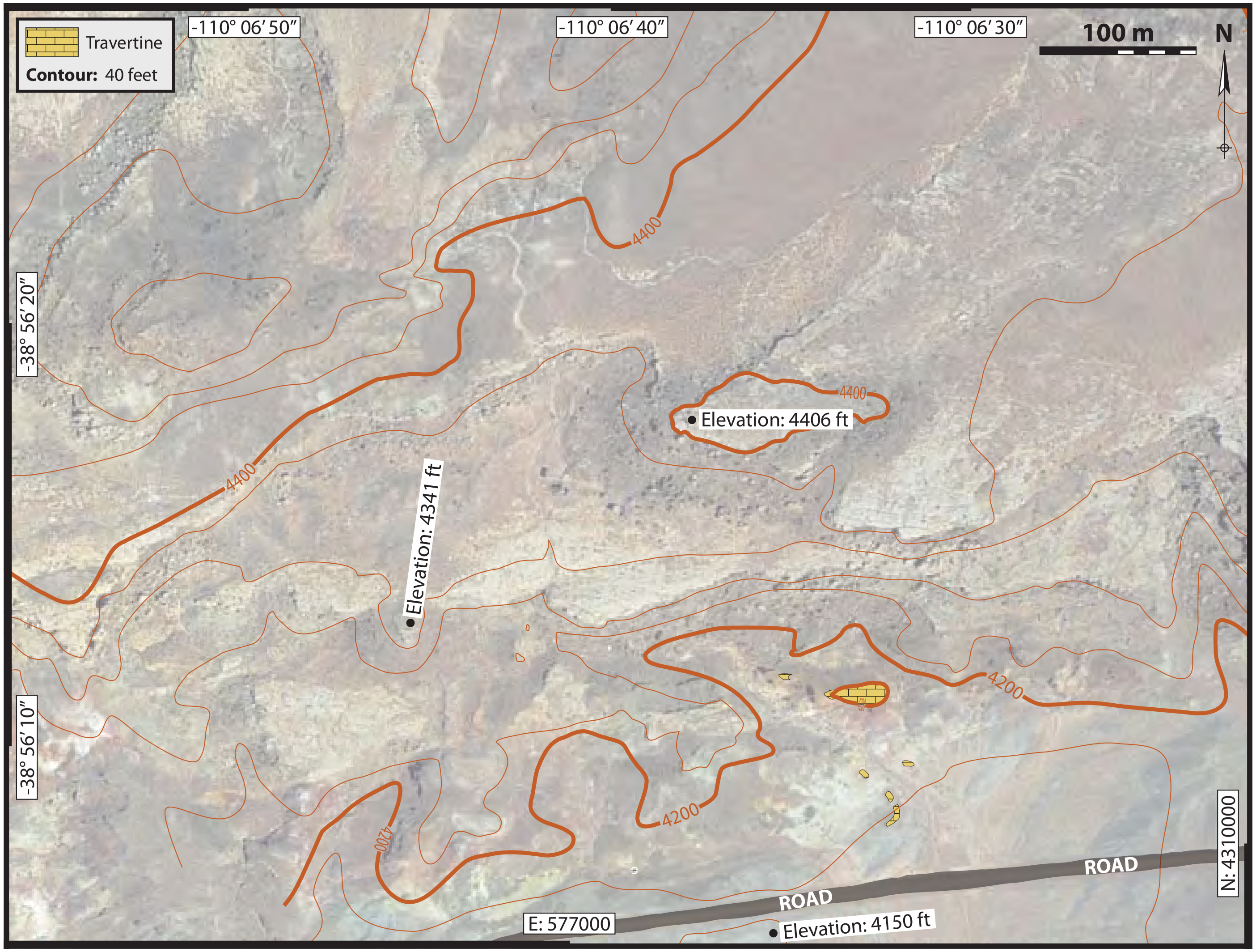

Figure 4: Topographic map of the field area. Little Grand Wash fault creates a roughly east-west-striking scarp. Note the travertine deposit located at the base of a long ravine.

formations that outcrop in and around the map area are Jurassic and Cretaceous in age (Figure 5): the Jurassic Summerville Formation ($J_{s}$); the Jurassic Morrison Formation, which is divided into three members—the Tidwell Member ($J_{mt}$), the Salt Wash Member ($J_{ms}$) and the Brushy Basin Member ($J_{mb}$); the Cretaceous Cedar Mountain Formation ($K_{cm}$); the Cretaceous Dakota Sandstone ($K_{d}$); and the Cretaceous Mancos Shale, which is divided into three members—the Tununk Shale ($K_{mt}$); the Ferron Sandstone ($K_{mf}$); and the Blue Gate Shale ($K_{mb}$). Unconsolidated Quaternary wind, stream and wash alluvium can also be found, in addition to travertine deposits.

Doelling (2002) recorded a regional description of these formations in the San Rafael Desert. Because the sandstones in these units are mostly discontinuous fluvial deposits, however, there is significant spatial heterogeneity in thickness, grain size and lithology. A local, near-fault description is therefore necessary for mapping and cross sections. The following is a site-specific adaptation of Doelling's stratigraphic descriptions, based on field observations of outcrops in and around the map area and beginning with the youngest units:

**Cretaceous Mancos Shale – Blue Gate Shale Member ($K_{mb}$):** The Blue Gate Shale member of the Mancos Shale does not outcrop in the map area. It is a massively thick (800–1,000-m) shallow marine shale (Doelling, 2002), the lower portion of which forms a series of low rounded hills several kilometers north of the map area.

**Cretaceous Mancos Shale – Ferron Sandstone Member ($K_{mf}$):** The Ferron Sandstone member of the Mancos Shale does not outcrop in the map area. It is a relatively thin (6–50-m) mixture of shallow marine sandstone and shale (Cotter, 1975; Doelling, 2002) that forms a flat-topped table directly east of the map area and outcrops in the

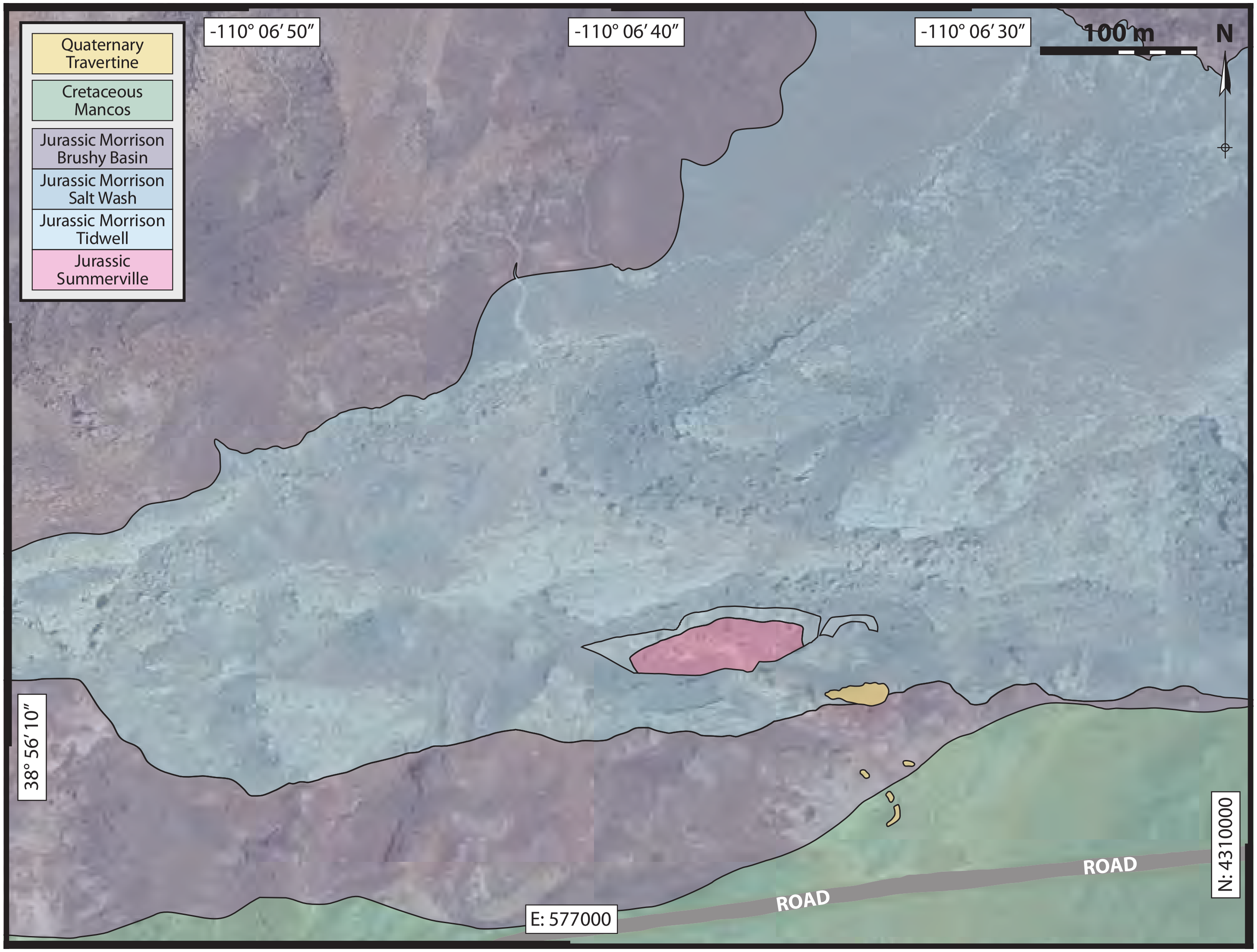

Figure 5: Geologic map of the field area.

shale hills north of the map area. This horizon of sandstone in the thick Mancos Shale shales is a helpful marker for estimating total throw on the fault.

**Cretaceous Mancos Shale – Tununk Shale Member ($K_{mt}$):** The Tununk Shale member of the Mancos Shale outcrops in the southernmost portion of the map area, as the overall Little Grand Wash hanging wall. It is a massive gray marine shale unit that forms a plain of low, rounded, wash-cut hillocks usually devoid of vegetation.

**Cretaceous Dakota Sandstone ($K_d$):** The Dakota Sandstone does not outcrop in the map area, but the access road cuts through outcrops about 1.75 km to the northeast. The outcrops are about 5 m thick, massive and tan-yellow in color. They are composed of cross-bedded coarse sandstone interbedded with conglomerate in a roughly 3:1 ratio. The rock is friable with platy weathering. Chert pebbles are abundant and yellow oxidation stains are also present. Other outcrops farther west include silicified wood in conglomerate beds. This outcrop is not continuous and, when traced to the west, pinches out entirely in some spots.

**Cretaceous Cedar Mountain Formation ($K_{cm}$):** The Cedar Mountain Formation does not outcrop in the map area, but can be found roughly 1 km to the north. It is composed mostly of thin siltstone beds and thick, slope-forming red, lavender and pale green shales (Doelling, 2002). The base of the Cedar Mountain Formation is the ledge-forming Buckhorn Conglomerate, a thick, dark, massively bedded chert-pebble conglomerate. The lower contact is defined as the bottom of this ledge.

**Jurassic Morrison Formation – Brushy Basin Member ($J_{mb}$):** The Brushy Basin Member of the Morrison Formation is prominent both in the fault zone and in the northern part of the map area. It is composed of thick lavender and maroon shale units interfingered with relatively thin silt and sandstone lenses. It represents a mixed fluvial and lacustrine depositional system (Mullens and Freeman, 1957; Peterson, 1980; Robinson and McCabe, 1997), with sandstones forming the lenticular, laterally discontinuous beds typical of channel deposits. Unlike shales in the Mancos Shale, shales in the Brushy Basin Member are non-marine, the earlier Morrison Formation having already flooded the Late Jurassic western interior seaway with terrestrial sediments (Brenner, 1983). In the map area, sandstones are thicker and more common towards the base; upsection, where shale sequences dominate, sandstone lenses become increasingly infrequent, thinner-bedded and more laterally discontinuous. The shale-rich upper portions are interspersed with small siltstone lenses (compared to the larger, stratigraphically lower sandstone deposits). Brushy Basin Member sandstones are commonly quartz-cemented and hard (Figure 6), ringing loudly when struck with a hammer. The hardness of the quartz-cemented sandstones causes them to weather with a dark varnish over the surface, unlike softer sandstones in the Salt Wash Member (described below).

Doelling (2002) notes several distinctive white bentonite deposits in the Brushy Basin Member. Although these are not present in the map area, they outcrop to the east (Appendix B: Figure B1) and can be used to confirm the identification of the Brushy Basin Member by lateral correlation. Large (8–10-cm) reddish fossil bone fragments are present in the lower, sandier portion of the Brushy Basin Member. Due to their size, these are likely dinosaur bones, which are abundant in the

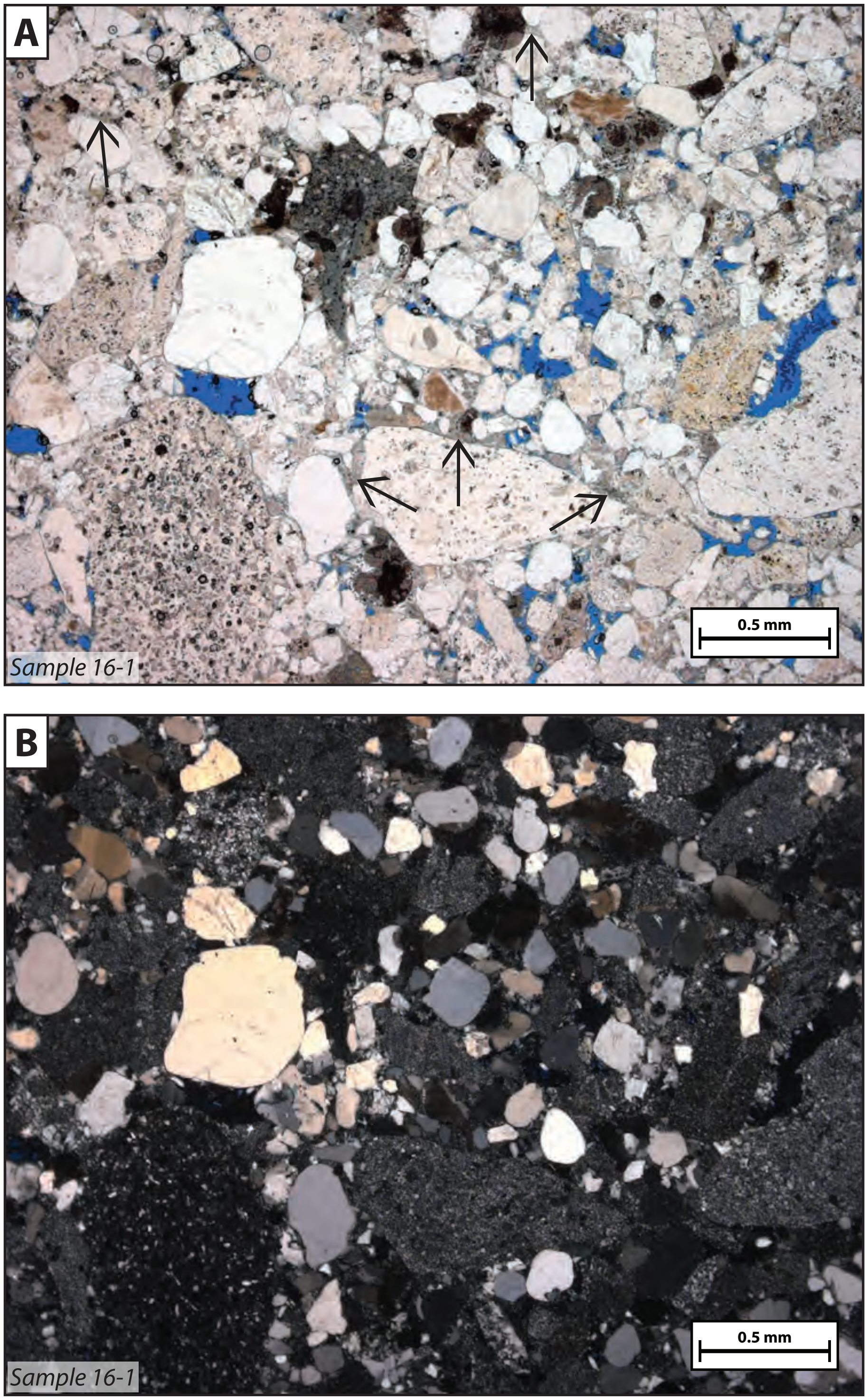

Figure 6: **A:** Quartz-cemented Brushy Basin Member sandstone (plane-polarized light); arrows indicate quartz cement. **B:** Same sample (cross-polarized light). Blue is porosity in all photomicrographs, unless otherwise noted.

Morrison Formation (Riggs and Farrington, 1901; Gillette, 1999). They are too fragmented to make a definite species identification, but are likely Sauropoda, which is a common large vertebrate in the upper Morrison Formation (Mook, 1916; Stokes, 1944; personal communication: Boyd, 2011; personal communication: Stocker, 2011). Volcanically altered thin mudstone beds cut by bright red septarian veins outcrop at a stratigraphically higher point in the Brushy Basin Member slightly north of the map area (Appendix B: Figure B2). The mudstone is in some places altered to chert-like hardness and has conchoidal fractures. Volcanic rock fragments with star-shaped quartz lathes are also present, possibly forming from devitrification of a red glassy matrix (Appendix C: Sample 100).

The shale-rich middle and upper sections of the Brushy Basin Member outcrop towards the southern end of the map area, in several down-dropped blocks within the fault zone. The base of the Brushy Basin Member outcrops extensively at the northern end of the map area, where it conformably contacts the underlying Salt Wash Member. The basal unit of the Brushy Basin Member is defined in the map area as the first shale sequence directly overlying the uppermost of the six correlatable Salt Wash Member sand units (described below).

**Jurassic Morrison Formation – Salt Wash Member ($J_{ms}$):** The Salt Wash Member of the Morrison Formation is the most conspicuous outcropping unit in the fault zone and, with the Brushy Basin Member, covers most of the map area. It is composed of thin to massive lenticular cross-bedded sandstones, mostly light-colored, and interbedded with bright red and pale green shales. Grain size in the sandstones varies from fine sand to a coarse chert-pebble conglomerate. The Salt Wash Member represents an alluvial plain depositional system eroding off the ancestral (Middle to Late Jurassic) Elko highlands in western Utah, intermediate between braided stream conglomerates farther west and distal floodplain claystones farther east (Mullens and Freeman, 1957; Peterson, 1980, as cited in Robinson et al., 1997; Peterson, 1987, 1994; Robinson and McCabe, 1997). The sand lenses are laterally discontinuous fluvial (channel fill) deposits with highly variable thickness; the red and green shales are abandoned channel fill and overbank deposits, more homogeneous and laterally continuous than the sandstones (Mook, 1916; Stokes, 1944; Craig et al., 1955; Peterson, 1980; Robinson and McCabe, 1997).

In the map area, the Brushy Basin Member and Salt Wash Member are distinguished from each other by the greater thickness and the color of Brushy Basin Member shale intervals, which tend to be in the darker purple range than the pale green and bright red Salt Wash Member shales; and by the sandstones, which tend to be thicker and more laterally extensive in the Salt Wash Member. Sandstones in the Salt Wash Member are rarely quartz-cemented and are therefore relatively soft compared to those in the Brushy Basin Member. They tend to be more friable and do not develop the dark varnish seen in Brushy Basin Member sandstones.

Because distinct shale beds cannot be discerned in the field, stratigraphic correlation across fault segments relies on recognizable sand beds to determine stratigraphic position. Although no beds are continuous throughout the entire map area, six lenses are sufficiently thick and continuous to use for correlation. These beds are critical markers for building an accurate map and cross sections. They are numbered $J_{ms}1$–$J_{ms}6$, where $J_{ms}1$ is the oldest correlatable bed and $J_{ms}6$ is the youngest correlatable bed. Each bed is predominantly sandstone, except for $J_{ms}6$, which is mostly a dark chert-pebble conglomerate cross-bedded with coarse-grained sandstone; chert pebbles range in size from 0.5–3.0 cm.

The Salt Wash Member and Brushy Basin Member have variable thicknesses. Because the Salt Wash Member–Brushy Basin Member contact is defined at the top of the last major Salt Wash Member channel sand, and channel deposits are by nature not uniformly distributed, the contact occurs at different stratigraphic heights between $J_{ms}4$ and $J_{ms}6$. This uneven contact creates a disparity of up to 20 m in the two members' thicknesses, where a thinner Salt Wash Member corresponds to a thicker Brushy Basin Member.

The base of the Salt Wash Member is defined at the base of the bottommost massive sandstone unit, where one exists; elsewhere it is defined at the contact between soft red Salt Wash Member shale and the thin-bedded, more brittlely weathered Tidwell Member siltstone. A red shale–red siltstone contact is sometimes difficult to pinpoint, especially in a slope with heavy boulder cover, so the exact contact is inferred where necessary.

**Jurassic Morrison Formation – Tidwell Member ($J_{mt}$):** The Tidwell Member of the Morrison Formation outcrops in only a small portion of the map area, in the ravine slope northwest of the travertine platform. It is composed of reddish finely bedded siltstone and forms a thin band in the slope rising above the ravine bed. The thick basal gypsum deposit mentioned in Doelling (2002) is not present in the map area, although it is seen in outcrops farther west, near the river (Appendix B: Figure B3).

The Tidwell Member is often obscured by cover eroding from the massive Salt Wash Member sandstones in the slope above it, but the base is identified where possible as the first semi-brittle siltstone overlying the softer shales of the Summerville Formation.

**Jurassic Summerville Formation ($J_s$):** The Summerville Formation similarly outcrops in only a small portion of the map area, where the ravine cuts shallowly into it immediately northwest of the travertine deposit. Its soft red shales form the base of the ravine slope and contact the Tidwell Member. Below these shales, harder platy red siltstone and very fine-grained sandstone form the ravine bed and are very well exposed.

Stratigraphy and thicknesses for all units in the region are shown in Table 1, down to the basement rock. Thicknesses are taken from field observations where possible and other sources where necessary. A site-specific stratigraphic column of map area outcrops is presented in the *Results* section (Figure 25).

| **Formation** | **Member** | **Lithology** | **Thickness** | **Source** | **Perm.** |
|---|---|---|---|---|---|
| Mancos | Blue Gate | shale | 900 m | Doelling 2002 | |
| | Ferron | sand | 30 m | Doelling 2002 | |
| | Tununk | shale | 91 m | Field Mapping | |
| Dakota | | sand | 3 m | Field Mapping | |
| Cedar Mountain | | shale | 27 m | Field Mapping | |
| | Buckhorn | conglom | 5 m | Doelling 2002 | |
| Morrison | Brushy Basin | conglom-sand-shale | 74 m | Field Mapping<br>Field Mapping | |
| | Salt Wash | sand 5 | 5 m | Field Mapping | 100 mD |
| | | shale | 5 m | Field Mapping | |
| | | sand 4 | 5 m | Field Mapping | 375 mD |
| | | shale | 5 m | Field Mapping | |
| | | sand 3 | 5 m | Field Mapping | 215 mD |
| | | shale | 15 m | Field Mapping | |
| | | sand 2 | 11 m | Field Mapping | 37 mD |
| | | shale | 10 m | Field Mapping | |
| | | sand 1 | 5 m | Field Mapping | 100 mD |
| | Tidwell | sand-silt | 6 m | Field Mapping | |
| Summerville | | silt | 30 m | Field Mapping | |
| Curtis | | sand-shale | 37 m | Field Mapping | |
| Entrada | | sand | 174 m | Greentown State 36-24H | 500 mD |
| Carmel | | silt | 45 m | Greentown State 36-24H | |
| Navajo | | sand | 140 m | Greentown State 36-24H | |
| Kayenta | | sand | 23 m | Greentown State 36-24H | |
| Wingate | | sand | 136 m | Greentown State 36-24H | |
| Chinle | | fine sand | 101 m | Greentown State 36-24H | |
| Shinarump | | no data | 7 m | Greentown State 36-24H | |
| Moenkopi | | silt | 136 m | Greentown State 36-24H | |
| Sinbad | | limestone | 64 m | Greentown State 36-24H | |
| White Rim | | sand | 112 m | Greentown State 36-24H | |
| Cutler | | sand | 66 m | Greentown State 36-24H | |
| Elephant Canyon | | limestone | 263 m | Greentown State 36-24H | |
| Honaker Trail | | sand-shale-lime | 373 m | Greentown State 36-24H | |
| Paradox Salt | | salt | 1000 m | Hintze 1982 | |
| Redwall | | limestone | 200 m | Hintze 1982 | |
| Devonian | | limestone | 100 m | Hintze 1982 | |
| Cambrian | | limestone | 300 m | Hintze 1982 | |
| Ophir | | shale | 60 m | Hintze 1982 | |
| Tintic | | quartzite | 60 m | Hintze 1982 | |
| Basement | | granite | | Hintze 1982 | |

Table 1: Local stratigraphy. Entrada permeability data are from Eichhubl et al. (2009).

# 2. METHODS AND RESULTS

## 2.1 Field Work

### 2.1.1 FIELD MAPPING

#### 2.1.1.1 Methods

The primary goal in mapping the fault zone is to produce a more detailed structural and stratigraphic map than those currently available. This is necessary to better analyze and understand the structural controls on leakage and diagenesis. Several good maps have previously been made of the fault zone (Doelling, 2002; Shipton et al., 2004; Vrolijk et al., 2005; Dockrill and Shipton, 2010), but none are sufficiently detailed or on a scale large enough to be used for this type of structural examination.

Field mapping was done over the course of three field trips to Little Grand Wash, for a total of 33 days of field work. To make a map of the fault zone and area surrounding the travertine, emphasis in the field was divided three ways: mapping lithology and stratigraphy; mapping fault segments and the internal structure of the fault zone; and mapping the distribution of diagenesis. These elements were mapped at a 1:700 scale, which enables representation of features as small as about one meter.

The mapped area at its widest is 990 m east-to-west and 690 m north-to-south. The fault zone is up to 200 m wide and extends across the map area. The final map includes: stratigraphy; outcrop lithology; fault segments and estimations of changing throw along each segment; topographic contours; sampling stations; field measurements such as fault attitudes and strike and dip; and rock alteration, including yellow coloration, dense veining, salt staining, and joints and deformation bands where their presence is conspicuous.

### 2.1.1.2 Field mapping results: Lithology, stratigraphy and structure

The Salt Wash Member and Brushy Basin Member are the major outcropping units within the fault zone; the Summerville Formation and Tidwell Member outcrop in the ravine west of the travertine, and the Mancos Shale outcrops in the southernmost downdropped block (Figure 7). Salt Wash Member channel fill deposits create a high sandstone-to-shale ratio relative to the nearby Brushy Basin Member and Mancos Shale (Figure 8). The mechanics of brittle siltstone, sandstone and conglomerate interbedded with relatively ductile shale result in a wide and complex fault zone where it intersects the Salt Wash Member and a substantially less complex fault in the shale-dominated Mancos Shale and Brushy Basin Member (Vrolijk et al., 2005). Brushy Basin Member outcrops in the southern portion of the fault zone are dominated by thick shales with scattered thin, quartz-cemented sandstone lenses and patches of siltstone. The uninterrupted, gray Mancos Shale forms the ultimate hanging wall and abuts the Brushy Basin Member shales in the southernmost part of the map area.

The greatest throw on the Little Grand Wash fault system has been estimated at 195–290 m, near the river, from which point it decreases towards the map area (McKnight, 1940; Vrolijk et al., 2005; Dockrill and Shipton, 2010). By the river the throw is divided between two major fault segments. In the map area, the fault system is composed of many subparallel fault segments. Some segments strike for hundreds of meters and account for offset of over 100 m; others are only a few meters long with less than 1 m of offset. Figure 9 shows the field area fault map and includes a simplified version in which the latter minor segments are omitted or extended where they can reasonably be interpreted. Incipient fault segments bound the fault zone to the north, where they fracture and barely offset $J_{ms}2$ pavement sandstones. The system as a whole is a south-dipping normal fault, though some

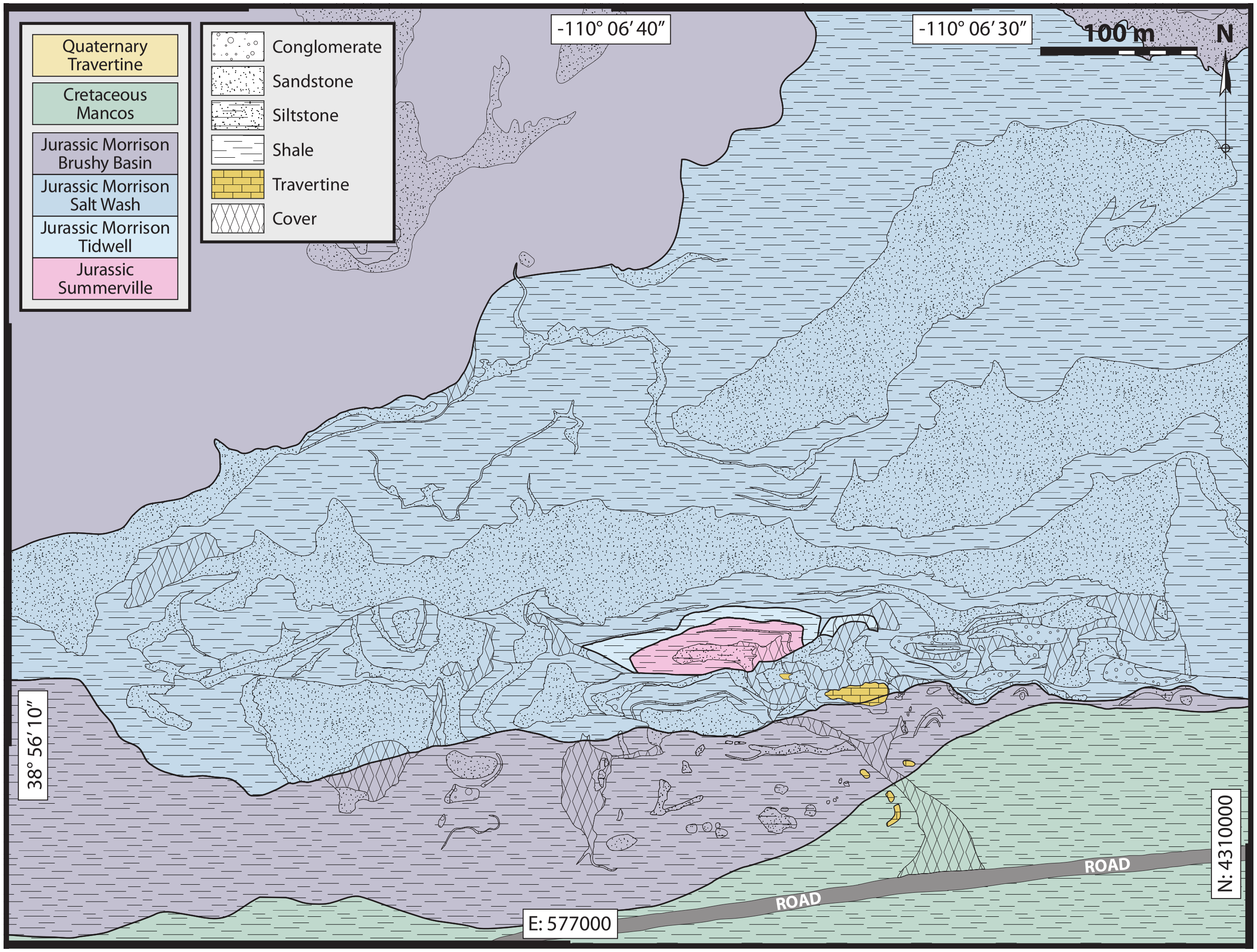

Figure 7: Field map showing stratigraphy and lithology.

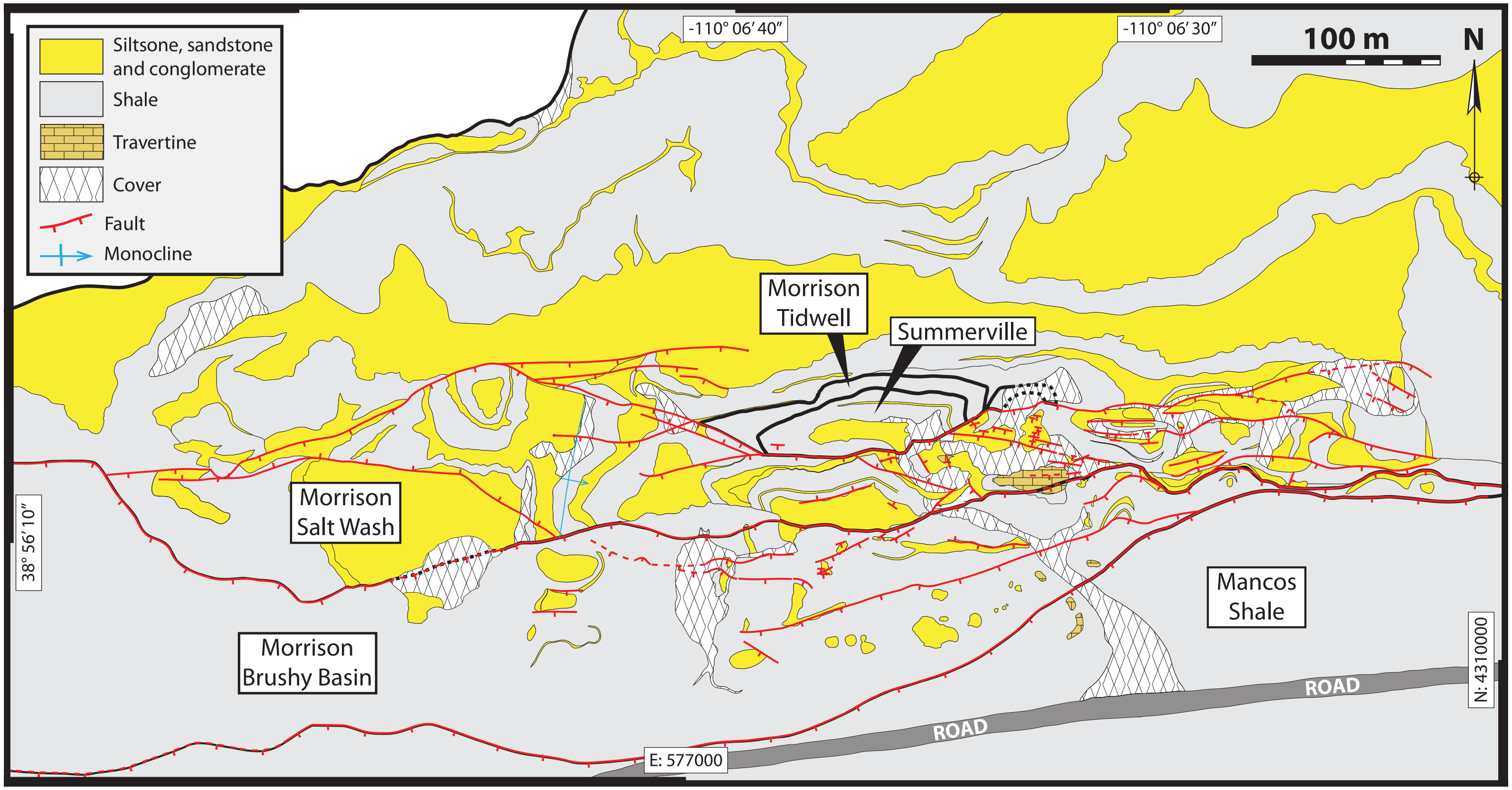

Figure 8: Comparison of map area shale (gray) with map area siltstone, sandstone and conglomerate (yellow). Note the greater fault complexity where brittle lithologies are more abundantly interbedded with shale and the simpler structure where shale predominates.

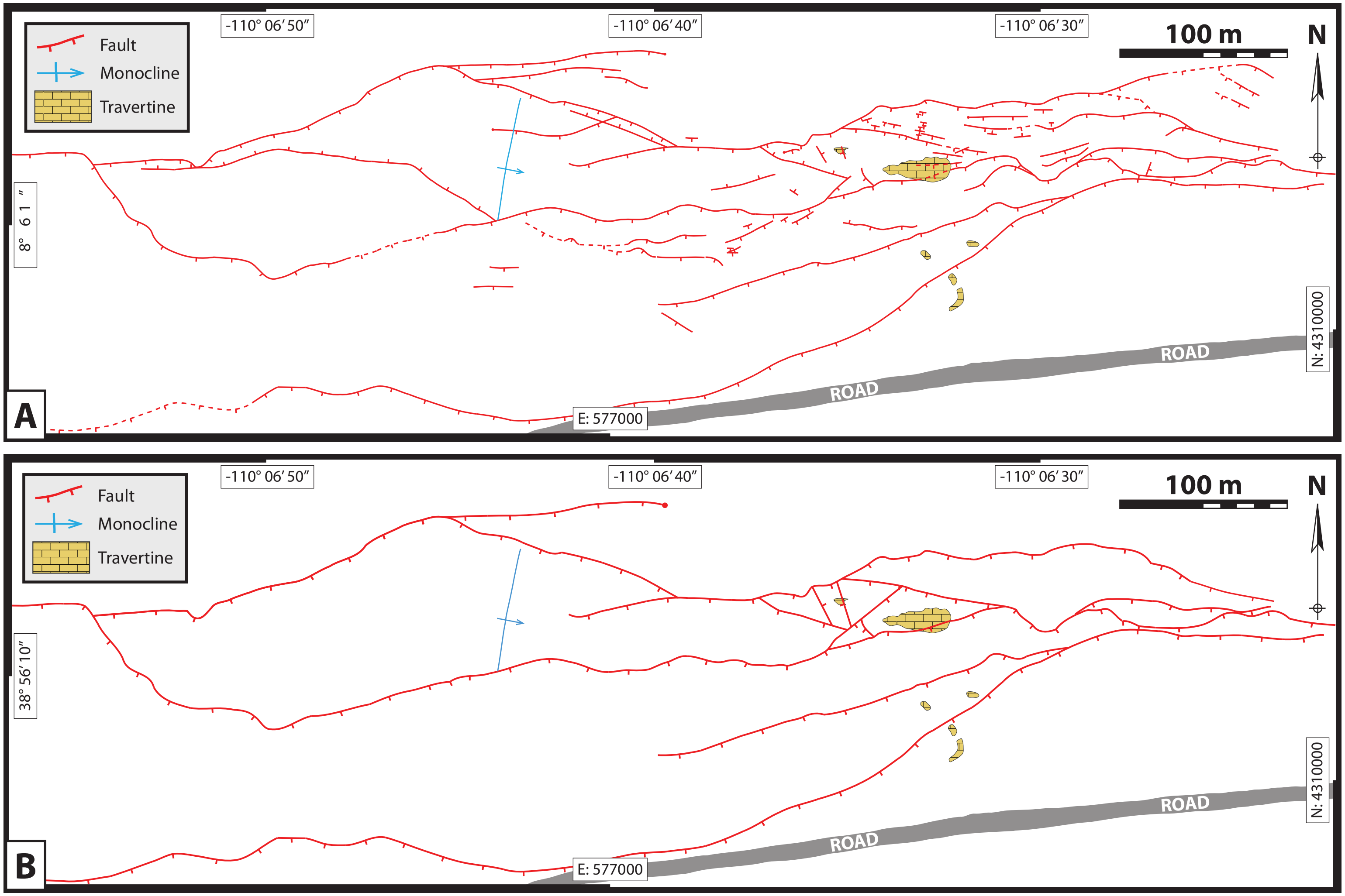

Figure 9: **A:** Field area fault map. The overall system is dropping down to the south. **B:** Simplified fault map emphasizing long faults and those with major offset, and projecting faults where they may reasonably be interpreted.

smaller faults dip to the north, indicating down-drop in the reverse direction. These are likely conjugate faults and are not associated with significant offset.

Bedding in the footwall is essentially flat-lying. In the sandy portion of the fault zone west of the travertine, bedding dips about 20° to the east, forming a monocline. At the base of the travertine bedding is mostly flat-lying, although along faults it dips to the south. The southern edge of this monocline abuts a shale-dominated fault block that dips 33° to the east. Throw along the northernmost fault (Fault 1) tapers from 72 m in the east to 13 m in the west, where it is truncated by the fault that separates the monocline from the shale block (Fault 2). Because the shale block dips east more steeply than the monocline, Fault 2 at first gains throw as it strikes east before losing it again around the travertine, where some offset is transferred onto other fault segments. The southernmost Little Grand Wash fault segment (Fault 3) loses throw to the east, from 180 m to about 100 m of offset across the map area.

Faults 1–3 are overlapping segments with tapering throw and associated inclined bedding. They appear to outline a pair of nested fault ramps—a sandstone-dominated 450-meter-long ramp "piggybacking" on a shale-dominated ramp that extends beyond the map area to the west (Figure 10). These structures transfer strain between discontinuous overlapping fault segments to accommodate throw across the entire fault zone (Peacock and Sanderson, 1991; Trudgill and Cartwright, 1994; Childs et al., 1995; Cartwright et al., 1996; Hus et al., 2005). The bounding faults of the sandstone-dominated ramp propagate into each other: At the west end of the ramp this occurs as a simple fault intersection; at the east end of the ramp it is accomplished by a more complex swarm of roughly north-south-striking fault segments. Breaching the continuous plane from footwall to hanging wall makes this a "hard-linked" ramp (Peacock and Sanderson, 1991, 1994; Walsh and Watterson, 1991; Childs et al., 1995; Crider and Peacock, 2004). The longer shale-rich ramp extends outside of the map area, but no breach is evident at its lower end, where throw on the southernmost

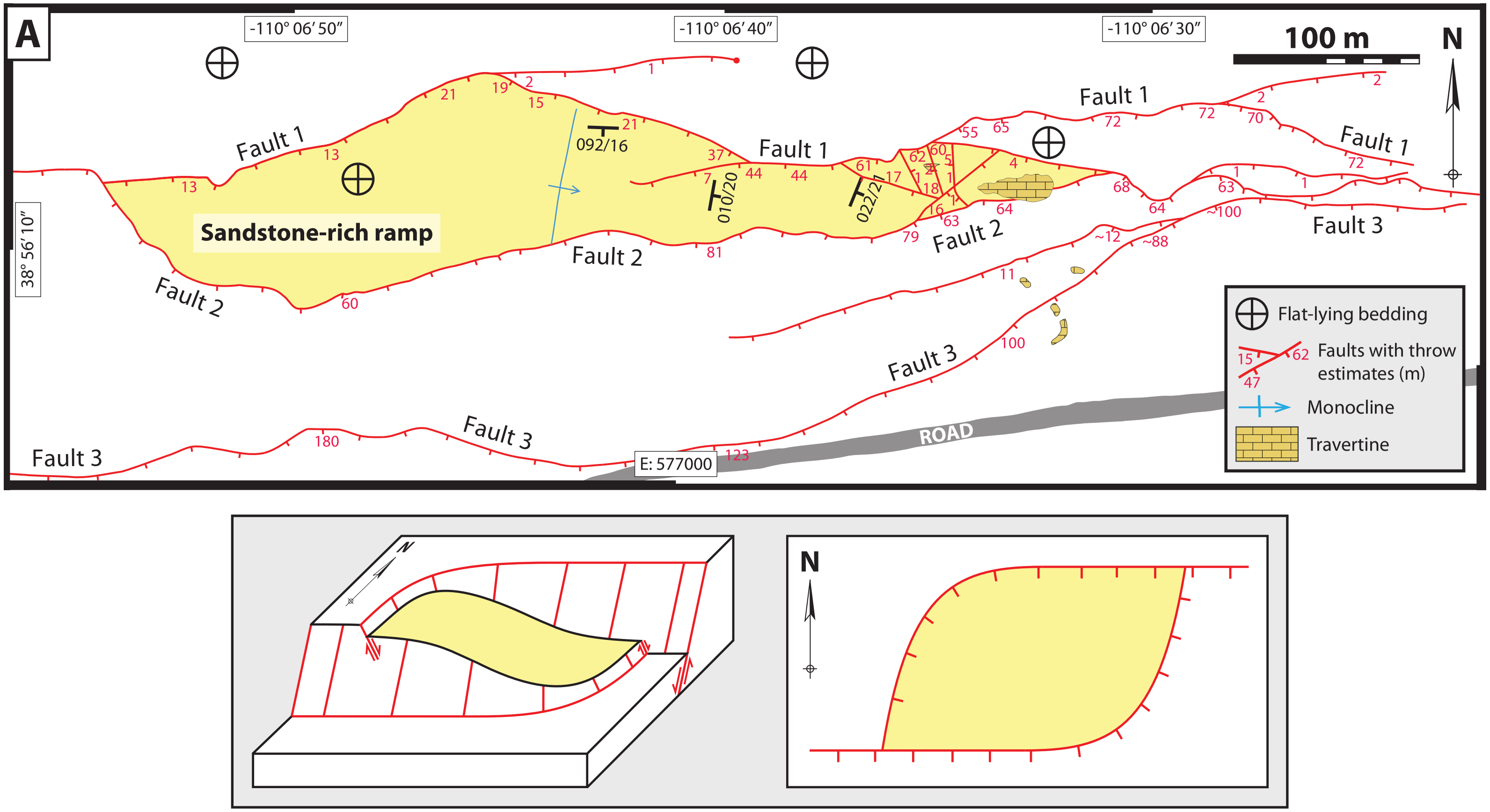

Figure 10: **A:** Overlapping fault segments form a large hard-linked fault ramp running down the center of the fault zone; the travertine was deposited where the overlapping faults are linked.

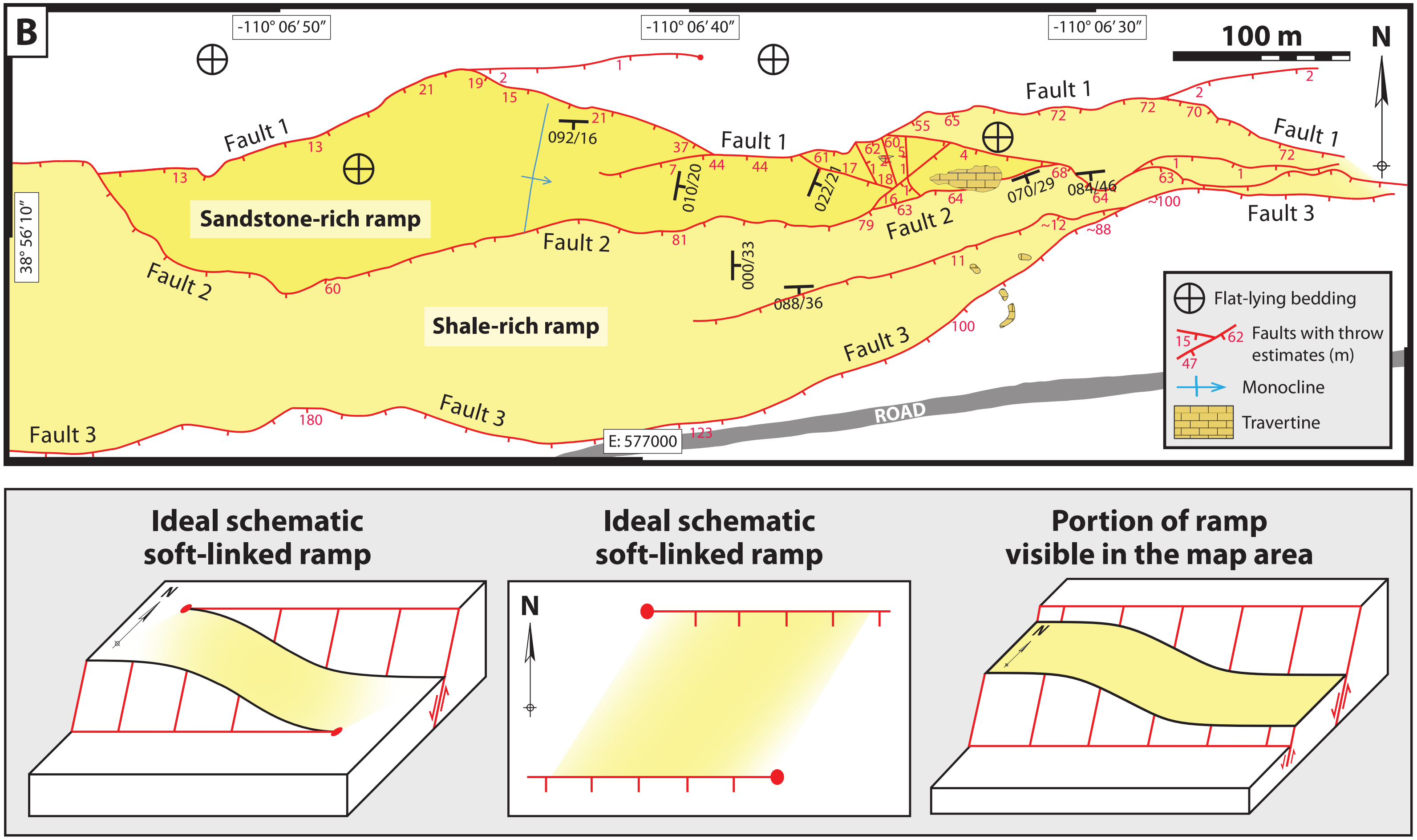

Figure 10: **B:** The hard-linked ramp is part of a longer, apparently soft-linked ramp that extends beyond the bounds of the map area. Although the fault tips are not seen in the map area, throw on the southernmost fault stops decreasing in the eastern region of the map area.

fault appears to stop decreasing (i.e., where the ramp stops dipping east and flattens out). This would make it a "soft-linked" ramp (Larsen, 1988), albeit one in which the ends have not been clearly identified.

#### *2.1.1.2.1 Travertine platform*

The travertine is located in a topographically low area, at the base of the fault scarp; at higher elevations travertine is absent. It was deposited on the $J_{ms}5$ sandstone and appears to form an erosion-resistant cap, as it now rises 5–10 m above its surroundings. Four additional small travertine deposits are located south of the main travertine platform, 9 m below it. Several of these are arranged in a linear, slightly arcuate shape that projects into the main travertine mound. These do not appear to represent unique leakage sights. There is no evidence to indicate that faults extend beneath them, and their linear orientation is in fact nearly perpendicular to the trends of nearby fault segments. Their orientation and shape is more consistent with runoff from the main travertine platform—a small distributary-like stream redepositing travertine material a few tens of meters downhill.

The travertine platform is 2.5 m thick and 635 $m^2$ in area (Dockrill, 2006, as cited in Burnside et al., 2009). This is considerably thinner than the 4.5–7.5 m thicknesses for deposits closer to the river reported by Doelling (1994), or 21.5 m of travertine reported by McKnight (1940) and Baer et al. (1978) (though Baer et al. noted that this estimate of travertine thickness is based on "driller's records which leave considerable information wanting").

### 2.1.1.3 Field mapping results: Nature of fault zone alteration

Five principal types of alteration are present in the fault zone: calcite cementation, yellow outcrop staining, salt staining, fracturing and deformation bands.

#### *2.1.1.3.1 Calcite cement and veins*

The most common type of alteration is calcite cement, which manifests as intergranular, pore-filling cement, pore-filling and matrix-related micrite, and occasionally massive sparry veins (Figure 11). Although they are closely related, a distinction is made between such carbonate alteration and the travertine deposit itself. Carbonate alteration is specifically the late-stage deposit of cement in Morrison Formation sandstones. Because it is a surface deposit and not a form of diagenesis, the travertine platform is considered to be a separate Quaternary deposit within the fault zone. It is nonetheless included in most figures as an important reference point within the map area.

#### *2.1.1.3.2 Yellow coloration*

Yellow coloration is a common type of alteration in the map area. Colored outcrops appear a bright yellow-orange, which laboratory analysis determines to be caused by the presence of iron oxides (Figure 12). As a feature easily identifiable in outcrop during field work, it was a useful characteristic in the development of the field map.

#### *2.1.1.3.3 Salt staining*

Salt staining (Figure 13) is a feature only observed and mappable in shales, where it forms a white crust on the surface. The pale stain on dark shale is vivid enough to appear on aerial photographs, which is helpful for mapping. Salt crystals are present in sandstones as well (Figure 13), but these are identified petrographically and are not apparent from observations in the field. The salt stain is a veneer of crystalline salt on aerially exposed shale and is associated in particular with damp outcrops. Such outcrops need be exposed for only a matter of hours before the rind of salt appears.

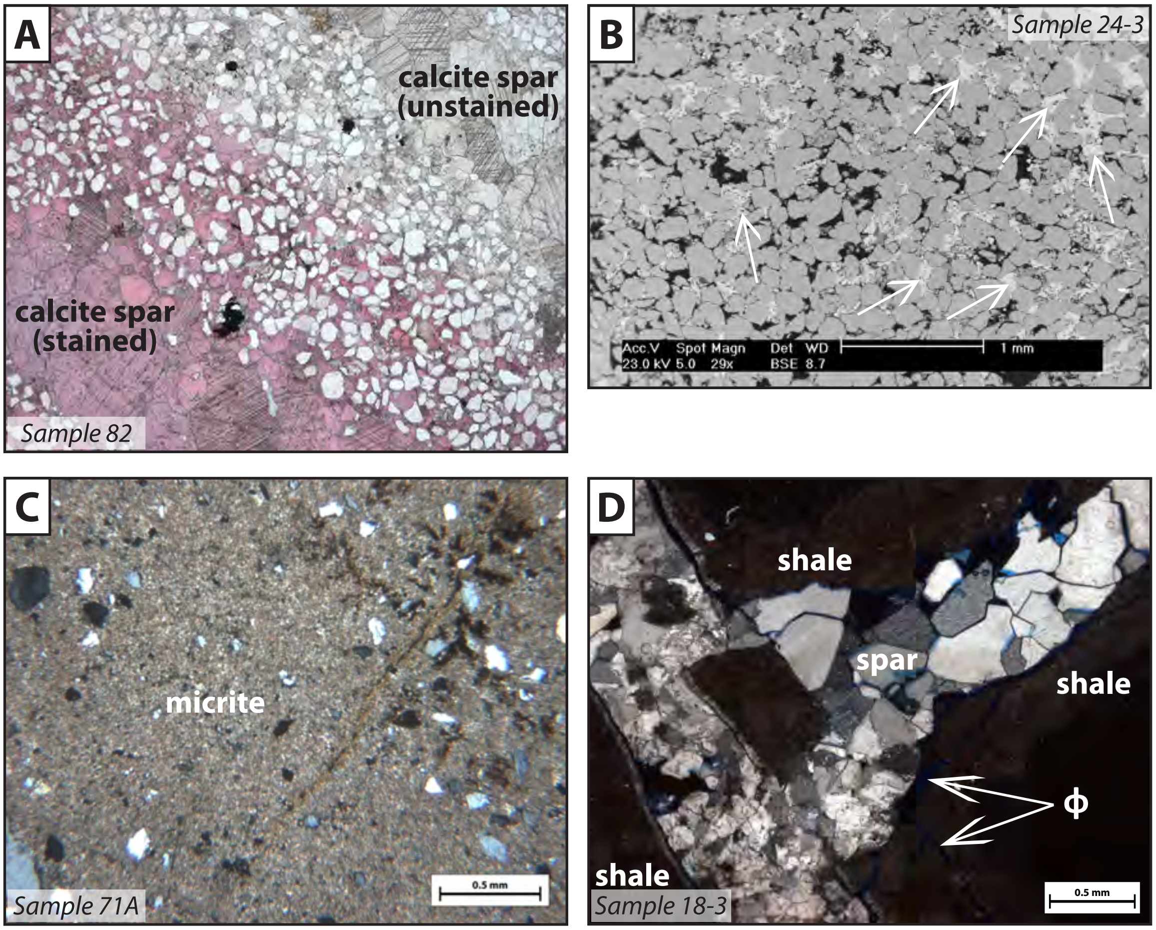

Figure 11: **A:** Complete pore and vein occlusion by calcite spar in a Salt Wash Member sandstone. **B**: Backscatter electron image showing partial pore occlusion by calcite spar (arrows) in a Salt Wash Member sandstone (gray: calcite; dark gray: quartz; black: porosity). **C:** Crossed-polars image of micritic matrix in the Salt Wash Member. **D:** Crossed-polars image of massive sparry calcite veins crisscrossing a Brushy Basin Member shale (ϕ: porosity).

Figure 12: **A:** Yellow coloration visible at outcrop scale in the Salt Wash Member north (left) of the travertine platform. **B:** Closer view of the same outcrop, showing pervasive yellow sandstone coloration.

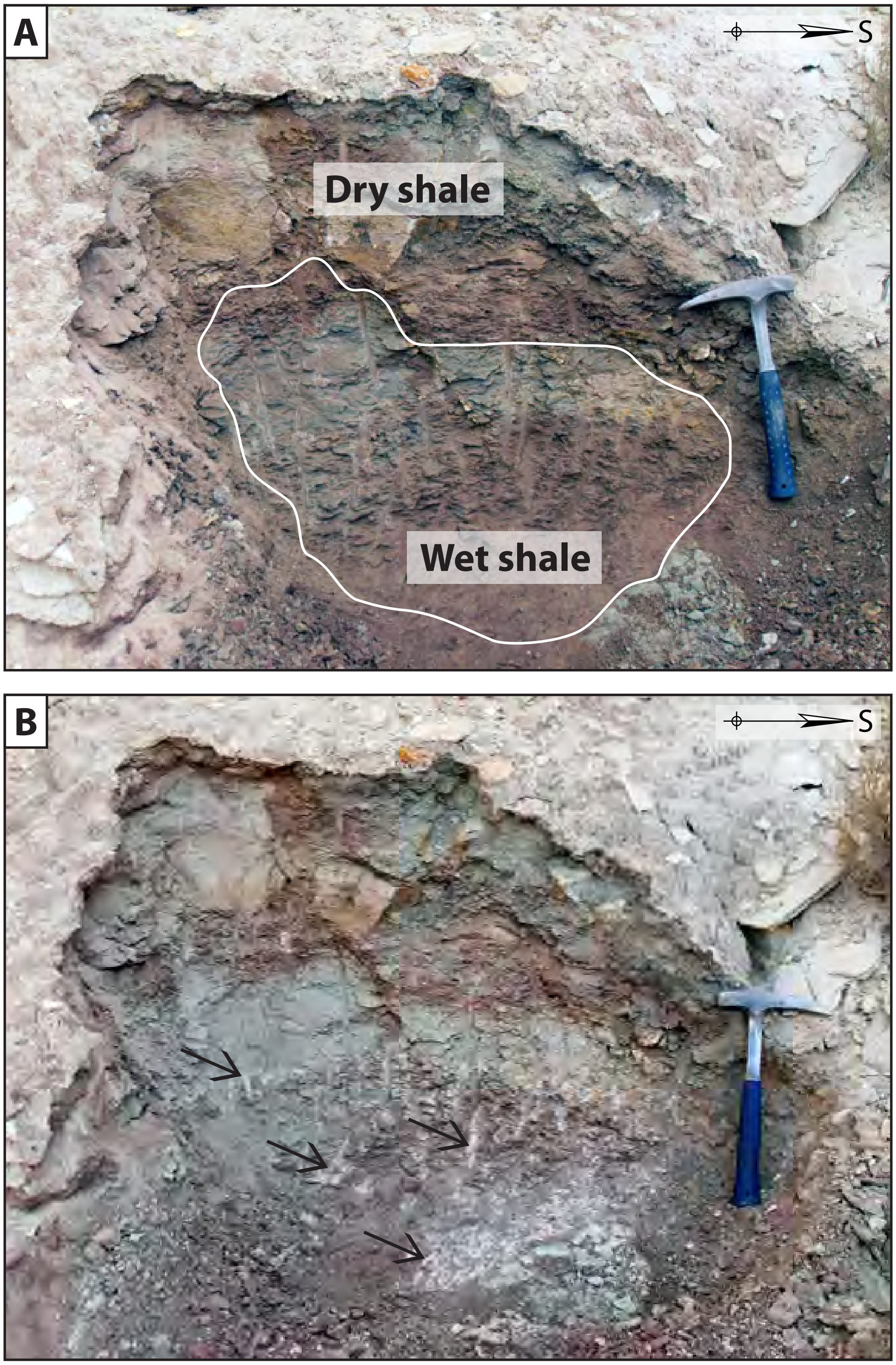

Figure 13: **A:** A damp exposure of Salt Wash Member shale moments after removing several inches of dried material; located on the slope of the western edge of the travertine deposit. **B:** A pale rind of salt is evident one day later (arrows).

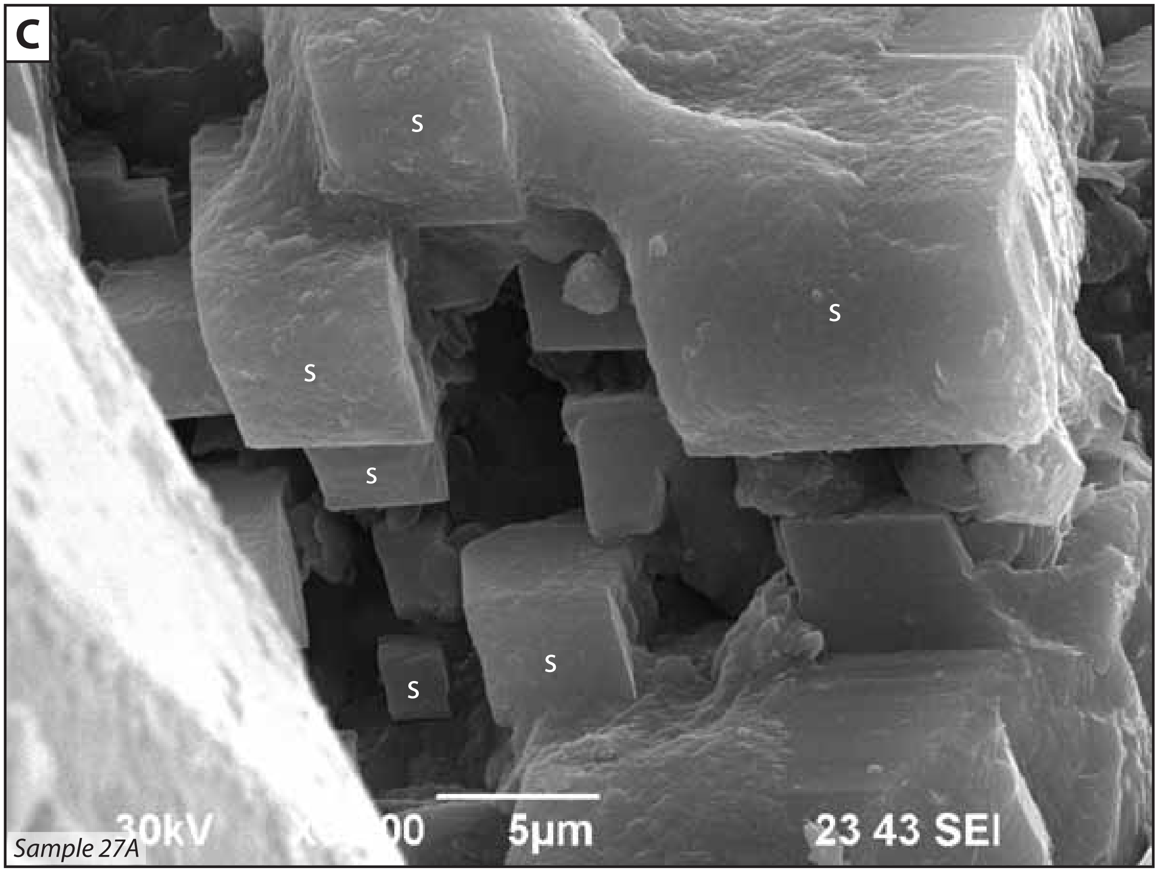

Figure 13: **C:** Secondary electron image of euhedral salt crystals (s) in a Salt Wash Member sandstone.

#### *2.1.1.3.4 Fractures and deformation bands*

Fractures (joints and uncemented opening-mode fractures) and deformation bands (zones of deformation-accommodating pore collapse and grain cataclasis, generally only a few grains wide) are structural forms of alteration probably unrelated to fluid flow or the presence of $CO_2$. Fractures can increase overall permeability, however, and deformation bands can act as relatively impermeable barriers within a sandstone (Jamison and Stearns, 1982; Antonellini and Aydin, 1994). Because they have bearing on fault zone permeability, they have the potential to exert control over the location of a spring within a fault zone. Although veins are a type of fracture (cement-filled), they are mapped separately, as a form of calcite alteration.

### 2.1.1.4 Field mapping results: Distribution of fault zone alteration

The distribution of all alteration within the fault zone is shown in Figure 14. The ability to accurately relate the distribution of alteration and travertine to fault geometry is crucial to understanding the structural controls on fault zone leakage and diagenesis. Outcrop coloration and areas of dense veining, the types of alteration most closely related to the presence of $CO_2$, are shown in Figure 15.

#### *2.1.1.4.1 Calcite cement and vein distribution*

Outcrops in the vicinity of the travertine contain abundant calcite-filled veins: The deposit itself is underlain by thick (2–10 cm) horizontal veins (Figure 16), and shales immediately adjacent to it are rendered nearly unrecognizable by a dense network of fabric-obliterating veins (Figure 17). Pore-filling carbonate cement is also pervasive in the immediate vicinity of the travertine platform (Figure 11A), where many of the rocks are hardened and ring loudly when hit with a hammer. Elsewhere in the fault zone, carbonate cement is patchy and less pervasive (Figure 11B). While many rocks have a slight to

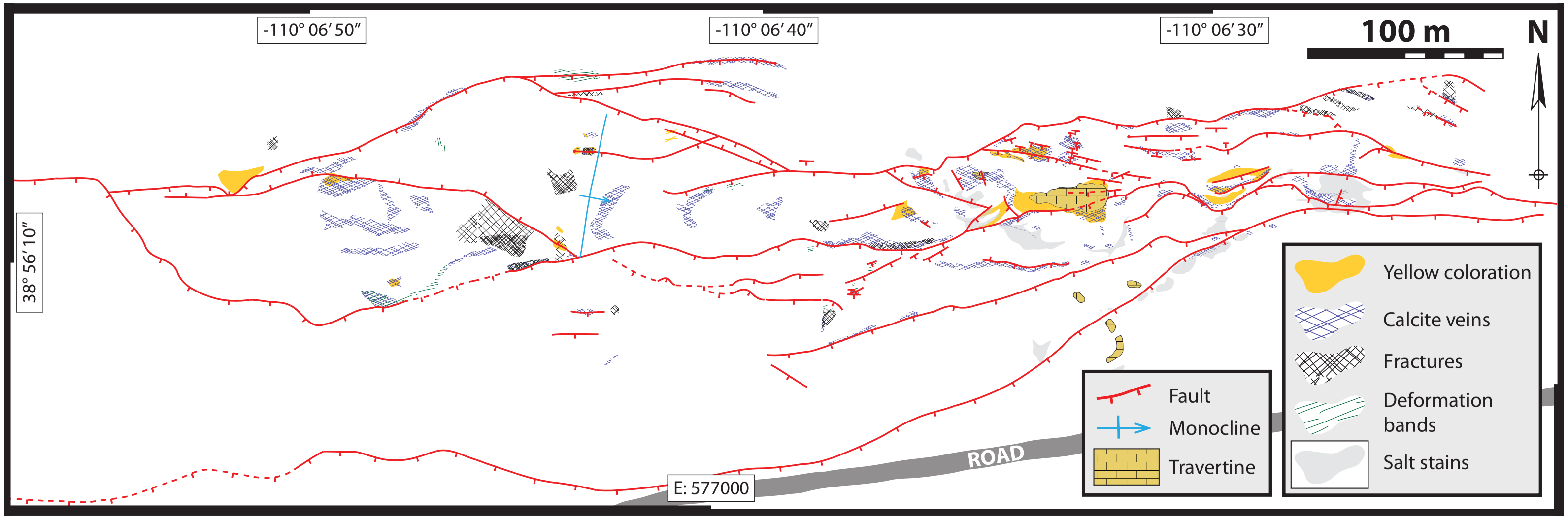

Figure 14: Field map simplified to show only fault zone structure and the distribution of alteration within the fault zone.

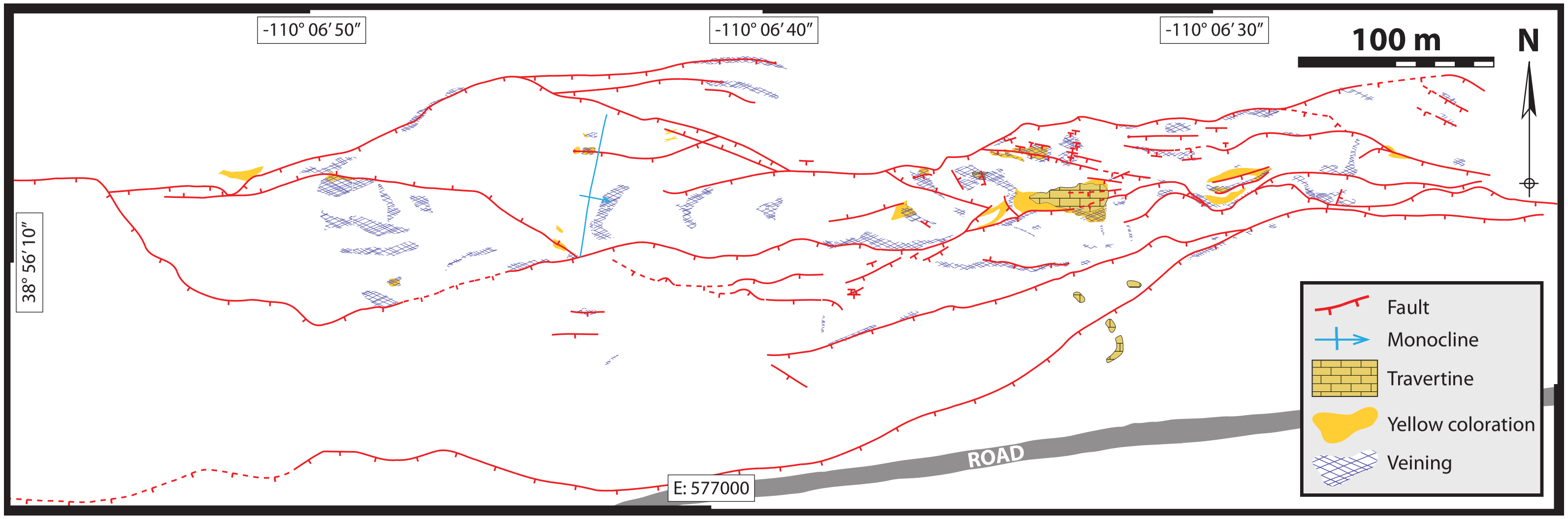

Figure 15: Field map with areas of dense veining and yellow outcrop coloration, the two forms of alteration most closely associated with the spring (travertine).

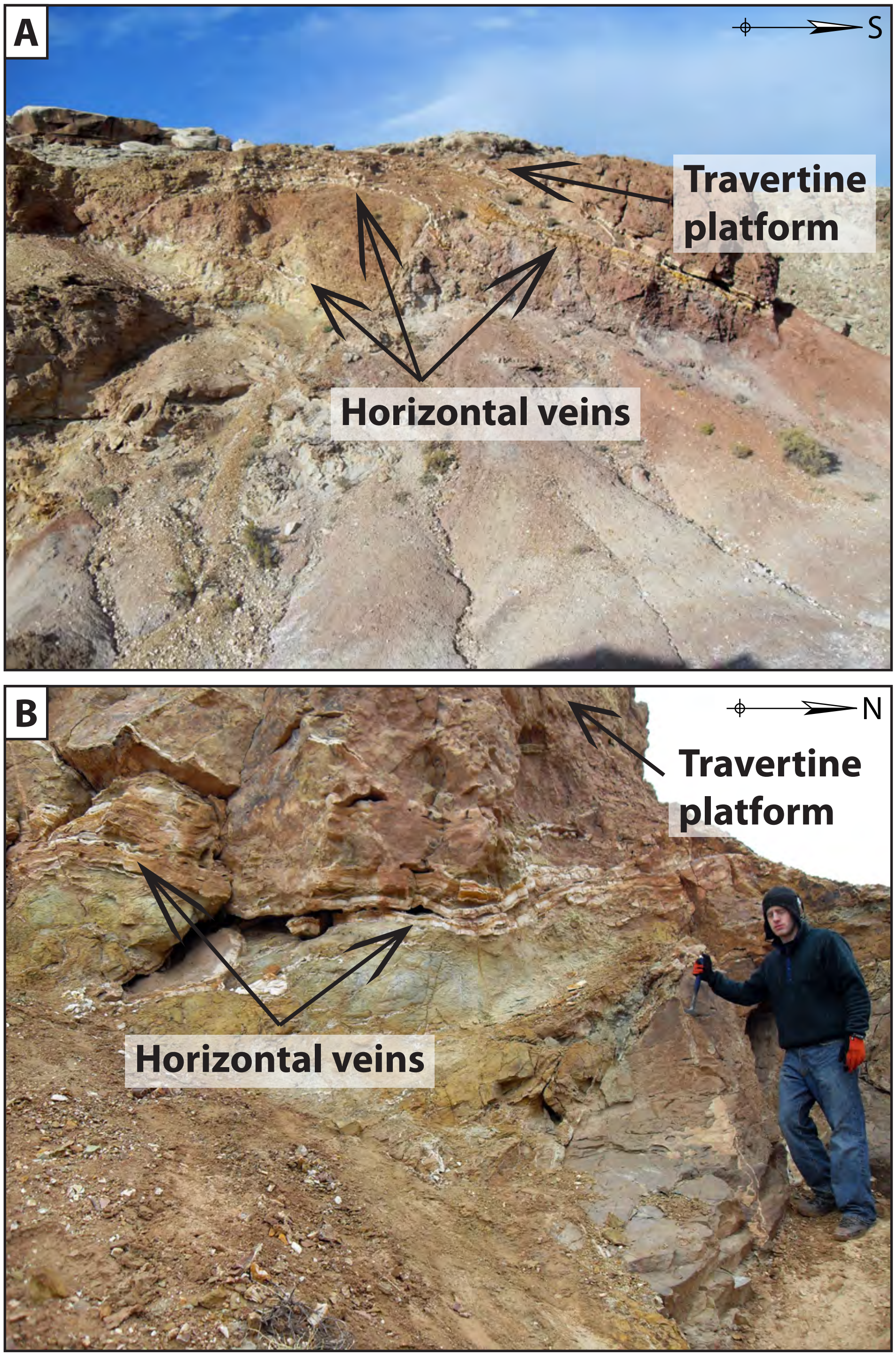

Figure 16: **A:** Thick horizontal veins cutting Salt Wash Member sandstone and Brushy Basin Member shale underneath the western edge of the travertine platform. **B:** Similar veins cutting Salt Wash Member sandstone on the eastern edge of the travertine platform (field assistant for scale).

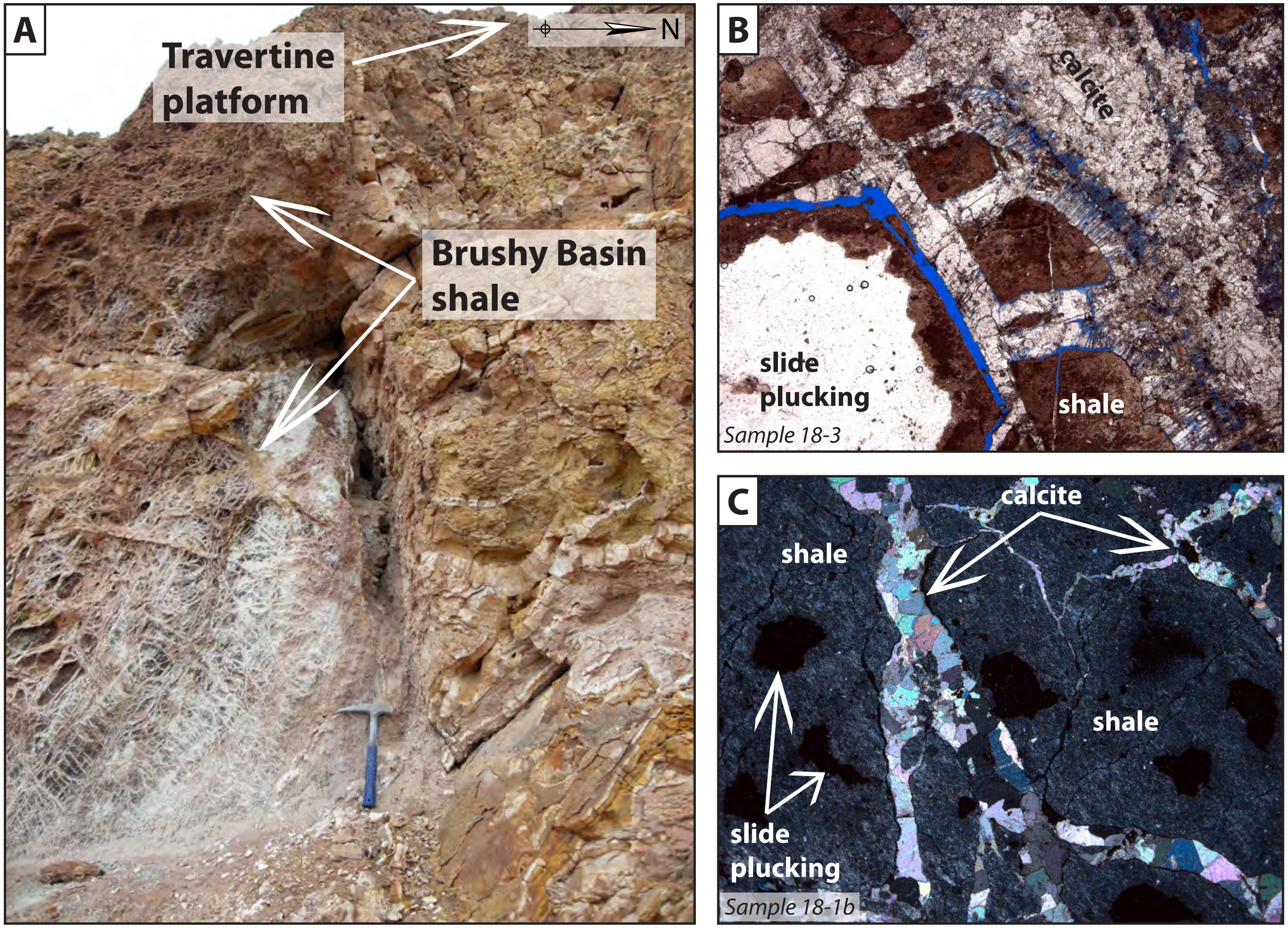

Figure 17: **A:** Red Brushy Basin Member shale underneath the eastern edge of the travertine platform crisscrossed by a dense network of calcite-filled veins. **B–C:** Photomicrographs of the same veins.

moderate reaction to hydrochloric acid, sandstones are rarely hardened by cement but are instead easily disaggregated, and shales are not penetrated by veins. Veins are usually found within about a meter of faults, striking parallel to them.

The extent of typical carbonate cement is related to location relative to the fault zone (Figure 18). Compared to cementation inside the fault zone near the travertine, cementation outside the fault zone is in most cases low (less than 14%) or absent. Sandstones show slight reaction to hydrochloric acid and veins are almost nonexistent. Not all outcrops are without carbonate content, however. There is at least one location with significant cementation—station 86, which is 60 m outside the fault zone (Figure 19). Isotope data show that this is not spring-related cementation, however (see *Discussion*). Other samples taken outside the fault zone show little to no calcite content, except for recycled sedimentary carbonate grains (see *Petrography*). An isopach map of calcite abundance (Figure 20) emphasizes the concentration of calcite around the travertine deposit. Precision is limited by the number of data points—25 stations, many concentrated around the travertine—but it is a good snapshot of the distribution of calcite cement throughout the map area.

#### ***2.1.1.4.2 Yellow coloration distribution***

Yellow coloration is mostly found in a halo of Salt Wash Member sandstone surrounding the travertine (Figure 21). Heavy cover on the north edge of the travertine prevents any observations of in-place rock, but it is likely that these outcrops are similarly stained. Scattered patches of similar coloration can be seen elsewhere in the fault zone, but these are always small in areal extent, covering only a few square meters. As with the large area around the travertine, these other patches are in almost every case located along faults, and especially at intersections of fault segments. Yellow coloration is not observed anywhere outside the fault zone.

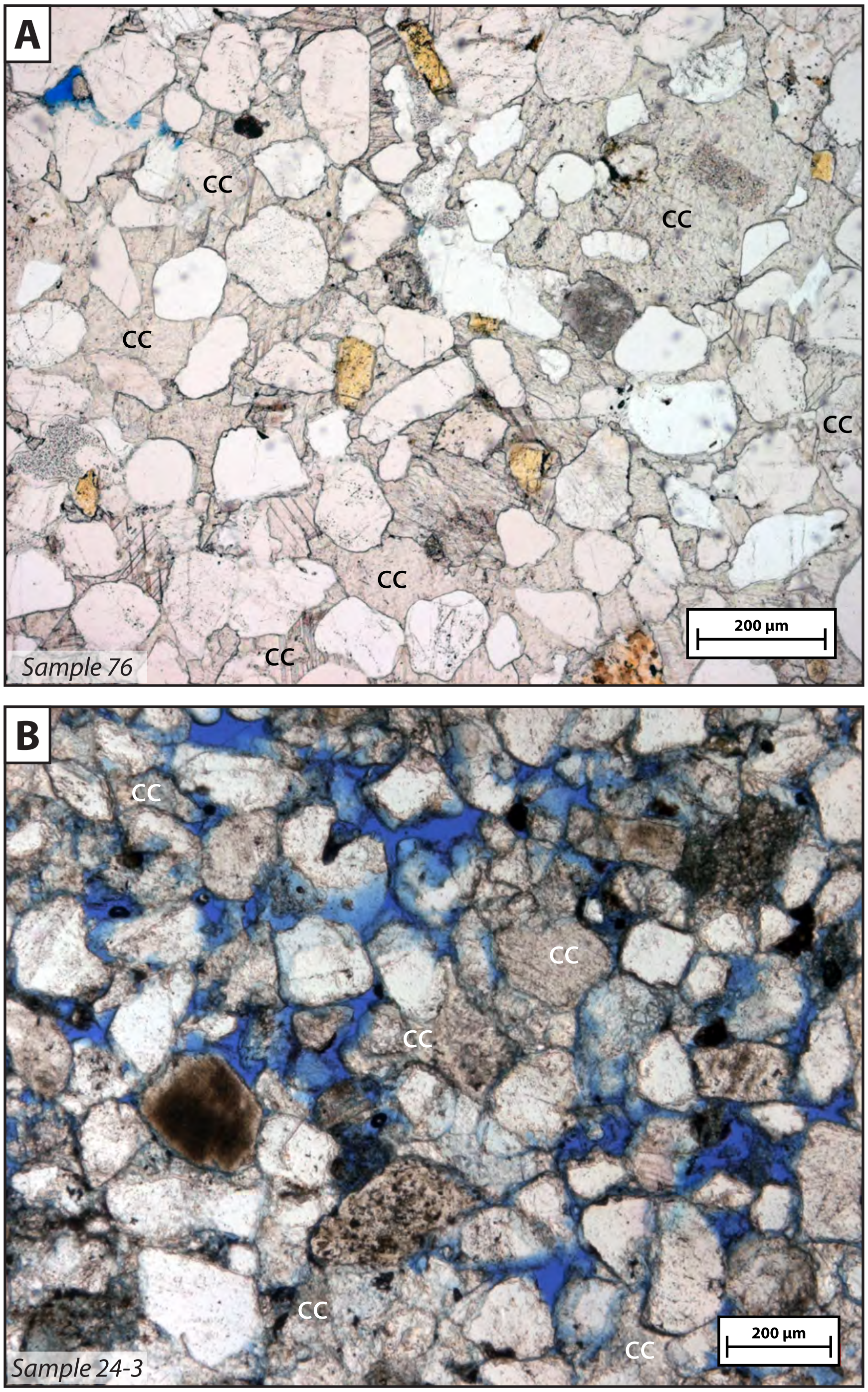

Figure 18: **A:** Salt Wash Member sandstone with pervasive pore-filling carbonate cement (cc), located adjacent to the travertine platform. **B:** Salt Wash Member sandstone with only patchy carbonate cement (cc) and retaining much of its porosity, located 150 m from the travertine.

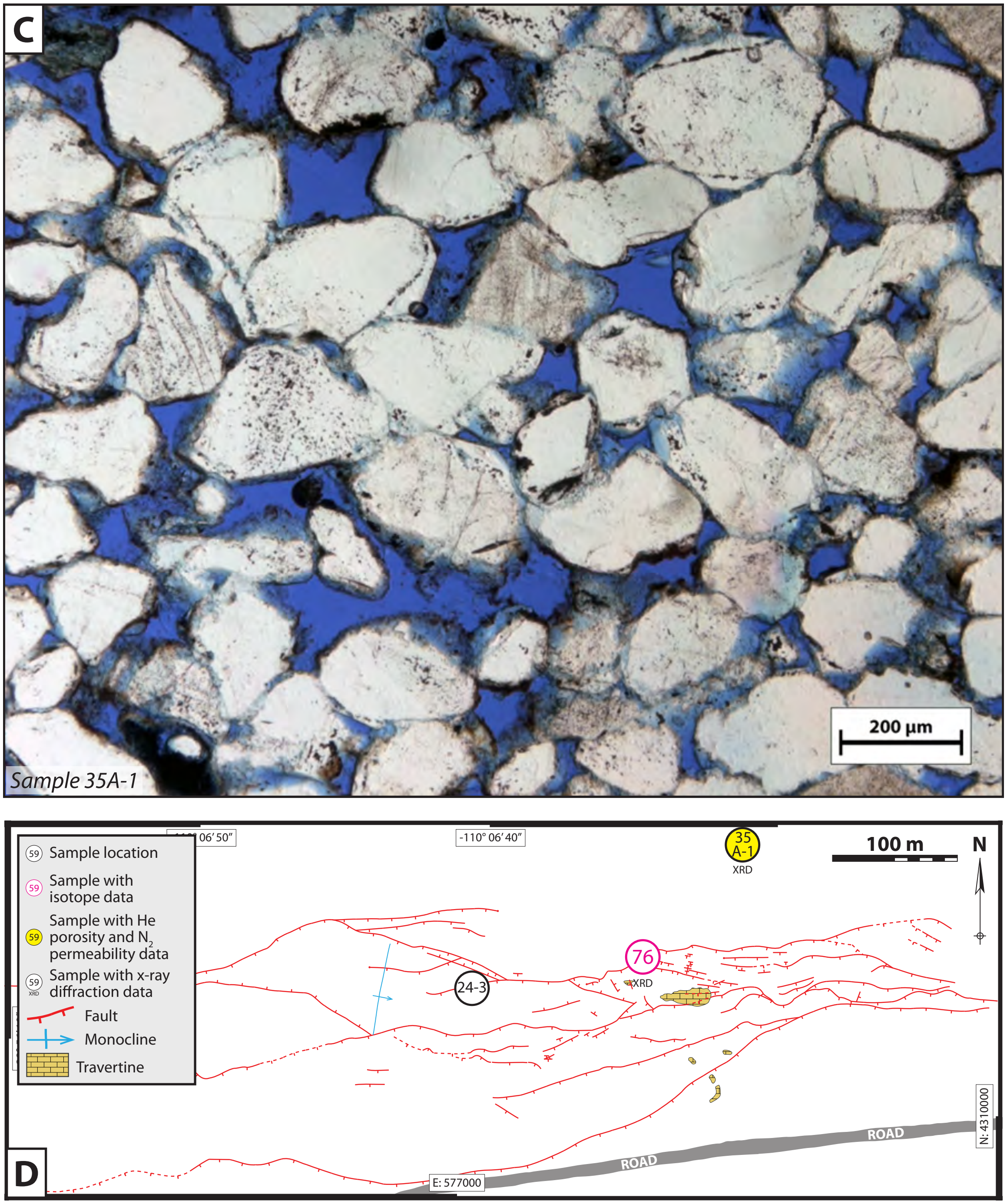

Figure 18: **C:** Salt Wash Member sandstone with no carbonate cement and high porosity, located outside the fault zone. **D:** Location map for these samples.

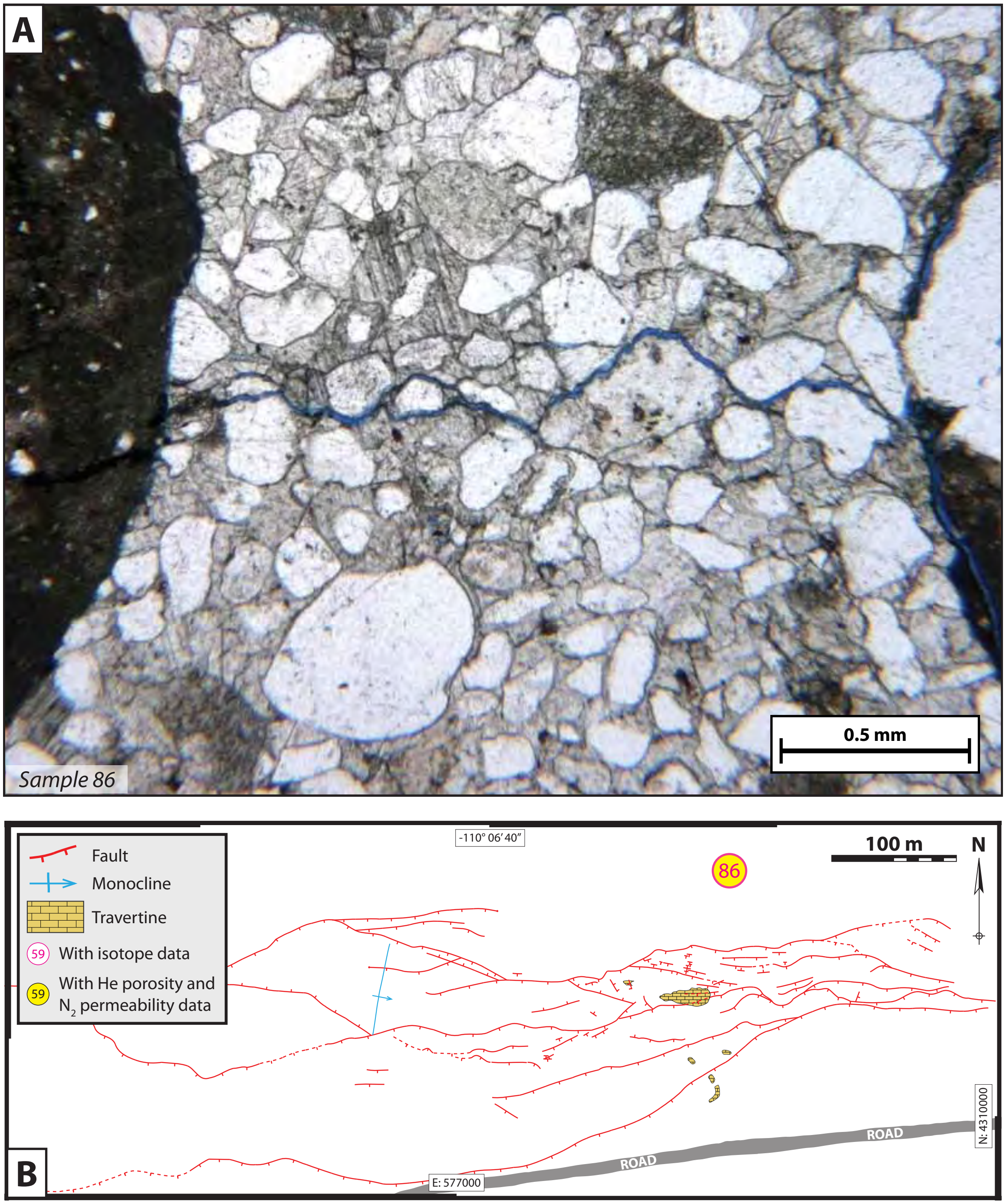

Figure 19: **A:** Photomicrograph of sandstone from station 86. Note the abundance of calcite cement and low porosity. **B:** Sample location map for station 86.

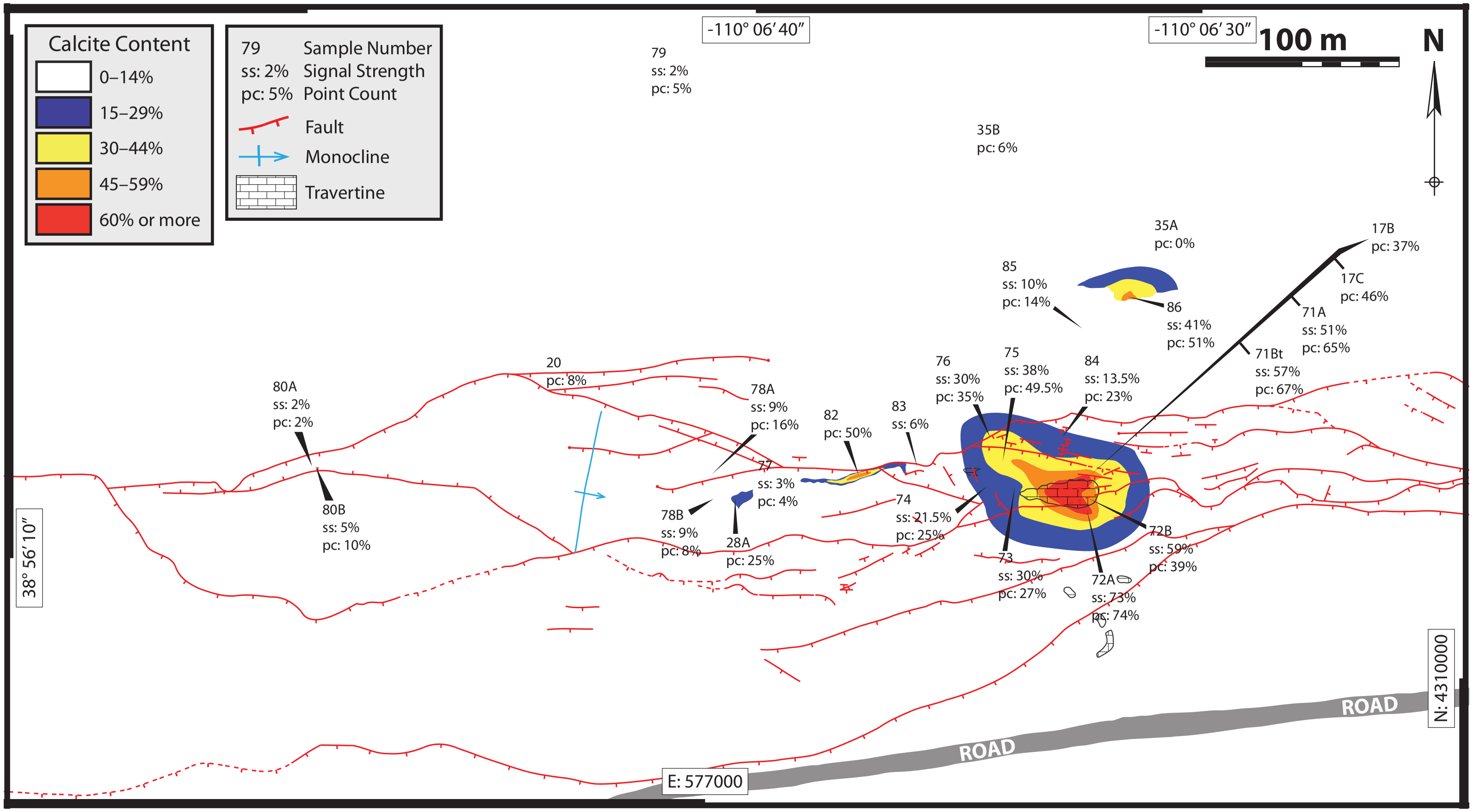

Figure 20: Isopach map of total calcite abundance (spar plus micrite). Precision is limited by a low number of data points throughout large parts of the map area, but an increase in intensity around the travertine is obvious.

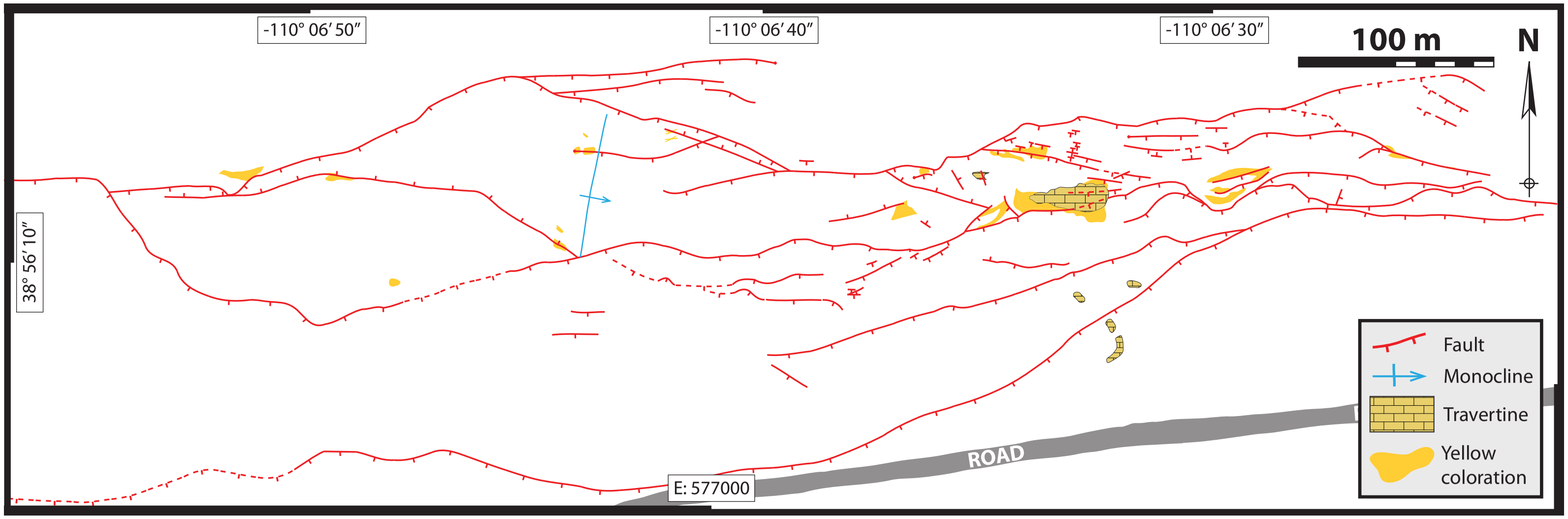

Figure 21: The distribution of yellow staining within the fault zone. Coloration is intense around the travertine and sparse elsewhere. Note that almost all instances occur along faults.

#### *2.1.1.4.3 Salt staining distribution*

Salt staining on shales appears only within the fault zone, and always in topographic lows (Figure 22). It shows up in the wash below the travertine and in the hanging wall at the southern edge of the map. It does not cover all low areas, however; it tends instead to form patches that are linearly aligned. These linear features are apparently fault traces. During an excursion west of the map area, salt stains observed in low-lying washes could be used to predict the trace of a fault segment from a distance of over 100 m. In one case, salt stains were observed in close proximity to an active (low output) spring, which confirmed the presence of a fault segment, although the area was mostly covered in thick desiccated shale.

#### *2.1.1.4.4 Fracture and deformation band distribution*

Fractures are ubiquitous throughout the fault zone, and even outside the fault zone. I have mapped them where they are both particularly intense and well exposed (Figure 23). The distribution of deformation bands in the map area is restricted to thin sandstone zones parallel and adjacent to faults (Figure 24). This is consistent with the tendency of deformation bands to form as a result of faulting (e.g., Aydin and Johnson, 1978; Pittman, 1981; Karig and Lundberg, 1990; Antonellini and Aydin, 1994; Crider and Peacock, 2004; Davatzes et al., 2005; Shipton et al., 2005b). Not all faults have associated deformation bands, however—the zone around the travertine is cut by many faults, but only one small outcrop exhibits deformation bands. Deformation bands were mapped where they were conspicuous features, but there was no emphasis during field work on searching for and comprehensively mapping them.

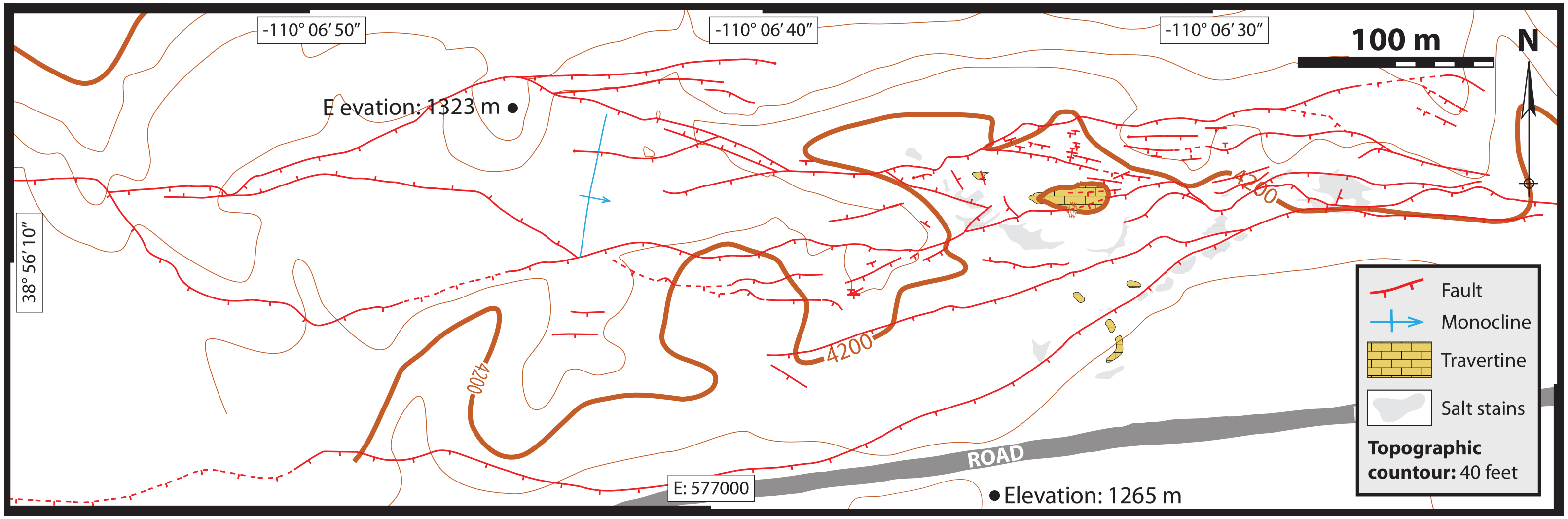

Figure 22: Map of salt staining in the fault zone. Topography shows that the stains are restricted to low-lying areas.

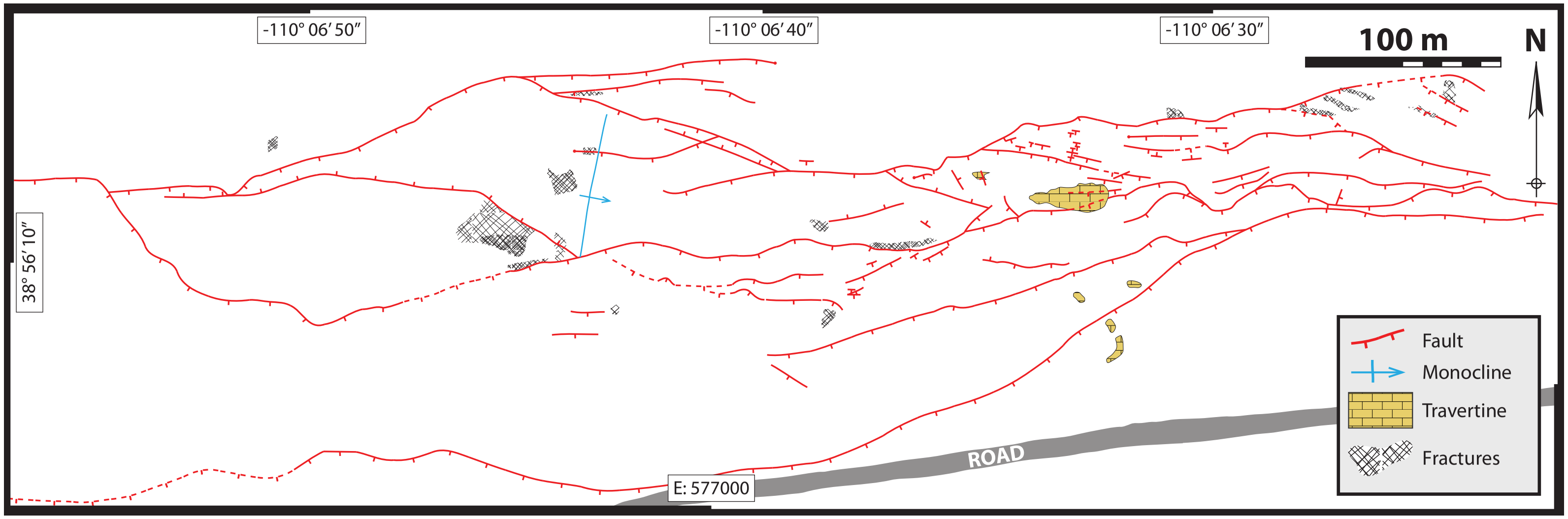

Figure 23: Map of high fracture density in the fault zone. Because they are ubiquitous, only areas with unusual fracture density have been noted.

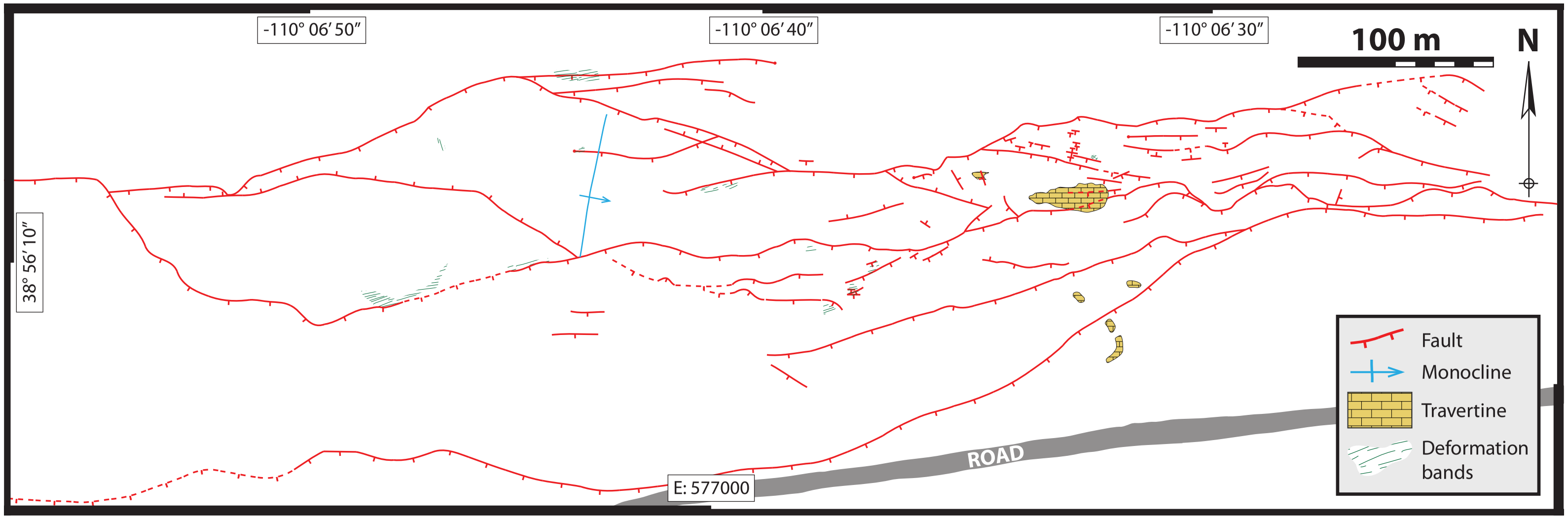

Figure 24: Distribution of deformation bands within the fault zone.

### 2.1.2 STRATIGRAPHIC SECTIONS AND CROSS SECTIONS

#### 2.1.2.1 Methods

Map area Morrison Formation sandstones are discontinuous, lithologically heterogeneous fluvial deposits. Some lenses pinch out over distances as short as 50–80 m, and no sandstone beds are continuous throughout the entire map area. The $J_{ms}1$–$J_{ms}6$ correlatable sandstones are therefore critical to making accurate cross sections. Without them there is too much stratigraphic ambiguity to determine which part of the Salt Wash Member is exposed at the surface and how much downdrop each fault block has undergone. The cross sections were therefore based on correlation of these sandstone marker beds as they were mapped in the field area.

It is also important to have accurate stratigraphic sections on which the cross sections can be based. Stratigraphic sections have been put together for the region (Trimble and Doelling, 1978; Hintze, 1988; Doelling, 2002), as well as specifically for the Little Grand Wash fault (Vrolijk et al., 2005; Dockrill, 2006; Burnside, 2010). These are specific to localities outside the map area, however, and due to the depositional heterogeneities that characterize much of the Morrison Formation, they are too generalized to be highly useful for this project. I have therefore drawn a new set of stratigraphic sections based on map area field observations (Figure 25).

Two north-south cross sections improve the fault zone structural analysis by resolving the amount of throw on each fault segment and confirming stratigraphic assignations, especially within the Salt Wash Member. These are especially useful for analyzing lithologic juxtapositions associated with alteration and better defining the nature of fluid flow paths to the surface.

The A–A' cross section cuts through the fault zone west of the travertine platform. This location was chosen to confirm the identification of sandstones exposed in the western

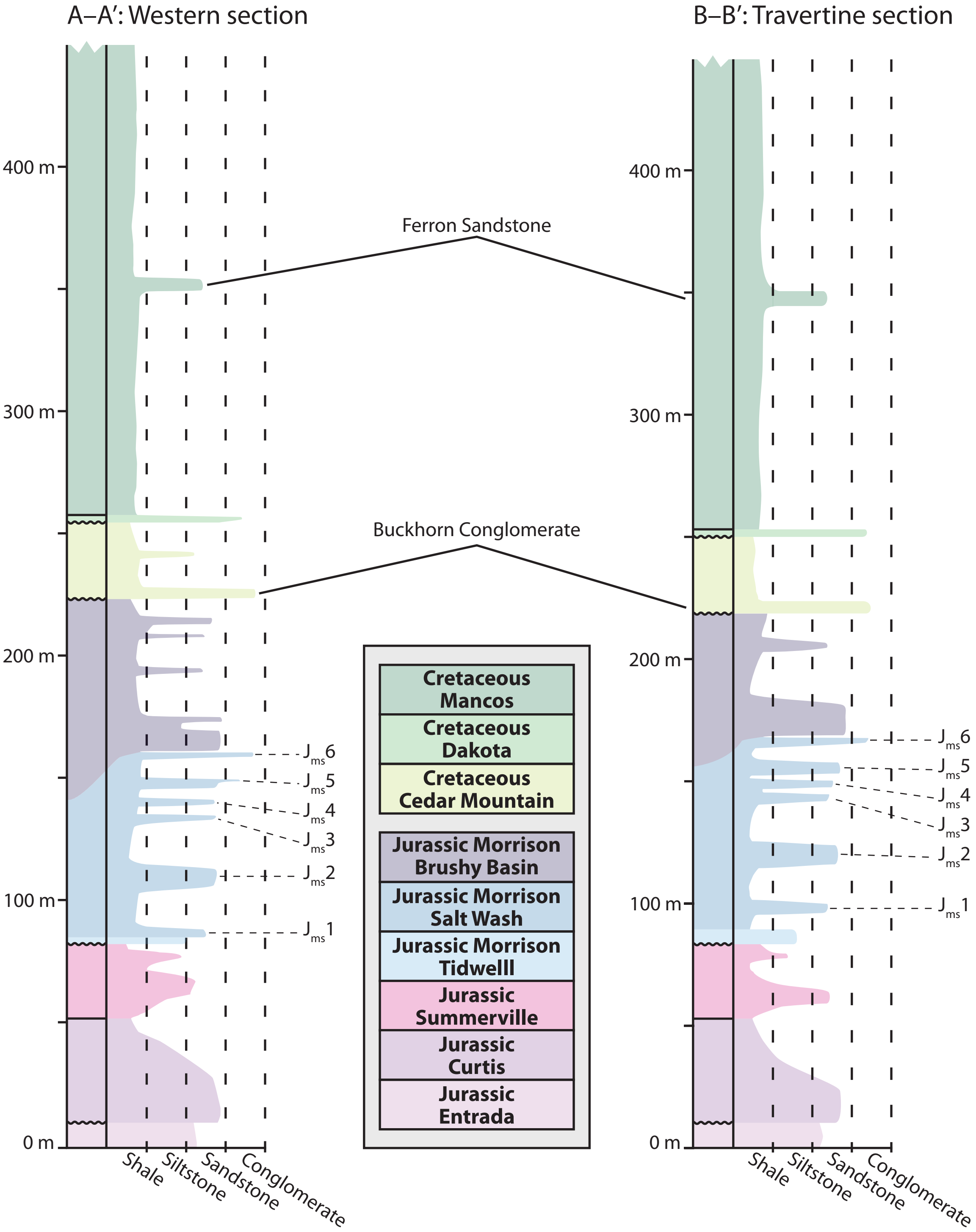

Figure 25: Schematic map area stratigraphic sections correlating to the A–A’ and B–B’ cross sections, from the western and eastern regions of the map area, respectively.

section of the fault zone, where field observations led to an ambiguous interpretation. The B–B' cross section cuts through the travertine platform. In addition to resolving throw on faults and confirming stratigraphic identifications, illustrating the subsurface in the area of interest around the travertine is important for facilitating a discussion of structural controls on leakage.

### 2.1.2.2 Cross sections

#### *2.1.2.2.1 Construction*

The A–A' and B–B' cross sections are presented in Figures 26 and 27. Data from the Greentown State 36-24H well (Delta Petroleum Corporation, 2009: API# 43-019-31519) are a useful reference against which to compare subsurface projections. Unfortunately the well is in the footwall and does not intersect any fault segments, but stratigraphic projections in the cross sections are all within a few meters' agreement of stratigraphy identified in the well completion log. The cross sections were constructed using an average measured fault dip of 84°.

Bedding is oriented with strike and dip measurements taken in the map area near the cross sections, where they are available. Elsewhere bedding is set at 1.65°, based on Doelling's (2002) map of the San Rafael Desert. Other factors used to configure the cross sections are less well constrained. Massive Brushy Basin Member shales abut the travertine platform and the fault ramp to the south. This shale is likely from the upper portion of the member because it is a thick section with thin and infrequent sandstone lenses, and the Brushy Basin Member becomes increasingly shale-rich upsection. It has no recognizable markers, though, so it is impossible to pinpoint the exact stratigraphic location.

The Mancos Ferron Sandstone forms a flat table where it caps a hill of shale about 1 km east of the map area, at a point overlooking a hairpin turn in the access road (Figure 28).

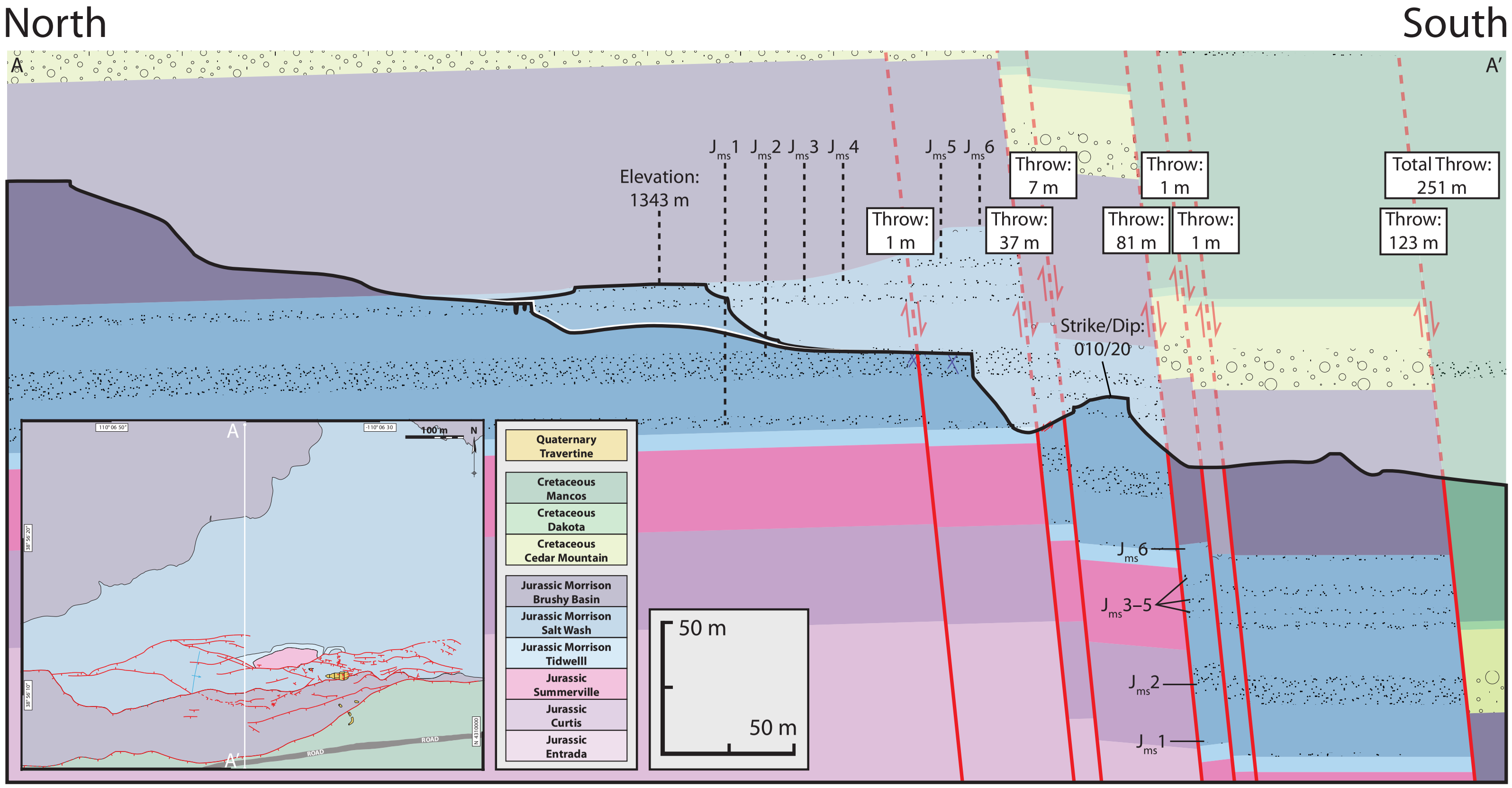

Figure 26: A–A' cross section cutting through the western region of the map area, including the fault ramp. Inset shows cross section location.

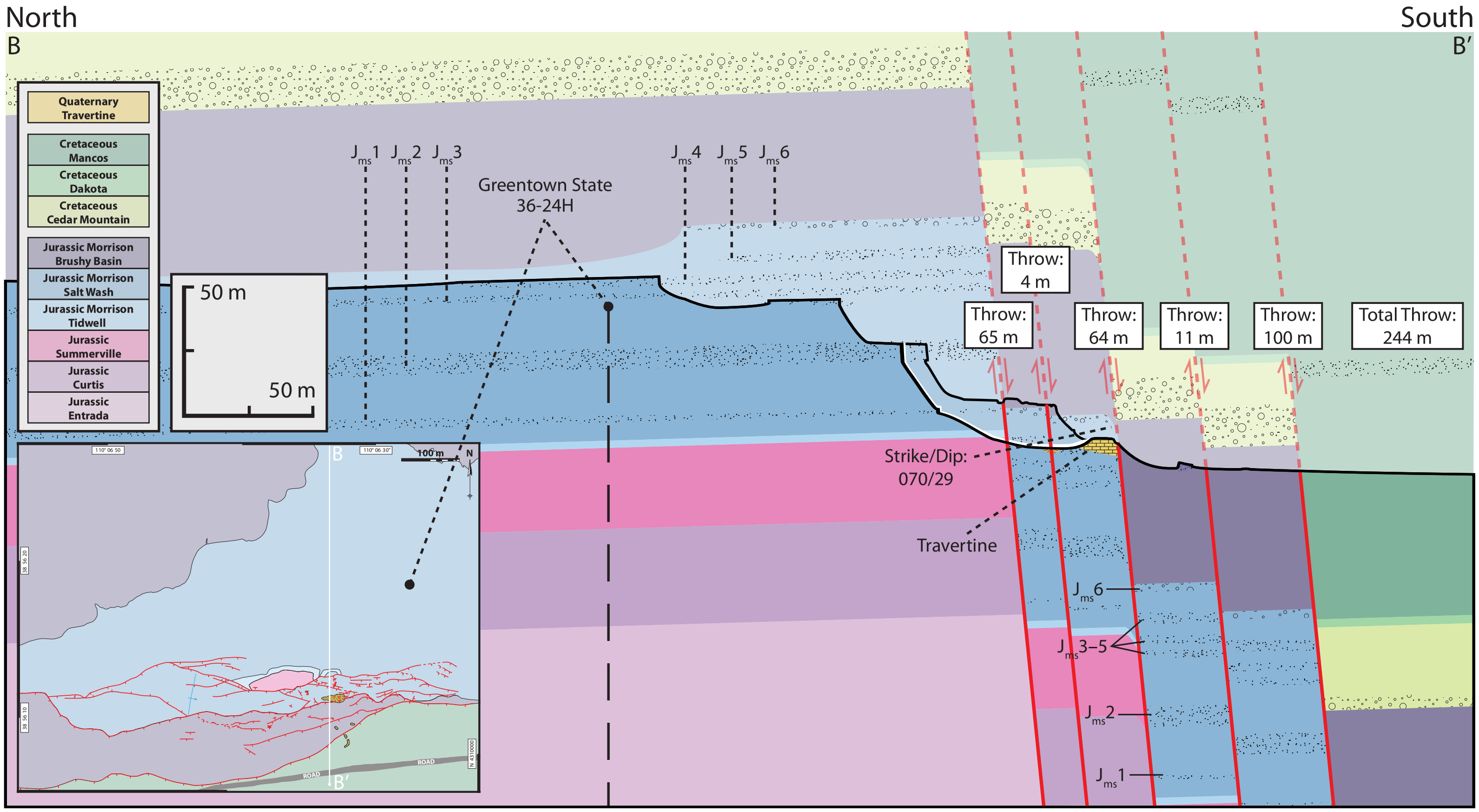

Figure 27: B–B' cross section cutting through the travertine deposit in the central part of the map area. Inset shows cross section location.

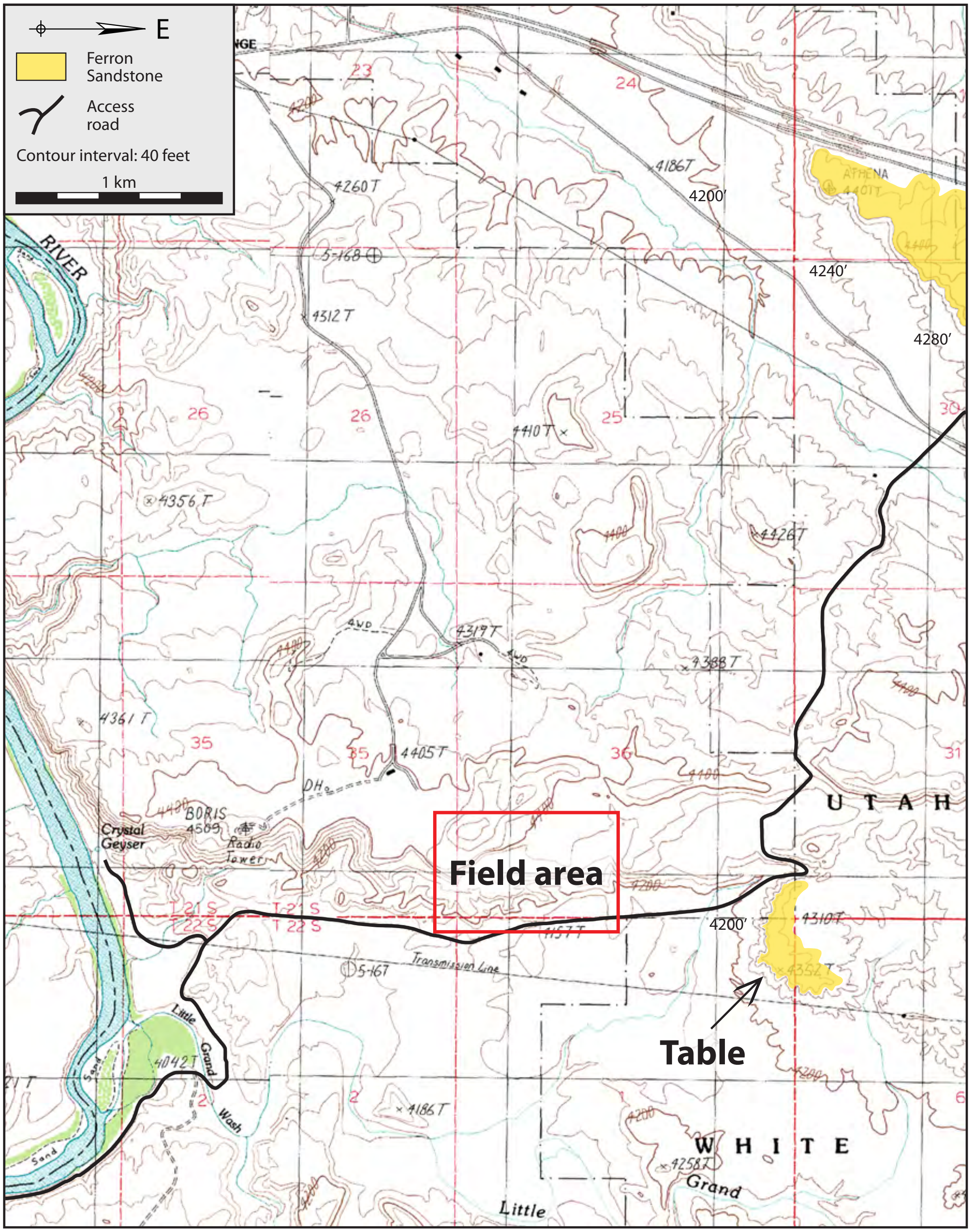

Figure 28: **A:** A map of the area around Little Grand Wash (after USGS, 1988) shows the Mancos Ferron Sandstone outcropping in a flat table east of the map area.

Figure 28: **B:** View from the fault scarp of the Ferron Sandstone table to the west. The base of the Ferron Sandstone outcrops near the top of the table (arrows). Foreground shows closely spaced arcuate joints in a Salt Wash Member sandstone.

The only control on placement of the Ferron Sandstone in the cross sections is that it cannot be raised above its position in this table, or throw would be increasing towards the east despite reports that maximum throw on the Little Grand Wash fault is at a point by the river, to the west (McKnight, 1940; Vrolijk et al., 2005; Dockrill and Shipton, 2010). In the map area, the shale outcropping in the hanging wall is the Mancos Tununk Shale, which underlies the Ferron Sandstone. In the cross sections, therefore, the Ferron Sandstone in the hanging wall must be placed between ground level and its position in the table to the east. Because so much throw is lost between the map area and the table (see below for a discussion of this), it is placed at the lower end of this range of possible positions.

#### ***2.1.2.2.2 Throw estimates***

Cross sections were used to calculate throw on individual fault segments (Figure 29), and across the fault zone. In A–A', fault offsets range from 1 to 123 m, for a total of 251 m across the fault zone; in B–B', offsets range from 4 to 100 m, for a total of 244 m across the fault zone. Throw estimates in Figure 29 are most accurate near the cross sections; moving away from either, estimates are skewed by the unknown amount of total throw reduction that occurs along strike with distance from the point of maximum offset, which is west of the field area (McKnight, 1940; Vrolijk et al., 2005; Dockrill and Shipton, 2010).

It is helpful to compare offset determined in the cross sections to offset reported by other researchers and calculated using cross-fault changes in the elevation of the Ferron Sandstone. The reported point of maximum throw on Little Grand Wash is near the river to the west; overall throw should diminish east of that point. The A–A' cross section is 1.9 km east of the river. The B–B' cross section is 153 m east of the A–A' cross section, and the Ferron Sandstone table is another 1.0 km farther east. Dockrill and Shipton (2010) put the maximum Little Grand Wash offset at 260 m, and McKnight (1940) reported 290 m. Both

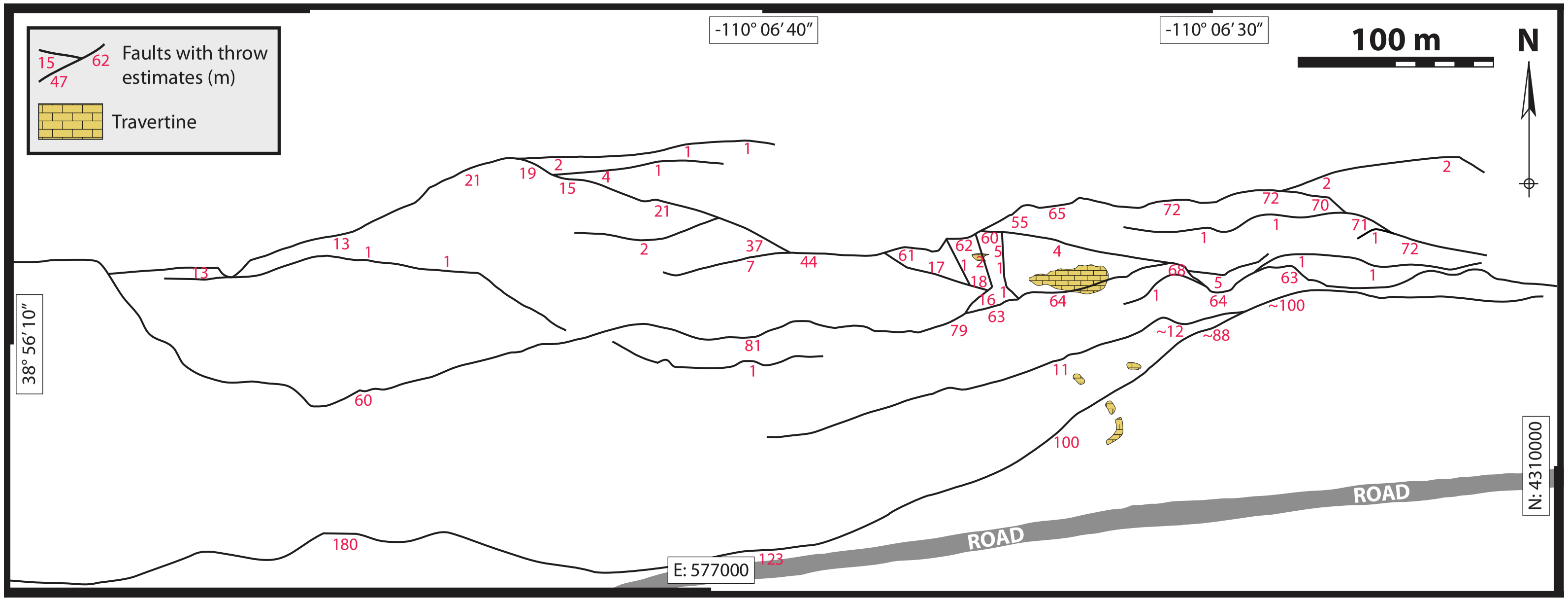

Figure 29: Throw estimates on fault segments throughout the fault zone. Total throw across the entire fault system should diminish to the east.

cross sections in the map area show about 250 m of throw. Offset along the fault therefore diminishes at an average rate of 5–20 m/km between the river and the A–A’ cross section. Assuming the rate of throw decrease is constant, the total offset at the Ferron Sandstone table (Figure 28) should be 228–244 m.

In the shale hills north of the map area, the Ferron Sandstone outcrops at an elevation of 4,360 ft (Figure 28). In the table east of the map area it outcrops at an elevation of 4,290 ft, according to elevation taken on April 4, 2010 with a Garmin GPS device. The distance between these outcrops is 8,475 ft. The increase in elevation due to regional dip should therefore be

$$8{,}475 \text{ ft}(\tan 1.65) = 244 \text{ ft}.$$

This makes the un-faulted elevation of the sandstone in the flat table 4,360 ft + 244 ft = 4,604 ft. The actual, faulted elevation is 4,290 ft, indicating a fault offset of 314 ft, or 96 m. This is far less than the 228–244 m predicted above.

If the rate of diminishing offset between the river and the Ferron Sandstone table were constant, 164–194 m of throw would need to be eliminated in about 3.1 km, requiring a throw loss rate of 52–62 m/km of fault trace. This would put the total offset on cross section A–A’ at 161–172 m and on cross section B–B’ at 153–163 m. Because the total throws determined in the cross sections (251 m and 244 m, respectively) are much higher than the calculated throw for the map area, the rate of offset diminishment does not appear to be linear.

The difference in throw between the two cross sections is consistent with a non-linear rate of offset decrease (although, at about 3%, it may be within the range of measurement error). The cross sections are 153 m apart with a difference in offset of 7 m, indicating a rate of throw reduction of about 46 m/km—much higher than the 5–20 m/km calculated between the river and the map area. Loss of offset along the fault is therefore unlikely to increase at a constant rate. Variations in fault mechanics due to changing lithologic juxtapositions may prevent throw reduction from being distributed uniformly along strike. Although offset in the map area is diminishing to the east, it is possible there are also segments of the fault where the amount of offset is constant along strike.

### 2.1.3 SAMPLE COLLECTION

For laboratory analysis I collected a total of 50 samples (see Appendix C: Table C1 for a full list). The emphasis of this project is on sandstone alteration, because the relative permeability of sandstone is conducive to fluid infiltration and alteration, making it a good proxy for former fluid flow. For this reason only two shale samples were collected. Specimens of interest included those seen in the field to be highly altered (obviously colored or showing a vigorous fizz in response to hydrochloric acid); correlative unaltered rocks; and samples taken along two transects through the map area (Figure 30). The transects are intended to assess the degree to which alteration is dependent on proximity to the $CO_2$ seep, and to compare to alteration (or lack thereof) in the fault zone away from the seep and outside the fault zone. Both transects begin at the travertine platform. One runs north, moving away from the travertine and out of the fault zone; the other runs west, moving away from the travertine but remaining within the fault zone and in close proximity to several fault segments.

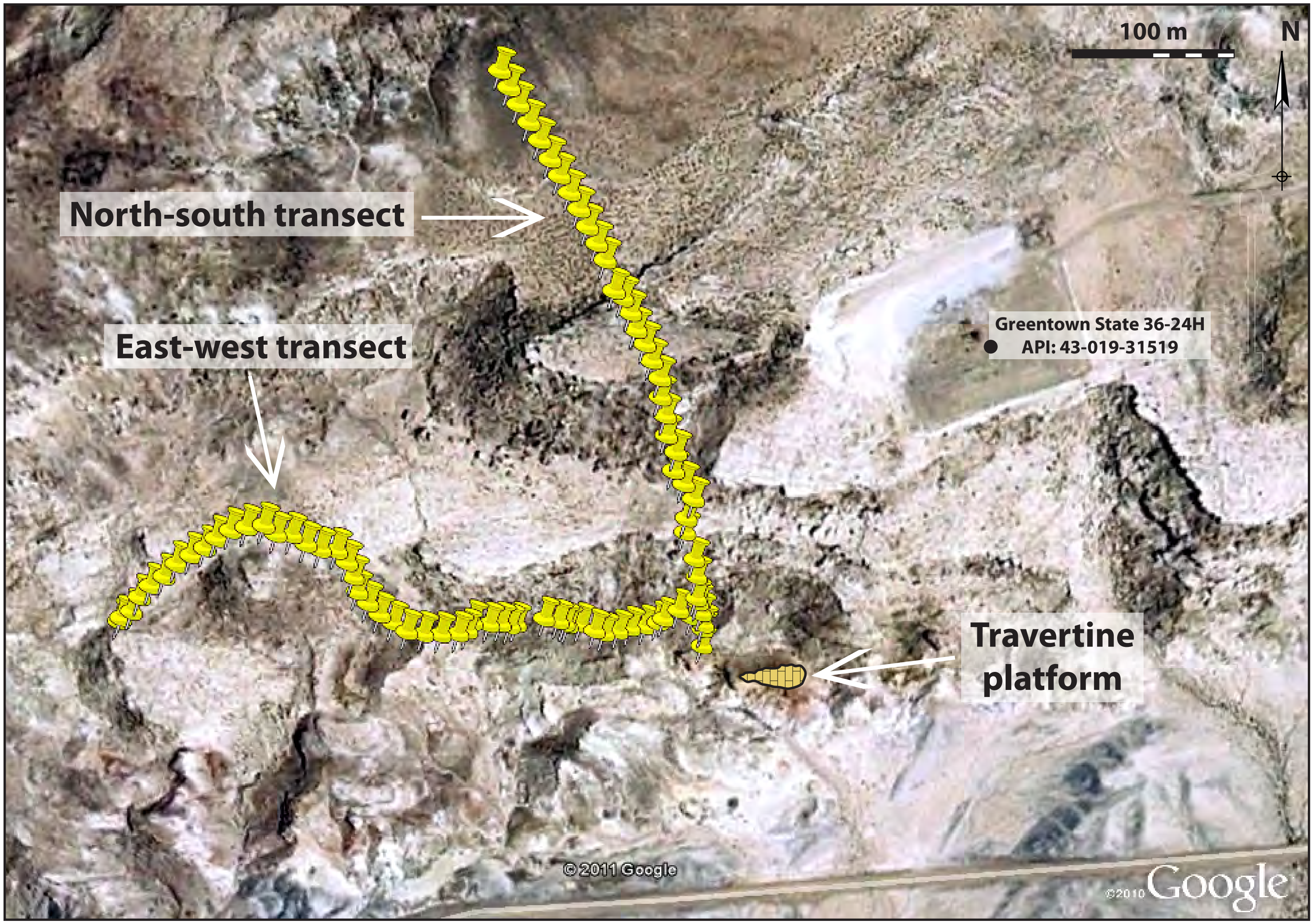

Figure 30: GPS data displayed in Google Earth trace north-south and east-west transects through the map area. Pins represent GPS data; see Figure 31 for sample locations.

## 2.2 Laboratory Analyses

A laboratory-based analytical approach is important to understanding the diagenetic processes associated with the Little Grand Wash fault system. The following sections present the results of this analytical work, which include standard petrography (optical and scanning electron microscopy), energy dispersive spectroscopy, X-ray diffraction analysis, porosity and permeability measurements and stable isotope analysis. Table 2 summarizes the techniques used to augment field work (microscopy is excluded—see Appendix C: Table C1 for a complete list of petrographic samples) and Figure 31 shows the location of each sample used in laboratory analysis. Appendix D contains detailed methodologies for each technique.

### 2.2.1 PETROGRAPHY AND POINT COUNTING

#### 2.2.1.1 Methods

Optical and electron microscopy are the most basic and the most useful approaches to describing the nature of diagenesis associated with $CO_2$-rich fluid flow. Seventy-nine thin sections were available for petrographic examination, representing altered and unaltered rocks from throughout the map area. All thin sections used in this project were vacuum-impregnated with blue-dyed epoxy to highlight porosity.

In order to facilitate optical petrography, 31 thin sections were stained for alkali feldspars and calcite. Following the suggestions outlined in Hutchison (1974), these stains were intended to confirm or refute the absence of dolomite; to make it easier to identify micrite, which can be amorphous and difficult to identify; to differentiate alkali and plagioclase feldspars from each other and from quartz grains, as feldspars can be difficult to identify if they do not exhibit twinning; and to identify feldspars rendered nearly unrecognizable by dissolution.

| **Sample** | **He injection porosity** | **$N_2$ injection permeability** | **Point counting** | **Weight % calcite (signal calibration)** | **C/O isotope** | **XRD: Clay-size sep., air-dried** | **XRD: Clay-size sep., glycolated** | **XRD: Clay-size sep., heated (375°C)** | **XRD: Bulk rock, air-dried** |
|---|---|---|---|---|---|---|---|---|---|
| 17B | yes | yes | yes | | | | | | |
| 17C | yes | yes | yes | | | yes | yes | | yes |
| 20A | yes | yes | yes | | | | | | |
| 28A | yes | yes | yes | | | | | | |
| 35A | yes | yes | yes | | | yes | yes | | yes |
| 35B | yes | yes | yes | | | yes | yes | yes | yes |
| 71A | yes | yes | yes | yes | yes | yes | yes | | yes |
| 71B | | | yes | yes | yes | | | | |
| 72A | yes | yes | yes | yes | yes | | | | |
| 72B | yes | yes | yes | yes | yes | | | | |
| 73 | yes | yes | yes | yes | yes | | | | |
| 74 | yes | yes | yes | yes | yes | yes | yes | | yes |
| 75 | yes | yes | yes | yes | yes | yes | yes | | yes |
| 76 | | | yes | yes | yes | yes | yes | | yes |
| 77 | yes | yes | yes | yes | yes | | | | |
| 78A | yes | yes | yes | yes | yes | yes | yes | | yes |
| 78B | yes | yes | yes | yes | yes | | | | |
| 79 | yes | yes | yes | yes | yes | yes | yes | | yes |
| 80A | yes | yes | yes | yes | yes | yes | yes | | yes |
| 80B | yes | yes | yes | yes | yes | yes | yes | yes | yes |
| 82 | yes | yes | yes | | | yes | yes | | yes |
| 83 | | | | yes | yes | | | | |
| 84 | yes | yes | yes | yes | yes | | | | |
| 85 | yes | yes | yes | yes | yes | | | | |
| 86 | yes | yes | yes | yes | yes | | | | |

Table 2: Summary of all laboratory experiments performed on each sample. See Table C1 for a summary of microscopy and energy dispersive spectroscopy.

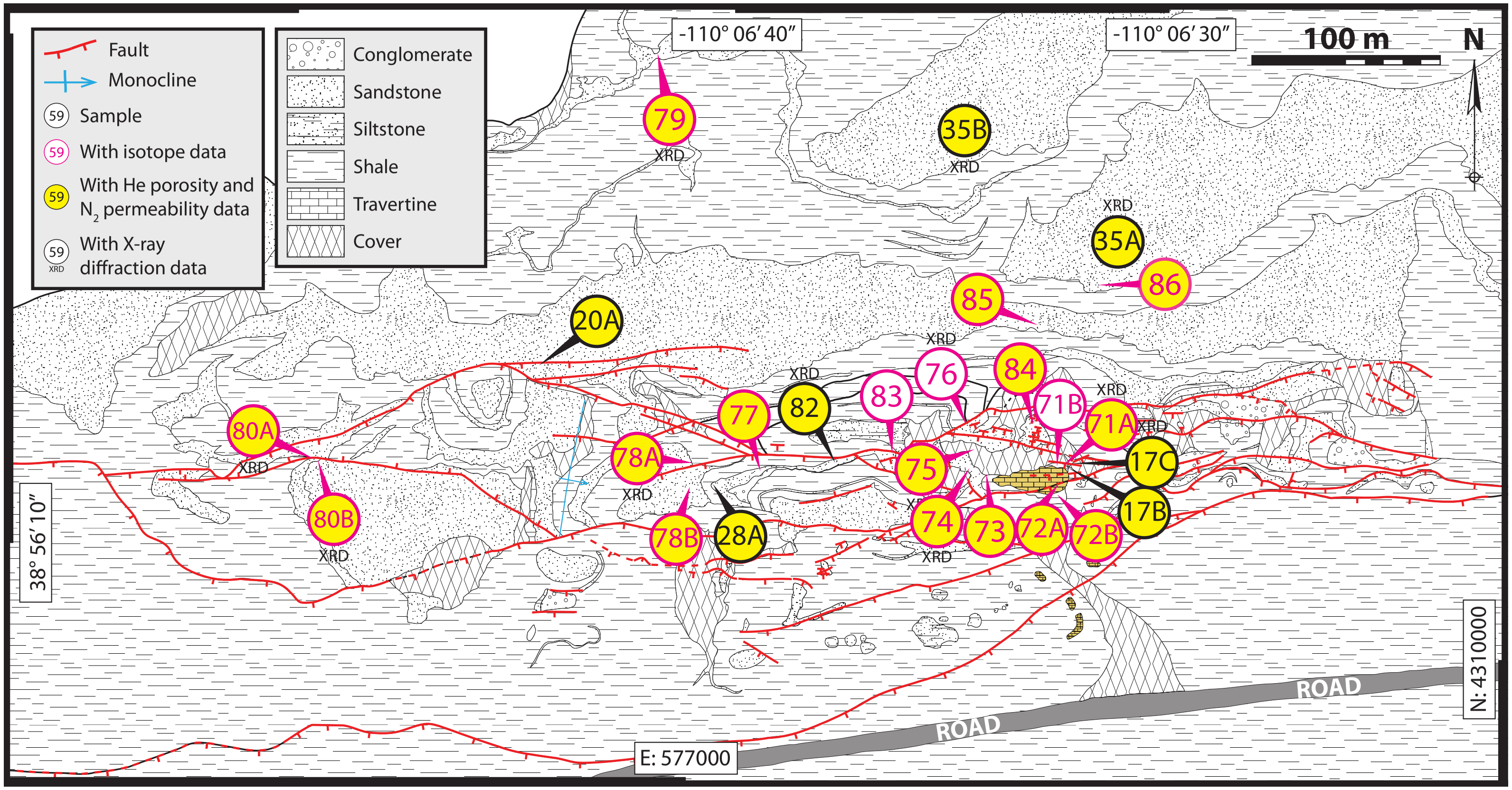

Figure 31: Reference map showing the locations of samples listed in Table 2.

My own efforts to apply various stains yielded a strong calcite stain but less successful feldspar stains. The Na-cobaltinitrite used to stain potassium feldspars did not produce an even stain and tended to stick on clays and microporous grains as well as alkali grains. Because of these mixed results, another batch of thin sections was sent away for commercial staining. On the advice of Kitty Milliken (personal communication, 2010), one end of each section was stained for calcite and the other end for alkali feldspars, while the middle remained unstained. No plagioclase stain was requested, as the process of applying overlapping stains risks ruining the first with the second. Preliminary analysis, moreover, showed that alkali feldspars are rarer and commonly quite dissolved. Being thus more difficult to identify, it was more helpful to stain for alkali feldspars than for plagioclase.

Clays and opaque minerals are difficult to identify in optical microscopy. In order to comprehensively describe sample compositions, additional work was needed to properly determine what minerals were present. To this end, 19 thin sections were polished for scanning electron microscope analysis—in order to find compositional data, see micro-scale morphologies and otherwise augment observations from optical microscopy. Backscatter electron mode was useful for highlighting contrasts in mineralogy, such as grain-coating cement or feldspar twinning, as well as getting images of samples at higher magnification and resolution than possible using optical microscopy. This was especially useful for looking at microcrystalline cement and matrix material. Using energy dispersive spectroscopy in tandem with backscatter mode enabled identification of unknown mineralogical composition by showing a spectrum of elemental composition. Secondary electron mode made it possible to search sample fragments for distinctive mineral morphologies, such as hexagonal kaolinite "booklets" or the euhedral crystal faces of quartz overgrowths.

For point counting, 19 petrographic categories were used to quantify the composition of 25 samples. The categories are:

- monocrystalline quartz
- polycrystalline quartz
- microcrystalline quartz and chert
- intact plagioclase feldspar
- dissolved plagioclase feldspar
- intact alkali feldspar
- dissolved alkali feldspar
- opaque lithic
- sedimentary lithic
- miscellaneous
- clay matrix
- spar cement (calcite)
- micrite cement (calcite)
- quartz cement
- clay cement
- intergranular porosity
- oversize porosity
- intragranular porosity
- microporosity.

Descriptions and examples of each category are included in Appendix E. Folk's (1980) nomograph indicates that counting 400 points per sample creates a maximum statistical error of slightly under 2.5% (Figure 32). The statistical error does not account for human error, but this should be minimized by extensive petrographic preparation such as staining and comparison to electron microscopy.

Supplementary calcite content data were collected at the Stanford University School of Earth Sciences. This method uses a mass spectrometer to measure $CO_2$ produced by the reaction of phosphoric acid with a sample with unknown calcite content. By comparing the $CO_2$ signal produced in this reaction with the $CO_2$ signal produced in the same reaction with a pure calcite standard of known mass, calcite content in the sample can be calculated. This method is henceforth referred to as the "signal calibration" method. See Appendix D for a more detailed explanation of the technique. These measurements are in the form of weight-percent calcite. Because the density of calcite (2.71 g/cc) is roughly equivalent to the density

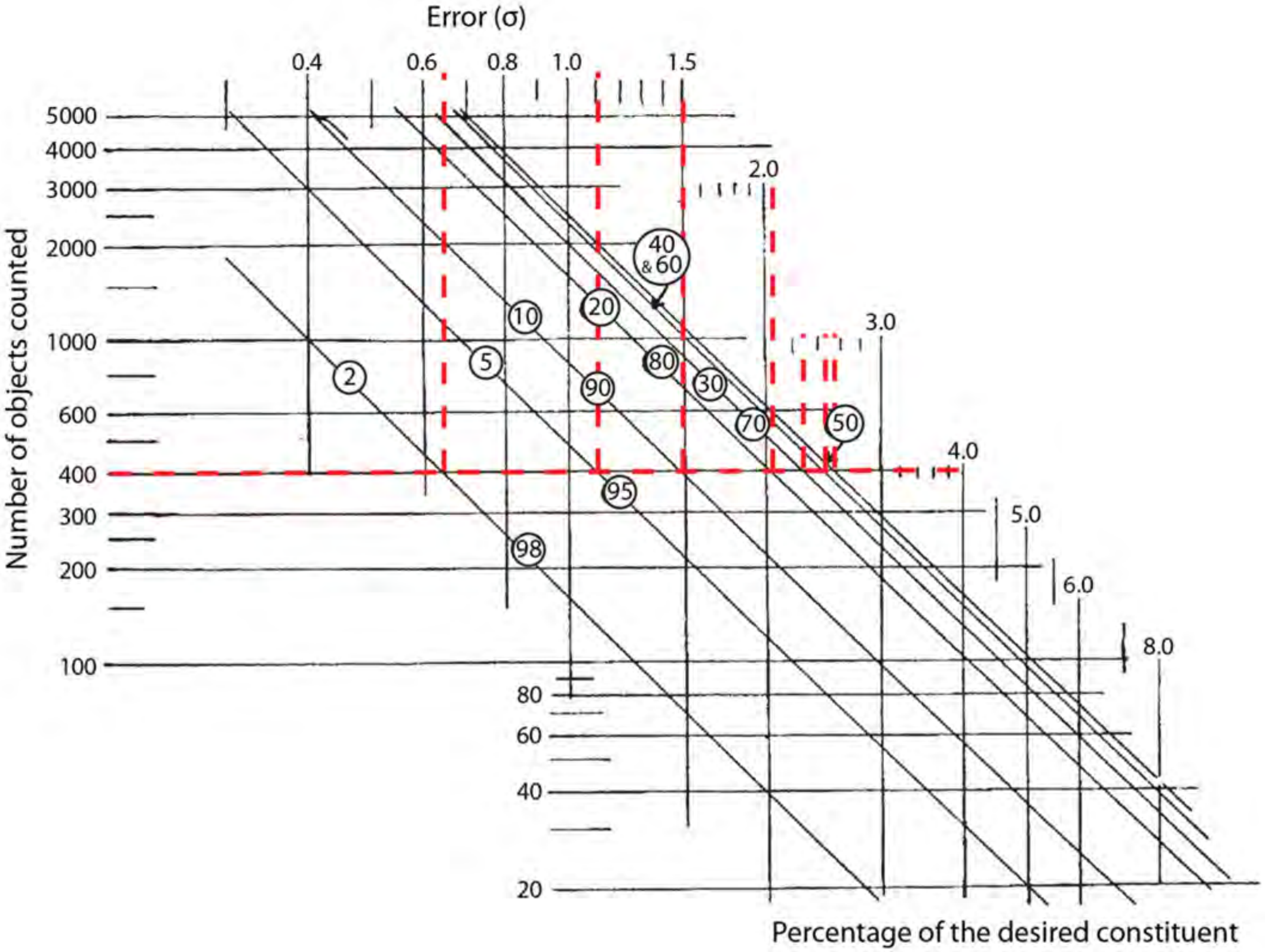

Figure 32: Nomograph used to determine the number of points counted per sample (after Folk, 1980, adapted from van der Plas and Tobi, 1965). Counting 400 points per slide limits the maximum statistical error to less than 2.5%.

of quartz (2.65 g/cc), and the two minerals comprise the bulk of sample material, the weight percent of calcite is a good measurement of its abundance in a sample.

#### 2.2.1.2 Petrographic results

The following is a summary of petrographic observations from point counting (see Appendix C for notes and images from each sample). Point counting exposes differences in bulk rock composition. Variations in cement volume are especially useful, as cementation is often a flow-related form of alteration, which is the focus of this project. Point count results are presented in Table 3.

##### *2.2.1.2.1 Lithologic classification and provenance*

Samples are mostly quartz-dominated sandstones. The quartz-feldspar-lithic (Q-F-L) ternary plot in Figure 33 shows that 21 of the 25 point-counted samples have a grain component of 90% or more quartz. Twelve samples have greater than 95% quartz, which makes them quartzarenites, according to Folk's (1980) classification scheme. The remaining samples are classified as subarkoses (three samples) and sublitharenites (nine samples). Sample 72B is a shale and does not appear on the plot. The Q-F-L data used to make Figure 33 are included in Table 4.

Applying provenance regions to the ternary plot indicates that all samples derive from cratonic interior or recycled orogenic sources (Dickinson and Suczek, 1979; Dickinson et al., 1983). Most samples are clustered near the quartz pole around the boundary between these two provenance regions. This is consistent with the source regions described in the *Stratigraphy* section above—fluvial deposits of material eroded and transported from the ancestral Elko highlands to the west.

| | Rock | Quartz | | | Plag | | Kspar | | Lithics | | Misc. | Clay | Cement | | | | Porosity | | | | Total | |
|---|---|---|---|---|---|---|---|---|---|---|---|---|---|---|---|---|---|---|---|---|---|---|
| Sample | Type | mono | poly | mic/ch | intact | diss | intact | diss | opaq | sed | Grains | Matrix | spar | mic | qtz | clay | inter | over | intra | micro | Points | IGV |
| 17B-2 | sand w/ matrix | 126 | 3 | 3 | 0 | 0 | 0 | 1 | 0 | 9 | 0 | 79 | 4 | 143 | 0 | 6 | 10 | 0 | 11 | 5 | 400 | 242 |
| | | 32% | 1% | 1% | 0% | 0% | 0% | 0% | 0% | 2% | 0% | 20% | 1% | 36% | 0% | 2% | 3% | 0% | 3% | 1% | | 61% |
| 17C-1 | sand | 177 | 6 | 6 | 0 | 0 | 1 | 0 | 1 | 12 | 2 | 0 | 183 | 0 | 0 | 7 | 0 | 0 | 2 | 3 | 400 | 190 |
| | | 44% | 2% | 2% | 0% | 0% | 0% | 0% | 0% | 3% | 1% | 0% | 46% | 0% | 0% | 2% | 0% | 0% | 1% | 1% | | 48% |
| 20A | sand | 234 | 7 | 17 | 0 | 0 | 0 | 0 | 0 | 4 | 0 | 0 | 27 | 4 | 30 | 6 | 49 | 5 | 14 | 3 | 400 | 116 |
| | | 59% | 2% | 4% | 0% | 0% | 0% | 0% | 0% | 1% | 0% | 0% | 7% | 1% | 8% | 2% | 12% | 1% | 4% | 1% | | 29% |
| 28A-1 | sand | 203 | 13 | 5 | 0 | 0 | 2 | 0 | 0 | 5 | 0 | 0 | 94 | 6 | 9 | 0 | 44 | 0 | 11 | 8 | 400 | 153 |
| | | 51% | 3% | 1% | 0% | 0% | 1% | 0% | 0% | 1% | 0% | 0% | 24% | 2% | 2% | 0% | 11% | 0% | 3% | 2% | | 38% |
| 35A-1 | sand | 240 | 9 | 6 | 3 | 3 | 2 | 2 | 0 | 3 | 1 | 0 | 1 | 0 | 17 | 16 | 64 | 8 | 22 | 3 | 400 | 98 |
| | | 60% | 2% | 2% | 1% | 1% | 1% | 1% | 0% | 1% | 0% | 0% | 0% | 0% | 4% | 4% | 16% | 2% | 6% | 1% | | 25% |
| 35B-1 | sand | 160 | 15 | 45 | 0 | 0 | 0 | 0 | 1 | 42 | 0 | 0 | 4 | 18 | 73 | 13 | 9 | 0 | 9 | 11 | 400 | 117 |
| | | 40% | 4% | 11% | 0% | 0% | 0% | 0% | 0% | 11% | 0% | 0% | 1% | 5% | 18% | 3% | 2% | 0% | 2% | 3% | | 29% |
| 71A | shaley matrix | 41 | 1 | 6 | 0 | 0 | 0 | 1 | 2 | 2 | 0 | 79 | 0 | 258 | 0 | 2 | 0 | 0 | 0 | 8 | 400 | 339 |
| | | 10% | 0% | 2% | 0% | 0% | 0% | 0% | 1% | 1% | 0% | 20% | 0% | 65% | 0% | 1% | 0% | 0% | 0% | 2% | | 85% |
| 71B | shaley matrix | 13 | 2 | 3 | 0 | 0 | 0 | 1 | 0 | 2 | 0 | 106 | 10 | 259 | 0 | 4 | 0 | 0 | 0 | 0 | 400 | 379 |
| | | 3% | 1% | 1% | 0% | 0% | 0% | 0% | 0% | 1% | 0% | 27% | 3% | 65% | 0% | 1% | 0% | 0% | 0% | 0% | | 95% |
| 72A | shale | 0 | 0 | 0 | 0 | 0 | 0 | 0 | 0 | 0 | 0 | 45 | 297 | 0 | 0 | 0 | 0 | 58 | 0 | 0 | 400 | 342 |
| | | 0% | 0% | 0% | 0% | 0% | 0% | 0% | 0% | 0% | 0% | 11% | 74% | 0% | 0% | 0% | 0% | 15% | 0% | 0% | | 86% |
| 72B | travertine | 38 | 0 | 30 | 0 | 0 | 0 | 0 | 0 | 23 | 0 | 125 | 7 | 149 | 0 | 10 | 14 | 0 | 0 | 4 | 400 | 305 |
| | | 10% | 0% | 8% | 0% | 0% | 0% | 0% | 0% | 6% | 0% | 31% | 2% | 37% | 0% | 3% | 4% | 0% | 0% | 1% | | 76% |
| 73 | sand w/ matrix | 139 | 4 | 8 | 0 | 1 | 0 | 0 | 0 | 0 | 1 | 133 | 0 | 108 | 0 | 6 | 0 | 0 | 0 | 0 | 400 | 247 |
| | | 35% | 1% | 2% | 0% | 0% | 0% | 0% | 0% | 0% | 0% | 33% | 0% | 27% | 0% | 2% | 0% | 0% | 0% | 0% | | 62% |
| 74 | sand | 223 | 5 | 9 | 0 | 0 | 1 | 1 | 0 | 1 | 0 | 0 | 65 | 34 | 0 | 16 | 40 | 0 | 4 | 1 | 400 | 155 |
| | | 56% | 1% | 2% | 0% | 0% | 0% | 0% | 0% | 0% | 0% | 0% | 16% | 9% | 0% | 4% | 10% | 0% | 1% | 0% | | 39% |
| 75-1 | sand w/ matrix | 144 | 3 | 14 | 0 | 0 | 0 | 0 | 0 | 3 | 0 | 65 | 12 | 154 | 0 | 4 | 0 | 0 | 0 | 1 | 400 | 235 |
| | | 36% | 1% | 4% | 0% | 0% | 0% | 0% | 0% | 1% | 0% | 16% | 3% | 39% | 0% | 1% | 0% | 0% | 0% | 0% | | 59% |
| 75-2 | sand w/ matrix | 116 | 6 | 4 | 0 | 0 | 1 | 0 | 0 | 1 | 0 | 30 | 8 | 218 | 0 | 16 | 0 | 0 | 0 | 0 | 400 | 272 |
| | | 29% | 2% | 1% | 0% | 0% | 0% | 0% | 0% | 0% | 0% | 8% | 2% | 55% | 0% | 4% | 0% | 0% | 0% | 0% | | 68% |

Table 3: Point count results from 25 map area samples.

mono: monocrystalline; poly: polycrystalline; mic/ch: microcrystalline/chert; spar: calcite spar; mic: micritic calcite; inter: intergranular; over: oversize; intra: intragranular; micro: microporosity; IGV: intergranular volume

| | Rock | Quartz | | | Plag | | Kspar | | Lithics | | Misc. | Clay | Cement | | | | Porosity | | | | Total | |
|---|---|---|---|---|---|---|---|---|---|---|---|---|---|---|---|---|---|---|---|---|---|---|
| Sample | Type | mono | poly | mic/ch | intact | diss | intact | diss | opaq | sed | Grains | Matrix | spar | mic | qtz | clay | inter | over | intra | micro | Points | IGV |
| 76 | sand | 201 | 12 | 21 | 1 | 2 | 5 | 3 | 0 | 3 | 1 | 0 | 139 | 0 | 0 | 7 | 4 | 0 | 0 | 1 | 400 | 150 |
| | | 50% | 3% | 5% | 0% | 1% | 1% | 1% | 0% | 1% | 0% | 0% | 35% | 0% | 0% | 2% | 1% | 0% | 0% | 0% | | 38% |
| 77 | sand | 231 | 8 | 20 | 0 | 1 | 2 | 5 | 0 | 3 | 0 | 0 | 9 | 5 | 9 | 9 | 74 | 5 | 9 | 10 | 400 | 106 |
| | | 58% | 2% | 5% | 0% | 0% | 1% | 1% | 0% | 1% | 0% | 0% | 2% | 1% | 2% | 2% | 19% | 1% | 2% | 3% | | 27% |
| 78A | sand | 238 | 8 | 9 | 1 | 1 | 0 | 0 | 0 | 14 | 0 | 0 | 60 | 3 | 9 | 3 | 34 | 3 | 14 | 3 | 400 | 109 |
| | | 60% | 2% | 2% | 0% | 0% | 0% | 0% | 0% | 4% | 0% | 0% | 15% | 1% | 2% | 1% | 9% | 1% | 4% | 1% | | 27% |
| 78B | sand | 248 | 7 | 14 | 0 | 2 | 1 | 5 | 0 | 2 | 0 | 0 | 29 | 3 | 6 | 7 | 60 | 0 | 15 | 1 | 400 | 105 |
| | | 62% | 2% | 4% | 0% | 1% | 0% | 1% | 0% | 1% | 0% | 0% | 7% | 1% | 2% | 2% | 15% | 0% | 4% | 0% | | 26% |
| 79 | sand | 254 | 8 | 11 | 1 | 6 | 0 | 0 | 0 | 15 | 0 | 0 | 9 | 9 | 4 | 3 | 59 | 1 | 16 | 4 | 400 | 84 |
| | | 64% | 2% | 3% | 0% | 2% | 0% | 0% | 0% | 4% | 0% | 0% | 2% | 2% | 1% | 1% | 15% | 0% | 4% | 1% | | 21% |
| 80A | sand | 247 | 16 | 12 | 1 | 5 | 2 | 2 | 0 | 18 | 0 | 0 | 0 | 6 | 24 | 16 | 30 | 7 | 12 | 2 | 400 | 76 |
| | | 62% | 4% | 3% | 0% | 1% | 1% | 1% | 0% | 5% | 0% | 0% | 0% | 2% | 6% | 4% | 8% | 2% | 3% | 1% | | 19% |
| 80B-1 | sand | 247 | 14 | 11 | 0 | 3 | 1 | 1 | 0 | 2 | 1 | 0 | 34 | 5 | 24 | 3 | 43 | 0 | 10 | 1 | 400 | 109 |
| | | 62% | 4% | 3% | 0% | 1% | 0% | 0% | 0% | 1% | 0% | 0% | 9% | 1% | 6% | 1% | 11% | 0% | 3% | 0% | | 27% |
| 82 | sand | 166 | 5 | 5 | 1 | 6 | 2 | 4 | 0 | 5 | 0 | 0 | 199 | 0 | 0 | 4 | 1 | 0 | 1 | 1 | 400 | 204 |
| | | 42% | 1% | 1% | 0% | 2% | 1% | 1% | 0% | 1% | 0% | 0% | 50% | 0% | 0% | 1% | 0% | 0% | 0% | 0% | | 51% |
| 84 | sand | 252 | 7 | 3 | 0 | 0 | 0 | 1 | 0 | 0 | 0 | 0 | 18 | 73 | 31 | 1 | 6 | 0 | 4 | 4 | 400 | 129 |
| | | 63% | 2% | 1% | 0% | 0% | 0% | 0% | 0% | 0% | 0% | 0% | 5% | 18% | 8% | 0% | 2% | 0% | 1% | 1% | | 32% |
| 85 | sand | 224 | 6 | 15 | 0 | 0 | 0 | 4 | 1 | 1 | 2 | 0 | 50 | 7 | 11 | 6 | 64 | 0 | 4 | 5 | 400 | 138 |
| | | 56% | 2% | 4% | 0% | 0% | 0% | 1% | 0% | 0% | 1% | 0% | 13% | 2% | 3% | 2% | 16% | 0% | 1% | 1% | | 35% |
| 86 | sand | 171 | 8 | 11 | 1 | 0 | 4 | 0 | 0 | 0 | 1 | 0 | 199 | 4 | 0 | 1 | 0 | 0 | 0 | 0 | 400 | 204 |
| | | 43% | 2% | 3% | 0% | 0% | 1% | 0% | 0% | 0% | 0% | 0% | 50% | 1% | 0% | 0% | 0% | 0% | 0% | 0% | | 51% |
| | Average: | 43% | 2% | 3% | 0% | 0% | 0% | 0% | 0% | 2% | 0% | 7% | 15% | 15% | 2% | 2% | 6% | 1% | 2% | 1% | | 46% |
| | Mode: | 62% | 2% | 1% | 0% | 0% | 0% | 0% | 0% | 1% | 0% | 0% | 0% | 0% | 0% | 2% | 0% | 0% | 0% | 0% | | 2% |

Table 3: Continued point count results from 25 map area samples.
mono: monocrystalline; poly: polycrystalline; mic/ch: microcrystalline/chert; spar: calcite spar; mic: micritic calcite; inter: intergranular; over: oversize; intra: intragranular; micro: microporosity; IGV: intergranular volume

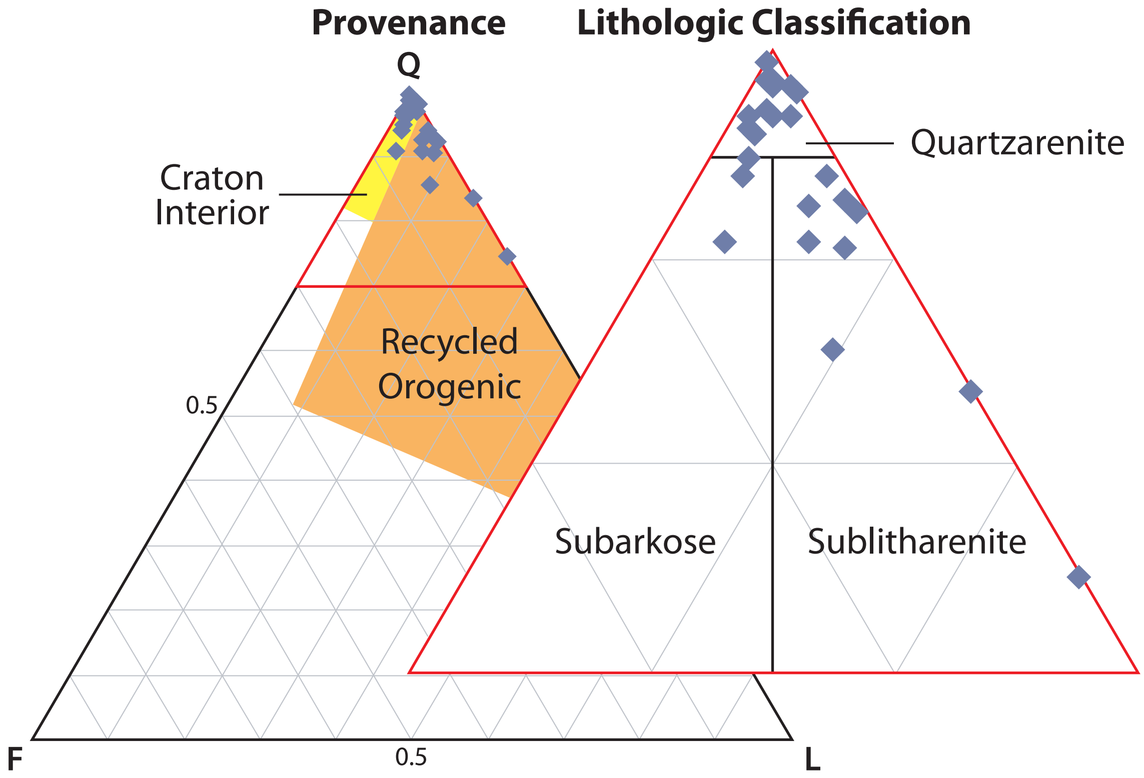

Figure 33: A quartz-feldspar-lithic plot shows samples are quartz-rich, with provenance from craton-interior mountains. Provenance after Dickinson et al. (1983) and Dickinson and Suczec (1979); lithologic classification after Folk (1980).

| Sample | Q | F | L |
|---|---|---|---|
| 17B-2 | 132 | 1 | 9 |
| 17C-1 | 189 | 1 | 15 |
| 20A | 258 | 0 | 4 |
| 28A-1 | 221 | 2 | 5 |
| 35A-1 | 255 | 10 | 4 |
| 35B-1 | 220 | 0 | 43 |
| 71A | 48 | 1 | 4 |
| 71B | 18 | 1 | 2 |
| 72A | 0 | 0 | 0 |
| 72B | 68 | 0 | 23 |
| 73 | 151 | 1 | 1 |
| 74 | 237 | 2 | 1 |
| 75-1 | 161 | 0 | 3 |

| Sample | Q | F | L |
|---|---|---|---|
| 75-2 | 126 | 1 | 1 |
| 76 | 234 | 11 | 4 |
| 77 | 259 | 8 | 3 |
| 78A | 255 | 2 | 14 |
| 78B | 269 | 8 | 2 |
| 79 | 273 | 7 | 15 |
| 80A | 275 | 10 | 18 |
| 80B-1 | 272 | 5 | 3 |
| 82 | 176 | 13 | 5 |
| 84 | 262 | 1 | 0 |
| 85 | 245 | 4 | 4 |
| 86 | 190 | 5 | 1 |

Table 4: Data used to populate the ternary plot above.

#### *2.2.1.2.2 Maturity*

A quartz-feldspar/lithic-matrix (Q-F/L-M) ternary plot (Figure 34) shows 16 out of 25 samples clustering around the quartz pole, with no matrix content and a grain component of 90% or more quartz. This indicates texturally and compositionally mature, mineralogically stable sandstones. Sample 35B-1 has the largest feldspar/lithic component (16%) due to 42 point-counted sedimentary lithic fragments, but also has no matrix. This indicates textural maturity with slightly less mineralogical stability due to the abundance of sedimentary lithics. The remaining 8 samples have matrix content of 19–100%, indicating lower textural maturity. Sample 72A, which shows 100% matrix, is a shale. Using a modified Dott classification (Boggs, 2009, after Williams et al., 1982, modified from Dott, 1964), which includes a matrix dimension to determine textural maturity, the 4 samples with matrix content of 5–49% are defined as quartz wackes (samples 17B-2, 73 75-1 and 75-2). The other 4 samples (71A, 71B, 72A and 72B) have 50–100% matrix and are defined in the modified Dott classification as mudstones, although it will be shown later that 71A, 71B and 72A are travertines. The Q-F/L-M data used to make Figure 34 are included in Table 5.

#### *2.2.1.2.3 Quartz*

The most abundant grains are quartz, commonly monocrystalline but also present as polycrystalline or microcrystalline and chert grains. The average total quartz for all point-counted samples is 48%; in sandstones the average is 60%.

Monocrystalline grains show no signs of dissolution. In many samples, however, some grains have a blue tinge and somewhat spongy texture (Figure 35); this is a sign of dissolution, the tinge resulting from impregnation of tiny dissolution features with blue-stained epoxy. Although these grains are unidentifiable in plane-polarized light, in cross-polarized light they often have the appearance of microcrystalline quartz—many small crystals with low birefringence and no axial alignment. Energy dispersive spectroscopy on

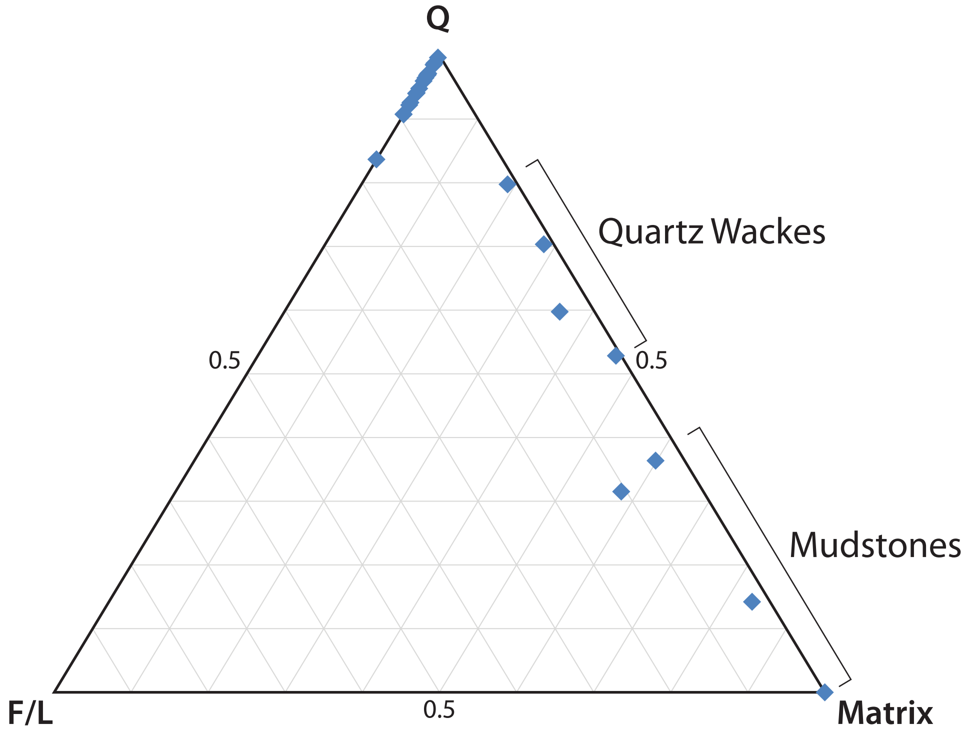

Figure 34: A quartz-feldspar/lithic-matrix plot shows significant matrix component in eight samples, making them quartz wackes and mudstones, according to the Dott classification system. Sample 72A (with 100% matrix) is a shale.

| Sample | Q | F+L | Matrix |
|---|---|---|---|
| 17B-2 | 132 | 10 | 79 |
| 17C-1 | 189 | 16 | 0 |
| 20A | 258 | 4 | 0 |
| 28A-1 | 221 | 7 | 0 |
| 35A-1 | 255 | 14 | 0 |
| 35B-1 | 220 | 43 | 0 |
| 71A | 48 | 5 | 79 |
| 71B | 18 | 3 | 106 |
| 72A | 0 | 0 | 45 |
| 72B | 68 | 23 | 125 |
| 73 | 151 | 2 | 133 |
| 74 | 237 | 3 | 0 |
| 75-1 | 161 | 3 | 65 |

| Sample | Q | F+L | Matrix |
|---|---|---|---|
| 75-2 | 126 | 2 | 30 |
| 76 | 234 | 15 | 0 |
| 77 | 259 | 11 | 0 |
| 78A | 255 | 16 | 0 |
| 78B | 269 | 10 | 0 |
| 79 | 273 | 22 | 0 |
| 80A | 275 | 28 | 0 |
| 80B-1 | 272 | 8 | 0 |
| 82 | 176 | 18 | 0 |
| 84 | 262 | 1 | 0 |
| 85 | 245 | 8 | 0 |
| 86 | 190 | 6 | 0 |

Table 5: Data used to populate the ternary plot above.

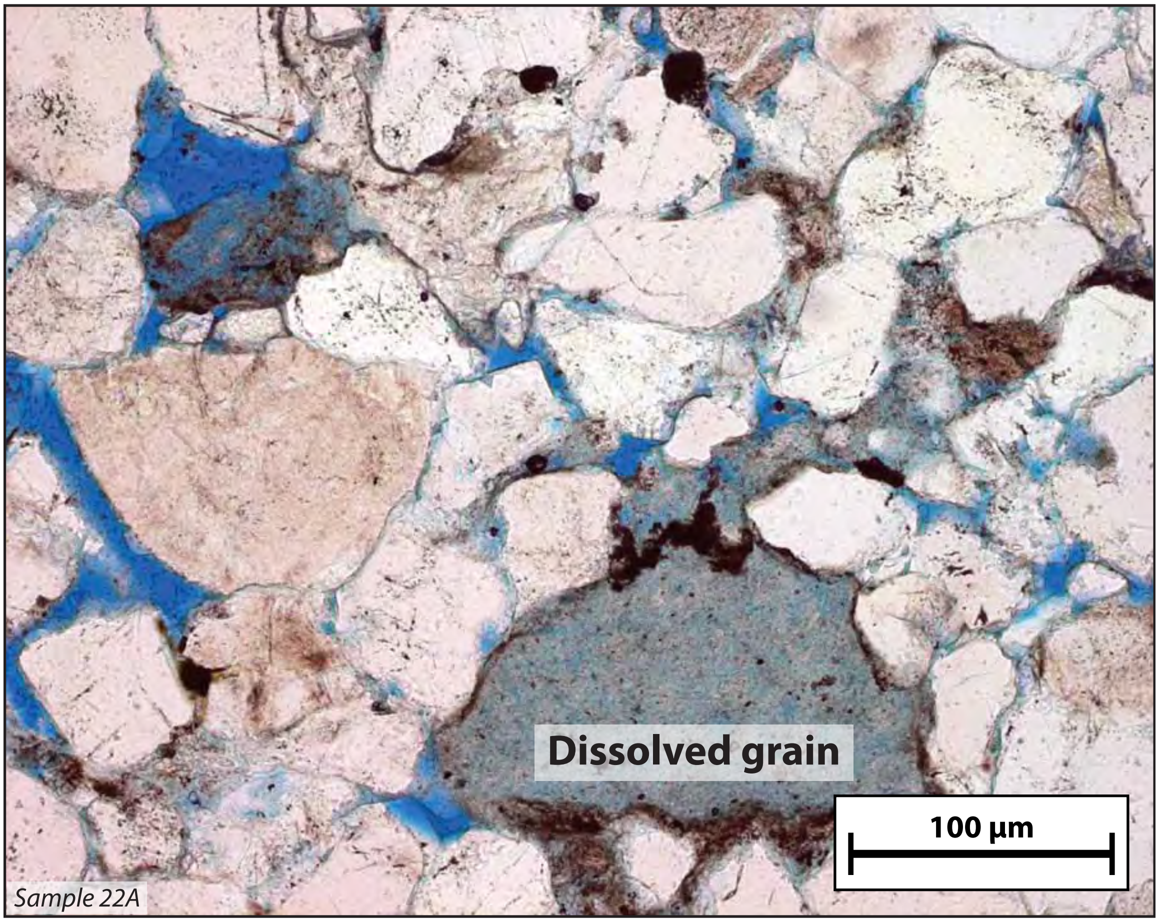

Figure 35: A dissolved grain appears spongy and green-to-blue in plane polarized light.

intact parts of these grains shows that they are composed of silicon and oxygen, suggesting that they are quartzose (Figure 36). This could indicate that these grains once had softer components, such as clays, which have since dissolved, leaving behind a quartzose framework. Evidence for this hypothesis exists in the widespread presence of partially dissolved sedimentary lithic grains, which are composed of a mixture of fine-grained quartz in a muddy matrix (Figure 37). Alternately, the texture could result from partial dissolution of chert or microcrystalline quartz grains. This would be surprising, however: Although these grains have many particle boundaries that might facilitate dissolution (Figure 37), other intact quartz grains have few signs of even minor dissolution. If some quartz grains had been extensively dissolved, other grains in the same sample would be expected to show similar, if less extensive, signs of diagenesis.

#### ***2.2.1.2.4 Feldspars***

Feldspars are not abundant in these samples: The maximum combined percentage of intact and dissolved plagioclase and alkali feldspars is 4%; the mode for both phases and both textures is 0%. Most feldspar grains in these samples are at least partially dissolved. Any feldspar showing obvious dissolution features (ragged edges or intragranular porosity) was counted as a "Dissolved Feldspar." Extent of dissolution was not recorded, so grains with only minor dissolution were counted in the same category as those with advanced dissolution. This insensibility to subtle distinction is somewhat attenuated, however, as any points landing on intragranular porosity (i.e., dissolved portions of a feldspar) were tallied as porosity, not as feldspars. Greater feldspar dissolution is therefore indirectly represented by greater intragranular porosity and microporosity. This method of counting underrepresents original feldspar abundance,

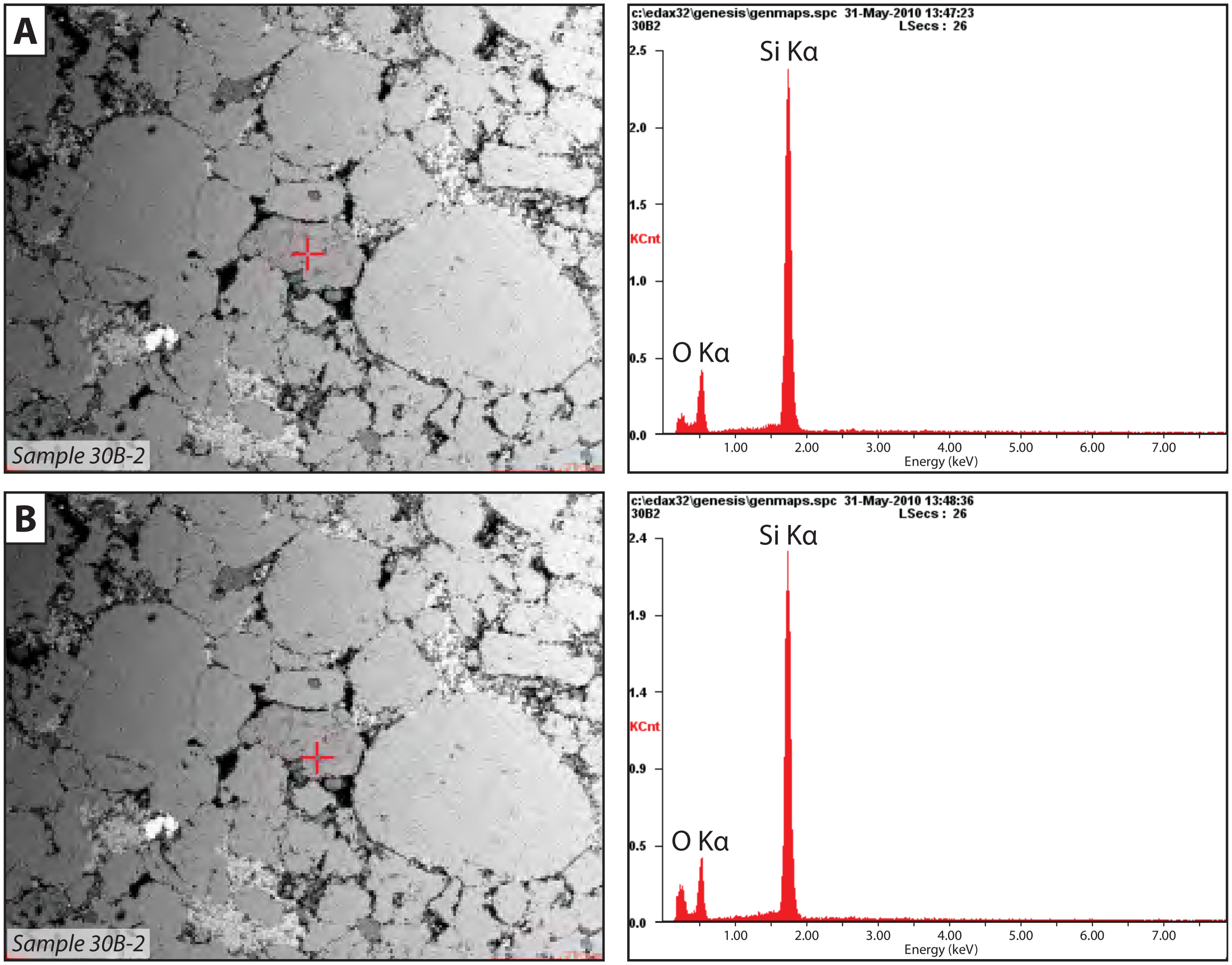

Figure 36: **A–B:** Analysis of points on a partially dissolved, spongy-looking grain using energy dispersive spectroscopy show that the remaining portions are composed of silicon and oxygen.

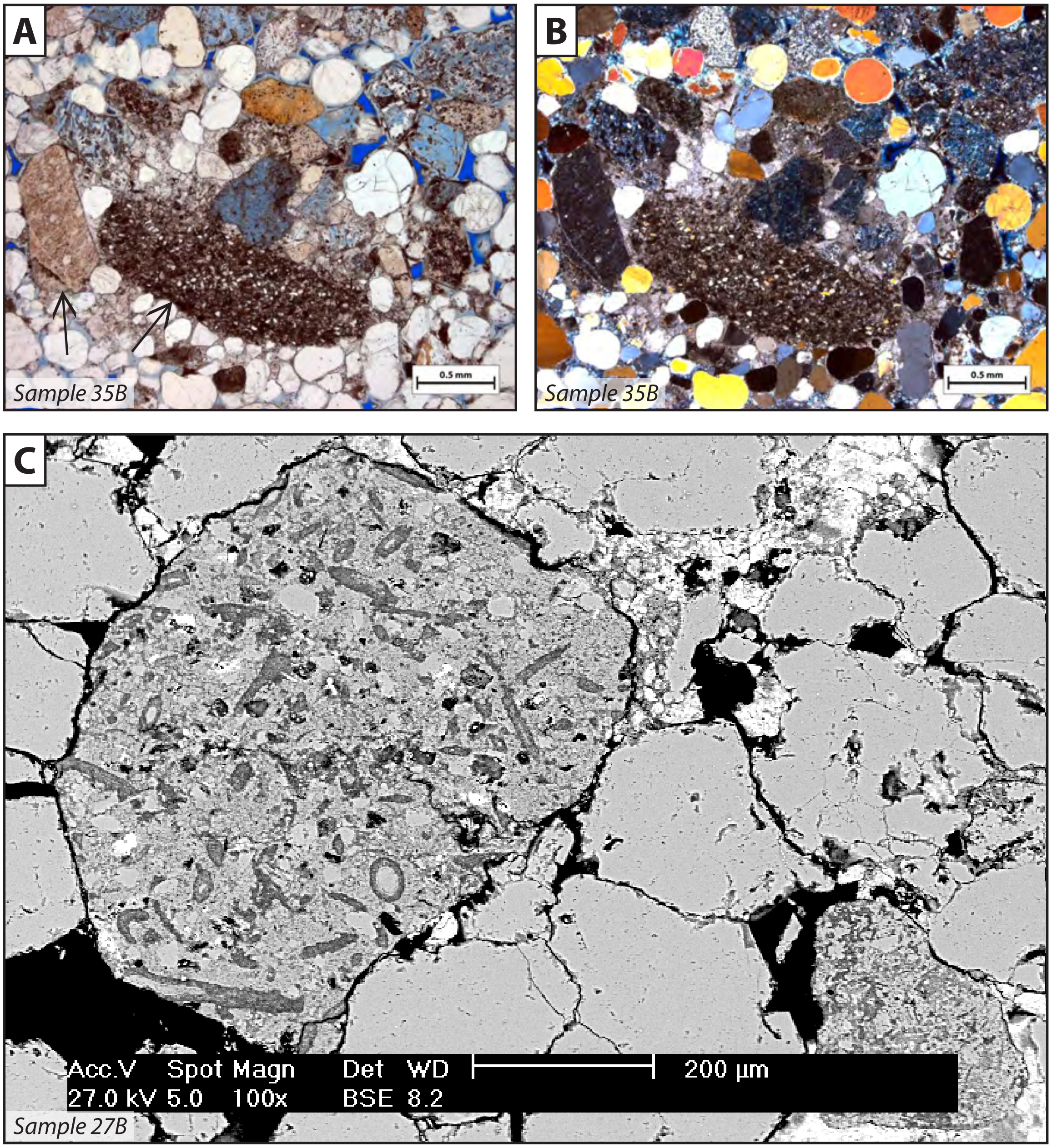

Figure 37: **A–B:** Sedimentary lithic grains (arrows) composed of small quartz fragments in a muddy matrix. These may be analogous to the pre-dissolution composition of grains such as the one in Figure 35. (The unusually high birefringence of quartz is due to a thicker-than-usual slide.) **C:** A backscatter electron image of a chert grain shows the many tiny particle boundaries that could act as spots of weakness for dissolution.

but correctly characterizes the current state of diagenesis, which is the focus of this project.

While most feldspars in these samples are at least partially dissolved, one sample (26-1) with virtually no remaining porosity due to calcite cementation has nearly pristine feldspars (Figure 38). This appears to show that the cement prevented dissolution reactions by acting as a shield (against, for example, silicate hydrolysis in the presence of acidic water). This does not indicate that seep-formed calcite has shielded the host rock from acidic spring water, however, as calcite in this sample appears to be burial-related—unassociated with $CO_2$ and predating the $CO_2$ seep (see *Discussion* for an explanation of this).

#### ***2.2.1.2.5 Opaque lithics***

Opaque lithics are rare, never comprising even 1% of these samples (and below the 2.5% margin of error from counting 400 points). Electron microscopy was the primary means of identifying opaque lithic grains, as they have few distinguishing features in optical microscopy. In backscatter electron imaging many appear bright white (Figure 39), meaning they are composed of heavy elements. Energy dispersive spectroscopy shows that these grains are often rich in iron, platinum, sulfur, and titanium or barium. Samples with a high proportion of titanium and iron are likely ilmenite (Figure 40). Because these grains are rare and not apparently diagenetic in nature, however, no great measures were taken to identify specific minerals.

#### ***2.2.1.2.6 Sedimentary lithics***

Sedimentary lithics are relatively abundant compared to other grain types, with a mode of 1% and often composing up to 4% of a sample. They are predominantly clay-rich. The most common are recycled fragments of shale and grains composed of a mixture

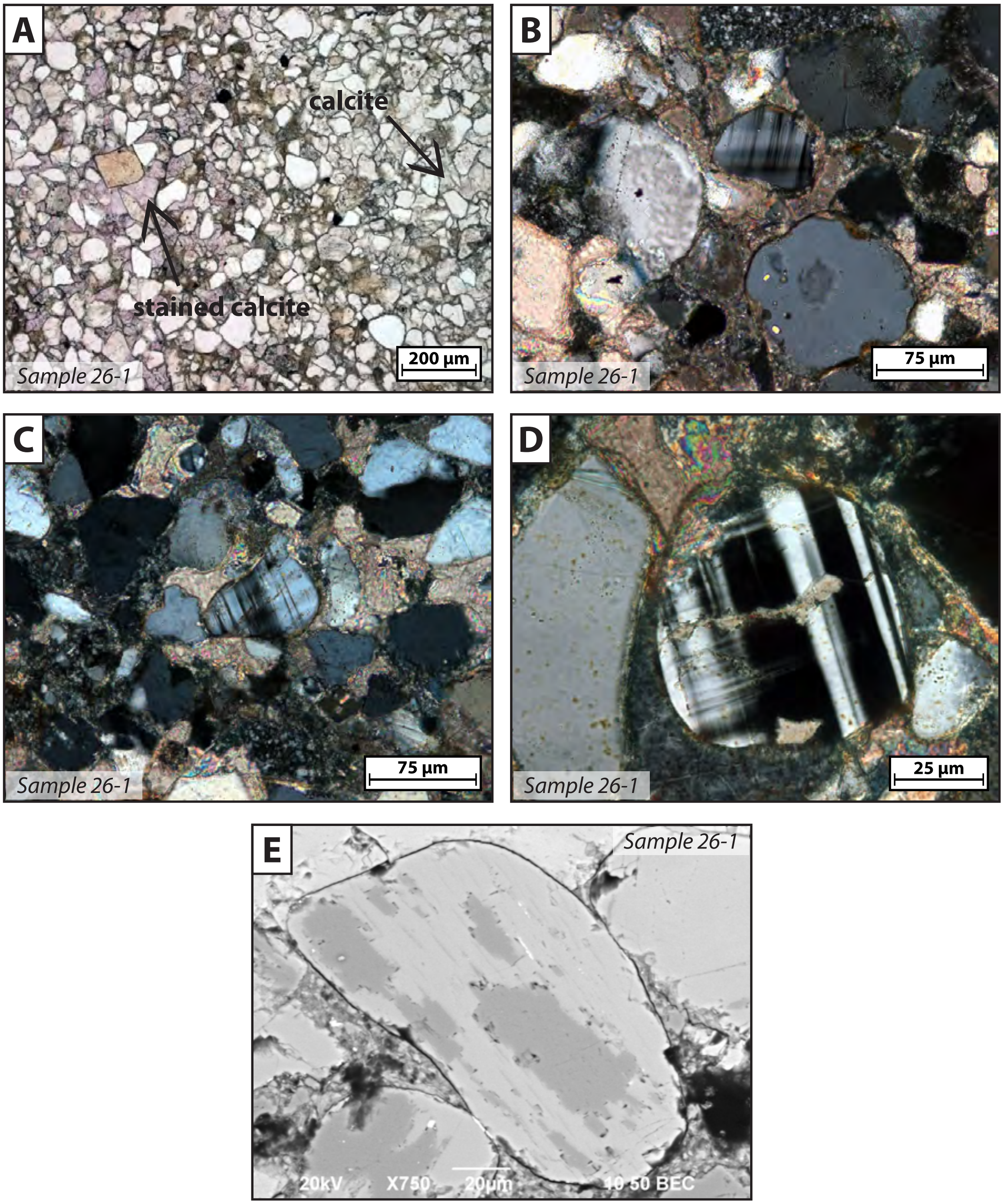

Figure 38: **A:** Samples from station 26 show nearly total porosity occlusion by calcite cement. **B–D:** Feldspars in these samples are better preserved than in other samples. **E:** The high resolution of a backscatter electron image of an alkali feldspar illustrates the high level of preservation.

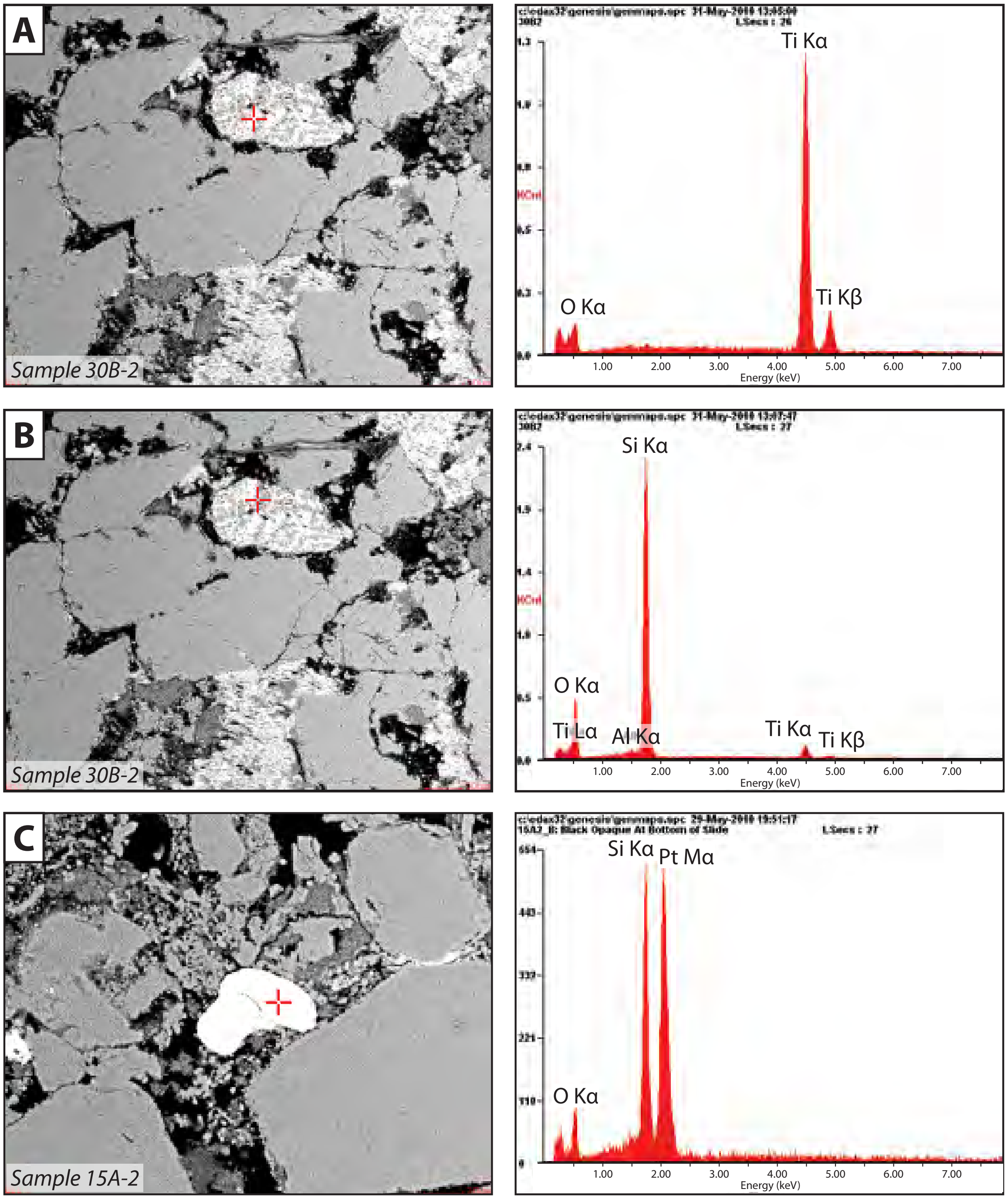

Figure 39: **A:** An opaque grain shows up brightly in backscatter electron mode due to heavy-element components. EDS shows it is composed in large part of titanium. **B:** The lighter regions are silicon-rich. **C:** Another opaque grain of more uniform composition contains a high proportion of platinum.

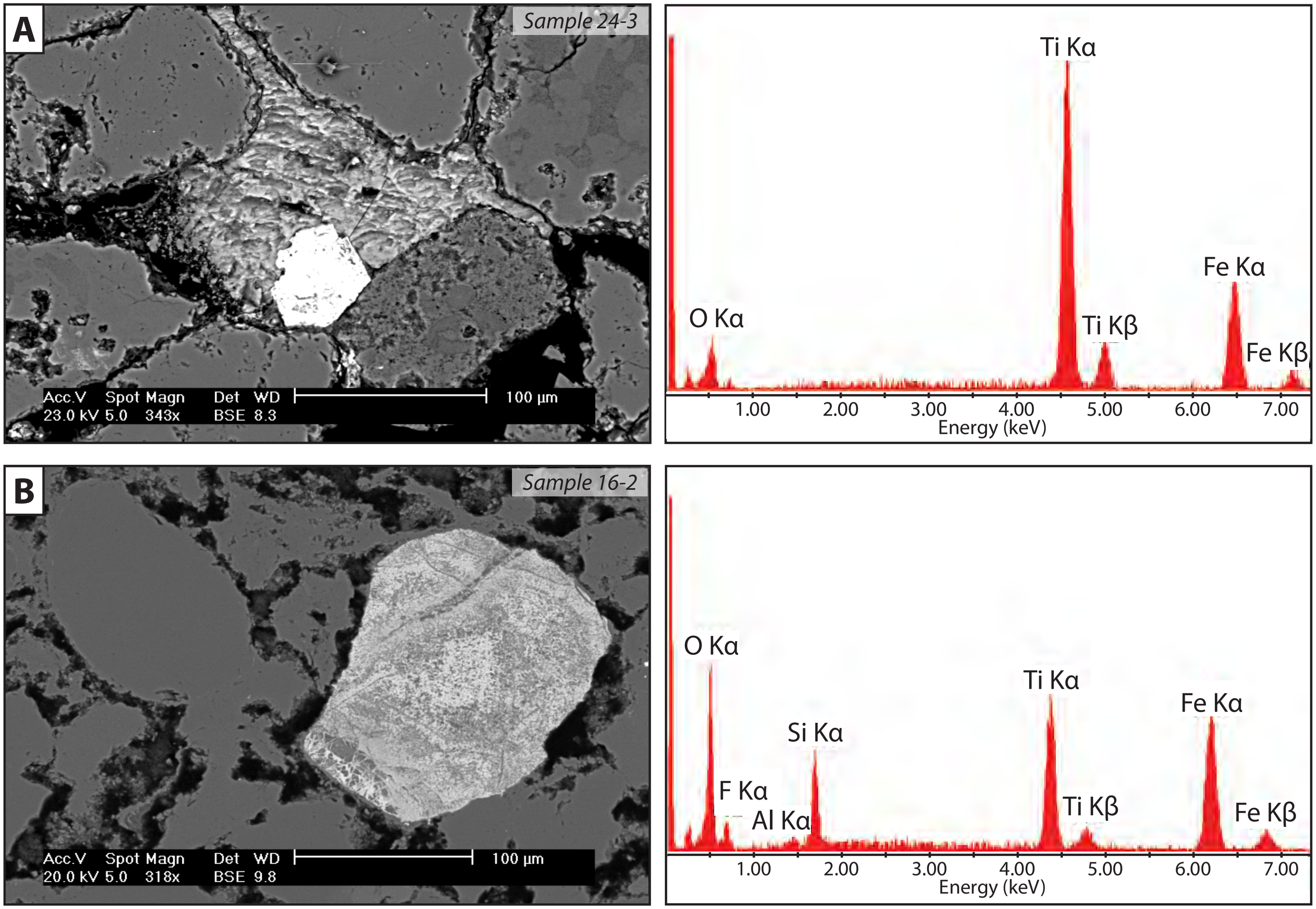

Figure 40: **A:** Backscatter electron image and EDS spectrum of an opaque lithic grain; it is composed in large part of iron and titanium, which indicates it may be ilmenite ($FeTiO_3$). **B:** Another opaque grain with similar composition.

of clay and silt-sized quartz particles (Figure 37). Recycled carbonate grains are another type, but these are less common.

The clay-rich grains are apparently soft, being in places impacted by other grains. In many instances they are also partially dissolved, sometimes almost entirely. In these cases, although there is evidence for the former presence of sedimentary lithics, the point count process is designed to count the pores, and the grains are therefore unrecorded.

#### *2.2.1.2.7 Miscellaneous grains*

Miscellaneous grains include those that could not be identified as well as those that could be identified but which were not sufficiently abundant to justify a unique category (Figure 41). Miscellaneous grains are rare: The average number counted was 0.3 per slide, with a mode of 0. Such a low number of uncategorized points indicates a satisfactory level of overall positive grain identification. Among the identifiable grains, zircons are common. They stand out well due to their high birefringence and high relief.

#### *2.2.1.2.8 Matrix: clay and micrite*

Matrix material is absent in most samples, the intergranular volumes of which are typically comprised of variable proportions of porosity and cement, but a few samples (17B-2, 71A, 71B, 73 and 75) do contain a pervasive matrix. In these samples it forms as much as 92% of the rock, with an average of 69%.

In plane-polarized light this matrix tends to be dark red or brown with a fine-grained, shale-like appearance (Figure 42). Cross-polarized light reveals a more mottled appearance: dark red, nearly opaque patches intermixed with brighter patches of relatively high birefringence microcrystalline material having the appearance of micrite (Figure 42). Energy dispersive spectroscopy shows that these bright patches are composed of the component elements of calcite (Ca, C and O), and the signal produced by this material is

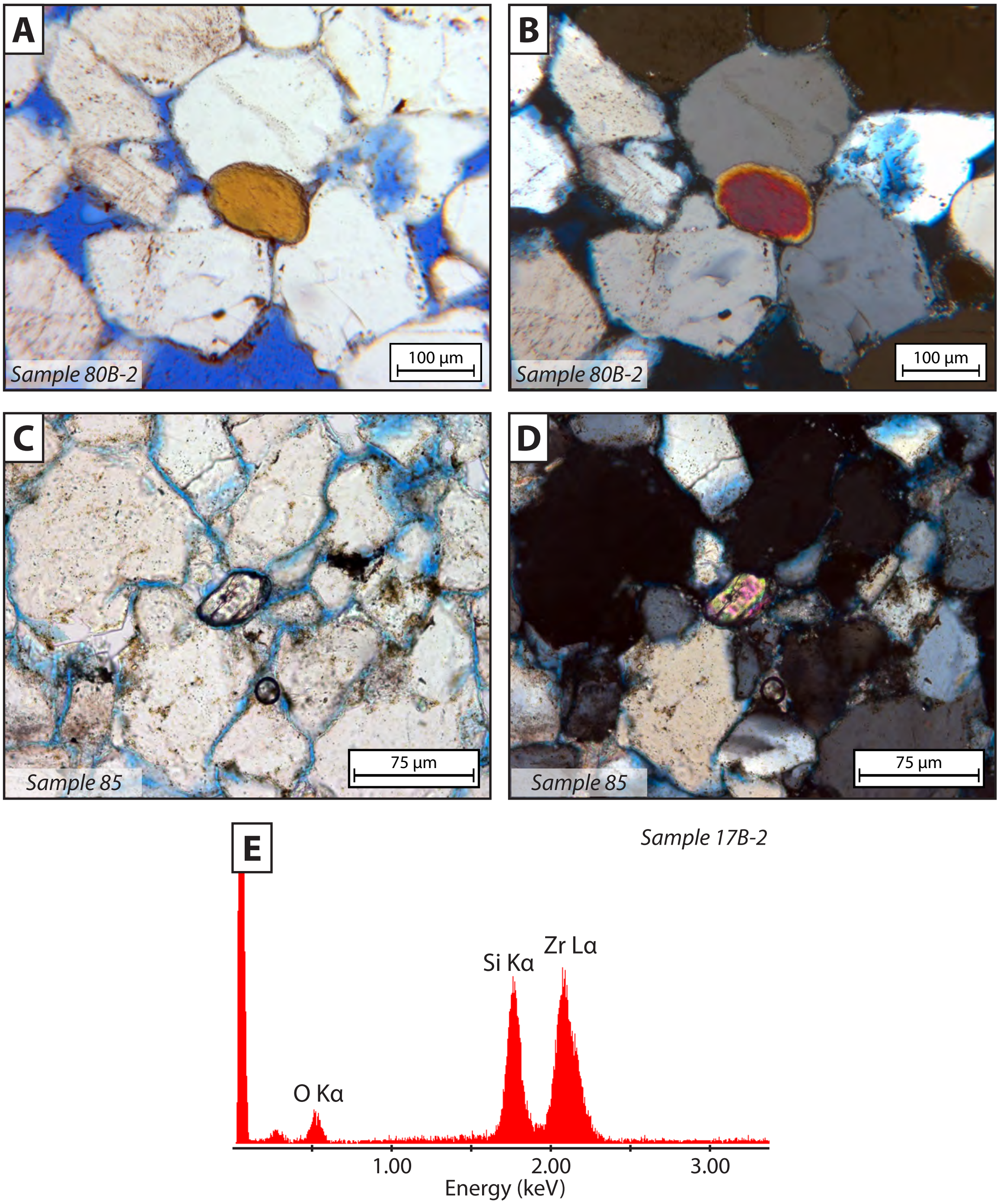

Figure 41: **A–B:** Photomicrographs of an unidentified grain. **C–D:** Photomicrographs of a high-relief, high-birefringence grain. **E:** The elemental composition of grains such as (C–D) is consistent with the chemical formula for zircon ($ZrSiO_4$).

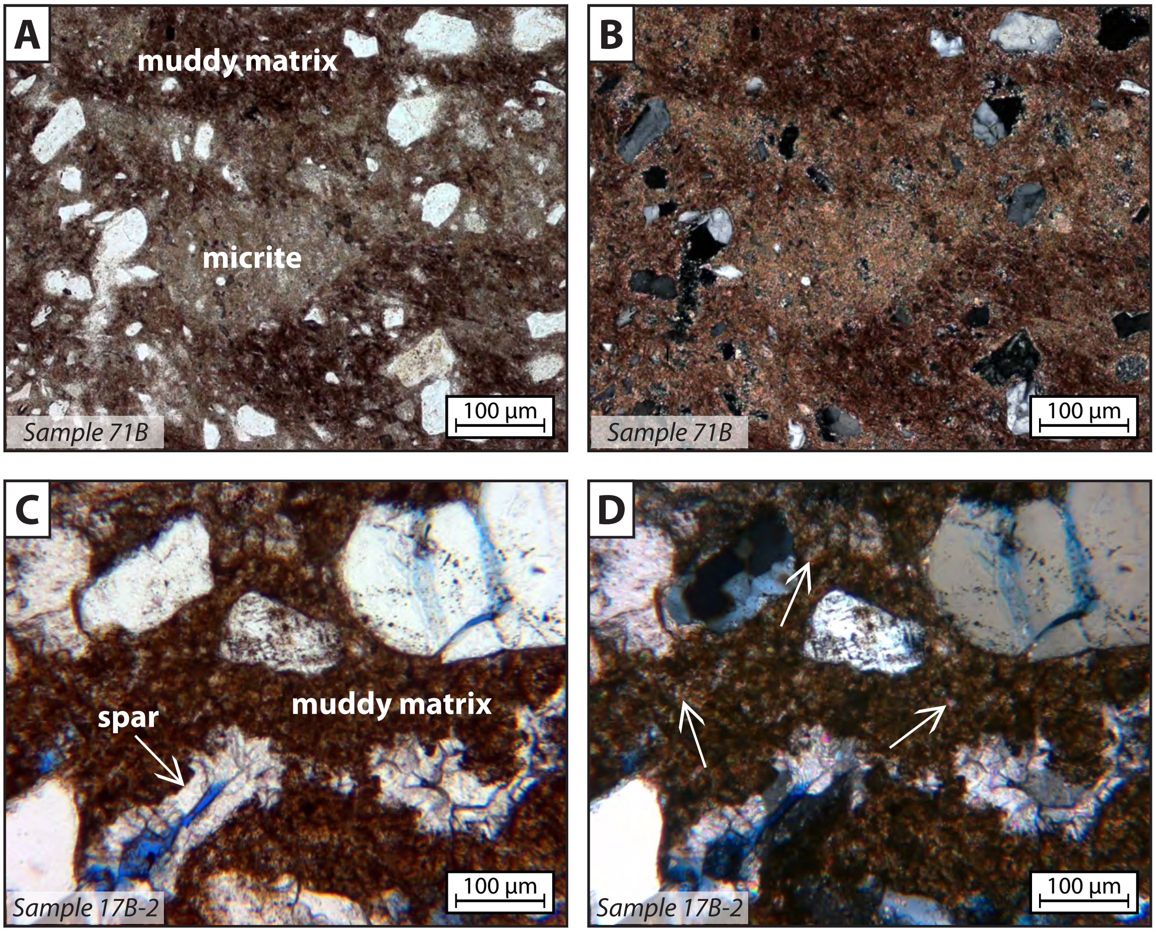

Figure 42: **A–D:** Plane light and crossed-polars photomicrographs of microcrystalline matrix suggest that it is composed of a mixture of clay (dark red) and micrite (bright, high-birefringence). (A) and (B) have a high proportion of micrite compared to (C) and (D), in which the matrix is dominated by muddier sediment.

virtually identical to that produced by euhedral calcite spar, confirming that it is micrite (Figure 43).

#### *2.2.1.2.9 Calcite cement: spar and micrite*

Calcite cement (spar and micrite) is abundant in these samples. The average total percentage of point-counted calcite is 29%. The amount of calcite is significantly higher near the travertine than it is elsewhere in the map area, however. Total calcite abundance begins to increase at a distance of less than 35 m from the travertine mound (Figure 44). The average for samples at distances closer to the travertine than 35 m is 45%, while the average for samples farther away is only 15%. Micrite shows an especially sharp spike with close proximity to the travertine: Farther away than 25 m, micrite content hovers around 1–5%; at closer range it averages 32% and reaches as high as 65%. Two more distant samples—samples 82 and 86, at 84 m and 98 m, respectively—have a higher-than-usual amount of spar content for their distance (50% and 51%, respectively). These data do not expand the radius at which calcite begins to systematically increase, however, as isotope data show that they are not seep-related cement (see *Discussion*). With the exception of these points, all samples farther than 35 m have less than 25% calcite content, and most have less than 10%.

Additional calcite abundance data were provided by signal calibration measurements made at the Stanford University School of Earth Sciences (Table 6). These data reiterate the same trends seen in point counting (Figure 45): high calcite content near the travertine (average: 37%), but greatly diminished at distances farther than that (average: 7%).

Calcite spar is in general distinctive and easy to identify, although it could be difficult to differentiate from dolomite. The combined Alizarin Red S and potassium ferricyanide stain applied to some slides stains calcite red or pink and leaves dolomite unstained. A ferrous component will cause calcite to stain purple to blue and dolomite blue (Evamy, 1963;

| Sample | Meters to travertine | Weight (µg) | Sig. strength (Vsec) | Wt. % $CaCO_3$ |
|---|---|---|---|---|
| 71A | 2 | 382 | 20.7 | 51 |
| 71B | 1 | 328 | 20.2 | 58 |
| 71B | 1 | 332 | 20.0 | 56 |
| Avrg. | 1 | 330 | 20.1 | 57 |
| 72A | 0 | 293 | 23.0 | 73 |
| 72B | 0 | 352 | 22.3 | 59 |
| 73 | 3 | 393 | 12.7 | 30 |
| 74 | 15 | 462 | 11.3 | 23 |
| 74 | 15 | 787 | 17.1 | 20 |
| Avrg. | 15 | 625 | 14.2 | 22 |
| 75 | 19 | 517 | 21.1 | 38 |
| 76 | 33 | 602 | 19.4 | 30 |
| 77 | 124 | 3,052 | 9.7 | 3 |
| 78A | 159 | 1,927 | 19.1 | 9 |
| 78B | 162 | 1,256 | 12.7 | 9 |
| 79 | 287 | 12,836 | 29.6 | 2 |
| "99" | 287 | 11,666 | 21.6 | 2 |
| "99" | 287 | 12,655 | 23.3 | 2 |
| Avrg. | 287 | 12,386 | 24.9 | 2 |
| 80A | 360 | 9,570 | 16.0 | 2 |
| 80B | 358 | 2,117 | 14.6 | 6 |
| 80B | 358 | 2,100 | 9.4 | 4 |
| Avrg. | 358 | 2,109 | 12.0 | 5 |
| 83 | 54 | 2,365 | 15.9 | 6 |
| 84 | 23 | 985 | 13.9 | 13 |
| "98" | 23 | 1,462 | 22.0 | 14 |
| Avrg. | 23 | 1,224 | 18.0 | 14 |
| 85 | 77 | 2,033 | 22.4 | 10 |
| 86 | 98 | 384 | 16.9 | 41 |

Table 6: Weight-percent calcite data collected via mass spectrometry signal strength calibration at the Stanford University School of Earth Sciences.

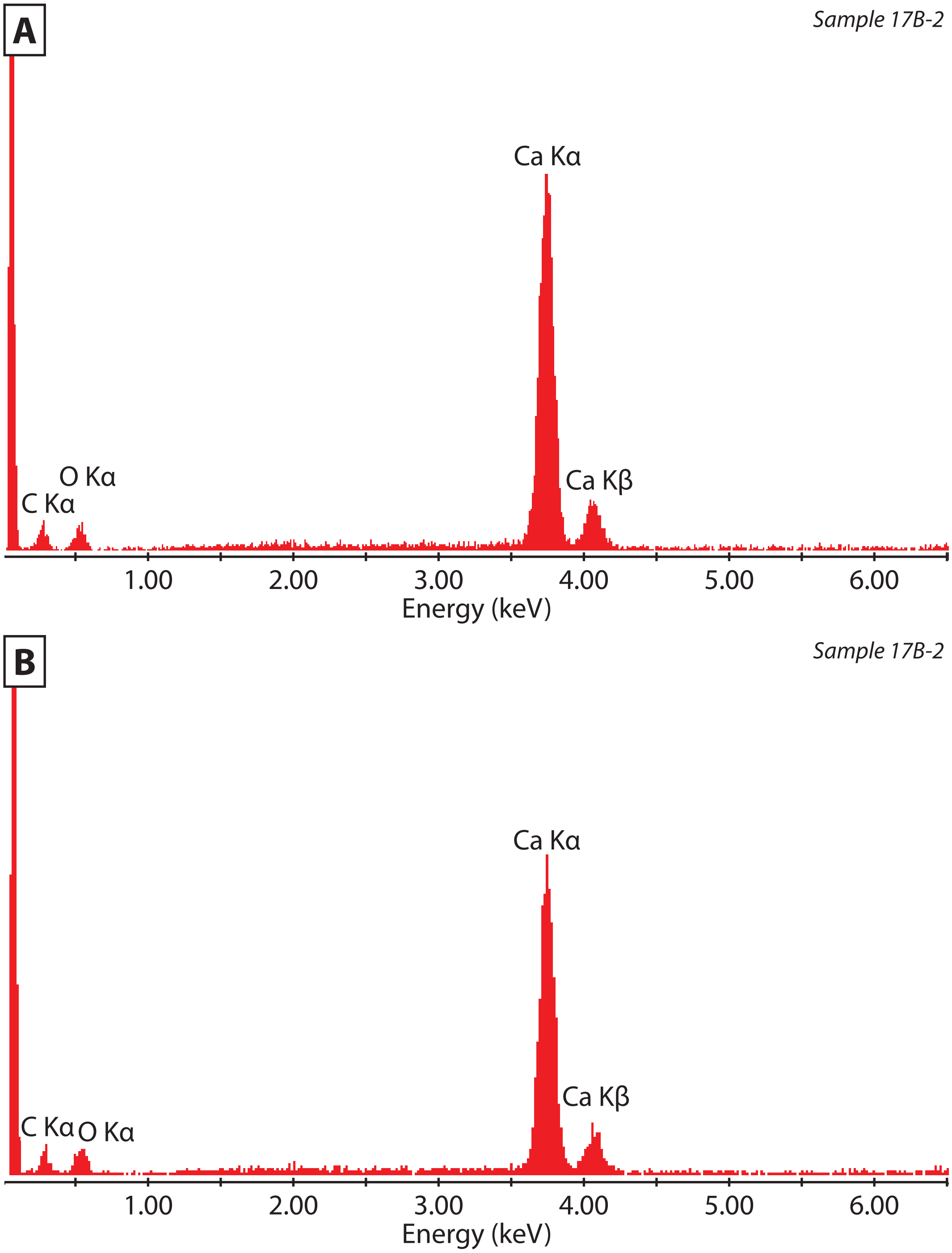

Figure 43: **A:** EDS signal from a euhedral calcite crystal. **B:** EDS signal from the bright, high-birefringence matrix material. It is identical to the euhedral calcite and confirms that this material is micrite.

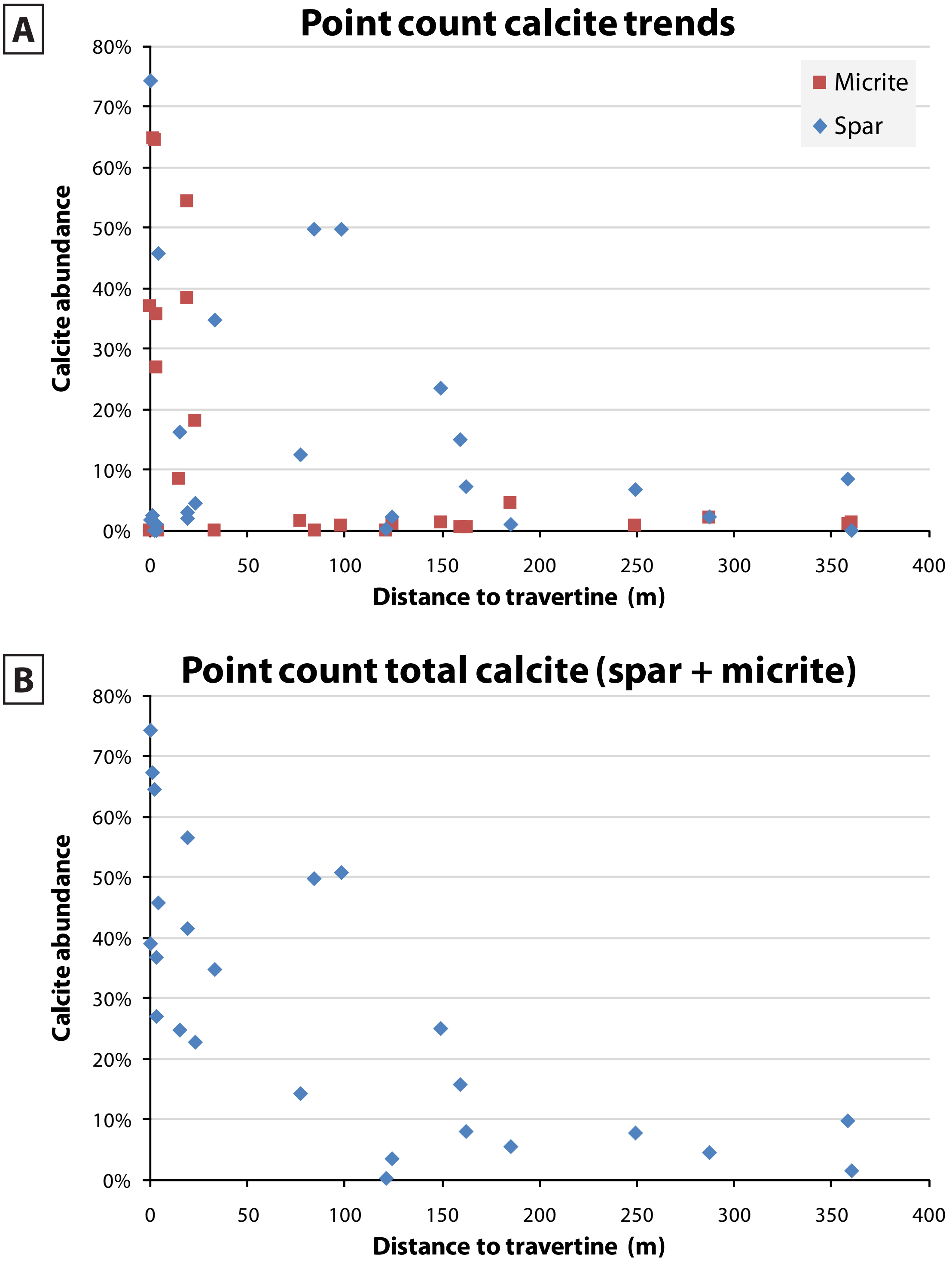

Figure 44: **A:** Both calcite spar and micrite increase with close proximity to the travertine. **B:** The same data, combined to show total calcite.

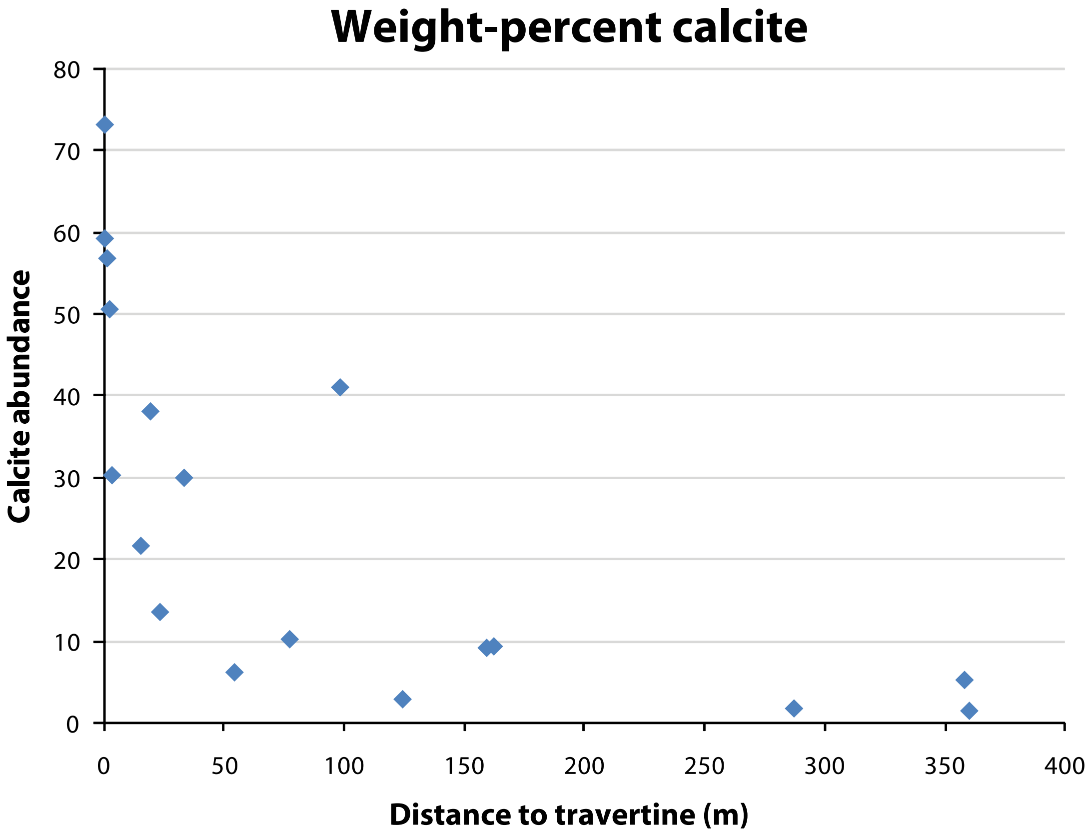

Figure 45: Weight-percent calcite data show much the same trend as point count data: low percentages of calcite abundance throughout most of the map area but a steep increase near the travertine.

Lindholm and Finkelman, 1972). Although carbonates in most stained samples turned uniformly pink, samples 17C-2, 78A, 79 and 87 include small regions of blue-to-purple stain, indicating the presence of either ferroan calcite or dolomite (Figure 46). In samples 17C-2 and 79, the stain highlights sharp boundaries within calcite that appear to show distinct generations of ferroan and non-ferroan cement. It is difficult to make the mineralogical distinction based solely on shades of blue, but this is most likely ferroan calcite: If it were ferrous dolomite, there would likely be non-ferrous dolomite present as well, but no carbonates failed to take a stain. X-ray diffraction data presented later also show that no dolomite is detectable in these samples. If it is ferroan calcite, the purple-blue color indicates that it likely contains 2.5–3.5% FeO (Lindholm and Finkelman, 1972).

#### *2.2.1.2.10 Quartz cement*

Quartz cement is common in Salt Wash Member sandstones and likely accumulated during the burial history of the rocks. Typical quartz overgrowths appear in 11 of the 17 sandstone samples that were point-counted. In those 11 samples, quartz cement averages 4%, with a maximum of 8%. In most cases quartz cement is in the form of large (grain-scale), optically aligned, euhedral quartz overgrowths (Figure 47).

One sample from the $J_{ms}4$ marker sandstone, however, contains abundant (18%) length-fast chalcedonic cement in the form of isopachous rims coating all grain types (sample 35B; Figure 48). This is a precipitate often associated with hydrothermal settings (Simonson, 1987), although there are no indications here of anomalous heat flow or hydrothermal activity. Its microcrystalline, non-euhedral habit indicates that it may have precipitated rapidly, which would be possible under highly silicic conditions where source material was readily available (Lander et al., 2008; personal communication: Milliken, 2011). Such precipitation would not require the high temperature (76–140°C) commonly associated

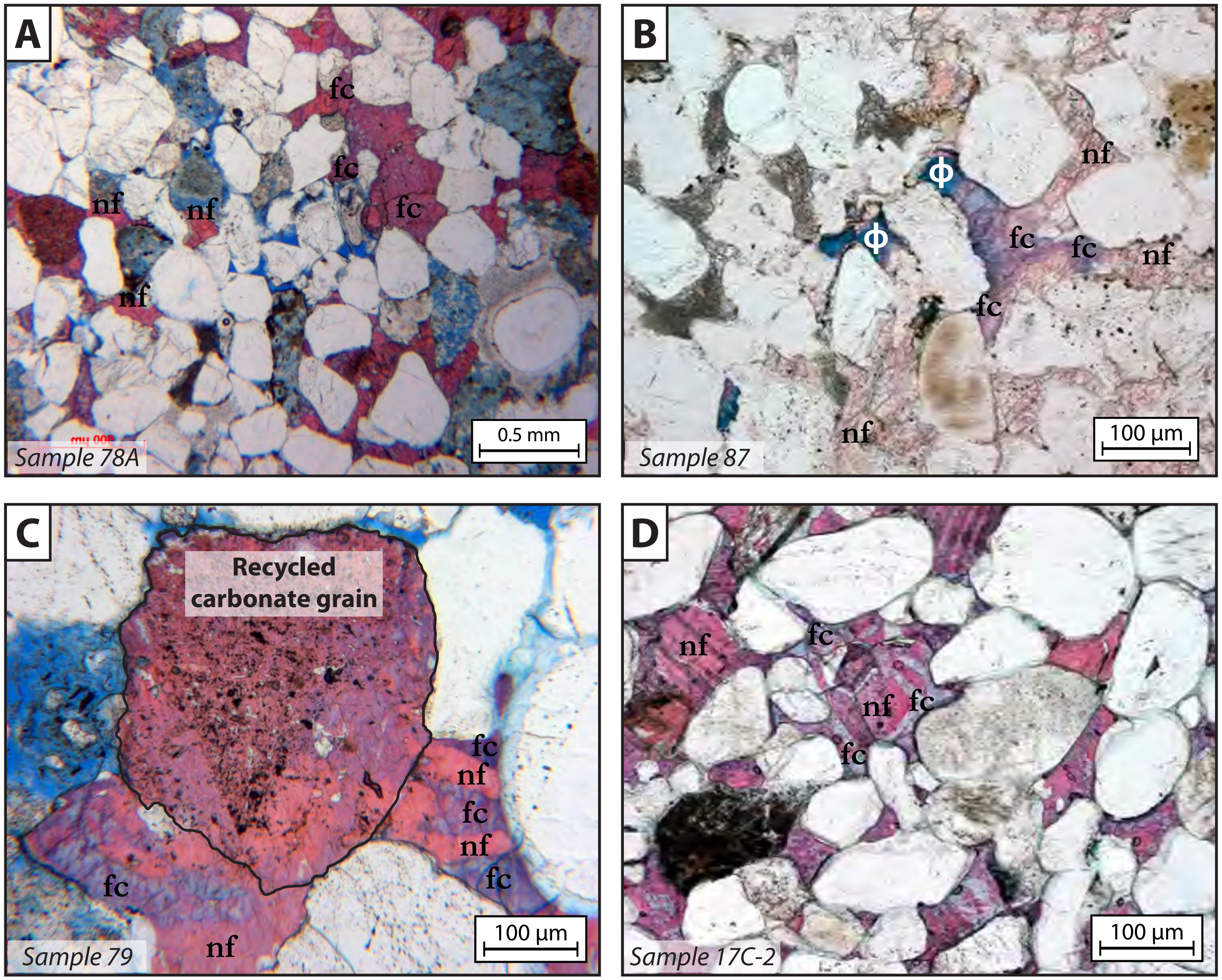

Figure 46: **A–B:** Ferroan calcite (fc) and non-ferroan calcite (nf) in sandstones. **C–D:** Sharp boundaries between purple- and pink-stained calcite appear to indicate distinct generations of ferroan and non-ferroan cement. (C) contains a large recycled carbonate grain; ϕ: porosity.

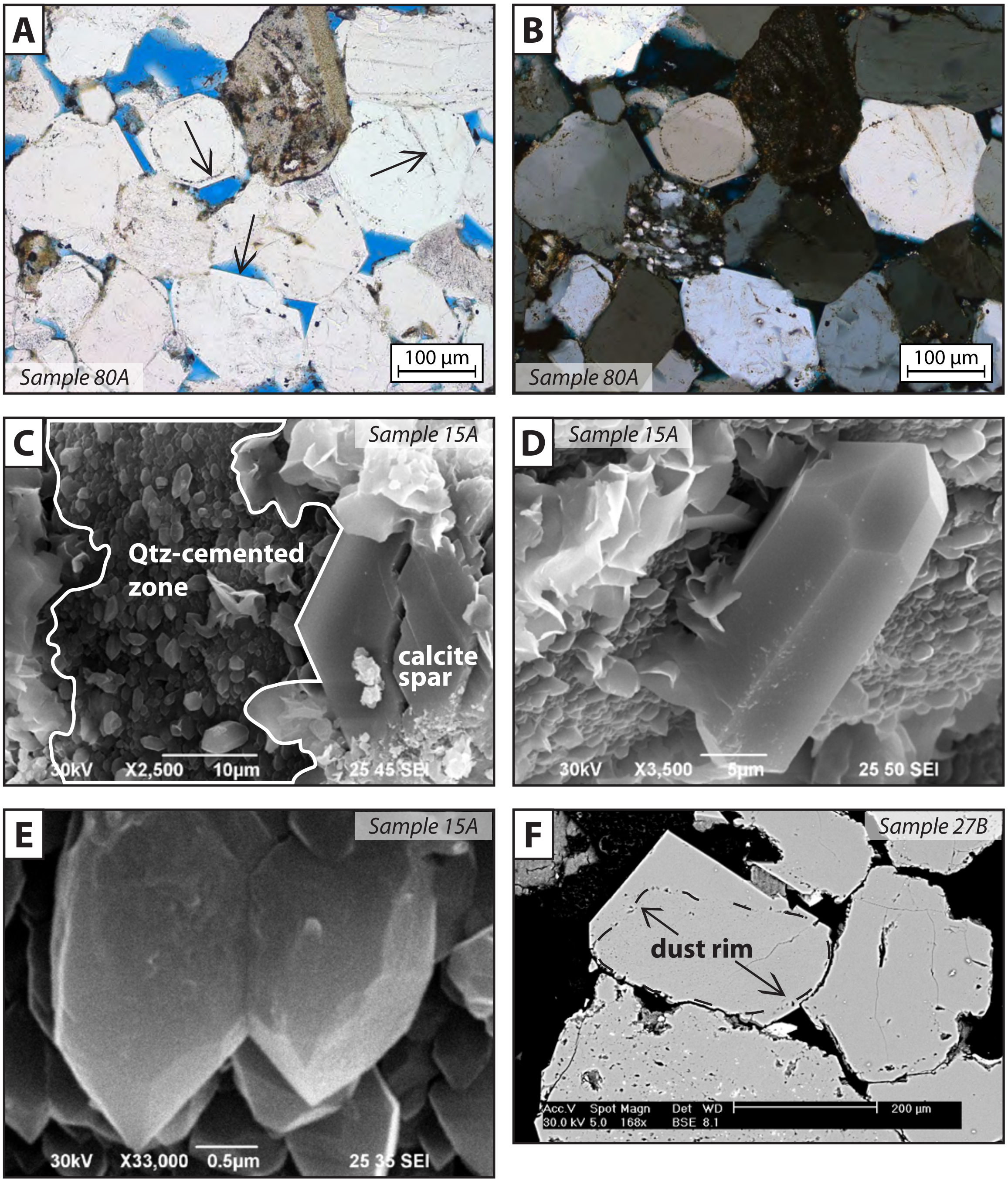

Figure 47: **A–B:** Euhedral quartz overgrowths, easily identified by their sharp edges and dust rims. **C–E:** Secondary electron images of euhedral quartz cement at increasing magnifications. **F:** Backscatter electron imaging captures the sharp edges typical of many quartz overgrowths.

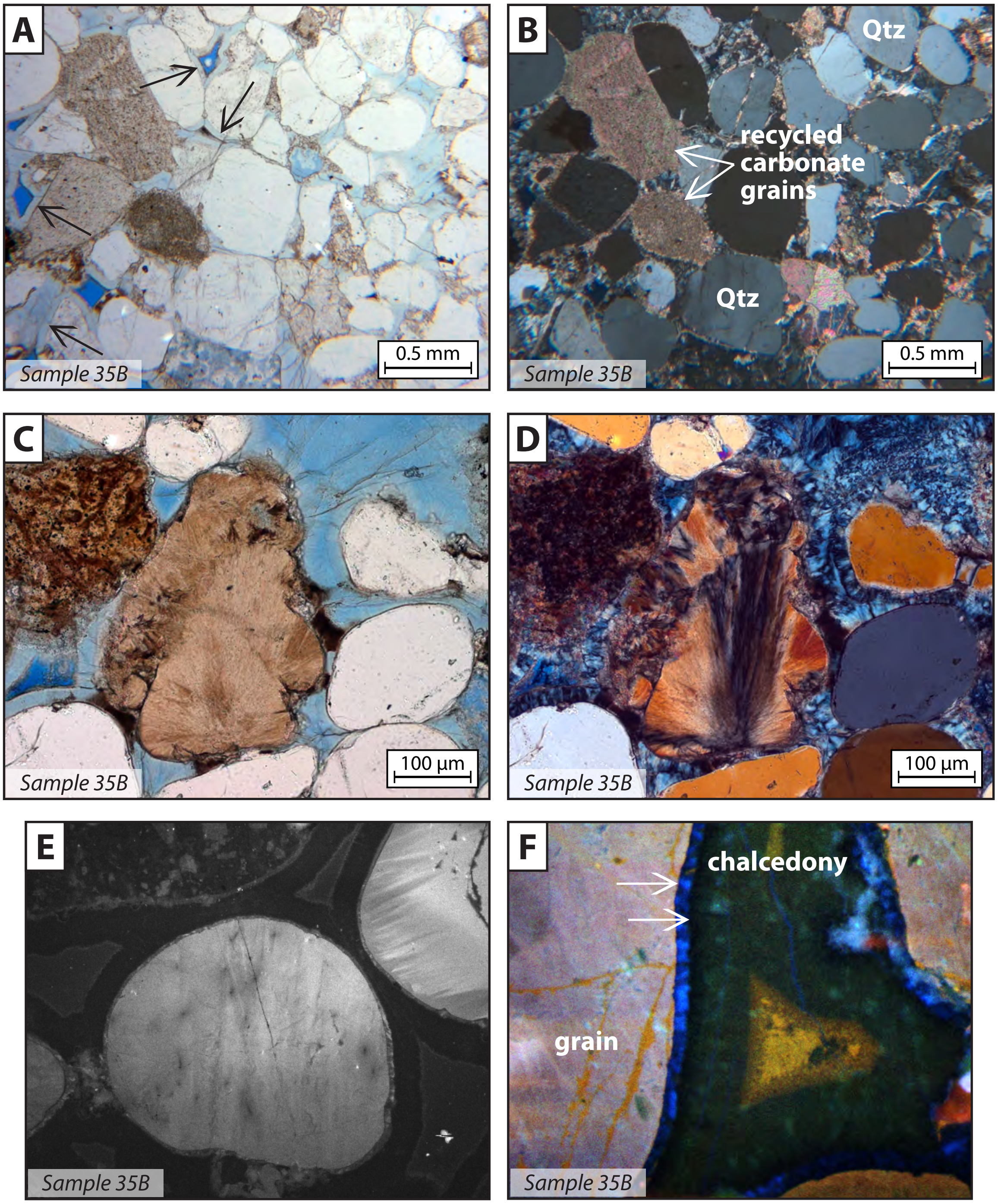

Figure 48: **A–B:** Isopachous chalcedonic cement appears pale blue in plane light and is not restricted to only quartz surfaces. **C–D:** At higher magnification the fibrous habit is more evident. **E–F:** Cathodoluminescence emphasizes the isopachous nature of the cement and exposes zoning typical of pedogenic precipitation.

with euhedral overgrowths forming during burial (Walderhaug, 1994; Lander and Walderhaug, 1999), but could have occurred at surface temperatures (Milliken, 1979). Cathodoluminescence imaging supports this interpretation by exposing zonation typical of pedogenic precipitation (the zoning results from variations in surface water chemistry that have a subtle effect on cement composition). A likely explanation is therefore that it this isopachous cement precipitated at the surface as a result of volcanism common during the late Jurassic, the ash from which provided silica-rich conditions. This type of cement is unique in the map area, both for its abundance and habit, and is not observed anywhere in the fault zone.

The presence and abundance of quartz cement appear to be inversely related to the presence and abundance of calcite spar. In samples with a large amount of calcite spar, quartz cement is almost totally absent (Figure 49). When spar cement drops below about 15%, however, the amount of quartz cement begins to increase.

#### *2.2.1.2.11 Clay cement*

Brown and black opaque cements are present in most point-counted samples (average: 2%; mode: 2%). These cements have variable composition: In some cases they are similar to opaque grains, with high proportions of sulfur, titanium or barium (Figure 50); others contain significant proportions of iron (Figure 51). Where it is growing in association with partially dissolved grains or oversize porosity, opaque cement is commonly composed of a mixture of lighter elements, presumably derived from the dissolving grains (Figure 51).

Clay minerals can sometimes be identified by their distinctive morphologies (e.g., kaolinite booklets or vermiculite “worms”), but no such diagnostic morphologies are apparent in optical microscopy. Following a guide to clay morphologies by Wilson et al. (1977), I also used electron microscopy to search for other common clays: illite, smectite,

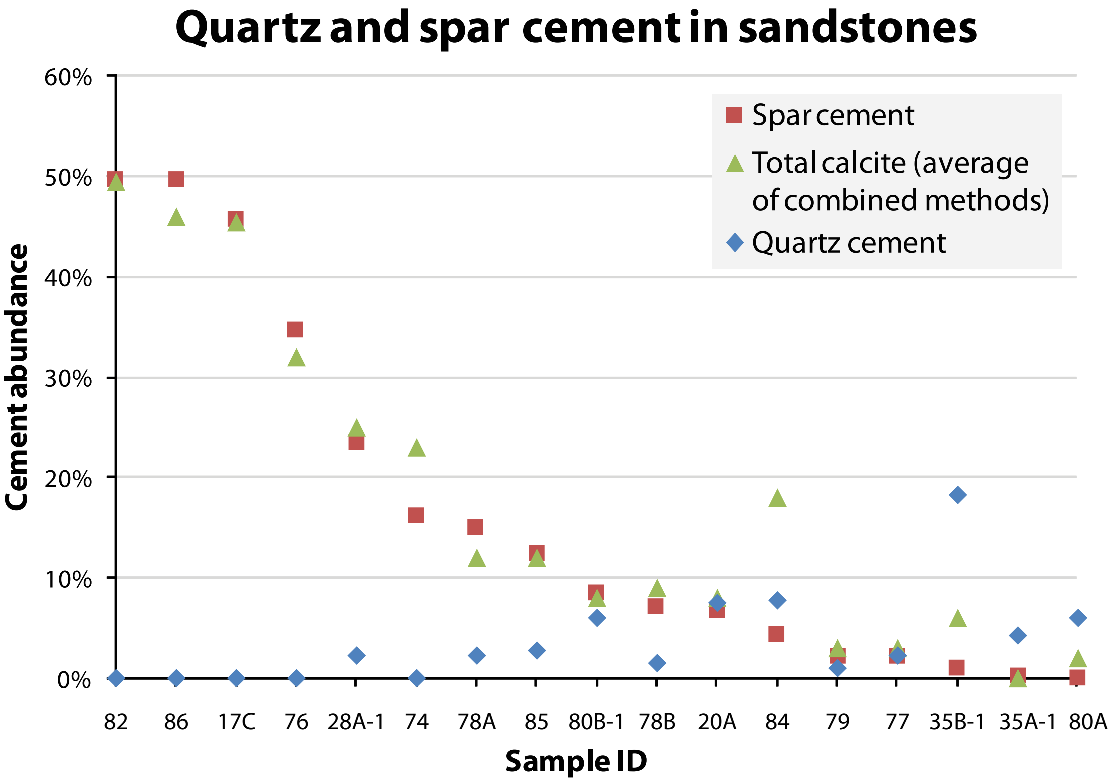

Figure 49: Quartz cement and calcite spar cement in sandstones show an inverse relationship. The average of combined methods of total calcite measurement (point count and He injection) is included for comparison, but this is not referenced because there is no distinction between spar and micrite.

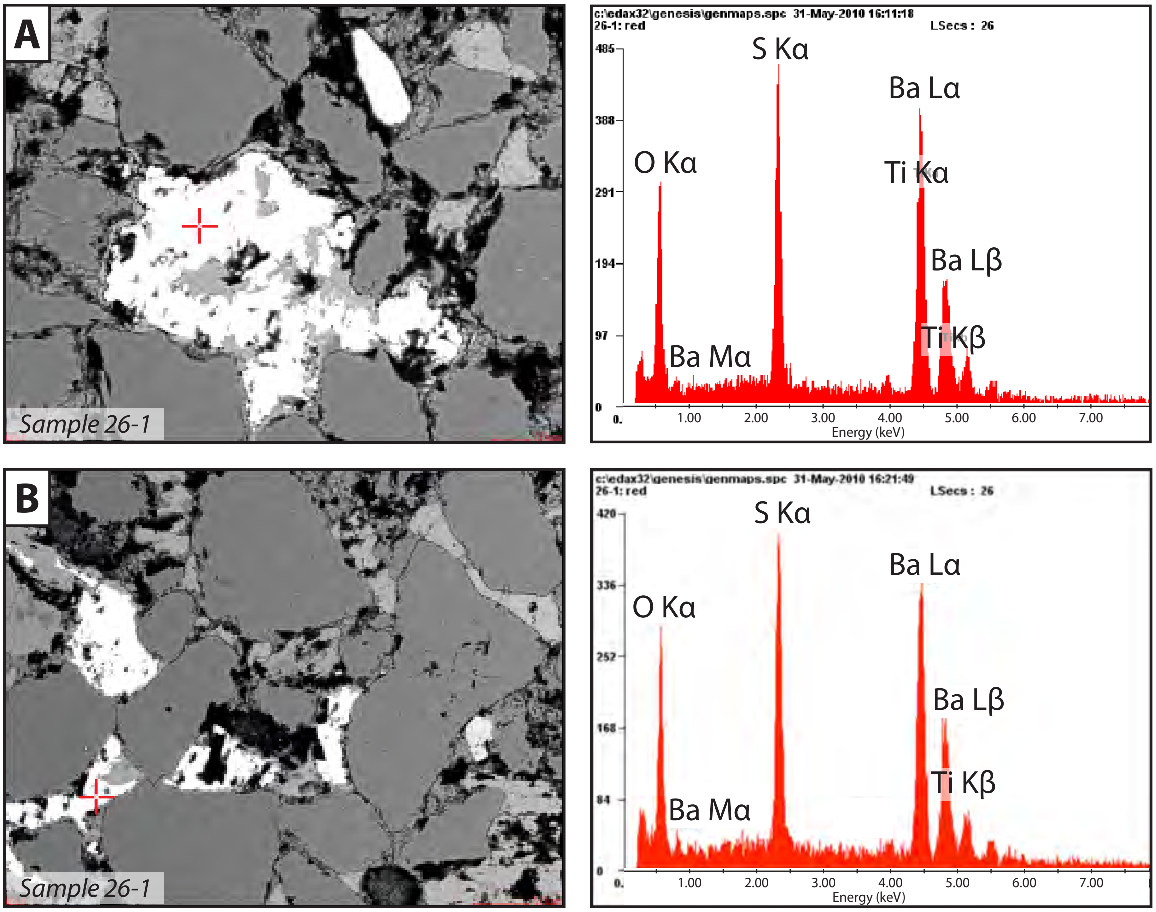

Figure 50: **A–B:** Opaque cements with compositions similar to the heavy opaque grains.

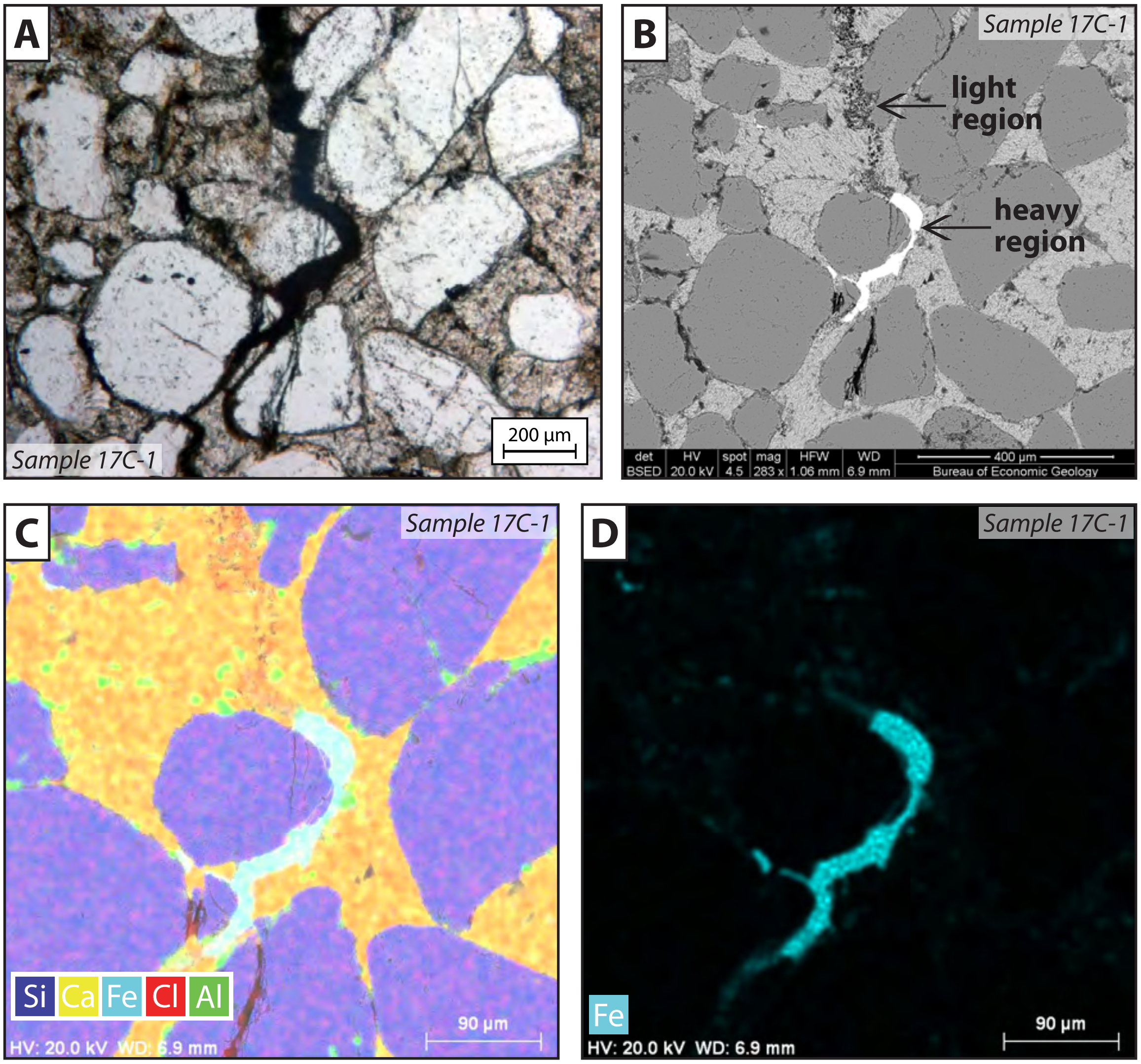

Figure 51: **A:** Opaque vein-filling clay-ey cement appears homogeneous in optical microscopy. **B:** Backscatter imaging exposes heavy and light regions. **C:** A composite EDS map shows that each region has a distinct composition. **D:** An EDS map of iron distribution explains why the lower portion of the vein is heavier.

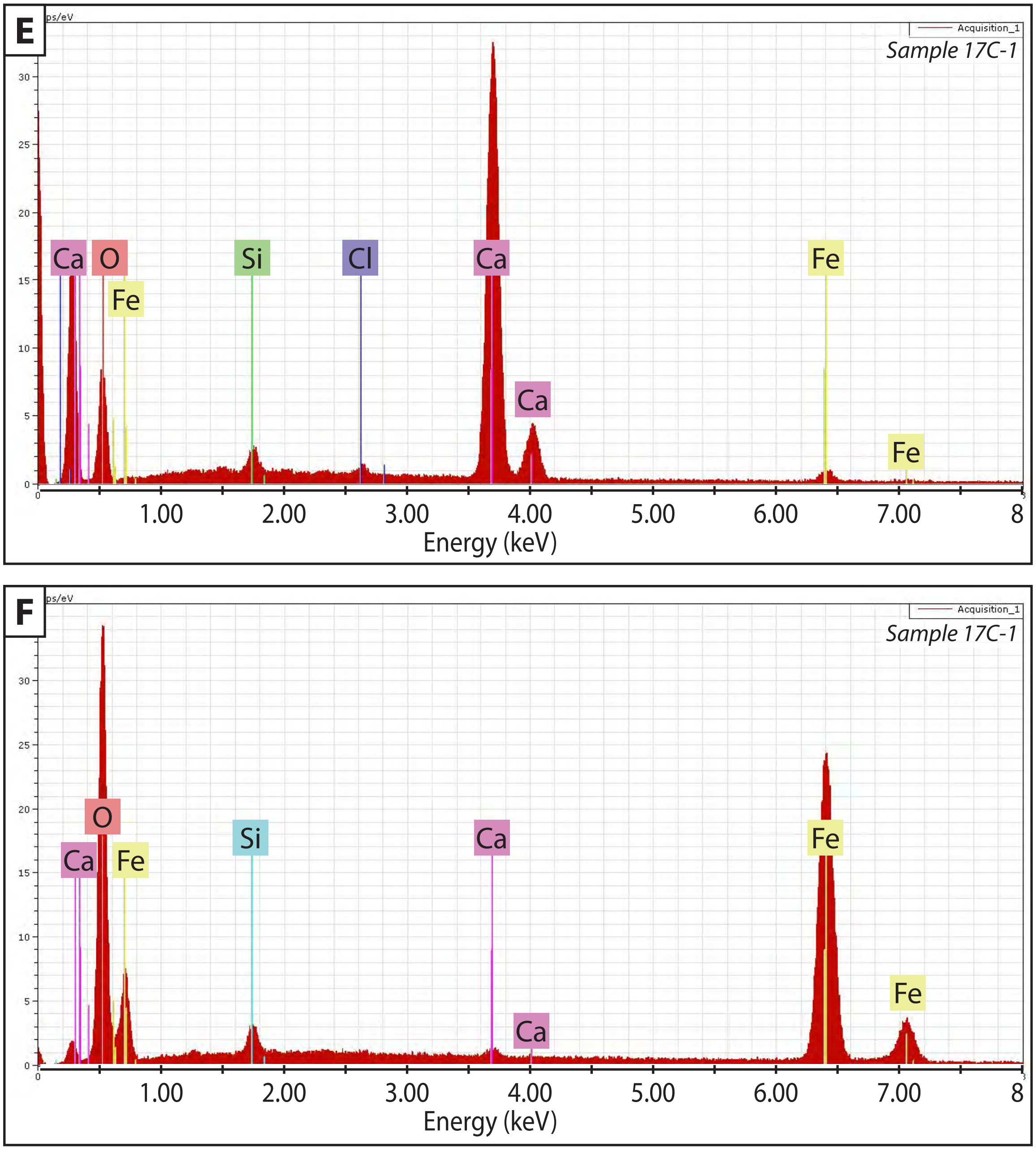

Figure 51: **E:** EDS from the upper portion shows a clay-like mélange of components.
**F:** EDS from the lower portion is mostly dominated by Fe and O, likely $FeO_2$.

chlorite and illite-smectite. None of these are obviously present, with the exception of what may be grain-coating chlorite flakes (sample 35B; Figure 52). These features, seen in polished thin section as opposed to a rock fragment, are somewhat indistinct, however, and appear slightly too stout for chlorite flakes.

More apparent are small rosette-like clusters that resemble a hybrid of authigenic chlorite honeycomb flakes and the box-work texture typical of smectite (sample 15A; Figure 52). Like smectite, individual particles cannot be discerned, only a webby mass. This morphology is a strong match to descriptions of chlorite-smectite in secondary electron imaging (Welton, 1984; Humphreys et al., 1989; Pay et al., 2000); it is an intermediate form between the morphologies of its two endmember minerals (Brigatti and Poppi, 1984). X-ray diffraction data presented below confirm that chlorite-smectite is present in these samples.

#### *2.2.1.2.12 Intergranular volume*

Intergranular volume is the total of intergranular porosity plus matrix material plus cement (Paxton et al., 2002). The average for all point-counted samples is 46% (Table 3). Intergranular volume is a useful measurement of volume between grains in sandstones, however, so matrix-dominated samples such as shales, travertines and matrix-supported rocks should be excluded from this average. The average intergranular volume for only sandstone samples without a major mud-matrix component is 33% (samples 17C-1, 20A, 28A-1, 35A-1, 35B-1, 74, 76, 77, 78A, 78B, 79, 80A, 80B-1, 82, 84, 85 and 86). The average amounts of intergranular porosity, matrix material and cement in these sandstones are 9%, 0% and 24%, respectively. Porosity is discussed in the next section.

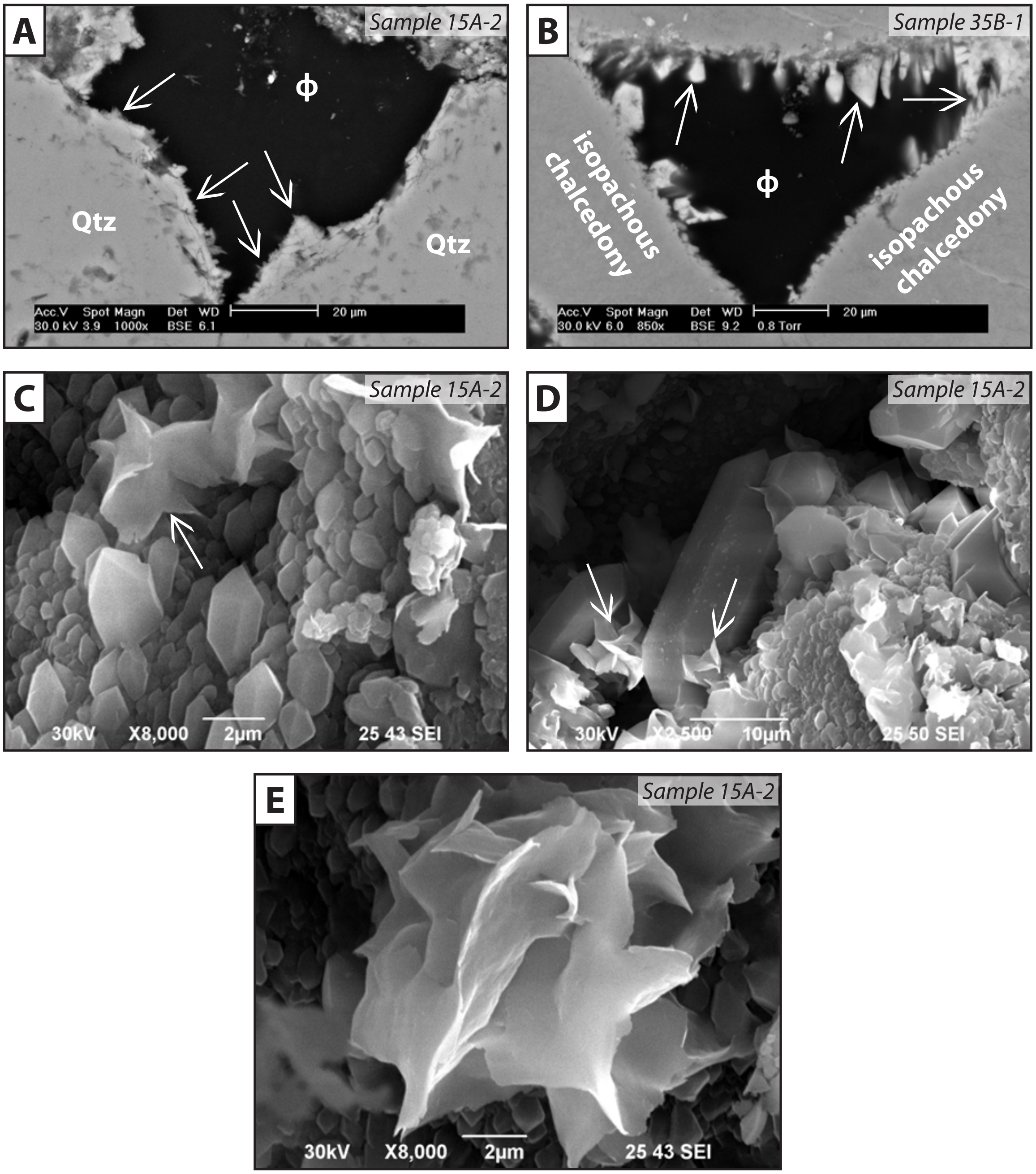

Figure 52: **A:** Backscatter electron image of possible grain-coating chlorite flakes in a polished thin section. **B:** A similar, albeit rather robust, morphology growing on isopachous chalcedonic quartz cement. **C–D:** Secondary electron images showing webby masses of unresolvable particles nested in euhedral quartz cement. **E:** A rosette-like cluster of the same material; this appears to be mixed-layer chlorite-smectite clay (corrensite).

## 2.2.2 POROSITY AND PERMEABILITY

### 2.2.2.1 Methods

Porosity and permeability data are important considerations for an assessment of leakage potential from possible injection reservoirs. Porosity data from the 25 point-counted samples were supplemented by helium injection measurements from 24 one-inch sample plugs. Nitrogen injection permeability was also obtained from the same set of plugs. The plugs submitted for porosity and permeability measurement were taken from samples collected on the two traverses (north and west from the travertine—see Figure 30). They are intended to describe changing porosity and permeability within the fault zone as a function of distance from the travertine. Helium and nitrogen injection measurements were made at the Department of Petroleum and Geosystems Engineering at the University of Texas at Austin (see Appendix D for a description of each technique).

### 2.2.2.2 Porosity results

All porosity data collected with both point counting and helium injection are shown in Table 7. The average amount of primary porosity in all point-counted samples is 6% but has high variability, reaching as much as 19%. Primary porosity is generally lower in samples near the travertine than in those taken from farther than about 50 m away (Figure 53). The average within 50 m of the travertine is 2%; the average at greater distance is 10%.

Secondary porosity is the total of three dissolution features: oversize porosity, intragranular porosity and microporosity. The average amount of secondary porosity is 3%. It follows a trend similar to that seen in primary porosity, increasing with distance from the travertine (Figure 53). At about 100 m, however, secondary porosity reaches a rough maximum abundance of about 5–6%. The outlier with nearly 15% secondary porosity (sample 72A) is a sample of vein-cut shale from near the travertine, which has a high

| Sample | Meters to travertine | Porosity | |
|---|---|---|---|
| | | He inject. | PC |
| 17B$^{P1}$ | 3 | 12.18% | -- |
| 17B$^{P2}$ | 3 | 11.12% | -- |
| He avrg. | 3 | 11.65% | -- |
| 17B-2 | 3 | -- | 7% |
| 17C$^{P1}$ | 4 | 9.46% | -- |
| 17C-1 | 4 | -- | 1% |
| 20A$^{P1}$ | 249 | 18.24% | -- |
| 20A | 249 | -- | 18% |
| 28A$^{P1}$ | 149 | 10.07% | -- |
| 28A-1 | 149 | -- | 16% |
| 35A$^{P1}$ | 121 | 32.38% | -- |
| 35A-1 | 121 | -- | 24% |
| 35B$^{P1}$ | 185 | 12.71% | -- |
| 35B-1 | 185 | -- | 7% |
| 71A$^{P1}$ | 2 | 13.97% | -- |
| 71A$^{P1}$ | 2 | 10.22% | -- |
| He avrg. | 2 | 12.10% | -- |
| 71A-3 | 2 | -- | 2% |
| 71B | 1 | -- | 0% |
| 72A$^{P1}$ | 0 | 19.20% | -- |
| 72A | 0 | -- | 15% |
| 72B$^{P1}$ | 0 | 12.51% | -- |
| 72B | 0 | -- | 5% |
| 73$^{P1}$ | 3 | 10.19% | -- |
| 73$^{P1}$ | 3 | 13.53% | -- |
| 73$^{P2}$ | 3 | 13.05% | -- |
| 73$^{P2}$ | 3 | 15.15% | -- |
| He avrg. | 3 | 14.10% | -- |
| 73 | 3 | -- | 0% |
| 74$^{P1}$ | 15 | 24.35% | -- |
| 74 | 15 | -- | 11% |
| 75$^{P1}$ | 19 | 10.22% | -- |
| 75-1 | 19 | -- | 0% |
| 75-2 | 19 | -- | 0% |
| PC Avrg. | 19 | -- | 0% |
| 76 | 33 | -- | 1% |
| 77$^{P1}$ | 124 | 33.46% | -- |
| 77 | 124 | -- | 25% |
| 78A$^{P1}$ | 159 | 15.10% | -- |
| 78A | 159 | -- | 14% |
| 78B$^{P1}$ | 162 | 23.99% | -- |
| 78B | 162 | -- | 19% |
| 79$^{P1}$ | 287 | 30.77% | -- |
| 79 | 287 | -- | 20% |
| 80A$^{P1}$ | 360 | 20.64% | -- |
| 80A | 360 | -- | 13% |
| 80B$^{P1}$ | 358 | 16.40% | -- |
| 80B-1 | 358 | -- | 14% |
| 82$^{P1}$ | 84 | 11.50% | -- |
| 82$^{P1}$ | 84 | 8.83% | -- |
| He avrg. | 84 | 10.17% | -- |
| 82 | 84 | -- | 1% |
| 84$^{P1}$ | 23 | 10.02% | -- |
| 84 | 23 | -- | 4% |
| 85$^{P1}$ | 77 | 20.13% | -- |
| 85 | 77 | -- | 18% |
| 86$^{P1}$ | 98 | 5.30% | -- |
| 86$^{P1}$ | 98 | 5.65% | -- |
| He avrg. | 98 | 5.48% | -- |
| 86 | 98 | -- | 0% |

Table 7: Point count and helium injection porosity data. P1 and P2 indicate unique plugs submitted for helium injection.

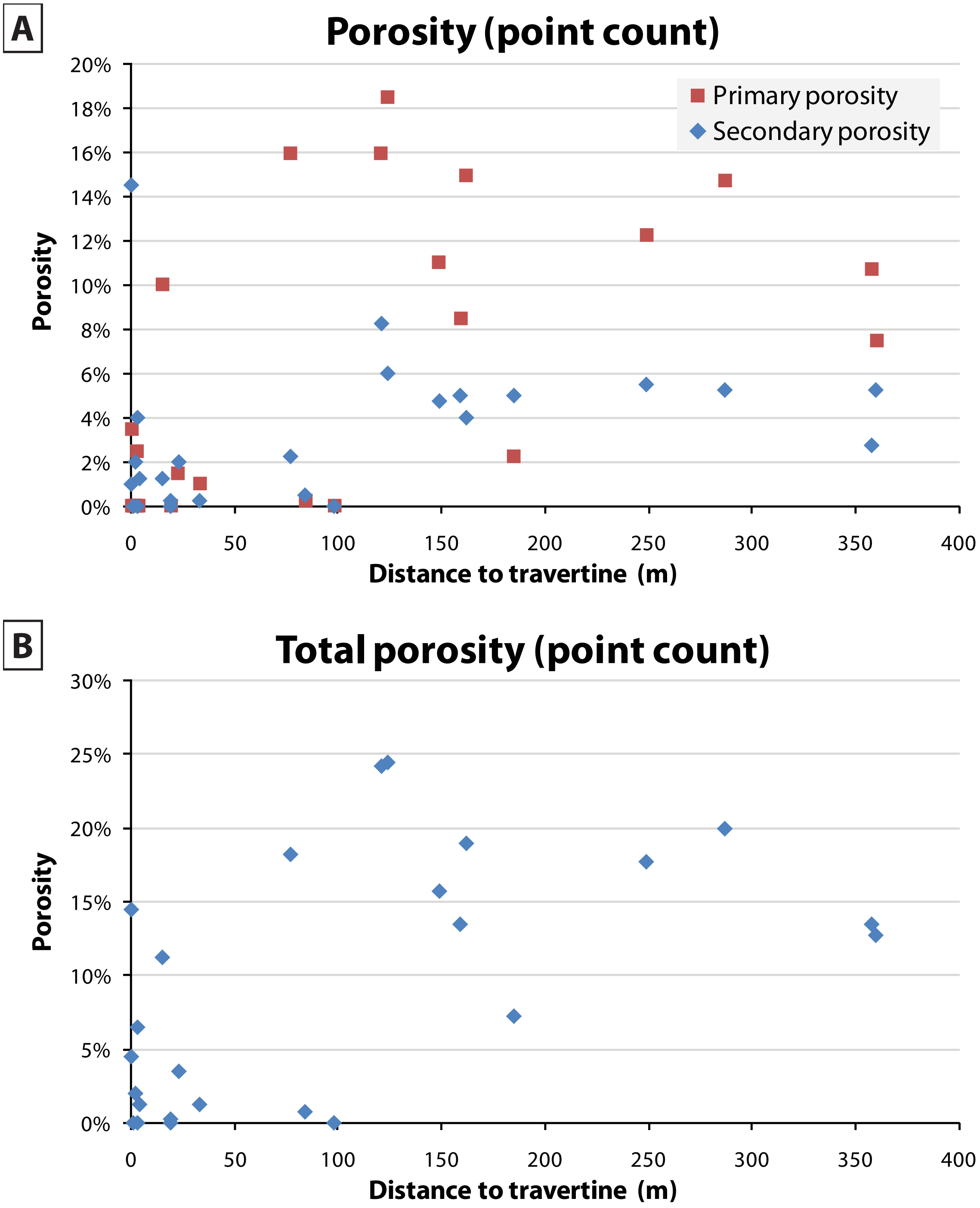

Figure 53: **A:** Primary and secondary porosity both increase with distance from the travertine. Secondary porosity hits a relatively low ceiling at 6%; primary porosity reaches almost 19% and has more variability. **B:** The same data, combined to show total point count porosity.

percentage of secondary porosity due to open and partially cemented fractures (Figure 17). Total combined primary and secondary porosity varies from 0% to 25% and averages 9%.

The helium injection method calculates total porosity but does not differentiate between primary and secondary. The average porosity measured with helium injection is 13%, and ranges from 5% to 34%. These data reproduce the same travertine-distal increase in porosity noted in the point count data (Figure 54).

Helium injection measurements for any given sample tend to be slightly higher than point count measurements. This is likely because helium gas penetrates and measures microporosity not observed in optical microscopy. There are also small chips and imperfections in some sample plugs; porosity calculations assume that the plug is a perfect cylinder (see Appendix D), so the effect of these chips would be to increase the overall porosity measurement.

#### 2.2.2.3 Permeability results

All permeability data are presented in Table 8. Several samples have permeabilities too low to be measured by nitrogen injection; these are given a value of 0.1 mD in order to place them on a logarithmic plot. Glen Baum, the electronic and mechanical technician who made the measurements, confirms that this is a reasonable adjustment given the limitations of the injection apparatus (personal communication, 2010). The average permeability throughout the map area is 142 mD. Measurements reach as high as 1,682 mD (sample 35A), but samples located near the travertine generally have reduced permeability. All five of the samples with permeability too low to detect are located within 19 m of the travertine (samples 17B, 17C, 71A, 72B and 75). The permeability trend is similar to the porosity trend, increasing with distance from the travertine (Figure 55): The average permeability nearer

| Sample | Meters to travertine | Perm. (mD) | Perm. on plot (mD) |
|---|---|---|---|
| 17B$^{P1}$ | 3 | too low | 0.1 |
| 17B$^{P2}$ | 3 | too low | 0.1 |
| Avrg. | 3 | too low | 0.1 |
| 17C$^{P1}$ | 4 | too low | 0.1 |
| 20A$^{P1}$ | 249 | 51.6 | 51.6 |
| 28A$^{P1}$ | 149 | 2.5 | 2.5 |
| 35A$^{P1}$ | 121 | 1,682.1 | 1,682.1 |
| 35B$^{P1}$ | 185 | 3.2 | 3.2 |
| 71A$^{P1}$ | 2 | too low | 0.1 |
| 71A$^{P1}$ | 2 | too low | 0.1 |
| Avrg. | 2 | too low | 0.1 |
| 72A$^{P1}$ | 0 | 14.1 | 14.1 |
| 72B$^{P1}$ | 0 | too low | 0.1 |
| 73$^{P1}$ | 3 | too low | 0.1 |
| 73$^{P1}$ | 3 | 0.8 | 0.8 |
| 73$^{P2}$ | 3 | 0.3 | 0.3 |
| 73$^{P2}$ | 3 | 4.9 | 4.9 |
| Avrg. | 3 | 1.5 | 1.5 |

| Sample | Meters to travertine | Perm. (mD) | Perm. on plot (mD) |
|---|---|---|---|
| 74$^{P1}$ | 15 | 310.2 | 310.2 |
| 75$^{P1}$ | 19 | too low | 0.1 |
| 77$^{P1}$ | 124 | 374.8 | 374.8 |
| 78A$^{P1}$ | 159 | 2.1 | 2.1 |
| 78B$^{P1}$ | 162 | 142.3 | 142.3 |
| 79$^{P1}$ | 287 | 215.4 | 215.4 |
| 80A$^{P1}$ | 360 | 198.8 | 198.8 |
| 80A$^{P1}$ | 360 | 198.0 | 198.0 |
| Avrg. | 360 | 198.4 | 198.4 |
| 80B$^{P1}$ | 358 | 69.9 | 69.9 |
| 82$^{P1}$ | 84 | 0.4 | 0.4 |
| 82$^{P1}$ | 84 | 8.9 | 8.9 |
| Avrg. | 84 | 4.7 | 4.7 |
| 84$^{P1}$ | 23 | 2.3 | 2.3 |
| 85$^{P1}$ | 77 | 36.9 | 36.9 |
| 86$^{P1}$ | 98 | 0.1 | 0.1 |
| 86$^{P1}$ | 98 | 2.1 | 2.1 |
| Avrg. | 98 | 1.1 | 1.1 |

Table 8: Nitrogen injection permeability data. P1 and P2 indicate unique plugs submitted for nitrogen injection.

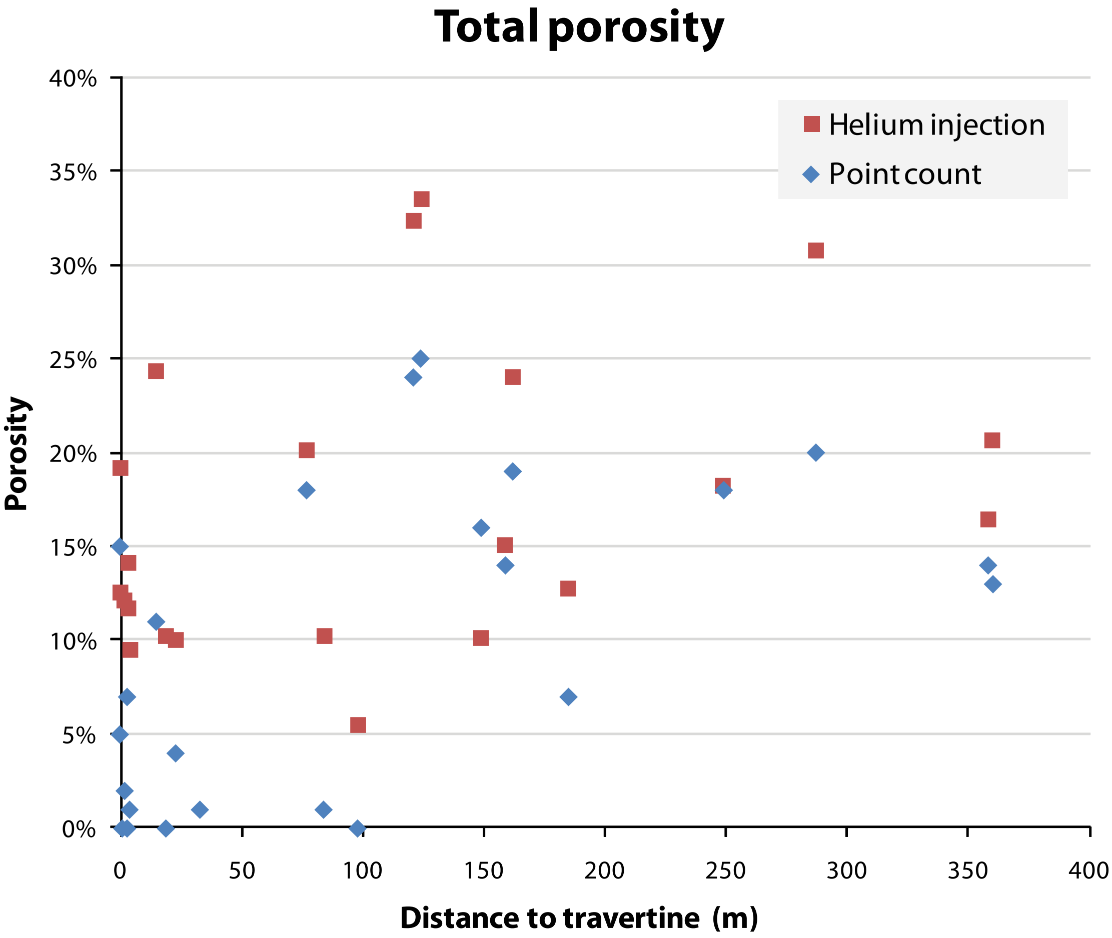

Figure 54: Total porosity measured with both point counting and helium injection; porosity is diminished in close proximity to the travertine.

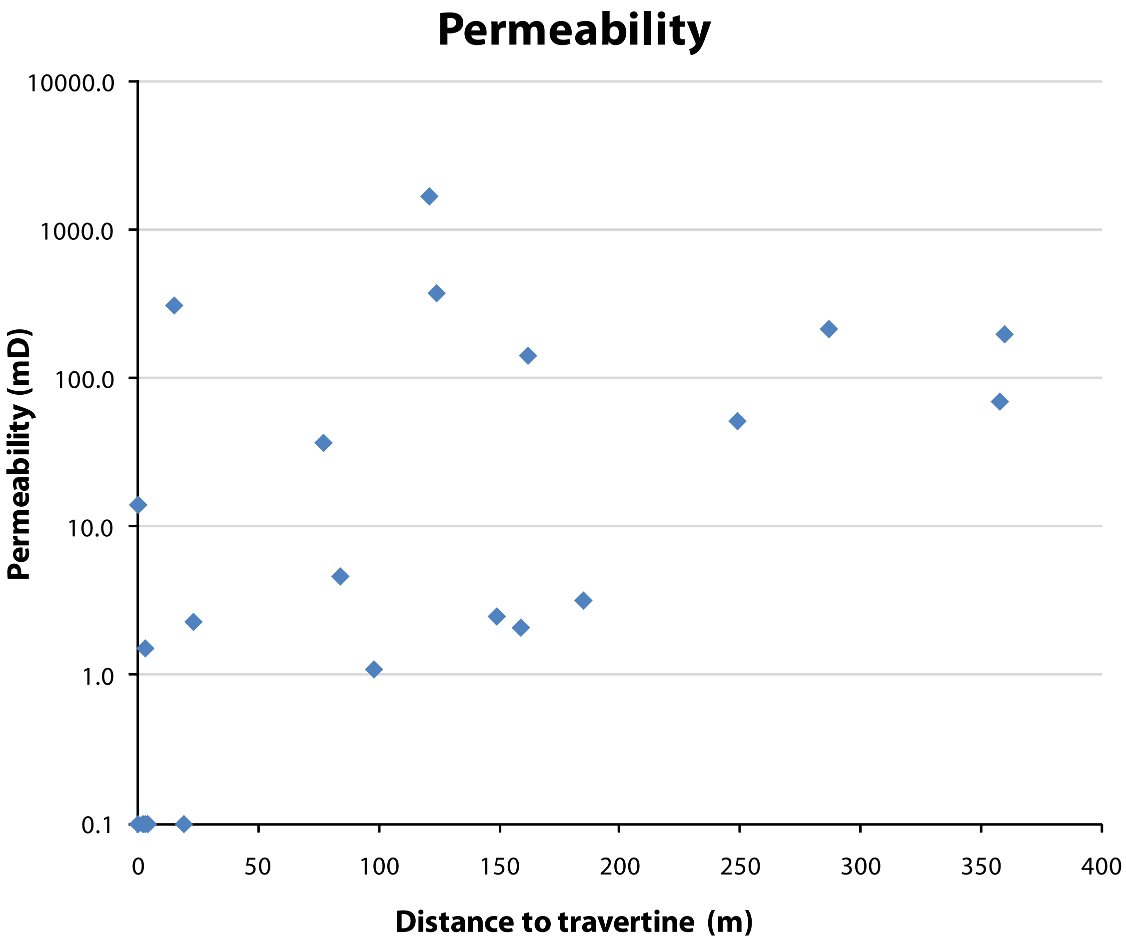

Figure 55: Permeability data display a trend similar to porosity data, decreasing with proximity to the travertine. Samples less than 25 m away from the travertine have permeability as much as three or four orders of magnitude lower than elsewhere in the map area.

than 25 m is 37 mD; it is only 2 mD if one anomalously permeable sample is excluded (sample 74, with 310 mD). At greater distances the average is 214 mD.

The porosity and permeability trends are the inverse of the calcite content trend (Figure 56). This is unsurprising, as calcite precipitation necessarily occludes porosity. Though there is not a linear relationship between porosity and permeability, they are closely linked and a reduction in porosity will cause a similar reduction in permeability.

### 2.2.3 STABLE ISOTOPES

#### 2.2.3.1 Method

It is important to be able to distinguish $CO_2$-related cementation from other diagenetic cements that could have formed independently of a $CO_2$-rich spring, such as weathering-related caliche carbonate and burial-related calcite. Carbonates derived from $CO_2$-rich fluids will have an isotopic signature that differs from these other forms of cementation, and this systematic difference can be used to isolate spring-related cementation.

To obtain stable isotope measurements I sent 20 preparations from 18 samples to the Stanford University School of Earth Sciences for analysis. Samples were collected along strike of the fault and perpendicular to the fault, with increasing distance from the travertine deposit in order to highlight patterns related to travertine proximity, and in order to cover the basic regions of the map area (travertine-proximal, travertine-distal, inside and outside the fault zone). Two samples were duplicated (sample 84, as “98,” and sample 79, as “99”). Four other samples were analyzed twice at the lab as an internal check on measurement precision (samples 71B, 74, “99” and 80B). All measurements are satisfactorily within the $1\sigma$ range. All carbonate isotope data are presented with reference to the Pee Dee Belemnite (PDB) standard.

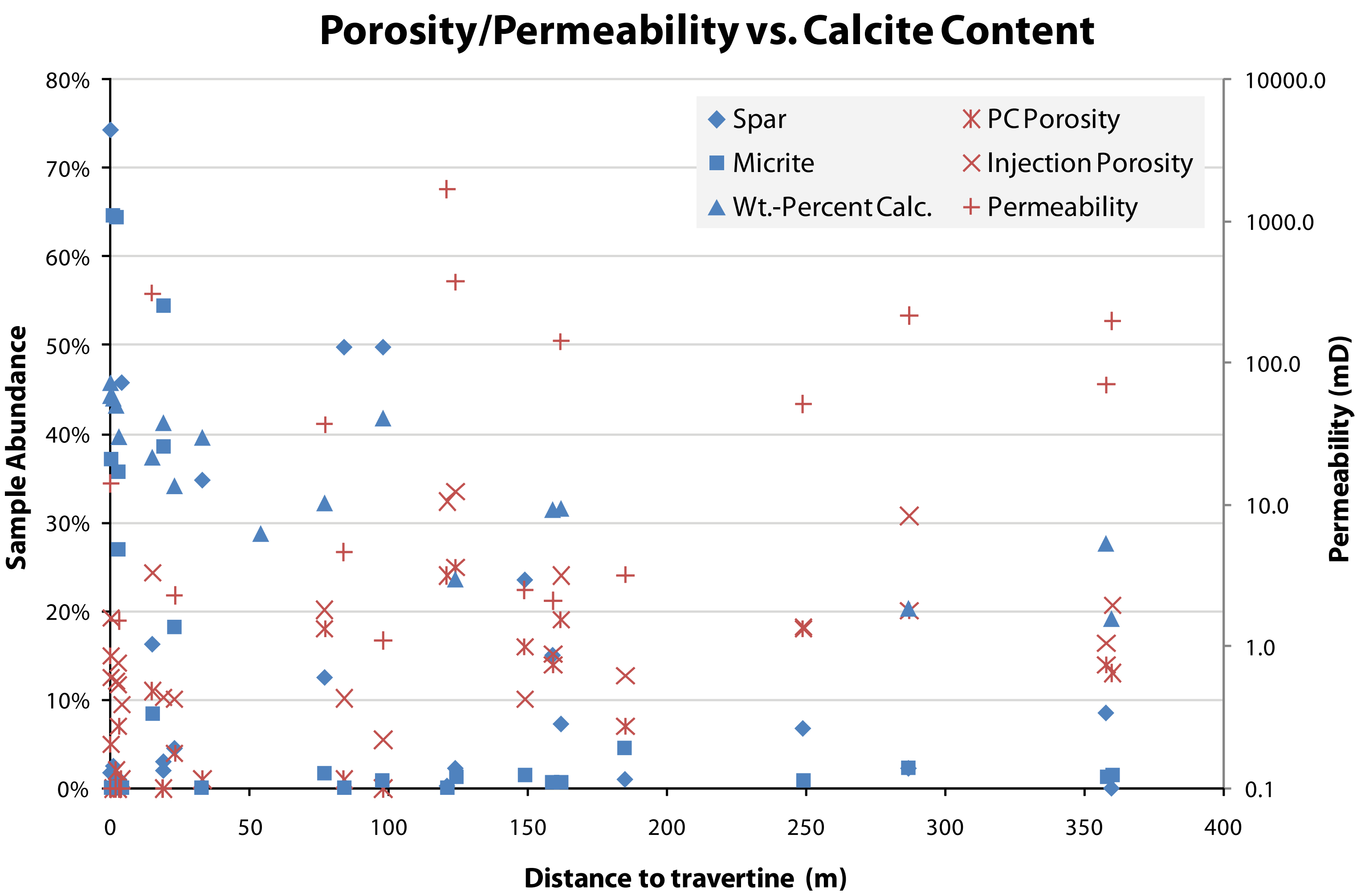

Figure 56: Comparing permeability and porosity to calcite content shows a roughly inverse relationship: Calcite is abundant near the travertine and dwindles at greater distances; porosity and permeability are low near the travertine but increase past about 35 m.

### 2.2.3.2 Stable isotope results

All carbon and oxygen isotope data are presented in Table 9. There is a noticeable increase in weight for each near the travertine (Figure 57). At distances greater than 25 m from the travertine, $\delta^{13}C$ averages -2.5‰, ranging between about -1.5‰ and -4.5‰. Nearer to the travertine than 25 m, however, it increases more than 6‰ to an average of 3.8‰, reaching as high as 5.4‰ in sample 72A. There is also an uptick in $\delta^{18}O$, though it is less pronounced: Distal from the travertine, $\delta^{18}O$ averages -11.9‰, ranging between around -12.0‰ and -15.0‰; nearer to the travertine than 25 m, however, it increases almost 2‰ to an average of -10.1‰, reaching as high as -9.3‰.

## 2.2.4 X-RAY DIFFRACTION

### 2.2.4.1 Methods

X-ray diffraction analysis is helpful for classifying clay minerals, which are often opaque and amorphous and could not be identified petrographically. It is well-suited to this purpose because it identifies mineralogy, unlike energy dispersive spectroscopy, which only generates compositional data. Although the primary impetus for X-ray diffraction is to identify clay minerals, it is also useful for detecting other minor sample components and differentiating mineral phases (e.g., types of feldspars).

Two X-ray diffraction preparations were created from one group of 12 samples: randomly oriented bulk rock powders and preferentially oriented clay-size separations. Bulk rock analysis is intended to make semi-quantitative measurements of the major components in each sample. These specimens were mixed with corundum in a ratio of 6:1 and prepared as powders of randomly oriented spherules (Appendix D: Figure D1) in order to avoid overemphasis of easily aligned minerals such as platy clays. The corundum was added to

|  | Meters to travertine | Weight (μg) | Sig. strength (Vsec) | $\delta^{18}O$ (PDB) |  | $\delta^{13}C$ (PDB) |  |
|---|---|---|---|---|---|---|---|
| Sample |  |  |  | ‰ | ±1σ | ‰ | ±1σ |
| 71A | 2 | 382 | 20.7 | -9.76 | 0.05 | 4.45 | 0.05 |
| 71B | 1 | 328 | 20.2 | -9.39 | 0.10 | 4.37 | 0.07 |
| 71B | 1 | 332 | 20.0 | -9.37 | 0.07 | 4.38 | 0.06 |
| Avrg. | 1 | 330 | 20.1 | -9.38 | 0.08 | 4.38 | 0.07 |
| 72A | 0 | 293 | 23.0 | -10.26 | 0.04 | 5.37 | 0.02 |
| 72B | 0 | 352 | 22.3 | -9.28 | 0.07 | 4.80 | 0.06 |
| 73 | 3 | 393 | 12.7 | -11.55 | 0.06 | 3.78 | 0.05 |
| 74 | 15 | 462 | 11.3 | -11.23 | 0.07 | 0.05 | 0.07 |
| 74 | 15 | 787 | 17.1 | -11.15 | 0.05 | 0.34 | 0.02 |
| Avrg. | 15 | 625 | 14.2 | -11.19 | 0.06 | 0.20 | 0.05 |
| 75 | 19 | 517 | 21.1 | -9.72 | 0.05 | 4.56 | 0.04 |
| 76 | 33 | 602 | 19.4 | -12.37 | 0.06 | -3.73 | 0.04 |
| 77 | 124 | 3,052 | 9.7 | -11.71 | 0.06 | -1.47 | 0.07 |
| 78A | 159 | 1,927 | 19.1 | -14.95 | 0.06 | -4.39 | 0.06 |
| 78B | 162 | 1,256 | 12.7 | -14.01 | 0.06 | -2.74 | 0.08 |
| 79 | 287 | 12,836 | 29.6 | -12.76 | 0.06 | -2.95 | 0.02 |
| "99" | 287 | 11,666 | 21.6 | -12.91 | 0.06 | -2.94 | 0.02 |
| "99" | 287 | 12,655 | 23.3 | -13.04 | 0.06 | -3.16 | 0.03 |
| Avrg. | 287 | 12,386 | 24.9 | -12.90 | 0.06 | -3.02 | 0.03 |
| 80A | 360 | 9,570 | 16.0 | -2.23 | 0.09 | 2.76 | 0.03 |
| 80B | 358 | 2,117 | 14.6 | -13.30 | 0.06 | -2.54 | 0.03 |
| 80B | 358 | 2,100 | 9.4 | -13.08 | 0.11 | -2.43 | 0.11 |
| Avrg. | 358 | 2,109 | 12.0 | -13.19 | 0.09 | -2.48 | 0.07 |
| 83 | 54 | 2,365 | 15.9 | -13.22 | 0.08 | -1.61 | 0.06 |
| 84 | 23 | 985 | 13.9 | -9.41 | 0.08 | 2.63 | 0.09 |
| "98" | 23 | 1,462 | 22.0 | -9.54 | 0.08 | 2.31 | 0.06 |
| Avrg. | 23 | 1,224 | 18.0 | -9.47 | 0.08 | 2.47 | 0.07 |
| 85 | 77 | 2,033 | 22.4 | -13.57 | 0.07 | -3.47 | 0.05 |
| 86 | 98 | 384 | 16.9 | -10.39 | 0.06 | -4.50 | 0.06 |

Table 9: Stable isotope (carbon and oxygen) results from calcite cement.

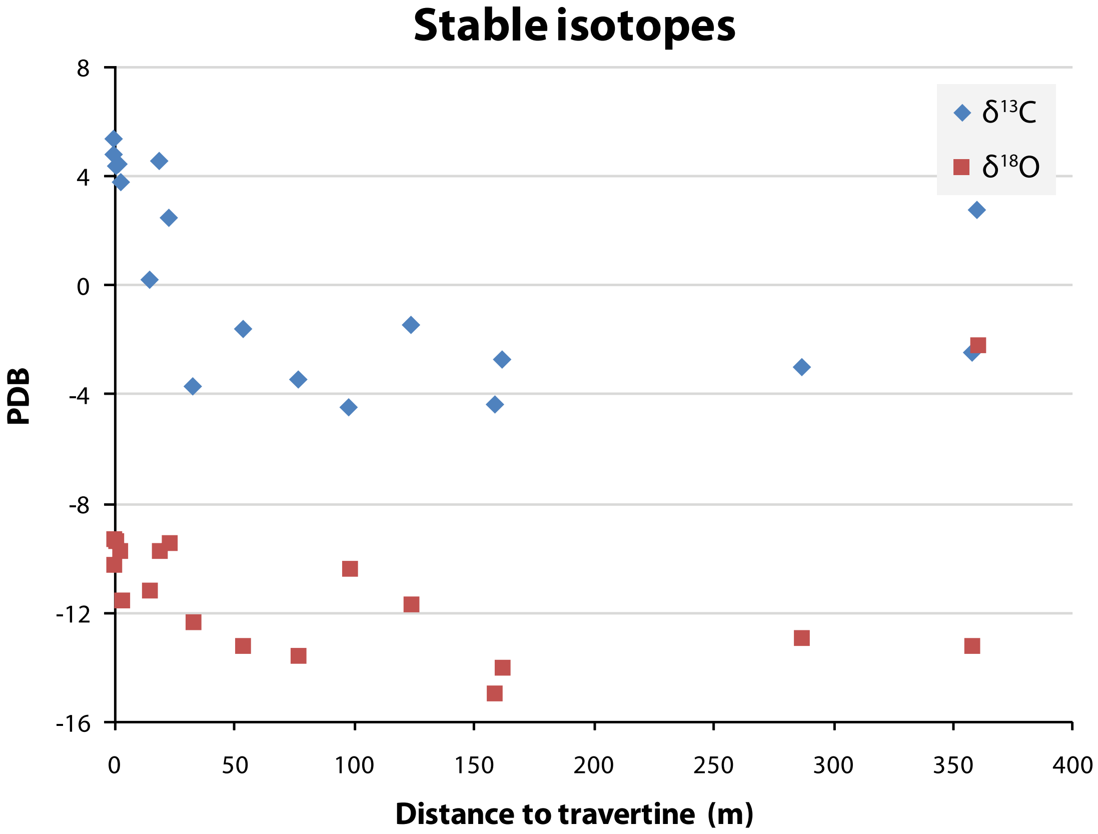

Figure 57: Stable isotope data from across the map area. Note the uptick in weight with proximity to the travertine platform.

facilitate quantification of the results: If a known quantity of a known material creates a peak of a certain intensity, then that peak can be used as a standard against which to compare the peak heights of other minerals.

Diffractometer sensitivity limitations prevent the reliable detection of minerals present in small amounts. Because the clay components in these samples are minor, their signals are overwhelmed and suppressed by major components, such as quartz, if those components are not removed. I therefore prepared clay-size separations for clay mineral analysis, following methods described by Moore et al. (1997). To remove carbonate material and disaggregate well-cemented samples I submerged the samples in 0.3 M acetic acid. This approach avoids the problem inherent to mortar-and-pestle disaggregation wherein clay-sized particles may be created by fracturing large grains, and Ostrom (1961) showed that acid will not damage clay minerals as long as there is carbonate present to act as a pH buffer. Centrifugation was then used to separate coarse-grained material and isolate clay-sized particles. These particles were deposited using a vacuum pump to induce a preferred orientation that would accentuate clay mineral peaks (Appendix D: Figure D2).

To analyze X-ray diffraction data for clay minerals, I limited the search to those likely to be found in sedimentary rocks: illite, vermiculite, kaolinite, chlorite, smectite, and the mixed-layer minerals chlorite-smectite and illite-smectite (Moore and Reynolds, 1997; Vrolijk and van der Pluijm, 1999).

Isolating clays by predominantly removing just quartz (grain-size separation) and calcite (acid treatment) has the corollary effect of broadening the field of detectable minerals. In addition to the 7 clays, therefore, X-ray diffraction results were also compared to 12 other diffraction patterns: those minerals expected based on petrographic and field observations, those generally expected in sedimentary rocks, and those that geochemical models have predicted to precipitate in high-$CO_2$ environments.

This suite includes quartz, feldspars and calcite, all observed during petrography. Quartz and feldspars can be fine-grained and therefore are not necessarily eliminated by grain-size separation. X-ray diffraction expands the simplistic plagioclase-or-alkali dichotomy by enabling differentiation of feldspar phases (albite, orthoclase and microcline). Iron oxides (hematite and goethite) were also suspected due to the yellow stain in some altered rocks and the Fe-rich heavy opaque cements observed during petrography.

In order to avoid damaging clays during preparation, the acid treatment was applied conservatively. Enough carbonate was dissolved to disaggregate the sample, but the treatment was halted before reacting all calcite in order to maintain the buffer protecting clay minerals. The premature termination of this process validates the search for calcite as well as other carbonates: aragonite and dolomite, in order to augment petrographic analyses and confirm or refute the absence of these minerals; and dawsonite, siderite and ankerite, to complete the suite of predicted $CO_2$-related and -sequestering minerals (Knauss et al., 2005; White et al., 2005; Xu et al., 2005; Zerai et al., 2006; Wilkinson et al., 2009b). Corundum is also identified in the bulk rock samples, though it is a laboratory additive.

Each sample was scanned first after being air-dried and then after glycol solvation. Glycolation is intended to identify swelling clays such as smectite by causing a shift in their diffraction patterns relative to their air-dried patterns. Two samples (35B and 80B) were also heated for an hour at 375°C in order to check for clays otherwise difficult to distinguish due to the similarity of their diffraction patterns with other minerals (chlorite-smectite and illite-smectite). The heating process should dehydrate and collapse them, causing a shift in their diffraction pattern.

These samples were selected as representative sets from key regions within the map area: inside the fault zone, near the travertine deposit; inside the fault zone, far from the travertine deposit; outside the fault zone entirely; and from a station within the fault zone, far from the travertine but exhibiting yellow coloration (station 80).

### 2.2.4.2 X-ray diffraction results: Clay-size separation

Because of the undefined bias created by preferential removal of some material, the clay-size separation results must be interpreted as relative abundances. Tables 10–13 present the results of the clay-size separation analysis as a qualitative comparison of mineral abundances based on their relative peak heights (all clay-size scans are included with their interpretations in Appendix F). Using calcite content as a proxy for alteration, samples in Tables 10–13 are ordered from most to least altered. The relative abundance of each mineral is graded on a scale from weak (+) to very strong (+ + + +). Only quartz and calcite ever have very strong peak intensities. These grades do not describe absolute peak intensity thresholds; rather, they describe the height of each peak relative to other peaks in the same sample. Grades were assigned as follows:

| | |
|---|---|
| **+ + + +** | **Very strong:** pronounced peaks |
| **+ + +** | **Strong:** easily distinguished tall peaks |
| **+ +** | **Moderate:** easily distinguished lower-intensity peaks |
| **+** | **Weak:** low intensity peaks difficult to distinguish |
| **n/d** | Mineral not detected. |
| **possible** | All major mineral peaks overlap with the peaks of more common minerals. |

#### *2.2.4.2.1 Quartz and calcite*

Quartz is overwhelmingly abundant in all samples, as is calcite in most samples. Even original (pre-acid treatment) measured calcite as low as 5–10% produces a strong calcite peak (sample 80B), despite the removal of an unquantified but significant portion of calcite. Signal intensity does not drop to moderate until original calcite is 2–5% (sample 79). Because of the acid treatment, detection of calcite in sample 79 suggests that mineral detection is sensitive to abundances below 2–5%, a range consistent with feldspar detection limits presented below. Sample 80A produces no calcite signal despite 2% measured

**Clay-size separation analysis: alteration, quartz and calcite**

| | Meters | | Percent calcite | | Porosity | | | |
|---|---|---|---|---|---|---|---|---|
| **Sample** | **to trav.** | **Color** | **Sig. calib.** | **PC** | **Helium** | **PC** | **Quartz** | **Calcite** |
| 71A | 2 | yellow | 51% | 65% | 10% | 2% | + + + + | + + + + |
| 82 | 84 | off-white | no data | 50% | 12% | 1% | + + + + | + + + + |
| 17C | 4 | off-white | no data | 46% | 9% | 1% | + + + + | + + + + |
| 75 | 19 | yellow | 38% | 42% | 10% | 0% | + + + + | + + + + |
| 76 | 33 | gray | 30% | 35% | no data | 1% | + + + + | + + + + |
| 74 | 15 | yellow | 22% | 25% | 24% | 11% | + + + + | + + + + |
| 78A | 159 | off-white | 9% | 16% | 15% | 14% | + + + + | + + + |
| 80B | 358 | off-white | 5% | 10% | 16% | 14% | + + + + | + + + |
| 35B | 185 | gray | no data | 6% | 13% | 7% | + + + + | + + + |
| 79 | 287 | off-white | 2% | 5% | 31% | 20% | + + + + | + + |
| 80A | 360 | yellow | 2% | 2% | 21% | 13% | + + + + | n/d |
| 35A | 121 | brown | no data | 0% | 32% | 24% | + + + + | n/d |

Table 10: Qualitative analysis of X-ray diffraction results of clay-size separations, showing the state of alteration of each sample and the relative abundance of quartz and calcite, which in most cases have very strong signals.
Sig. calib. = signal strength calibration method

**Clay-size separation analysis: clay minerals**

| Sample | Illite | Vermiculite | Kaolinite | Chlorite | Smectite | Chlor-smec | Illite-smec |
|---|---|---|---|---|---|---|---|
| 71A | + + + | n/d | n/d | n/d | n/d | n/d | n/d |
| 82 | + | n/d | n/d | + + | n/d | n/d | n/d |
| 17C | + | n/d | n/d | + + + | n/d | n/d | n/d |
| 75 | + + | n/d | n/d | n/d | n/d | + + | possible |
| 76 | + + | n/d | possible | + + | n/d | + + | n/d |
| 74 | + + | n/d | possible | + + | n/d | + + | n/d |
| 78A | + + | n/d | possible | + + + | n/d | + + + | n/d |
| 80B | + + | n/d | possible | + + + | n/d | + + + | n/d |
| 35B | + | n/d | n/d | + | n/d | + + | n/d |
| 79 | + + | n/d | possible | + + + | n/d | + + + | n/d |
| 80A | + | n/d | possible | + + | n/d | + + | n/d |
| 35A | + + | n/d | possible | + + + | n/d | + + + | n/d |

Table 11: Qualitative analysis of clay mineral abundance in clay-size separations.
Chlor-smec = chlorite-smectite mixed-layer clay (corrensite);
Illite-smec = illite-smectite mixed-layer clay

**Clay-size separation analysis: feldspars**

| Sample | Albite | Orthoclase | Microcline |
|---|---|---|---|
| 71A | n/d | + | n/d |
| 82 | + + | n/d | + |
| 17C | + + | n/d | + |
| 75 | + | + | n/d |
| 76 | + + + | n/d | + + + |
| 74 | + + + | n/d | n/d |
| 78A | + + | n/d | n/d |
| 80B | + + + | n/d | + + |
| 35B | + | n/d | n/d |
| 79 | + + + | n/d | + |
| 80A | + + + | n/d | n/d |
| 35A | + + + | n/d | + + |

Table 12: Qualitative analysis of feldspar abundance in clay-size separations.

**Clay-size separation analysis: other possible minerals**

| Sample | Goethite | Hematite | Siderite | Ankerite | Aragonite | Dolomite | Dawsonite |
|---|---|---|---|---|---|---|---|
| 71A | + + | n/d | n/d | n/d | n/d | n/d | n/d |
| 82 | n/d | n/d | n/d | n/d | n/d | n/d | n/d |
| 17C | n/d | n/d | n/d | n/d | n/d | n/d | n/d |
| 75 | + + | possible | n/d | n/d | n/d | n/d | n/d |
| 76 | n/d | n/d | n/d | n/d | n/d | n/d | n/d |
| 74 | + | + + | n/d | n/d | n/d | n/d | n/d |
| 78A | n/d | n/d | n/d | n/d | n/d | n/d | n/d |
| 80B | n/d | + + | n/d | n/d | n/d | n/d | n/d |
| 35B | n/d | n/d | n/d | n/d | n/d | n/d | n/d |
| 79 | n/d | + | n/d | n/d | n/d | n/d | n/d |
| 80A | + + | + | n/d | n/d | n/d | n/d | n/d |
| 35A | n/d | + | n/d | n/d | n/d | n/d | n/d |

Table 13: Qualitative analysis of other possible minor components in clay-size separations.

abundance, but the loss of calcite during acid treatment means actual scanned abundance is less than 2%.

#### ***2.2.4.2.2 Clay minerals***

Of the clay minerals, only illite, chlorite and mixed-layer chlorite-smectite (corrensite) have recognizable patterns in these samples. In the clay-size separations, illite is identified by its peaks at 8.9° 2θ and 19.7° 2θ, which are the strongest peaks and are not overlapped by other mineral patterns. The latter of these distinctive illite peaks has a broad shoulder on the right-hand side. A scan of smectite in the RRUFF online database (Downs, 2006: montmorillonite, ID# R050050) shows a similarly shaped peak at 19.7° 2θ. Samples 17C and 71A show this peak, however, and clearly have no smectite (Figure 58). Illite is present in all samples, although generally the signal is relatively weak compared to minerals like chlorite and albite that show strong peaks. There are no apparent trends in illite abundance.

The presence of strong peaks at 6.2° 2θ and 18.8° 2θ is a good positive indication of the presence of chlorite (Moore and Reynolds, 1997). The major peaks of chlorite and chlorite-smectite overlap almost perfectly, however. In these cases, the presence or absence of chlorite can be determined using glycol-solvated peaks: If, in addition to an adjacent treated peak (indicating chlorite-smectite shift), there is another treated peak overlapping the untreated peak at 6.2° 2θ, this indicates the presence of chlorite, which should not shift when glycolated. This distinction is more difficult in the presence of high-chlorite mixtures of chlorite-smectite, especially when peak intensities are low. The high-chlorite mixtures are identified by a down-shift in the treated peak from about 6.2° 2θ to 5.9° 2θ. In other peaks, however, the mixed-layer shift is very slight, and low peak intensities make it difficult to say for sure if there is a pure chlorite peak.

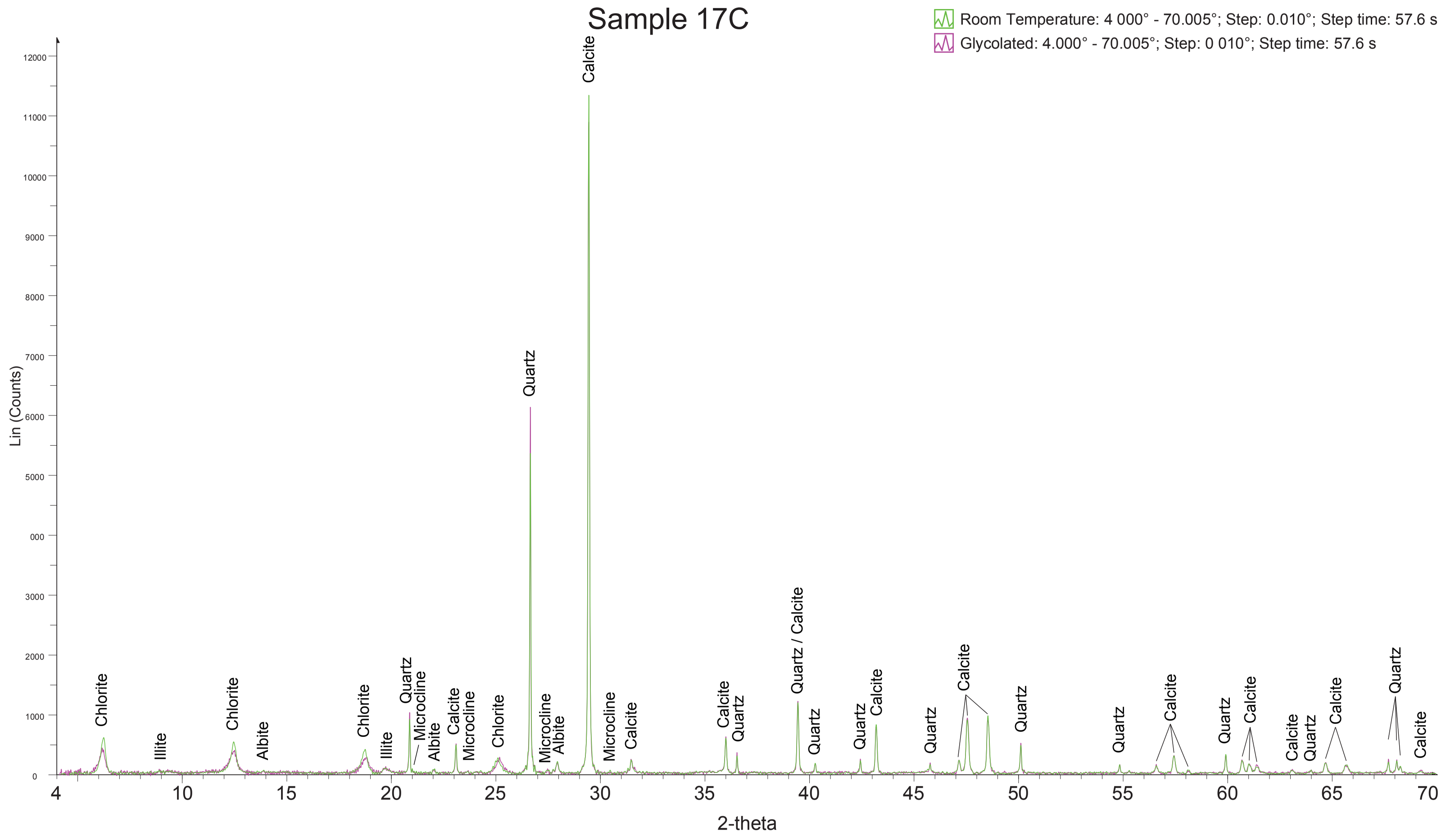

Figure 58: Clay-size separation scans from samples 17C and 71A show the typical illite peak at 19.7° 2θ. The peak can be discounted as indicative of smectite presence because these two samples clearly lack the diagnostic glycol-shifted peak around 6.0° 2θ.

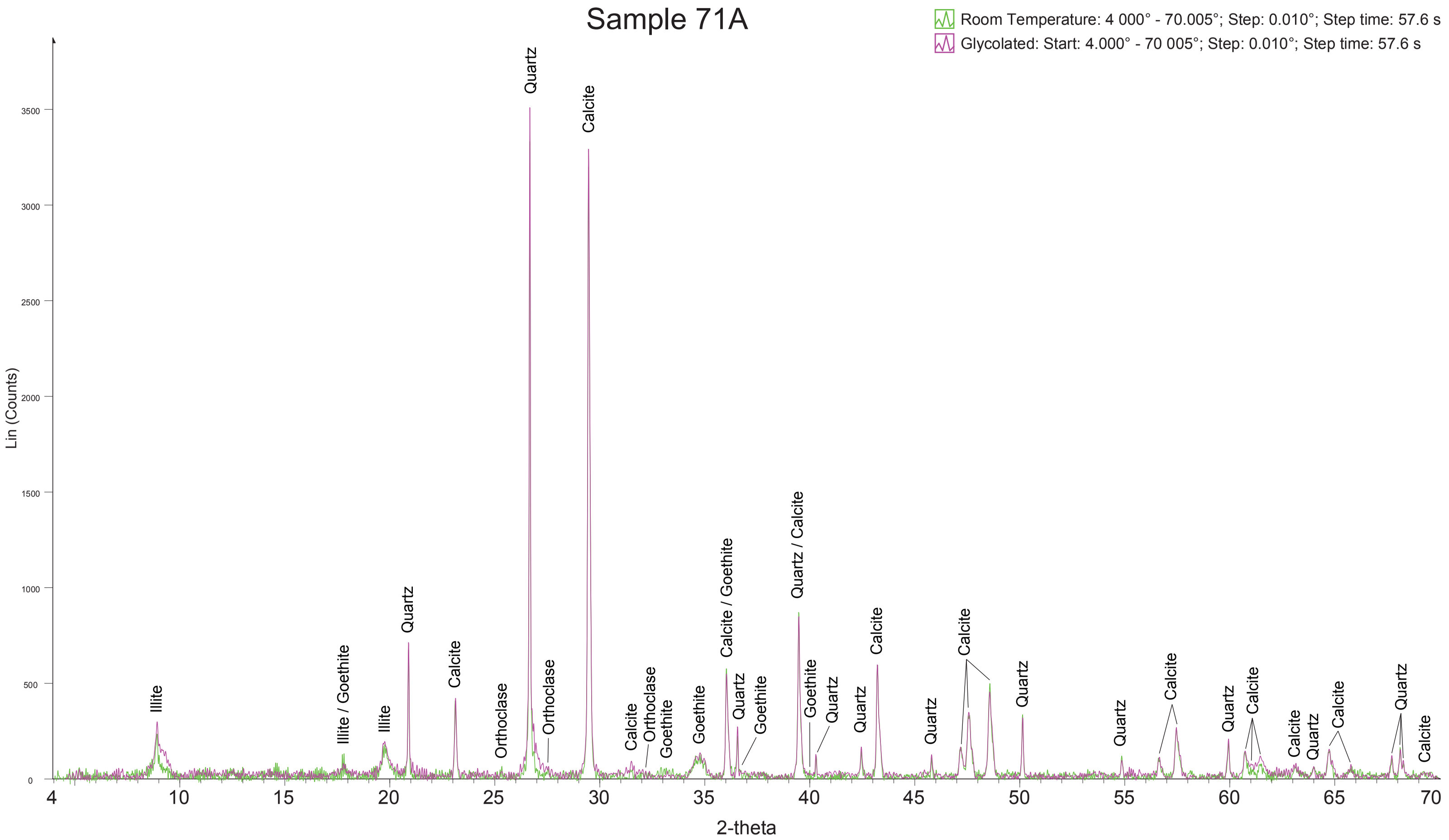

Figure 58: Clay-size separation scans from samples 17C and 71A show the typical illite peak at 19.7° 2θ. The peak can be discounted as indicative of smectite presence because these two samples clearly lack the diagnostic glycol-shifted peak around 6.0° 2θ.

The chlorite-smectite peak is expected to shift by about 0.7° after heating to 375°C (Moore and Reynolds, 1997). The chlorite-smectite peak in sample 80B, which was heated for an hour at 375°, shifted only about 0.1°. This could be affected by the transportation and set-up time between the oven used to heat the sample and the diffractometer. Immediate re-scans of both heated samples (35B and 80B) showed a slight retrogressive shift to their pre-heating patterns, indicating that the dehydrating effect diminishes rapidly.

Arranging samples by their level of alteration renders a trend in chlorite-smectite abundance, and a slightly weaker trend in chlorite abundance (Table 11). These patterns are the only ones to emerge among the clay minerals. In the three most altered samples, chlorite-smectite is not detectable at all. In the next three, it has moderate peaks, and of the six least altered samples, four have strong peaks and two (35B and 80A) have moderate peaks. The quartz peak in 35B has an unusually high intensity of 17,500 counts, which has the effect of suppressing all other constituent peaks—even albite, normally highly abundant, has a weak peak (Figure 59). It is likely that the chlorite-smectite peak would be strong if more quartz had been removed.

Pure chlorite shows less reduction as a result of alteration, but, if values are assigned to the mineral signal strength grades from 0 (for n/d) to 4 (for very strong), the average of the least altered samples (78A, 80B, 35B, 79, 80A and 35A) is a moderate-to-strong peak (2.5). Among the most altered samples (71A, 82, 17C, 75, 76 and 74), the average is a weak-to-moderate peak (1.5), showing that there is a slight decrease in chlorite among altered samples.

The yellow-colored samples (71A, 74, 75 and 80A) all have reduced chlorite and chlorite-smectite signals (average chlorite: weak (1.0); average chlorite-smectite: weak-to-moderate (1.5)) compared to samples with low alteration (78A, 80B, 35B, 79 and 35A; average for both minerals: moderate-to-strong (2.6 and 2.8, respectively)). Sample 80A is

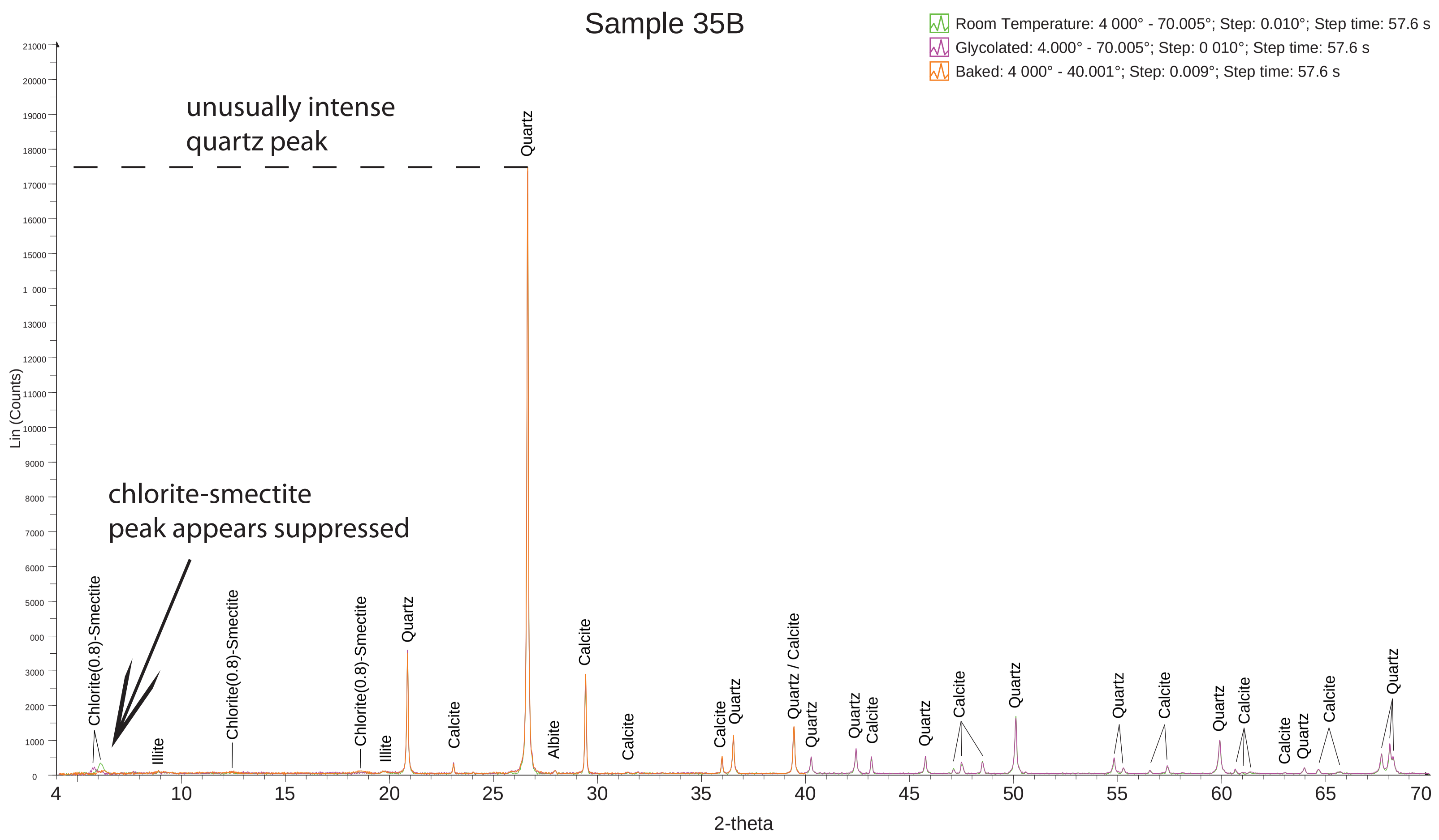

Figure 59: Chlorite-smectite is given a moderate peak in sample 35B, but it would likely have a strong peak if more quartz had been removed during preparation.

yellow but has low calcite content (2%), while the other 3 yellow samples have 22–65% calcite content, suggesting that a reduction in chlorite and chlorite-smectite may result from coloration processes, rather than other diagenesis such as cementation. It is notable that chlorite is present in both diminished minerals, and may therefore be the catalyst that facilitates the reduction.

No other clay minerals are detected in the clay-size separations. Illite-smectite is a common mixed-layer clay in sedimentary rocks; using peak positions described in several studies of illite-smectite (Reynolds, 1992; Moore and Reynolds, 1997; Mannan, 2002), however, and searching for it in compositions from 30% to 70% illite, it does not appear in these samples. In sample 75, the presence of illite-smectite is possible, but there is no need to invoke it as the same peaks are formed by minerals already known to be present (chlorite-smectite, illite and quartz); in all other samples, the appropriate combination of peak locations is absent. Illite-smectite is therefore absent, or present in such low abundance that the X-ray diffractometer cannot detect it.

Smectite does not appear to be present in any sample. Glycol solvation is specifically intended to identify smectite and smectite-bearing minerals, the peaks of which should shift due to swelling of the clay. There are clear shifts in the peaks for chlorite-smectite (Figure 60), which verifies that the treatment was effective. Smectite should have strong glycol-solvated peaks at about 10.2° $2\theta$ and 15.6° $2\theta$ (Moore and Reynolds, 1997), but these are absent in all cases. The success of the glycolation and the lack of diagnostic glycolated smectite peaks establish that there is no smectite present in these samples, or that it is present in such small quantities as to be undetectable.

The primary diagnostic vermiculite peak is located around 7.5–8.5° $2\theta$ and is more or less unaffected by glycol solvation (Moore and Reynolds, 1997). Its other peaks overlap with those for chlorite. Identification of vermiculite therefore relies heavily on the presence of the

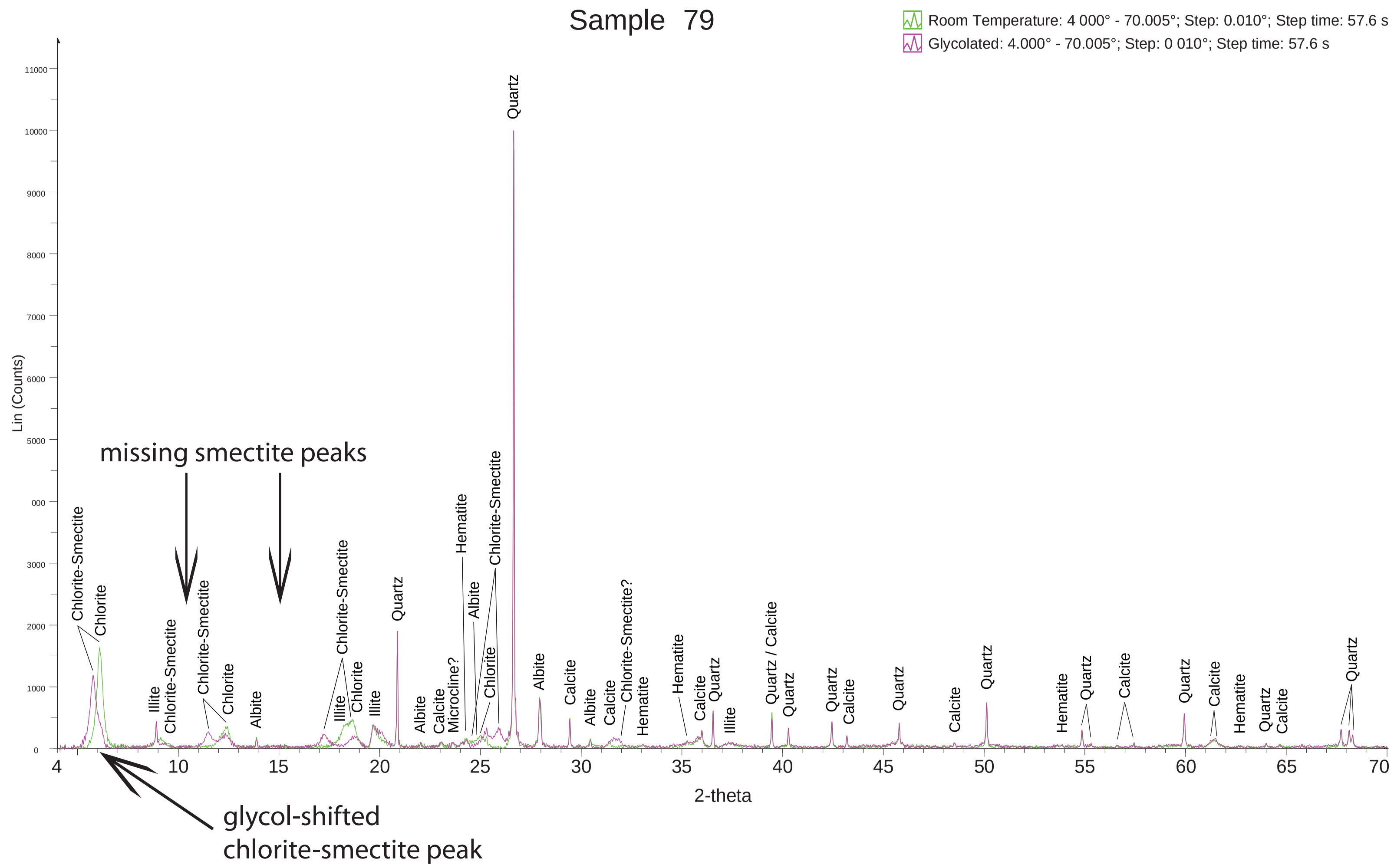

Figure 60: Sample 79 shows a strong chlorite-smectite peak, easily identifiable by the leftward shift resulting from glycol solvation. This indicates that the glycol treatment was successful and smectite is absent, else it would have its own glycol-shifted peaks.

primary peak; absent that, the other peaks can all be identified as chlorite, which is known from optical petrography to be present in these rocks. A definitive vermiculite peak does not appear in any sample, but because this diagnostic peak is near to that for chlorite and chlorite-smectite, the presence of vermiculite is slightly ambiguous. It is prudent, then, to augment the interpretation with other petrographic observations: Searches in both optical and electron microscopy failed to find any of the typical vermiculite vermicules. Vermiculite, moreover, is commonly a diagenetic product of biotite (Deer et al., 1966), which is not observed in petrography. Although it is common in sedimentary rocks, there is no evidence to suggest vermiculite is present in these samples.

The presence of kaolinite is ambiguous but unlikely. In half of the samples, it is not detected at all, lacking important peaks at 12.1° 2θ and 24.9° 2θ (Moore and Reynolds, 1997; Poppe et al., 2001). Both of these peaks underlie the more prominent chlorite and albite peaks, the presence of which is well established. Where chlorite and albite have prominent peaks, therefore, kaolinite is listed as possible, since the presence of peaks in those positions prevents positive confirmation of its absence. Because of this ambiguity, electron microscopy was used to search for diagnostic kaolinite booklets; no such morphologies were observed. These observations demonstrate that kaolinite is absent from these samples.

#### *2.2.4.2.3 Feldspars*

Albite (plagioclase) has a distinctive diagnostic peak at about 27.9° 2θ. It is present in all samples but 71A, and in 9 out of 11 it gives a moderate to strong signal. There is a slight trend of decreasing intensity among the most highly altered samples (17C, 71A, 75 and 82). The change is not great, however, as two of these still have a moderate signal.

The overall abundance of albite is rather surprising, considering that, of these 12 samples, the highest percentage tallied during point counting was 1.75% (samples 79 and 82), and five were recorded as having no plagioclase at all (samples 17C, 35B, 71A, 74 and 75). The X-ray diffractometer is capable of detecting mineral abundances lower than 2–5%, as shown by the moderate calcite peak in sample 79 (despite acid treatment). The disparity between X-ray diffraction and point count results, although unquantifiable, may indicate that point counting systematically misses plagioclase. These feldspars are not stained and can be mistaken for monocrystalline quartz in the absence of strong diagnostic twinning or obvious cleavage planes. It is also possible that the sample preparation process increases the concentration of albite in sample material; this could result from the advanced dissolution observed in some feldspar grains, which could facilitate granular breakdown into clay-sized particles not removed during centrifugation.

Alkali feldspars microcline and orthoclase are less common than albite. They are detected in 8 of 12 samples, but their signal is commonly weak. The single sample with a strong microcline signal (sample 76) is consistent with the point count results, which record 2.0% alkali feldspar—the highest alkali point count tally for any of the twelve samples analyzed in X-ray diffraction. This agreement indicates that point count estimates of alkali feldspar abundance are more accurate than those for plagioclase. This is unsurprising, as alkali feldspars in thin section are easier to identify: Their diagnostic tartan twinning is hard to miss and they are stained yellow to facilitate identification.

#### *2.2.4.2.4 Iron oxides*

Four of these 12 samples have yellow coloration. To test the hypothesis that coloration is caused by iron oxidation, all samples were examined for goethite and hematite. Goethite has major peaks at 17.8° 2θ, 21.2° 2θ, 33.3° 2θ and 36.7° 2θ (Moore and Reynolds, 1997; Downs, 2006: ID# R050142). The peak at 17.8° 2θ is often covered by illite and chlorite-smectite peaks, and the 36.7° 2θ peak is located on the shoulder of a quartz peak, so

21.2° 2θ and 33.3° 2θ are the best peaks to use for identification. The 21.2° 2θ peak can overlap with a microcline or orthoclase peak, but if there is no strong primary feldspar peak at 27.5° 2θ then a peak at 21.2° 2θ is likely a goethite peak. All four yellow-colored samples (71A, 74, 75, 80A) contain goethite, and these are the only samples that contain goethite. Three have moderate signals, while 74 has a weak signal. It is likely, then, that goethite is largely responsible for the coloration.

Hematite has distinctive peaks at 24.3° 2θ, 33.3° 2θ and 35.8° 2θ (Moore and Reynolds, 1997; Downs, 2006). Five samples (35A, 74, 79, 80A and 80B) contain hematite, including two of those with goethite. Because it is found in yellow as well as non-colored rocks, hematite cannot be responsible for the yellow staining. It more likely comprises a portion of the opaque cements observed in many samples, which have already been shown by energy dispersive spectroscopy to contain iron (Figure 51). In optical microscopy some of these cements have a dark red color at their edges, where they are thin—further suggestive of iron content. Such opaque cements appear in most thin sections; they are sparse in samples 35A and 79, but this is consistent with the weak X-ray diffraction signal for hematite in both of these samples.

##### *2.2.4.2.5 Additional carbonates*

Because other researchers have noted its presence in the Little Grand Wash area (Doelling, 1994; Shipton et al., 2004), X-ray diffraction samples were analyzed for aragonite. The major aragonite peak, at 26.2° 2θ, is too near the primary quartz peak to be useful. Other peaks are therefore used instead, located at 33.2° 2θ, 36.2° 2θ and 45.8° 2θ (Moore and Reynolds, 1997). There is no indication in any sample that aragonite is present. This augments petrographic observations, which found no obvious signs of aragonite, such as acicular or botryoidal crystals often typical of the cement (Tucker and Wright, 1990).

Dolomite can be elusive in standard petrography, so X-ray diffraction is helpful to confirm or refute its absence. The 31.0° $2\theta$ and 41.2° $2\theta$ peaks are the largest with which there is little interference from other mineral patterns. These peaks do not appear in any sample. This confirms conclusions from microscopy, in which staining does not indicate the presence of dolomite and the diamond-shaped crystals that typify it are not observed in any sample.

Geochemical models predict that an influx of $CO_2$ into sandstone formations containing abundant plagioclase feldspar should result in authigenic dawsonite ($NaAlCO_3(OH)_2$) after the feldspar dissolves to provide the necessary $N^+$ and $Al^{3+}$ (Knauss et al., 2005; White et al., 2005; Xu et al., 2005; Zerai et al., 2006; Wilkinson et al., 2009b). X-ray diffraction does not show dawsonite in any sample, however. The dominant peak should appear at 15.7° $2\theta$ (Bénézeth et al., 2007). This is a portion of the $2\theta$ scale that in all samples is virtually flat, making the search for dawsonite straightforward and giving a high degree of confidence to the conclusion that it is not present. The absence of dawsonite is confirmed by the lack of typical dawsonite morphologies—pore-filling acicular bundles, splays and vermicules (Baker et al., 1995)—in either optical or electron microscopy. X-ray diffraction data clearly show that albite is plentiful in these samples, and optical petrography shows extensive dissolution of both alkali and plagioclase feldspars. The models predict as much as 4% volume fraction of dawsonite after 10,000 years (Xu et al., 2005), which is roughly the amount of time this $CO_2$-charged spring is estimated to have been active. An abundance of 4% is within the detection sensitivity of the machine, as shown by the recognition of as little as 2% calcite and alkali feldspar. It is interesting, then, that dawsonite is absent at Little Grand Wash.

Siderite and ankerite precipitation are also predicted to result from an influx of $CO_2$ into sandstone strata, reaching as much as 7.5% (siderite) and 2.5% (ankerite) volume fraction after 10,000 years (Xu et al., 2005). Siderite has major peaks at 32.0° 2θ and 24.8° 2θ (Moore and Reynolds, 1997; Downs, 2006). These peaks are not detected in any sample. Ankerite has a major peak at 30.8° 2θ and smaller peaks at 24.0° 2θ and 41.0° 2θ, but it is not detected either—the major peak is absent in all samples and the lesser peaks are either absent or are already associated with other confirmed minerals. Both carbonates require $Fe^{2+}$ to precipitate, and X-ray diffraction shows that either chlorite or hematite, which could act as sources of $Fe^{2+}$, are present in most samples. It is therefore reasonable to expect these minerals in proximity to the spring, and interesting that they are absent.

### *2.2.4.2.6 Comparison to petrography*

At the highest optical magnification (250–500X), very thin (3–10-μm) chlorite grain coats can be seen in several thin sections as a fringe of slightly blurred, green, sometimes tabular crystal growths (Figure 61). The size and habit of these growths are consistent with authigenic chlorite cement in sandstones (Wilson and Pittman, 1977). In general chlorite does not appear in large accumulations (large chlorite crystals or massively pore-filling chlorite cement). In one case (sample 80A) there is a grain that may be partially replaced by chlorite (Figure 61), but it is small and its reddish tint could indicate iron oxide.

The abundance of chlorite observed in thin sections is roughly consistent with the intensities detected in X-ray diffraction results. The two patterns without detectable chlorite (samples 71A and 75) correspond to samples in which no chlorite is apparent in microscopy. Sample 35B, which has no apparent chlorite in microscopy, corresponds to a weak X-ray diffraction chlorite signal. In sample 80A, chlorite is fairly apparent, although high magnification is needed to view it; this abundance is evident in X-ray diffraction, where chlorite has a moderate signal. Because the chlorite presence is easy to miss at low

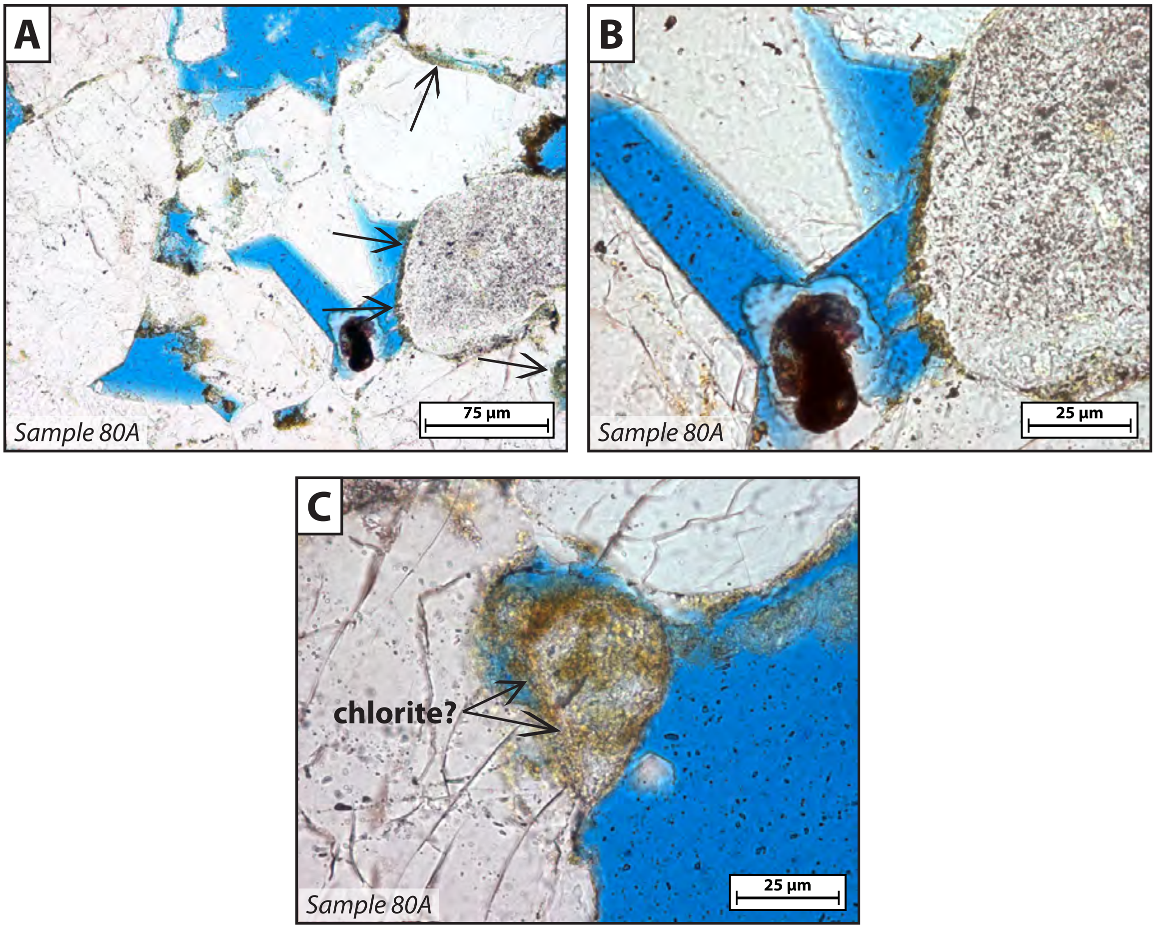

Figure 61: **A:** Thin chlorite grain coatings can be seen at very high magnification in some samples. **B:** The same grain coat at higher magnification; it is too blurry to distinguish individual crystals. **C:** A small grain that may be partly replaced with chlorite; the reddish hue where cement is thicker indicates this may be an iron oxide, however.

magnifications, it went unnoticed until X-ray diffraction results spurred a reexamination of thin sections to look carefully and specifically for it.

Many samples have brown translucent or black opaque cements. Energy dispersive spectroscopy shows that these cements commonly have iron content. The cement is not pervasive in any sample, however; it appears patchily, filling in spotty intragranular dissolution, or heterogeneously filling veins and small pores, so its overall volume is low. Such low abundance is consistent with the "average" of undetectable-to-weak goethite and hematite X-ray diffraction signals. The stronger goethite signals (in samples 71A, 75 and 80A) correspond to yellow-colored samples that could be predicted to contain iron oxides from their outcrop appearance.

#### 2.2.4.3 X-ray diffraction results: Bulk rock powder

The bulk rock X-ray diffraction results are semi-quantitative because there is no bias created by partial removal of sample material, and because a known quantity of corundum is included in each sample. To interpret the bulk rock data there must be a primary reference peak for each mineral to compare against the corundum peak. I use the peak that consistently has the highest intensity as this abundance indicator; these peaks are listed in Table 14. To analyze each sample, the intensity of each mineral's reference peak was measured and recorded as a ratio against the corundum peak. These results are compiled in Tables 15–18. All bulk rock scans are included with their interpretations in Appendix F. Because most of these samples are extensively cemented sandstones, quartz sand and calcite cement tend to dominate the diffractograms, with the corundum additive forming another shorter peak. Figure 62 shows results typical of the bulk rock analysis, with large quartz and calcite peaks, a clearly apparent corundum peak, and no other obviously detectable minerals.

| Mineral | Peak Position (2Θ) |
|---|---|
| **Corundum** | 35.1° |
| **Quartz** | 26.6° |
| **Calcite** | 29.4° |
| **Albite** | 27.9° |
| **Microcline** | 27.5° |
| **Illite** | 19.7° or 24.0° |
| **Goethite** | 34.7° |

Table 14: Two-theta positions for the primary (highest-intensity) reference peak of each mineral identified in bulk rock X-ray diffraction analysis.

**Bulk rock analysis: alteration and corundum intensity**

|  | Meters to trav. |  | Percent Calcite |  | Porosity |  | Corundum |  |
|---|---|---|---|---|---|---|---|---|
| Sample |  | Color | Sig. calib. | PC | Helium | PC | Intens. | Ratio |
| 71A | 2 | yellow | 51% | 65% | 10% | 2% | 390 | 1.00 |
| 82 | 84 | off-white | no data | 50% | 12% | 1% | 490 | 1.00 |
| 17C | 4 | off-white | no data | 46% | 9% | 1% | 490 | 1.00 |
| 75 | 19 | yellow | 38% | 42% | 10% | 0% | 460 | 1.00 |
| 76 | 33 | gray | 30% | 35% | no data | 1% | 480 | 1.00 |
| 74 | 15 | yellow | 22% | 25% | 24% | 11% | 520 | 1.00 |
| 78A | 159 | off-white | 9% | 16% | 15% | 14% | 520 | 1.00 |
| 80B | 358 | off-white | 5% | 10% | 16% | 14% | 580 | 1.00 |
| 35B | 185 | gray | no data | 6% | 13% | 7% | 600 | 1.00 |
| 79 | 287 | off-white | 2% | 5% | 31% | 20% | 590 | 1.00 |
| 80A | 360 | yellow | 2% | 2% | 21% | 13% | 610 | 1.00 |
| 35A | 121 | brown | no data | 0% | 32% | 24% | 610 | 1.00 |

Table 15: Semi-quantitative analysis of X-ray diffraction results of randomly oriented bulk rock powders, showing the state of alteration of each sample and the intensity of the corundum additive.
Sig. calib. = signal strength calibration method

**Bulk rock analysis: quartz, calcite, feldspars**

|  | Quartz |  | Calcite |  | Albite |  | Microcline |  |  |
|---|---|---|---|---|---|---|---|---|---|
| Sample | Intens. | Ratio | Intens. | Ratio | Intens. | Ratio | Intens. | Ratio | Orthoclase |
| 71A | 2,830 | 7.26 | 3,550 | 9.10 | n/d | -- | n/d | -- | n/d |
| 82 | 10,870 | 22.18 | 3,480 | 7.10 | 70 | 0.14 | 70 | 0.14 | n/d |
| 17C | 12,480 | 25.47 | 3,180 | 6.49 | n/d | -- | n/d | -- | n/d |
| 75 | 7,270 | 15.80 | 2,750 | 5.98 | n/d | -- | n/d | -- | n/d |
| 76 | 12,500 | 26.04 | 3,370 | 7.02 | 110 | 0.23 | 70 | 0.15 | n/d |
| 74 | 15,630 | 30.06 | 2,100 | 4.04 | 100 | 0.19 | n/d | -- | n/d |
| 78A | 18,620 | 35.81 | 1,550 | 2.98 | 190 | 0.37 | n/d | -- | n/d |
| 80B | 20,120 | 34.69 | 1,070 | 1.84 | 140 | 0.24 | n/d | -- | n/d |
| 35B | 18,020 | 30.03 | 980 | 1.63 | n/d | -- | n/d | -- | n/d |
| 79 | 19,640 | 33.29 | 620 | 1.05 | 110 | 0.19 | n/d | -- | n/d |
| 80A | 21,270 | 34.87 | 270 | 0.44 | 160 | 0.26 | n/d | -- | n/d |
| 35A | 21,470 | 35.20 | n/d | -- | n/d | -- | n/d | -- | n/d |

Table 16: Semi-quantitative analysis of quartz, calcite and feldspars in bulk rock powders. The mineral ratio is the quotient of a mineral's intensity over corundum intensity in the same sample.

**Bulk rock analysis: clay minerals**

| Sample | Illite Intens. | Illite Ratio | Verm. | Kaol. | Chlorite | Smectite | Chlorite-smectite | Illite-smectite |
|---|---|---|---|---|---|---|---|---|
| 71A | 130 | 0.33 | n/d | n/d | n/d | n/d | n/d | n/d |
| 82 | 60 | 0.12 | n/d | n/d | n/d | n/d | n/d | n/d |
| 17C | n/d | -- | n/d | n/d | n/d | n/d | n/d | n/d |
| 75 | 100 | 0.22 | n/d | n/d | n/d | n/d | n/d | n/d |
| 76 | 80 | 0.17 | n/d | n/d | n/d | n/d | n/d | n/d |
| 74 | 110 | 0.21 | n/d | n/d | n/d | n/d | n/d | n/d |
| 78A | 200 | 0.38 | n/d | n/d | n/d | n/d | n/d | n/d |
| 80B | n/d | -- | n/d | n/d | n/d | n/d | n/d | n/d |
| 35B | 110 | 0.18 | n/d | n/d | n/d | n/d | n/d | n/d |
| 79 | n/d | -- | n/d | n/d | n/d | n/d | n/d | n/d |
| 80A | 120 | 0.20 | n/d | n/d | n/d | n/d | n/d | n/d |
| 35A | 120 | 0.20 | n/d | n/d | n/d | n/d | n/d | n/d |

Table 17: Semi-quantitative analysis of clay minerals in bulk rock powders. The mineral ratio is the quotient of a mineral's intensity over corundum intensity in the same sample.
Verm. = vermiculite; Kaol. = kaolinite

**Bulk rock analysis: other possible minerals**

| Sample | Goethite Intens. | Ratio | Sid. | Hem. | Arag. | Dol. | Dawsonite | Ankerite |
|---|---|---|---|---|---|---|---|---|
| 71A | 80 | 0.21 | n/d | n/d | n/d | n/d | n/d | n/d |
| 82 | n/d | -- | n/d | n/d | n/d | n/d | n/d | n/d |
| 17C | n/d | -- | n/d | n/d | n/d | n/d | n/d | n/d |
| 75 | 90 | 0.20 | n/d | n/d | n/d | n/d | n/d | n/d |
| 76 | n/d | -- | n/d | n/d | n/d | n/d | n/d | n/d |
| 74 | n/d | -- | n/d | n/d | n/d | n/d | n/d | n/d |
| 78A | n/d | -- | n/d | n/d | n/d | n/d | n/d | n/d |
| 80B | n/d | -- | n/d | n/d | n/d | n/d | n/d | n/d |
| 35B | n/d | -- | n/d | n/d | n/d | n/d | n/d | n/d |
| 79 | n/d | -- | n/d | n/d | n/d | n/d | n/d | n/d |
| 80A | n/d | -- | n/d | n/d | n/d | n/d | n/d | n/d |
| 35A | n/d | -- | n/d | n/d | n/d | n/d | n/d | n/d |

Table 18: Semi-quantitative analysis of other possible mineral components in bulk rock powders. The mineral ratio is the quotient of a mineral's intensity over corundum intensity in the same sample.
Sid. = siderite; Hem. = hematite; Arag. = aragonite; Dol. = dolomite

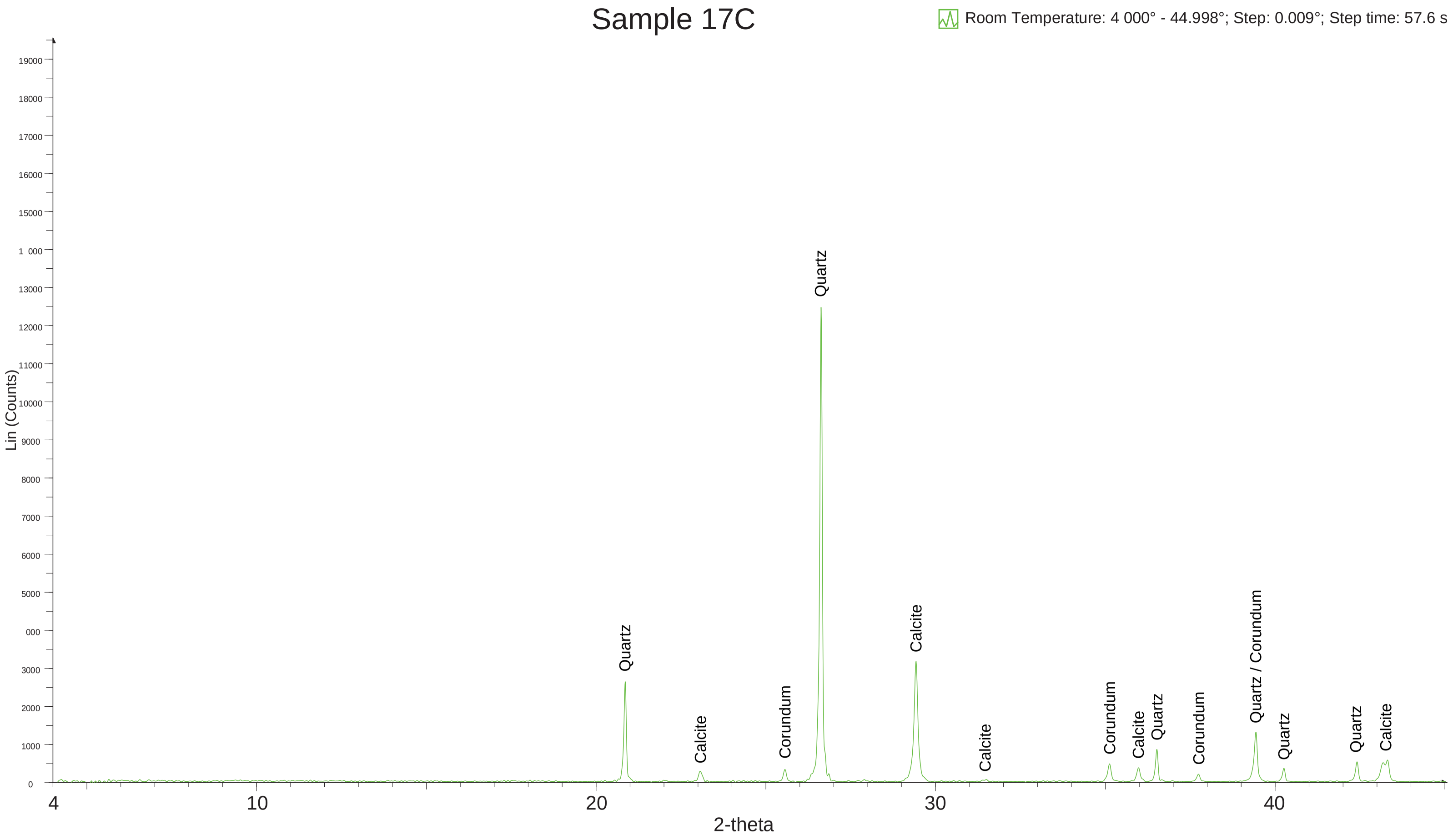

Figure 62: Bulk rock X-ray analysis from sample 17C shows obvious quartz, calcite and corundum peaks. No other minerals are evident.

Most constituent minerals detected in the clay-size separations constitute such proportionally small amounts of the bulk rock powders that their diffraction patterns are below the detectable limit. Aside from quartz, calcite and corundum, the only minerals sufficiently abundant to appear in any of these scans are albite, microcline, goethite, and illite. The peaks that emerge have low relative intensities, but can nonetheless provide semi-quantitative impressions of the minerals' relative abundances. Figure 63 shows the results from a sample (76) with detectable minor components.

Figure 64 compares the rough abundance (ratio to corundum) of each mineral in each sample. The samples are ordered from most to least altered, based on their measured (point count and signal calibration) calcite content. The declining trend of the calcite:corundum ratio is as expected based on this ordering. Both signal calibration measurement and point counting estimate the calcite content of sample 80A at about 2%, which yields a calcite:corundum ratio of 0.44. Sample 79 contains 2–5% calcite, and has a calcite:corundum ratio of 1.05. The increased ratio compared to 80A is about proportional to the increase in measured calcite. This helps outline the rough abundance of minor components, which have ratios between 0.12 and 0.38, corresponding to contents of about 0.5–1.7%. Minor components are isolated in Figure 65. Albite has a relatively strong signal in 7 of the 12 samples, which is unsurprising given its frequency and high intensity in the clay-size separations. Microcline appears only twice, which is also consistent with the relatively lower frequency of its appearance in clay-size separations. Pie charts showing the mineral assemblage of each sample are included in Figure 66; the amount of pie allotted to each mineral corresponds to the mineral's corundum ratio.

After consulting with Jiemin Lu (personal communication, 2011), two peaks at 19.7° $2\theta$ and 24.0° $2\theta$ were identified as illite. These peaks are not identified in Moore et al. (1997), but an international powder diffraction database (ICDD, 2008) has illite patterns

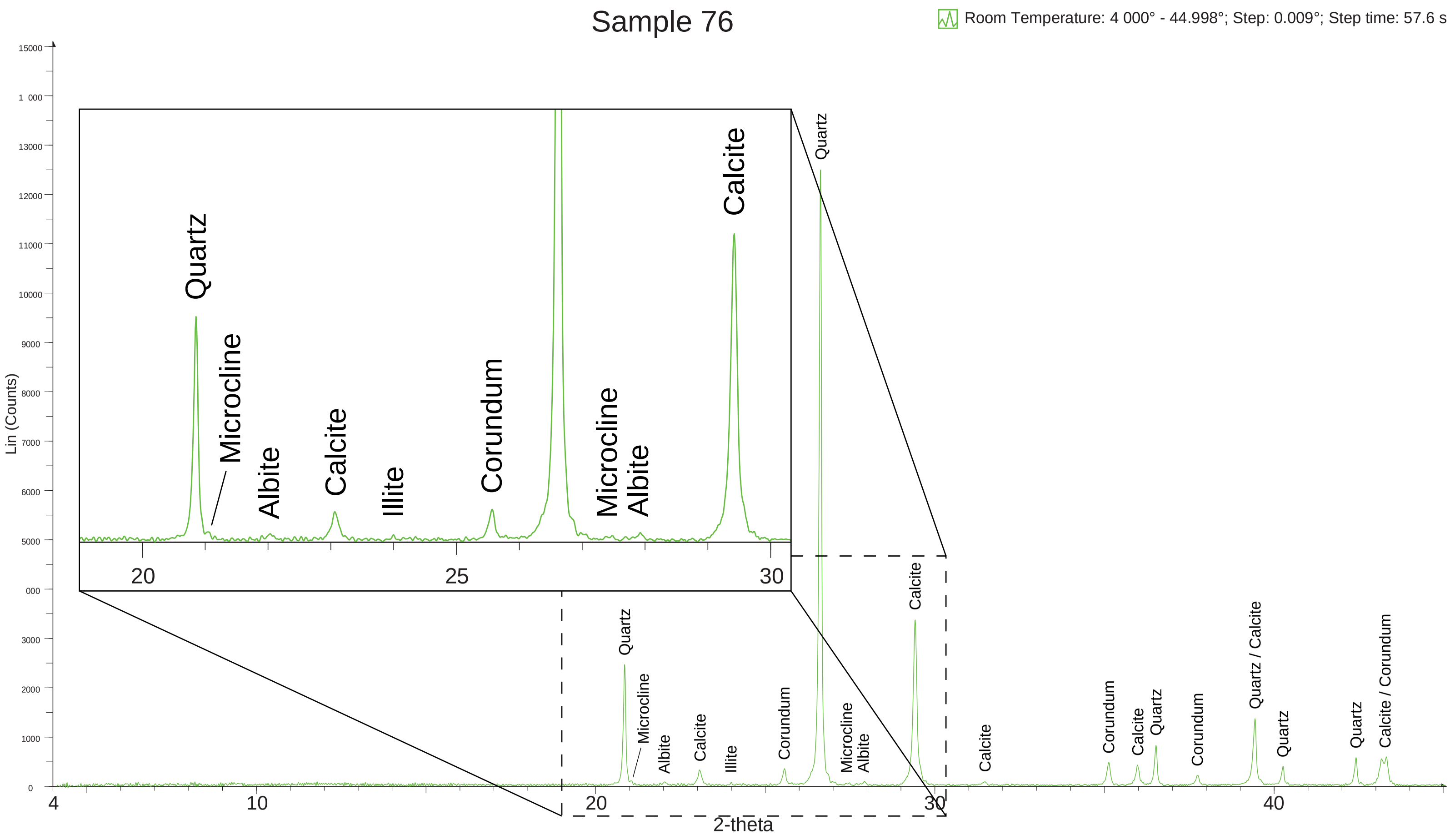

Figure 63: Bulk rock analysis from sample 76 shows low-intensity peaks indicating the presence of minor components in addition to quartz and calcite.

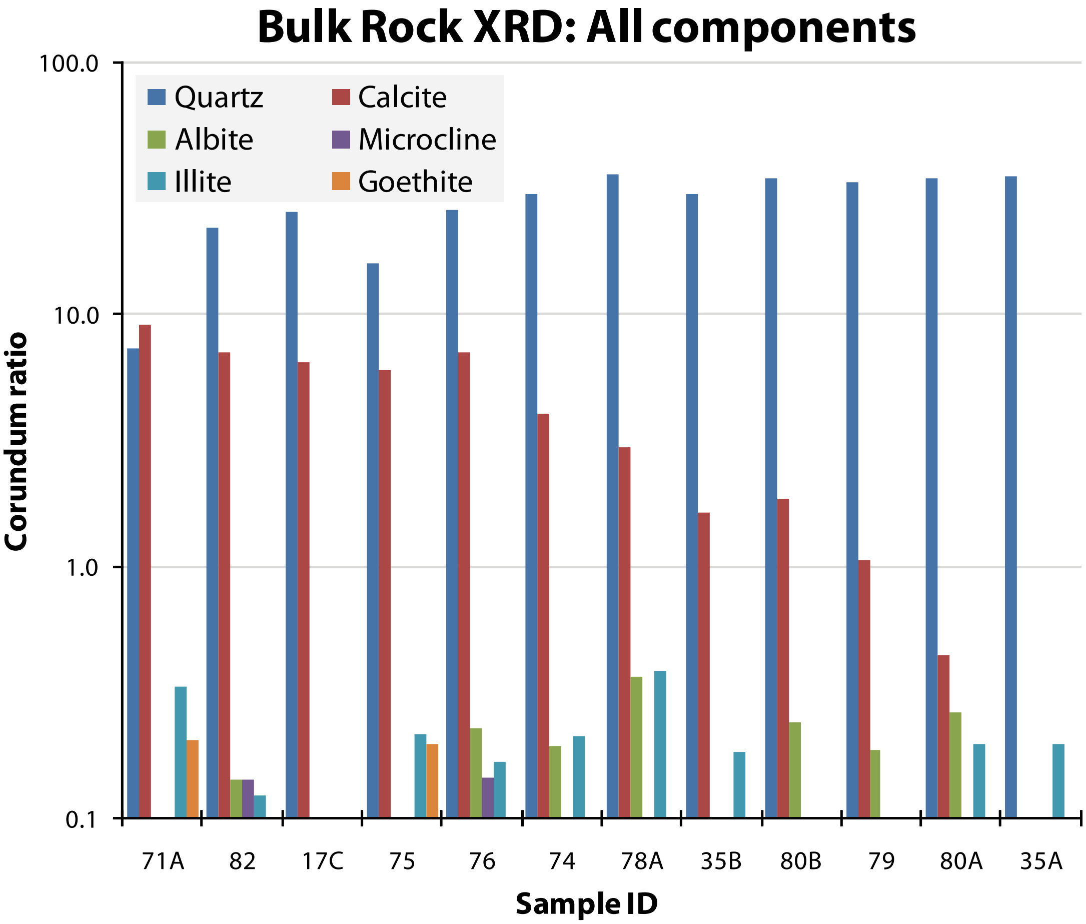

Figure 64: Comparison of mineral ratios (to corundum) in each bulk rock sample. Samples are arranged from most to least altered, based on measured calcite content (point count and signal strength calibration).

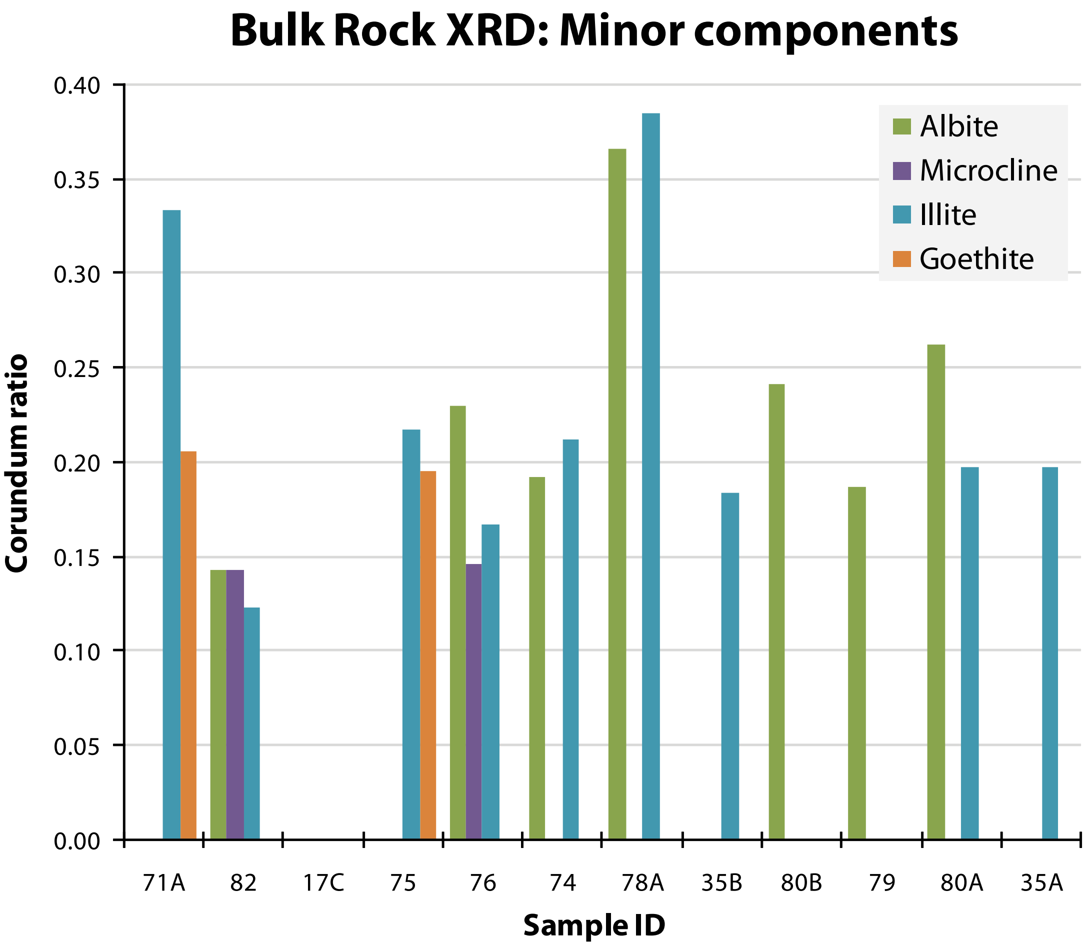

Figure 65: Comparison of the minor components in each bulk rock sample (excluding quartz and calcite). Samples are arranged from most to least altered, based on measured calcite content (point count and signal strength calibration).

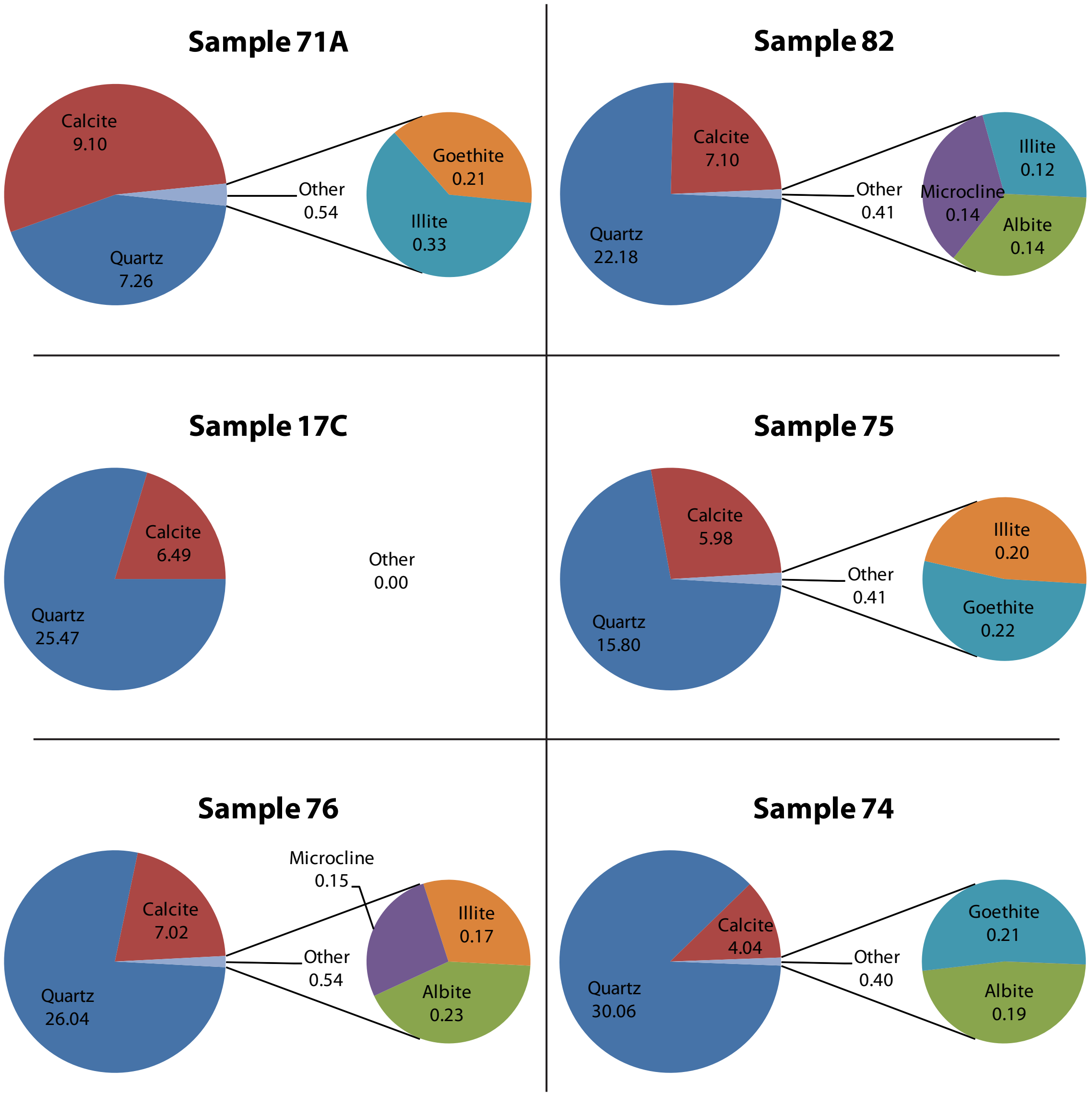

Figure 66: Pie chart representation for each bulk rock sample of the detectable mineral assemblage, based on corundum ratios. Samples are arranged left to right and top to bottom from most to least altered, based on calcite content.

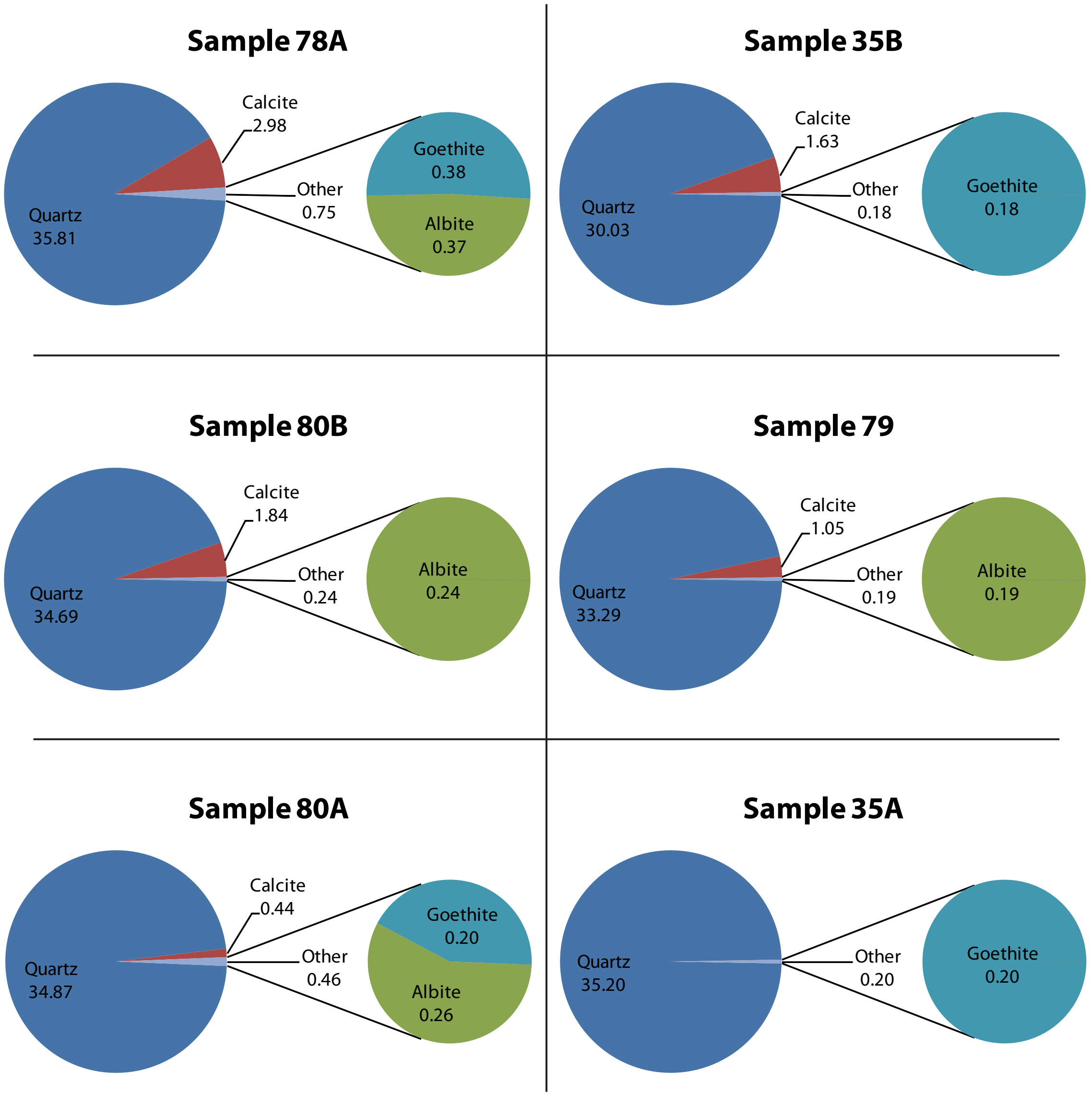

Figure 66: Pie chart representation for each bulk rock sample of the detectable mineral assemblage, based on corundum ratios. Samples are arranged left to right and top to bottom from most to least altered, based on calcite content.

corresponding to these locations, as does the RRUFF online database, under entries for muscovite (Downs, 2006: ID# R040104 and R050198). Using these peaks as the primary peaks, illite has a relatively strong showing in the bulk rock powders (nine of twelve samples), especially considering that no other clay minerals are detectable.

Goethite is detectable in two of the four yellow-colored samples (71A and 75). It may be detectable in the remaining yellow samples as well (74 and 80A), but the strongest goethite peaks are at about 21.2° 2θ and 36.1° 2θ and are overlapped by strong quartz and calcite peaks, respectively. The relatively weak peak at about 34.7° 2θ is instead used to identify goethite in bulk rock scans; the lack of this particular peak in samples 74 and 80A does not necessarily mean goethite has no detectable peaks, only that they may be "hidden" underneath stronger quartz and calcite peaks. The appearance of goethite even in bulk rock analysis enforces the explanation for the yellow coloration seen in rocks mainly around the travertine platform. Mineral detection by X-ray diffraction is limited to minerals present in abundances of around 2% or more, and an iron oxide presence as low as 1–3% can cause yellow-red coloration (Torrent and Schwertmann, 1987; Eichhubl et al., 2004). If goethite is detected in bulk rock powder, therefore, it is likely present in sufficient quantity to stain the sample yellow.

# 3. DISCUSSION

## 3.1 Carbonate Cementation in Response to $CO_2$-Rich Seepage

### 3.1.1 DISTRIBUTION AND ISOTOPIC SIGNATURE OF ANOMALOUS CEMENTATION

The presence of a travertine platform in the map area indicates the presence of an inactive flow conduit, similar to the currently active Crystal Geyser. Three datasets—calcite content, porosity and permeability—show corresponding trends with distance from the travertine. The amount of total calcite content (the average of point count and signal strength calibration data) increases within 50–100 m of the travertine (Figure 67). Porosity and permeability data have considerable scatter but show correlated trends, both with decreasing values within about 100 m of the travertine (Figure 68). Trends in all three datasets deflect either up or down at about the same point because they are genetically related: Cementation reduces porosity, which tends to reduce permeability. These datasets outline a cement anomaly—a zone of intense alteration of up to 100 m around the travertine platform. Although weathering and burial processes can result in calcite precipitation, the spatial association of increased cementation with the travertine platform is consistent with expected calcite precipitation in sandstone resulting from a $CO_2$-degassing seep. Carbon dioxide exsolves from rising water due to the drop in hydrostatic pressure and the difference between aqueous and atmospheric $P_{CO2}$ (Ellis, 1959; Pearson, et al., 1978; Eichhubl and Boles, 2000; Heath, 2004; Burnside, 2010). The solubility of calcite also decreases with decreasing aqueous $P_{CO2}$ (Miller, 1952; Ellis, 1959). As $CO_2$-rich water degasses, therefore, calcite precipitates according to the carbonate equilibrium equation (Clark and Fritz, 1997):

$$\mathrm{Ca^{2+} + 2HCO_3^- \leftrightarrow CO_{2(g)} + H_2O + CaCO_3.}$$

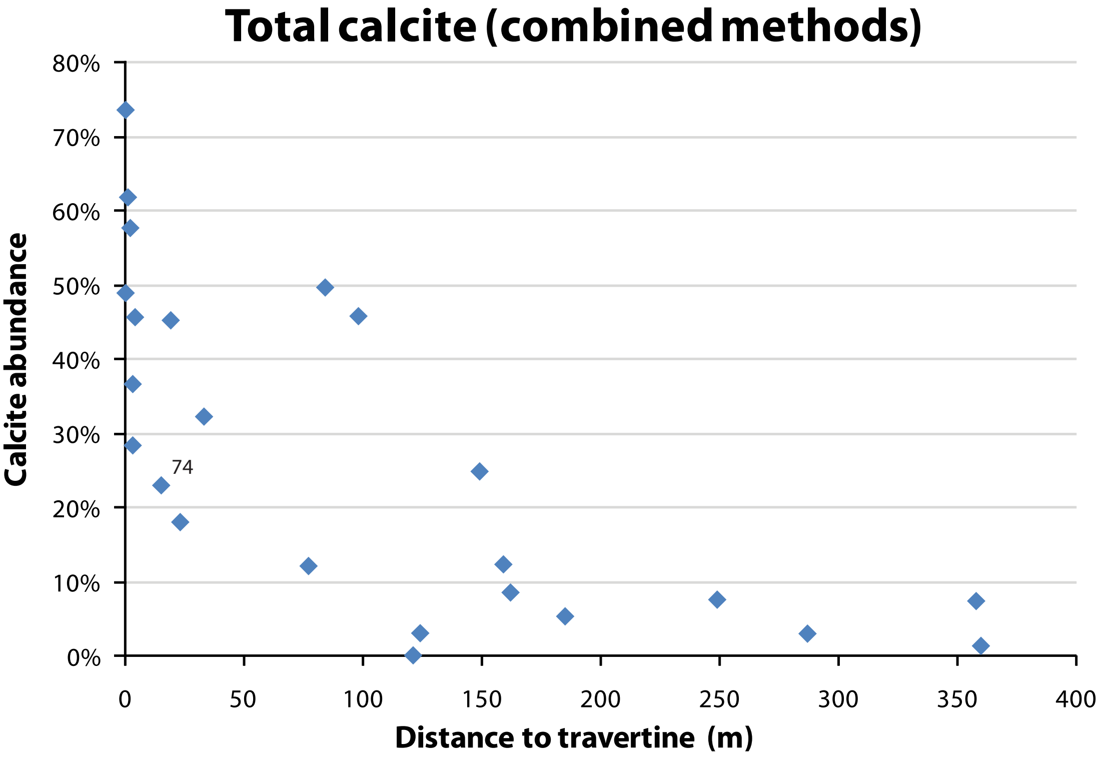

Figure 67: The average of results from both methods used to measure total calcite (point counting and signal strength calibration); an uptick in the data is evident within about 50–100 m of the travertine. Sample 74 has slightly exaggerated porosity due to late calcite dissolution.

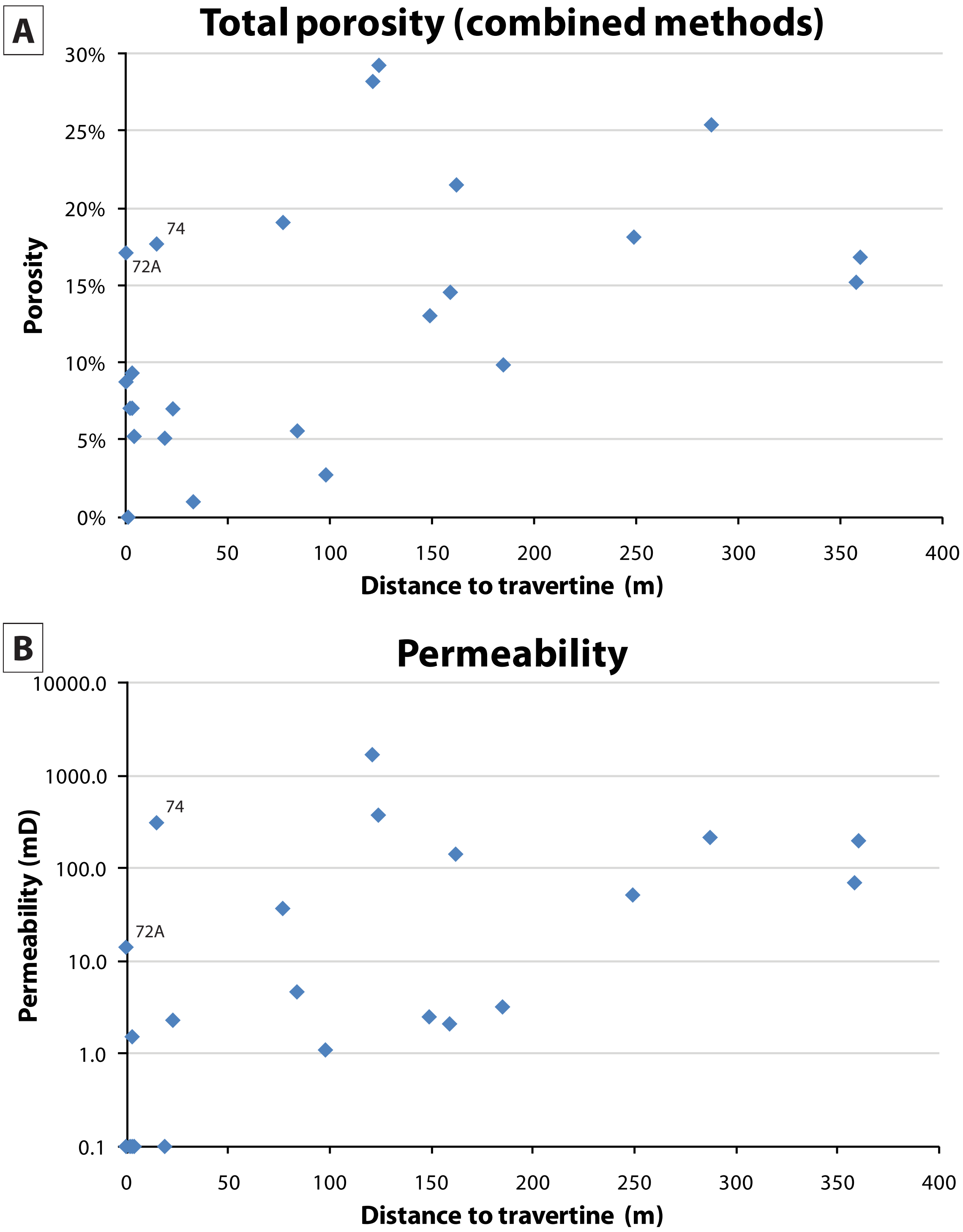

Figure 68: **A:** The average of results from both methods used to measure total porosity (point counting and He injection); a downward trend is apparent closer than 100 m from the travertine. **B:** The same trend is present in permeability data.

Water evaporation at the surface and rising pH due to degassing also facilitate calcite precipitation (see Appendix A for a more detailed description of this reaction).

In addition, the observed stable isotopic trends in pore-filling calcite also suggest that the calcite cement anomaly is a result of $CO_2$ seepage and not other processes. Heavier travertine-proximal $\delta^{18}O$ and $\delta^{13}C$ calcite values could reflect differences in the temperature and isotopic composition of water prior to $CO_2$ degassing, as well as the effects of degassing and evaporation.

Carbon dioxide degassing from spring water depletes the water of lighter isotopes (Shipton et al., 2004). The effect of preferential degassing will be slight for oxygen because of its natural abundance as a molecular component of water, but more pronounced for carbon isotopes. This effect should be recorded in calcite as an increase (relative to non–$CO_2$-related calcite) in $\delta^{13}C$ values. In addition to $CO_2$ degassing, evaporation at the seep location would deplete emanating waters in $^{16}O$, leading to heavier oxygen isotopic compositions in precipitating calcite.

The isotope data show a relatively uniform range of values throughout most of the map area: Excluding one anomalously heavy outlier (sample 80A, discussed later), $\delta^{18}O$ remains around -13‰ PDB and $\delta^{13}C$ around -3‰ PDB. Within a radius of 25 m around the travertine, however, the isotope ratios are heavier, with $\delta^{18}O$ averaging about -10‰ PDB and $\delta^{13}C$ averaging nearly 4‰ PDB. These relatively heavier values in proximity to the travertine define a chemically unique zone within the high-cementation anomaly, distinct from calcite precipitated from non–$CO_2$-rich water or as a result of surface weathering elsewhere in the map area. This trend is consistent with light isotope depletion due to $CO_2$ degassing and evaporation. The rise in $\delta^{13}C$ values is more pronounced than that for $\delta^{18}O$ values, suggesting the effect of $CO_2$ degassing is predominant over that from evaporation. This demonstrates that cementation near the travertine formed from a $CO_2$-rich spring similar to Crystal Geyser. Such a spring represents a conduit through which $CO_2$-rich fluids escaped to the surface.

The water erupting at Crystal Geyser is similar in temperature to average regional surface water: Crystal Geyser waters are 15–18°C (Baer and Rigby, 1978; Heath, 2004; Gouveia and Friedmann, 2006; Heath et al., 2009); the annual mean temperature for Green River, UT is 12°C (U.S. Climate Data), similar to the water temperature of the nearby Price River of 9–13°C (USGS, 2011) (no nearby water temperature data are available for the Green River). Lighter isotope ratios would be expected for carbonates precipitating from warmer seep water compared to cooler surface water because increasing temperature corresponds to a decrease in isotopic fractionation between $CO_{2(gas)}$ and $CO_{2(aqu)}$ and between aqueous solution and mineral. The 2–9°C higher temperature of seep water relative to surface water should decrease the $\delta^{18}O$ composition of seep-related calcite by 0.5–2.1‰ relative to (soil) calcite precipitation unassociated with the seep (see Appendix G for these calculations). This temperature-dependent decrease is opposite to the observed 3–6‰ increase in $\delta^{18}O$ values for calcite adjacent to the travertine relative to calcite distant from the travertine, consistent with $CO_2$ degassing as the dominant mechanism for the trend in $\delta^{18}O$. Due to the mass balance reasons noted above, carbon dioxide degassing has an even more pronounced effect on calcite $\delta^{13}C$ values.

Water sampled from Crystal Geyser has $\delta^{18}O$ composition (-14.3‰ SMOW) similar to local surface and river water (-14 to -16‰ SMOW) (Mayo et al., 1991, 2003), suggesting that $CO_2$ degassing does not significantly affect the water isotopic composition at Crystal Geyser. The extent of fractionation is expected to vary from seep to seep, however, depending on the ratio of degassing $CO_2$ to water flow rate. The proximity of Crystal Geyser to the Green River and its open drill hole conduit likely result in a higher water flow rate than more distant, rock-hosted inactive seep sites such as the one analyzed in this study.

The 25-m-wide calcite isotopic anomaly is distinctly smaller than the 50–100-m cementation anomaly indicated by calcite content, porosity and permeability. I explain this difference as a result of $CO_2$ degassing being confined to a small area around the active flow conduit immediately above and adjacent to the zone of fluid depressurization. Carbonate cementation, on the other hand, reflects the spatial extent of groundwater supersaturation with respect to calcite. Compared to the zone of depressurization, conditions of supersaturation can extend farther from the flow conduit, depending on the rate of groundwater flow away from the conduit and the distance of flow over which groundwater attains chemical equilibrium with the host sandstone.

In the following discussion, I use the 25-m isotope-defined radius around the travertine to indicate the zone of intense $CO_2$-related alteration. The radius is superimposed on each dataset (porosity, permeability, calcite content and also isotope) in Figure 69. This helps identify variability in each dataset that requires additional analysis—for example samples inside the 25-m alteration radius that have high porosity, or samples outside the alteration radius that have unusually high calcite content.

#### 3.1.1.1 High porosity inside the 25-m alteration radius

Two samples within 25 m of the travertine exhibit unusually high porosity compared to other samples in this area. Sample 72A is a heavily fractured, not fully cemented shale with 17% porosity, collected directly under the travertine. Sample 74 is a fairly well cemented sandstone (calcite content: 23%) located near the travertine (15 m), but contains high porosity (18%). It has average grain size (0.3–0.4 mm) and no outstanding compositional features. The diverse lithologies associated with Salt Wash Member sandstones could hypothetically create variations in pH buffering due to more or less abundant feldspars or zeolites (Gunter et al., 1993; Hutcheon et al., 1993; Clark and Fritz, 1997; Baines and

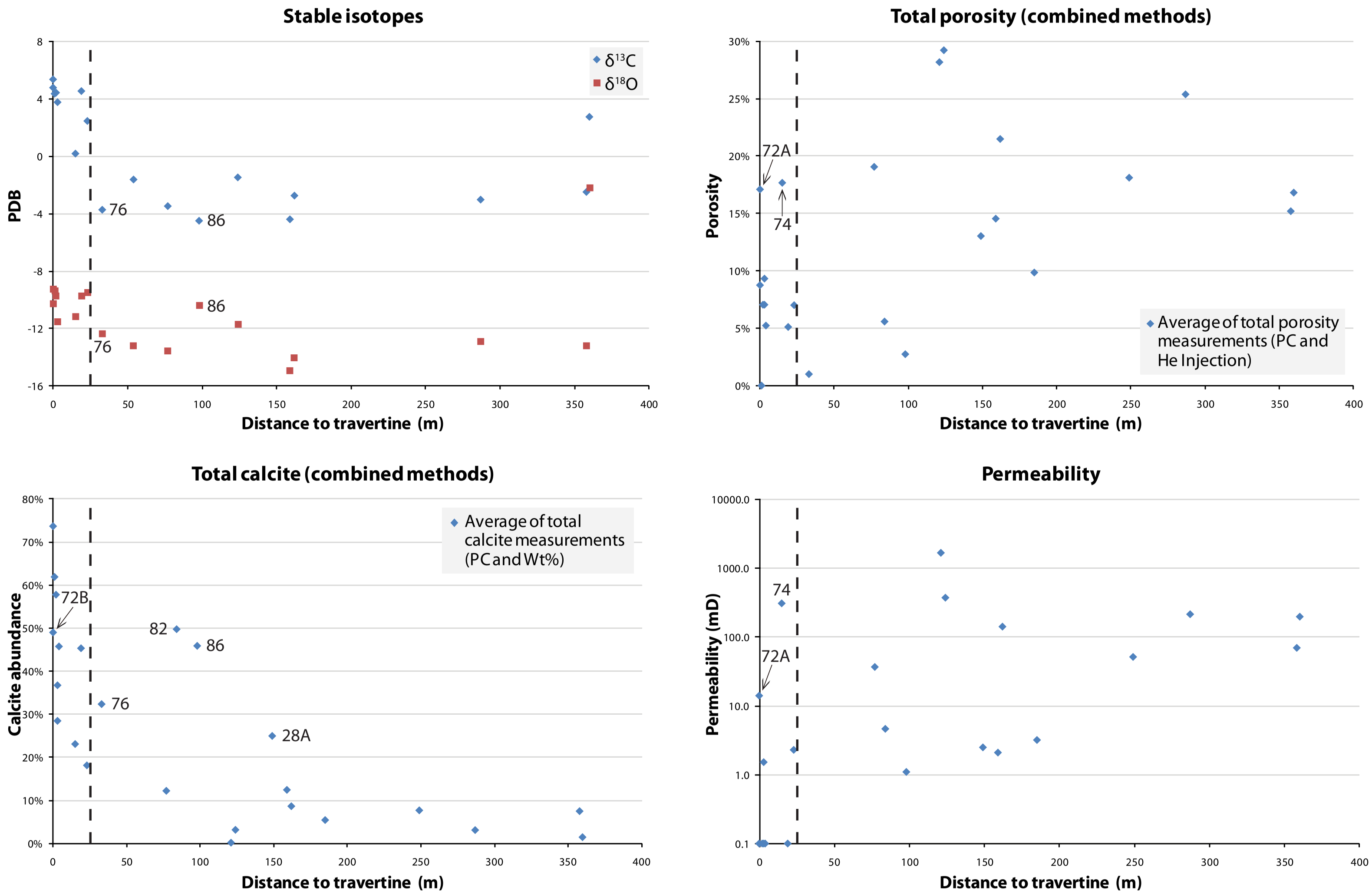

Figure 69: Applying the isotopically defined 25-m radius to other petrographic datasets indicates trends that are somewhat obscured by high variability in the data. Labeled samples require additional examination in order to more carefully define any trends.

Worden, 2004), but water-rock reactions occur on timescales too slow to create small-scale heterogeneities in acidity. Although the sample is well cemented, it contains circumgranular (grain-rimming) porosity (Figure 70). Spar needs a nucleation surface, so a halo of porosity between grain boundaries and spar indicates that some material may have been dissolved. Because sample 74 has the isotope signature of recent, seep-related calcite ($\delta^{18}O$: -11.2‰; $\delta^{13}C$: 0.2‰), this dissolution would have to be recent. Surface weathering is a possible explanation for dissolution, but other samples taken in the vicinity of the travertine show no signs of such circumgranular porosity.

#### 3.1.1.2 High calcite content outside the 25-m alteration radius

Samples 28A, 76, 82 and 86 stand out for being located outside the isotopically unique zone of calcite cementation but nonetheless containing high calcite content. Such samples require additional scrutiny. The locations of these anomalies are shown in Figure 71. It is tempting to explain three of them by their proximity to a major fault: 28A, 76 and 82 are all located near a major fault in the relay ramp. Faults commonly transport fluid to the surface (Curewitz and Karson, 1997). If meteoric and therefore acidic, these fluids could hypothetically dissolve limestone at depth and reprecipitate calcite in overlying sandstones containing sufficient pH buffering capacity. Water leaking through Little Grand Wash is charged with $CO_2$, however, and sample 76, for which there is isotope data, does not exhibit the $CO_2$-related isotopic signature. This is consistent with trends in the isotope data, which show that $CO_2$-related calcite is restricted to the conduit. This indicates that faults outside the conduit are not currently transporting significant amounts of water to the surface, and such instances of calcite cementation therefore require a different explanation.

Sample 86 is located outside the fault zone, far from any faults and therefore unrelated to fault-related flow. Cementation could be a surficial effect, but surface

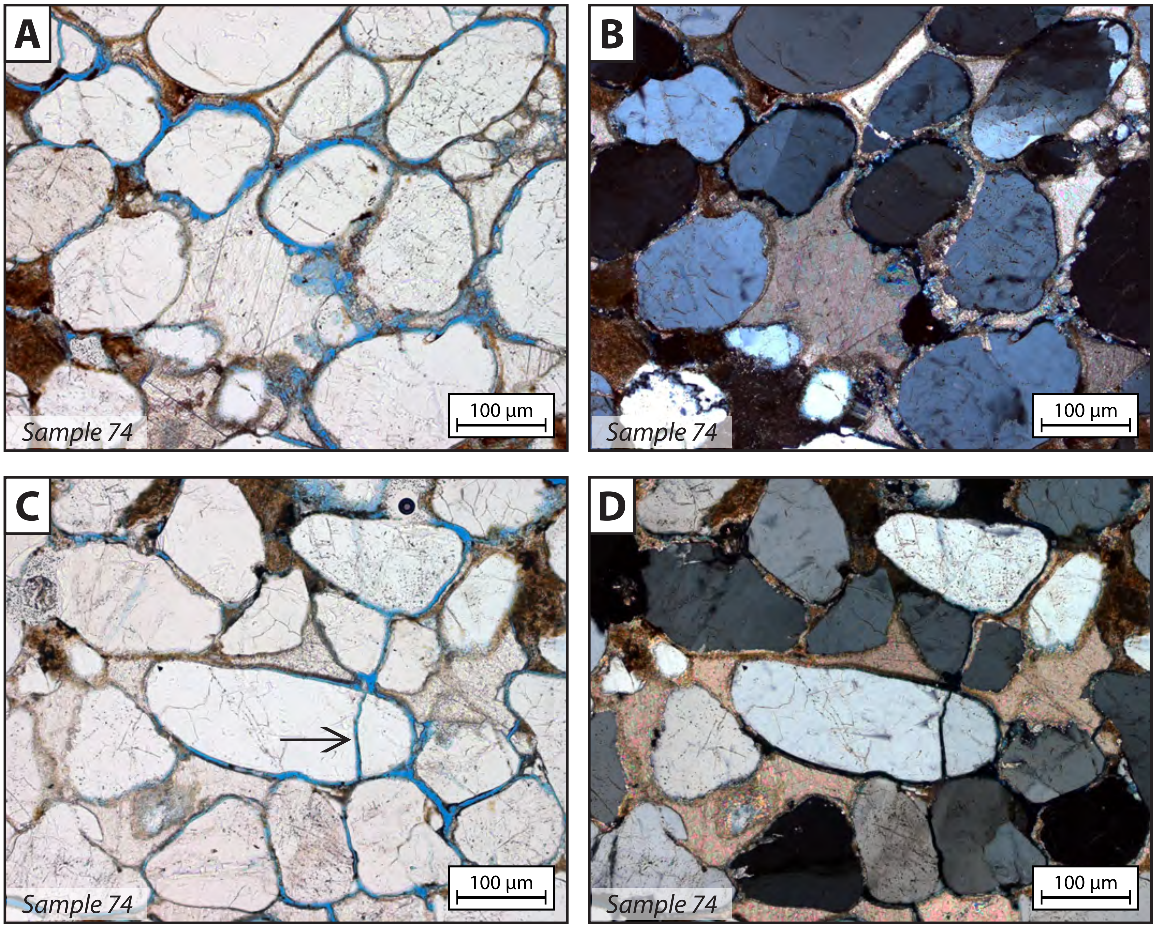

Figure 70: **A–D:** Sample 74 has been extensively cemented, and the isotopic signature confirms that cement is seep-related. Despite being located only 15 m from the spring, it has unusually high 10% porosity. This is due to circumgranular porosity, evident here. In (C) and (D) an epoxy-filled quartz grain fracture (arrow) suggests recent, possibly collection-related damage to the sample.

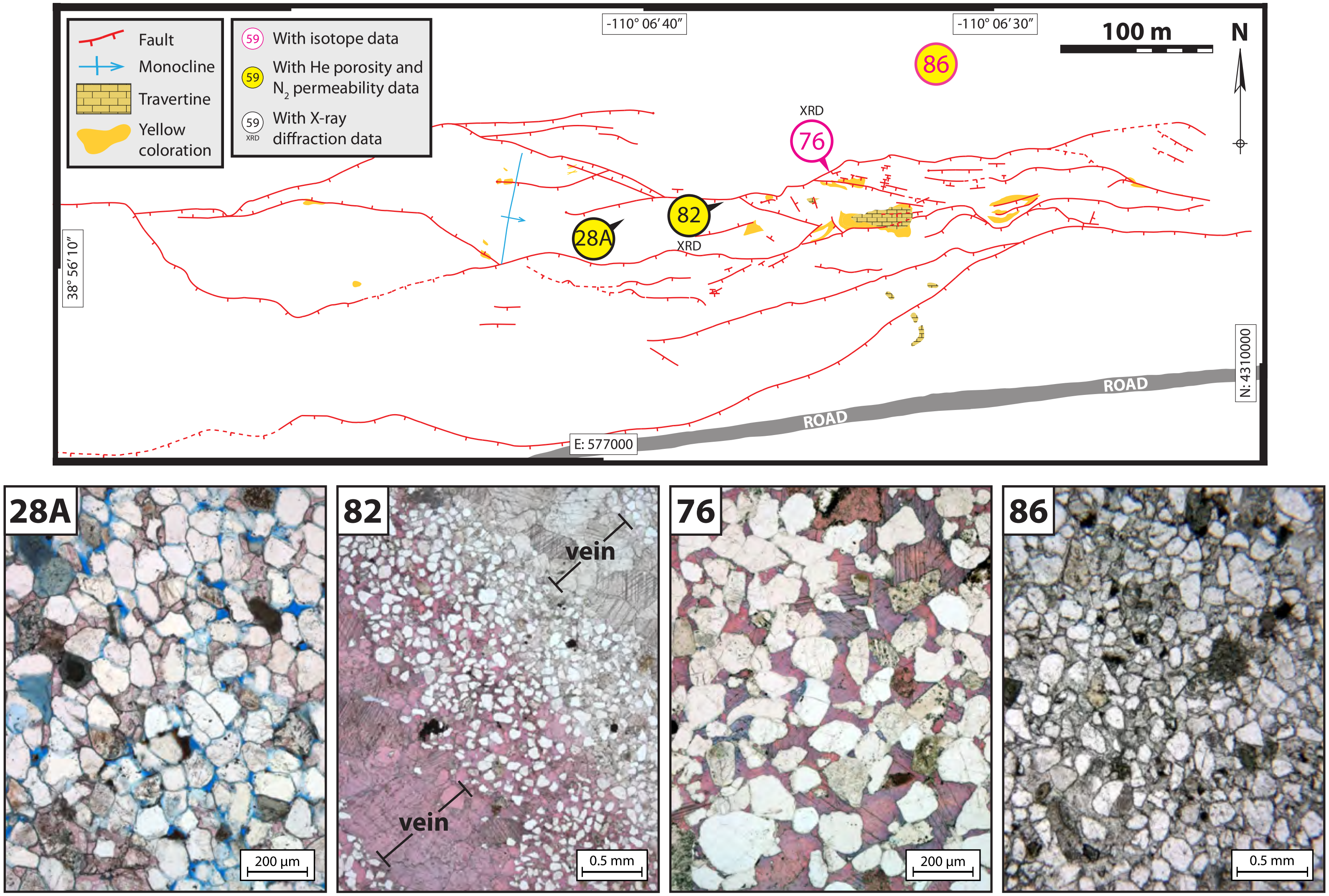

Figure 71: Locations and photomicrographs of samples with apparently anomalous high calcite content.

weathering tends to form micritic caliche (Zhou and Chafetz, 2009a, 2009b), not the well-developed calcite spar seen in sample 86. Cementation could be controlled by lithologic heterogeneities. If that were true, extensive secondary porosity (calcite-occluded) would be expected where original depositional features had been dissolved to provide material for the cement. I did not observe any such dissolution, though there are a few conspicuous recycled carbonate grains. Although the material could be allochthonous, the only nearby source is the $J_{ms}4$ sandstone. This is an overlying unit, however, and contains insufficient suitable minerals: Total calcite cement in $J_{ms}4$ (sample 35B) is 6%, and the total abundance of sedimentary grains is 11%, of which only a portion are recycled carbonate grains—not enough to create 41–51% calcite cement in an underlying sandstone lens. No other nearby sources contain significant calcite.

#### *3.1.1.2.1 Early-diagenetic calcite*

The relationship in sandstones between calcite spar and quartz cement (Figure 72) provides a better explanation for these highly cemented yet non–spring-related samples. The inverse nature of this relationship seems to imply that one stymies the other: Either quartz restricts the precipitation of spar or spar restricts the precipitation of quartz. While spar cement can form on most surfaces in these samples, including quartz cement, quartz overgrowths require a quartz substrate on which to nucleate (Land and Dutton, 1978; Dixon et al., 1989), and cannot grow if that substrate has been covered in spar. It therefore seems that the presence of spar should be the controlling factor: Pervasive spar uses up all available quartz precipitation surfaces, preventing quartz overgrowths from being able to nucleate. At and below about 15% spar abundance, according to the sandstone point count data, there still seem to be enough suitable substrates remaining for quartz overgrowths to gain a foothold.

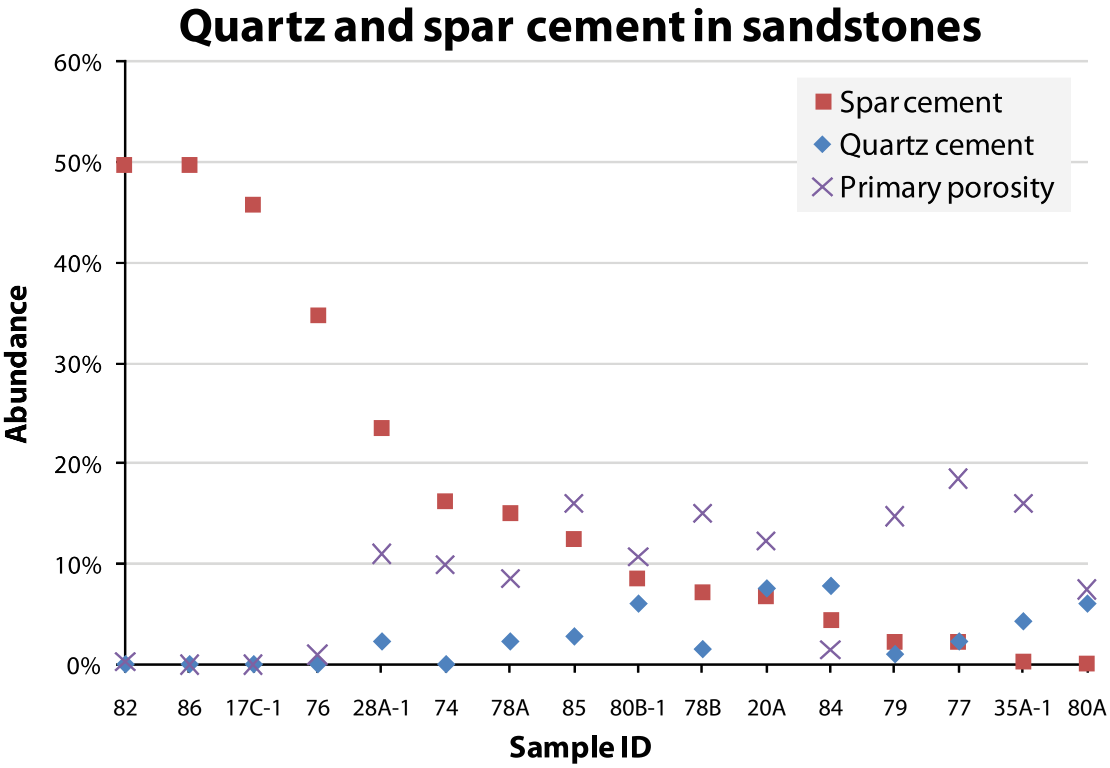

Figure 72: The inverse relationship between quartz and calcite cement. The lack of porosity and lack of quartz cement in the first four samples indicate that calcite growth limits quartz growth. This in turn indicates that some map area calcite cement is old. Samples 28A-1, 76, 82 and 86 are those with high calcite content found outside the conduit; samples 74 and 84 contain recent spring-related cement. Sample 35B is excluded, as it contains isopachous chalcedony not comparable to quartz cement elsewhere in the field; it is included in Figure 49.

If the calcite cement is recent, however, this interpretation is problematic. Quartz must have been emplaced long before calcite, as it requires elevated temperatures and long periods of time to precipitate in large euhedral form (Walderhaug, 1994). Two of the sandstone samples (74 and 84) bear the isotopic signature of spring-formed calcite, verifying that they are modern precipitates and not ancient cements that could have predated or precipitated synchronously with quartz. There is less control on the timing of precipitation in other samples.

Assuming the relationship between cements is not coincidental, it must be controlled by the amount of available pore space and suitable nucleation sites remaining after formation of one or the other cement. The slow growth rate of quartz compared to calcite would limit its ability to compete for available space if calcite were precipitating synchronously, but quartz is presumably an old cement and had a long time to grow during burial and exhumation of the Colorado Plateau. In samples with no remaining primary porosity, the decrease in spar should therefore be equal to the abundance of preexisting quartz cement, which consumed potential growth space but did not eliminate nucleation surfaces. As long as there is remaining porosity, however, the amount of quartz and calcite cement should be decoupled: Quartz cement has a maximum of 8% abundance, which is too low to reduce permeability to the point where calcite-saturated waters would be unable to infiltrate a sandstone, so the loss of pore space due to preexisting quartz cement is not a limiting factor on calcite cement until there is no remaining space to fill (Figure 73).

Some primary porosity remains in most samples (Figure 72). Assuming quartz precipitated first, this means neither calcite nor quartz should be a limiting factor on the other and there should be no relationship between them. If this were true, the apparent inverse relationship in Figure 72 would be merely coincidental. The sample size is 17—all of the sandstones for which point count data were collected. While a larger sample size would

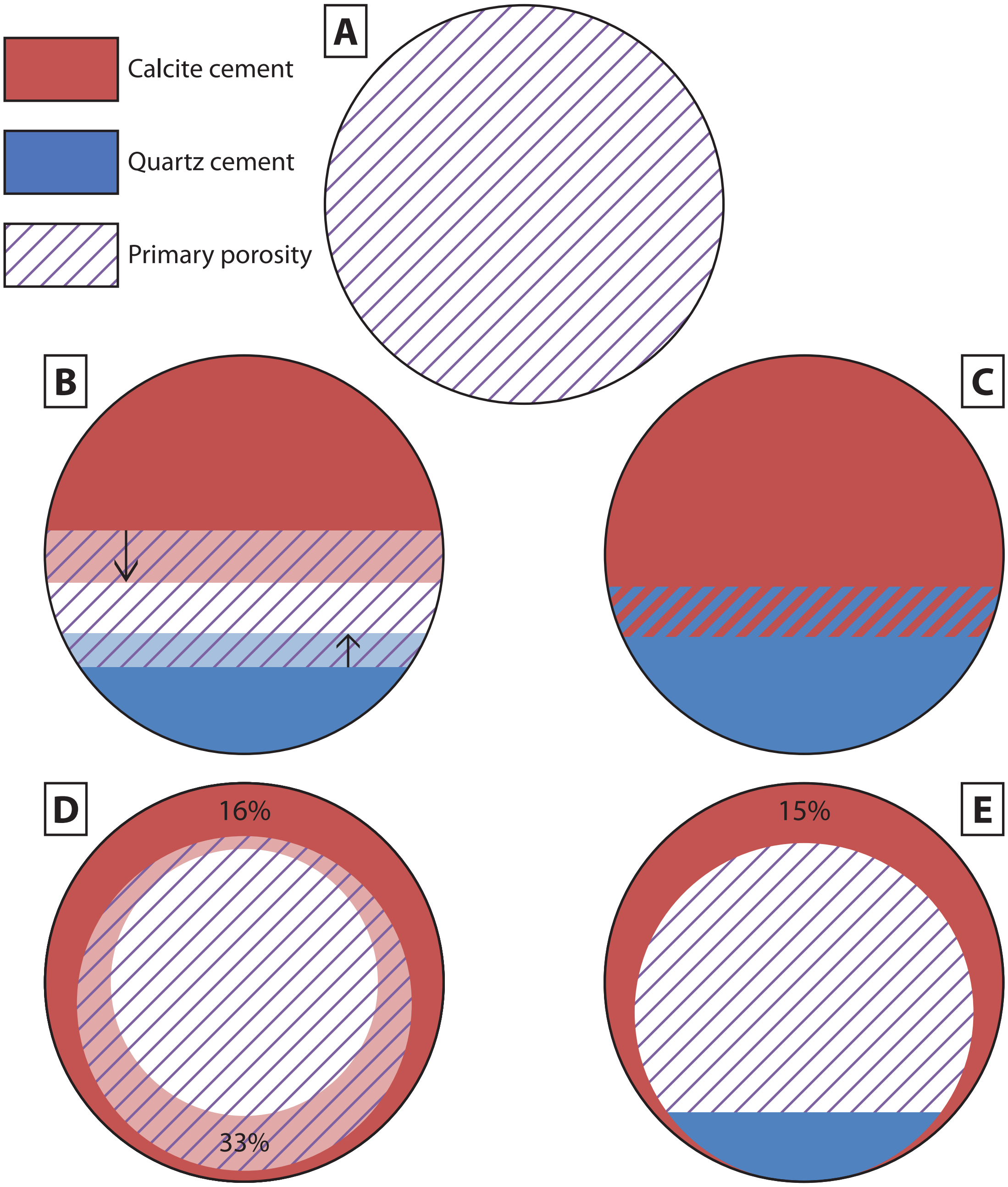

Figure 73: **A:** Unfilled porosity. **B:** With porosity remaining, neither cement limits precipitation of the other. **C:** With no porosity remaining, the amount of preexisting cement directly limits the amount of possible late cement. **D:** If calcite cement predates quartz cement, it covers suitable nucleation surfaces and prevents quartz growth. The minimum to prevent quartz overgrowths appears to be 16%. **E:** Calcite content of 15% or less appears to leave quartz nucleation surfaces open and the only limiting factor is available porosity.

be helpful, the relationship is nonetheless quite convincing. The persistence of primary porosity therefore means quartz cement cannot have predated calcite cement: Quartz exerts only a spatial control, whereas calcite exerts a textural control as well—quartz overgrowths require a quartz surface for nucleation and cannot grow where that substrate has been covered by calcite (Cecil and Heald, 1971; Land and Dutton, 1978; Dixon et al., 1989). This interpretation is bolstered by looking at the first four samples: These have no remaining primary porosity (one has 1%), meaning that a controlling relationship will be in effect regardless of which cement came first. In these samples there is 0% quartz cement and 35–50% calcite cement. If one cement limited the other, then calcite limited quartz, so calcite had to precede quartz. Quartz cement generally requires elevated temperature (burial conditions of greater than 60–80°C) and time in order to precipitate. The calcite in these samples must therefore be old, likely burial-related cement. Such cement can form with considerable spatial heterogeneity based largely on differences in depositional energy (Dutton and Willis, 1998). This could explain the patchy distribution of non–$CO_2$-related calcite in the map area (Figure 20).

Ideally this emplacement history could be drawn solely from petrographic analysis of the growth relationship between cements. Although petrographic observations are consistent with the conclusions, however, they are too equivocal to stand on their own. Absolute proof that calcite preceded quartz, based on growth relationships, would require the precipitation of quartz cement on top of calcite cement, which I did not observe. The lack of such a relationship may reflect that quartz cement prefers a quartz substrate, which is in agreement with findings by Dixon et al. (1989) and Land and Dutton (1978).

Assuming that calcite inhibits quartz growth, however, a supportive though less definitive relationship is present: in quartz-cemented samples, the absence of quartz cement where calcite cement covers grain surfaces. If antecedent calcite cementation were patchy and incomplete, then later quartz cementation would be free to grow on a portion of grain surfaces that remained open. Such a relationship can be seen in Figure 74. Quartz overgrowths are well developed and consume much of the available space, indicating that cementation was extensive and may have been able to fully occlude porosity were it not for preexisting calcite. Such a relationship is compelling but not incontrovertible. It is possible that early quartz cementation was simply incomplete, and remaining porosity was later filled during a period of calcite precipitation.

A final growth relationship—calcite precipitation on quartz cement—is observed in most sandstones (Figure 75). Calcite can grow under both burial and surface conditions, and this relationship shows that at least one period of calcite precipitation has occurred since quartz was emplaced. Combined with earlier conclusions (based on cement abundances) showing that some calcite must precede quartz, this indicates multiple periods of calcite precipitation: at least one before and one after quartz precipitation.

The apparently feldspar-preserving effect of calcite in sample 26-1 (Figure 38) lends additional support to the early-calcite conclusion. The precipitation of calcite in the presence of high concentrations of $CO_2$ must be preceded by feldspar hydrolysis (and other aluminosilicate dissolution), which consumes $H^+$ to dissolve feldspars and buffer the water, allowing carbonates to precipitate (Gunter et al., 1993; Baines and Worden, 2004; Zerai et al., 2006; Kampman et al., 2009; Lu et al., 2011). Many feldspars throughout the map area have been highly dissolved due to acidic groundwater. If feldspars are undissolved, however, this implies they were likely shielded from acidic waters. Early calcite precipitation in a non–$CO_2$-saturated setting could provide this shield.

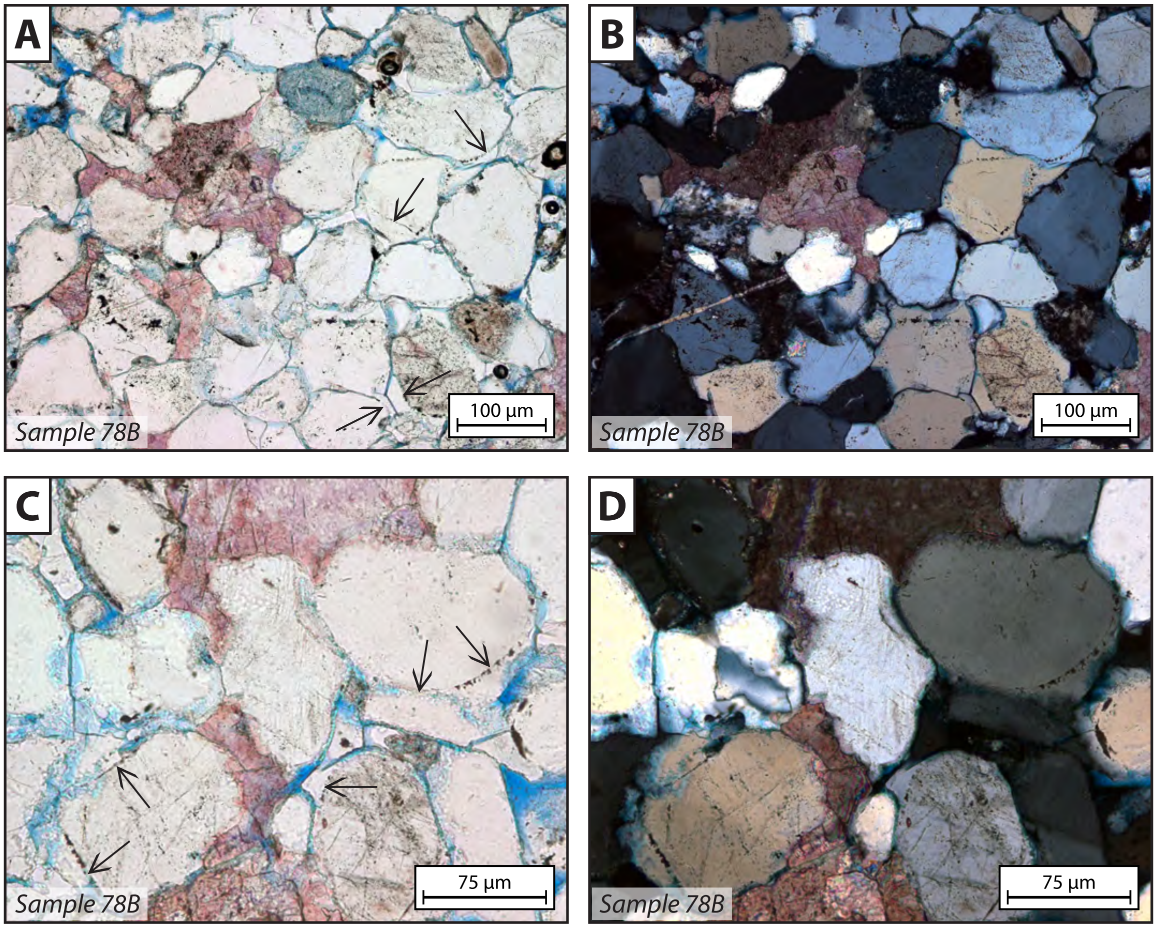

Figure 74: **A–D:** Quartz cement (arrows) in extensively quartz-cemented sandstones is absent where calcite (stained pink) appears to have preceded it. This history presumes the extensive nature of quartz precipitation to indicate that it is limited only by antecedent calcite, which destroyed suitable substrates and consumed porosity; otherwise quartz would have used much more of the available space. It is also possible, however, that quartz cementation preceded calcite and was simply incomplete, not using all available space in which to grow; calcite then grew into the remaining porosity.

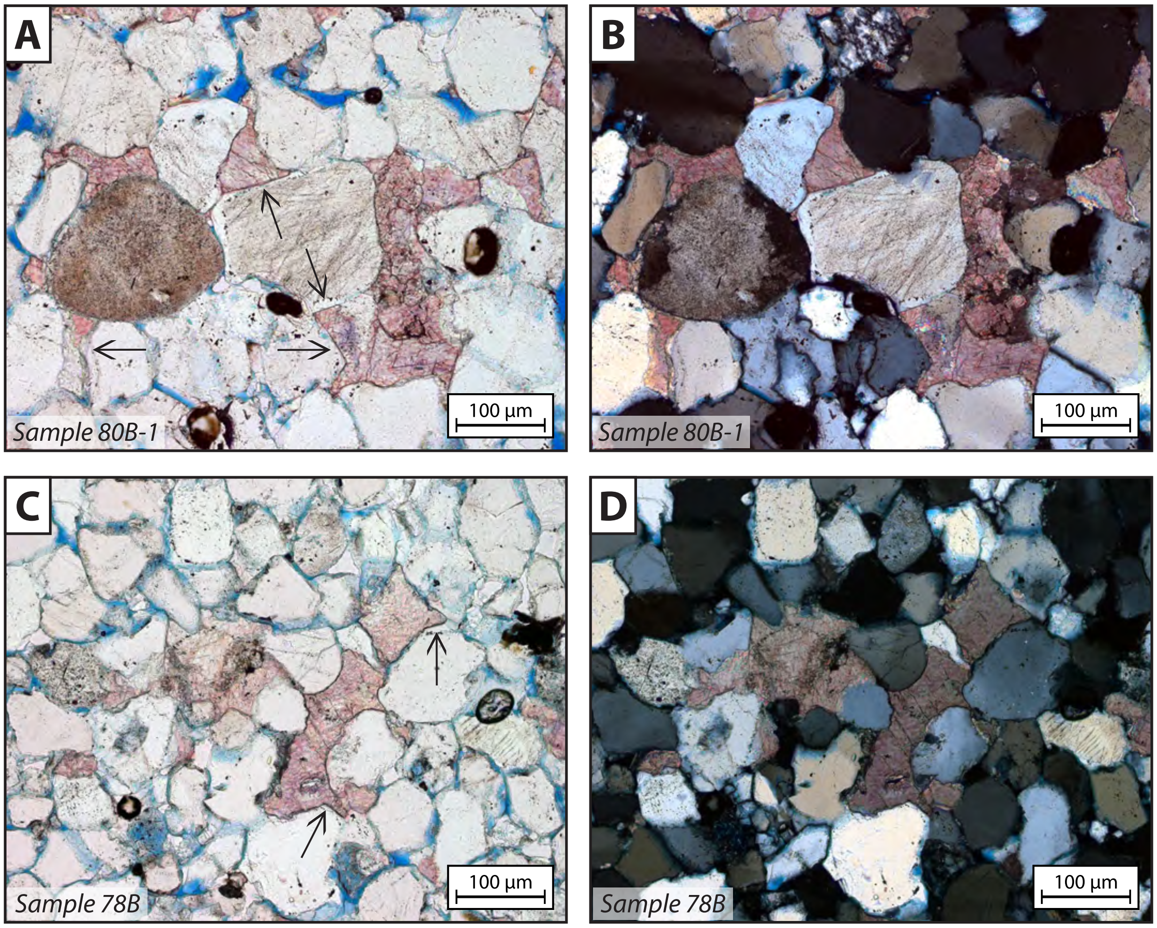

Figure 75: **A–D:** Calcite cement (stained pink) precipitating on quartz cement (arrows) means that at least one period of calcite growth must postdate quartz growth.

#### 3.1.1.3 Using cementation history to refine the calcite content trend

The highly cemented samples located outside the conduit (28A, 76, 82 and 86) are included in the quartz-calcite relationship shown in Figure 72. The above cementation history demonstrates that the best explanation for such calcite content anomalies—shown with isotope data to be non–$CO_2$-related—is that they are early cement emplaced by diagenetic processes predating $CO_2$ alteration. Such pre-$CO_2$ cementation can be pervasive, as observed in sample 86.

For the purposes of illustrating a conduit-related calcite trend, these four samples should be ignored. Sample 72B is a piece of travertine taken from the platform and can also be discounted when tracing a seep-related calcite trend. Although it has the elevated $CO_2$-related isotopic signature, it is surface precipitation and therefore not representative of a rock-hosted conduit (see Appendix H for a more detailed discussion of travertine petrography and isotopic analysis). If samples 28A, 72B, 76, 82 and 86 are removed from the calcite content data, another underlying trend appears that more closely matches the isotopically defined conduit, showing a sharp increase within the 25-m radius (Figure 76).

### 3.1.2 EXPLANATION FOR SAMPLES WITH EXTREMELY HIGH CALCITE CONTENT

Samples 82 and 86 are sandstones with 41–51% calcite content. The accepted maximum porosity for even unconsolidated river sand at the surface is 40–42% (Paxton et al., 2002), and the ceiling of secondary porosity in the map area is 6–8%, so the absolute maximum possible cementation in the map area should be about 46–50%. Morrison Formation sandstones have been buried and compacted, however. The highest measurement of field area porosity is 33% (He injection measurement on sample 77), so the upper limit of porosity (and therefore cementation) should be around 41%.

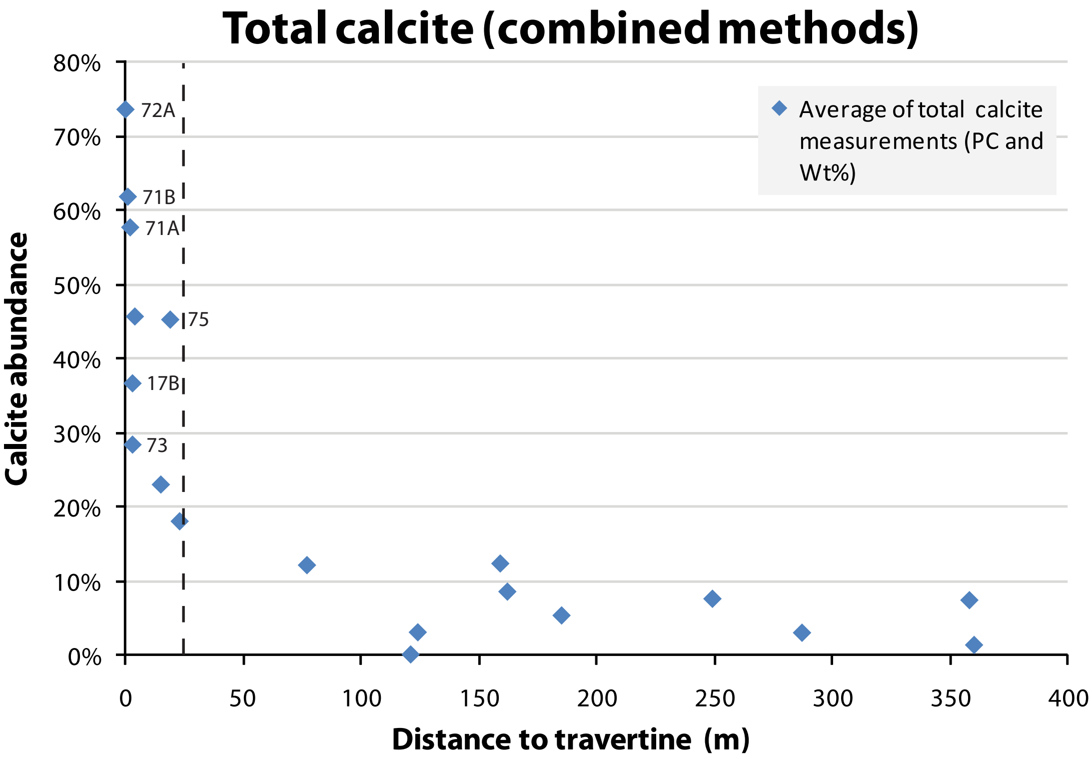

Figure 76: After removing travertine and samples with ancient calcite cement, the 25-m conduit defined by isotope data is apparent as well in calcite content data, in the form of a sharp spike. Labeled samples will receive further examination, however, as petrographic observations indicate that additional analysis is necessary to ensure that they are accurate representations of the spike in calcite cementation.

Estimates of maximum secondary porosity do not take into account veins, though. Sample 82 contains extensive calcite-filled veins (Figure 71), which increase its intergranular volume to 51% and explain its high calcite content. Sample 72A, which contains 74% calcite, is a highly veined sample of Brushy Basin Member shale that underlies the travertine deposit (Figure 17).

Sample 86 does not contain veins, but weight-percent (signal calibration) measurement shows it has total calcite of 41%—equal to the hypothetical maximum calcite content of map area samples. The signal calibration method would measure calcite from the large recycled carbonate grains in sample 86, however, meaning that actual measured calcite cement should be slightly less than 41%.

## 3.2 Formation and Closure of the Conduit

The above petrographic data demonstrate the former existence of a conduit similar to the one currently feeding Crystal Geyser. The following sections describe the life cycle of the conduit. I first assess the structural and diagenetic factors that controlled conduit formation and location. I then examine the factors that contributed to the eventual cessation of flow through the conduit.

### 3.2.1 FORMATION OF THE CONDUIT

The development of a conduit within the Little Grand Wash fault zone resulted from three controlling factors: 1) Overlapping fault segments were linked and created a damage zone; 2) permeability anisotropies within the damage zone formed a conduit, while permeability anisotropies along fault segments channeled water towards the conduit; 3) although other overlapping fault segments may share the above conditions, location of the conduit was topographically controlled to occur at a low point in the fault zone. Other conditions, such as the cross-fault juxtaposition of lithologies, also contributed to development of the conduit, but these circumstances are highly variable, difficult to predict and have limited applicability to other scenarios. The following sections examine each of these factors in more detail.

#### 3.2.1.1 Linkage of fault segments creates a damage zone

Much of the area abutting the travertine is covered, but where small pavement outcrops are exposed several meters to the north, they are dissected by low-throw (<1 m) faults. Four to five other fault segments with offset ranging from 1–18 m are exposed on the west side of the travertine where they cut roughly north-south through the wash. It is likely there are more such faults underlying the travertine and adjacent cover, but these cannot be observed. This group of north-south-striking low-offset faults breaches the relay ramp by linking the two overlapping high-throw faults that define the ramp. Such a breach is consistent with research showing that links between overlapping faults typically have a low amount of throw (Ellis and Dunlap, 1988; Peacock and Sanderson, 1991, 1994).

Most sandstones in the map area, both inside and outside the fault zone, are to some extent fractured. I have not mapped uncemented fractures, but I have mapped faults and veins (cemented fractures). The cluster of low-throw faults described above is accompanied by abundant veining. I interpret the unusual concentration of faults and veins around and underneath the travertine as evidence of a highly fractured damage zone forming at the ramp hard link. Such a damage zone is typical in the presence of overlapping fault tips and fault linkups such as those in a relay ramp (Trudgill and Cartwright, 1994; Crider and Peacock, 2004; Rotevatn et al., 2007; Anderson and Fairley, 2008). The increased fracturing in these zones is a result of elevated stress due to interaction of stress fields where the tips of propagating fault segments overlap (Cruikshank et al., 1991; Cruikshank and Aydin, 1994; Curewitz and Karson, 1997; Willemse and Pollard, 1998).

### 3.2.1.2 Permeability anisotropies form and feed a conduit

#### *3.2.1.2.1 Damage zone fractures form a conduit*

The travertine platform is deposited on top of the fault link damage zone. Runoff from the main travertine deposit appears to have formed the cluster of smaller deposits downslope to the south; excepting these secondary deposits, however, no travertine is evident elsewhere in the map area. Such spatial restriction indicates that the location of travertine at the hard link is not coincidental: The ramp breach is apparently the primary structural control on seep location.

Travertine is currently precipitating around Crystal Geyser as a result of water being channeled through a narrow conduit to the surface. At the surface, degassing $CO_2$ causes the precipitation of calcite, which forms the travertine platform. Travertine in the map area is assumed to have formed by reactions similar to those at Crystal Geyser—a $CO_2$-charged spring degassing at the surface—which indicates that the damage zone on which the travertine is deposited constitutes a preferred conduit for fluid flow. This increased-permeability conduit results from the local concentration of fractures, which can be paths for vertical fluid flow (Eichhubl and Boles, 2000). Such enhanced permeability through fractures underlying the travertine can be seen where a vein rises up a fault as it crosses from the footwall to the hanging wall (Figure 77).

Such a conduit is consistent with research showing that damage zone fractures can be an important factor in the evolution of flow paths, as they create regions of relatively high permeability along faults and especially at strain transfer zones (Antonellini and Aydin, 1995; Caine et al., 1996; Martel and Boger, 1998; Davatzes et al., 2005; Wibberley et al., 2008; Eichhubl et al., 2009). Several studies have shown that fault ramps such as the one in the map area can act as cross-fault conduits, bypassing otherwise impermeable fault-associated barriers (Rotevatn et al., 2007; Rotevatn et al., 2009; Fossen et al., 2010), but fracture zones associated with such fault linkups can also act as vertical conduits (Curewitz and Karson, 1997; Rawling et al., 2001; Rowland and Sibson, 2004; Anderson and Fairley, 2008; Annunziatellis et al., 2008). Water migrating through the relatively impermeable surrounding rock is channeled into this high-permeability conduit because it provides a preferential flow path to the surface (Forster and Smith, 1988; Eichhubl and Boles, 2000).

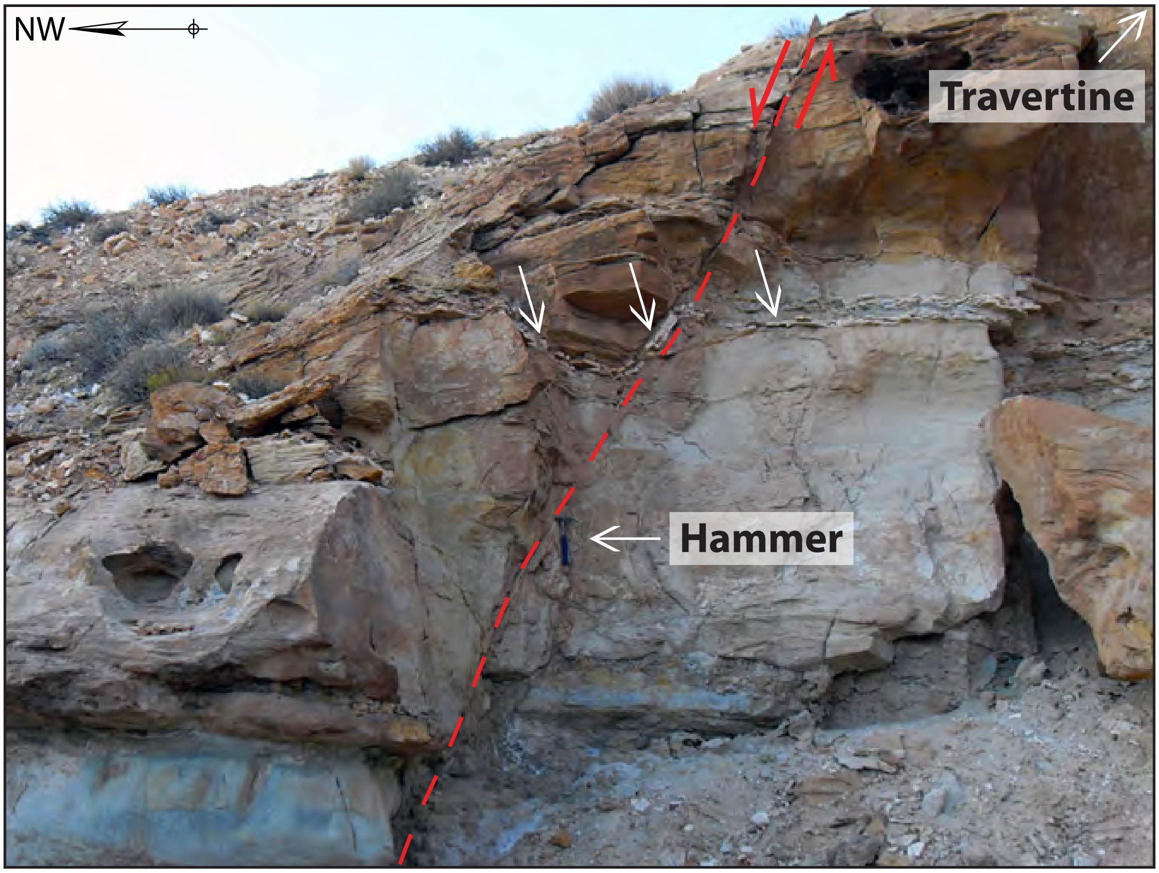

Figure 77: One of several low-throw faults offsetting a Salt Wash Member sandstone and linking the two major overlapping fault segments of the hard-linked relay ramp. Such damage zone faults form a conduit that underlies the travertine (barely out of photo to the right). Their vertical permeability is evident in a vein that rises up the fault as it crosses from the hanging wall to the footwall.

#### *3.2.1.2.2 Along-fault flow from shale gouge feeds the conduit*

Salt Wash Member sandstones are interstratified with intervals of shale that can be dragged into faults to create shale gouge (Figure 78). Shale gouge reduces permeability through the fault, but as a vertical barrier it does not interfere with along-fault (fault-parallel) permeability (Yielding et al., 1997; Shipton et al., 2004; Vrolijk et al., 2005; Wibberley et al., 2008). Damage zone fractures surrounding the fault allow fluid flow to circumvent the impermeable gouge by following adjacent parallel vertical flow paths instead of the migrating through the fault core itself (Rawling et al., 2001). Water prevented from migrating through the fault is thus directed along the fault, towards the conduit.

#### *3.2.1.2.3 Along-fault flow from deformation bands feeds the conduit*

Deformation bands are damage features that commonly form within and adjacent to brittle faults (Aydin and Johnson, 1978; Underhill and Woodcock, 1987; Davatzes et al., 2005; Shipton et al., 2005b; Eichhubl et al., 2009). In the map area, deformation bands occur along the southern segment of the hard-linked fault ramp. Unlike other sandstone faults that are composed primarily of deformation bands (e.g., Karig and Lundberg, 1990; Davatzes et al., 2005; Eichhubl et al., 2005; Eichhubl et al., 2009), deformation bands in the map area are a lesser component of the fault architecture compared to joints and veins. Where they are observed, however, they occur in tight fault-parallel clusters (Figure 79).

Deformation bands can have porosity and permeability up to three orders of magnitude lower than the host rock in which they are formed (Jamison and Stearns, 1982; Antonellini and Aydin, 1994); only a few closely spaced, low-permeability deformation bands are necessary to reduce permeability through a fault ramp (Rotevatn et al., 2007). Zones of deformation bands can therefore form low-permeability barriers and cause compartmentalization in otherwise porous and permeable sandstone (Pittman, 1981;

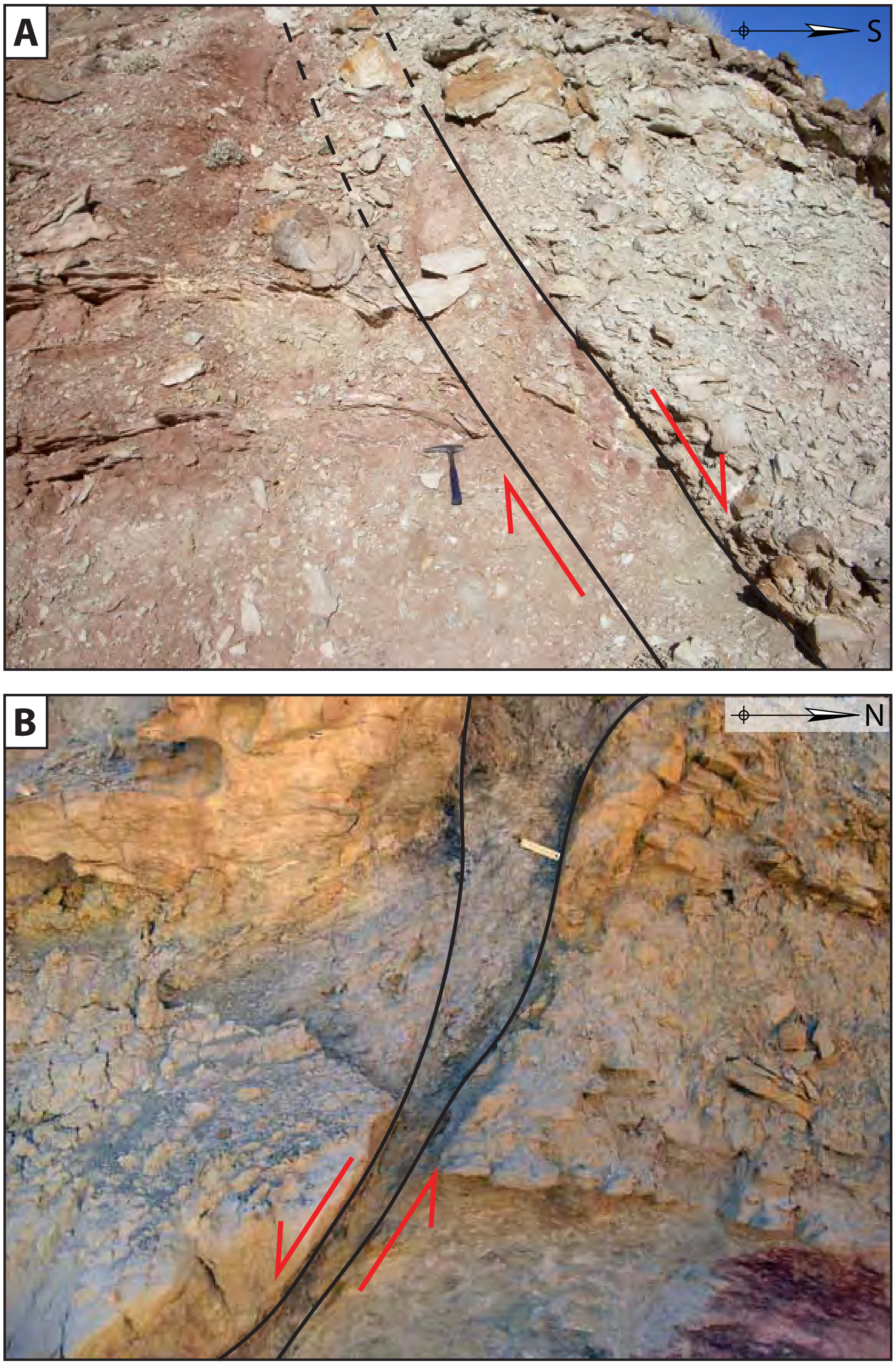

Figure 78: **A:** Shale gouge smeared along a fault juxtaposing Salt Wash Member sandstones and shales; located 40 m northwest of the travertine platform. **B:** Shale gouge in another Salt Wash Member-cutting fault 20 m west of the travertine platform; ruler is 15 cm long.

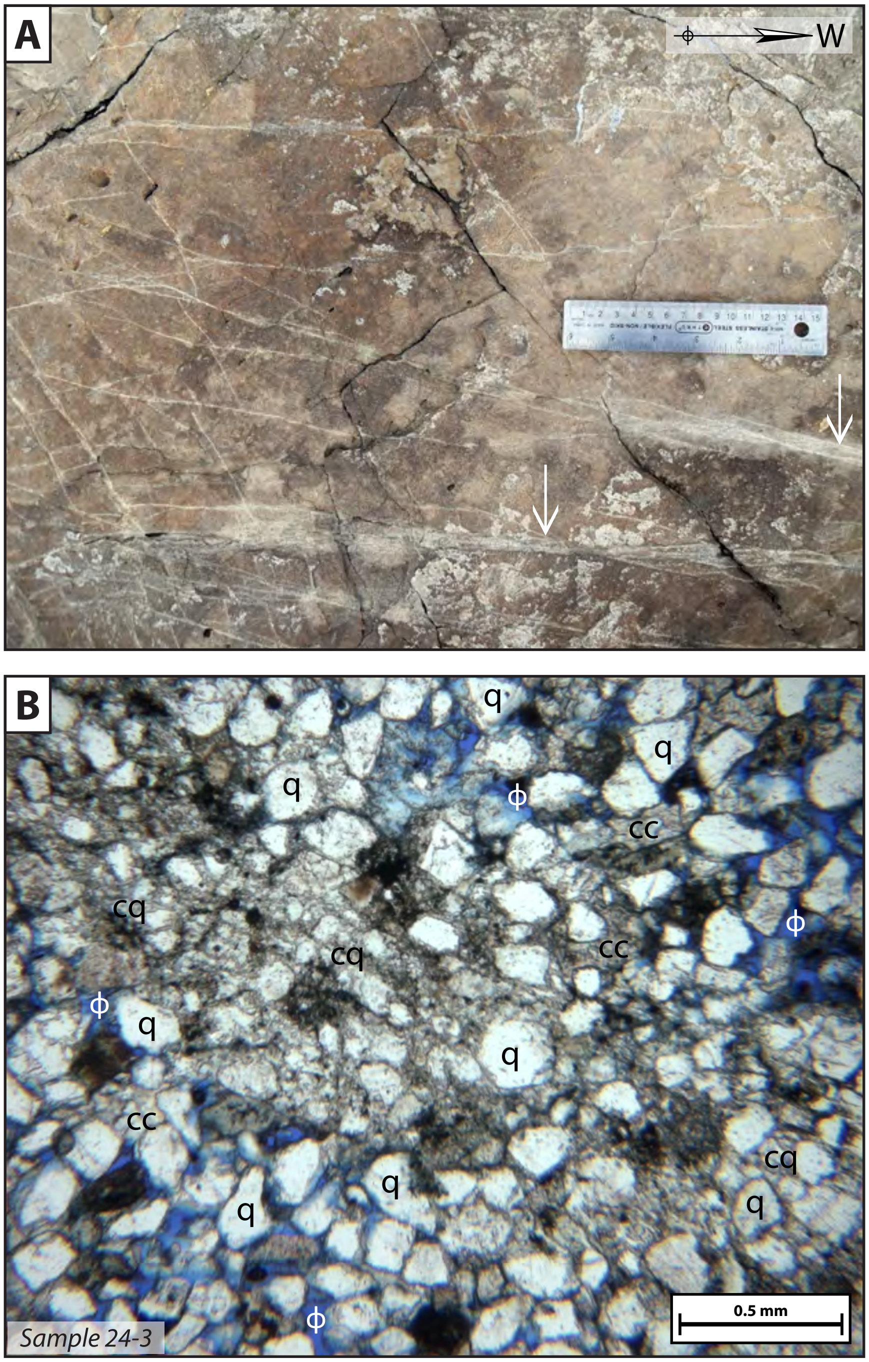

Figure 79: **A:** Deformation bands in Salt Wash Member sandstone along Fault 2 (Figure 10); note the tight clusters (arrows). **B:** Photomicrograph of a Salt Wash Member deformation band showing typical reduction in porosity due to pore collapse and grain cataclasis (q: quartz; cq: cataclastic quartz; cc: calcite cement; ϕ: porosity).

Antonellini and Aydin, 1994; Eichhubl et al., 2004; Rotevatn et al., 2007; Wibberley et al., 2008; Rotevatn et al., 2009).

At the macro scale, deformation bands in the fault zone may be too discontinuous to cause extensive interference with fluid flow. The abundance of deformation bands is underreported in this project because they were mapped only where they were conspicuous. Where they are present, however, they will form barriers to cross-fault flow (Rawling et al., 2001; Rotevatn et al., 2007; Rotevatn et al., 2009). Where these barriers exist, migrating fluids will be channeled towards the fault link and its associated vertical fracture permeability. This will augment the similar permeability anisotropies created by shale gouge by directing the flow of escaping fluids into the conduit from which the spring is sourced.

#### 3.2.1.3 Topography discriminates among potential seep locations

The travertine is located at the base of the fault scarp, about 35 m below the top of the footwall, and lies at the end of a 200-meter-long ravine that begins about 25 m above it. Currently the travertine rises 5–10 m above its surroundings. It was deposited 27 ka (Burnside et al., 2009), however, and the average rate of erosion in the Colorado Plateau is about 0.2 m/ka (Woodward-Clyde Consultants, 1983), meaning about 6 m have been eroded since travertine deposition. This shows that the travertine was originally deposited on level ground (its current elevation above its surroundings indicates that it forms an erosion-resistant cap). In the past the scarp and ravine likely rose even higher above the travertine, as the washes coming off the fault likely caused a greater rate of erosion due to the high energy resulting from a steep gradient. The travertine location was therefore a topographic low point along the fault.

This topographic control is consistent with research showing that topography is a factor affecting seep location (Chan et al., 2000; Anderson and Fairley, 2008). The fault zone contains many intersecting fault segments, and fracturing is nearly ubiquitous. No other overlapping fault segments in the map area show cement or travertine representative of an ancient $CO_2$ seep, however. Assuming there are multiple zones suitable to act as conduits, the spring is likely to erupt at the topographically lowest of them, where topography intersects the water table or comes closest to it (Forster and Smith, 1988). Rather than rise the additional 30–40 m necessary to reach the surface via alternate potential escape paths such as the upper hard link, water is likely to be channeled into the conduit through which the least amount of work is required to escape.

### 3.2.1.4 Additional locality-specific conditions

Cross section B–B' indicates that shallow subsurface conditions beneath the travertine may be fortuitously arranged to enhance formation of the conduit. Because shale sequences constitute much of the Morrison Formation, thick low-permeability horizontal barriers to vertical flow are common. The $J_{ms}1$–$J_{ms}5$ sandstone markers that underlie the travertine are each locally 3–8 m thick. Their considerable thicknesses create a lithologic column in the immediate subsurface more conducive to vertical permeability than shale-dominated sequences.

Sandstone-rich conditions are augmented by favorable cross-fault juxtapositions among the $J_{ms}3$–$J_{ms}5$ sandstones, which are 3–5 m thick, each separated by 2–3 m of shale. Because fault throw underneath the travertine is low (about 4 m), offset through these beds creates an almost continuous 20-m vertical column of sandstone (Figure 80). In strata composed of interbedded shales and sandstones, greater vertical sandstone distribution via fault offset will increase overall vertical permeability: If truncated sandstones are vertically stacked in close succession, they can form a permeable column through which upward flow avoids shale strata on one side of the fault or the other (Figure 80). Shale gouge, if present,

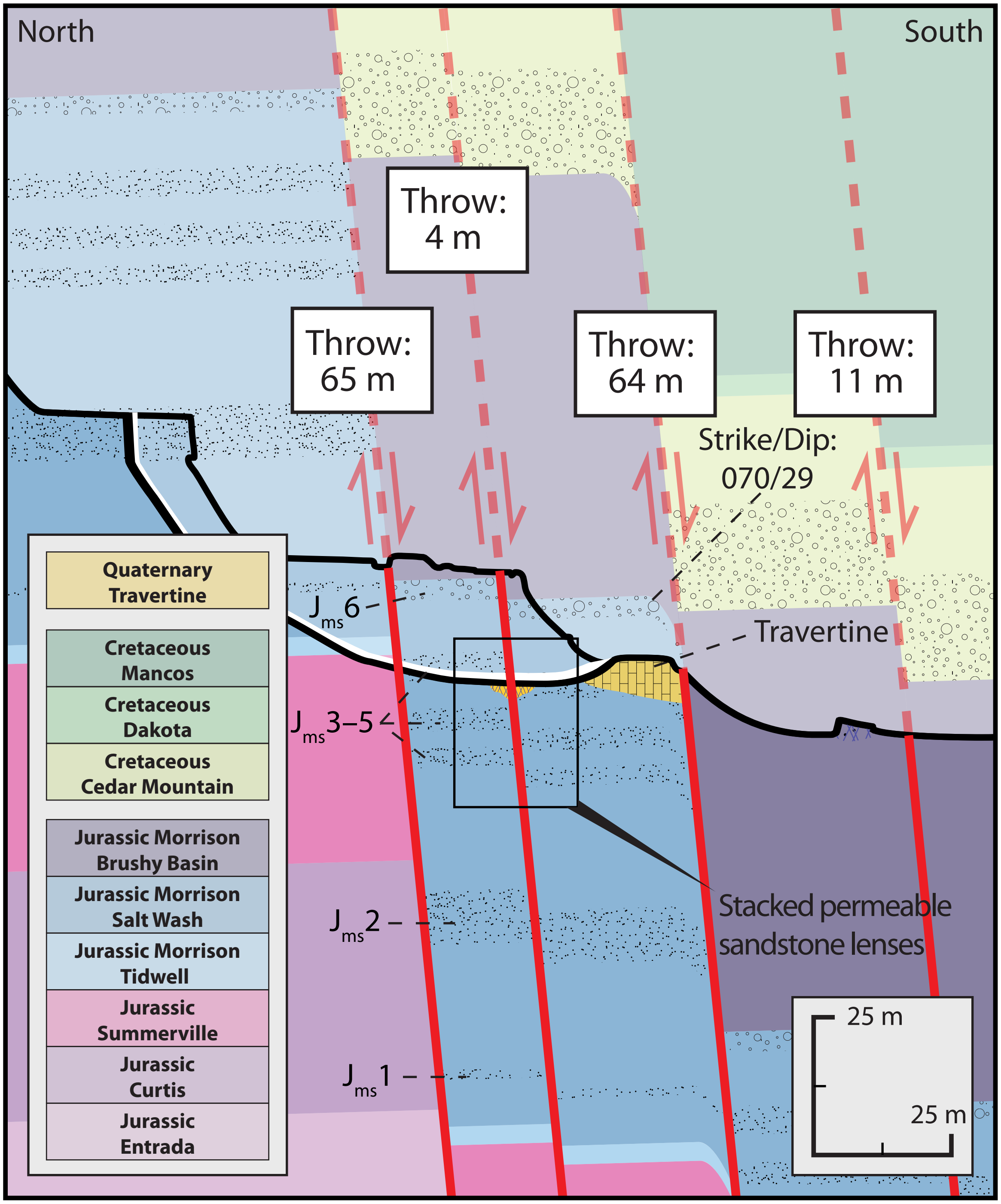

Figure 80: A portion of cross section B–B' shows that fault throw underneath the travertine offsets Salt Wash marker sands to create an almost continuous column of permeable sandstone at this location. Increased vertical sandstone distribution on one side of the fault or the other facilitates the ability of rising fluids to circumvent low-permeability shale strata.

will interfere with fluid flow across the fault, but the cumulative stacking effect nonetheless increases vertical permeability—the vertical barriers presented by shale gouge, inhibiting cross-fault flow, are generally thinner than 1 m (Figure 78), whereas the horizontal barriers presented by in-place shale strata, hindering vertical flow, are often 5 m thick or more. Once having flowed across the fault, the fluid can then circumvent the more imposing barrier of thick shale strata by flowing instead through the sandstone. Shipton et al. (2004) interpret the shale underneath the travertine as vein-dissected fault gouge. If this interpretation is correct, then the dense boxwork of veins demonstrates the viability of cross-gouge flow.

The cross-fault juxtapositions of sandstone and shale strata are unique and highly variable along every fault. Accurate prediction therefore requires low-level, location-specific knowledge of sub-formation-scale stratal thicknesses and fault offset. Conditions in the map area consequently offer little prescriptive, universal ability to better characterize potentially leaky faults—only the readily evident fact that knowledge of the nature and arrangement of subsurface strata are useful, as these juxtapositions will inevitably have some effect on local permeability.

The following points summarize controls on the creation and location of leaking springs in a complex fault zone incorporating interbedded sandstones and shales:

**1.** A conduit will form in the high-permeability damage zone associated with major intersecting or overlapping faults, such as a fault ramp hard link.

**2.** The fluid-channeling effect of this flow-favorable permeability anisotropy can be augmented by the lateral presence of fault-associated shale gouge and deformation bands, which will tend to form barriers to cross-fault flow and channel water towards the conduit.

3. Given multiple zones with suitable permeability conditions, a location will be preferred for conduit formation if it intersects the surface at a topographic low.
4. The subsurface arrangement of high-permeability sandstone zones relative to low-permeability shale barriers may also facilitate the creation of a conduit. These conditions are location-specific with high spatial variability, however. Effective prediction of such flow paths and barriers requires sub-formation-scale knowledge of stratal thicknesses and lithologies, as well as fault offset.

### 3.2.2 OVERALL FAULT SYSTEM FLOW CHARACTERIZATION

Most fluid escape through the Little Grand Wash fault zone occurs through conduits such as the one in the map area. Alignment of salt staining with faults and its association with damp outcrops indicate that saline water is evaporating at the surface after migrating vertically through fault segments. This shows that some migration of brine occurs outside of the spring setting, but at such low volume as to be nearly unnoticeable—essentially the diffusion rate of evaporation. Although no calculations have been done to compare the cumulative volume of water expelled through slow diffusion to the volume lost via springs arrayed along Little Grand Wash, the great majority appears to be escaping from the springs.

Hard-linked ramps appear to make good vertical conduits, but the conduits are only point seeps. In a section of fault zone 3 kilometers long, $CO_2$-charged water is escaping only from scattered narrow conduits. Compared to the potential for expulsion along the entire length of the fault, this distribution imposes significant limitations on the amount of fluid that can escape.

### 3.2.3 CLOSURE OF THE CONDUIT BY ALTERATION

Trends in porosity, permeability and calcite cementation are used to identify the conduit and define the extent of associated alteration because they directly result from the presence of $CO_2$-rich water: As water flows through the conduit, the presence of degassing $CO_2$ induces extensive cementation. The corresponding reductions in porosity and permeability are good representations of the extent of spring infiltration into the host rock. This also provides an explanation for the current inactivity of the spring. Cementation closes not only intergranular primary porosity, but fracture porosity and permeability as well—calcite-filled veins representing sealed fractures abound in the immediate vicinity of the travertine platform. The conduit formed by taking advantage of these damage zone fractures to channel water through a relatively high-permeability pipe. Although there are scattered outcrops that maintain relatively high permeability (Figure 55), pervasive mineralization appears to have shut off the conduit by eliminating the permeability anisotropy that led to its formation.

#### 3.2.3.1 Conduits have finite lifetimes

Because of degassing-induced cementation, once $CO_2$-rich fluid begins to take advantage of a damage zone, that path has a limited lifetime. Burnside et al. (2007, 2009) use uranium-series dating to show that this lifetime is in the 10,000-year range for a travertine deposit of much greater volume than that in the map area (69,660 $m^3$ vs. 1,588 $m^3$). In addition to the areal restrictions on fluid escape imposed by point leakage, this adds an additional temporal limitation.

When one of these conduits shuts off, however, it appears that another opens up along the next point of least resistance (Burnside, 2010). Uranium-series dating on Little

Grand Wash travertines shows that they precipitated at different times and that the fault system as a whole has been leaking for over 100 ka (Burnside, 2010). Leakage is not continuous, however. Burnside constructed a timeline of Little Grand Wash travertine deposition by determining the age of each travertine deposit and using multiple samples to determine the lifespan of six out of eight deposits. He concluded that gaps of 4–32 ka exist between deposition of consecutive platforms, during which times leakage from the fault zone would have been greatly reduced if not entirely halted. It is not clear if the process of path switching will continue indefinitely, taking advantage of less and less efficient pathways over time, or if there will come a point at which all feasible conduits have been used and sealed. The fault zone is complex, however, containing many intersecting fault segments. These provide a large supply of potential conduits for escape.

## 3.3 Yellow Coloration as Evidence of a Possible Failed Conduit

Heath (2004) noted the yellow coloration that exists in the map area and attributed it to the supersaturation of spring waters with respect to iron oxides. This is consistent with X-ray diffraction results from this project, which show goethite and hematite in each of the yellow-stained samples. Chlorite and chlorite-smectite in these samples are present in reduced amounts. It is possible that chlorite could form from the combined dissolution of preexisting iron oxides and aluminosilicates (Land and Dutton, 1978). Because chlorite shows up throughout the fault zone and iron oxides are absent in most samples, however, it is more likely the opposite: Dissolution of chlorite acts as a source of iron for goethite and hematite. This would explain the reduced chlorite in colored samples. The yellow-colored sample 80A has relatively abundant chlorite and chlorite-smectite, each producing a moderate peak in X-ray diffraction analysis (Figure 81), but only a small portion of iron oxides is necessary to stain a rock yellow (Torrent and Schwertmann, 1987; Eichhubl et al., 2004). It is likely that chlorite in sample 80A was once even more abundant than at present and was reduced to its current level by a small amount of dissolution.

Sample 80A is a sandstone from the western edge of the map area, near the upper hard link. It is a clear isotopic outlier: Figure 82 shows that it has anomalously high isotopic weight compared to other samples near it and that the ratio of $\delta^{18}O$ to $\delta^{13}C$ falls far outside the trend defined by other field samples. This is not an analytical artifact, as re-runs of the sample produce identical $\delta^{18}O$ measurements (-2.23‰) and very similar $\delta^{13}C$ measurements (2.76‰ and 2.91‰). The coloration and isotopic aberration appear to be related—sample 80B is a non-colored sandstone from the same station immediately adjacent to 80A. It has nearly identical primary (depositional) lithology, but shows none of the isotopic irregularity

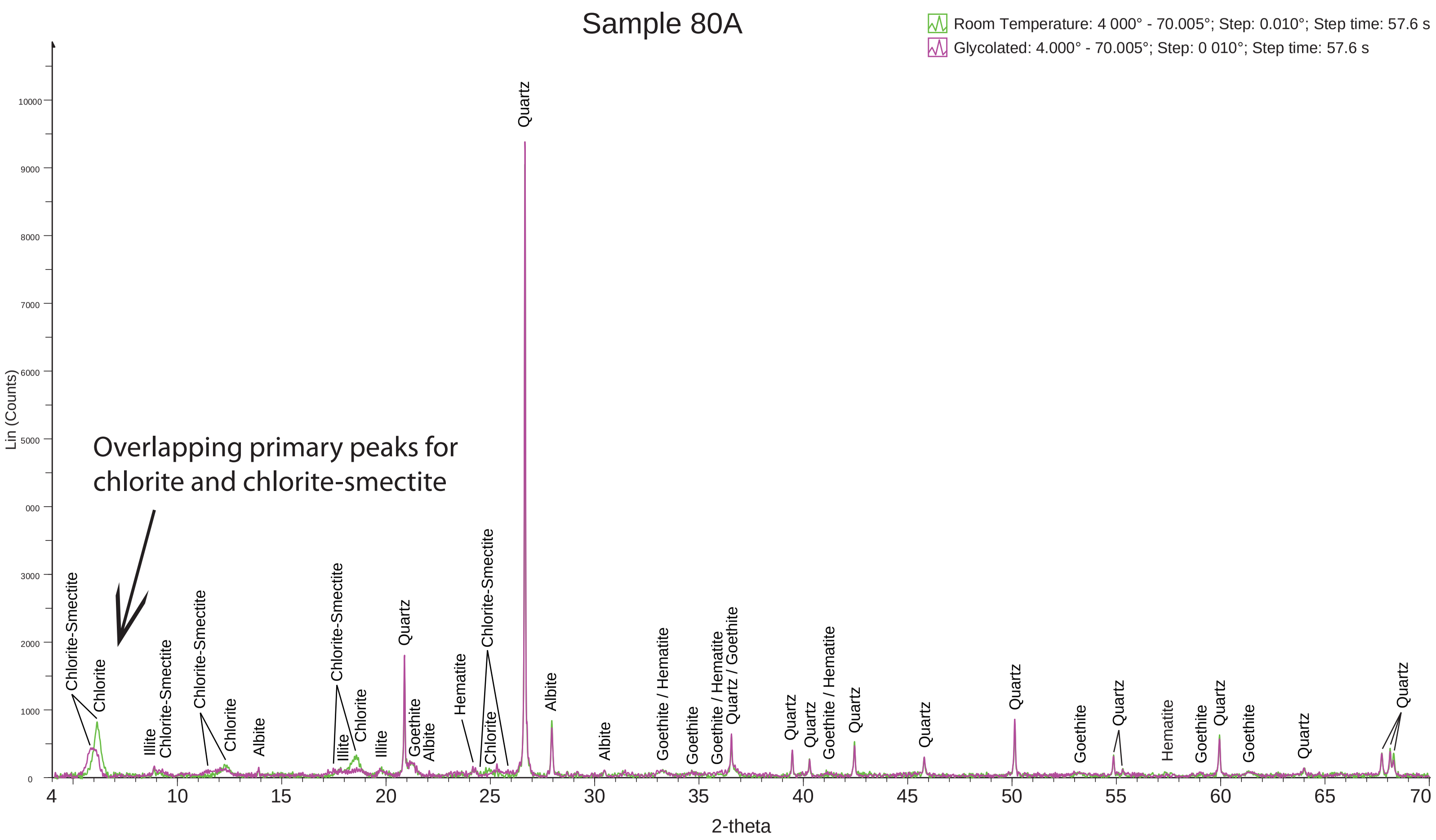

Figure 81: X-ray diffraction analysis of the clay-size separation of sample 80A shows moderate chlorite and chlorite-smectite peaks.

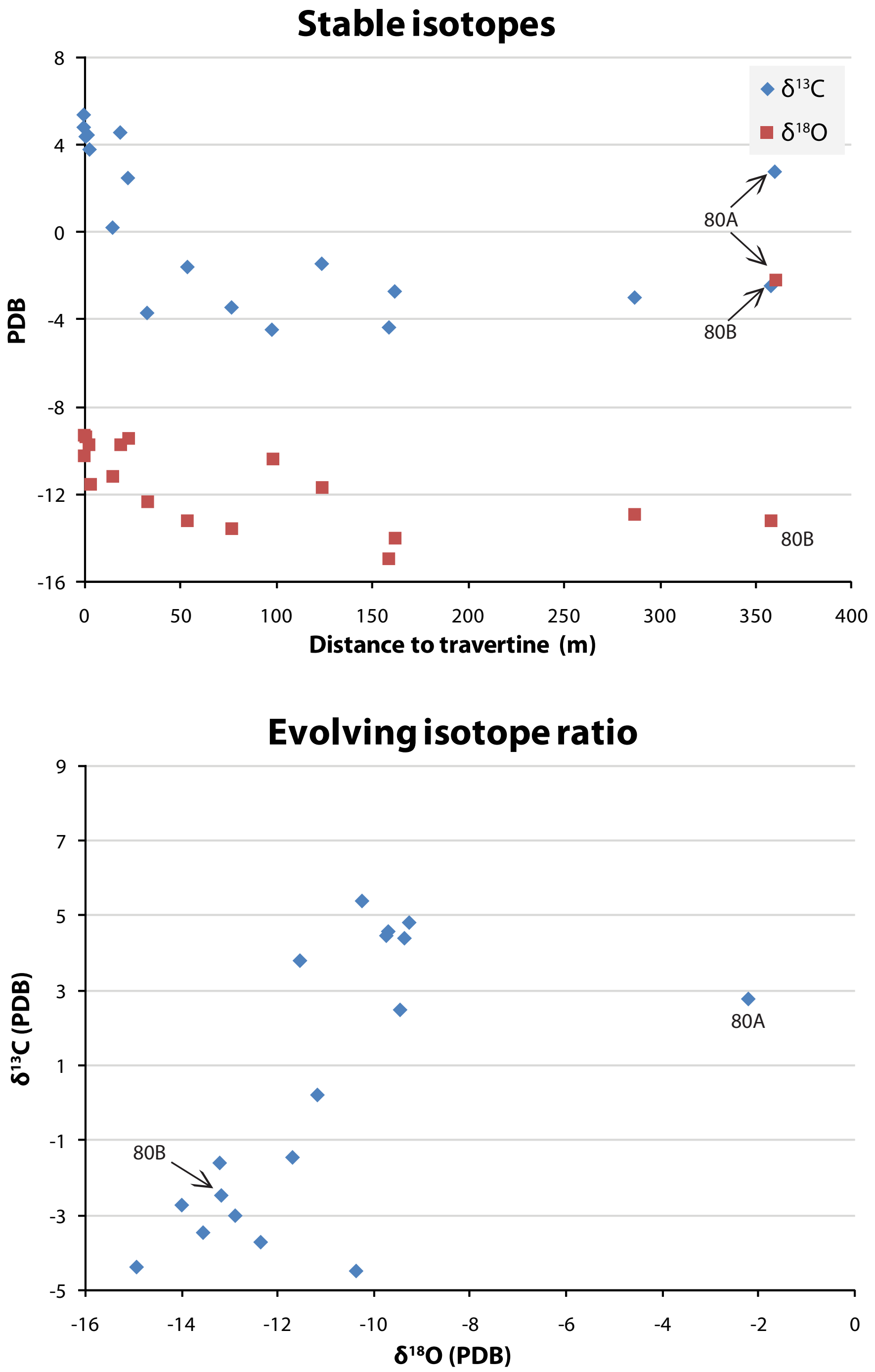

Figure 82: Sample 80A has anomalously high $\delta^{18}$O and $\delta^{13}$C values, even compared to samples from within the conduit. The ratio of $\delta^{18}$O and $\delta^{13}$C also places it far outside the trend defined by other map area samples. Sample 80B, not stained but taken from virtually the same location, has none of these abnormalities.

of its neighbor. No other yellow-colored samples from the map area have the same isotope signature, however, so the relationship cannot be causal.

Sample 80A has 6% secondary porosity, indicating fairly average dissolution for samples outside the conduit. It has a small amount of micrite but no calcite spar, while 80B has 9% spar (Figure 83). Sample 80A contains 4% opaque cement, and X-ray diffraction results from the clay-size separation show a moderate goethite peak and weak hematite peak. Yellow-red coloration can result from iron oxide abundance as low as <1–3% (Torrent and Schwertmann, 1987; Eichhubl et al., 2004), so these opaque minerals (visible in Figure 83) are likely responsible for the coloration in sample 80A.

In 80A there are obvious and abundant chlorite growths on some grain surfaces and even partially replacing some grains (Figure 61). Chlorite rims are present in 80B as well, but they are not as thick or pervasive. Early chlorite cementation will prevent the growth of quartz cement (Dixon et al., 1989; Warren and Pulham, 2001; Berger et al., 2009; Gould et al., 2010), but it does not hinder calcite precipitation (Land and Dutton, 1978; Berger et al., 2009; Gould et al., 2010). The abundance of chlorite in sample 80A cannot therefore be invoked to explain the discrepancy in calcite cement.

No likely unique source of material for authigenic cement exists at station 80. Although formation lithologies in the map area can be quite heterogeneous, all other samples fall within a well defined isotopic trend, including sample 80B. It may be possible that processes resulting in iron oxide formation are associated with a heavy isotopic signature. Within the alteration radius of the travertine-associated conduit, this heavy signature would be suppressed by the abundance of spring-related calcite bearing its own unique isotopic signature; in 80A, the paucity of spar would prevent this signature suppression. This could be confirmed or refuted with isotope data from the other non–spring-related patches of yellow coloration, but I do not have this data.

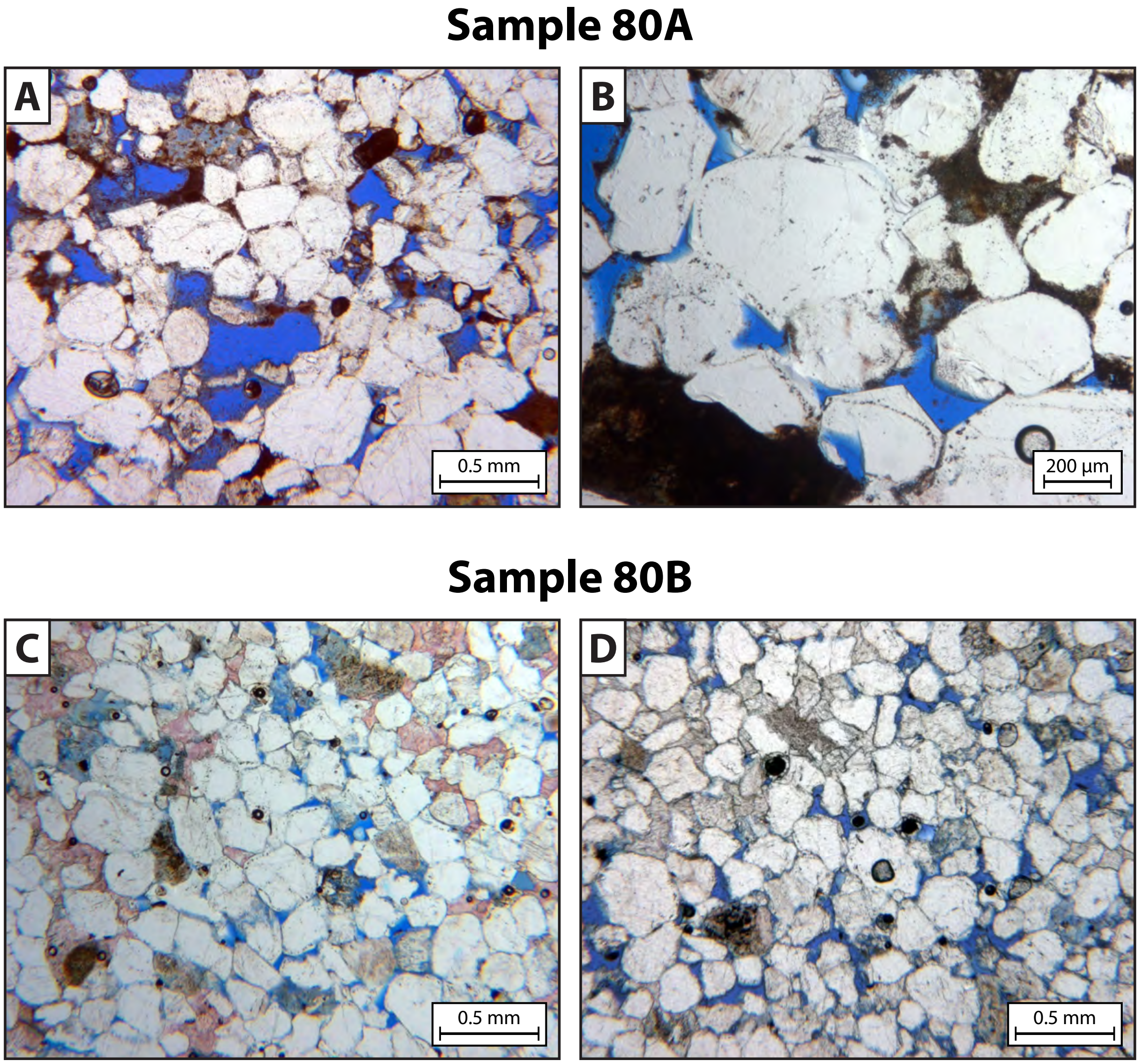

Figure 83: **A–B:** Sample 80A has high porosity and no calcite. Opaque cements are sufficiently abundant to register in X-ray diffraction analysis as goethite and hematite and likely give it its yellow color. **C–D:** Its immediate neighbor, sample 80B, contains more calcite cement and fewer opaque cements.

Sample 80A is unique among colored samples in being unrelated to the conduit: It is located 360 m from travertine platform and has no point-counted calcite—the evidence originally used to identify the conduit. It is situated near the intersection of two faults, however, including the western end of the northern segment of the hard-linked ramp, making the location a likely candidate for a $CO_2$ seep. It is therefore possible that station 80 represents a short-lived or "failed" $CO_2$ conduit. Because it is located 25 m above the travertine platform, although it was structurally suitable for escaping fluids, they may only have migrated through it for a brief period before switching paths to a topographically lower pathway.

The brevity of this seep would explain the dearth of calcite spar, as well as the low level of dissolution (secondary porosity). Chlorite is prone to dissolution due to its high reactive surface area and small crystal size (Baines and Worden, 2004; White et al., 2005), however, so even a brief period of dissolution may have been sufficient to provide material for the precipitation of iron oxides. Station 80 contains both altered rock (sample 80A) and unaltered rock (sample 80B) and the average permeability is 134 mD. This confirms that the $CO_2$ seep would have had to be short-lived: If it had lasted a long time, the relatively high host rock permeability would have led to horizontal infiltration and alteration.

## 3.4 Comparing Findings to Geochemical Models

Numerous geochemical simulations have been employed that predict the mineral storage potential of reactions that will occur as a result of $CO_2$ sequestration in sandstone reservoirs (Hellevang et al., 2005; Knauss et al., 2005; Moore et al., 2005; White et al., 2005; Xu et al., 2005; Zerai et al., 2006; Bénézeth et al., 2007). The models themselves have been compared, and their predictions are in reasonable agreement with each other (Pruess et al., 2004), but it is interesting to compare $CO_2$-related mineralization observed in this study with modeled reactions. Such a comparison can provide informative feedback on model accuracy and applicability, as a lack of well-understood geochemical kinetic data is commonly cited as foremost among the models' limitations (Baines and Worden, 2004; Knauss et al., 2005; Xu et al., 2005; Bénézeth et al., 2007). Moreover, uncertainty about the ability of faults to self-seal through mineralization is a major concern for the feasibility of carbon sequestration (Knipe, 1993; Yielding et al., 1997; Heath et al., 2009). It is important to keep in mind that most models simulate at-depth reservoir reactions, however, with the shallowest modeled reactions occurring at 100–400 m; White et al. (2005) ran their simulations up to the surface, but showed no precipitation of any minerals at depths shallower than 100 m. Pressure and temperature parameters are therefore higher than those in the map area.

### 3.4.1 MODEL PREDICTIONS

Because the introduction of $CO_2$ will initially acidify formation waters, models generally define three stages of evolution: First, carbonate minerals react quickly to changes in acidity and dissolve as a result of reduced pH; then aluminosilicate minerals, which react more slowly, also begin to dissolve and in doing so raise the pH; finally carbonates will reprecipitate as pH reaches a range in which they are stable (Baines and Worden, 2004; Zerai et al., 2006).

The dissolution of aluminosilicates such as feldspars, zeolites and Fe- and Mg-clays frees metal ions for the precipitation of a range of carbonates (Baines and Worden, 2004; Xu et al., 2005; Zerai et al., 2006). The models commonly predict calcite, dolomite, siderite, ankerite, kaolinite and dawsonite, the last of which is included in every model (Baines and Worden, 2004; Knauss et al., 2005; Moore et al., 2005; White et al., 2005; Xu et al., 2005; Zerai et al., 2006; Wilkinson et al., 2009b). Additionally, Heath (2004) shows positive saturation indices in Crystal Geyser waters for calcite, aragonite, dolomite and hematite, where a positive saturation index indicates the thermodynamic tendency for water to precipitate, rather than dissolve, a mineral.

### 3.4.2 COMPARISON OF PREDICTIONS TO PETROGRAPHIC RESULTS

In the map area, $CO_2$-related calcite is present in great abundance. I do not observe any of the other predicted minerals, however. It is possible that carbonates may have been completely removed by the acid treatment during preparation of clay-size separations for X-ray diffraction analysis. This is only likely, however, if they were originally present in low abundance, as the acid was applied conservatively and calcite very plainly shows up in most samples. Moreover, the model-predicted carbonates do not appear in bulk rock X-ray diffraction analyses either, and these samples were not subjected to acid treatment during preparation.

Dawsonite appears in all models. Hellevang et al. (2005) showed that it is stable at $CO_2$ fugacities as low as 0.1, and that its stability increases with decreasing temperature, although they do not extend their calculations into the low range of map area water temperatures (15–18°C). Simulations by White et al. (2005) predict dawsonite precipitation at depths as shallow as 100 m, though only in small amounts, and the simulations show nothing at the surface or shallow subsurface.

The total absence of dawsonite in field samples despite its association with high $CO_2$ concentrations may be explained by several mechanisms. Zerai et al. (2006) predict that dawsonite will precipitate and then completely dissolve within 500–4,000 years. If the conduit has a lifetime on the order of several thousand years, dawsonite may already have been removed. Another model shows dawsonite becoming unstable in reservoirs due to the decreasing partial pressure of $CO_2$ after injection ends (Hellevang et al., 2005); vertical migration of $CO_2$ is of particular concern, leading to reduced $CO_2$ partial pressure and dawsonite destabilization. Dawsonite might then be unstable in map area springs, where $CO_2$ at the current analogue, Crystal Geyser, is degassing and therefore decreasing its partial pressure as spring water rises to the surface.

The above interpretations are somewhat simplistic applications of geochemical models at the surface. Trumping alternate explanations by virtue of precedence, it is most likely that dawsonite formation is prevented by unsuitable water chemistry or kinetics. In order to precipitate, dawsonite ($NaAlCO_3(OH)_2$) requires a supply of $Na^+$ and $Al^{3+}$ in addition to $CO_2$. Heath (2004) reported 166.0 meq/L $Na^+$ in Crystal Geyser waters, possibly from ion exchange processes where the water contacts shales; I have not been able to find any published $Al^{3+}$ data for local spring waters, however. In the models $Al^{3+}$ is supplied by a buildup from dissolving aluminosilicates, but $Al^{3+}$ tends to complex with other metals present in groundwater and is not highly mobile. Wilkinson et al. (2009a) showed that 80–90% of the water erupting from Little Grand Wash is recharged from the nearby San Rafael Swell. Concentrations of $Al^{3+}$ in these dominantly meteoric waters are likely too low for dawsonite to precipitate.

Although the remaining predicted minerals—kaolinite, siderite, ankerite and dolomite—are common and stable at the surface, a similar host of conditions prevents them from precipitating. One model (White et al., 2005) predicts more kaolinite precipitation than any other mineral, but the absence of kaolinite in the field can be similarly explained by the contrast in flow dynamics between surface conduits and subsurface reservoirs. In the models, kaolinite ($Al_2Si_2O_5(OH)_4$) is a product of feldspar dissolution, which provides the necessary $Al^{3+}$ (Baines and Worden, 2004; Moore et al., 2005; White et al., 2005). In non–$Al^{3+}$-saturated water, its precipitation therefore requires a buildup of free ions that cannot occur in a system dominated by water expulsion and recharge.

Siderite ($FeCO_3$) and ankerite ($Ca(Fe,Mg)(CO_3)_2$) require $Fe^{2+}$. The models provide this through dissolution of Fe-clays and -lithics such as chlorite, hematite and volcanics (Baines and Worden, 2004; Xu et al., 2005; Zerai et al., 2006). Heath (2004) showed that Little Grand Wash water is supersaturated with respect to iron oxide, and this is confirmed by the presence of hematite and goethite in some conduit samples. Although this indicates $Fe^{3+}$ availability, the necessary redox reaction (to $Fe^{2+}$) may present a barrier to the precipitation of iron carbonates. Because this reaction would take time to occur, siderite and ankerite are therefore subject to the same limitation on ion availability that prevents the precipitation of dawsonite and kaolinite (i.e., a non-evolving system of continuous expulsion and recharge). Furthermore, Zerai et al. (2006) indicated that, in low-temperature water with low $CO_2$ fugacity, such as the water erupting along Little Grand Wash, siderite will dissolve.

Crystal Geyser waters are supersaturated with respect to dolomite ($CaMg(CO_3)_2$) and aragonite ($CaCO_3$) (Heath, 2004), and dolomite precipitation is a common model prediction (Baines and Worden, 2004; Zerai et al., 2006; Bénézeth et al., 2007; Wilkinson et al., 2009b). Dolomite precipitation should not be affected by low $CO_2$ fugacities, and calcite, which has the same chemical formula as aragonite, is more stable at low $CO_2$ fugacities (Zerai et al., 2006). These minerals do not appear in the study area, however. The absence of dolomite is unsurprising, as the kinetics and thermodynamics of dolomite precipitation under surface conditions are so poorly understood that the paucity of modern dolomite is commonly referred to as the "dolomite problem" (Land, 1998; Arvidson and Mackenzie, 1999; Fenter et al., 2007). Sea water, for example, is oversaturated with respect to dolomite, but dolomite is rare or absent even in warm waters where it is predicted to form (Land, 1998; Arvidson and Mackenzie, 1999). The absence of aragonite may simply reflect a kinetic preference to precipitate calcite.

Zerai et al. (2006) showed the total mass of carbonates increasing with decreasing temperature, although they do not extend their model to temperatures below 35°C. In spite of this, Little Grand Wash fault at the surface is not an ideal environment for $CO_2$-related precipitation of any predicted mineral, at least by measures of suitable pH, $CO_2$ fugacity, or availability of metal ions. Because spring water is by nature constantly recharged and expelled, it cannot achieve equilibrium with the host rock. Reactions in the host rock will likely be comparable to those that would occur in a $CO_2$-rich reservoir setting (i.e., the constant presence of $CO_2$ will have a similar effect on lithology), but metal ions will not be able to accumulate in the water. Rather, freed ions are rapidly flushed out at the surface, preventing the precipitation of minerals such as kaolinite and dawsonite. Similarly, pH cannot equilibrate because there is no static volume of water that can be buffered by the dissolution of aluminosilicates; buffering requires hundreds to thousands of years, while as much as 90% of erupting water is seasonally recharged at the nearby San Rafael Swell (Hood and Patterson, 1982; Wilkinson et al., 2009a). Constant recharge of both water and $CO_2$ means that the water remains permanently acidic. The fact that calcite is able to precipitate in such an unsuitable environment is due to the controlling effects of the difference between aqueous and atmospheric $P_{CO2}$ and the pressure drop as water rises, which result in $CO_2$ degassing.

### 3.4.3 MODEL APPLICABILITY AT THE SURFACE

These results show that existing geochemical models are in general not applicable to near-surface conditions. This is not a criticism of the models, which are intended to simulate reactions at depth. Minerals such as dawsonite precipitate only under a specific range of conditions, so their absence at the surface is not a refutation of their likelihood in the subsurface. Some faults may intersect the surface, however, and these are where the threat of storage failure jeopardizes the mission of carbon sequestration. It is therefore highly desirable to have a better predictive understanding of geochemical reactions at the surface.

## 3.5 Conclusions

### 3.5.1 $CO_2$ SEEPAGE ALONG THE LITTLE GRAND WASH FAULT ZONE

The Little Grand Wash fault is composed of a complex network of overlapping and splaying fault segments that contribute to a total offset of about 250 m in the map area. A hard-linked fault ramp is the main structural feature. The ramp is 450 m long and incorporates the largest fault segments to transfer a majority of throw (up to 140 m) in the brittle part of the fault zone.

Intense fracturing is exhibited in the small zone around a major fault overlap and intersection, the hard link of a strain transfer fault ramp. In addition to the presence of a travertine platform, this damage zone is characterized by intense alteration in the form of pervasive, pore-occluding and fracture-filling calcite cement. Stable isotope analysis of this calcite shows that, within a 25-m radius of the travertine, it bears a unique isotopic signature, having relatively light-isotope-depleted $\delta^{18}O$ and $\delta^{13}C$ values relative to calcite elsewhere in the map area. These heavier isotopes can be attributed to the fractionation effect of precipitation from $CO_2$-degassing parental water. Elevated levels of cementation with a heavier-than-usual ($CO_2$-related) isotopic signature show that the fracture zone was once a conduit for the escape of $CO_2$-rich fluids, similar to the currently active $CO_2$-degassing Crystal Geyser. Other calcite in the field area does not bear the $CO_2$-related isotope signature and was likely formed during burial or as caliche from surface weathering.

Fluid does not escape uniformly throughout the fault zone, but is restricted to the damage zone conduit. The location of this conduit is predominantly the result of three structural properties within the fault zone: 1) Major fault segment intersections or overlaps create enhanced damage zones; 2) fracturing in these damage zones increases vertical permeability and creates a preferred-flow pipe through the fault zone, while shale gouge and deformation bands form barriers to cross-fault flow, channeling fluids towards the conduit;

3) if multiple locations exhibit the first two properties, locations in topographically low areas will be the most suitable for conduit formation, as these present the shortest path to the surface.

If the conduit transmits $CO_2$-charged water, degassing near the surface results in extensive calcite precipitation that cements rocks in a halo of about 25 m. Such cementation reduces porosity in the conduit, eliminating the permeability advantage that caused fluids to migrate through it. This effectively seals it off as a preferential flow path. Because of the structural properties necessary for conduit formation, conduits are narrow and this process can occur quite rapidly—on the order of 10 ka. The elimination of one damage zone conduit does not seal the larger fault system, however. In a fault zone composed of many intersecting fault segments, the complexity is sufficient to provide multiple possible escape paths. When one is sealed, migrating fluids appear to shift to another. Although this has been occurring at Little Grand Wash for over 100 ka, individual springs are separated by as much as 32 ka, indicating that path switching, during which leakage is dramatically reduced, may be a slow process.

Some sandstones in the map area have a distinctive yellow coloration in outcrop. X-ray diffraction and point counting show sufficient goethite and hematite in these rocks to account for this coloration. X-ray diffraction analysis also indicates that the abundance of chlorite and chlorite-smectite in such yellow-colored samples is reduced compared to non-colored samples. This suggests that the iron oxides form with iron made available by the dissolution of chlorite.

A comparison of model-predicted $CO_2$-related cementation and actual cementation identified around the $CO_2$ seep reveals striking disparities. While the models predict an array of carbonates and silicates—most notably dawsonite, dolomite, siderite, ankerite and kaolinite—extensive petrography, including X-ray diffraction analysis, shows that cementation at the surface is restricted almost entirely to calcite, with small amounts of iron carbonate. This discrepancy shows that current models cannot be reliably applied at the surface. Current geochemical models are calibrated for deep subsurface reservoir (sealed) conditions, as opposed to surface conduit (escape) conditions. Conduits are constantly recharged and therefore unable to equilibrate the way formation waters in a reservoir would do. Spring water saturation indices also predict minerals (aragonite and dolomite) that are not observed in field samples. The reasons are not entirely understood, but the constantly recharged, acidic, low-temperature, low-pressure ($CO_2$-degassing) conditions at the surface appear to favor calcite precipitation over other likely or possible reactions. These inconsistencies suggest a need for simulations calibrated to predict precipitation under surface conditions. Escape to the atmosphere indicates a critical failure of $CO_2$ sequestration and many models rely on mineralization to seal leaks and prevent such escape. It is therefore important to develop models that accurately characterize the $CO_2$-related reactions that take place in conduits through this last barrier.

### 3.5.2 IMPLICATIONS FOR CARBON SEQUESTRATION

The areally limited nature of $CO_2$ escape conduits through a broad inactive fault zone should help define points of concern for surface monitoring of leakage. This is important because $CO_2$ disperses quickly in the atmosphere and can be undetectable at distances as short as 100 m, making it difficult to detect even with a dense grid of monitors. Being able to identify zones of concern around injection sites will allow informed, targeted monitoring.

Because this system of prediction relies partly on where topography intersects the water table, it is primarily useful at the surface. The knowledge also improves our ability to assess possible injection sites, however. As most potential reservoirs are likely to be faulted, it is important to predict whether or not faults present a major escape path, or if $CO_2$ will be contained. Being channeled through point conduits within a broad fault zone limits the total amount of $CO_2$ that can escape over time, as a leaking conduit is more likely to seal than a long fault. If faults leaked uniformly, mineralization at any one point would be minimal because the source of cement would be diffused along the entire fault. The reduced rate of precipitation and the increased volume necessary to seal an entire fault (as opposed to a single vertical pipe) increase the possibility that the fault would never be entirely sealed. This would allow carbon dioxide to escape indefinitely. Even if mineralization eventually did seal the fault, the amount of escaping $CO_2$ associated with so much calcite precipitation would likely be orders of magnitude greater than the amount released during occlusion of a narrow pipe.

Channeling water from the entire length of the fault through a narrow point conduit concentrates mineralization and facilitates sealing of the conduit. It also increases the rate of precipitation so that conduits are active for relatively short periods of time (roughly 10 ka). Because the reduced-leakage period of path switching can take as much time or more (4–32 ka), the rapidity of the sealing process greatly increases the total time during which relatively little $CO_2$ is escaping. There is no evidence, however, to suggest that leakage will not continue indefinitely, if intermittently, at different locations throughout the fault zone. In an inactive fault, its tendency to do so is likely determined by fault zone complexity.

# Appendix A: Explanation of Calcite Precipitation from Degassing Water

Calcite cement along the Little Grand Wash fault is an important indicator of past leakage through the fault. In order to use such cementation as a proxy for past leakage, however, it is important to show that precipitation can be directly related to leaking $CO_2$-rich water. The following is a description of the $CO_2$-related processes and reactions that result in calcite precipitation.

As $CO_2$-rich water rises to the surface, the drop in hydrostatic pressure reduces $P_{CO2}$ in the water (Eichhubl and Boles, 2000; Burnside, 2010). This drop in partial pressure and the difference between relatively high aqueous $P_{CO2}$ and low atmospheric $P_{CO2}$ at the surface cause $CO_2$ to degas (Ellis, 1959; Pearson et al., 1978; Eichhubl and Boles, 2000; Heath, 2004; Burnside, 2010). Calcite solubility decreases with decreasing $P_{CO2}$ (Miller, 1952; Ellis, 1959). As $CO_2$ exsolves from bicarbonate- and $Ca^{2+}$-rich water, C and O are freed to bond with $Ca^{2+}$ and precipitate calcite. The carbonate equilibrium equation (Clark and Fritz, 1997) describes this reaction:

$$\mathrm{Ca^{2+} + 2HCO_3^- \leftrightarrow CO_{2(g)} + H_2O + CaCO_3}.$$

Degassing $CO_2$ causes an increase in pH, which is sensitive to $P_{CO2}$ (Ellis, 1959; Pearson et al., 1978). This enhances the ability of calcite to precipitate even while being flooded by $CO_2$-bearing (i.e., ostensibly acidic) water. Water evaporation at the surface may also facilitate calcite precipitation, by increasing the $Ca^{2+}$ saturation of emanating waters. Burnside (2010) summarizes other possible factors that may contribute to calcite precipitation (e.g., ion concentration, biotic mediation), as well as alternate reaction histories that have been proposed by other researchers.

# Appendix B: Additional Photographs

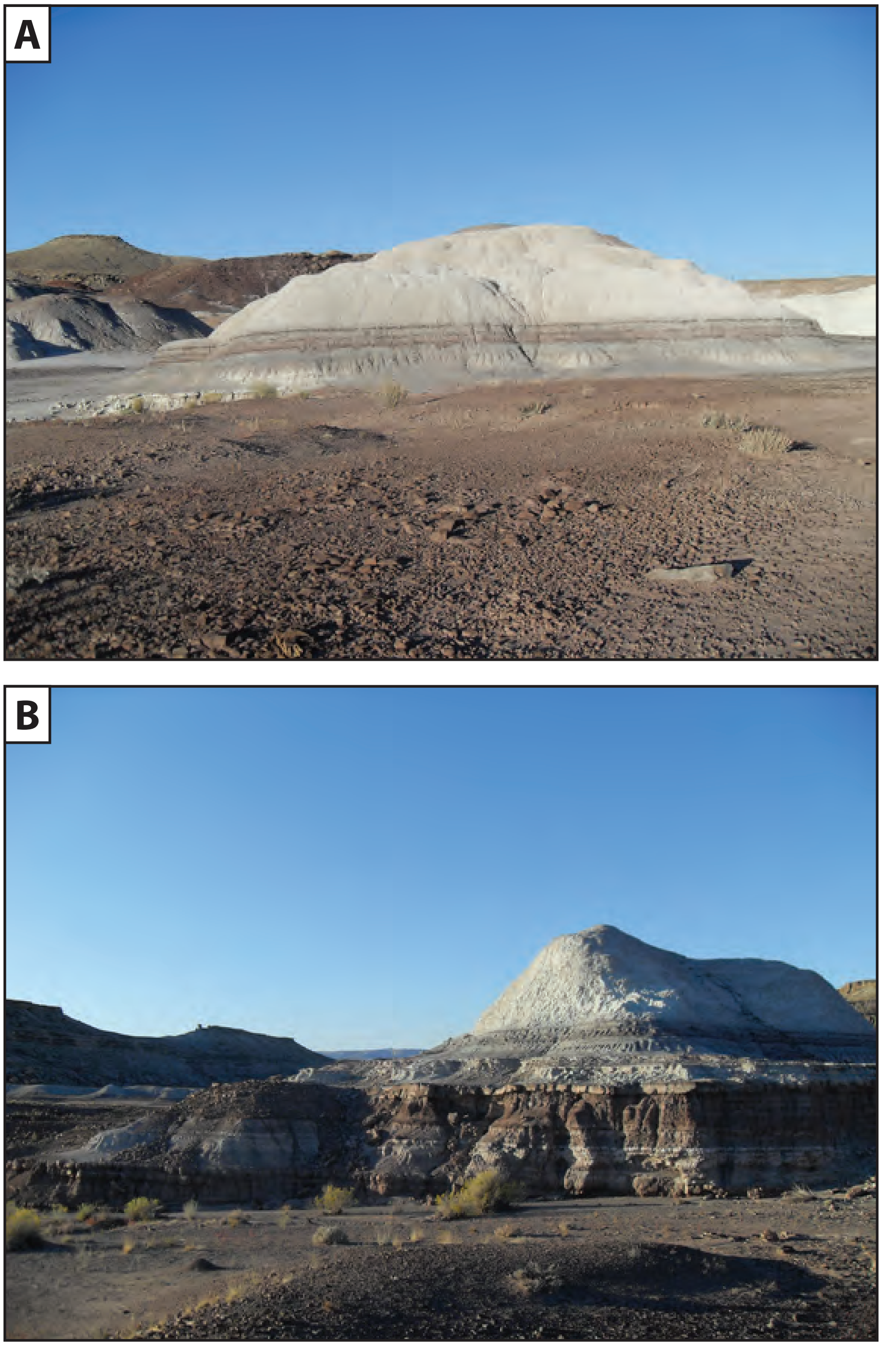

Figure B1: **A–B:** Distinctive white bentonite beds deposited among Brushy Basin shales and are helpful for differentiating the Brushy Basin from the Salt Wash, as the thick shale outcrops in each member are often insufficient to make the distinction.

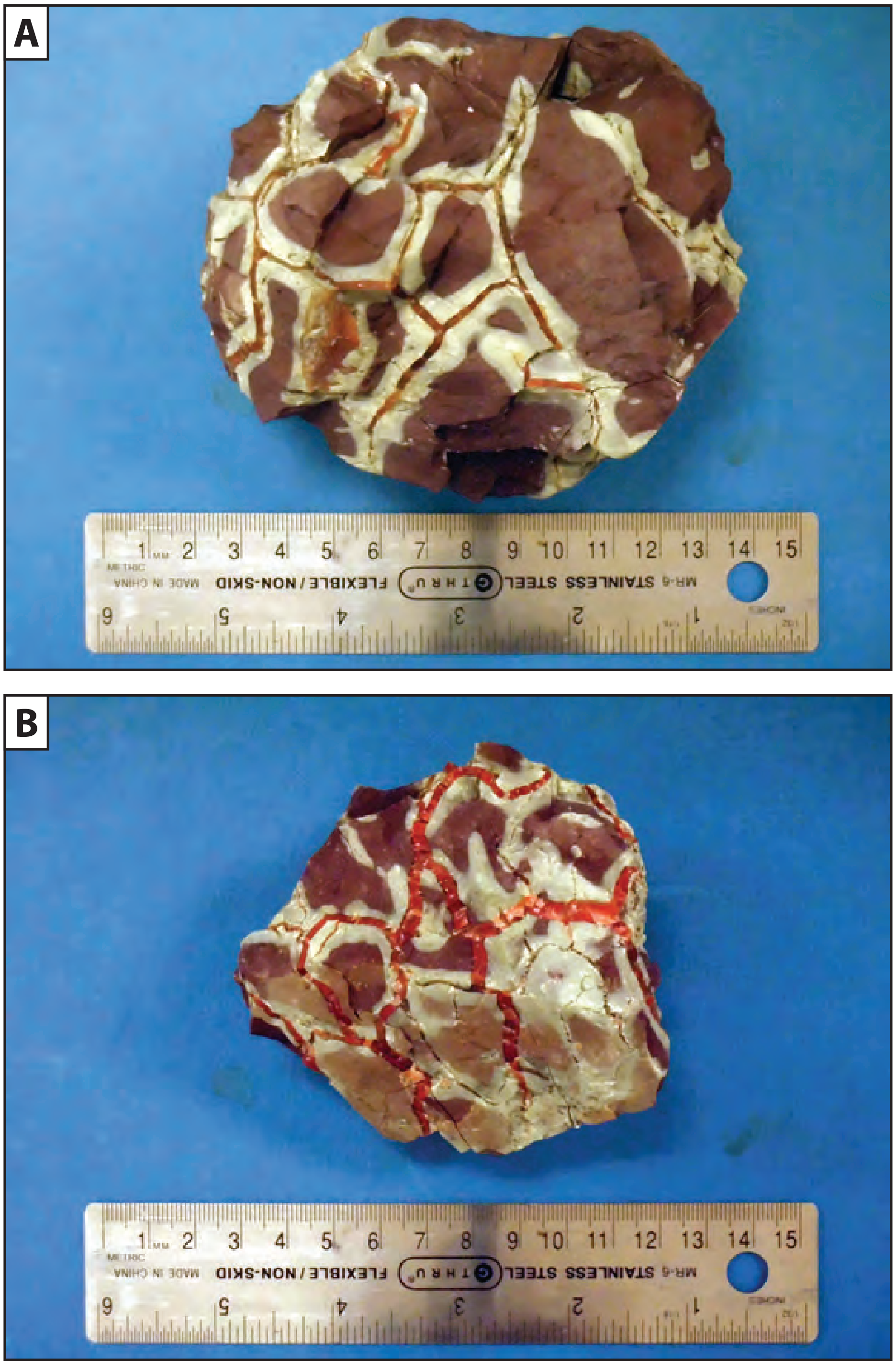

Figure B2: **A–B:** Red septarian quartz veins in altered Brushy Basin shale. These are not concretions but blocks out of a thin bed, likely altered by the volcanic processes common in the Brushy Basin.

Figure B3: Interbedded gypsum in the Morrison Tidwell, near Green River, west of the field area; advisor and hammer for scale.

# Appendix C: Notes from Petrography

The following are observations I made during petrography for each thin section. Table C1 lists all thin sections and summarizes the petrographic data (imagery) I have collected for each. I include with the observation sheets thin section scans, photomicrographs, electron microscope images and energy dispersive spectra of interesting details in each slide. Most available images are not shown, but are electronically preserved. Where I have the data, isotope and point count information are also included.

**List of thin sections and available petrographic data**

| | | | | | Stained | | | | | | |
|---|---|---|---|---|---|---|---|---|---|---|---|
| **Sample** | **Formation** | **Lithology** | **Std.** | **Pol.** | **Calcite** | **Kspar** | **Optical** | **SE** | **BSE** | **EDS** | **CL** |
| 15A-1 | Salt Wash | sandstone | x | | x | x | x | | | | |
| 15A-2 | Salt Wash | sandstone | | x | | | x | x | x | x | |
| 15A-2 | Salt Wash | sandstone | x | | | | x | x | | | |
| 15B-1 | Salt Wash | sandstone | x | | | | x | | | | |
| 15B-2 | Salt Wash | sandstone | x | | | | x | | | | |
| 16-1 | Brushy Basin | sand/cong | x | | | | x | | | | |
| 16-2 | Brushy Basin | sandstone | | x | | | x | | x | x | |
| 17A | Quaternary | travertine | | x | | | x | x | x | x | |
| 17B-1 | Quaternary | travertine | x | | | | x | | | | |
| 17B-2 | Quaternary | travertine | | x | | | x | | | x | |
| 17C-1 | Salt Wash | sandstone | | x | | | x | x | x | x | |
| 17C-2 | Salt Wash | sandstone | x | | x | x | x | | | | |
| 18-1 | Brushy Basin | shale | | x | | | x | | | x | |
| 18-1b | Brushy Basin | shale | x | | | | x | | | | |
| 18-2 | Brushy Basin | shale | x | | | | x | | | | |
| 18-3 | Brushy Basin | shale | x | | | | x | | | | |
| 20A | Salt Wash | sandstone | x | | | | x | | | | |
| 21A | Salt Wash | sandstone | x | | x | x | x | | | | |
| 21B | Salt Wash | sandstone | x | | | | x | | | | |
| 22A | Salt Wash | sandstone | x | | x | x | x | | | | |
| 22B | Salt Wash | sandstone | x | | | | x | | | | |
| 22C-1 | Salt Wash | sandstone | x | | | | x | | | | |
| 22C-2 | Salt Wash | sandstone | x | | | | x | | | | |
| 24-1 | Salt Wash | sandstone | x | | | | x | | | | |
| 24-2 | Salt Wash | sandstone | x | | x | x | x | | | | |
| 24-3 | Salt Wash | sandstone | | x | | | x | | x | x | |
| 26-1 | Salt Wash | sandstone | x | | x | x | x | | | | |
| 26-1 | Salt Wash | sandstone | | x | | | x | | x | x | |

Table C1: List of all thin sections and a summary of microscopy and energy dispersive data collected for each.
Std. = standard slide preparation; Pol. = polished slide preparation;
SE = secondary electron (rock fragment); BSE = backscatter electron;
EDS = energy dispersive spectroscopy; CL = cathodoluminescence

**List of thin sections and available petrographic data**

| | | | | | Stained | | | | | | |
|---|---|---|---|---|---|---|---|---|---|---|---|
| **Sample** | **Formation** | **Lithology** | **Std.** | **Pol.** | **Calcite** | **Kspar** | **Optical** | **SE** | **BSE** | **EDS** | **CL** |
| 26-2 | Salt Wash | sandstone | | x | | | x | | | | |
| 26-2 | Salt Wash | sandstone | x | | | | x | | | | |
| 27A-1 | Salt Wash | sandstone | x | | | | x | x | | | |
| 27B | Salt Wash | sandstone | | x | | | x | | x | x | x |
| 28A-1 | Salt Wash | sandstone | x | | x | x | x | | | | |
| 28A-2 | Salt Wash | sandstone | x | | | | x | | | | |
| 30A | Brushy Basin | sandstone | x | | | | x | | | | |
| 30B-1 | Brushy Basin | sandstone | x | | | | x | | | | |
| 30B-2 | Brushy Basin | sandstone | | x | | | x | | x | x | |
| 32A | Salt Wash | sandstone | | x | | | x | | x | x | |
| 32B | Salt Wash | sandstone | x | | | | x | | | | |
| 32C | Salt Wash | sandstone | x | | | | x | | | | |
| 32D-1 | Salt Wash | sandstone | x | | x | x | x | | | | |
| 32D-2 | Salt Wash | sandstone | x | | | | x | | | | |
| 34A-1 | Brushy Basin | sandstone | | x | | | x | | | | |
| 34A-2 | Brushy Basin | sandstone | x | | x | x | x | | | | |
| 35A-1 | Salt Wash | sandstone | | x | | | x | | x | x | |
| 35A-2 | Salt Wash | sandstone | x | | x | x | x | | | | |
| 35B-1 | Salt Wash | conglom. | | x | | | x | | x | | x |
| 35B-2 | Salt Wash | conglom. | x | | x | x | x | | | | |
| 36A-1 | Salt Wash | sandstone | | x | | | x | | | | |
| 36A-2 | Salt Wash | sandstone | x | | | | x | | | | |
| 71A | Quaternary | travertine | ruined | | x | x | x | x | | | |
| 71A-2 | Quaternary | travertine | | x | | | see 71A | x | | | |
| 71A-3 | Quaternary | travertine | | x | | | see 71A | x | | | |
| 71A-3 | Quaternary | travertine | x | | | | see 71A | x | | | |
| 71B | Quaternary | travertine | x | | x | x | x | | | | |
| 72A | Brushy Basin | shale | x | | | | x | | | | |
| 72B | Quaternary | travertine | x | | | | x | | | | |

Table C1: List of all thin sections and a summary of microscopy and energy dispersive data collected for each.
Std. = standard slide preparation; Pol. = polished slide preparation;
SE = secondary electron (rock fragment); BSE = backscatter electron;
EDS = energy dispersive spectroscopy; CL = cathodoluminescence

## List of thin sections and available petrographic data

| | | | | | Stained | | | | | | |
|---|---|---|---|---|---|---|---|---|---|---|---|
| **Sample** | **Formation** | **Lithology** | **Std.** | **Pol.** | **Calcite** | **Kspar** | **Optical** | **SE** | **BSE** | **EDS** | **CL** |
| 73 | Quaternary | travertine | x | | x | x | x | | | | |
| 74 | Salt Wash | sandstone | x | | x | x | x | | | | |
| 75-1 | Quaternary | travertine | x | | x | x | x | | | | |
| 75-2 | Quaternary | travertine | x | | x | x | x | | | | |
| 76 | Salt Wash | sandstone | x | | x | x | x | | | | |
| 77 | Salt Wash | sandstone | x | | x | x | x | | | | |
| 78A | Salt Wash | sandstone | x | | x | x | x | | | | |
| 78B | Salt Wash | sandstone | x | | x | x | x | | | | |
| 79 | Salt Wash | sandstone | x | | x | x | x | | | | |
| 80A | Salt Wash | sandstone | x | | x | x | x | x | | | |
| 80B-1 | Salt Wash | sandstone | x | | x | x | x | | | | |
| 80B-2 | Salt Wash | sandstone | x | | x | x | x | | | | |
| 82 | Salt Wash | sandstone | x | | x | x | x | | | | |
| 83 | Salt Wash | sandstone | x | | x | x | x | | | | |
| 84 | Salt Wash | sandstone | x | | x | x | x | | | | |
| 85 | Salt Wash | sandstone | x | | x | x | x | | | | |
| 86 | Salt Wash | sandstone | x | | x | x | x | | | | |
| 87 | Brushy Basin | sandstone | x | | x | x | x | | | | |
| 87 | Brushy Basin | sandstone | | x | | | x | | | | |
| 100 | Brushy Basin | volcanic? | x | | | | | | | | |
| 100 | Brushy Basin | volcanic? | | x | | | x | | | | |
| X | Quaternary | ooid-like | x | | | | x | | | | |

Table C1: List of all thin sections and a summary of microscopy and energy dispersive data collected for each.
Std. = standard slide preparation; Pol. = polished slide preparation;
SE = secondary electron (rock fragment); BSE = backscatter electron;
EDS = energy dispersive spectroscopy; CL = cathodoluminescence

**Sample #:** 15A-1

## Petrographic Summary

**Date:** 7/20/10

**Location Description:** Sliver of sandstone outcropping in shale slope between travertine and miniature, raised ramp to the northeast.

**Field Trip:** ☑ April, '09 ☐ Oct., '09

**Formation:** Salt Wash

**Rock Type:** sandstone

**Grain Size:** 0.1-0.6 mm

**Grain Types:** mostly quartz, some plag

**F-M-C-P:** F: M: C: P:

**Porosity (%):** Point Count: - -

Measured: - -

**Perm (mD):** - -

**Isotopes (‰):** $\delta^{18}$O: - -

$\delta^{13}$C: - -

Other: - -

**Thin Section Map**

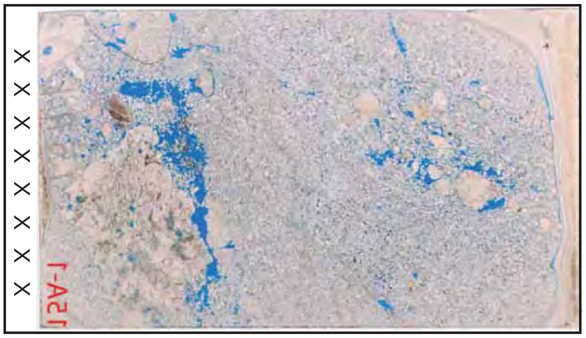

**Oriented thin section:** ☐ Yes ☑ No

**Orientation?:**

**Preparation** ☐ Thick ☑ Conventional ☐ Polished

**Stains:** ☑ Carbonate ☐ Plag ☐ Kspar

**Point Count:**

**Cement:** (types, sequence)
clay-ey, green spongy
no carbonates

**Comments:**
Some thin-layered deformed clays; some plag grains
Some frac porosity; most intergranular space filled w/ green spongy material
Grains a combo of mono qtz and micro qtz (chert). Also some less abundant zebraic qtz.
Crushed ductile high-B grains (micas?)
No carbonate grains OR carbonate cement
Some opaque cements and grains

**Sketches:**

**Sample #: 15A-1**

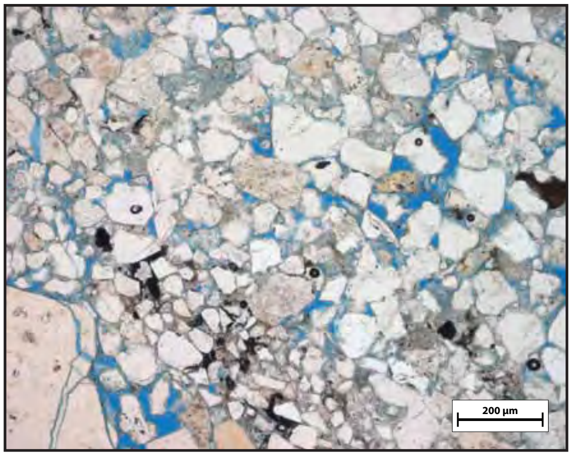

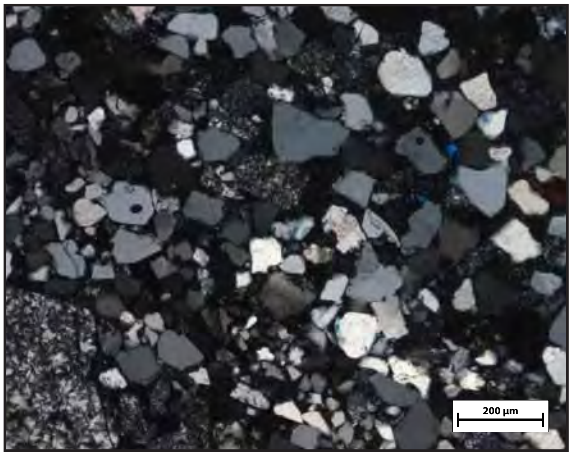

**Sample #:** 15A-2 (conventional)

## Petrographic Summary

**Date:** / /

**Location Description:** Sliver of sandstone outcropping in shale slope between travertine and miniature, raised ramp to the northeast.

**Field Trip:** ☑ April, '09 ☐ Oct., '09

**Formation:** Salt Wash

**Rock Type:** sandstone

**Grain Size:** 0.1-0.6 mm

**Grain Types:** quartz

**F-M-C-P:** F: M: C: P:

**Porosity (%):** Point Count: - -

Measured: - -

**Perm (mD):** - -

**Isotopes (‰ ):** $\delta^{18}O$: - -

$\delta^{13}C$: - -

Other: - -

**Thin Section Map**

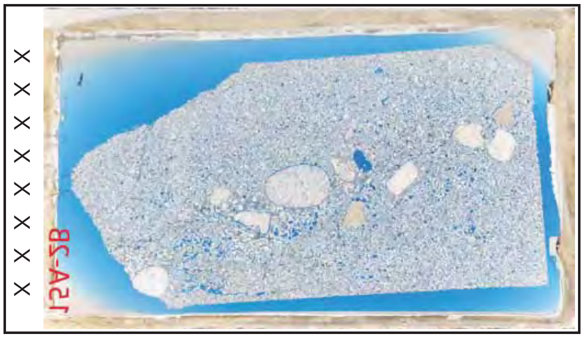

**Oriented thin section:** ☐ Yes ☑ No

**Orientation?:**

**Preparation** ☐ Thick ☑ Conventional ☐ Polished

**Stains:** ☐ Carbonate ☐ Plag ☐ Kspar

**Point Count:**

**Cement:** (types, sequence) Green spongy dissolved clay; smaller portion of brown/opaque cement

**Comments:** Feldspars very rare; miscellaneous, high-B, high-relief grains are more common than feldspars.

High porosity

**Sketches:**

**Sample #: 15A-2** (conventional)

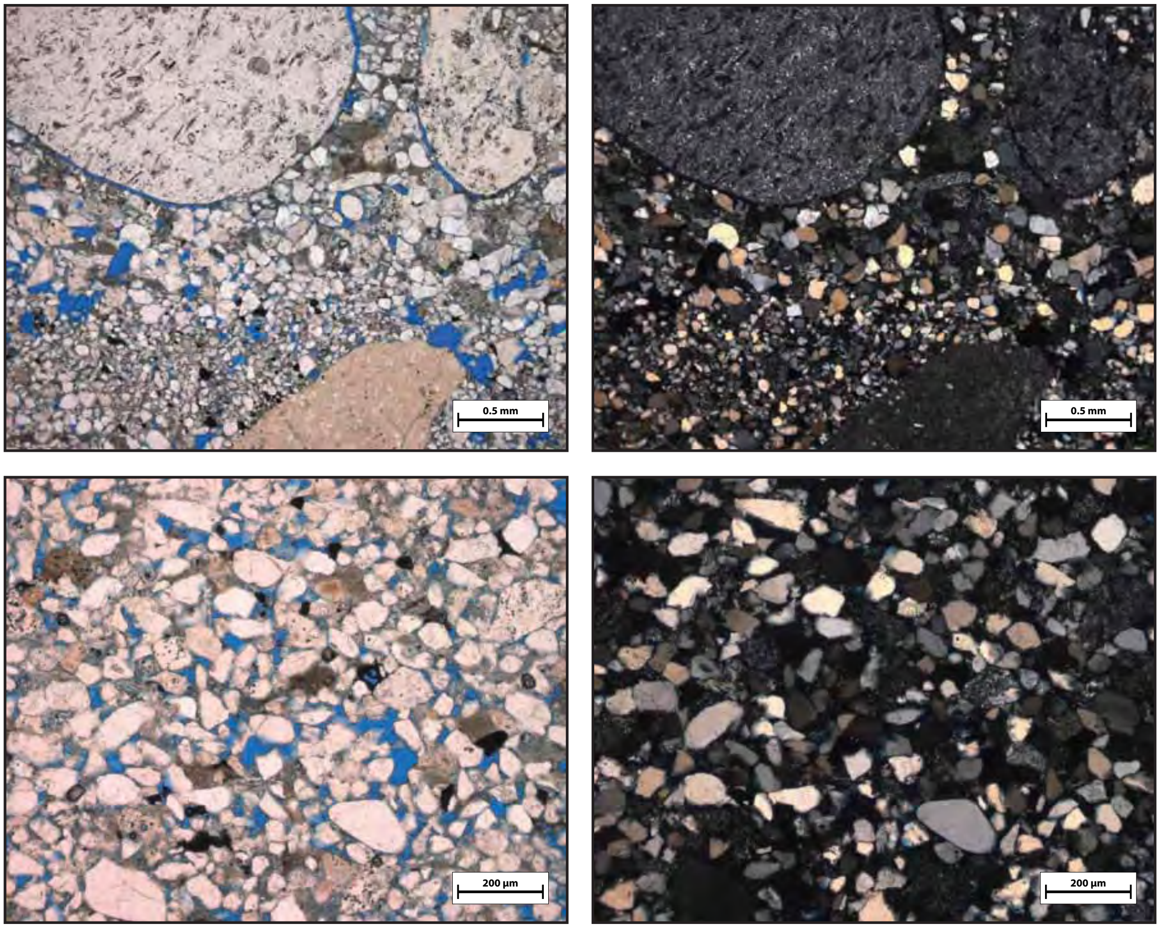

**Sample #:** 15A-2

## Petrographic Summary

**Date:** / /

**Location Description:** Sliver of sandstone outcropping in shale slope between travertine and miniature, raised ramp to the northeast.

**Field Trip:** ☑ April, '09 ☐ Oct., '09

**Formation:** Salt wash

**Rock Type:** sandstone

**Grain Size:** 0.1-0.8 mm

**Grain Types:** quartz, opaque, some felds

**F-M-C-P:** F: M: C: P:

**Porosity (%):** Point Count: - -

Measured: - -

**Perm (mD):** - -

**Isotopes (‰ ):** $\delta^{18}$O: - -

$\delta^{13}$C: - -

Other: - -

**Thin Section Map**

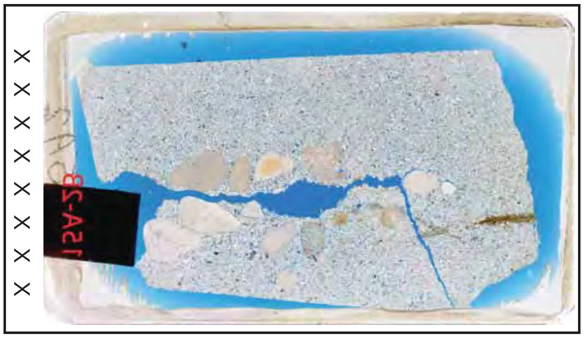

**Oriented thin section:** ☐ Yes ☑ No

**Orientation?:**

**Preparation** ☐ Thick ☐ Conventional ☑ Polished

**Stains:** ☐ Carbonate ☐ Plag ☐ Kspar

**Point Count:**

**Cement:** (types, sequence) Spongy, clay-ey partially dissolved. Almost no calcite. Some brown/opaque clay cement.

**Comments:** Deformations bands. Lots of spongy, pale-green-looking cement. Some dissolved grains with clay-ey-looking residue; quite grungy-looking.

High porosity

Some feldspars, especially plagioclase.

**Sketches:**

**Sample #: 15A-2**
(polished)

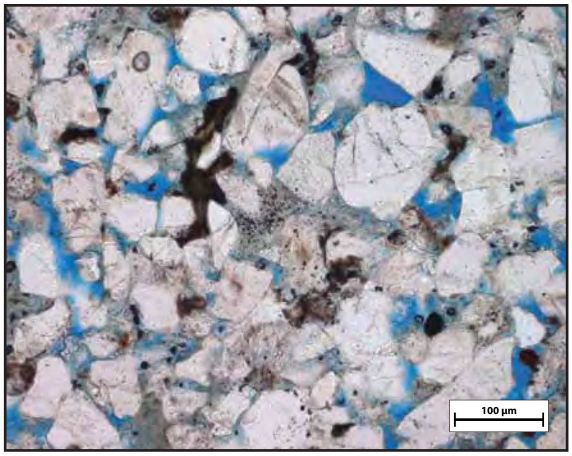

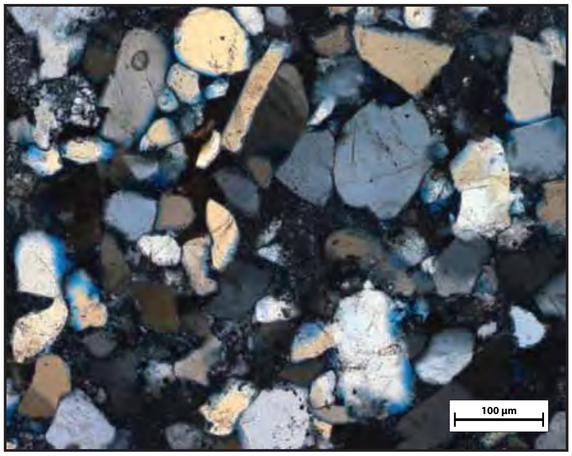

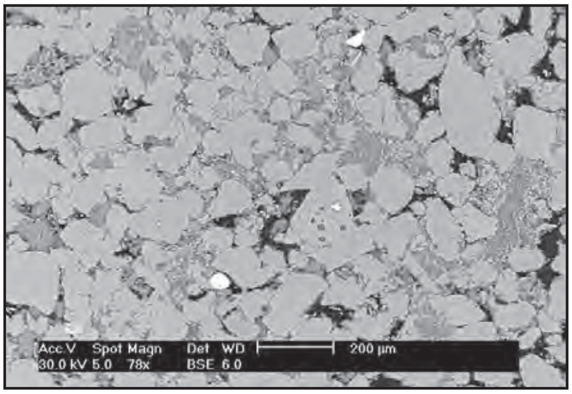

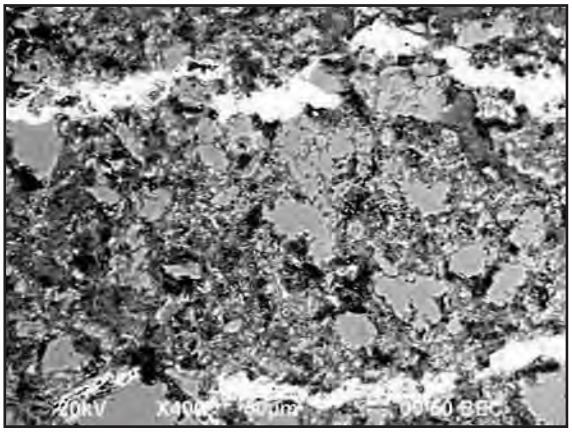

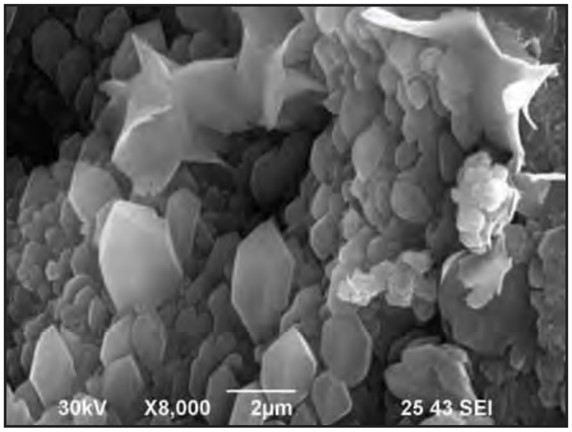

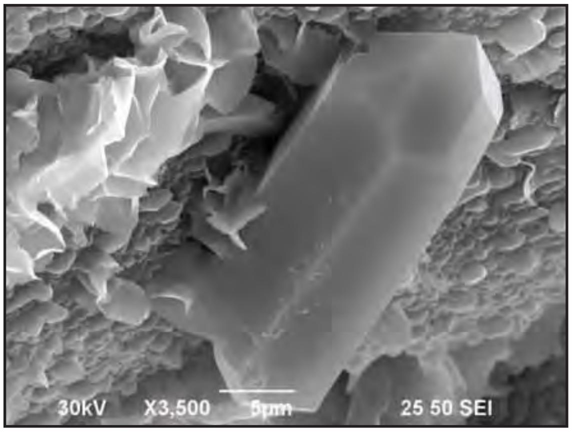

**Sample #:** **15B-1**

## Petrographic Summary

**Date:** / /

**Location Description:** Sliver of sandstone outcropping in shale slope between travertine and miniature, raised ramp to the northeast. From more veiny outcrop underneath 15A.

**Field Trip:** ☑ April, '09 ☐ Oct., '09

**Formation:** Salt Wash

**Rock Type:** sandstone

**Grain Size:** 0.1-1.0 mm

**Grain Types:** quartz, feldspar

**F-M-C-P:** F: M: C: P:

**Porosity (%):** Point Count: --

Measured: --

**Perm (mD):** --

**Isotopes (‰):** $\delta^{18}O$: --

$\delta^{13}C$: --

Other: --

**Thin Section Map**

**Oriented thin section:** ☐ Yes ☑ No

**Orientation?:**

**Preparation** ☑ Thick ☐ Conventional ☐ Polished

**Stains:** ☐ Carbonate ☐ Plag ☐ Kspar

**Point Count:**

**Cement:** brown-opaque clay cement

(types, sequence)

**Comments:** Grungier than 15B-2 due to brown clay cement.

Feldspars uncommon; lots of microcrystalline quartz.

High porosity

**Sketches:**

**Sample #: 15B-1**

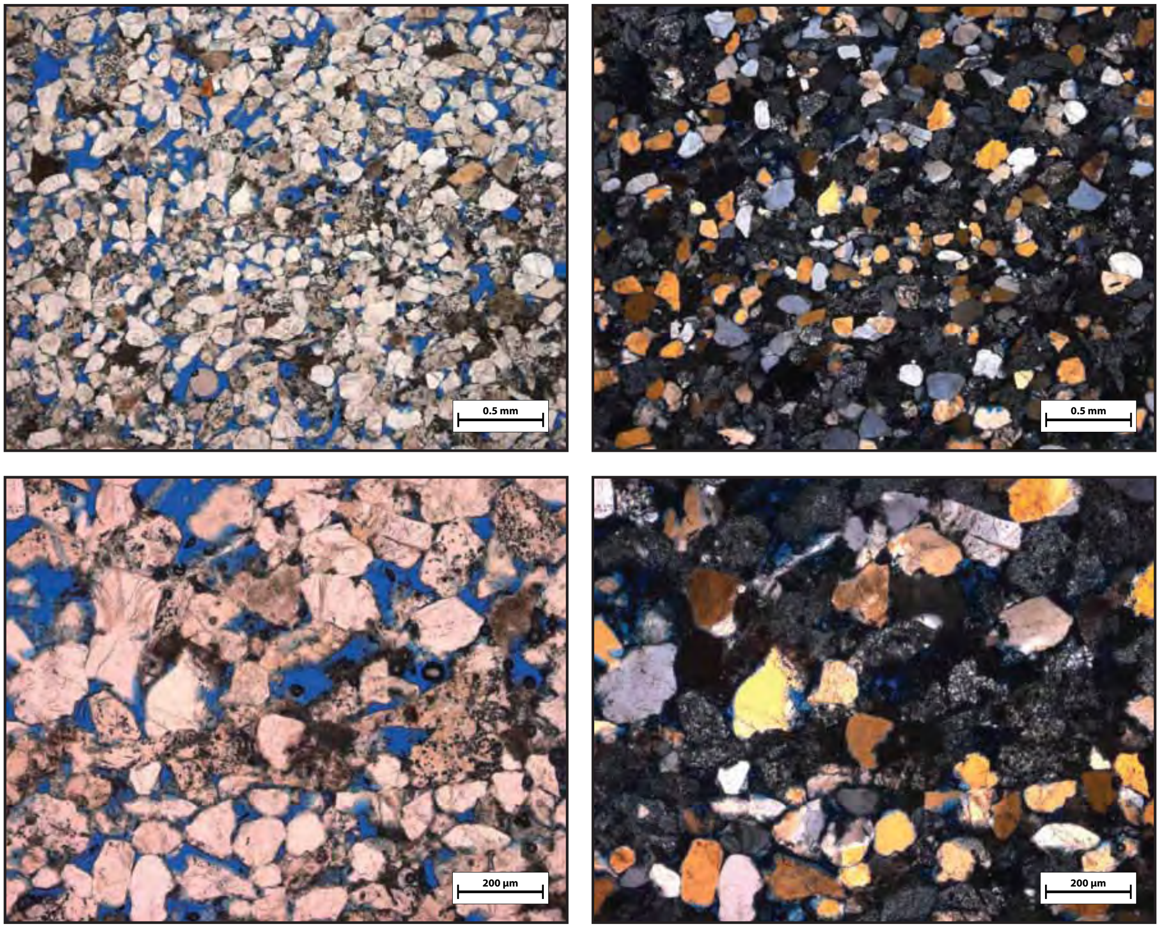

**Sample #:** 15B-2

## Petrographic Summary

**Date:** / /

**Location Description:** Sliver of sandstone outcropping in shale slope between travertine and miniature, raised ramp to the northeast. From more veiny outcrop underneath 15A.

**Field Trip:** ☑ April, '09 ☐ Oct., '09

**Formation:** Salt Wash

**Rock Type:** sandstone

**Grain Size:** 0.1-1.0 mm

**Grain Types:** quartz, opaque, some felds

**F-M-C-P:** F: M: C: P:

**Porosity (%):** Point Count: --

Measured: --

**Perm (mD):** --

**Isotopes (‰):** $\delta^{18}O$: --

$\delta^{13}C$: --

Other: --

**Thin Section Map**

**Oriented thin section:** ☐ Yes ☑ No

**Orientation?:**

**Preparation** ☐ Thick ☑ Conventional ☐ Polished

**Stains:** ☐ Carbonate ☐ Plag ☐ Kspar

**Point Count:**

**Cement:** (types, sequence) spongy green clay-ey cement; quartz overgrowths look recycled;

**Comments:** high porosity

Lots of microcrystalline quartz grains

Fewer opaques than 15A slides.

**Sketches:**

## Sample #: **15B-2**

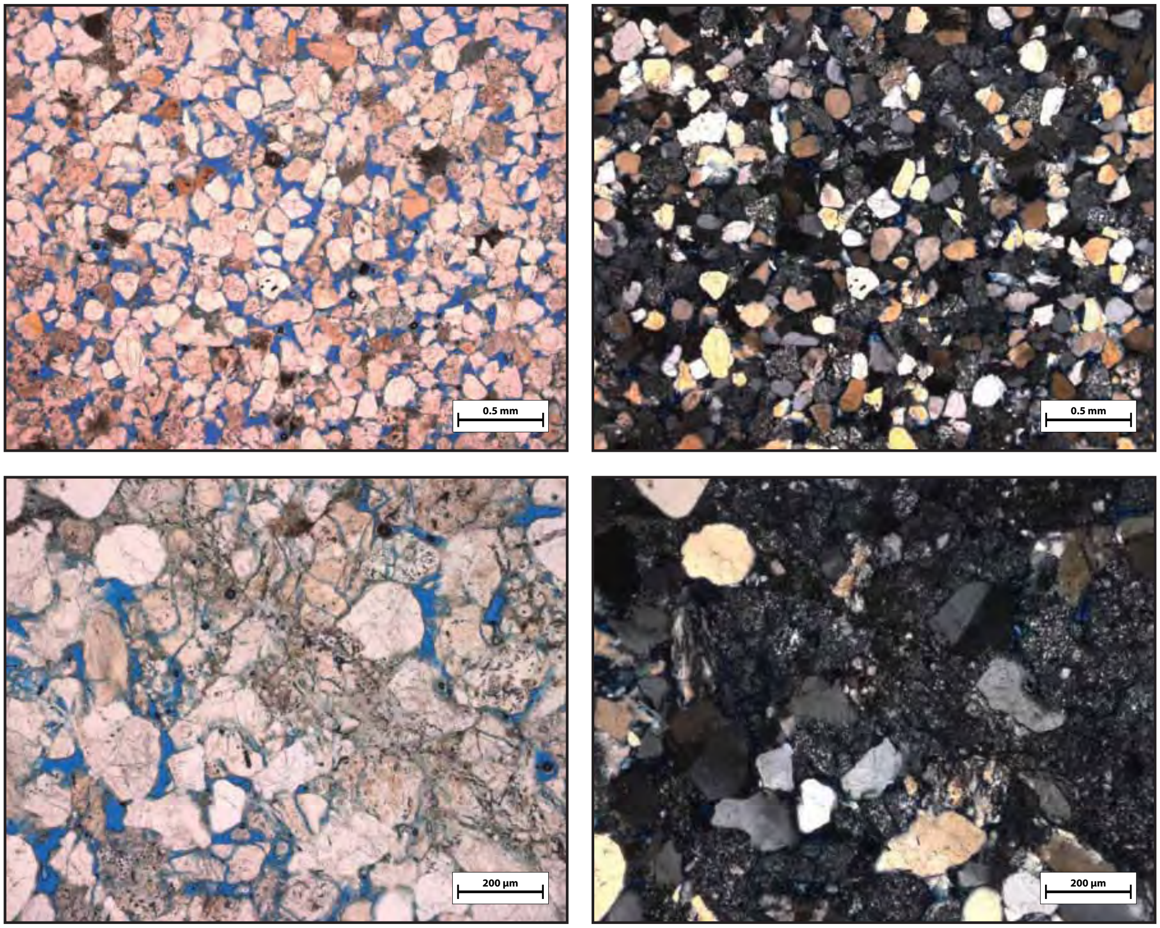

**Sample #:** 16-1

## Petrographic Summary

**Date:** / /

**Location Description:** Coarser-grained sand outcrop in shale hillock immediately east of travertine.

**Field Trip:** ☑ April, '09 ☐ Oct., '09

**Formation:** Brushy Basin

**Rock Type:** sandstone/conglomerate

**Grain Size:** 0.3-3.0 mm

**Grain Types:** mostly chert

**F-M-C-P:** F: M: C: P:

**Porosity (%):** Point Count: - -

Measured: - -

**Perm (mD):** - -

**Isotopes (‰ ):** $\delta^{18}O$: - -

$\delta^{13}C$: - -

Other: - -

**Thin Section Map**

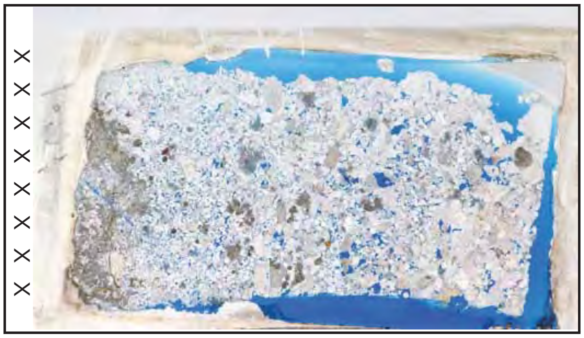

**Oriented thin section:** ☐ Yes ☑ No

**Orientation?:**

**Preparation** ☑ Thick ☐ Conventional ☐ Polished

**Stains:** ☐ Carbonate ☐ Plag ☐ Kspar

**Point Count:**

**Cement:** (types, sequence) some spongy green dissolved-looking clay; quartz cement appears to be recycled; some brown-opaque clay

**Comments:** Dominated by large chert grains; monocrystalline quartz grains are notably smaller.

Medium-high porosity

Samples from Station 16 should more appropriately be labeled 16A and 16B, as they are from lithologically different outcrops at the same station.

**Sketches:**

**Sample #: 16-1**

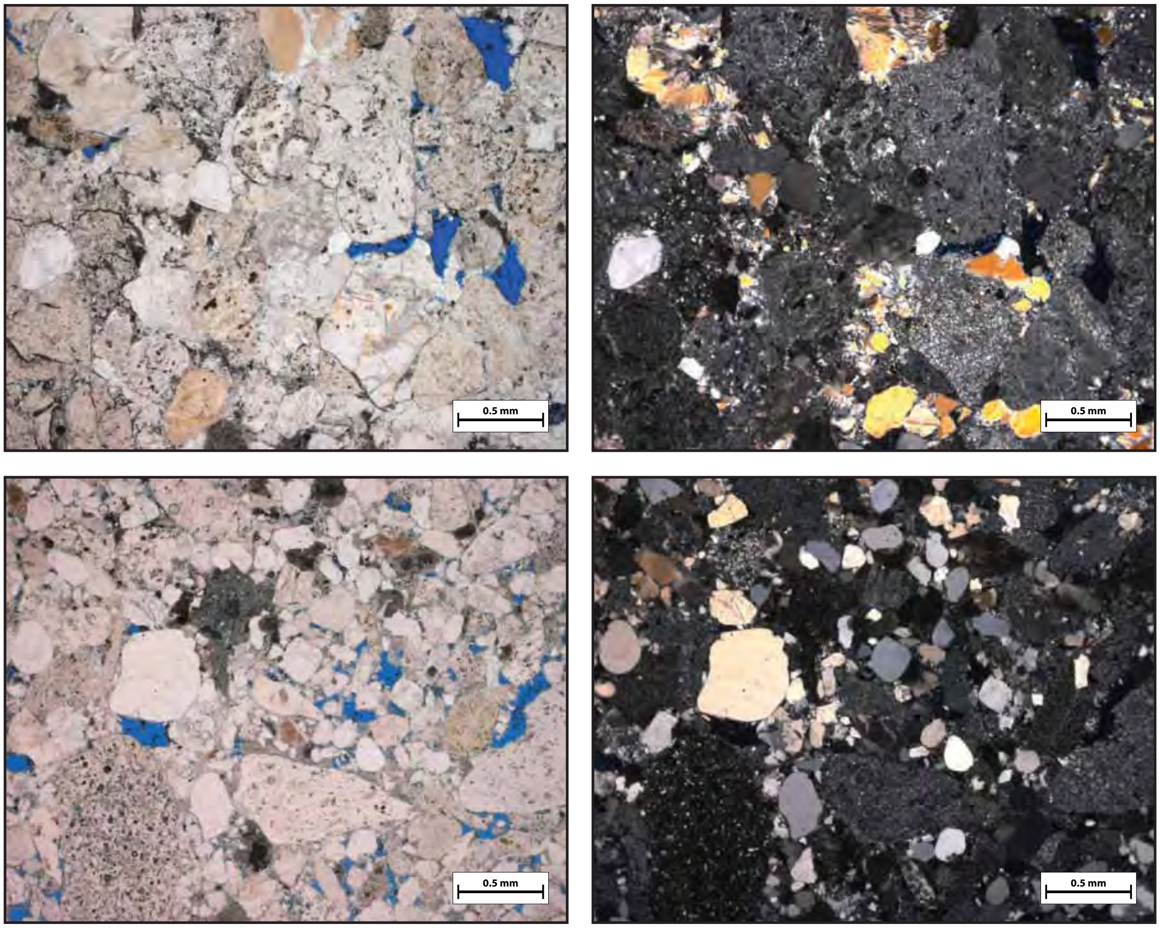

**Sample #:** 16-2

## Petrographic Summary

**Date:** / /

**Location Description:** Small rusty-colored fine-grained sand outcrop in shale hillock immediately east of travertine platform.

**Field Trip:** ☑ April, '09 ☐ Oct., '09

**Formation:** Brushy Basin

**Rock Type:** sandstone

**Grain Size:** 0.05-0.35 mm

**Grain Types:** quartz, opaques

**F-M-C-P:** F: M: C: P:

**Porosity (%):** Point Count: --

Measured: --

**Perm (mD):** --

**Isotopes (‰):** $\delta^{18}O$: --

$\delta^{13}C$: --

Other: --

**Thin Section Map**

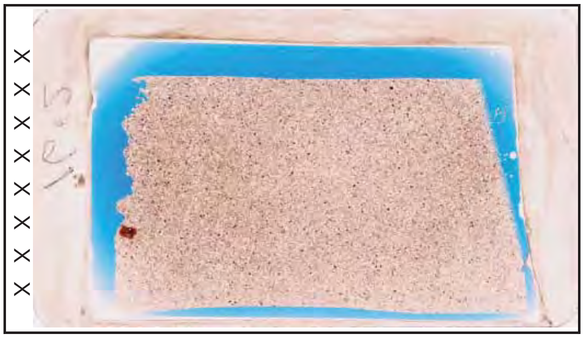

**Oriented thin section:** ☐ Yes ☑ No

**Orientation?:**

**Preparation** ☐ Thick ☐ Conventional ☑ Polished

**Stains:** ☐ Carbonate ☐ Plag ☐ Kspar

**Point Count:**

**Cement:** (types, sequence) Pervasively quartz-cemented. Fine-grained, microcrystalline, non-isopachous quartz (not euhedral overgrowths). Opaque clay mixed in.

**Comments:** Virtually zero porosity.

Pervasive quartz cement has a grungy opaque component that appears to be clay.

Samples from Station 16 should more appropriately be labeled 16A and 16B, as they are from lithologically different outcrops at the same station.

**Sketches:**

## Sample #: 16-2

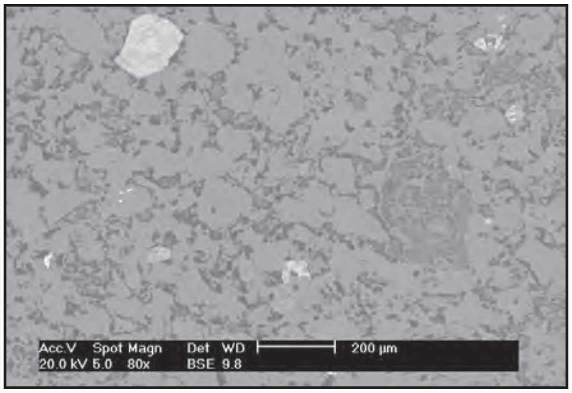
Acc.V Spot Magn Det WD 200 µm
20.0 kV 5.0 80x BSE 9.8

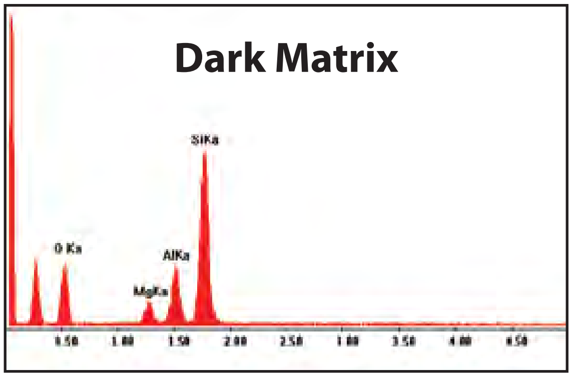
Dark Matrix
SiKa
O Ka
AlKa
MgKa
0.50
1.00
1.50
2.00
2.50
3.00
3.50
4.00
4.50

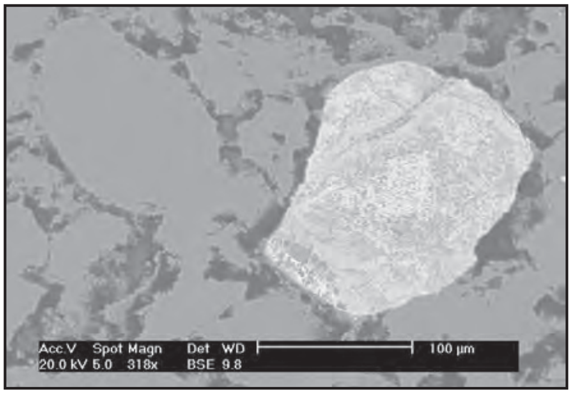
Acc.V Spot Magn Det WD 100 µm
20.0 kV 5.0 318x BSE 9.8

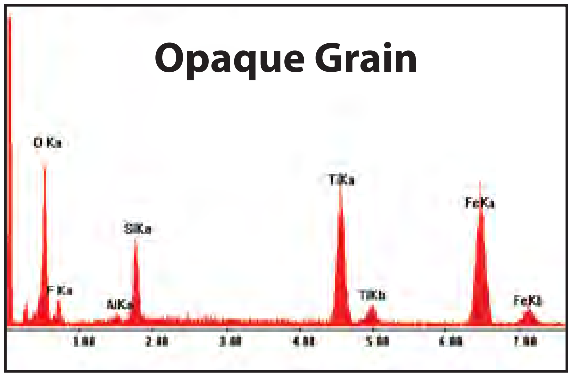
Opaque Grain
O Ka
TiKa
FeKa
SiKa
F Ka
AlKa
TiKb
FeKb
1.00
2.00
3.00
4.00
5.00
6.00
7.00

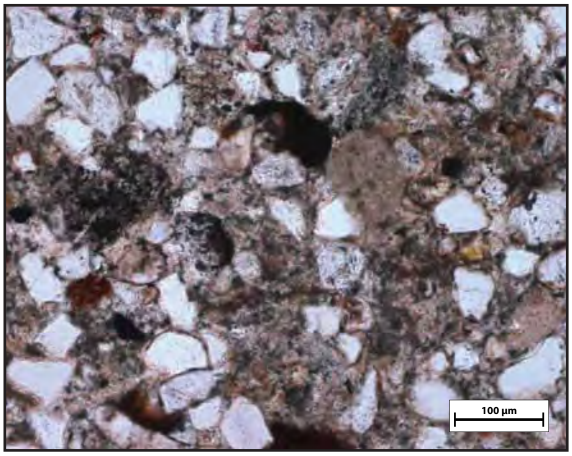
100 µm

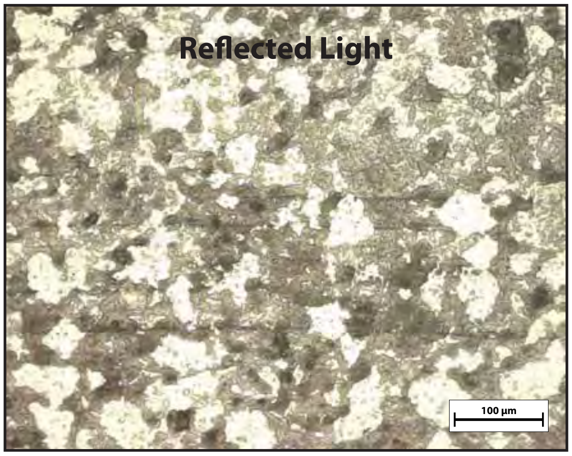
Reflected Light
100 µm

**Sample #:** 17A

## Petrographic Summary

**Date:** 11/ 3 /09

**Location Description:** Crumbly green silt/mud (altered?) part of ledgy sandstone outcrop immediately northeast of the travertine platform.

**Field Trip:** ☑ April, '09 ☐ Oct., '09

**Formation:** Jms5? travertine?

**Rock Type:** silty mud

**Grain Size:** mud - 0.5mm

**Grain Types:** qtz, chert, occasional opaques

**F-M-C-P:** F: 10 M: 90 C: 0 P: 0

**Porosity (%):** Point Count: --

Measured: --

**Perm (mD):** --

**Isotopes (‰ ):** $\delta^{18}O$: --

$\delta^{13}C$: --

Other: --

### Thin Section Map

**Oriented thin section:** ☐ Yes ☑ No

**Orientation?:**

**Preparation** ☐ Thick ☐ Conventional ☑ Polished

**Stains:** ☐ Carbonate ☐ Plag ☐ Kspar

**Point Count:**

**Cement:** (types, sequence) pervasive micrite

**Comments:** Grains are floating entirely in a dominantly micritic matrix (not a lot of clay content in this one, as compared to 17B).

Hypothesis about these samples (17A and B): they are actually part of the travertine deposit; while micrite was precipitating at the surface, varying amounts of sediment (little in 17A, lots in 17B) were washed or blown into it and encased in micrite.

**Sketches:**

**Sample #: 17A**

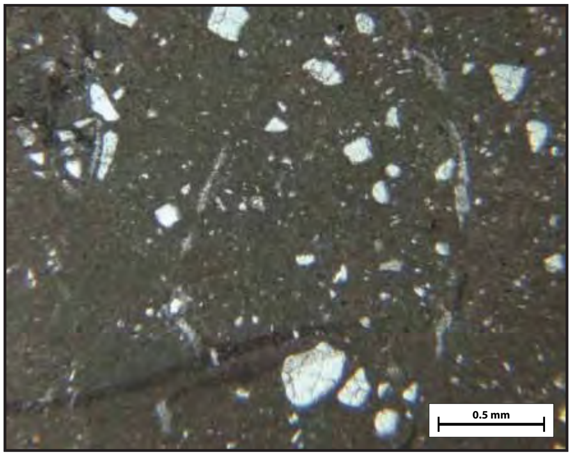

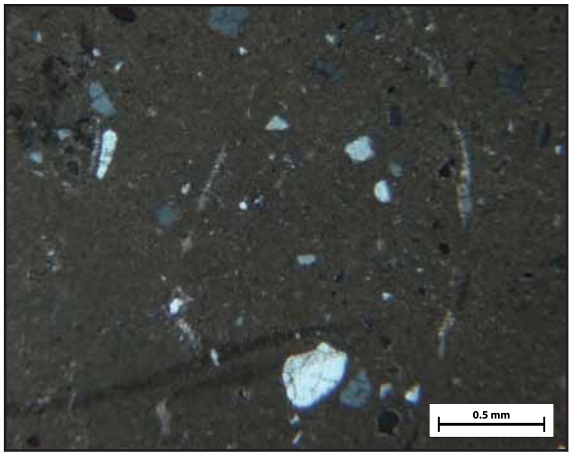

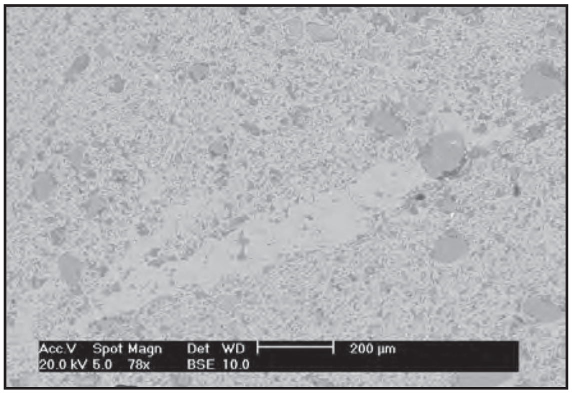

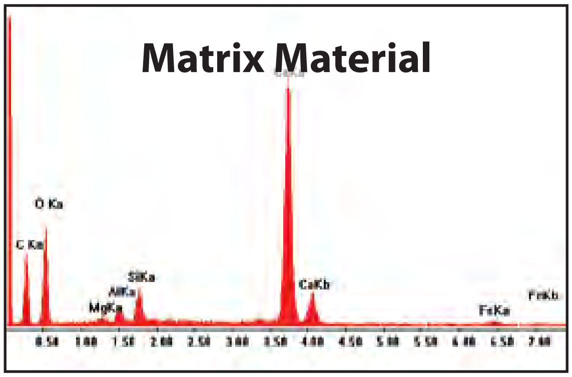
Matrix Material

**Sample #:** 17B-1

## Petrographic Summary

**Date:** / /

**Location Description:** Yellow/orange part of ledgy sandstone outcrop immediately northeast of the travertine platform.

**Field Trip:** ☑ April, '09 ☐ Oct., '09

**Formation:** Salt Wash? travertine?

**Rock Type:** muddy sand

**Grain Size:** 0.1-0.2 mm

**Grain Types:** quartz

**F-M-C-P:** F: M: C: P:

**Porosity (%):** Point Count: - -

Measured: - -

**Perm (mD):** - -

**Isotopes (‰ ):** $\delta^{18}$O: - -

$\delta^{13}$C: - -

Other: - -

**Thin Section Map**

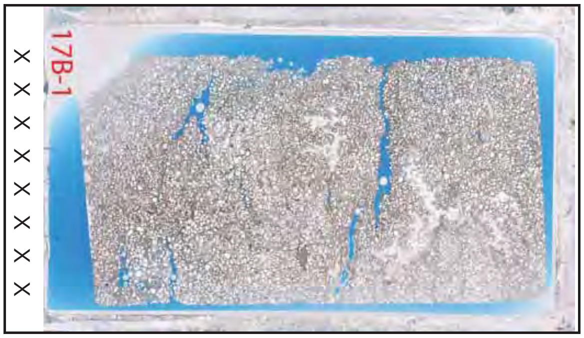

**Oriented thin section:** ☐ Yes ☑ No

**Orientation?:**

**Preparation** ☐ Thick ☑ Conventional ☐ Polished

**Stains:** ☐ Carbonate ☐ Plag ☐ Kspar

**Point Count:**

**Cement:** (types, sequence) pervasive mixture of clay and micrite matrix surrounding all grains

**Comments:** Grains are matrix-supported, "floating" in micrite/clay cement. Hard to actually call this a sandstone. Micrite cement evident from birefringence in crossed-polars; clay matrix is assigned to material that is dark brown/opaque with no birefringence. Both surround all grains. Possibly formed in the travertine by simultaneous precipitation/deposition of micrite and fine sediments. See notes for 17B-2.

**Sketches:**

## Sample #: 17B-1

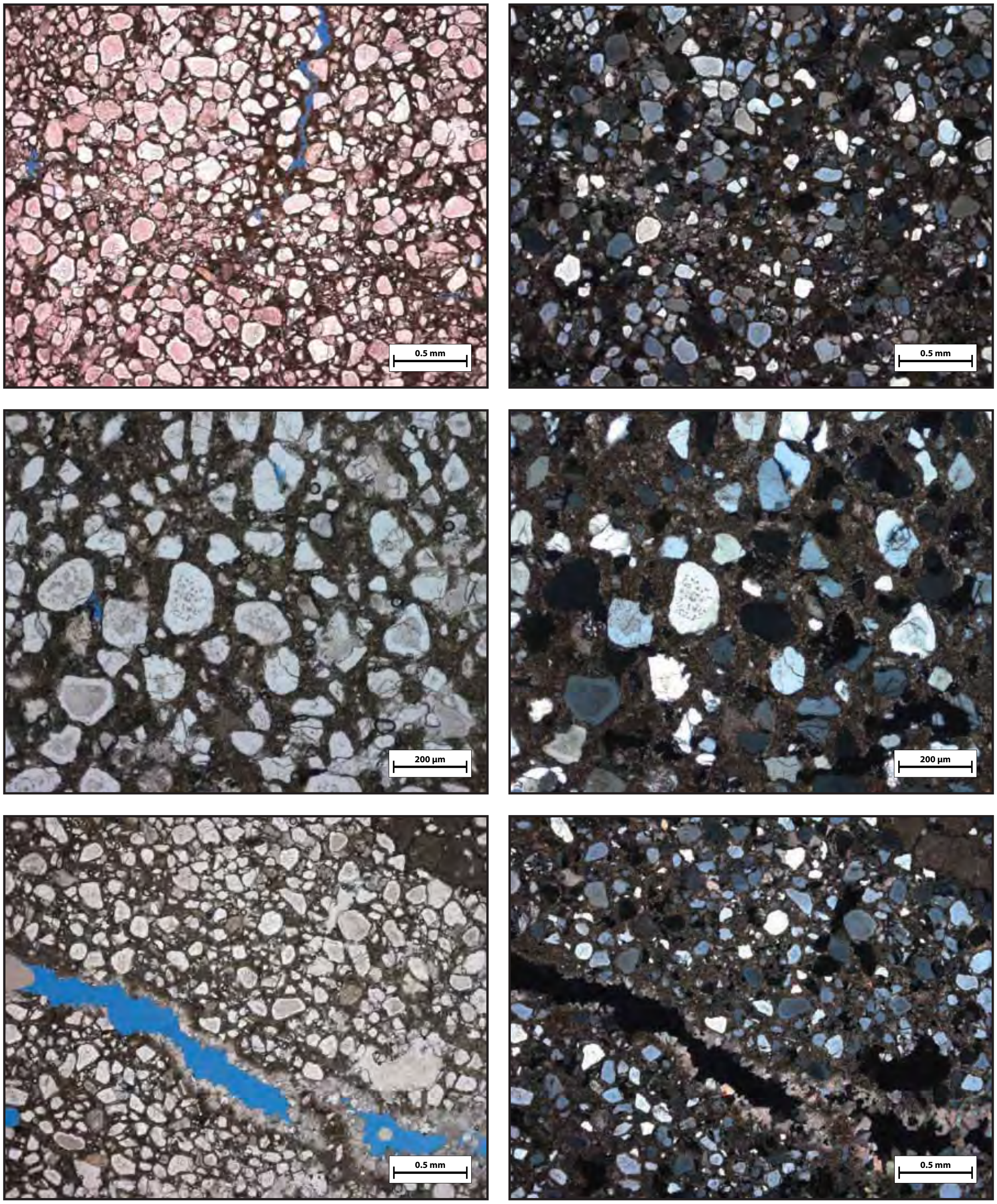

**Sample #:** 17B-2

## Petrographic Summary

**Date:** 11/ 3 /09

**Location Description:** Yellow/orange part of ledgy sandstone outcrop immediately northeast of the travertine platform.

**Field Trip:** ☑ April, '09 ☐ Oct., '09

**Formation:** Jms5

**Rock Type:** sandstone

**Grain Size:** mud -> 0.05-0.40 mm

**Grain Types:** qtz, felds, chert

**F-M-C-P:** F: 55 M: 40 C: x P: 5

**Porosity (%):** Point Count: 7%

Measured: --

**Perm (mD):** --

**Isotopes (‰):** $\delta^{18}O$: --

$\delta^{13}C$: --

Other:

### Thin Section Map

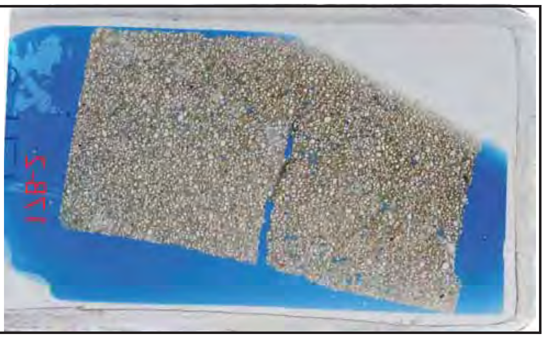

**Oriented thin section:** ☐ Yes ☑ No

**Orientation?:**

**Preparation**

☐ Thick

☐ Conventional

☑ Polished

**Stains:**

☐ Carbonate

☐ Plag ☐ Kspar

**Point Count:**

| Quartz | | | Plagioclase Feld. | | Alkali Feld. | | Lithics | | Misc. | Clay | Cement | | | | Porosity | | | | Total |
|---|---|---|---|---|---|---|---|---|---|---|---|---|---|---|---|---|---|---|---|
| mono | poly | mic/chert | intact | dissolved | intact | dissolved | opaque | sed | Grains | Matrix | spar | micrite | quartz | clay | inter | oversize | intra | micro | Points |
| 126 | 3 | 3 | 0 | 0 | 0 | 1 | 0 | 9 | 0 | 79 | 4 | 143 | 0 | 6 | 10 | 0 | 11 | 5 | 400 |
| 32% | 1% | 1% | 0% | 0% | 0% | 0% | 0% | 2% | 0% | 20% | 1% | 36% | 0% | 2% | 3% | 0% | 3% | 1% | |

**Cement:** (types, sequence)

some calcite cement growing into porosity very euhedrally

**Comments:** Mostly qtz grains "suspended" in opaque mud

This is highly altered sandstone -- need to determine clay composition.

Similar to Sample 73 -- dense micritic matrix mixed with clay matrix, but much more porosity and significant fracture porosity (w/ calcite crystals growing into fractures)

**Sketches:**

**Sample #: 17B-2**

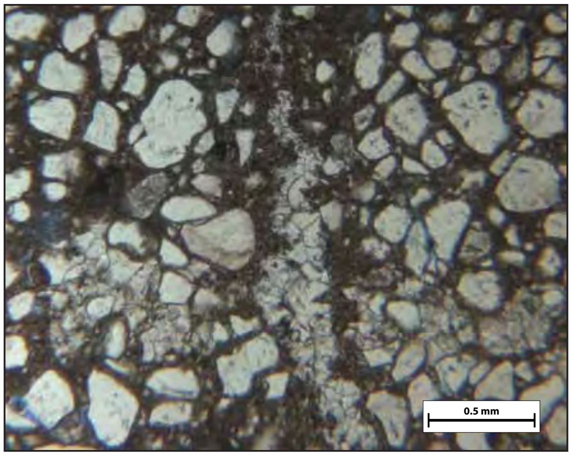

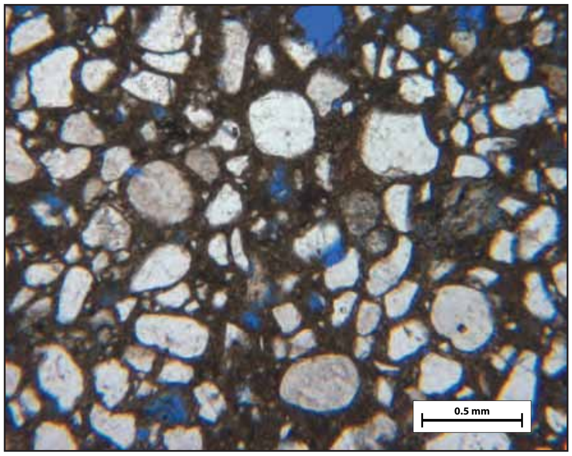

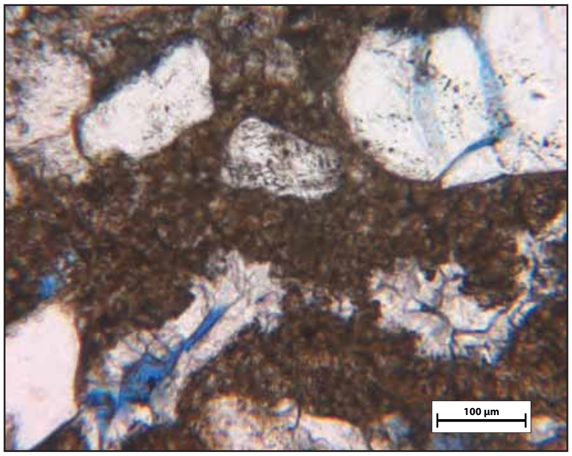

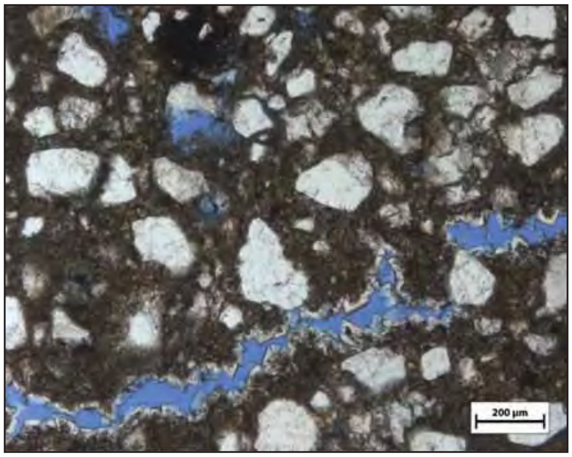

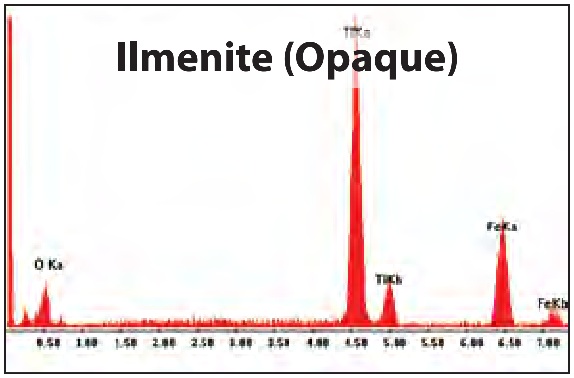
Ilmenite (Opaque)

**Sample #:** 17C-1

## Petrographic Summary

**Date:** 8/ 5 /10

**Location Description:** White/gray, well-cemented part of ledgy sandstone outcrop immediately northeast of the travertine platform.

**Field Trip:** ☑ April, '09 ☐ Oct., '09

**Formation:** Jms5

**Rock Type:** sandstone

**Grain Size:** 0.12-.05mm

**Grain Types:** mostly qtz

**F-M-C-P:** F: M: C: P:

**Porosity (%):** Point Count: 1%

Measured: --

**Perm (mD):** --

**Isotopes (‰ ):** $\delta^{18}O$: --

$\delta^{13}C$: --

Other:

**Thin Section Map**

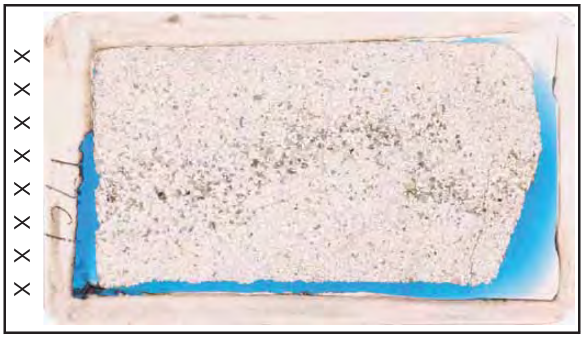

**Oriented thin section:** ☐ Yes ☑ No

**Orientation?:**

**Preparation** ☐ Thick ☐ Conventional ☑ Polished

**Stains:** ☐ Carbonate ☐ Plag ☐ Kspar

**Point Count:**

| Quartz | | | Plagioclase Feld. | | Alkali Feld. | | Lithics | | Misc. | Clay | Cement | | | | Porosity | | | | Total |
|---|---|---|---|---|---|---|---|---|---|---|---|---|---|---|---|---|---|---|---|
| mono | poly | mic/chert | intact | dissolved | intact | dissolved | opaque | sed | Grains | Matrix | spar | micrite | quartz | clay | inter | oversize | intra | micro | Points |
| 177 | 6 | 6 | 0 | 0 | 1 | 0 | 1 | 12 | 2 | 0 | 183 | 0 | 0 | 7 | 0 | 0 | 2 | 3 | 400 |
| 44% | 2% | 2% | 0% | 0% | 0% | 0% | 0% | 3% | 1% | 0% | 46% | 0% | 0% | 2% | 0% | 0% | 1% | 1% | |

**Cement:** (types, sequence) calcite spar

**Comments:** A few kspar grains - very good condition, not at all dissolved.

See photo of zebraic-style grain (qtz?)... could be a zeolite, maybe pyrophyllite

Virtually no secondary porosity

**Sketches:**

## Sample #: 17C-1

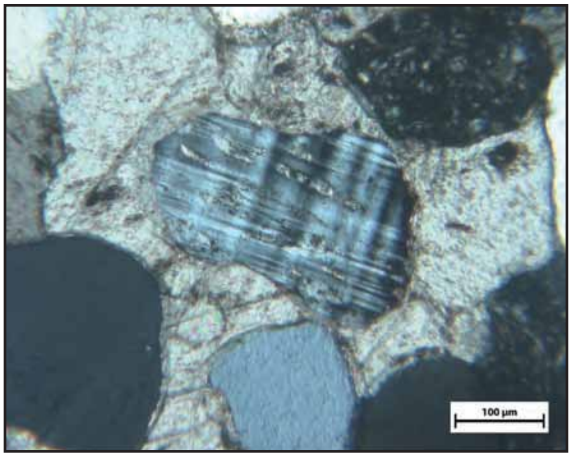
100 µm


100 µm

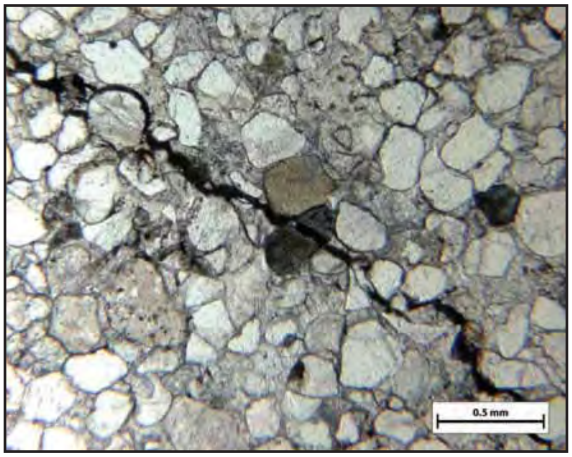
0.5 mm

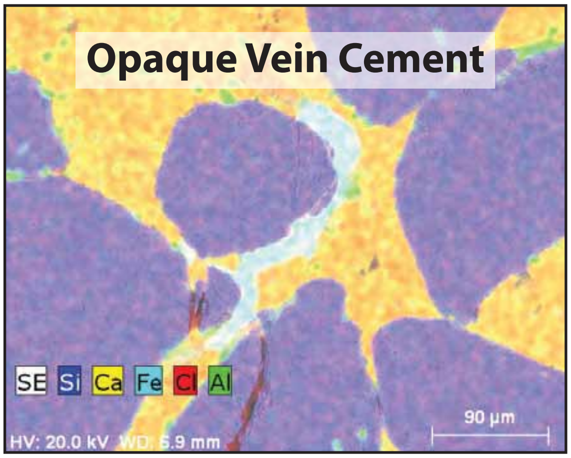
Opaque Vein Cement
SE Si Ca Fe Cl Al
90 µm
HV: 20.0 kV WD: 6.9 mm

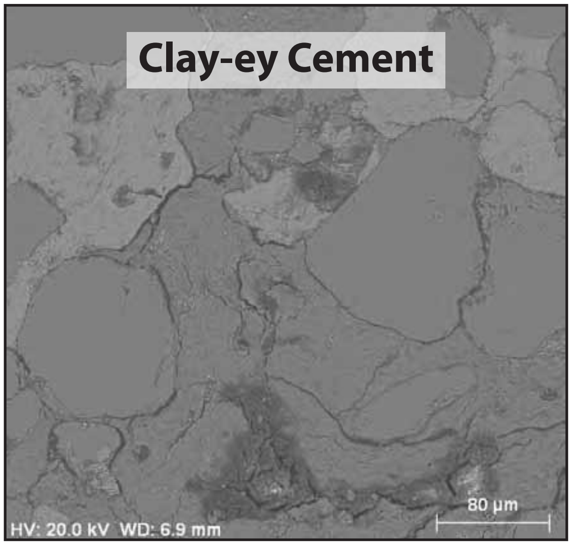
Clay-ey Cement
80 µm
HV: 20.0 kV WD: 6.9 mm

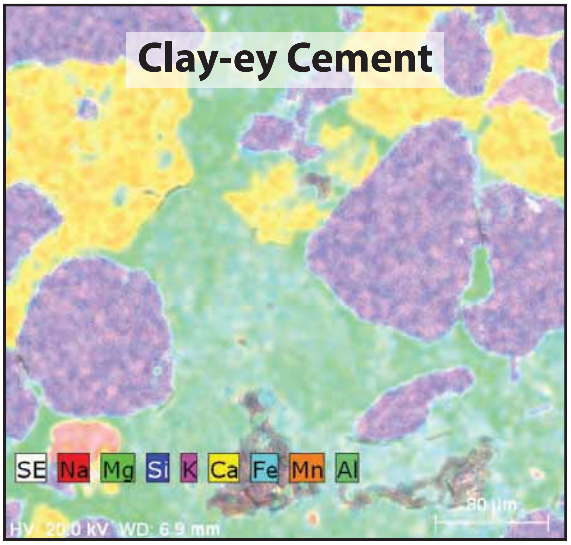
Clay-ey Cement
SE Na Mg Si K Ca Fe Mn Al
80 µm
HV: 20.0 kV WD: 6.9 mm

**Sample #:** 17C-2

## Petrographic Summary

**Date:** 5/20/10

**Location Description:** White/gray, well-cemented part of ledgy sandstone outcrop immediately northeast of the travertine platform.

**Field Trip:** ☑ April, '09 ☐ Oct., '09

**Formation:** Jms5

**Rock Type:** sandstone

**Grain Size:** 0.15-0.80 mm

**Grain Types:** quartz, rare felds

**F-M-C-P:** F: M: C: P:

**Porosity (%):** Point Count: --

Measured: --

**Perm (mD):** --

**Isotopes (‰):** $\delta^{18}O$: --

$\delta^{13}C$: --

Other: --

**Thin Section Map**

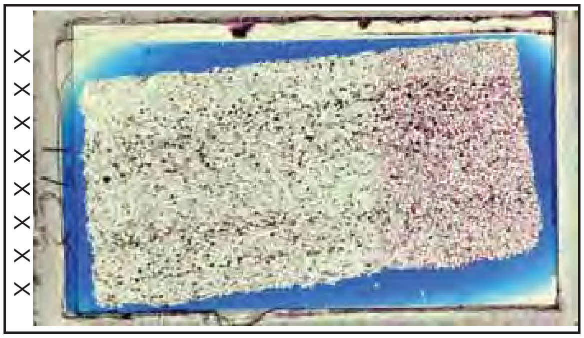

**Oriented thin section:** ☐ Yes ☑ No

**Orientation?:**

**Preparation** ☐ Thick ☑ Conventional ☐ Polished

**Stains:** ☑ Carbonate ☐ Plag ☑ Kspar

**Point Count:**

**Cement:** Abundant calcite spar

(types, sequence)

**Comments:** kspars: pale yellow stain, but on grains that are not clearly kspars, look more like poly/micro quartz

Photo above is sample of pink-stained calcite cement

very low porosity, almost totally filled in by calcite spar

Some dissolved spongy green grains

**Sketches:**

**Sample #: 17C-2**

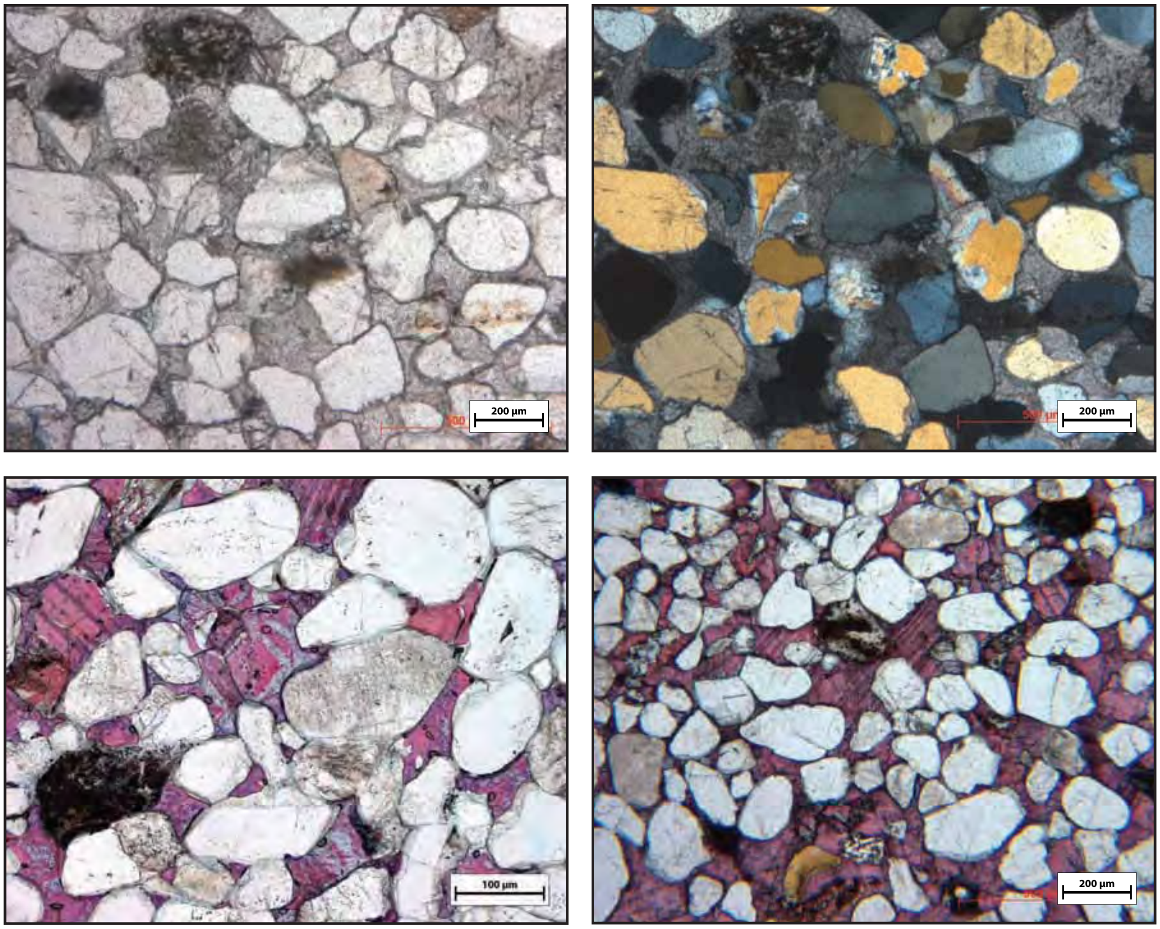

**Sample #:** 18-1

## Petrographic Summary

**Date:** 11/ 3 /09

**Location Description:** Vein-blasted red-green mottled shale from bottom of the outcrop jutting out of travertine platform

**Field Trip:** ☑ April, '09 ☐ Oct., '09

**Formation:** Jmb shale

**Rock Type:** altered shale w/ heavy veins

**Grain Size:** mud

**Grain Types:** ashes of ashes, dust of dust

**F-M-C-P:** F: x M: 55 C: 35 P: 10

**Porosity (%):** Point Count: - -

Measured: - -

**Perm (mD):** - -

**Isotopes (‰ ):** $\delta^{18}O$: - -

$\delta^{13}C$: - -

Other: - -

**Thin Section Map**

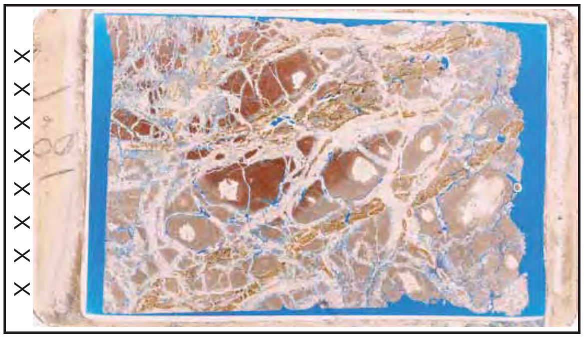

**Oriented thin section:** ☐ Yes ☑ No

**Orientation?:**

**Preparation** ☐ Thick ☐ Conventional ☑ Polished

**Stains:** ☐ Carbonate ☐ Plag ☐ Kspar

**Point Count:**

**Cement:** (types, sequence)
heavy calcite veining
something close to irregularly distributed grain-coating hematite

**Comments:** Difficult to determine porosity because it looks like sample was quite damaged, and circumgranular porosity could be an artifact of thin section preparation.

"Grains" are massively plucked.

This slide should be 18-1a (since there's an 18-1b).

**Sketches:**

## Sample #: 18-1

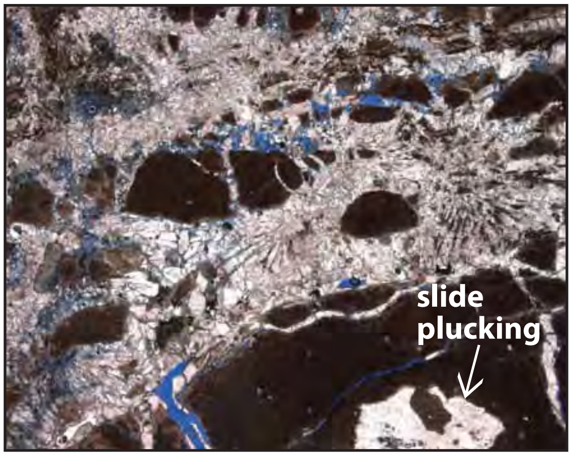

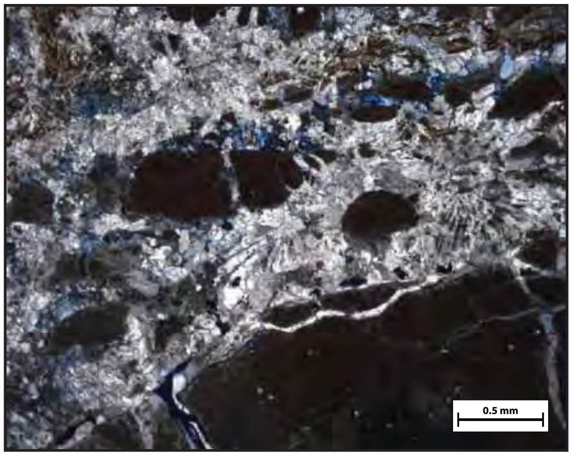

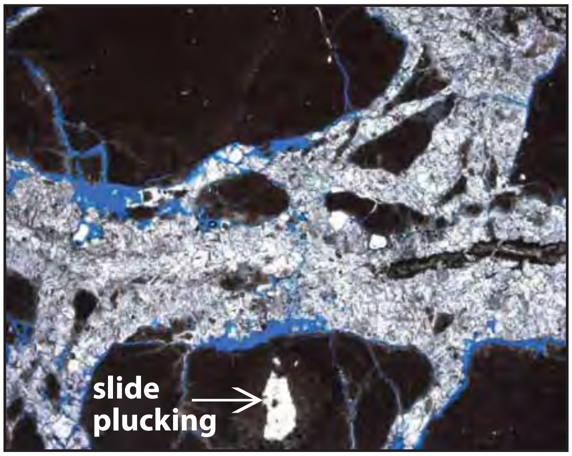

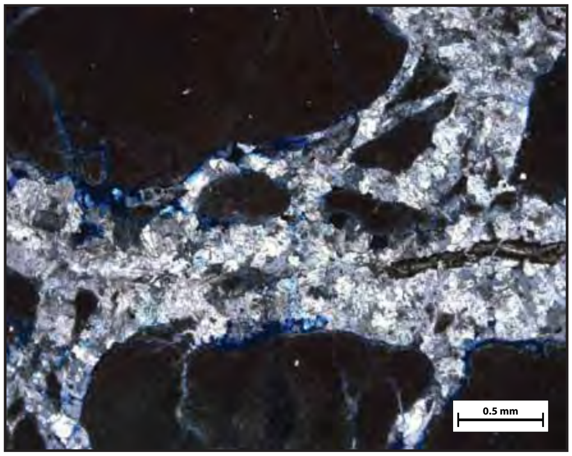

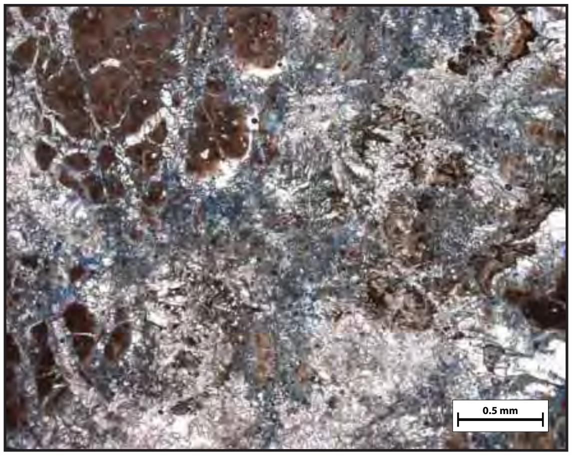

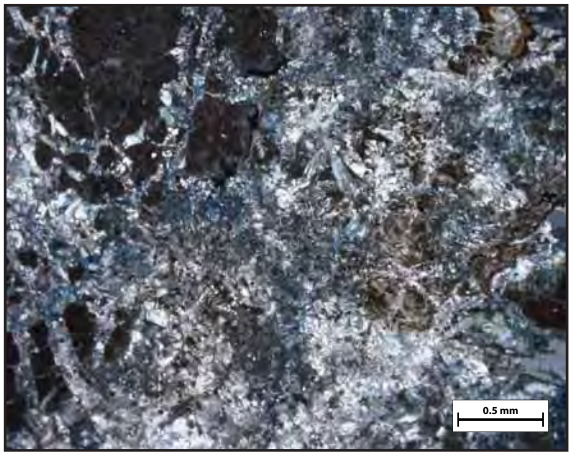

**Sample #:** 18-1b

## Petrographic Summary

**Date:** / /

**Location Description:** Vein-blasted red-green mottled shale from bottom of the outcrop jutting out of travertine platform

**Field Trip:** ☑ April, '09 ☐ Oct., '09

**Formation:** Brushy Basin

**Rock Type:** shale

**Grain Size:** clay-mud

**Grain Types:** --

**F-M-C-P:** F: M: C: P:

**Porosity (%):** Point Count: --

Measured: --

**Perm (mD):** --

**Isotopes (‰):** $\delta^{18}$O: --

$\delta^{13}$C: --

Other: --

**Thin Section Map**

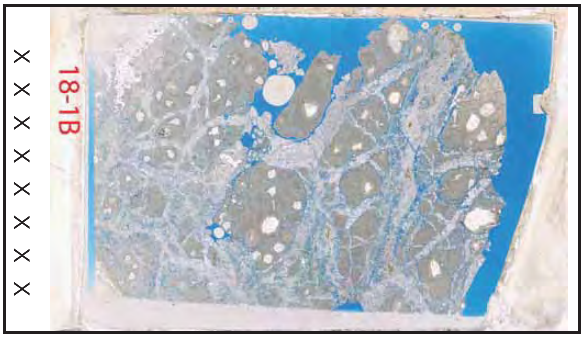

**Oriented thin section:** ☐ Yes ☑ No

**Orientation?:**

**Preparation** ☐ Thick ☑ Conventional ☐ Polished

**Stains:** ☐ Carbonate ☐ Plag ☐ Kspar

**Point Count:**

**Cement:** (types, sequence) Heavy calcite spar filling in veins that crosscut the shale all over

**Comments:** Lots of slide damage (plucking).

Thin slivers of porosity circumscribe the veins. Possible this was induced when I collected the sample (spar cement may have loosened from shale host when broken with a hammer).

**Sketches:**

**Sample #: 18-1b**

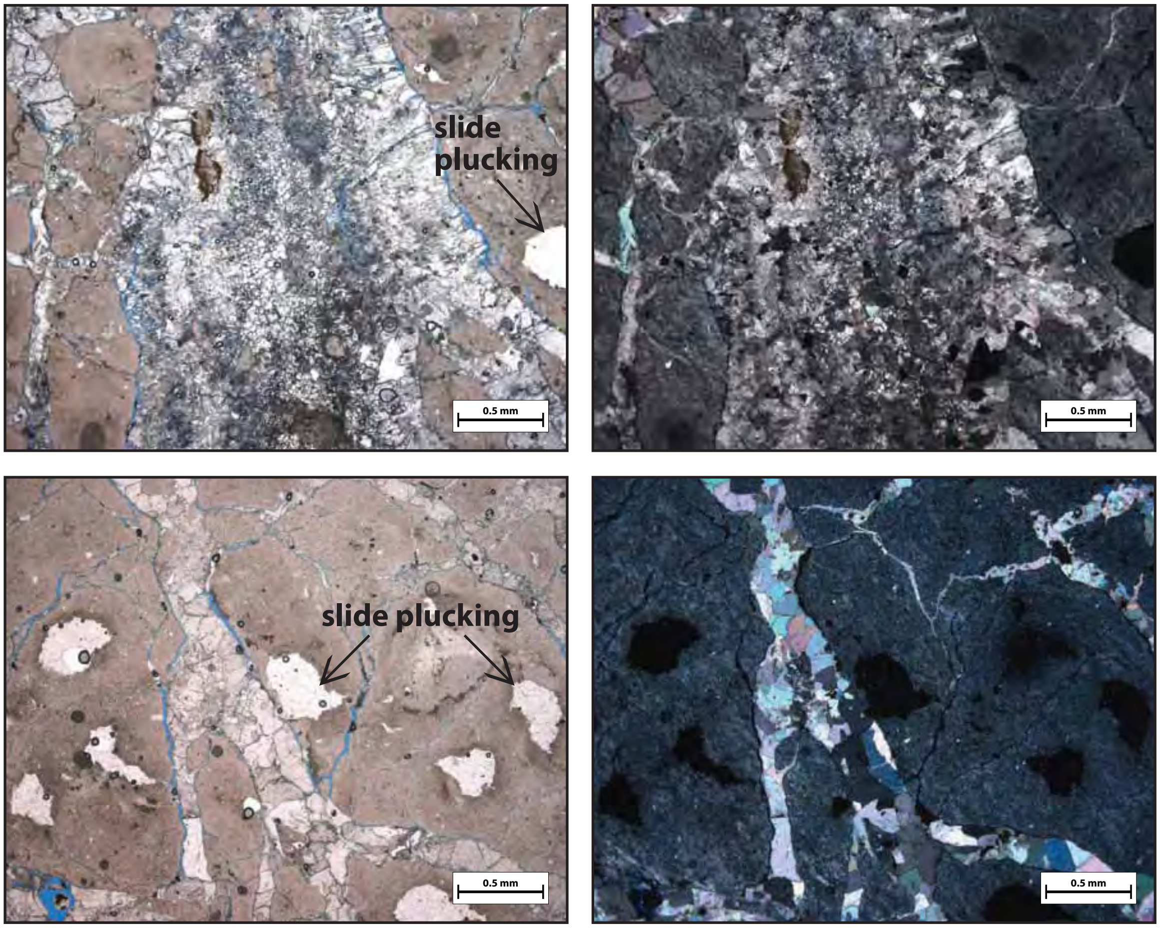

**Sample #:** 18-2

## Petrographic Summary

**Date:** / /

**Location Description:** Vein-blasted red-green mottled shale from bottom of the outcrop jutting out of travertine platform

**Field Trip:** ☑ April, '09 ☐ Oct., '09
**Formation:** Brushy Basin
**Rock Type:** shale
**Grain Size:** clay-mud
**Grain Types:** shale matrix
**F-M-C-P:** F: M: C: P:
**Porosity (%):** Point Count: --
Measured: --
**Perm (mD):** --
**Isotopes (‰):** $\delta^{18}O$: --
$\delta^{13}C$: --
Other: --

### Thin Section Map

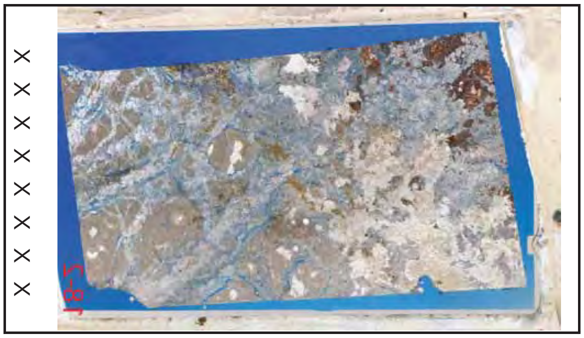

**Oriented thin section:** ☐ Yes ☑ No
**Orientation?:**

**Preparation**
☐ Thick
☑ Conventional
☐ Polished

**Stains:**
☐ Carbonate
☐ Plag ☐ Kspar

**Point Count:**

**Cement:** (types, sequence) Massive spar-filled veins

**Comments:** In places the spar appears to be somewhat dissolved, leaving behind a green spongy texture.
Lots of fracture porosity.
Some shale is bright red; some is duller buff/brown in color, resembling the opaque cements seen in other slides.
Spar is highly fractured, but that may be damage from slide preparation.

**Sketches:**

## Sample #: **18-2**

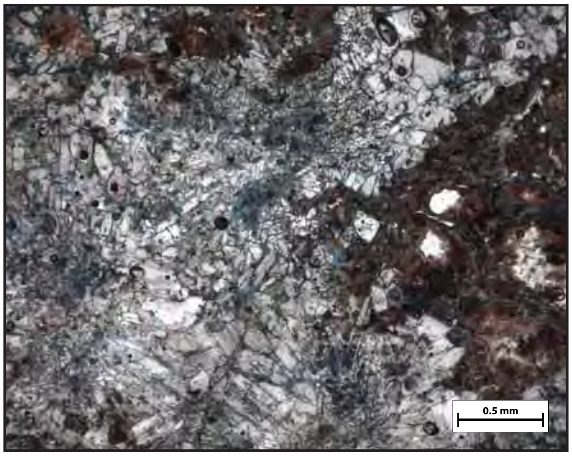

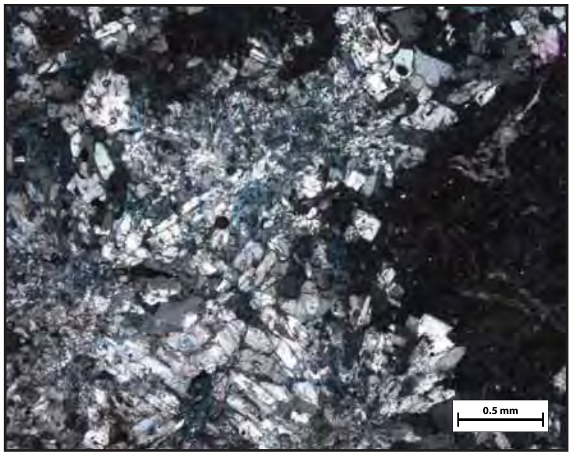

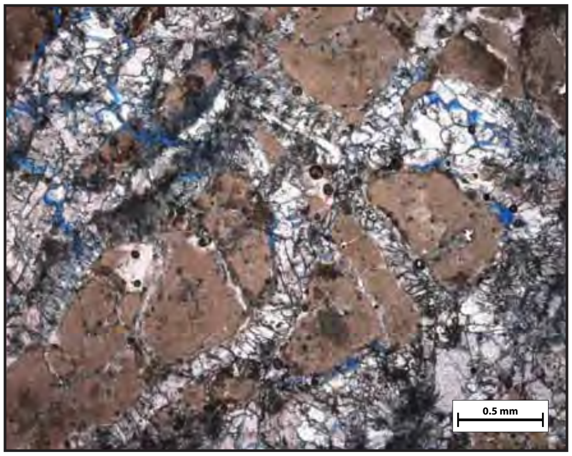

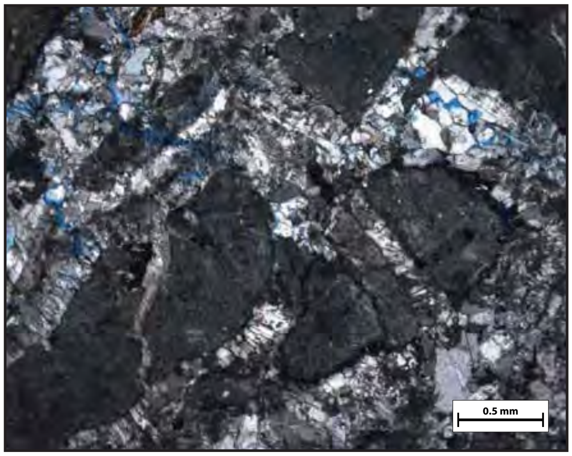

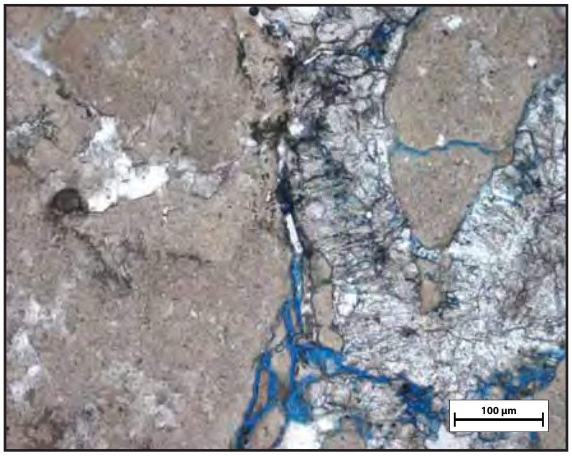

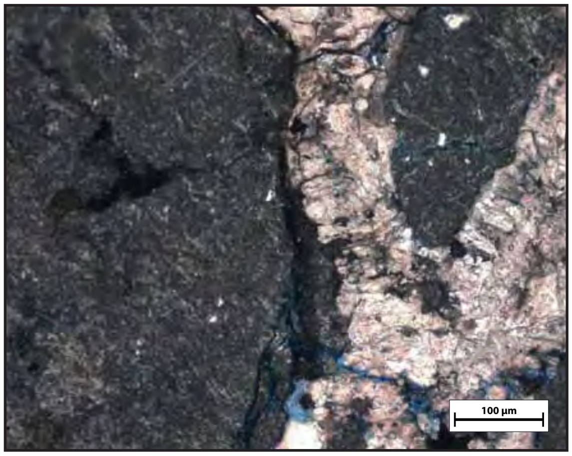

**Sample #:** 18-3

## Petrographic Summary

**Date:** / /

**Location Description:** Vein-blasted red-green mottled shale from bottom of the outcrop jutting out of travertine platform

**Field Trip:** ☑ April, '09 ☐ Oct., '09

**Formation:** Brushy Basin

**Rock Type:** shale

**Grain Size:** clay-mud

**Grain Types:** shale matrix

**F-M-C-P:** F: M: C: P:

**Porosity (%):** Point Count: - -

Measured: - -

**Perm (mD):** - -

**Isotopes (‰ ):** $\delta^{18}O$: - -

$\delta^{13}C$: - -

Other: - -

**Thin Section Map**

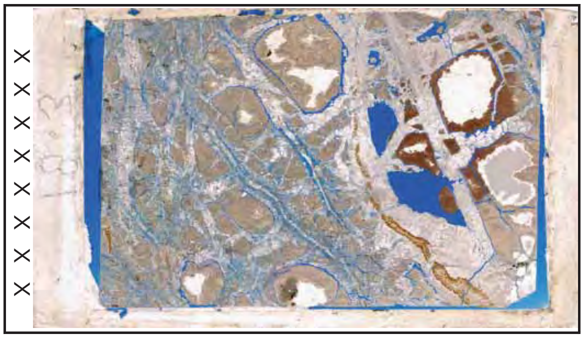

**Oriented thin section:** ☐ Yes ☑ No

**Orientation?:**

**Preparation** ☐ Thick ☑ Conventional ☐ Polished

**Stains:** ☐ Carbonate ☐ Plag ☐ Kspar

**Point Count:**

**Cement:** massive calcite spar filling in veins and cavities
(types, sequence)

**Comments:** Shale is heavily plucked in spots (obvious even in section map above).

Large zones of porosity where massive spar didn't fill in.

**Sketches:**

## Sample #: 18-3

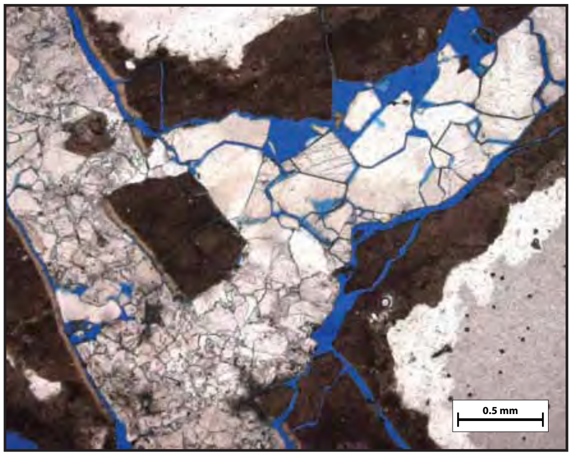

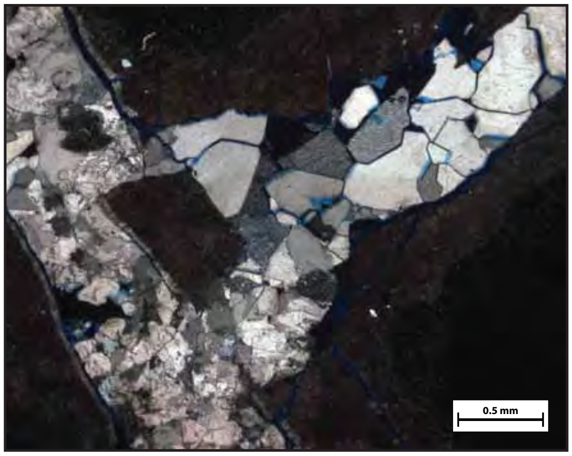

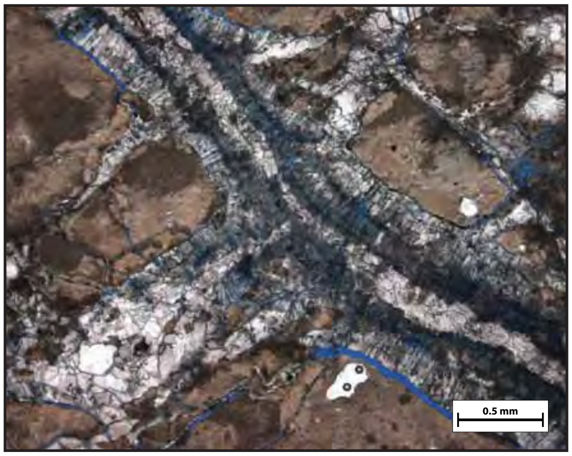

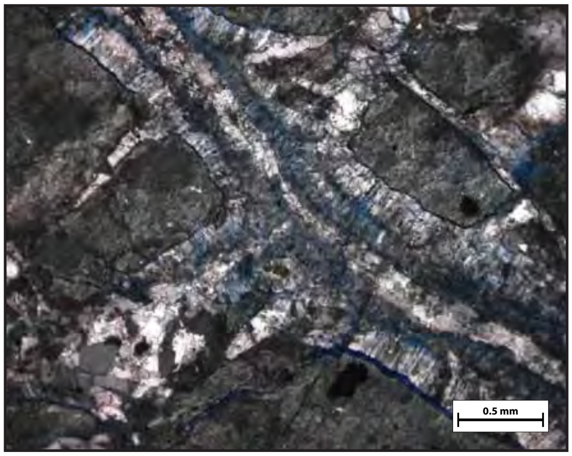

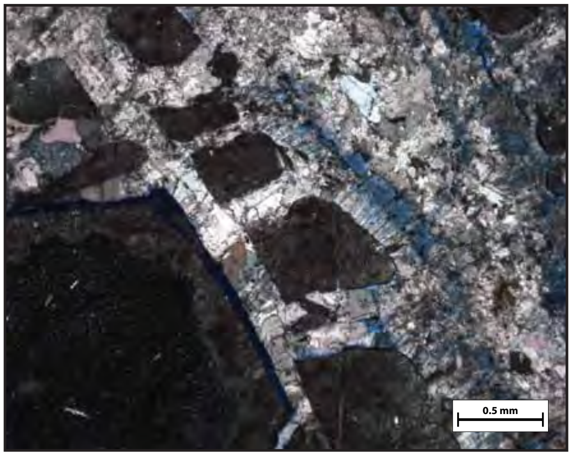

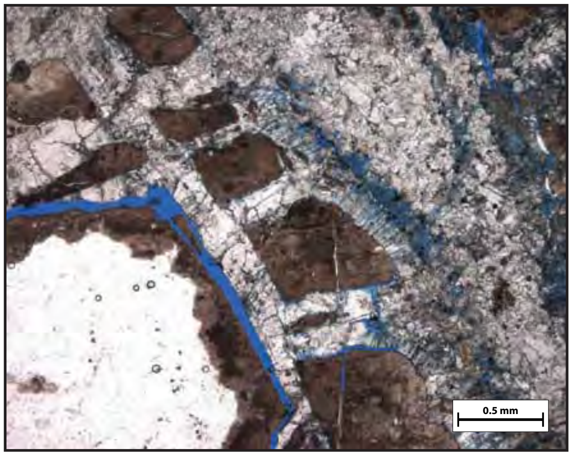

**Sample #:** 20A

## Petrographic Summary

**Date:** 1/11/11

**Location Description:** Low-offset (<0.5 m) scarp at north boundary of fault zone, 5-10 m NE of round hill (E:0576931 N: 4310188)

**Field Trip:** ☑ April, '09 ☐ Oct., '09
**Formation:** Jms2
**Rock Type:** Sandstone
**Grain Size:** 0.2-1.0 mm
**Grain Types:** Quartz and sed lithics
**F-M-C-P:** F: M: C: P:
**Porosity (%):** Point Count: 18%
Measured: --
**Perm (mD):** --
**Isotopes (‰):** $\delta^{18}O$: --
$\delta^{13}C$: --
Other:

**Thin Section Map**

**Oriented thin section:** ☑ Yes ☐ No
**Orientation?:**

**Preparation** ☐ Thick ☑ Conventional ☐ Polished

**Stains:** ☐ Carbonate ☐ Plag ☐ Kspar

**Point Count:**

| Quartz | | | Plagioclase Feld. | | Alkali Feld. | | Lithics | | Misc. | Clay | Cement | | | | Porosity | | | | Total |
|---|---|---|---|---|---|---|---|---|---|---|---|---|---|---|---|---|---|---|---|
| mono | poly | mic/chert | intact | dissolved | intact | dissolved | opaque | sed | Grains | Matrix | spar | micrite | quartz | clay | inter | oversize | intra | micro | Points |
| 234 | 7 | 17 | 0 | 0 | 0 | 0 | 0 | 4 | 0 | 0 | 27 | 4 | 30 | 6 | 49 | 5 | 14 | 3 | 400 |
| 59% | 2% | 4% | 0% | 0% | 0% | 0% | 0% | 1% | 0% | 0% | 7% | 1% | 8% | 2% | 12% | 1% | 4% | 1% | |

**Cement:** (types, sequence) Low calcite presence; lots of euhedral quartz overgrowths

**Comments:** Lots of clay-rich partially dissolved sedimentary lithic fragments. Oversize pores present as well, likely from fully dissolved such grains.
Overall quite a clean sandstone -- not a lot of clay or cement in the interstices.

Many qtz grains have large elongate inclusions. Rutilation?
Cut quite thick -- quartz very yellow.

**Sketches:**

## **Sample #: 20A**

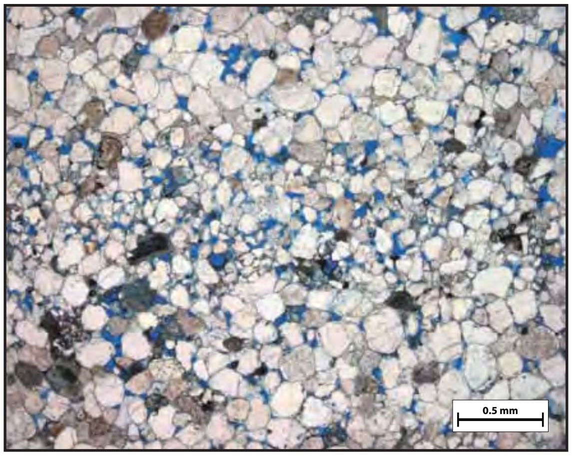

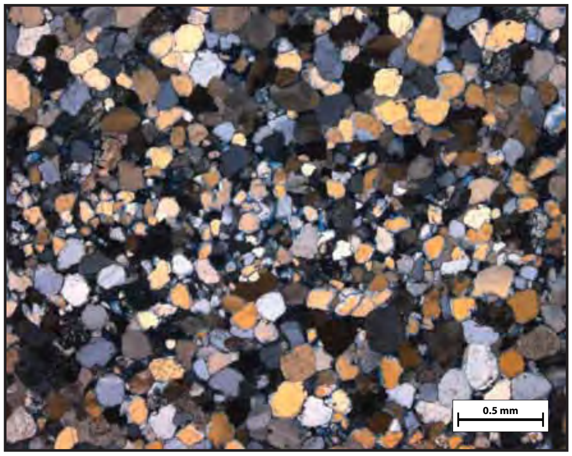

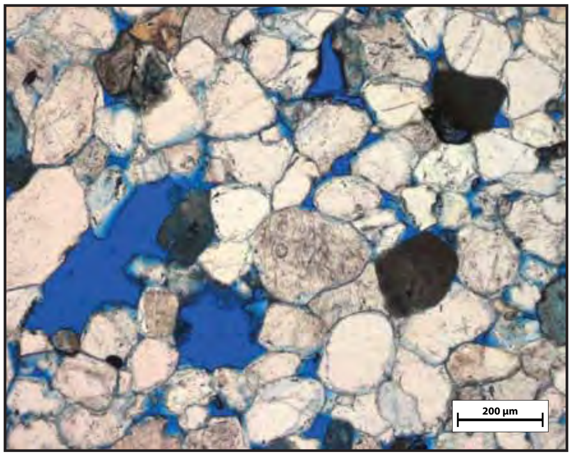

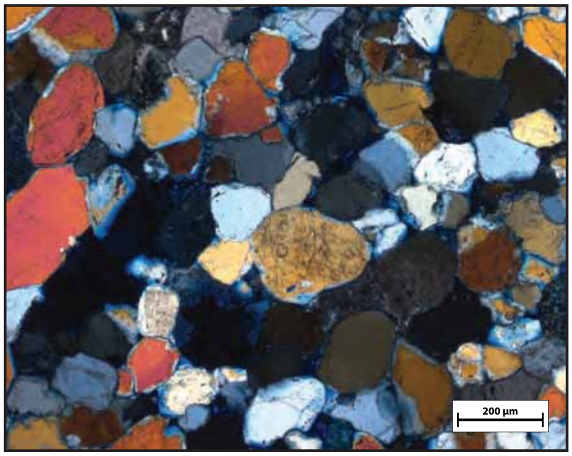

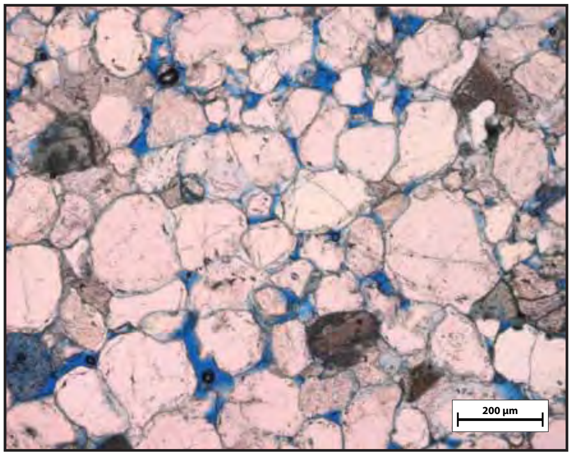

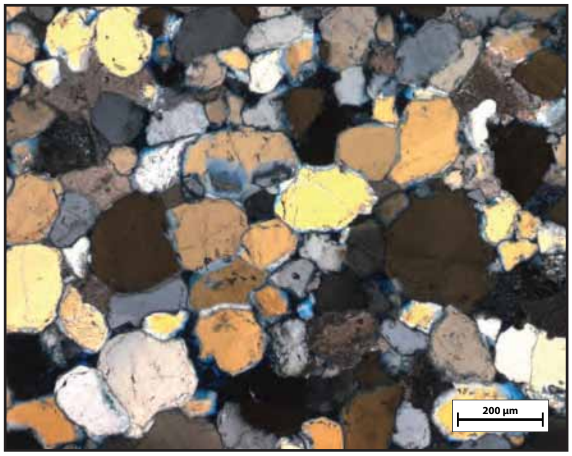

**Sample #:** 21A

## Petrographic Summary

**Date:** 7/22/10

**Location Description:** Highly fractured platform at head (west end) of ravine, about 20 m northwest of Station 22 platform

**Field Trip:** ☑ April, '09 ☐ Oct., '09

**Formation:** Jms3

**Rock Type:** sandstone

**Grain Size:** 0.15-0.60 mm

**Grain Types:** quartz, opaques, rare plag

**F-M-C-P:** F: M: C: P:

**Porosity (%):** Point Count: --

Measured: --

**Perm (mD):** --

**Isotopes (‰):** $\delta^{18}O$: --

$\delta^{13}C$: --

Other: --

**Thin Section Map**

**Oriented thin section:** ☐ Yes ☑ No

**Orientation?:**

**Preparation** ☐ Thick ☑ Conventional ☐ Polished

**Stains:** ☑ Carbonate ☐ Plag ☑ Kspar

**Point Count:**

**Cement:** (types, sequence)

sparse patchy carbonate (spar and micrite) cement

some opaque clay cements

quartz overgrowths appear to be recycled

**Comments:**

High-porosity, many green-blue spongy grains

Opaque grains are fairly common.

Clay cement forms cuticles on many grains, sporadically fills in small pores.

Feldspars rare: saw only one plagioclase, half-dissolved

**Sketches:**

## Sample #: **21A**

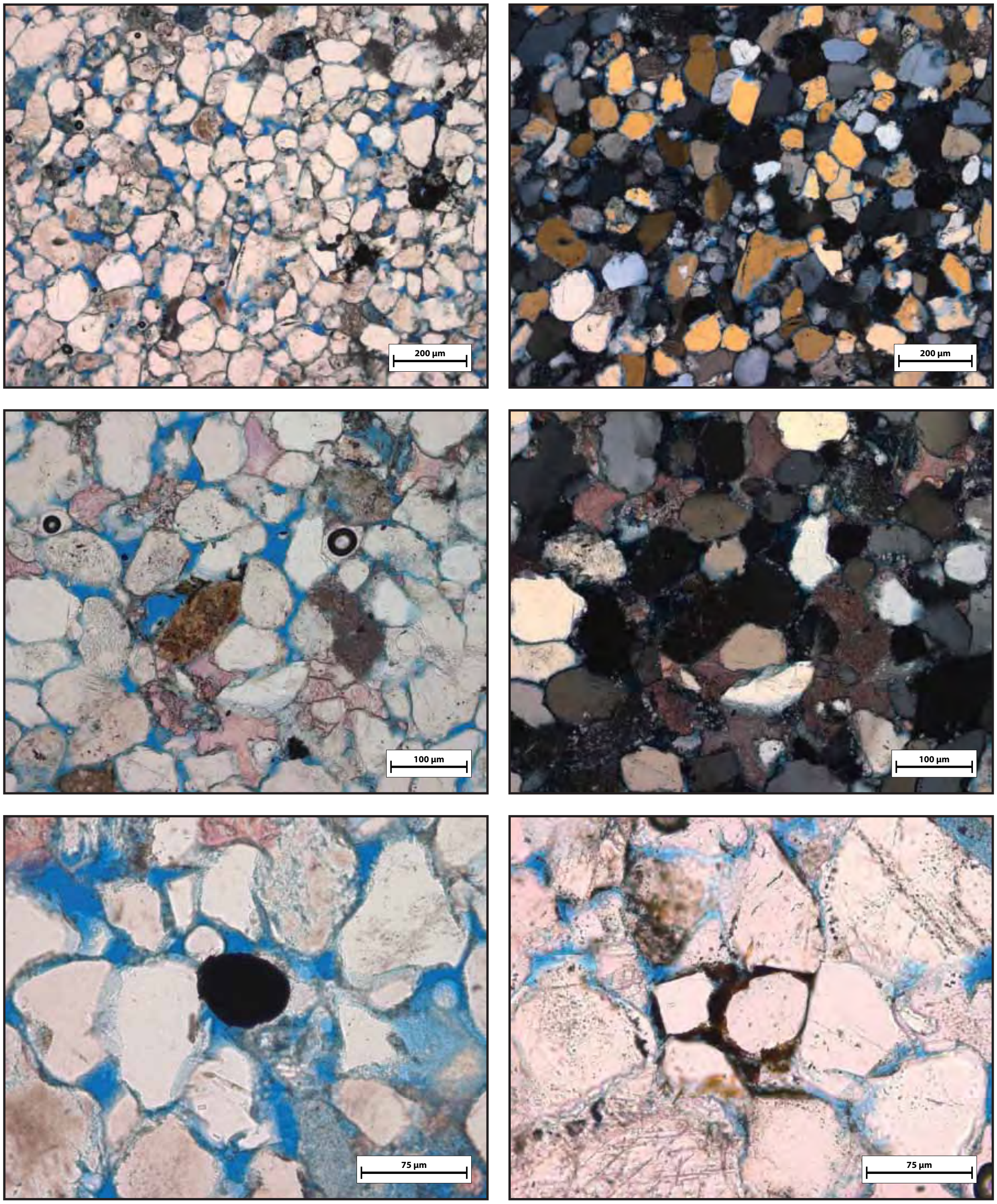

**Sample #:** 21B

## Petrographic Summary

**Date:** / /

**Location Description:** Highly fractured platform at head (west end) of ravine, about 20 m northwest of Station 22 platform

**Field Trip:** ☑ April, '09 ☐ Oct., '09

**Formation:** Jms3

**Rock Type:** sandstone

**Grain Size:** 0.1-0.6 mm

**Grain Types:** qtz, opaques

**F-M-C-P:** F: M: C: P:

**Porosity (%):** Point Count: --

Measured: --

**Perm (mD):** --

**Isotopes (‰):** $\delta^{18}O$: --

$\delta^{13}C$: --

Other: --

**Thin Section Map**

**Oriented thin section:** ☐ Yes ☑ No

**Orientation?:**

**Preparation** ☑ Thick ☐ Conventional ☐ Polished

**Stains:** ☐ Carbonate ☐ Plag ☐ Kspar

**Point Count:**

**Cement:** (types, sequence)

Some patchy calcite spar

Some patchy black-to-brown clay cement

Quartz overgrowths appear to be recycled

**Comments:**

Feldspars are very rare, observed only in state of advanced dissolution

High porosity

Green spongy dissolved grains are common.

**Sketches:**

**Sample #: 21B**

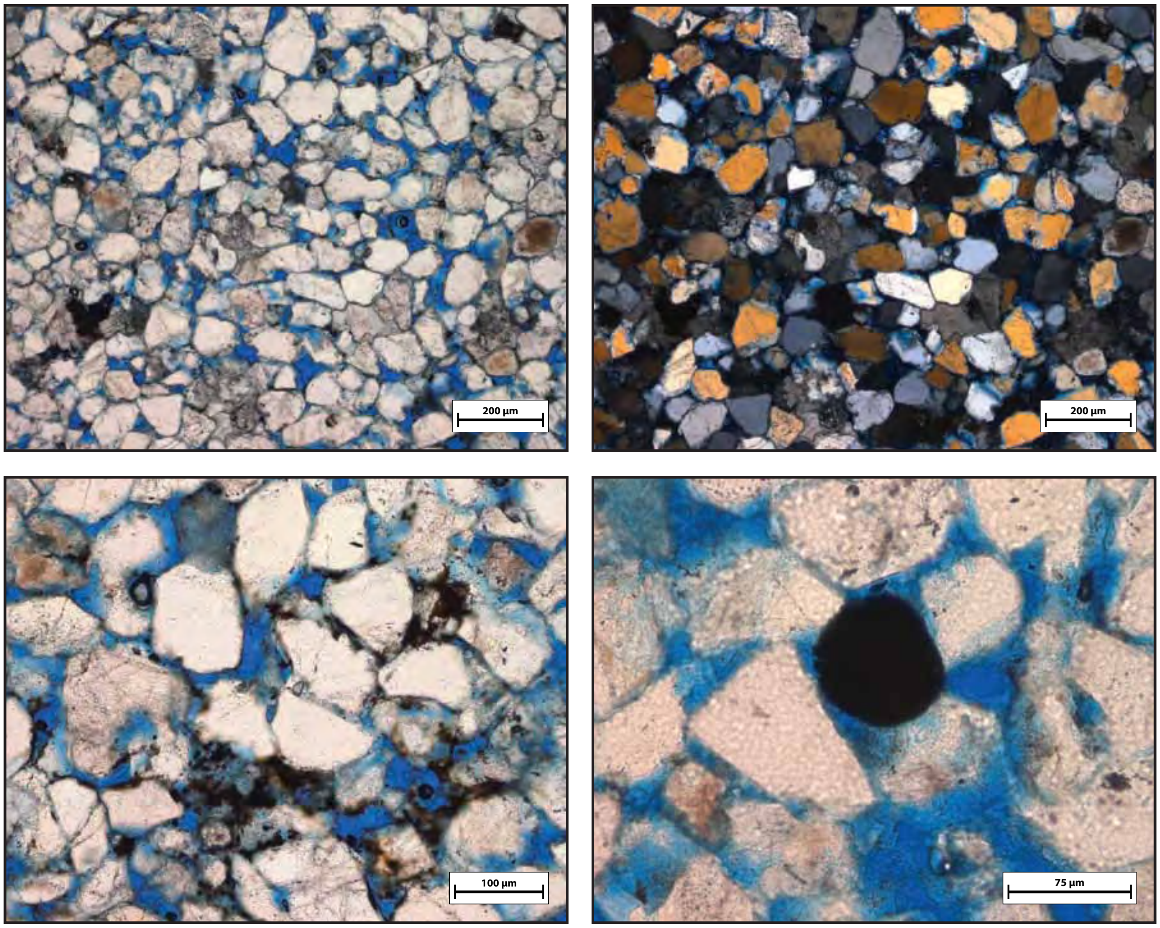

**Sample #:** 22A

## Petrographic Summary

**Date:** 7/22/10

**Location Description:** Top edge of platform separated from west end of ramp by the incipient fault that cuts across the ramp and forms southern edge of a slightly raised platform.

**Field Trip:** ☑ April, '09 ☐ Oct., '09

**Thin Section Map**

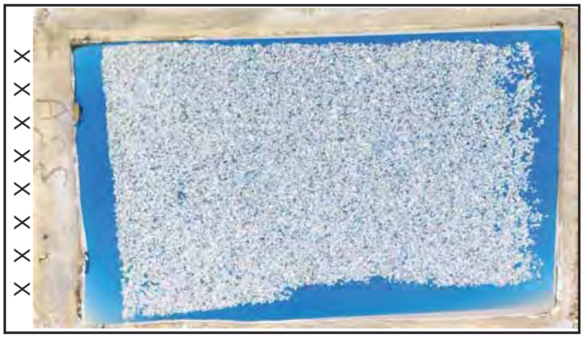

**Formation:** Jms3

**Rock Type:** sandstone

**Grain Size:** 0.1-0.6mm

**Grain Types:** quartz, rare opaque & plag

**F-M-C-P:** F: M: C: P:

**Porosity (%):** Point Count: --

Measured: --

**Perm (mD):** --

**Isotopes (‰ ):** $\delta^{18}$O: --

$\delta^{13}$C: --

Other: --

**Oriented thin section:** ☐ Yes ☑ No

**Orientation?:**

**Preparation** ☐ Thick ☑ Conventional ☐ Polished

**Stains:** ☑ Carbonate ☐ Plag ☑ Kspar

**Point Count:**

**Cement:** (types, sequence)

very small amount of carbonate cement

some brown/opaque clay cement (cuticle and pore-filling)

many qtz overgrowths (seen in dust rims and euhedral edges)

**Comments:**

High-porosity, very similar to Sample 21A

Qtz overgrowths NOT obviously grown in place, but could be

Many green/spongy grains

Feldspars are rare and in advanced state of dissolution

Brown clay cement forms thin cuticles on some grains, completely fills pores in rare instances.

**Sketches:**

## Sample #: 22A

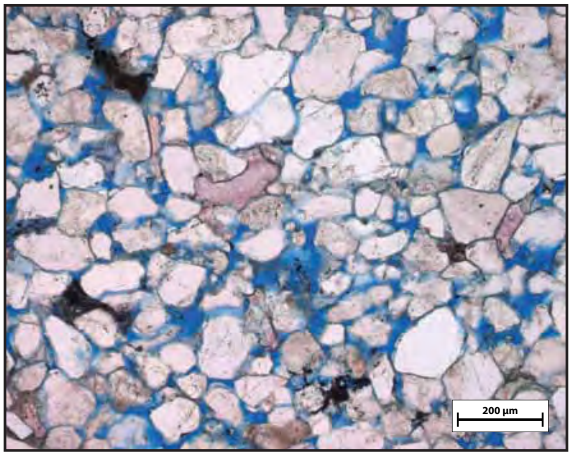

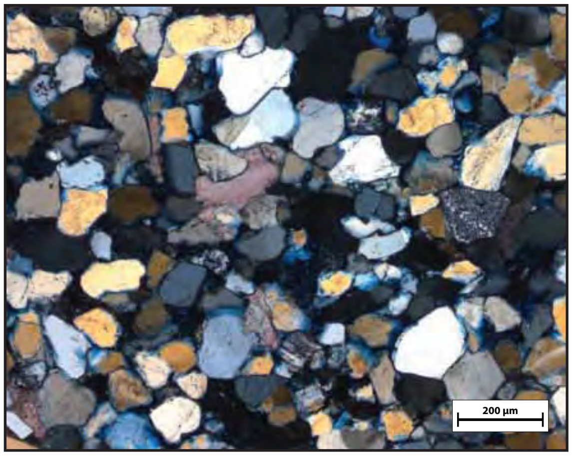

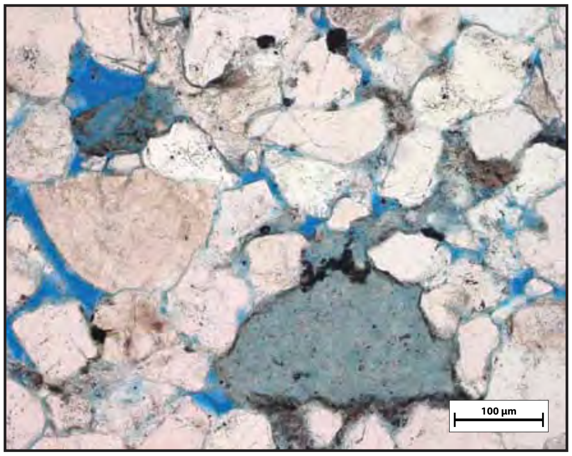

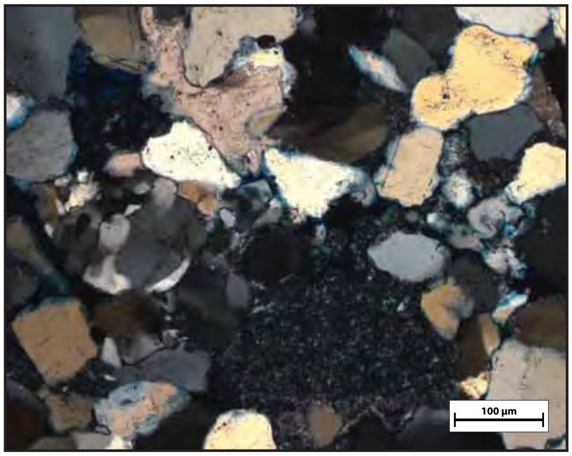

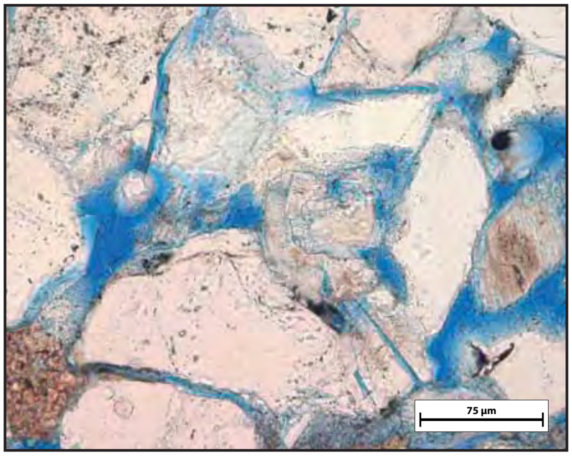

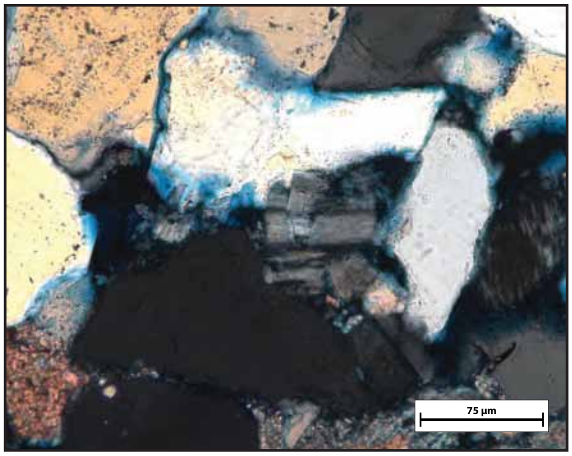

**Sample #:** 22B

## Petrographic Summary

**Date:** / /

**Location Description:** South edge platform separated from west end of ramp by the incipient fault that cuts across the ramp and forms southern edge of a slightly raised platform.

**Field Trip:** ☑ April, '09 ☐ Oct., '09
**Formation:** Jms3
**Rock Type:** sandstone
**Grain Size:** 0.2-0.6 mm
**Grain Types:** quartz, dissolved grains
**F-M-C-P:** F: M: C: P:
**Porosity (%):** Point Count: --
Measured: --
**Perm (mD):** --
**Isotopes (‰):** $\delta^{18}$O: --
$\delta^{13}$C: --
Other: --

**Thin Section Map**

**Oriented thin section:** ☐ Yes ☑ No
**Orientation?:**

**Preparation** ☑ Thick ☐ Conventional ☐ Polished
**Stains:** ☐ Carbonate ☐ Plag ☐ Kspar

**Point Count:**

**Cement:** (types, sequence)
Patchy brown/opaque clay cement cuticles
Patchy calcite spar is present but uncommon

**Comments:** Some opaque grains; many green spongy dissolved grains; feldspars not apparent. It's possible some of the spongy grains are dissolved feldspars, but they are unrecognizable as such, showing only clay residue, intragranular porosity and fragmentary parts of (usually) low-B original grain.

**Sketches:**

**Sample #: 22B**

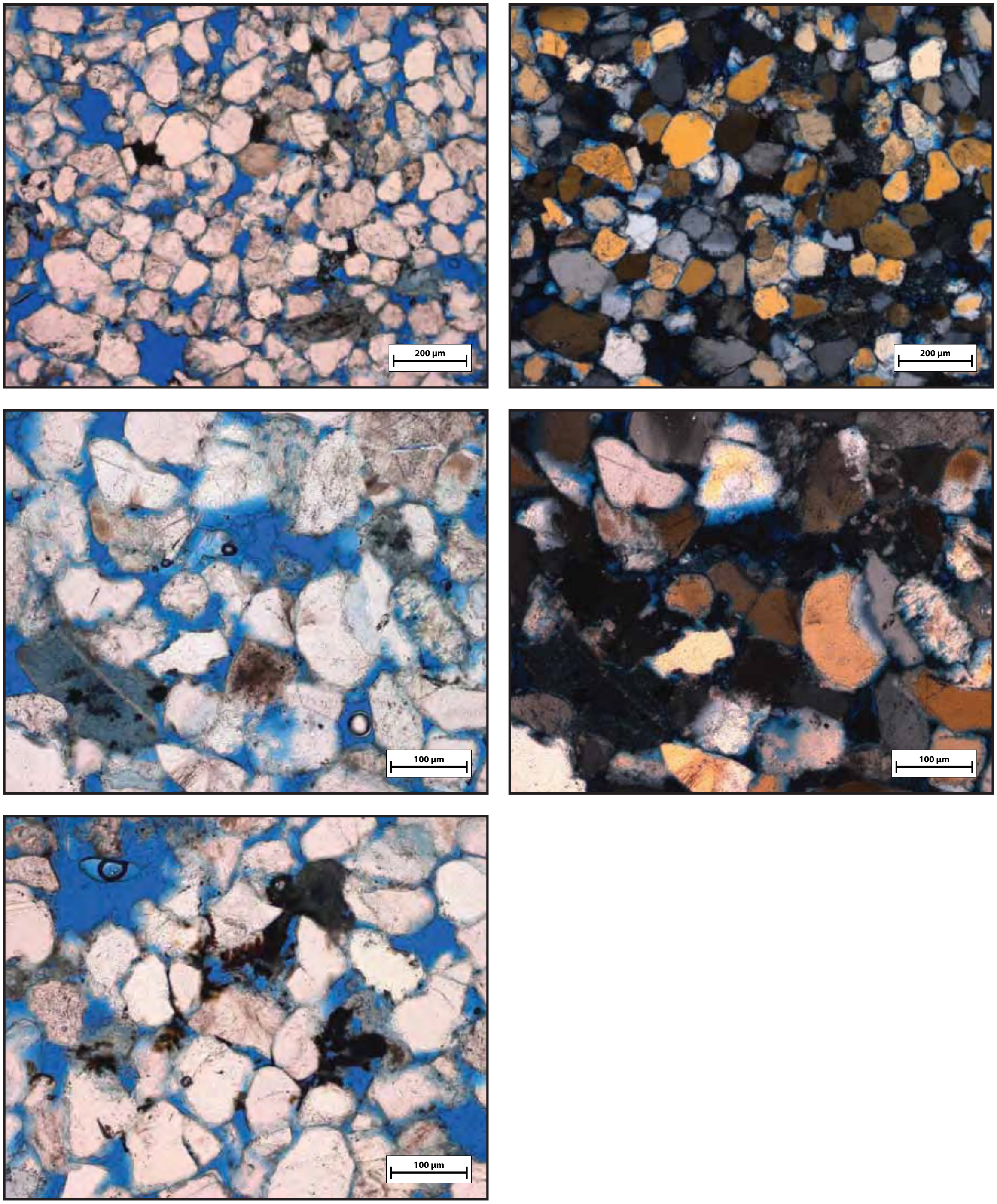

**Sample #:** 22C-1

## Petrographic Summary

**Date:** / /

**Location Description:** Underside of platform separated from west end of ramp by the incipient fault that cuts across the ramp and forms southern edge of a slightly raised platform.

**Field Trip:** ☑ April, '09 ☐ Oct., '09

**Formation:** Jms3

**Rock Type:** sandstone

**Grain Size:** 0.2-0.8 mm

**Grain Types:** mostly qtz, some feldspars

**F-M-C-P:** F: M: C: P:

**Porosity (%):** Point Count: --

Measured: --

**Perm (mD):** --

**Isotopes (‰ ):** $\delta^{18}O$: --

$\delta^{13}C$: --

Other: --

**Thin Section Map**

**Oriented thin section:** ☐ Yes ☑ No

**Orientation?:**

**Preparation**

☐ Thick
☑ Conventional
☐ Polished

**Stains:**

☐ Carbonate
☐ Plag ☐ Kspar

**Point Count:**

**Cement:** (types, sequence) Massively spar cemented; small amounts of brown/opaque cement

**Comments:** Sample from the contact of white and brown sandstone -- this effect (brown sandstone) is determined to be bedding controlled, as it tends to follow beds and remains independent of location within the field area.

Spar cement occludes nearly all porosity; looks like spar is dissolving out of one fracture.

Feldspars are mostly plagioclase.

Some dissolved, blue-spongy grains.

**Sketches:**

**Sample #: 22C-1**

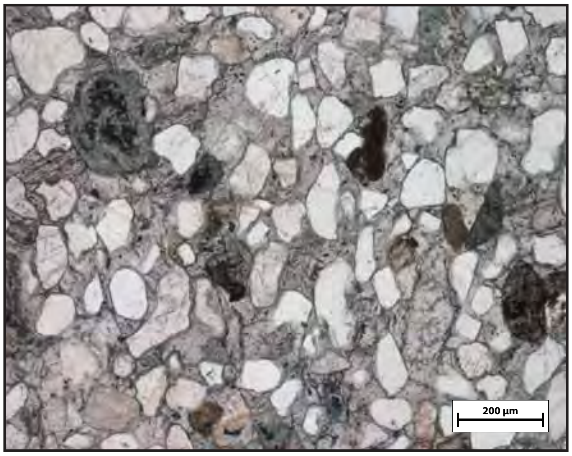

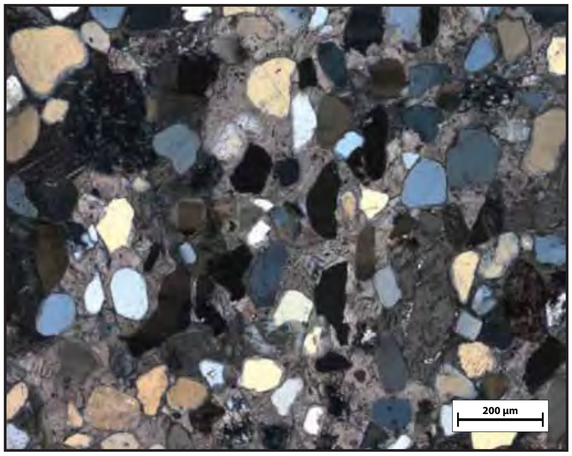

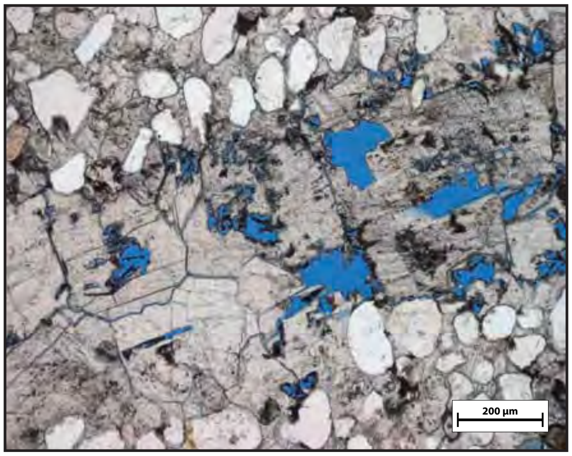

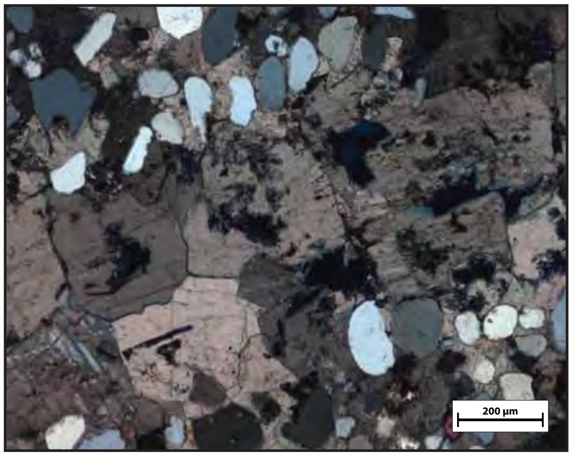

**Sample #:** 22C-2

## Petrographic Summary

**Date:** / /

**Location Description:** Underside of platform separated from west end of ramp by the incipient fault that cuts across the ramp and forms southern edge of a slightly raised platform.

**Field Trip:** ☑ April, '09 ☐ Oct., '09

**Formation:** Jms3

**Rock Type:** sandstone

**Grain Size:** 0.2-0.8 mm

**Grain Types:** quartz, some plagioclase

**F-M-C-P:** F: M: C: P:

**Porosity (%):** Point Count: - -

Measured: - -

**Perm (mD):** - -

**Isotopes (‰ ):** $\delta^{18}$O: - -

$\delta^{13}$C: - -

Other: - -

**Thin Section Map**

**Oriented thin section:** ☐ Yes ☑ No

**Orientation?:**

**Preparation** ☐ Thick ☑ Conventional ☐ Polished

**Stains:** ☐ Carbonate ☐ Plag ☐ Kspar

**Point Count:**

**Cement:** (types, sequence) pervasive spar

**Comments:** No noticeable differences from 22C-1; see notes for that slide.

**Sketches:**

**Sample #: 22C-2**

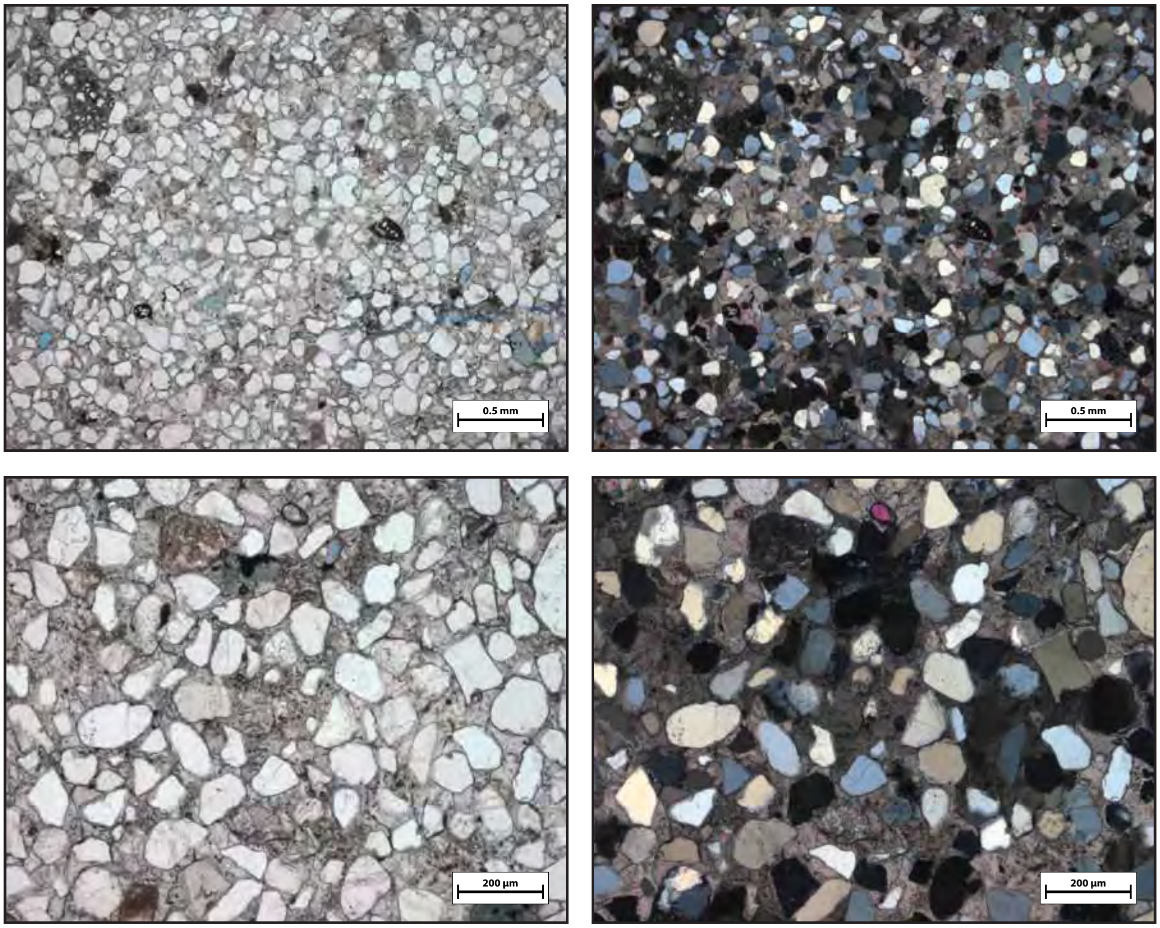

**Sample #:** 24-1

## Petrographic Summary

**Date:** / /

**Location Description:** Adjacent to the fault, on the downdropped portion of the Jms3 outcropping platform at the west end of the ramp

**Field Trip:** ☑ April, '09 ☐ Oct., '09

**Formation:** Jms3

**Rock Type:** sandstone

**Grain Size:** 0.15-0.55 mm

**Grain Types:** dominated by quartz

**F-M-C-P:** F: M: C: P:

**Porosity (%):** Point Count: - -

Measured: - -

**Perm (mD):** - -

**Isotopes (‰ ):** $\delta^{18}$O: - -

$\delta^{13}$C: - -

Other: - -

**Thin Section Map**

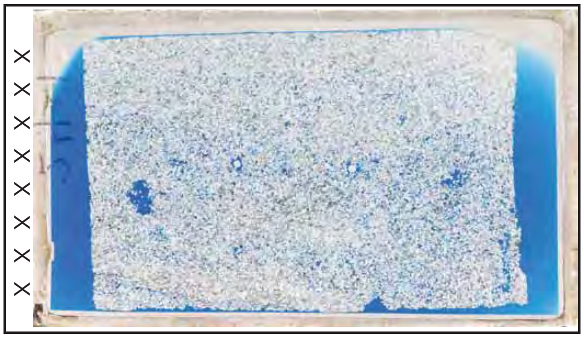

**Oriented thin section:** ☐ Yes ☑ No

**Orientation?:**

**Preparation** ☐ Thick ☑ Conventional ☐ Polished

**Stains:** ☐ Carbonate ☐ Plag ☐ Kspar

**Point Count:**

**Cement:** (types, sequence)
some spar cement (more than Station 22)
pore-filling clay (brown/opaque) cement

**Comments:**
High porosity
Lots of green spongy dissolved grains,
Several deformation bands
Feldspars are rare.

**Sketches:**

**Sample #: 24-1**

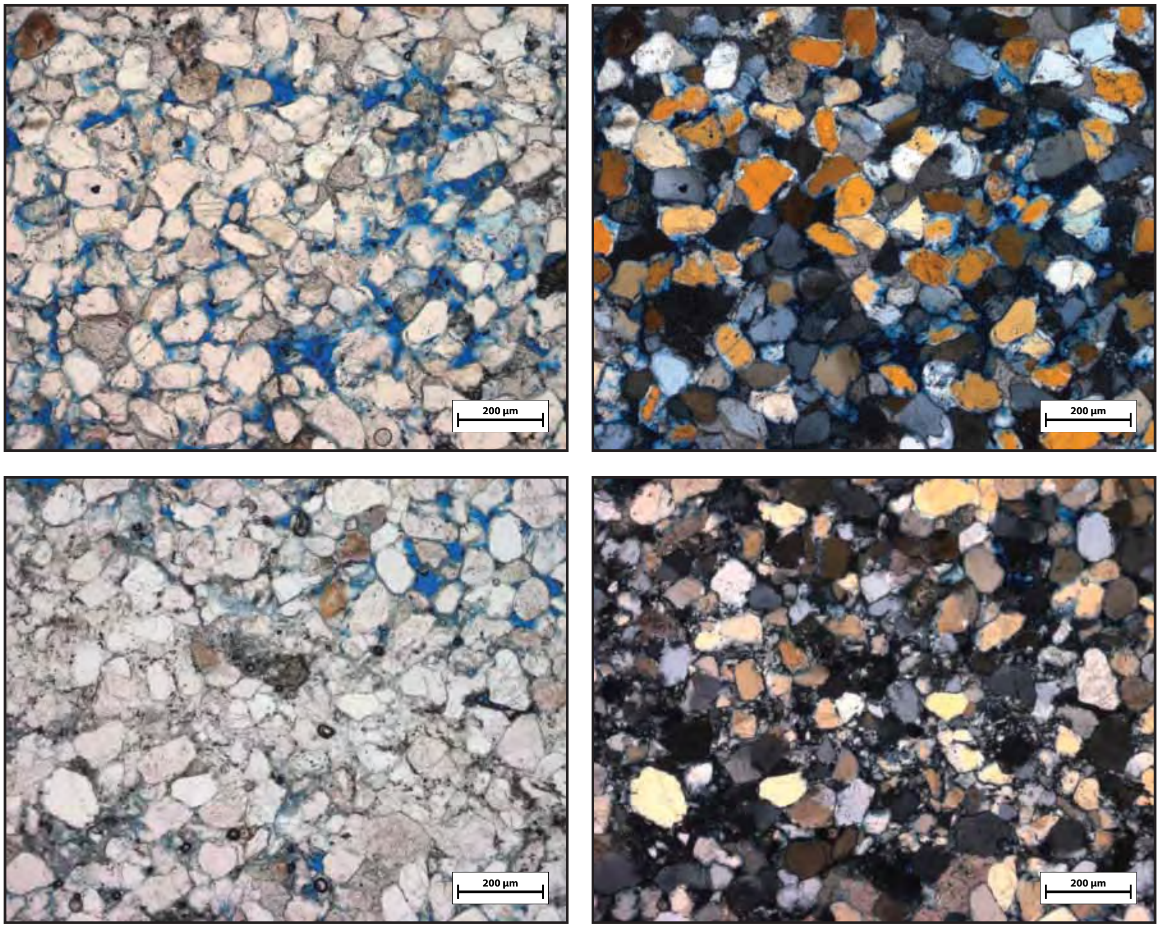

**Sample #:** 24-2

## Petrographic Summary

**Date:** 7/22/10

**Location Description:** Adjacent to the fault, on the downdropped portion of the Jms3 outcropping platform at the west end of the ramp

**Field Trip:** ☑ April, '09 ☐ Oct., '09

**Formation:** Jms3

**Rock Type:** sandstone

**Grain Size:** 0.1-0.5 mm

**Grain Types:** quartz,

**F-M-C-P:** F: M: C: P:

**Porosity (%):** Point Count:

Measured:

**Perm (mD):**

**Isotopes (‰ ):** $\delta^{18}O$:

$\delta^{13}C$:

Other:

**Thin Section Map**

**Oriented thin section:** ☐ Yes ☑ No

**Orientation?:**

**Preparation**

☐ Thick

☑ Conventional

☐ Polished

**Stains:**

☑ Carbonate

☐ Plag ☑ Kspar

**Point Count:**

**Cement:** (types, sequence)

some spar cement

small amount of clay cement

**Comments:**

Notably more carbonate (spar) cement Station 22, but still high porosity. Clay cement notably rarer than Station 22.

Spongy green dissolved grains

Deformation band in the lower half of slide

Some plagioclase grains, 50+ percent dissolved.

Grungy brown grains look like they have clay component or clay residue left from dissolution.

**Sketches:**

## Sample #: 24-2

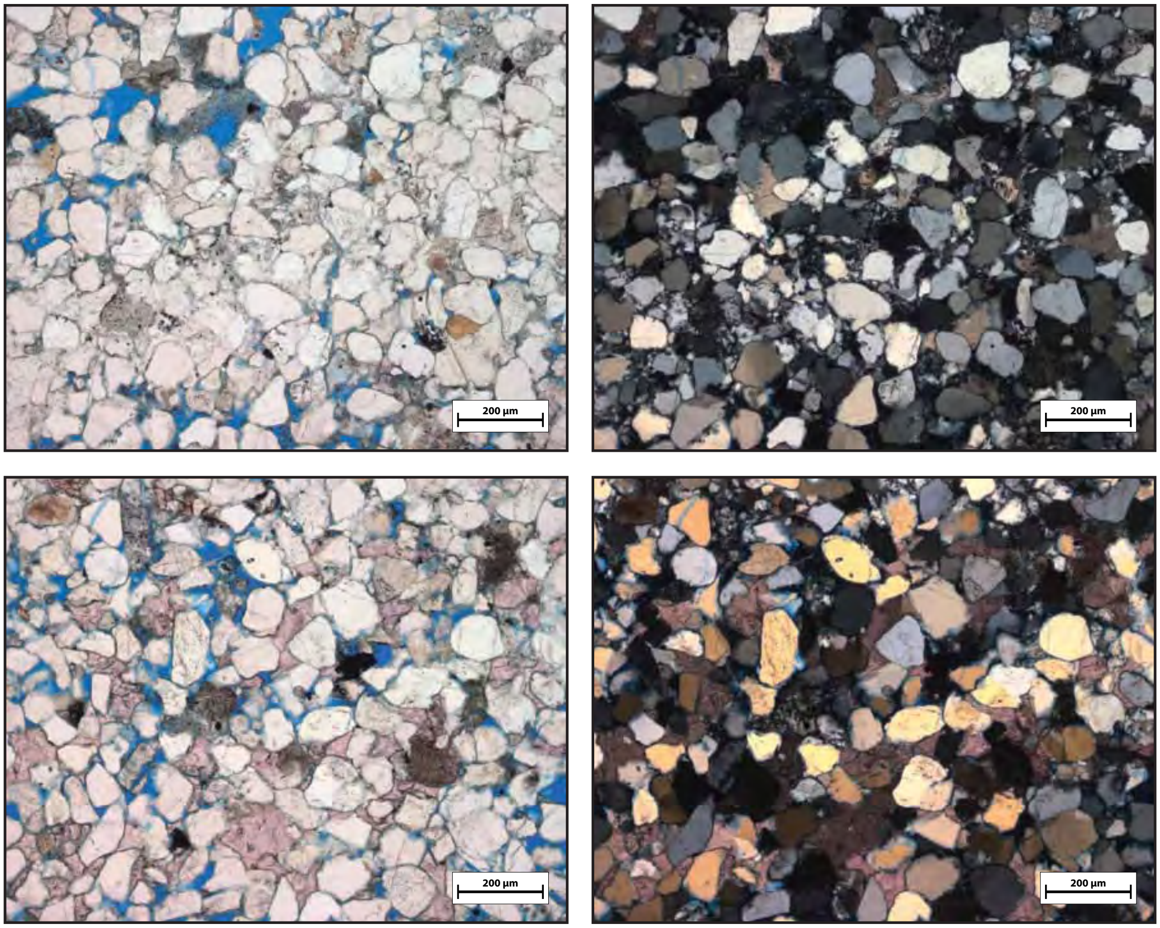

**Sample #:** 24-3

## Petrographic Summary

**Date:** 11/ 8 /09

**Location Description:** West end of ravine fault, where fault strikes into Jms platform - deformation bands apparent along edge of Jms ledge

**Field Trip:** ☑ April, '09 ☐ Oct., '09

**Formation:** Jms

**Rock Type:** sandstone

**Grain Size:** 0.12-0.3mm

**Grain Types:** qtz, some chert, unknown lithics

**F-M-C-P:** F: 65 M: 0 C: 20 P: 15

**Porosity (%):** Point Count: --

Measured: --

**Perm (mD):** --

**Isotopes (‰ ):** $\delta^{18}O$: --

$\delta^{13}C$: --

Other: --

**Thin Section Map**

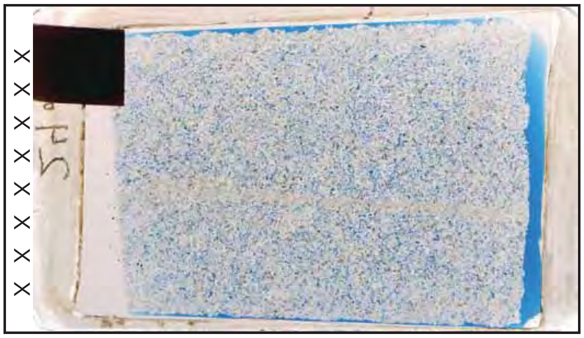

**Oriented thin section:** ☐ Yes ☑ No

**Orientation?:**

**Preparation**

☐ Thick

☐ Conventional

☑ Polished

**Stains:**

☐ Carbonate

☐ Plag ☐ Kspar

**Point Count:**

**Cement:** (types, sequence) calcite spar is dominant, often porosity-filling but NOT pervasive; some qtz overgrowths; some opaque (hematite?) cements

**Comments:** Note deformation band

Note relatively high porosity and some calcite spar cement

Interesting comparison to relatively unaltered (35A-1) and highly altered (32ABC) sands -- major difference seems to be % calcite cement

**Sketches:**

**Sample #: 24-3**

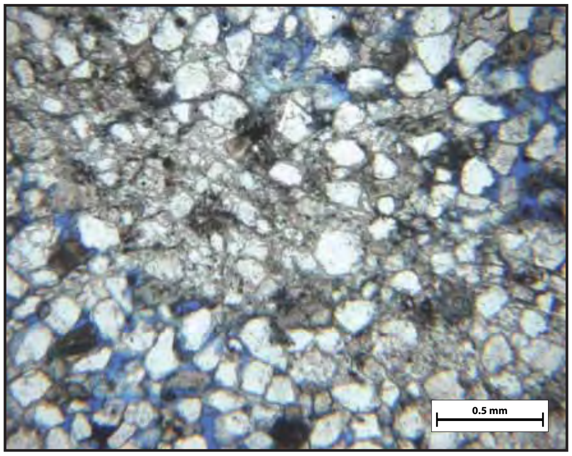

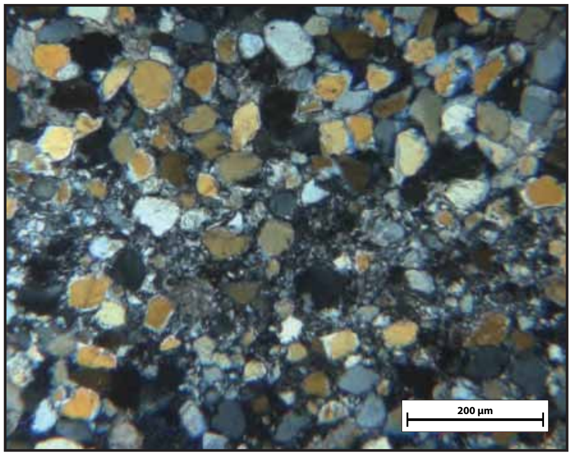

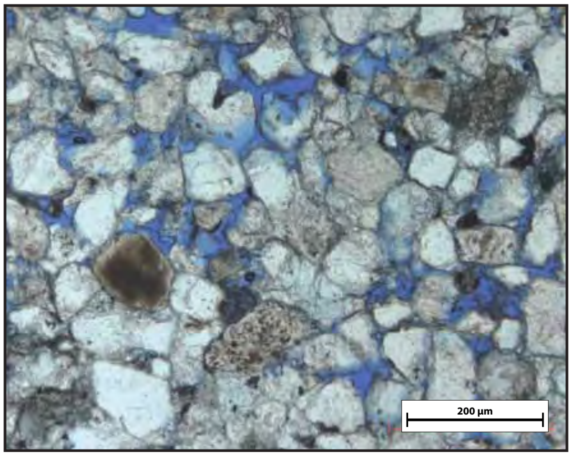

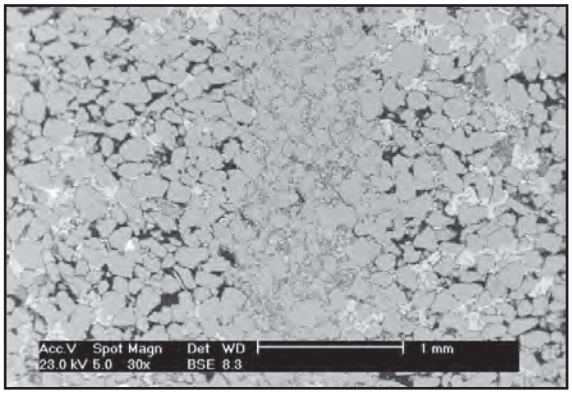

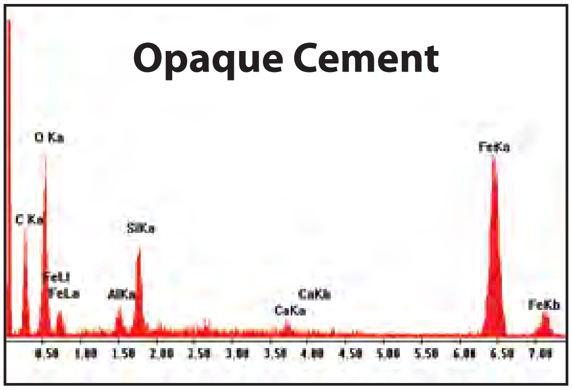
Opaque Cement

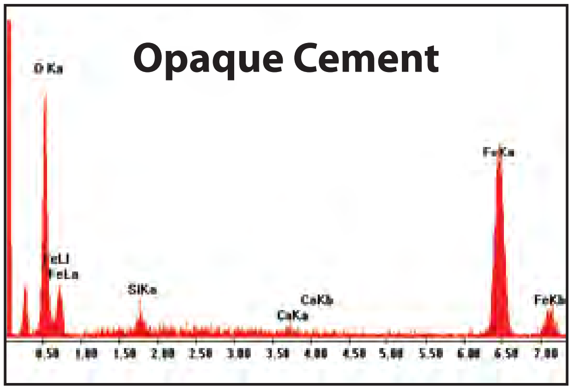
Opaque Cement

**Sample #:** 26-1 (polished)

## Petrographic Summary

**Date:** 11/ 3 /09

**Location Description:** In the shale slope directly below Jms5, about half-way up the ramp -- this is the continuous green fine-grained sandstone that outcrops amid the shale

**Field Trip:** ☑ April, '09 ☐ Oct., '09

**Formation:** Jms green unit

**Rock Type:** fine-grained sandstone

**Grain Size:** 0.06-0.30mm + some 0.60mm

**Grain Types:** qtz, chert, opaques, felds

**F-M-C-P:** F: 85 M: x C: 15 P: 0

**Porosity (%):** Point Count: - -

Measured: - -

**Perm (mD):** - -

**Isotopes (‰ ):** $\delta^{18}O$: - -

$\delta^{13}C$: - -

Other: - -

**Thin Section Map**

**Oriented thin section:** ☐ Yes ☑ No

**Orientation?:**

**Preparation**

☐ Thick
☐ Conventional
☑ Polished

**Stains:**

☐ Carbonate
☐ Plag ☐ Kspar

**Point Count:**

**Cement:** (types, sequence)

See 26-1a (26-1 stained)... spar cement very present (massively fills vein in this slide)
Grungy appearance likely due to clay-ey cement

**Comments:**

Very low porosity, completely filled with spar and clay cement (chlorite?)

Easily traceable unit

Mostly quartz, but feldspars are very well preserved.

**Sketches:**

**Sample #: 26-1**
(polished)

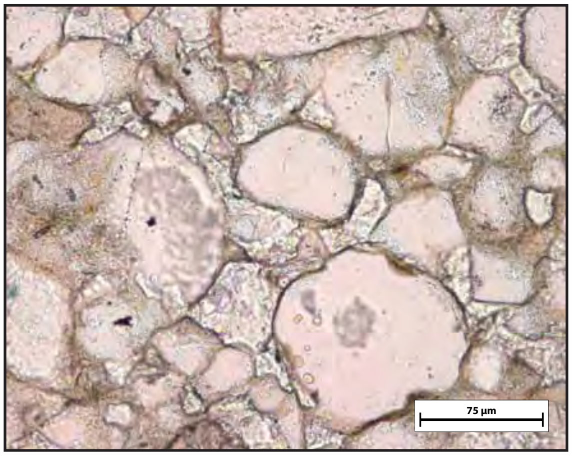

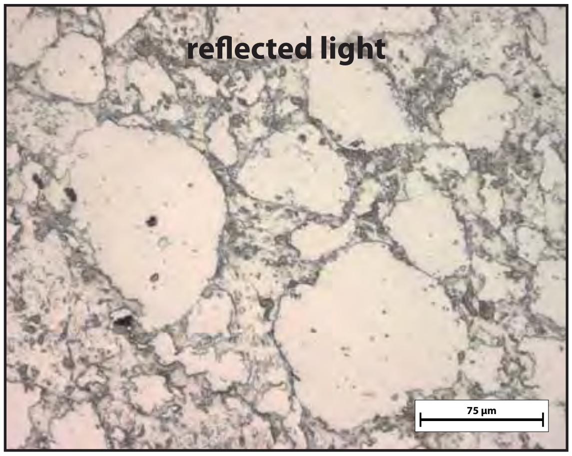

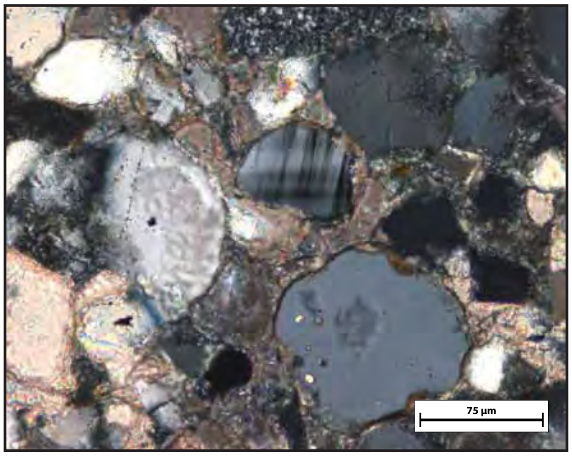

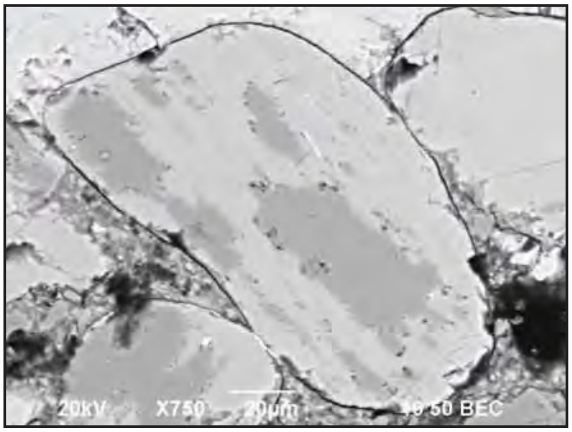

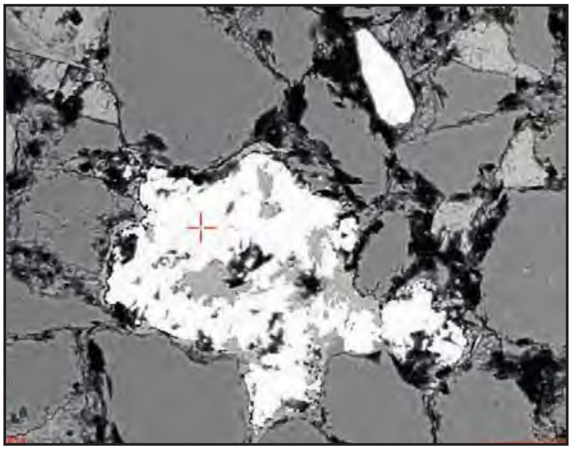

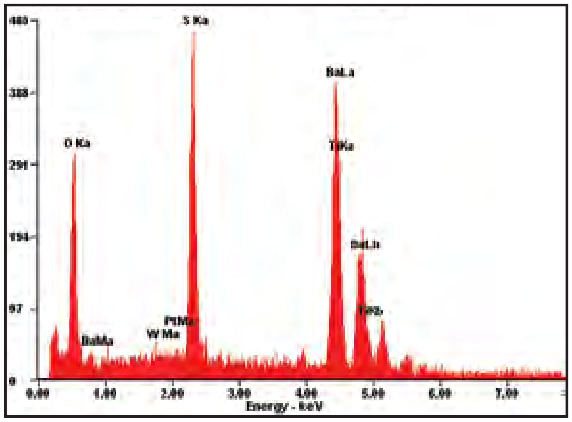

**Sample #:** 26-1 (conventional, stained)

## Petrographic Summary

**Date:** 7/22/10

**Location Description:** In the shale slope directly below Jms5, about half-way up the ramp -- this is the continuous green fine-grained sandstone that outcrops amid the shale

**Field Trip:** ☑ April, '09 ☐ Oct., '09

**Formation:** Salt Wash green sand

**Rock Type:** fine-grained sandstone

**Grain Size:** 0.05-0.40 mm

**Grain Types:** qtz, sed lith, plag/kspar

**F-M-C-P:** F: M: C: P:

**Porosity (%):** Point Count: - -

Measured: - -

**Perm (mD):** - -

**Isotopes (‰):** $\delta^{18}O$: - -

$\delta^{13}C$: - -

Other: - -

**Thin Section Map**

**Oriented thin section:** ☐ Yes ☑ No

**Orientation?:**

**Preparation** ☐ Thick ☑ Conventional ☐ Polished

**Stains:** ☑ Carbonate ☐ Plag ☑ Kspar

**Point Count:**

**Cement:** (types, sequence)

Calcite spar

Something clay-ey, possibly chlorite

**Comments:** Stain very helpful for bringing out calcite -- grunge appears NOT to be micrite... check in EDS. May be chlorite, which would give rocks their green color.

Virtually no porosity

Some plagioclase and kspar grains -- feldspars are very well preserved.

**Sketches:**

## Sample #: 26-1
(conventional, stained)

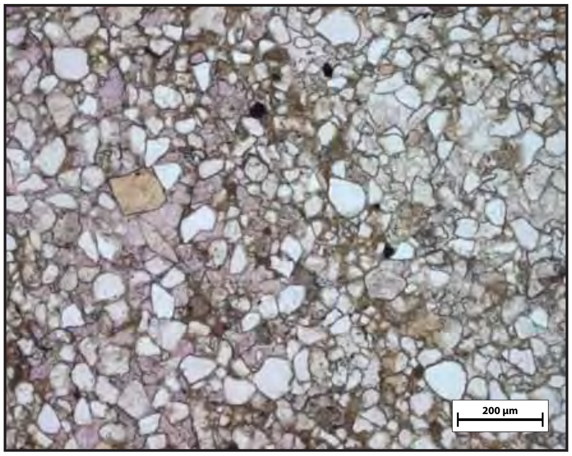

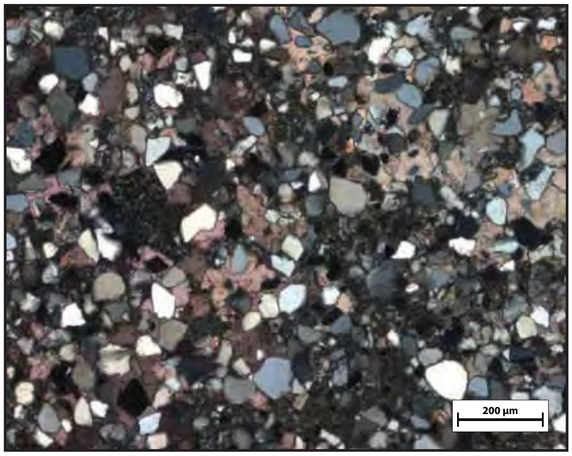

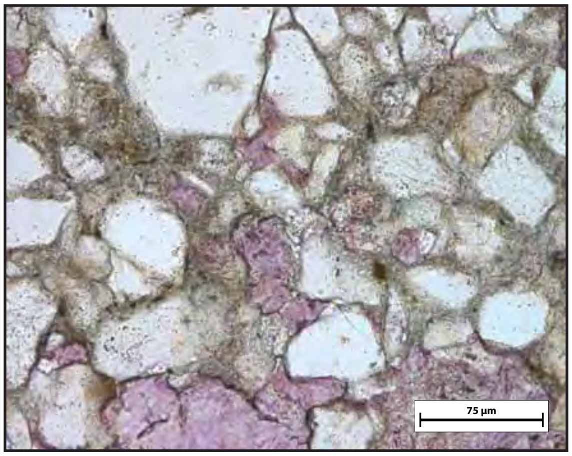

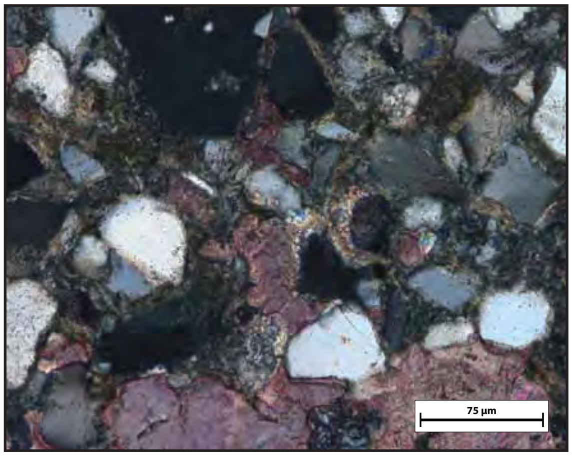

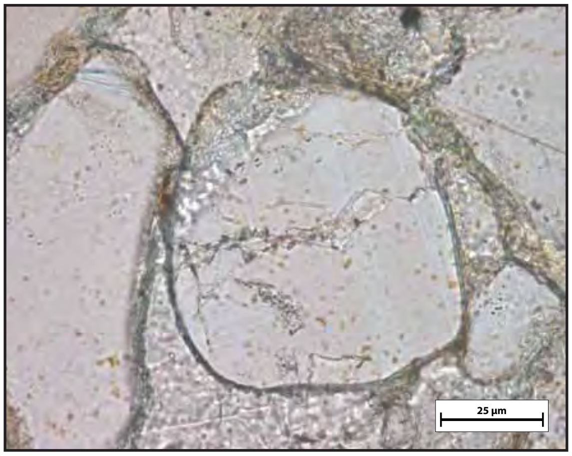

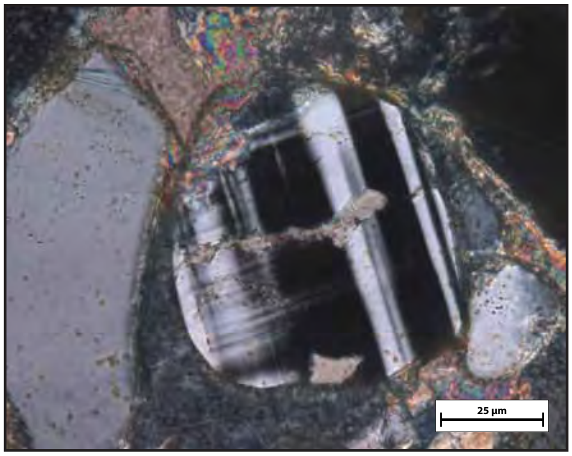

**Sample #:** 26-2 (conventional)

## Petrographic Summary

**Date:** / /

**Location Description:** In the shale slope directly below Jms5, about half-way up the ramp -- this is the continuous green fine-grained sandstone that outcrops amid the shale

**Field Trip:** ☑ April, '09 ☐ Oct., '09

**Formation:** Salt Wash green sandstone

**Rock Type:** fine-grained sandstone

**Grain Size:** 0.05-0.40 mm

**Grain Types:** quartz, sed liths, felds

**F-M-C-P:** F: M: C: P:

**Porosity (%):** Point Count: - -

Measured: - -

**Perm (mD):** - -

**Isotopes (‰):** $\delta^{18}O$: - -

$\delta^{13}C$: - -

Other: - -

### Thin Section Map

**Oriented thin section:** ☐ Yes ☑ No

**Orientation?:**

**Preparation**

☐ Thick

☑ Conventional

☐ Polished

**Stains:**

☐ Carbonate

☐ Plag ☐ Kspar

**Point Count:**

**Cement:** (types, sequence)

Grungy green interstitial (non-replacement) clay (chlorite?)

Calcite spar

**Comments:** Virtually no porosity except for fracture porosity.

Feldspars well-preserved

**Sketches:**

**Sample #: 26-2 (conventional)**

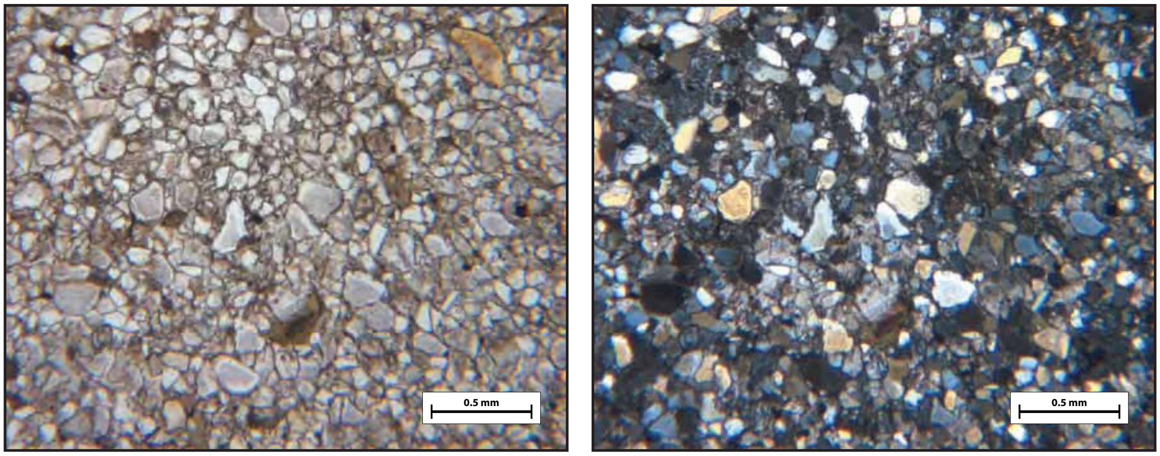

**Sample #:** 26-2 (polished)

## Petrographic Summary

**Date:** 4/21/10

**Location Description:** In the shale slope directly below Jms5, about half-way up the ramp -- this is the continuous green fine-grained sandstone that outcrops amid the shale

**Field Trip:** ☑ April, '09 ☐ Oct., '09

**Formation:** Salt Wash green sandstone

**Rock Type:** fine-grained sandstone

**Grain Size:** 0.05-0.40 mm

**Grain Types:** qtz, sed liths, felds

**F-M-C-P:** F: M: C: P:

**Porosity (%):** Point Count: 0.25%

Measured: --

**Perm (mD):** --

**Isotopes (‰):** $\delta^{18}O$: --

$\delta^{13}C$: --

Other: --

**Thin Section Map**

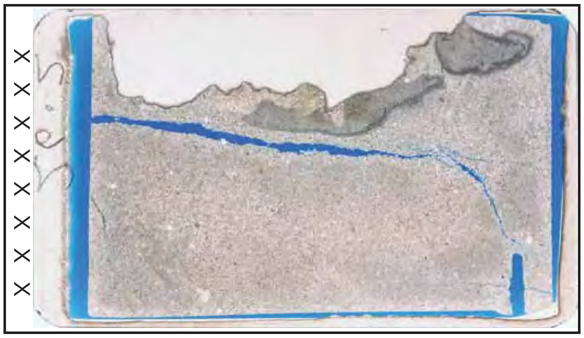

**Oriented thin section:** ☐ Yes ☑ No

**Orientation?:**

**Preparation** ☐ Thick ☐ Conventional ☑ Polished

**Stains:** ☐ Carbonate ☐ Plag ☐ Kspar

**Point Count:**

**Cement:** (types, sequence)

calcite spar

grungy greenish clay-ey interstitial cement (possibly chlorite)

**Comments:**

Thin section heavily damaged in preparation.

Very low porosity.

Feldspars mostly plagioclase, very well preserved.

**Sketches:**

**Sample #: 26-2 (polished)**

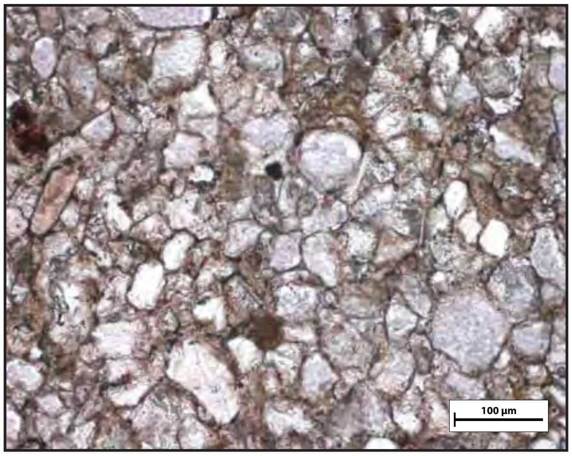

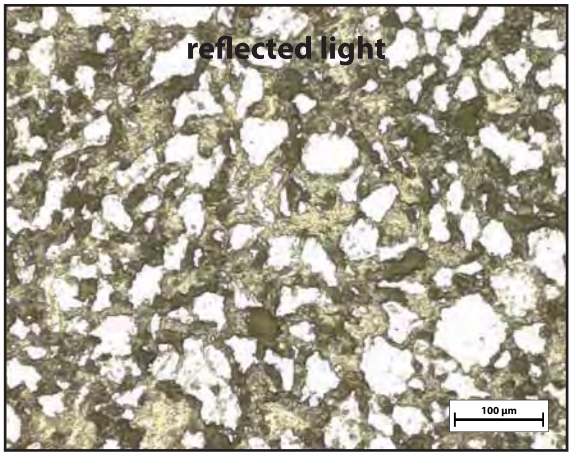

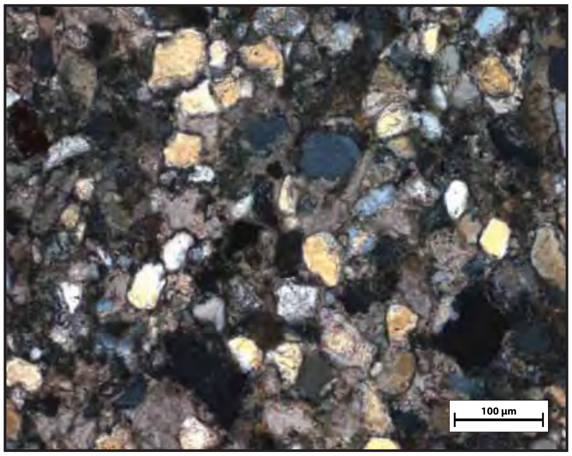

**Sample #:** 27A-1

## Petrographic Summary

**Date:** / /

**Location Description:** Gray sand from top (stratigraphically) Jms in main ramp; light acid reaction, harder, better cemented than brown sandstone (27B)

**Field Trip:** ☑ April, '09 ☐ Oct., '09

**Formation:** Jms5

**Rock Type:** sandstone

**Grain Size:** 0.1-0.8 mm

**Grain Types:** qtz, sed lithics

**F-M-C-P:** F: M: C: P:

**Porosity (%):** Point Count: - -

Measured: - -

**Perm (mD):** - -

**Isotopes (‰ ):** $\delta^{18}O$: - -

$\delta^{13}C$: - -

Other: - -

**Thin Section Map**

**Oriented thin section:** ☐ Yes ☑ No

**Orientation?:**

**Preparation** ☐ Thick ☑ Conventional ☐ Polished

**Stains:** ☐ Carbonate ☐ Plag ☐ Kspar

**Point Count:**

**Cement:** (types, sequence)

lots of opaque clay cement

very little spar cement

some quartz overgrowths, look in-place

**Comments:** Far more clay cement and much grungier appearance than 27B; surprising, since 27B is the brown rotten sandstone.

Fewer dissolved grains than 27B, but still a fair number present.

Grains cracked from slide preparation. There is no 27A-2.

**Sketches:**

**Sample #: 27A-1**

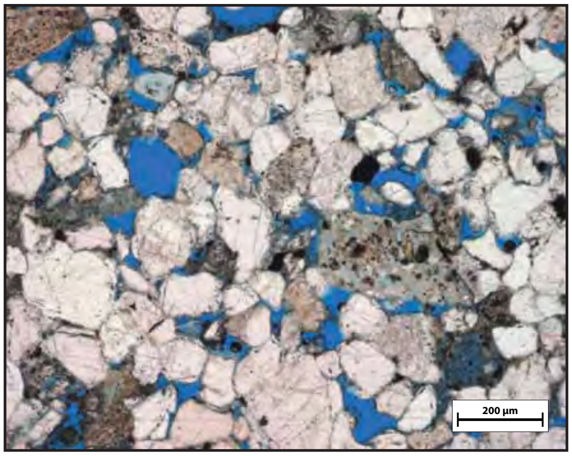
200 µm

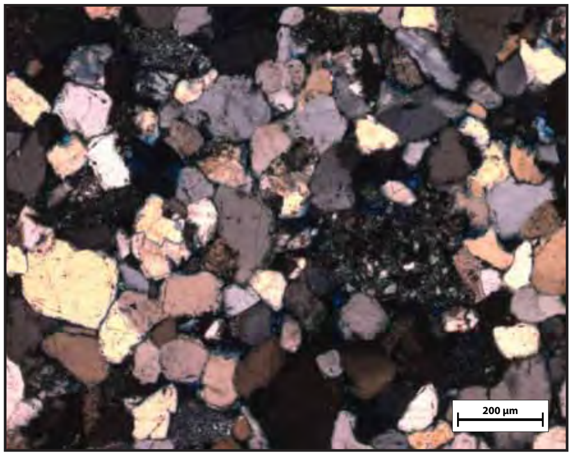
200 µm

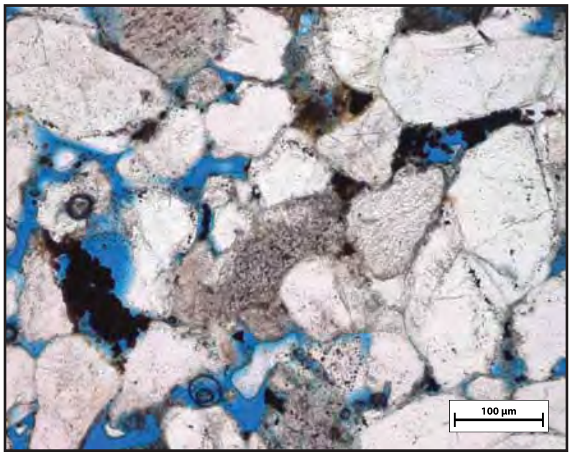
100 µm

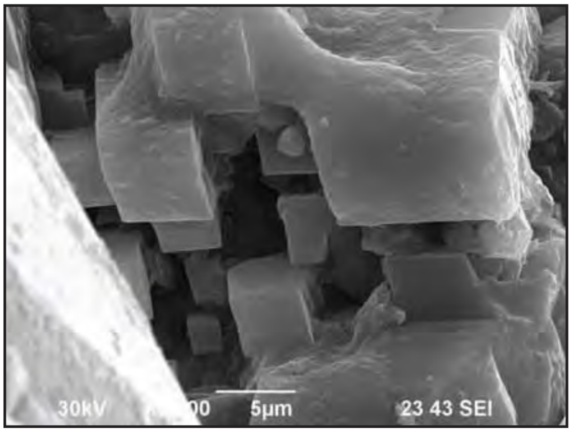
30kV
00
5µm
23 43 SEI

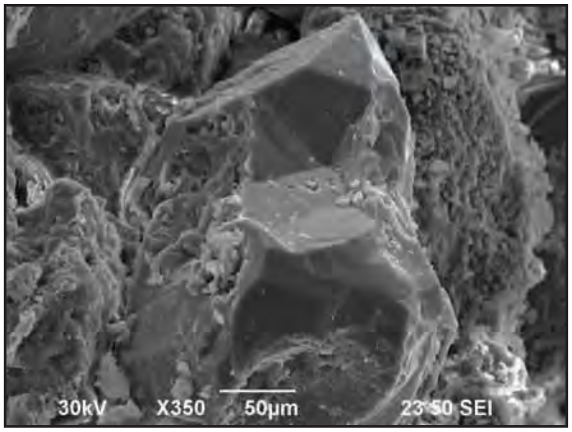
30kV
X350
50µm
23 50 SEI

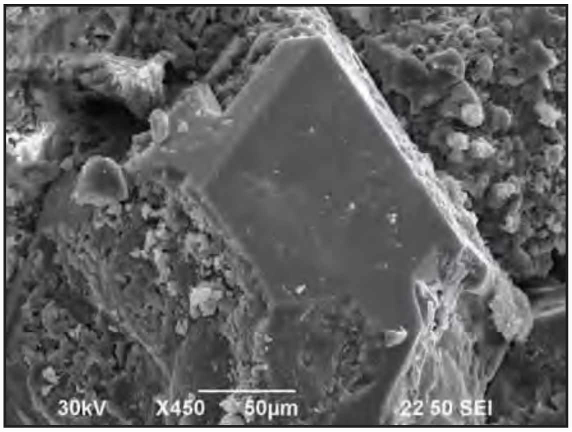
30kV
X450
50µm
22 50 SEI

**Sample #:** 27B

# Petrographic Summary

**Date:** 11/ 3 /09

**Location Description:** Brown "rotten" sand from top (stratigraphically) Jms in main ramp

**Field Trip:** ☑ April, '09 ☐ Oct., '09
**Formation:** Jms5
**Rock Type:** sandstone
**Grain Size:** 0.25-0.50mm
**Grain Types:** qtz, dissolved feldspars
**F-M-C-P:** F: 70 M: x C: 15 P: 15
**Porosity (%):** Point Count: --
Measured: --
**Perm (mD):** --
**Isotopes (‰ ):** $\delta^{18}O$: --
$\delta^{13}C$: --
Other: --

**Thin Section Map**

**Oriented thin section:** ☐ Yes ☑ No
**Orientation?:**

**Preparation** ☐ Thick ☐ Conventional ☑ Polished

**Stains:** ☐ Carbonate ☐ Plag ☐ Kspar

**Point Count:**

**Cement:** (types, sequence) Porosity-filling micrite, some spar; quartz overgrowths; small amounts of clay cement, mostly associated with dissolved grains

**Comments:** Compare to similar-lithology 27A to find difference between brown and grey alteration; and 32A to see if brown sandstones are similar.
Many grains with green-blue texture indicating dissolution.
Oversize pores are common.
Feldspars not common, always partially dissolved.

**Sketches:**

**Sample #: 27B**

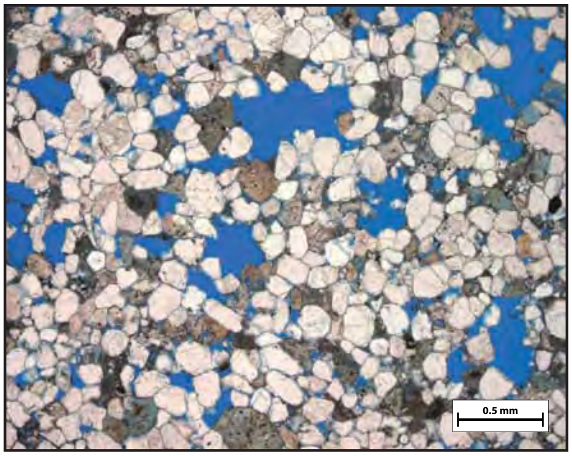
0.5 mm

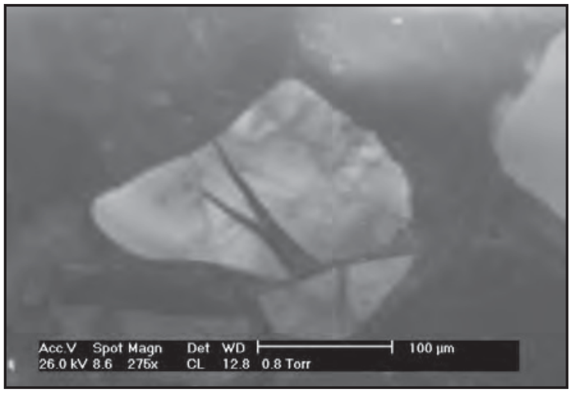
Acc.V Spot Magn Det WD 100 µm
26.0 kV 8.6 275x CL 12.8 0.8 Torr

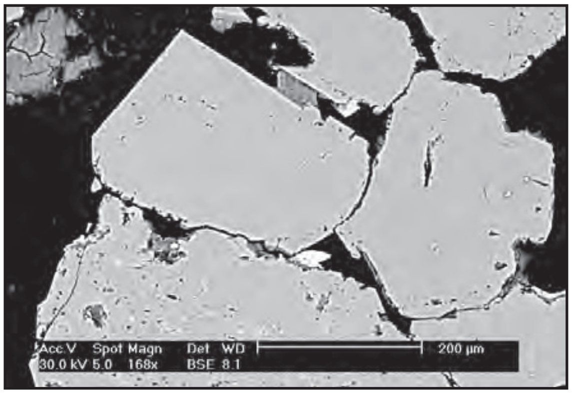
Acc.V Spot Magn Det WD 200 µm
30.0 kV 5.0 168x BSE 8.1

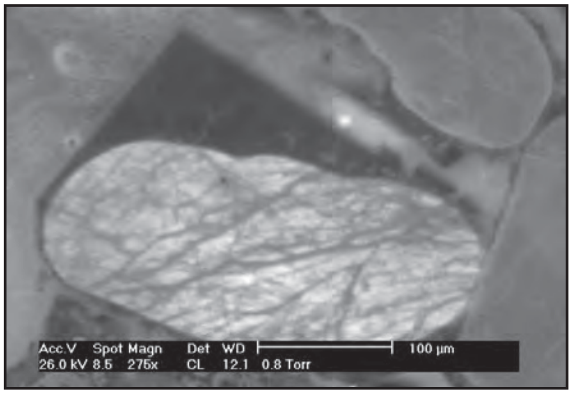
Acc.V Spot Magn Det WD 100 µm
26.0 kV 8.5 275x CL 12.1 0.8 Torr

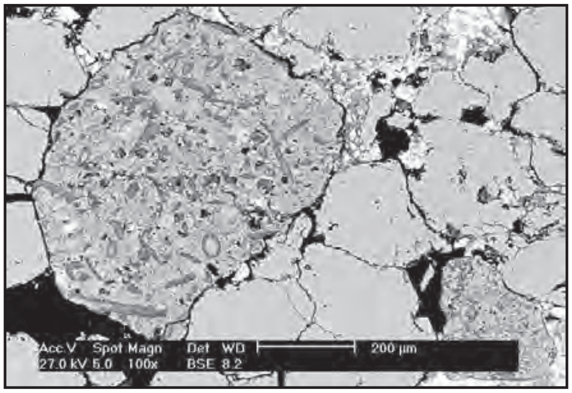
Acc.V Spot Magn Det WD 200 µm
27.0 kV 5.0 100x BSE 8.2

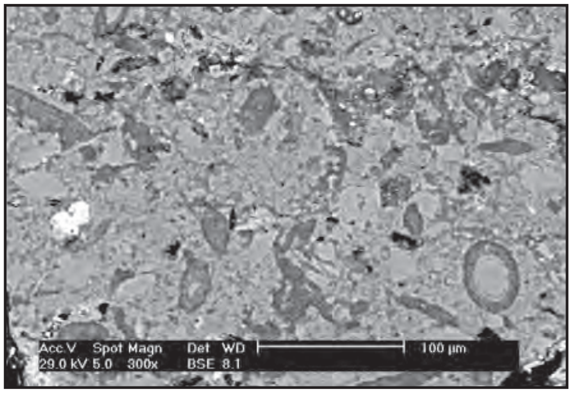
Acc.V Spot Magn Det WD 100 µm
29.0 kV 5.0 300x BSE 8.1

**Sample #:** **28A-1**

## Petrographic Summary

**Date:** 7/22/10

**Location Description:** Western tip of the ramp, dipping slightly to east (but east of large steeply east-dipping platform) (E:0577027 N:4310120)

**Field Trip:** ☑ April, '09 ☐ Oct., '09

**Formation:** Jms4

**Rock Type:** spar-cemented sandstone

**Grain Size:** 0.1-0.6 mm

**Grain Types:** Mostly quartz

**F-M-C-P:** F: M: C: P:

**Porosity (%):** Point Count: 16%

Measured: --

**Perm (mD):** --

**Isotopes (‰):** $\delta^{18}$O: --

$\delta^{13}$C: --

Other:

**Thin Section Map**

**Oriented thin section:** ☐ Yes ☑ No

**Orientation?:**

**Preparation** ☐ Thick ☑ Conventional ☐ Polished

**Stains:** ☑ Carbonate ☐ Plag ☑ Kspar

**Point Count:**

| Quartz | | | Plagioclase Feld. | | Alkali Feld. | | Lithics | | Misc. | Clay | Cement | | | | Porosity | | | | Total |
|---|---|---|---|---|---|---|---|---|---|---|---|---|---|---|---|---|---|---|---|
| mono | poly | mic/chert | intact | dissolved | intact | dissolved | opaque | sed | Grains | Matrix | spar | micrite | quartz | clay | inter | oversize | intra | micro | Points |
| 203 | 13 | 5 | 0 | 0 | 2 | 0 | 0 | 5 | 0 | 0 | 94 | 6 | 9 | 0 | 44 | 0 | 11 | 8 | 400 |
| 51% | 3% | 1% | 0% | 0% | 1% | 0% | 0% | 1% | 0% | 0% | 24% | 2% | 2% | 0% | 11% | 0% | 3% | 2% | |

**Cement:** (types, sequence)

Lots of carbonate cement

**Comments:**

Closely packed sand -- some but not lots of porosity (as compared to 22, 26)

Quite clean -- practically no clay cement

More carbonate cement than 22, 26

Green, spongy grains

Few recognizable feldspars

There is no 28B sample

**Sketches:**

**Sample #: 28A-1**

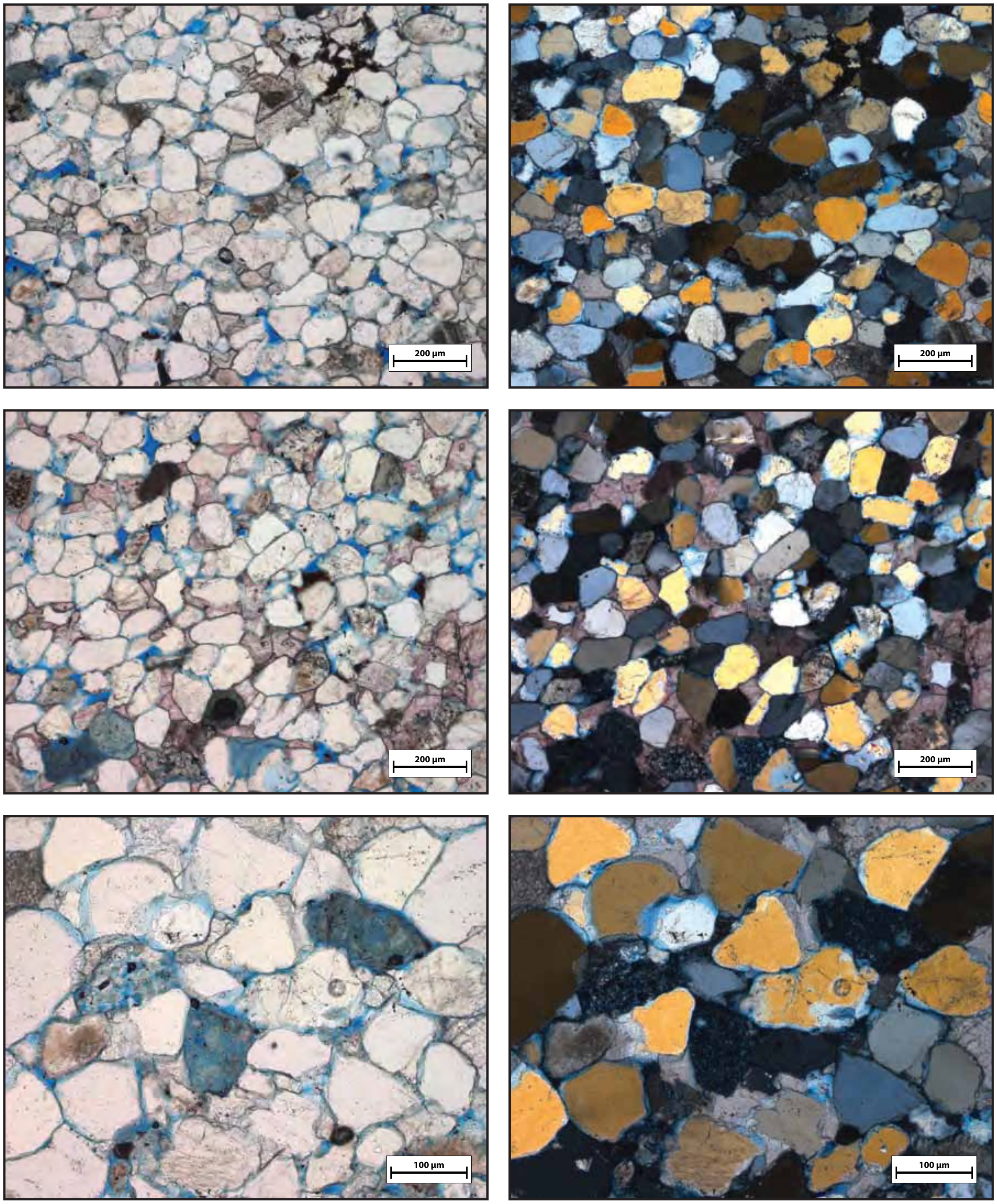

**Sample #:** 28A-2

## Petrographic Summary

**Date:** / /

**Location Description:** Western tip of the ramp, dipping slightly to east (but east of large steeply east-dipping platform) (E:0577027 N:4310120 )

**Field Trip:** ☑ April, '09 ☐ Oct., '09

**Formation:** Jms4

**Rock Type:** sandstone

**Grain Size:** 0.2-0.6 mm

**Grain Types:** quartz, sed liths,

**F-M-C-P:** F: M: C: P:

**Porosity (%):** Point Count: --

Measured: --

**Perm (mD):** --

**Isotopes (‰ ):** $\delta^{18}O$: --

$\delta^{13}C$: --

Other: --

### Thin Section Map

**Oriented thin section:** ☐ Yes ☑ No

**Orientation?:**

**Preparation**

☑ Thick
☐ Conventional
☐ Polished

**Stains:**
☐ Carbonate
☐ Plag ☐ Kspar

**Point Count:**

**Cement:** (types, sequence)

lots of spar cement
some clay cement

**Comments:** Med-low porosity -- grains quite closely packed together, not as much dissolution as in other samples (e.g., 27A and B).
Clay cement is mostly associated with grains, doesn't accumulate in large amounts but leaves a sort of residue where grains appear to have dissolved.
Feldspars rare
There is no 28B sample.

**Sketches:**

## Sample #: 28A-2

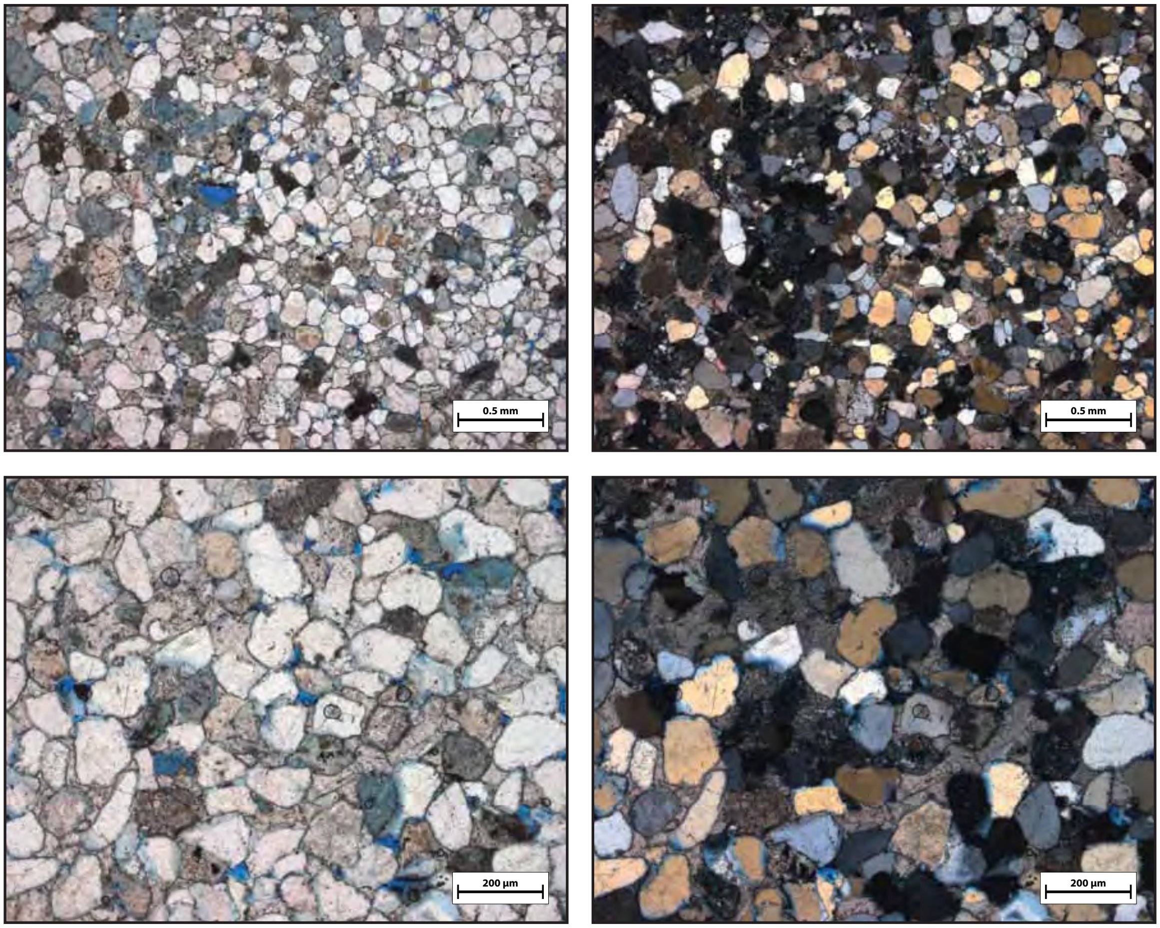

**Sample #:** 30A

## Petrographic Summary

**Date:** / /

**Location Description:** Small outcrop of fault-offset sandstone 10 m south of the Salt Wash-Brushy Basin fault contact at the top of the ramp

**Field Trip:** ☑ April, '09 ☐ Oct., '09

**Formation:** Brushy Basin

**Rock Type:** fine-grained sandstone

**Grain Size:** 0.05-0.30 mm

**Grain Types:** qtz, plag, kspar

**F-M-C-P:** F: M: C: P:

**Porosity (%):** Point Count: --

Measured: --

**Perm (mD):** --

**Isotopes (‰):** $\delta^{18}O$: --

$\delta^{13}C$: --

Other: --

### Thin Section Map

**Oriented thin section:** ☐ Yes ☑ No

**Orientation?:**

**Preparation**

☐ Thick
☑ Conventional
☐ Polished

**Stains:**
☐ Carbonate
☐ Plag ☐ Kspar

**Point Count:**

**Cement:** (types, sequence) pervasive calcite spar; patches of micrite are common but not pervasive; small amount of brown/black opaque cement

**Comments:** Almost no porosity due to calcite spar and small grain size (greater packing).

This sample is very different from sample 30B (lower porosity, more spar, smaller grain size). Possibly due to lithologic differences between beds.

A pair of deformation bands intersects in an X, and one slightly offsets the other.

**Sketches:**

**Sample #: 30A**

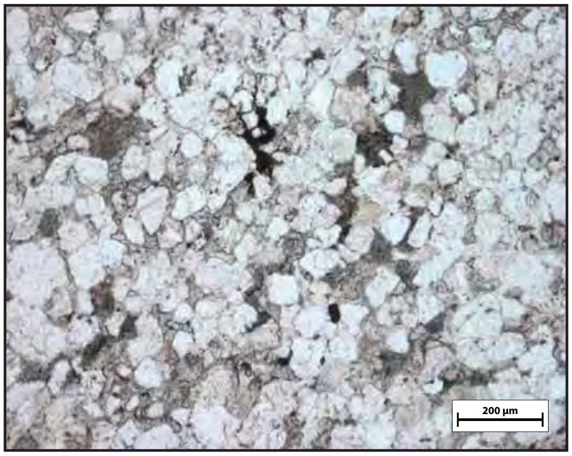

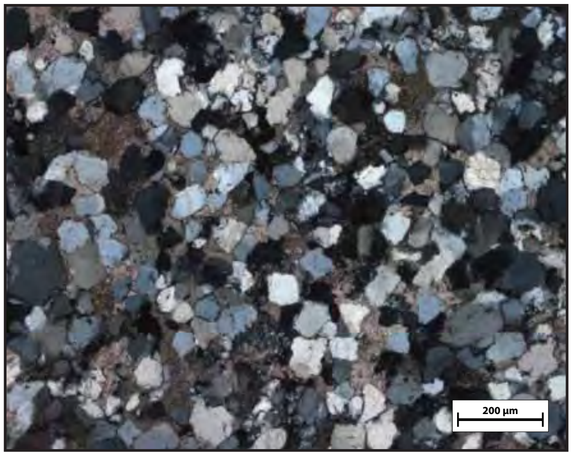

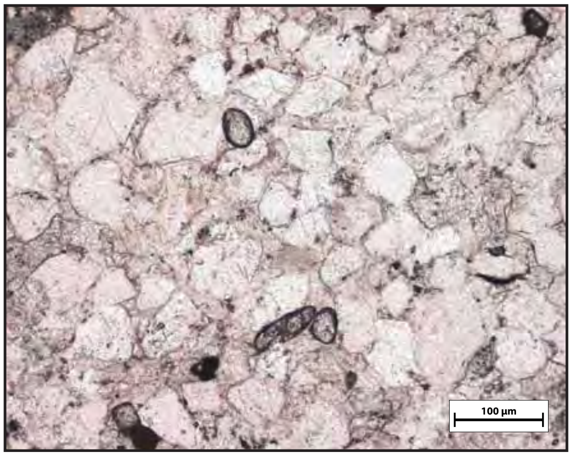

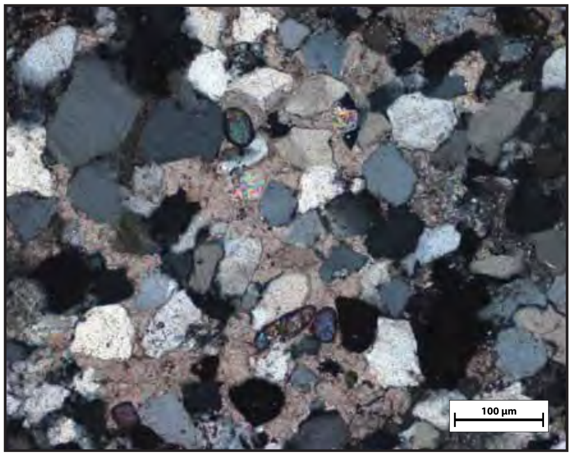

**Sample #:** 30B-1

## Petrographic Summary

**Date:** / /

**Location Description:** Small outcrop of fault-offset sandstone 10 m south of the Salt Wash-Brushy Basin fault contact at the top of the ramp

**Field Trip:** ☑ April, '09 ☐ Oct., '09

**Formation:** Brushy Basin

**Rock Type:** sandstone

**Grain Size:** 0.10-0.40 mm

**Grain Types:** qtz, clay-ey sed liths

**F-M-C-P:** F: M: C: P:

**Porosity (%):** Point Count: - -

Measured: - -

**Perm (mD):** - -

**Isotopes (‰ ):** $\delta^{18}$O: - -

$\delta^{13}$C: - -

Other: - -

### Thin Section Map

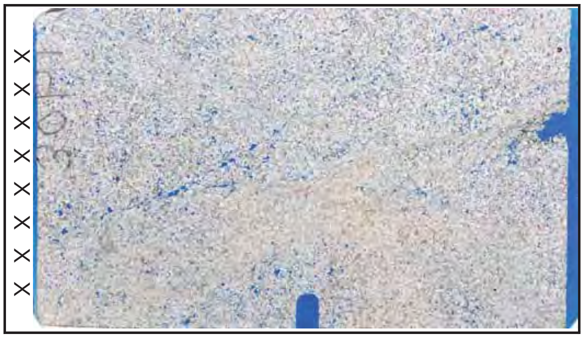

**Oriented thin section:** ☐ Yes ☑ No

**Orientation?:**

**Preparation**

☑ Thick

☑ Conventional

☐ Polished

**Stains:**

☐ Carbonate

☐ Plag ☐ Kspar

**Point Count:**

**Cement:** (types, sequence) Patches of micrite cement are common but not pervasive; spar also common but not pervasive; small amounts of clay cement; quartz cement

**Comments:** Fairly high porosity; many green spongy dissolved grains, often with a clay-ey residue left at their core.

Several deformation bands.

Hard to tell if some grains are dissolved, clay-replaced grains (e.g., former feldspars), or sedimentary lithic grains.

**Sketches:**

**Sample #: 30B-1**

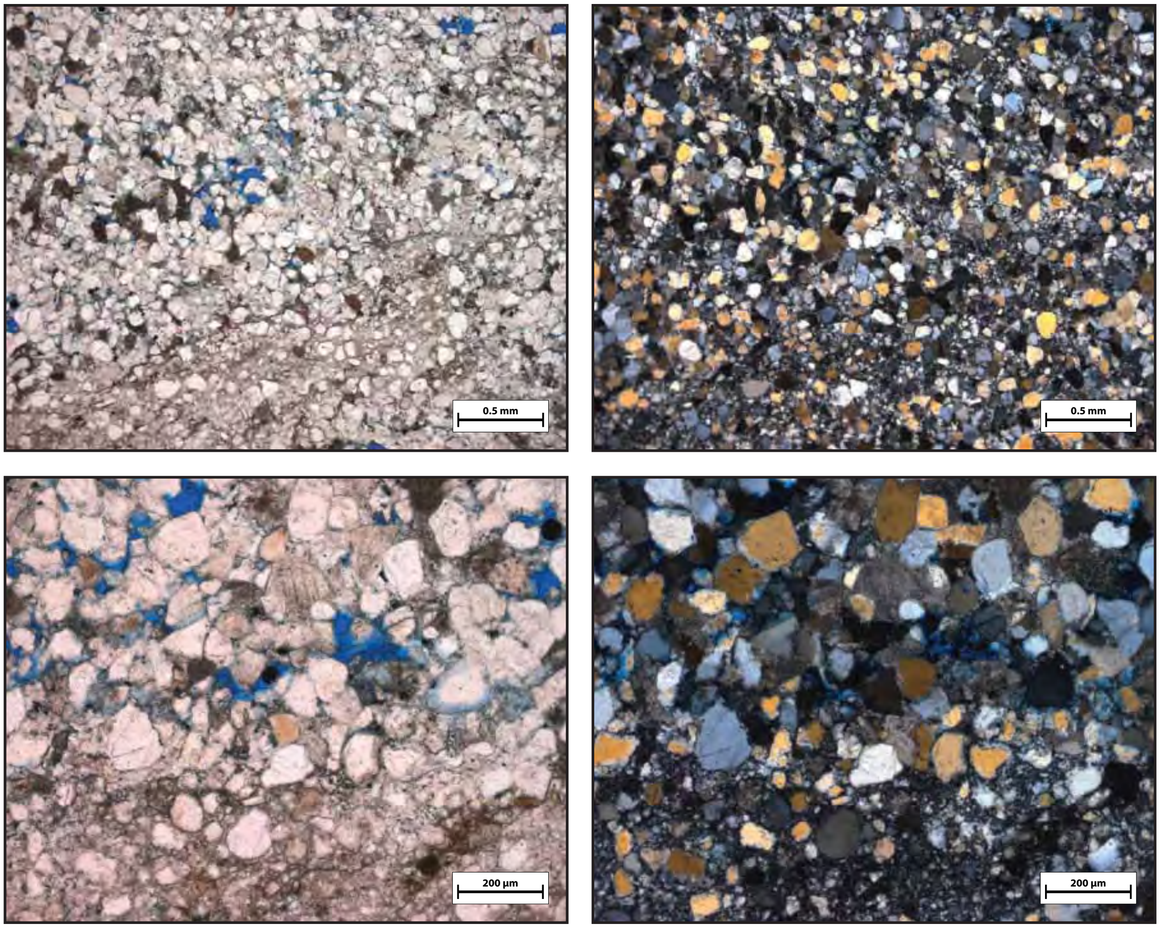

**Sample #:** 30B-2

**Petrographic Summary**

**Date:** / /

**Location Description:** Small outcrop of fault-offset sandstone 10 m south of the Salt Wash-Brushy Basin fault contact at the top of the ramp

**Field Trip:** ☑ April, '09 ☐ Oct., '09

**Formation:** Brushy Basin

**Rock Type:** sandstone

**Grain Size:** mostly 0.10-0.40 mm

**Grain Types:** quartz, sed. lithics

**F-M-C-P:** F: M: C: P:

**Porosity (%):** Point Count: - -

Measured: - -

**Perm (mD):** - -

**Isotopes (‰ ):** δ$^{18}$O: - -

δ$^{13}$C: - -

Other: - -

**Thin Section Map**

**Oriented thin section:** ☐ Yes ☑ No

**Orientation?:**

**Preparation**
☐ Thick
☐ Conventional
☑ Polished

**Stains:**
☐ Carbonate
☐ Plag ☐ Kspar

**Point Count:**

**Cement:** (types, sequence) Patchy micritic calcite; small amounts of calcite spar, generally associated with open porosity.
Quartz overgrowhts abundant, often growing into each other.

**Comments:** Porosity overall quite low. Where it's present it occurs in bands. Deformation bands and micrite cement occur in broad swathes that have little or no porosity.
"Grungy" appearance due to scattered micrite.
Some "spongy" blue-green dissolved grains, but dissolution is overall quite low, possibly due to the extent of quartz overgrowths and deformation band-related cataclastic quartz.

**Sketches:**

**Sample #: 30B-2**

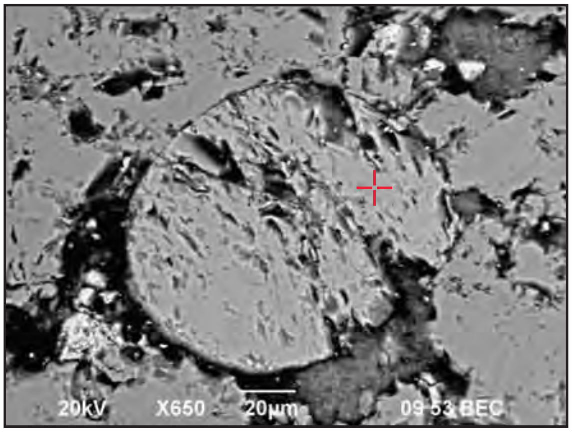
20kV
X650
20μm
09 53 BEC

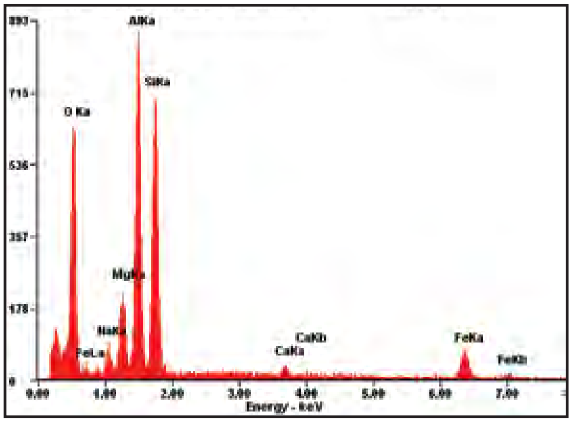
893
715
536
357
178
0
AlKa
SiKa
O Ka
MgKa
NaKa
FeLa
CaKb
CaKa
FeKa
FeKb
0.00
1.00
2.00
3.00
4.00
5.00
6.00
7.00
Energy - keV

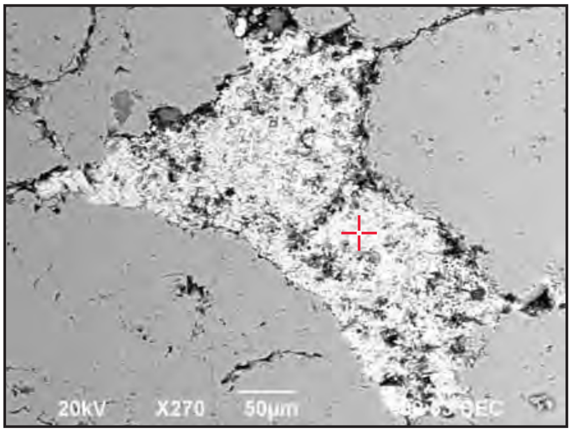
20kV
X270
50μm
BEC

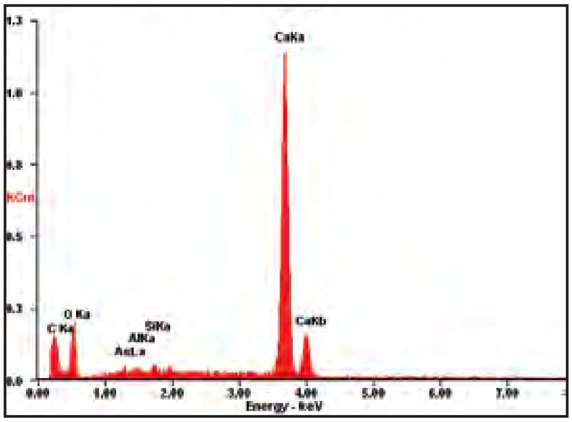
1.3
1.0
0.8
KCnt
0.5
0.3
0.0
CaKa
O Ka
C Ka
SiKa
AlKa
AuLa
CaKb
0.00
1.00
2.00
3.00
4.00
5.00
6.00
7.00
Energy - keV

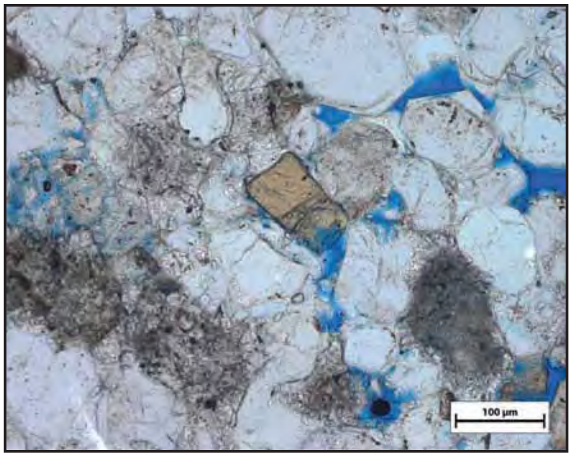
100 μm

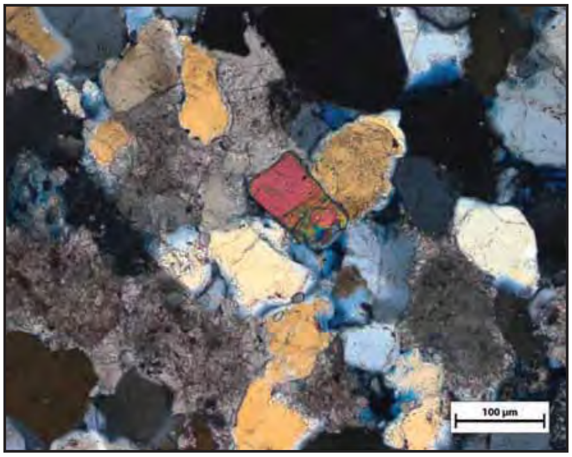
100 μm

**Sample #:** 32A

## Petrographic Summary

**Date:** 11/ 3 /09

**Location Description:** Jms brown sand under travertine mound (northeast corner)

**Field Trip:** ☑ April, '09 ☐ Oct., '09

**Formation:** should be Jms5

**Rock Type:** sandstone

**Grain Size:** 0.15-0.55mm

**Grain Types:** qtz, chert

**F-M-C-P:** F: 85 M: x C: <5 P: 10

**Porosity (%):** Point Count:

Measured:

**Perm (mD):**

**Isotopes (‰ ):** $\delta^{18}$O:

$\delta^{13}$C:

Other:

**Thin Section Map**

**Oriented thin section:** ☐ Yes ☑ No

**Orientation?:**

**Preparation** ☐ Thick ☑ Conventional ☑ Polished

**Stains:** ☐ Carbonate ☐ Plag ☐ Kspar

**Point Count:**

**Cement:** (types, sequence)

Some fine-grained calcite
Some clay (maybe hematite), but not abundant

**Comments:**

Interesting that this has such high porosity and 32B (a few meters away) has almost none, due to spar cement
Good brown sand to compare with white/gray sand (27B)

Slide was later polished. Notes from after polishing:
Many highly dissolved grains;
Qtz overgrowths
Small volume of porosity-filling spar

**Sketches:**

**Sample #: 32A**

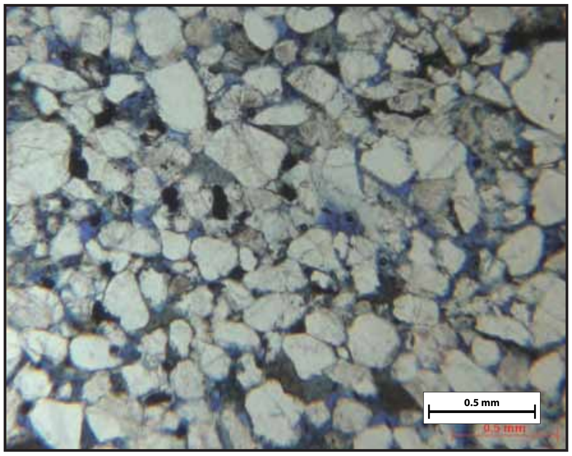
0.5 mm

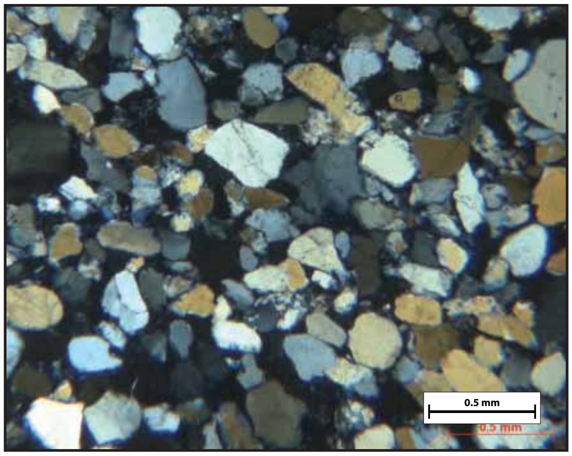
0.5 mm

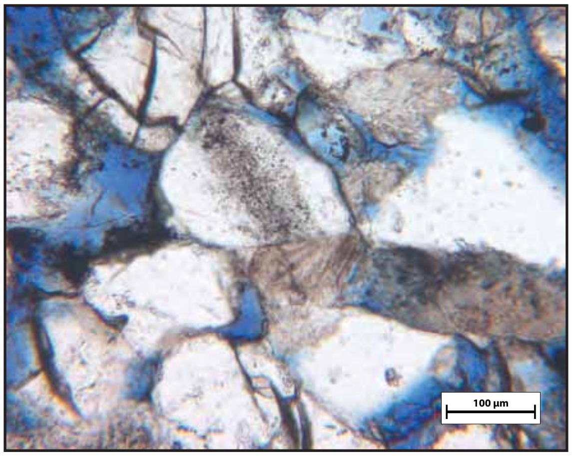
100 µm

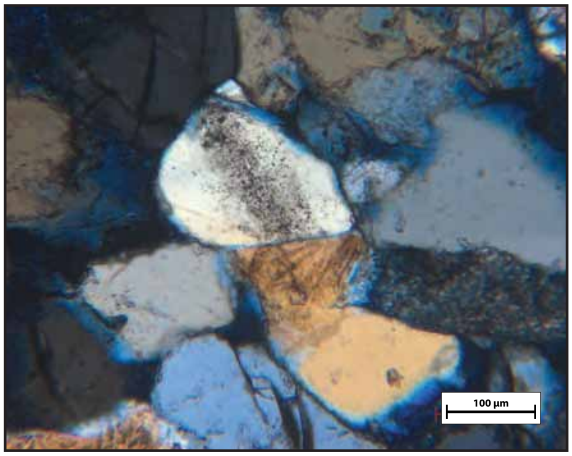
100 µm

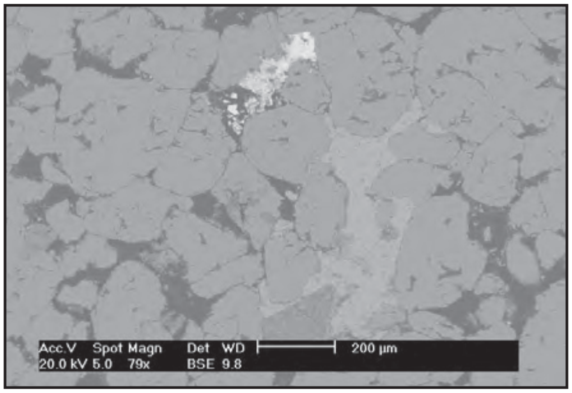
Acc.V Spot Magn Det WD 200 µm
20.0 kV 5.0 79x BSE 9.8

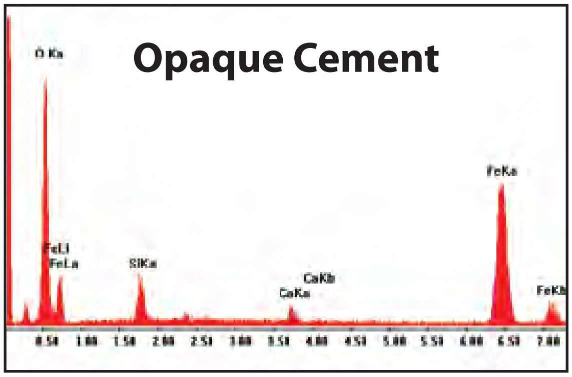
Opaque Cement
O Ka
FeLl
FeLa
SiKa
CaKb
CaKa
FeKa
FeKb
0.50
1.00
1.50
2.00
2.50
3.00
3.50
4.00
4.50
5.00
5.50
6.00
6.50
7.00

**Sample #:** 32B

## Petrographic Summary

**Date:** 11/ 3 /09

**Location Description:** Jms sand (white-gray w/ yellow patches) from ledgy bowl directly adjacent to travertine mound (east)

**Field Trip:** ☑ April, '09 ☐ Oct., '09

**Formation:** should be Jms5

**Rock Type:** sandstone

**Grain Size:** 0.15-0.60mm

**Grain Types:** qtz, chert

**F-M-C-P:** F: 65 M: x C: 35 P: 0

**Porosity (%):** Point Count:

Measured:

**Perm (mD):**

**Isotopes (‰ ):** $\delta^{18}$O:

$\delta^{13}$C:

Other:

**Thin Section Map**

**Oriented thin section:** ☐ Yes ☑ No

**Orientation?:**

**Preparation** ☐ Thick ☑ Conventional ☐ Polished

**Stains:** ☐ Carbonate ☐ Plag ☐ Kspar

**Point Count:**

**Cement:** (types, sequence) Fully pore-occluding calcite spar

**Comments:** Compare to nearby 32A, which has much less cement and more porosity

**Sketches:**

## Sample #: **32B**

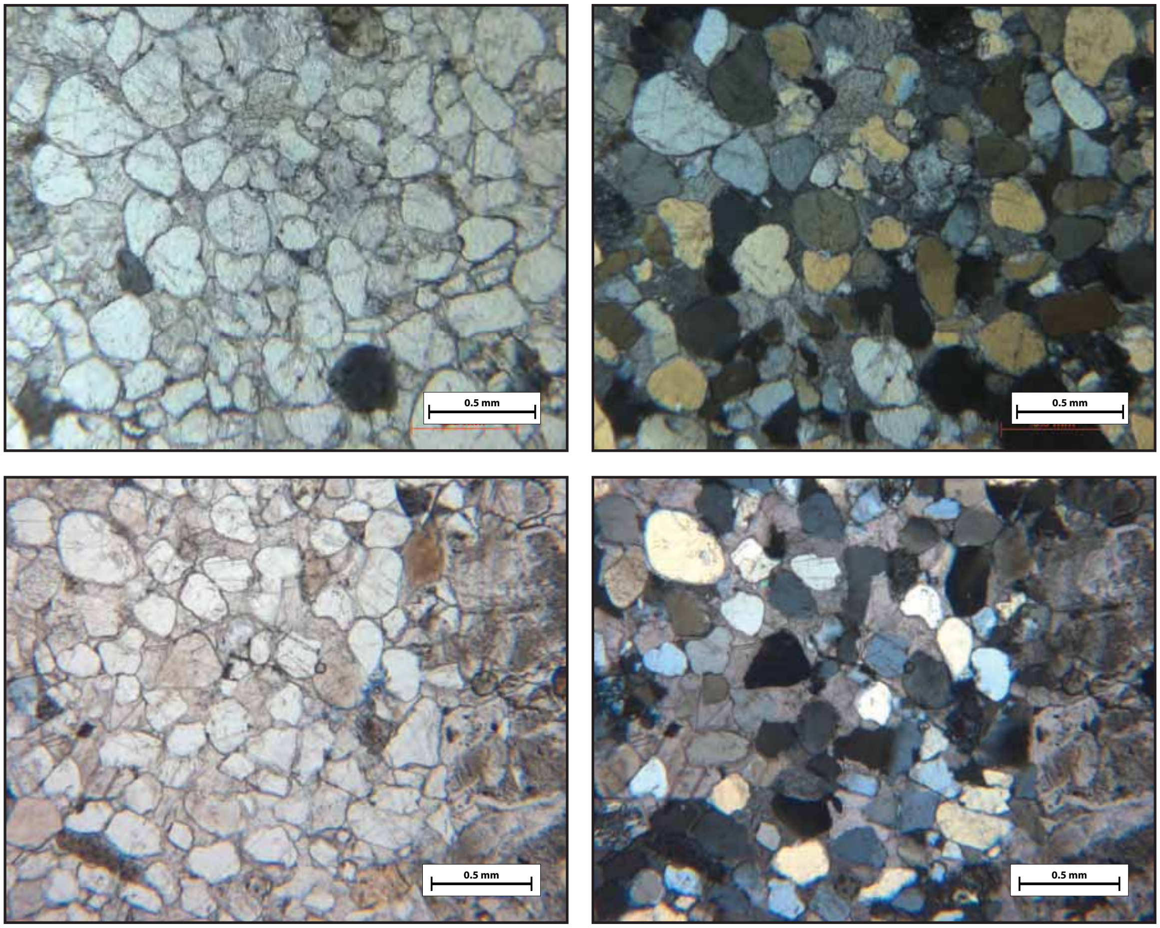

**Sample #:** 32C

## Petrographic Summary

**Date:** / /

**Location Description:** About 3/4 of the way east on the arc-shaped ledge that outcrops at the head of the wash that runs down the east side of the travertine deposit

**Field Trip:** ☑ April, '09 ☐ Oct., '09

**Formation:** Jms5

**Rock Type:** sandstone

**Grain Size:** 0.10-0.50

**Grain Types:** mostly quartz

**F-M-C-P:** F: M: C: P:

**Porosity (%):** Point Count: --

Measured: --

**Perm (mD):** --

**Isotopes (‰):** $\delta^{18}O$: --

$\delta^{13}C$: --

Other: --

**Thin Section Map**

**Oriented thin section:** ☐ Yes ☑ No

**Orientation?:**

**Preparation** ☐ Thick ☑ Conventional ☐ Polished

**Stains:** ☐ Carbonate ☐ Plag ☐ Kspar

**Point Count:**

**Cement:** (types, sequence) Calcite spar and micrite
Small amounts of clay (opaque brown/black) cement near dissolution features

**Comments:** Porosity is fairly high, considerably greater than 32D. Spar and micrite cement are present, but not pervasive. Green spongy dissolved grains are more numerous than in 32D.
Strange band running through the slide -- looks like a deformation band, but no cataclastic quartz, just smaller quartz grains mixed with micrite cement. Not apparently a fracture (i.e., didn't open up and fill with cement)

**Sketches:**

**Sample #: 32C**

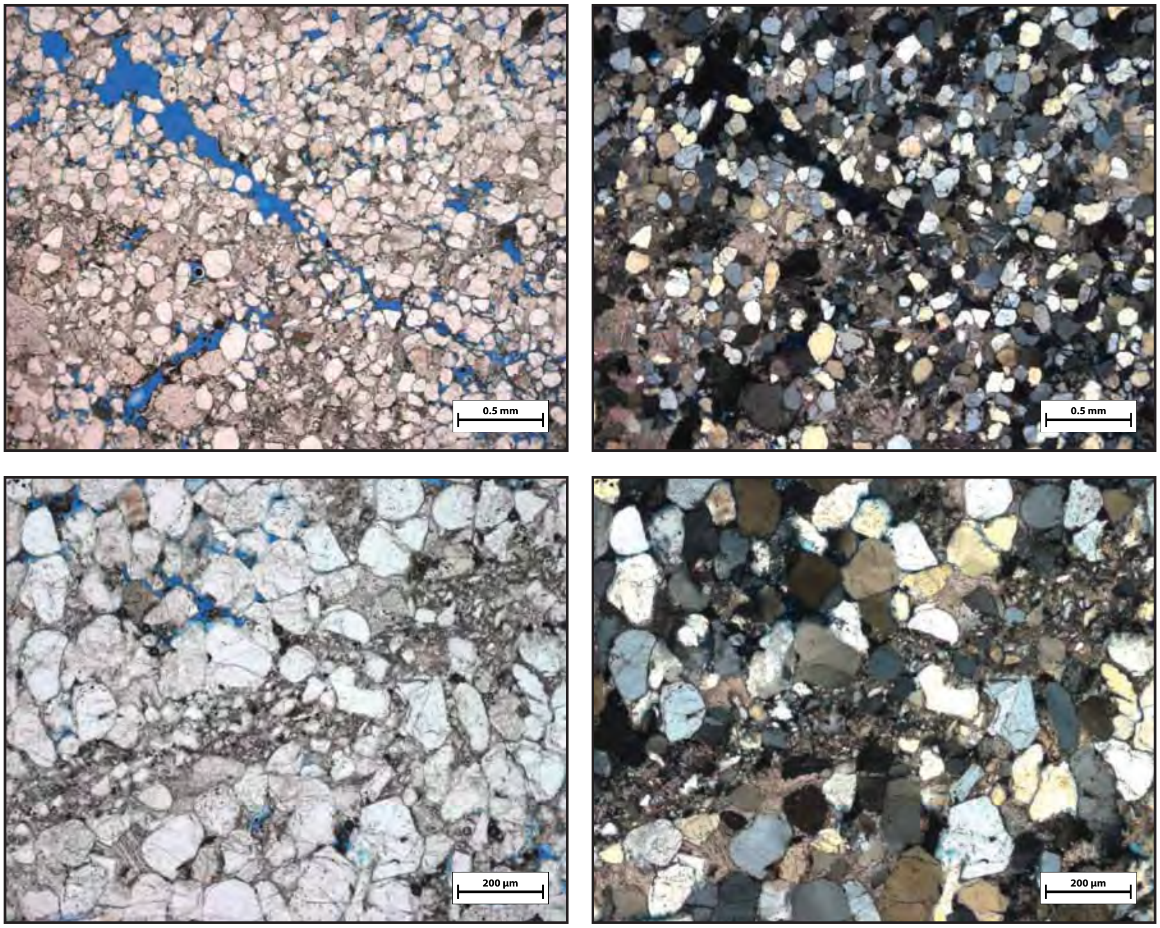

**Sample #:** **32D-1**

## Petrographic Summary

**Date:** 7/22/10

**Location Description:** Far east corner of the arc-shaped ledge that outcrops at the head of the wash that runs down the east side of the travertine deposit

**Field Trip:** ☑ April, '09 ☐ Oct., '09

**Formation:** Jms5

**Rock Type:** sandstone

**Grain Size:** 0.15-0.45 mm

**Grain Types:** qtz, kspar, plag,

**F-M-C-P:** F: M: C: P:

**Porosity (%):** Point Count: --

Measured: --

**Perm (mD):** --

**Isotopes (‰):** $\delta^{18}O$: --

$\delta^{13}C$: --

Other: --

**Thin Section Map**

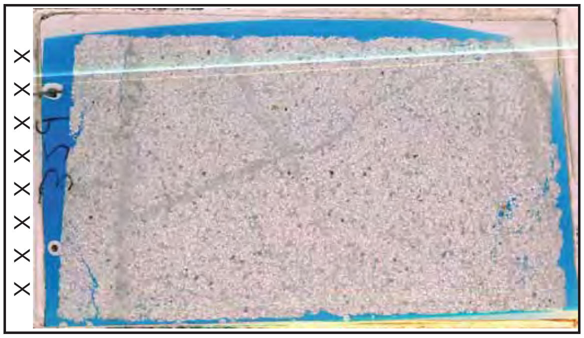

**Oriented thin section:** ☐ Yes ☑ No

**Orientation?:**

**Preparation**
☐ Thick
☑ Conventional
☐ Polished

**Stains:**
☑ Carbonate
☐ Plag ☑ Kspar

**Point Count:**

**Cement:** Fully carbonate-cemented
(types, sequence)

**Comments:** Very low porosity (all filled in w/ carbonate cement -- mostly large spar and some smaller crystals; no micrite)
Mostly mono-qtz, some poly-qtz, lots of feldspars
Green spongy dissolved grains are relatively rare (compared to samples like 17C).
Abundant brown-speckled grains, like boring Easter eggs
Fracture in one corner (northwest corner, above) appears to have some bridges growing across it

**Sketches:**

## Sample #: **32D-1**

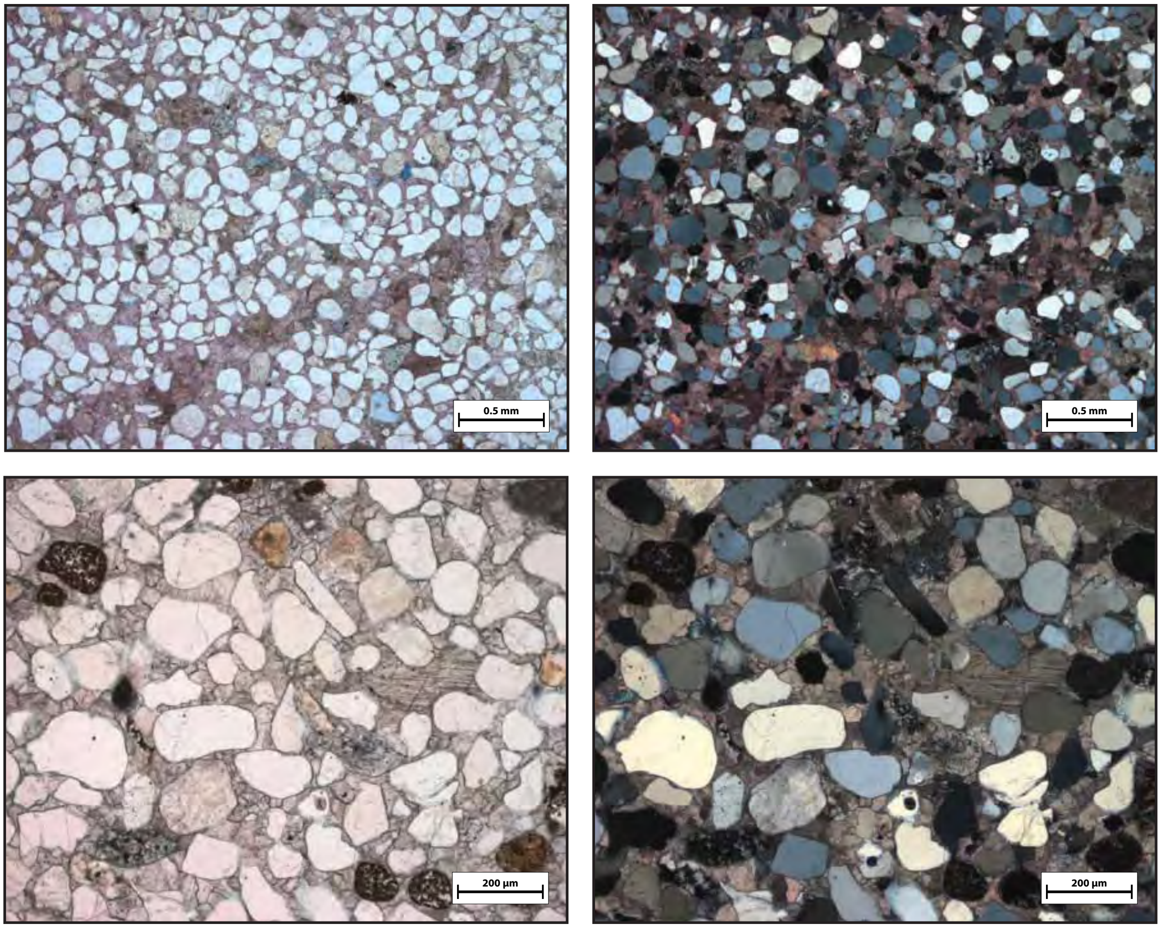

**Sample #:** **32D-2**

## Petrographic Summary

**Date:** / /

**Location Description:** Far east corner of the arc-shaped ledge that outcrops at the head of the wash that runs down the east side of the travertine deposit

**Field Trip:** ☑ April, '09 ☐ Oct., '09

**Formation:** Jms5

**Rock Type:** sandstone

**Grain Size:** 0.10-0.50 mm

**Grain Types:** quartz, plag, kspar

**F-M-C-P:** F: M: C: P:

**Porosity (%):** Point Count: --

Measured: --

**Perm (mD):** --

**Isotopes (‰ ):** $\delta^{18}O$: --

$\delta^{13}C$: --

Other: --

**Thin Section Map**

**Oriented thin section:** ☐ Yes ☑ No

**Orientation?:**

**Preparation**

☐ Thick

☑ Conventional

☐ Polished

**Stains:**

☐ Carbonate

☐ Plag ☐ Kspar

**Point Count:**

**Cement:** (types, sequence)

Pervasive calcite spar; some patches of micrite

Uncommon patches of black/brown opaque clay cement

**Comments:** Low porosity, few dissolved grains; IGV almost completely filled with calcite spar; fractures filled with very large calcite crystals. Interesting comparison to 32C, just a few meters to the west. 32D has very little dissolution, possibly due to the low porosity (high volume of cement), and 32C has quite a lot of dissolution, possibly due to the high porosity (limited cementation). Which comes first? Low cement or dissolution (low cement due to dissolution?).

**Sketches:**

**Sample #: 32D-2**

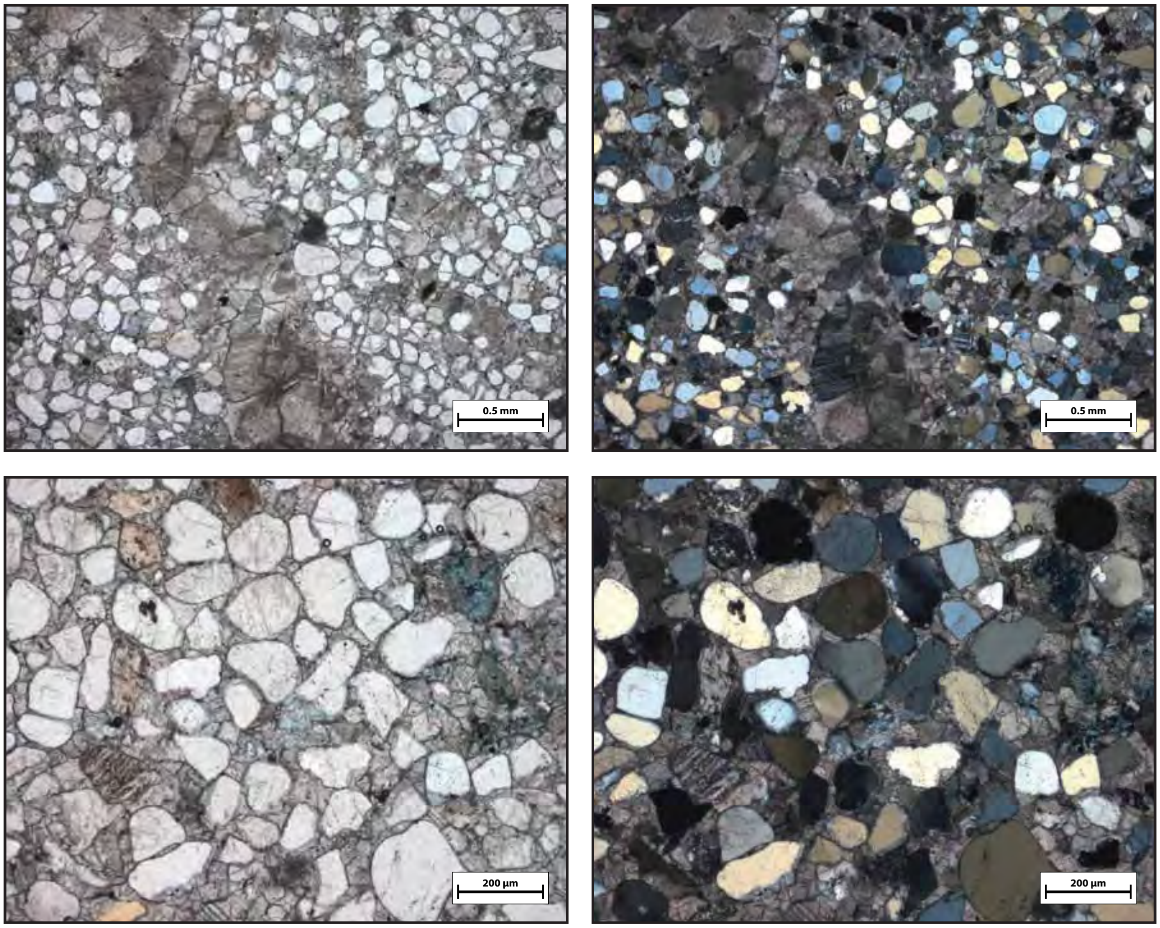

**Sample #:** **34A-1**

## Petrographic Summary

**Date:** / /

**Location Description:** From veiny, hard, non-reactive (quartz-cemented) white sandstone 45 m directly east of travertine platform.

**Field Trip:** ☐ April, '09 ☑ Oct., '09

**Formation:** Salt Wash, just below Jms6

**Rock Type:** coarse-grained sandstone

**Grain Size:** 0.3-1.0 mm

**Grain Types:** quartz, chert,

**F-M-C-P:** F: M: C: P:

**Porosity (%):** Point Count: - -

Measured: - -

**Perm (mD):** - -

**Isotopes (‰ ):** $\delta^{18}$O: - -

$\delta^{13}$C: - -

Other: - -

**Thin Section Map**

**Oriented thin section:** ☐ Yes ☑ No

**Orientation?:**

**Preparation**

☑ Thick
☐ Conventional
☑ Polished

**Stains:**

☐ Carbonate
☐ Plag ☐ Kspar

**Point Count:**

**Cement:** (types, sequence)

Abundant opaque clay cuticles -- form euhedral crystals in some places; some pore-filling clay

Abundant euhedral quartz overgowths

**Comments:**

High porosity, including unevenly distributed oversize porosity and relatively abundant green spongy dissolved grains.

Deformations bands full of cataclastic quartz in addition to the quartz overgrowths.

No apparent calcite.

Lots of chert and occasional extra large grains (4-6 mm)

Feldspars very rare

**Sketches:**

**Sample #: 34A-1**

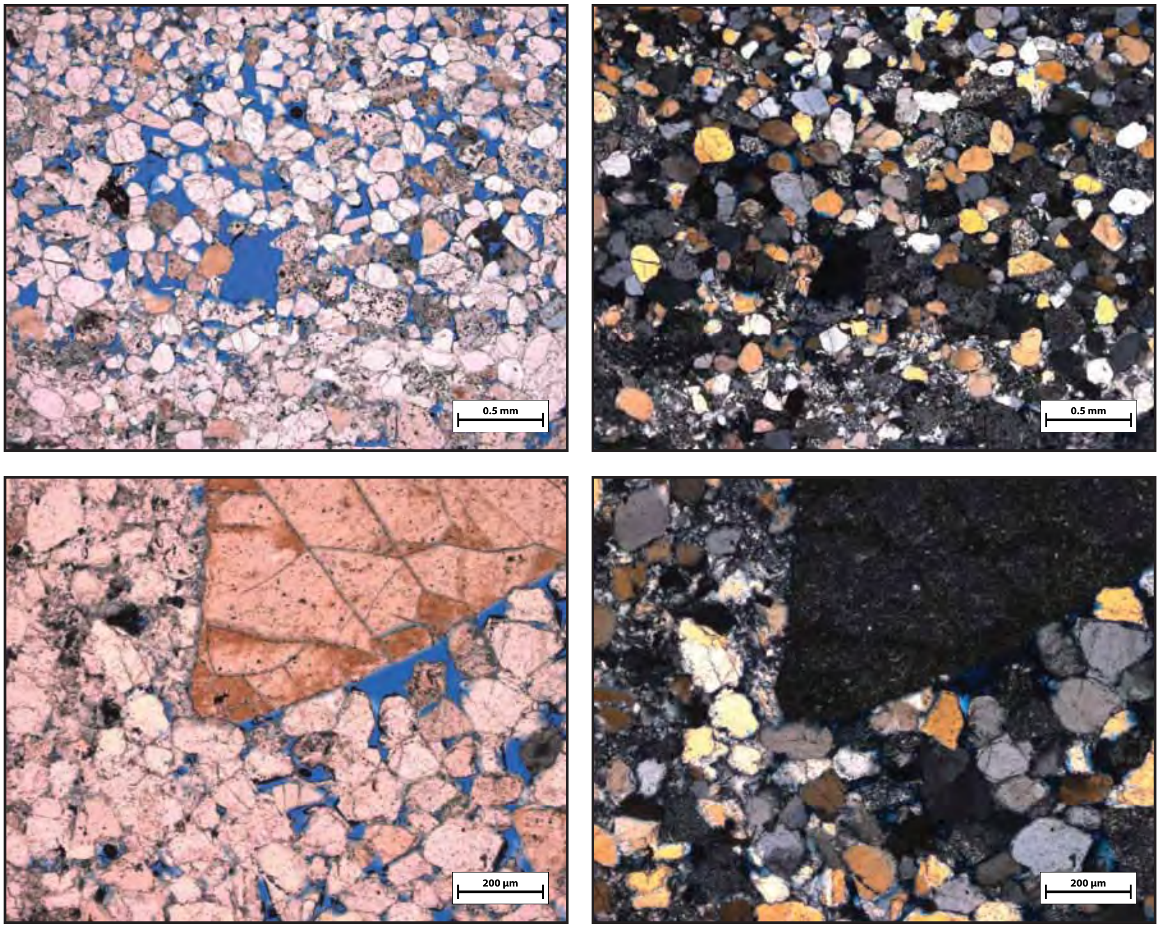

**Sample #:** 34A-2

## Petrographic Summary

**Date:** 7/22/10

**Location Description:** From veiny, hard, non-reactive (quartz-cemented) white sandstone 45 m directly east of travertine platform.

**Field Trip:** ☑ April, '09 ☐ Oct., '09

**Formation:** Salt Wash, just below Jms6

**Rock Type:** coarse-grained sandstone

**Grain Size:** 0.4-4.0 mm

**Grain Types:** chert, quartz, sed lithics

**F-M-C-P:** F: M: C: P:

**Porosity (%):** Point Count: --

Measured: --

**Perm (mD):** --

**Isotopes (‰):** $\delta^{18}O$: --

$\delta^{13}C$: --

Other: --

**Thin Section Map**

**Oriented thin section:** ☐ Yes ☑ No

**Orientation?:**

**Preparation**

☐ Thick

☑ Conventional

☐ Polished

**Stains:**

☑ Carbonate

☐ Plag ☑ Kspar

**Point Count:**

**Cement:** (types, sequence)

Heavy qtz overgrowths -- appear to have grown in place

NO carbonate cement

**Comments:**

Well-formed euhedral quartz overgrowths

Some large chert grains

No carbonate cement or grains

High porosity, lots of oversize pores, lots of partially to mostly dissolved grains

Feldspars RARE, only saw two: one 50% and one 90% dissolved. Stain does not highlight any feldspars.

**Sketches:**

**Sample #: 34A-2**

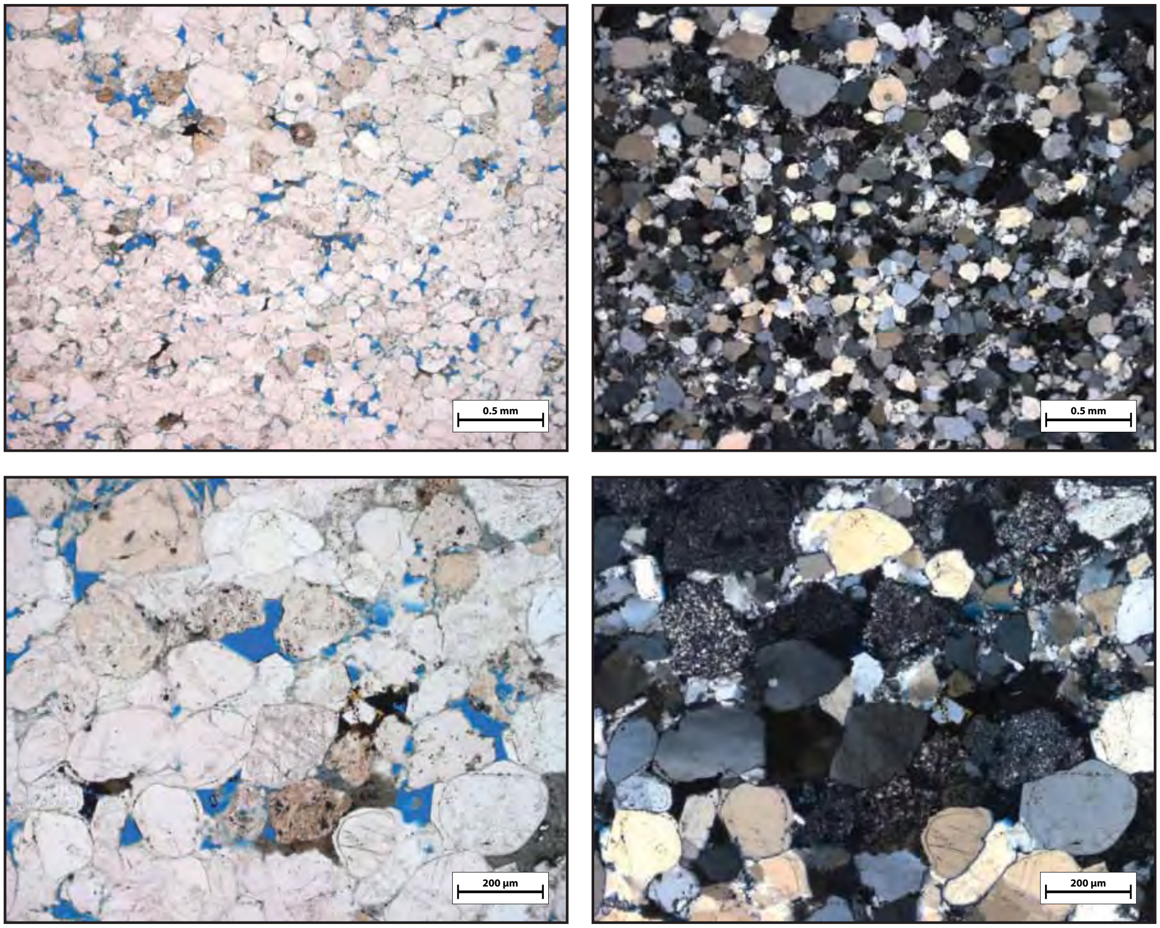

**Sample #:** 35A-1

## Petrographic Summary

**Date:** 11/ 3 /09

**Location Description:** Fault-distal Jms sand (north of mapping transparency) Visible in aerials in platform sand w/ large fracture sets, NE of travertine mound, above Jms2

**Field Trip:** ☑ April, '09 ☐ Oct., '09

**Formation:** Jms sand between Jms2 + 3

**Rock Type:** sandstone

**Grain Size:** 0.15-0.50mm

**Grain Types:** qtz, chert, clay clasts, felds

**F-M-C-P:** F: 75 M: x C: <5 P: 20

**Porosity (%):** Point Count: 24%

Measured: --

**Perm (mD):** --

**Isotopes (‰ ):** $\delta^{18}O$: --

$\delta^{13}C$: --

Other:

**Thin Section Map**

**Oriented thin section:** ☐ Yes ☑ No

**Orientation?:**

**Preparation** ☐ Thick ☐ Conventional ☑ Polished

**Stains:** ☐ Carbonate ☐ Plag ☐ Kspar

**Point Count:**

| Quartz | | | Plagioclase Feld. | | Alkali Feld. | | Lithics | | Misc. | Clay | Cement | | | | Porosity | | | | Total |
|---|---|---|---|---|---|---|---|---|---|---|---|---|---|---|---|---|---|---|---|
| mono | poly | mic/chert | intact | dissolved | intact | dissolved | opaque | sed | Grains | Matrix | spar | micrite | quartz | clay | inter | oversize | intra | micro | Points |
| 240 | 9 | 6 | 3 | 3 | 2 | 2 | 0 | 3 | 1 | 0 | 1 | 0 | 17 | 16 | 64 | 8 | 22 | 3 | 400 |
| 60% | 2% | 2% | 1% | 1% | 1% | 1% | 0% | 1% | 0% | 0% | 0% | 0% | 4% | 4% | 16% | 2% | 6% | 1% | |

**Cement:** (types, sequence) Some euhedral qtz overgrowths; some opaque grain coats and pore-fillers, very irregularly + sparsely distributed

**Comments:** Evidence of dissolving grains

Some polycrystalline quartz

Some kspar grains w/ associated clay: partially dissolved, but not highly so

Some plag grains -- not as common as kspar

**Sketches:**

## Sample #: 35A-1

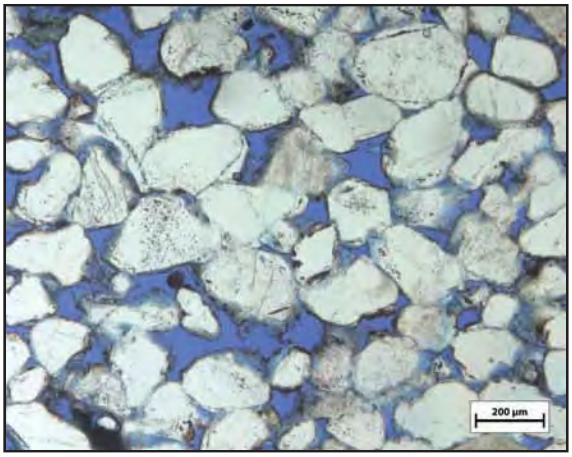
200 µm

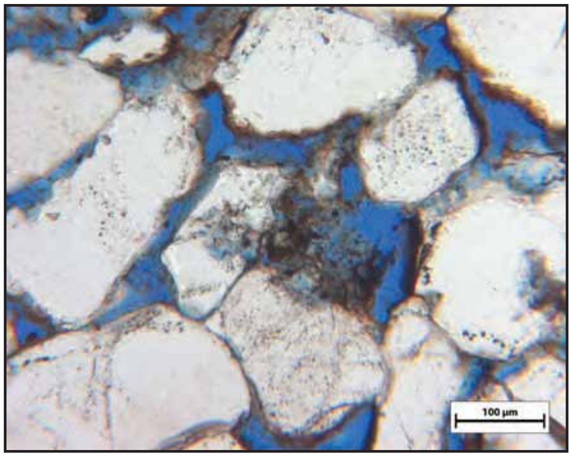
100 µm

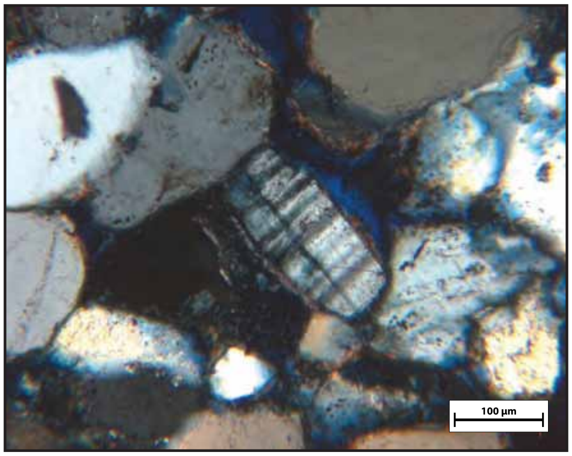
100 µm

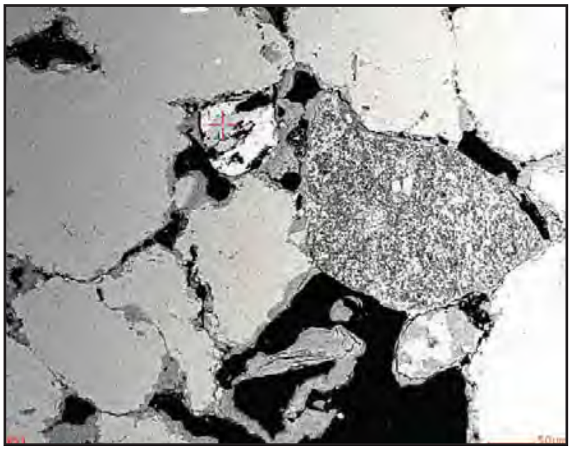

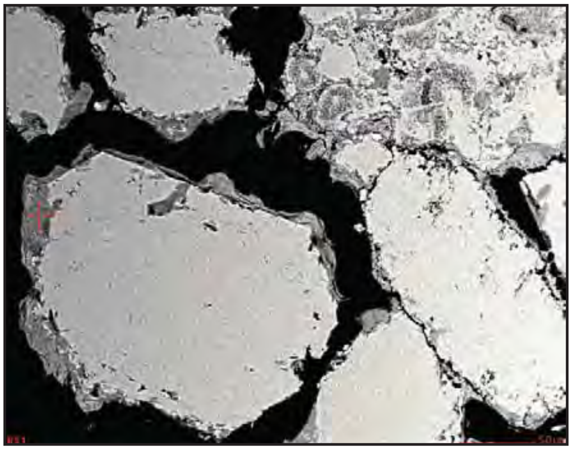

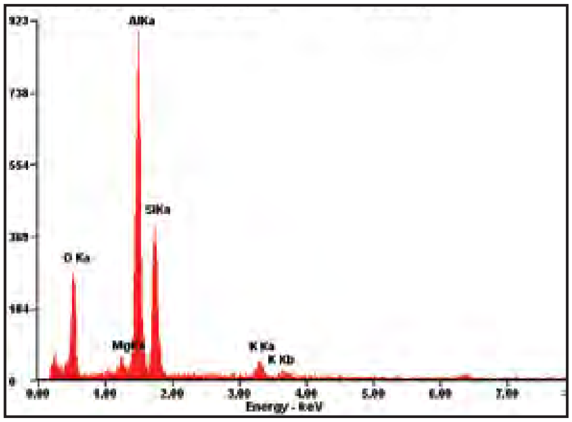
923
738
554
369
184
0
AlKa
SiKa
O Ka
MgKa
K Ka
K Kb
0.00
1.00
2.00
3.00
4.00
5.00
6.00
7.00
Energy - keV

**Sample #:** 35A-2

## Petrographic Summary

**Date:** 5/20/10

**Location Description:** Fault-distal Jms sand (north of mapping transparency) Visible in aerials in platform sand w/ large fracture sets, NE of travertine mound, above Jms2

**Field Trip:** ☑ April, '09 ☐ Oct., '09

**Formation:** Salt Wash

**Rock Type:** sandstone

**Grain Size:** 0.15-0.75 mm

**Grain Types:** quartz, kspar, plag, sed lithics

**F-M-C-P:** F: M: C: P:

**Porosity (%):** Point Count: --

Measured: --

**Perm (mD):** --

**Isotopes (‰):** $\delta^{18}O$: --

$\delta^{13}C$: --

Other: --

**Thin Section Map**

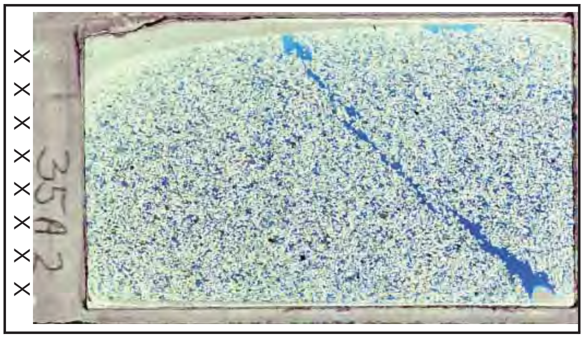

**Oriented thin section:** ☐ Yes ☑ No

**Orientation?:**

**Preparation** ☐ Thick ☑ Conventional ☐ Polished

**Stains:** ☑ Carbonate ☐ Plag ☑ Kspar

**Point Count:**

**Cement:** (types, sequence) No calcite. Lots of euhedral quartz cement Some clay (brown/black opaque) cement, especially around oversize pores.

**Comments:** NO CALCITE
Some feldspars, often quite dissolved.
Very high porosity; lots of oversize pores and heavily dissolved (green spongy) grains. Clay cement is usually associated with these partially or totally dissolved grains.

**Sketches:**

**Sample #: 35A-2**

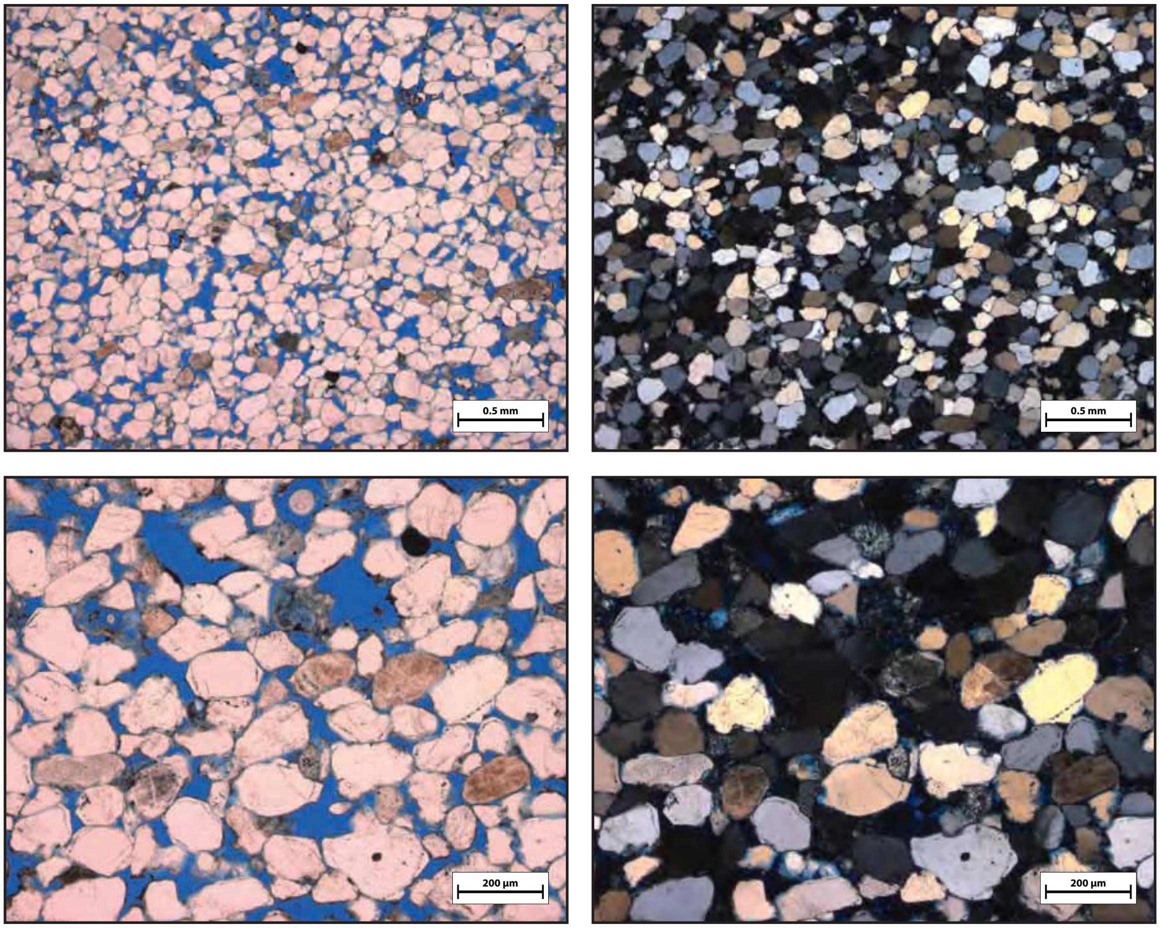

**Sample #:** 35B-1

## Petrographic Summary

**Date:** 5/20/10

**Location Description:** fault-distal conglomerate from out of aerial coverage -- see notes to Station 35 (E:0577141 N:4310316)

**Field Trip:** ☑ April, '09 ☐ Oct., '09

**Formation:** Jms4

**Rock Type:** conglomerate/coarse sand

**Grain Size:** 0.30-1.20mm and larger

**Grain Types:** qtz, chalcedony, chert, poly qtz

**F-M-C-P:** F: 70 M: 0 C: 15 P: 10-15

**Porosity (%):** Point Count: 7%

Measured: --

**Perm (mD):** --

**Isotopes (‰):** $\delta^{18}O$: --

$\delta^{13}C$: --

Other: --

**Thin Section Map**

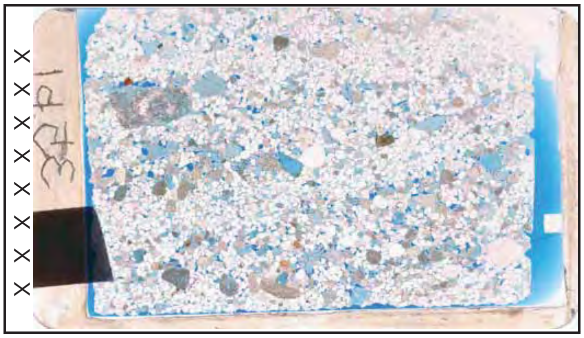

**Oriented thin section:** ☐ Yes ☑ No

**Orientation?:**

**Preparation**

☐ Thick
☐ Conventional
☑ Polished

**Stains:**
☐ Carbonate
☐ Plag ☐ Kspar

**Point Count:**

| Quartz | | | Plagioclase Feld. | | Alkali Feld. | | Lithics | | Misc. | Clay | Cement | | | | Porosity | | | | Total |
|---|---|---|---|---|---|---|---|---|---|---|---|---|---|---|---|---|---|---|---|
| mono | poly | mic/chert | intact | dissolved | intact | dissolved | opaque | sed | Grains | Matrix | spar | micrite | quartz | clay | inter | oversize | intra | micro | Points |
| 160 | 15 | 45 | 0 | 0 | 0 | 0 | 1 | 42 | 0 | 0 | 4 | 18 | 73 | 13 | 9 | 0 | 9 | 11 | 400 |
| 40% | 4% | 11% | 0% | 0% | 0% | 0% | 0% | 11% | 0% | 0% | 1% | 5% | 18% | 3% | 2% | 0% | 2% | 3% | |

**Cement:** (types, sequence)

Very interesting isopachous qtz cements -- occurs in
multiple generations
Some calcite

**Comments:**

Many cement-filled fractures in grains
Well rounded grains
Some splotchy clay distribution
No obvious feldspar grains
Some grains with calcite-filled veins
isopach qtz cements all pale blue, might indicate micropor;
sed grains commonly micrite, sometimes dissolved; a few
giant sed grains account for almost half of sed counts

**Sketches:**

**Sample #: 35B-1**

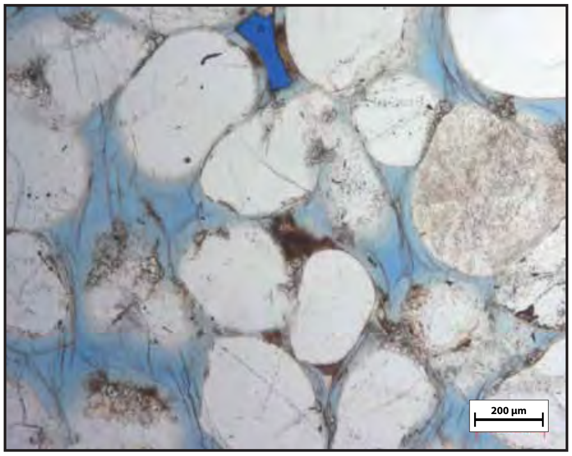
200 µm

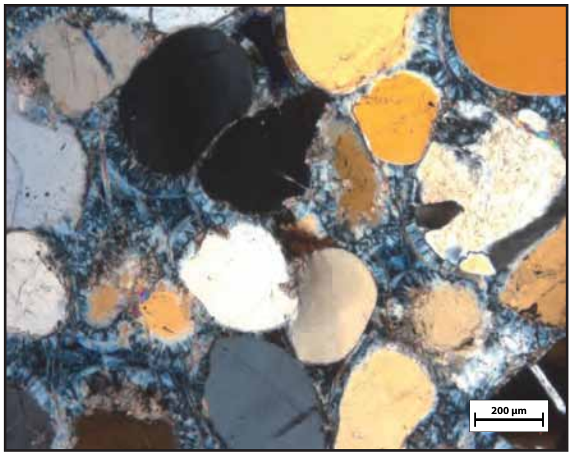
200 µm


100 µm

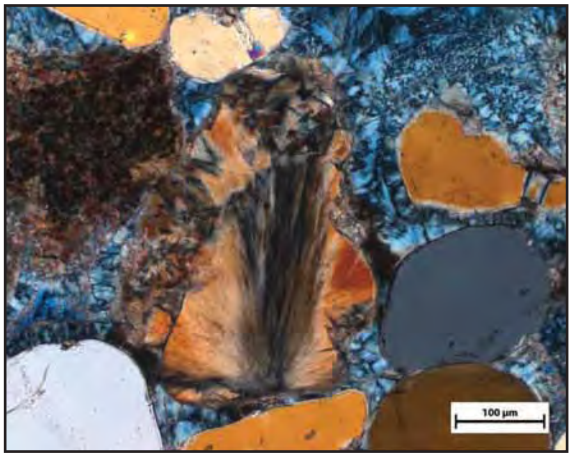
100 µm

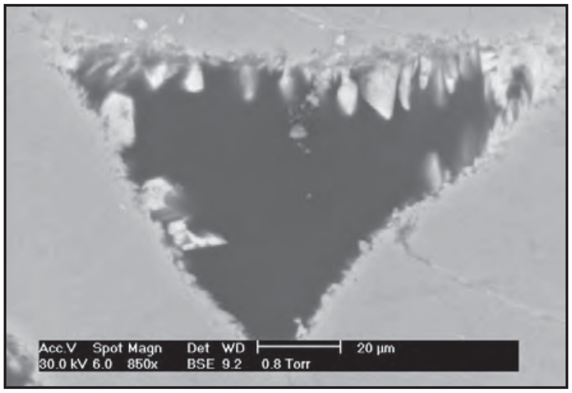
Acc.V Spot Magn Det WD 20 µm
30.0 kV 6.0 850x BSE 9.2 0.8 Torr

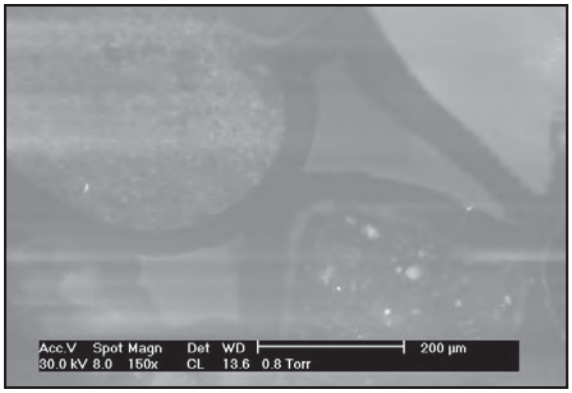
Acc.V Spot Magn Det WD 200 µm
30.0 kV 8.0 150x CL 13.6 0.8 Torr

**Sample #:** 35B-2

## Petrographic Summary

**Date:** 5/20/10

**Location Description:** fault-distal conglomerate from out of aerial coverage -- see notes to Station 35 (E:0577141 N:4310316)

**Field Trip:** ☑ April, '09 ☐ Oct., '09

**Formation:** Jms4

**Rock Type:** conglomerate/coarse sand

**Grain Size:** 0.30-1.20mm and larger

**Grain Types:** qtz, chert, chalcedony

**F-M-C-P:** F: M: C: P:

**Porosity (%):** Point Count: --

Measured: --

**Perm (mD):** --

**Isotopes (‰ ):** $\delta^{18}O$: --

$\delta^{13}C$: --

Other: --

### Thin Section Map

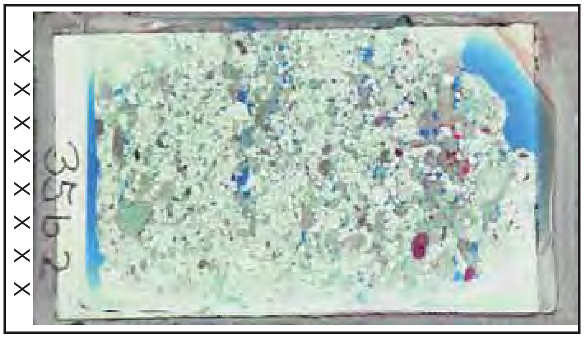

**Oriented thin section:** ☐ Yes ☑ No

**Orientation?:**

**Preparation** ☐ Thick ☑ Conventional ☐ Polished

**Stains:** ☑ Carbonate ☐ Plag ☑ Kspar

**Point Count:**

**Cement:** (types, sequence) Isopachous qtz overgrowths (microcrystalline) w/ some pore-filling spar

**Comments:** No feldspars

Some spar growth AFTER qtz overgrowths

Some carbonate grains -- can be seen stained bright pink/red in the thin section scan above.

**Sketches:**

**Sample #: 35B-2**

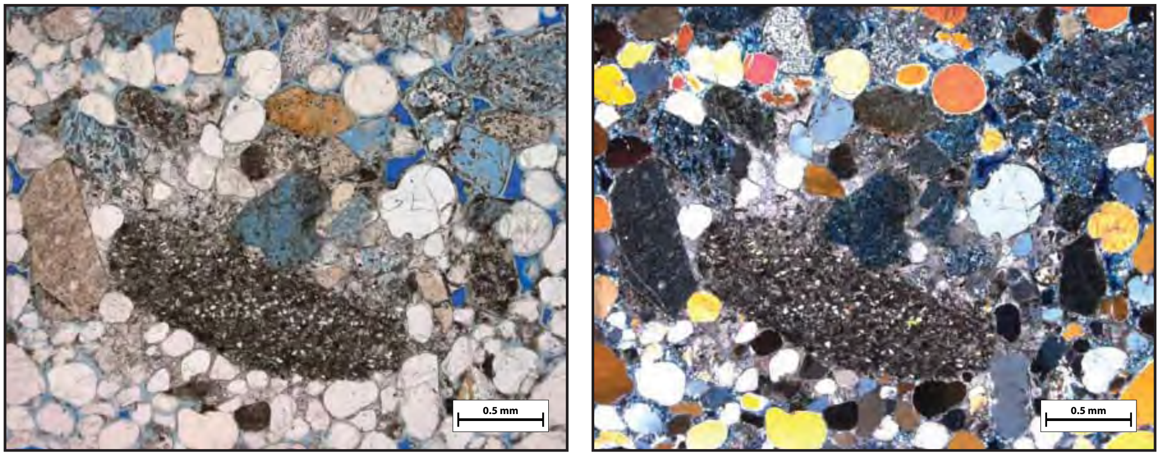

**Sample #:** 36A-1

## Petrographic Summary

**Date:** 11/ 3 /09

**Location Description:** Well-cemented yellow conglomerate from above altered spot east of travertine mound

**Field Trip:** ☑ April, '09 ☐ Oct., '09

**Formation:** Jms6

**Rock Type:** conglomerate

**Grain Size:** up to a centimeter across

**Grain Types:** chert, quartz

**F-M-C-P:** F: 60 M: 22 C: 15 P: <3

**Porosity (%):** Point Count:

Measured: --

**Perm (mD):** --

**Isotopes (‰ ):** $\delta^{18}O$: --

$\delta^{13}C$: --

Other: --

**Thin Section Map**

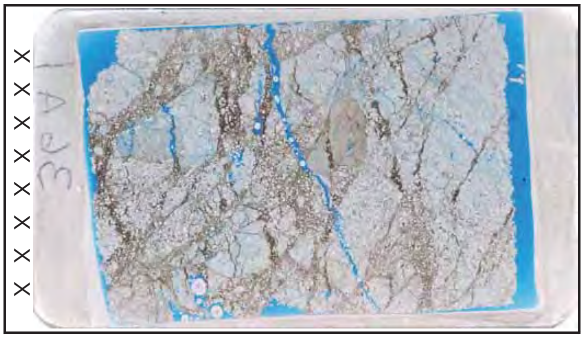

**Oriented thin section:** ☐ Yes ☑ No

**Orientation?:**

**Preparation** ☐ Thick ☐ Conventional ☑ Polished

**Stains:** ☐ Carbonate ☐ Plag ☐ Kspar

**Point Count:**

**Cement:** (types, sequence) Clay-ey (yellow in outcrop; brown in plane light) frac- and pore-filling cement

**Comments:** Hard in outcrop

Highly fractured grains

Interesting that 32A-2 has much smaller clasts but similar "cement"

**Sketches:**

**Sample #: 36A-1**

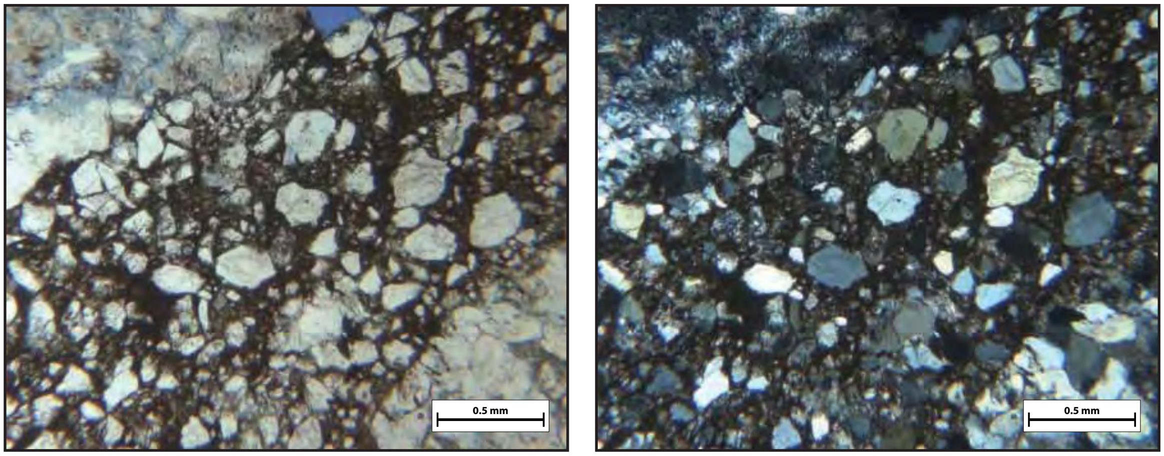

**Sample #:** 36A-2

## Petrographic Summary

**Date:** / /

**Location Description:** From vein-blasted, yellow-colored area of alteration 60 m directly east of travertine platform.

**Field Trip:** ☑ April, '09 ☐ Oct., '09

**Formation:** Jms6

**Rock Type:** mixed conglomerate & sand

**Grain Size:** 0.2-4.0 mm

**Grain Types:** quartz, chert

**F-M-C-P:** F: M: C: P:

**Porosity (%):** Point Count: --

Measured: --

**Perm (mD):** --

**Isotopes (‰ ):** $\delta^{18}O$: --

$\delta^{13}C$: --

Other: --

**Thin Section Map**

**Oriented thin section:** ☐ Yes ☑ No

**Orientation?:**

**Preparation** ☐ Thick ☑ Conventional ☐ Polished

**Stains:** ☐ Carbonate ☐ Plag ☐ Kspar

**Point Count:**

**Cement:** (types, sequence) pervasive micrite and clay mixture
some darker brown/opaque authigenic clay cement, but proportionally rare

**Comments:** Small grains are matrix-supported in a mixture of micrite and clay. Appears to be a similar lithology to samples from Station 71 and some from Station 17 -- possibly sand and mud entrained in calcite at the surface while a travertine platform precipitated.
Very low porosity -- limited to fractures and a few small areas of partial dissolution.
Lots of chert, no feldspars

**Sketches:**

## Sample #: 36A-2

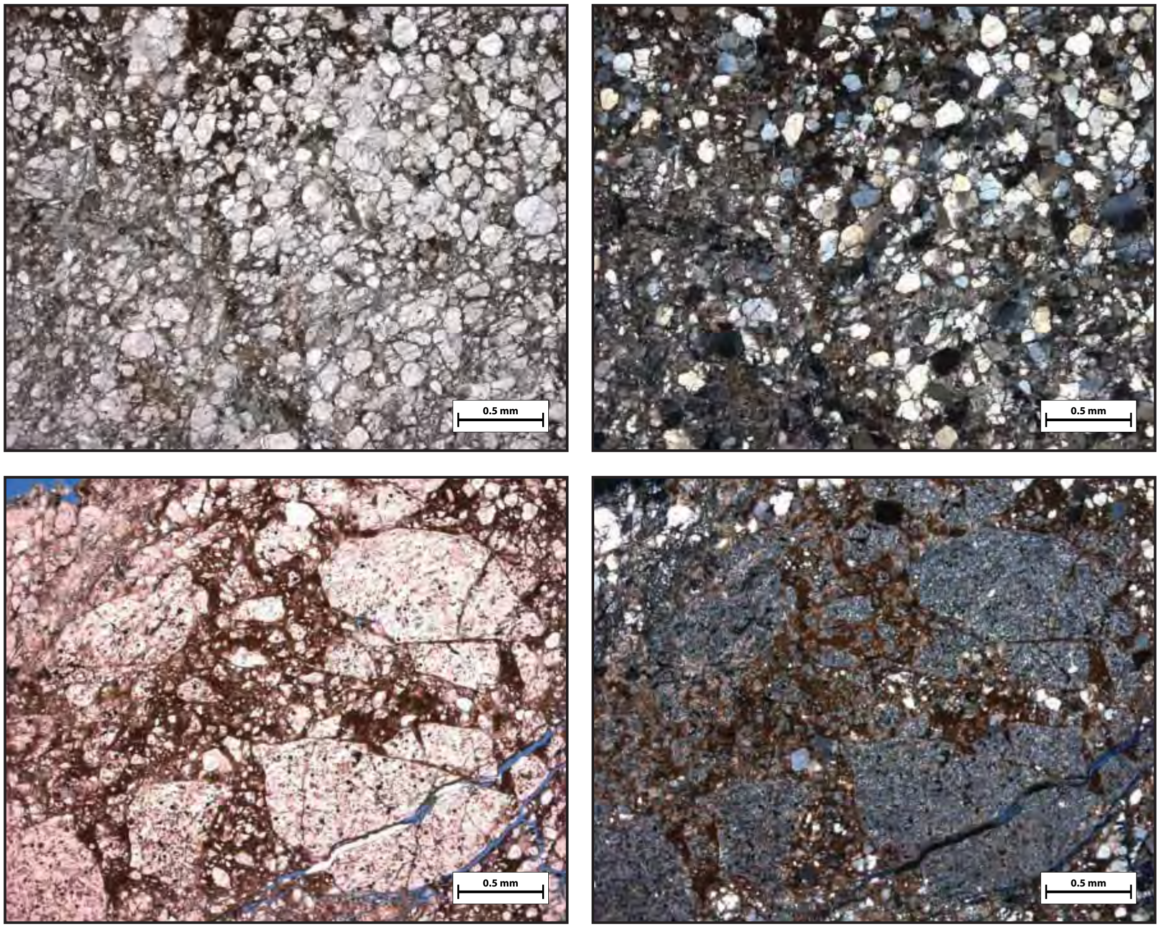

**Sample #:** 71A

## Petrographic Summary

**Date:** 4/11/10

**Location Description:** Outcrop directly beneath travertine mound; silty, highly altered; off northeast corner of mound

**Field Trip:** ☐ April, '09 ☑ Oct., '09

**Formation:** Jms5

**Rock Type:** silty, grains afloat in micrite

**Grain Size:** 0.10-0.50mm, mostly at small end

**Grain Types:** qtz

**F-M-C-P:** F: 15 M: 84 C: 1 P: 0

**Porosity (%):** Point Count: --

Measured: 13.97% (??)

**Perm (mD):** too low to measure

**Isotopes (‰):** $\delta^{18}O$: -9.76 (PDB)

$\delta^{13}C$: 4.45 (PDB)

Other:

**Thin Section Map**

**Oriented thin section:** ☐ Yes ☑ No

**Orientation?:**

**Preparation**

☐ Thick
☑ Conventional
☑ Polished

**Stains:**

☐ Carbonate
☐ Plag ☐ Kspar

**Point Count:**

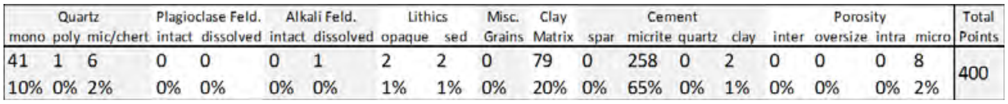

| Quartz | | | Plagioclase Feld. | | Alkali Feld. | | Lithics | | Misc. | Clay | Cement | | | | Porosity | | | | Total |
|---|---|---|---|---|---|---|---|---|---|---|---|---|---|---|---|---|---|---|---|
| mono | poly | mic/chert | intact | dissolved | intact | dissolved | opaque | sed | Grains | Matrix | spar | micrite | quartz | clay | inter | oversize | intra | micro | Points |
| 41 | 1 | 6 | 0 | 0 | 0 | 1 | 2 | 2 | 0 | 79 | 0 | 258 | 0 | 2 | 0 | 0 | 0 | 8 | 400 |
| 10% | 0% | 2% | 0% | 0% | 0% | 0% | 1% | 1% | 0% | 20% | 0% | 65% | 0% | 1% | 0% | 0% | 0% | 2% | |

**Cement:** (types, sequence) Micrite, mixed with a lot of clay-ey material

**Comments:** Some opaque(hematite?)-filled fracs: see photomicrographs
Don't be fooled by webby, linear dark zones: these are plucking zones, not a different cement.
Rare qtz grain-sized carbonate grains (microcrystalline)
Some grains took up yellow stain, but these look more like clay grains than kspar
This slide was destroyed when I tried to stain it.
Replacements were made (71A-2, 71A-3); slide shown = 71A-2

**Sketches:**

**Sample #: 71A**

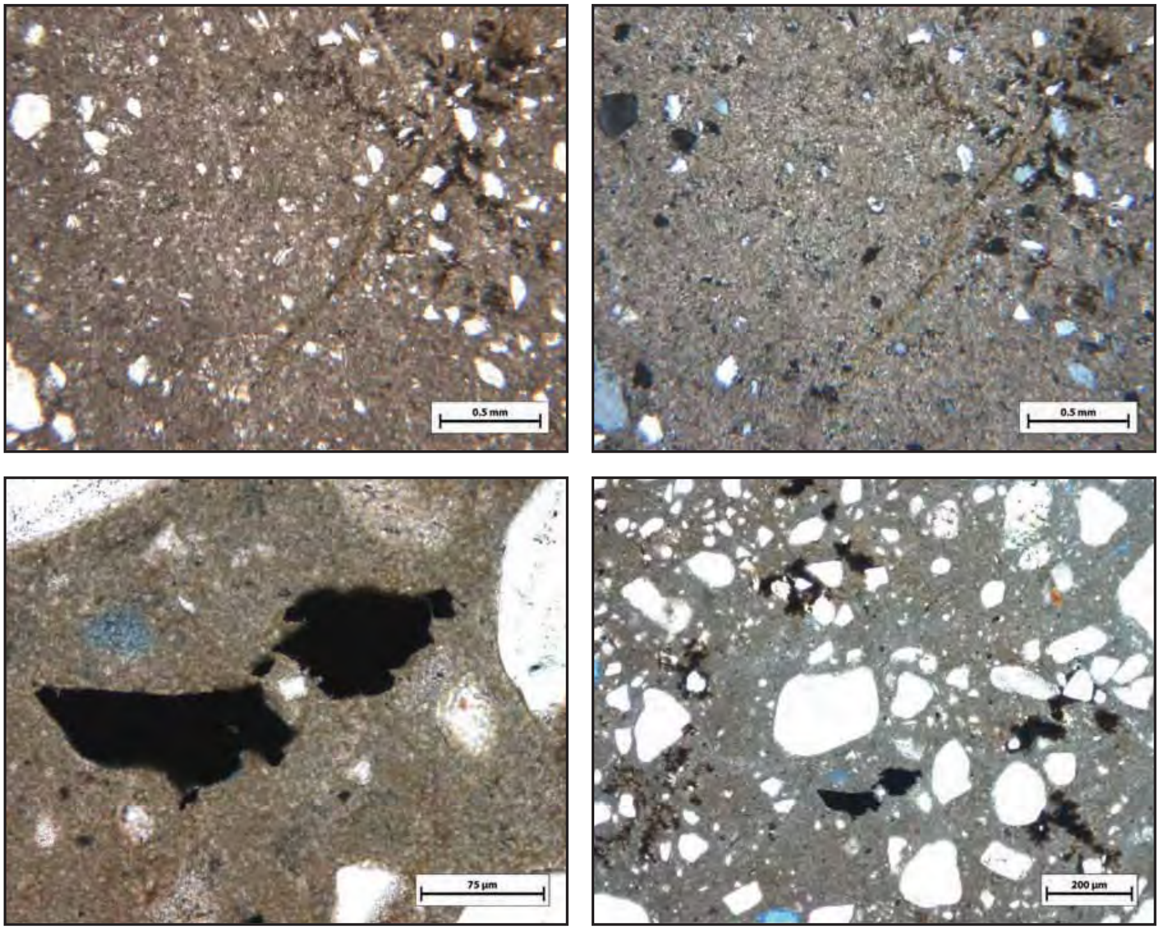

**Sample #:** 71B

## Petrographic Summary

**Date:** 5/ 1 /10

**Location Description:** Next to 71A (silty outcropping underneath travertine at northeast corner of mound)

**Field Trip:** ☐ April, '09 ☑ Oct., '09

**Formation:** Jms5? possibly travertine?

**Rock Type:** silty altered

**Grain Size:** matrix + quartz

**Grain Types:** silt-sized qtz + shaley matrix

**F-M-C-P:** F: M: C: P:

**Porosity (%):** Point Count: 0%

Measured: --

**Perm (mD):** --

**Isotopes (‰ ):** $\delta^{18}O$: -9.39 and -9.37 (PDB)

$\delta^{13}C$: 4.37 and 4.38 (PDB)

Other:

**Thin Section Map**

**Oriented thin section:** ☐ Yes ☑ No

**Orientation?:**

**Preparation** ☐ Thick ☑ Conventional ☐ Polished

**Stains:** ☑ Carbonate ☐ Plag ☑ Kspar

**Point Count:**

| Quartz | | | Plagioclase Feld. | | Alkali Feld. | | Lithics | | Misc. | Clay | Cement | | | | Porosity | | | | Total |
|---|---|---|---|---|---|---|---|---|---|---|---|---|---|---|---|---|---|---|---|
| mono | poly | mic/chert | intact | dissolved | intact | dissolved | opaque | sed | Grains | Matrix | spar | micrite | quartz | clay | inter | oversize | intra | micro | Points |
| 13 | 2 | 3 | 0 | 0 | 0 | 1 | 0 | 2 | 0 | 106 | 10 | 259 | 0 | 4 | 0 | 0 | 0 | 0 | 400 |
| 3% | 1% | 1% | 0% | 0% | 0% | 0% | 0% | 1% | 0% | 27% | 3% | 65% | 0% | 1% | 0% | 0% | 0% | 0% | |

**Cement:** micrite and spar

(types, sequence)

**Comments:** Largely red shaley-looking matrix; large part micrite Large spar-filled veins -- avoided during point counting. Some veins bordered by brown euhedral crystals that preceded spar development. Some fracs bordered by calcite (yellow transparent) and opaque xstals. Clay matrix has taken carbonate stain -- could be micrite? or just clay absorbing the stain? Think this formed at the surface w/ influx of allogenic fine-grained seds into carbonate precip

**Sketches:**

## Sample #: 71B

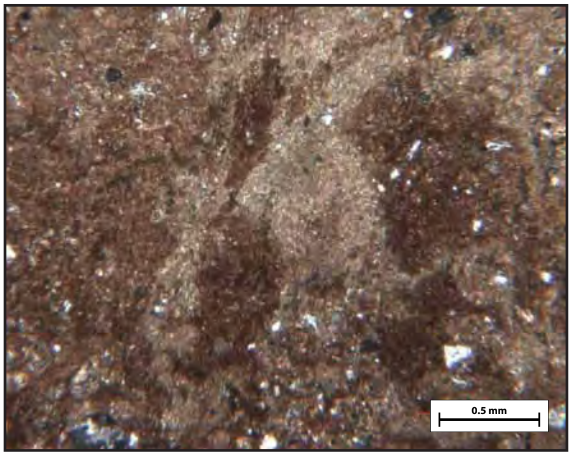

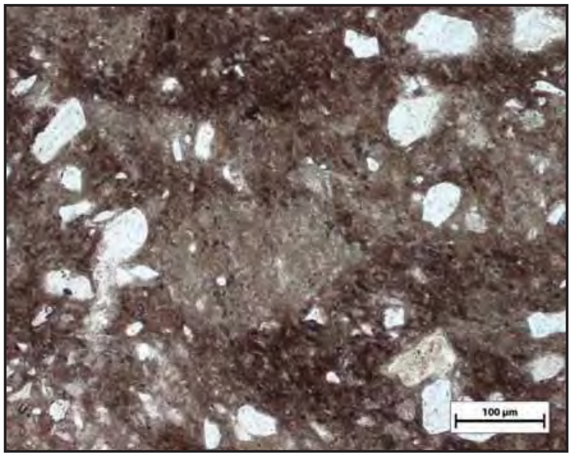

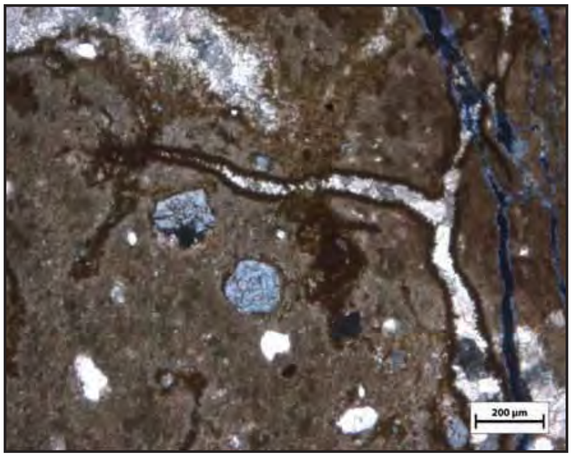

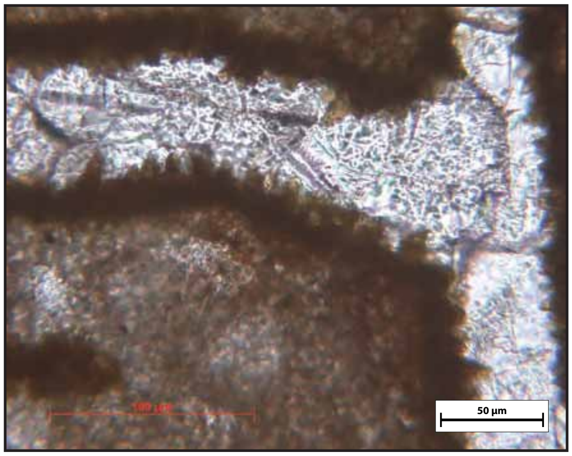

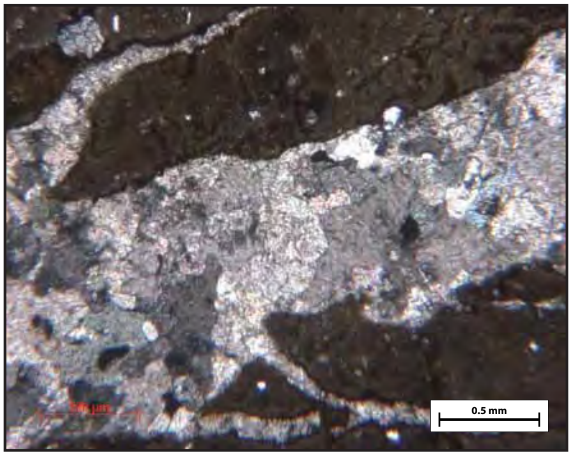

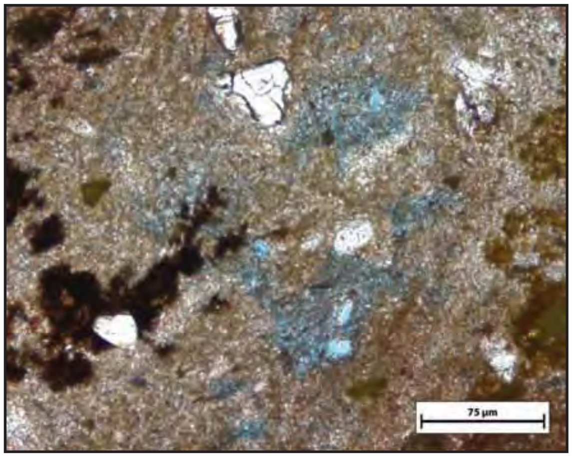

**Sample #:** 72A

## Petrographic Summary

**Date:** 1/12/11

**Location Description:** Red vein-blasted shale from immediately next to the travertine platform

**Field Trip:** ☐ April, '09 ☑ Oct., '09

**Formation:** Brushy Basin

**Rock Type:** Red shale with many veins

**Grain Size:** clay-sized

**Grain Types:** shale

**F-M-C-P:** F: M: C: P:

**Porosity (%):** Point Count: 15%

Measured: 19.2%

**Perm (mD):** 14.1 mD

**Isotopes (‰):** $\delta^{18}$O: -10.26 (PDB)

$\delta^{13}$C: 5.37 (PDB)

Other:

**Thin Section Map**

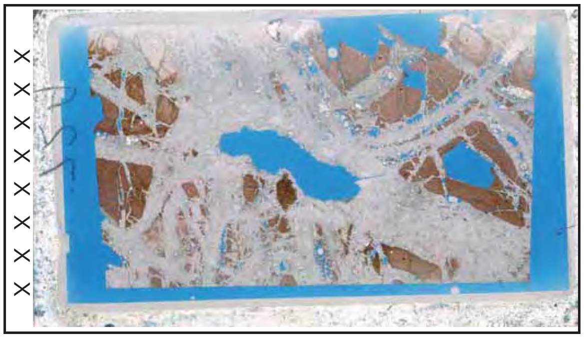

**Oriented thin section:** ☐ Yes ☑ No

**Orientation?:**

**Preparation** ☐ Thick ☑ Conventional ☐ Polished

**Stains:** ☐ Carbonate ☐ Plag ☐ Kspar

**Point Count:**

| Quartz | | | Plagioclase Feld. | | Alkali Feld. | | Lithics | | Misc. | Clay | Cement | | | | Porosity | | | | Total |
|---|---|---|---|---|---|---|---|---|---|---|---|---|---|---|---|---|---|---|---|
| mono | poly | mic/chert | intact | dissolved | intact | dissolved | opaque | sed | Grains | Matrix | spar | micrite | quartz | clay | inter | oversize | intra | micro | Points |
| 0 | 0 | 0 | 0 | 0 | 0 | 0 | 0 | 0 | 0 | 45 | 297 | 0 | 0 | 0 | 0 | 58 | 0 | 0 | 400 |
| 0% | 0% | 0% | 0% | 0% | 0% | 0% | 0% | 0% | 0% | 11% | 74% | 0% | 0% | 0% | 0% | 15% | 0% | 0% | |

**Cement:** (types, sequence) Massive spar cement (more spar than shale in this thin section)

**Comments:** Possibly some tiny (~0.001) quartz grains mixed in with shale. All counted as shale, though. Represented in point counting as "clay matrix."

Some very fine, jagged and spar-crystal-cutting clay-ey-looking lines through spar may be fracs that received small clay deposit before being filled in with more spar

**Sketches:**

**Sample #: 72A**

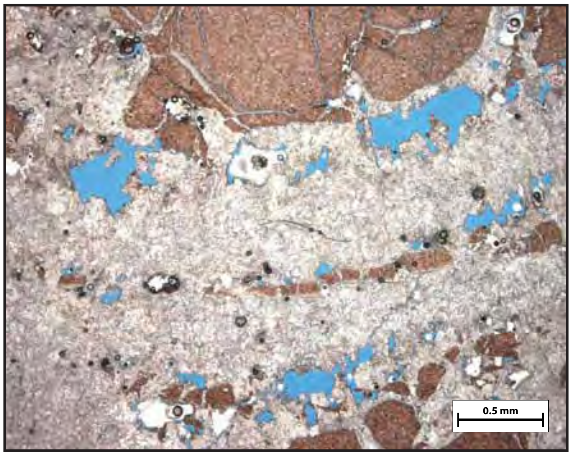

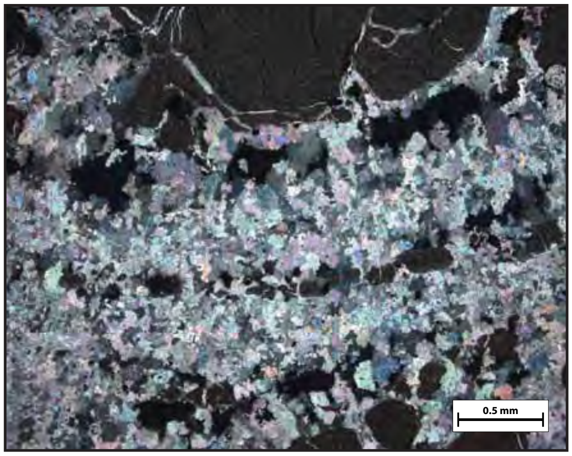

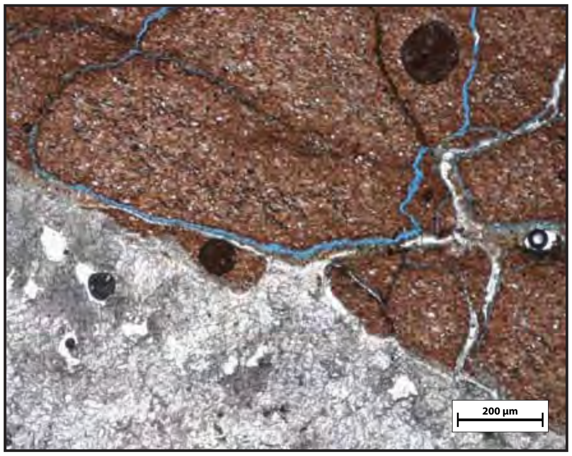

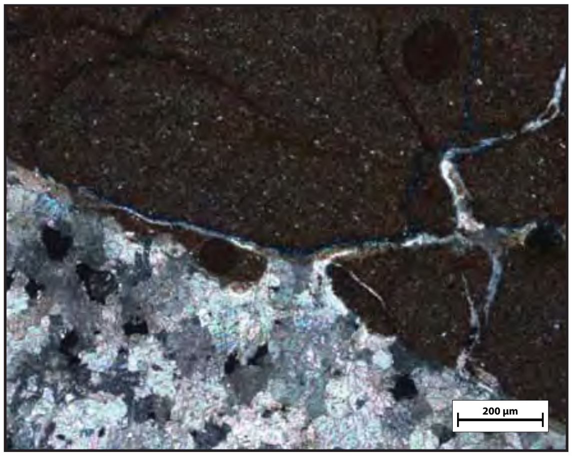

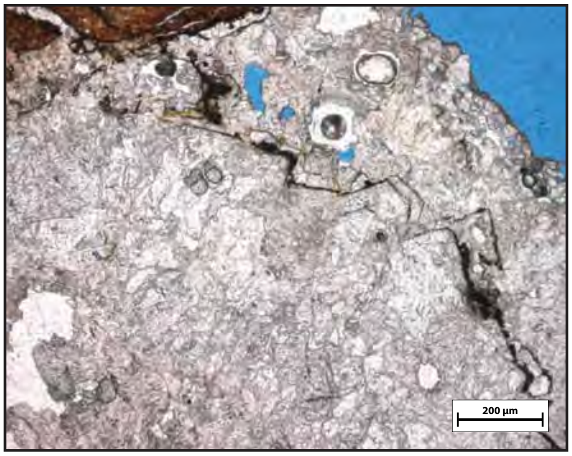

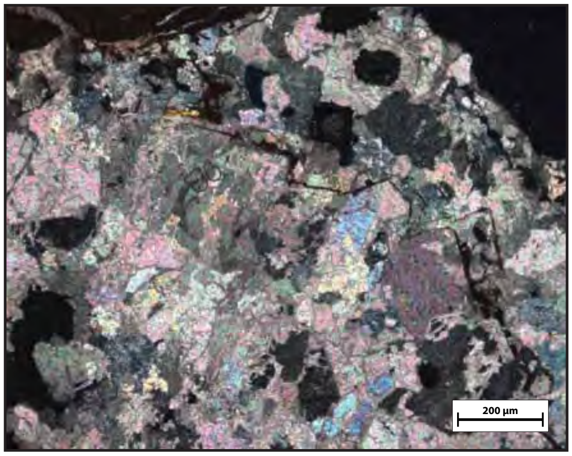

**Sample #:** 72B

## Petrographic Summary

**Date:** 1/11/11

**Location Description:** This is a sample from the travertine platform itself

**Field Trip:** ☐ April, '09 ☑ Oct., '09

**Formation:** Quaternary travertine

**Rock Type:** travertine

**Grain Size:** clay to pebble

**Grain Types:** mixed qtz + sed grains

**F-M-C-P:** F: M: C: P:

**Porosity (%):** Point Count: 5%

Measured: 12.51%

**Perm (mD):** too low for machine

**Isotopes (‰ ):** $\delta^{18}$O: -9.28 (PDB)

$\delta^{13}$C: 4.80 (PDB)

Other:

**Thin Section Map**

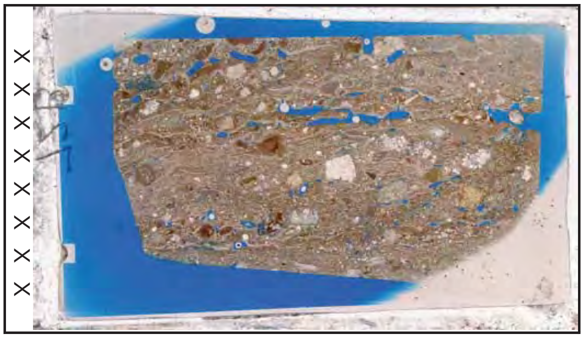

**Oriented thin section:** ☐ Yes ☑ No

**Orientation?:**

**Preparation** ☐ Thick ☑ Conventional ☐ Polished

**Stains:** ☐ Carbonate ☐ Plag ☐ Kspar

**Point Count:**

| Quartz | | | Plagioclase Feld. | | Alkali Feld. | | Lithics | | Misc. | Clay | Cement | | | | Porosity | | | | Total |
|---|---|---|---|---|---|---|---|---|---|---|---|---|---|---|---|---|---|---|---|
| mono | poly | mic/chert | intact | dissolved | intact | dissolved | opaque | sed | Grains | Matrix | spar | micrite | quartz | clay | inter | oversize | intra | micro | Points |
| 38 | 0 | 30 | 0 | 0 | 0 | 0 | 0 | 23 | 0 | 125 | 7 | 149 | 0 | 10 | 14 | 0 | 0 | 4 | 400 |
| 10% | 0% | 8% | 0% | 0% | 0% | 0% | 0% | 6% | 0% | 31% | 2% | 37% | 0% | 3% | 4% | 0% | 0% | 1% | |

**Cement:** (types, sequence) Micrite mixed with clay matrix

**Comments:** Compare to Sample X. I think matrix is composed of carbonate that was precipitating at the surface while allogenic sediment washed into it and was included in the agglomerate.

**Sketches:**

**Sample #: 72B**

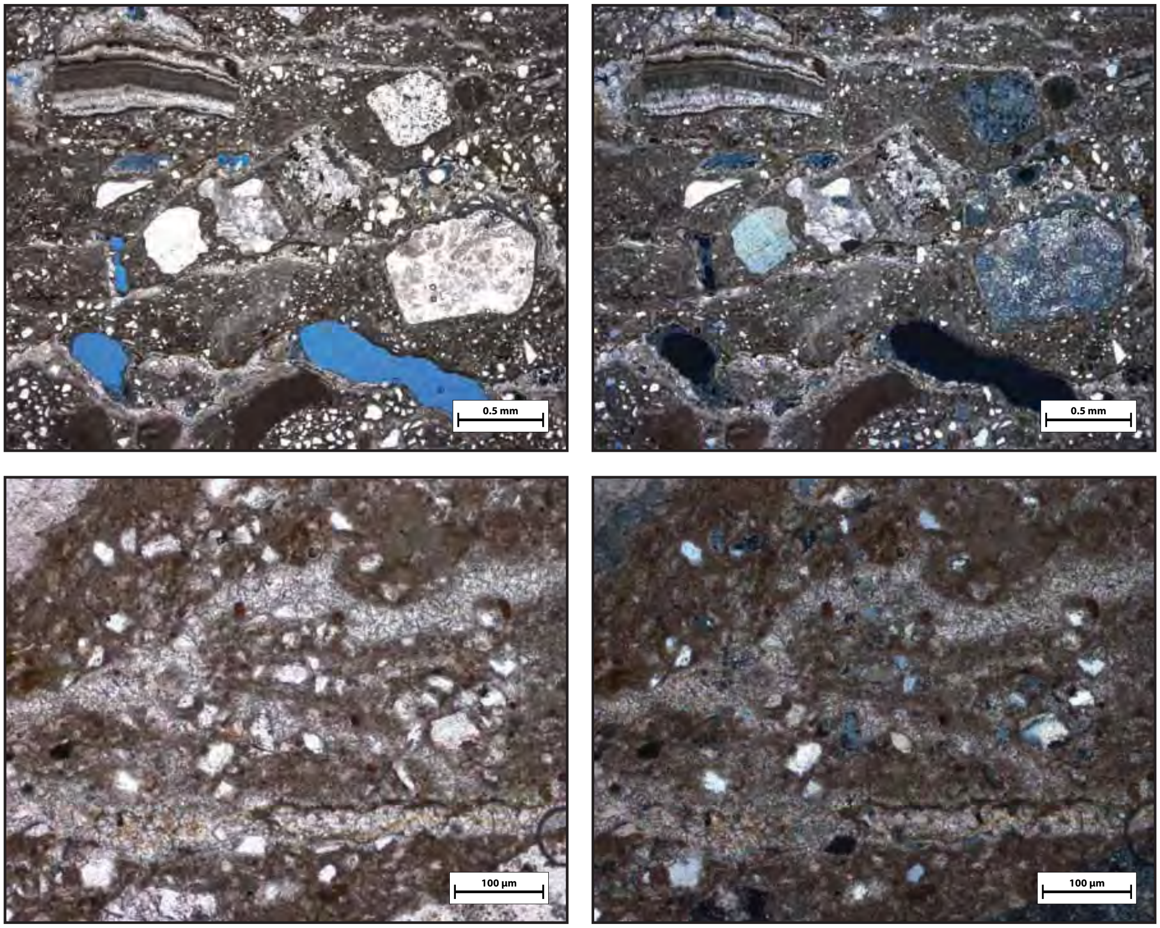

**Sample #:** 73

## Petrographic Summary

**Date:** 4/21/10

**Location Description:** sand at west extension of travertine mound (NOT overhanging ravine)

**Field Trip:** ☐ April, '09 ☑ Oct., '09

**Formation:** Jms5?

**Rock Type:** sand-floating-in-clay

**Grain Size:** 0.1-0.4 mm

**Grain Types:** quartz

**F-M-C-P:** F: M: C: P:

**Porosity (%):** Point Count: 0%

Measured: 13.53% - 15.15%

**Perm (mD):** 0.8 - 4.9 mD

**Isotopes (‰):** $\delta^{18}O$: -11.55 (PDB)

$\delta^{13}C$: 3.78 (PDB)

Other:

**Thin Section Map**

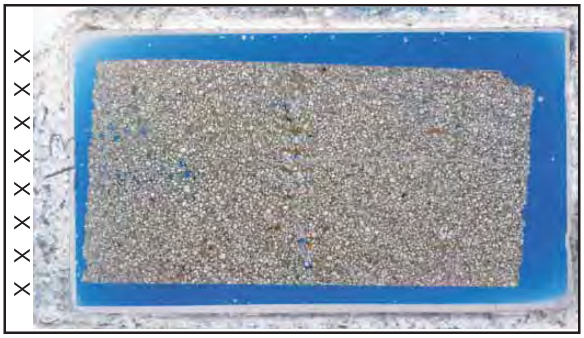

**Oriented thin section:** ☐ Yes ☑ No

**Orientation?:**

**Preparation** ☐ Thick ☑ Conventional ☐ Polished

**Stains:** ☑ Carbonate ☐ Plag ☑ Kspar

**Point Count:**

| Quartz | | | Plagioclase Feld. | | Alkali Feld. | | Lithics | | Misc. | Clay | Cement | | | | Porosity | | | | Total |
|---|---|---|---|---|---|---|---|---|---|---|---|---|---|---|---|---|---|---|---|
| mono | poly | mic/chert | intact | dissolved | intact | dissolved | opaque | sed | Grains | Matrix | spar | micrite | quartz | clay | inter | oversize | intra | micro | Points |
| 139 | 4 | 8 | 0 | 1 | 0 | 0 | 0 | 0 | 1 | 133 | 0 | 108 | 0 | 6 | 0 | 0 | 0 | 0 | 400 |
| 35% | 1% | 2% | 0% | 0% | 0% | 0% | 0% | 0% | 0% | 33% | 0% | 27% | 0% | 2% | 0% | 0% | 0% | 0% | |

**Cement:** (types, sequence) Lot of clay-ey matrix

**Comments:**
Altered sample, heavy intergranular micrite matrix
Very small amount of microporosity
Like Sample 71, matrix picks up stain -- could be micrite
Several calcite GRAINS
A few plagioclase grains
Possible rings around grains -- maybe image w/ CL?
Look at Sample X for possible genetic history -- grains
wash into micrite/clay matrix, become trapped by precip.

**Sketches:**

## Sample #: 73

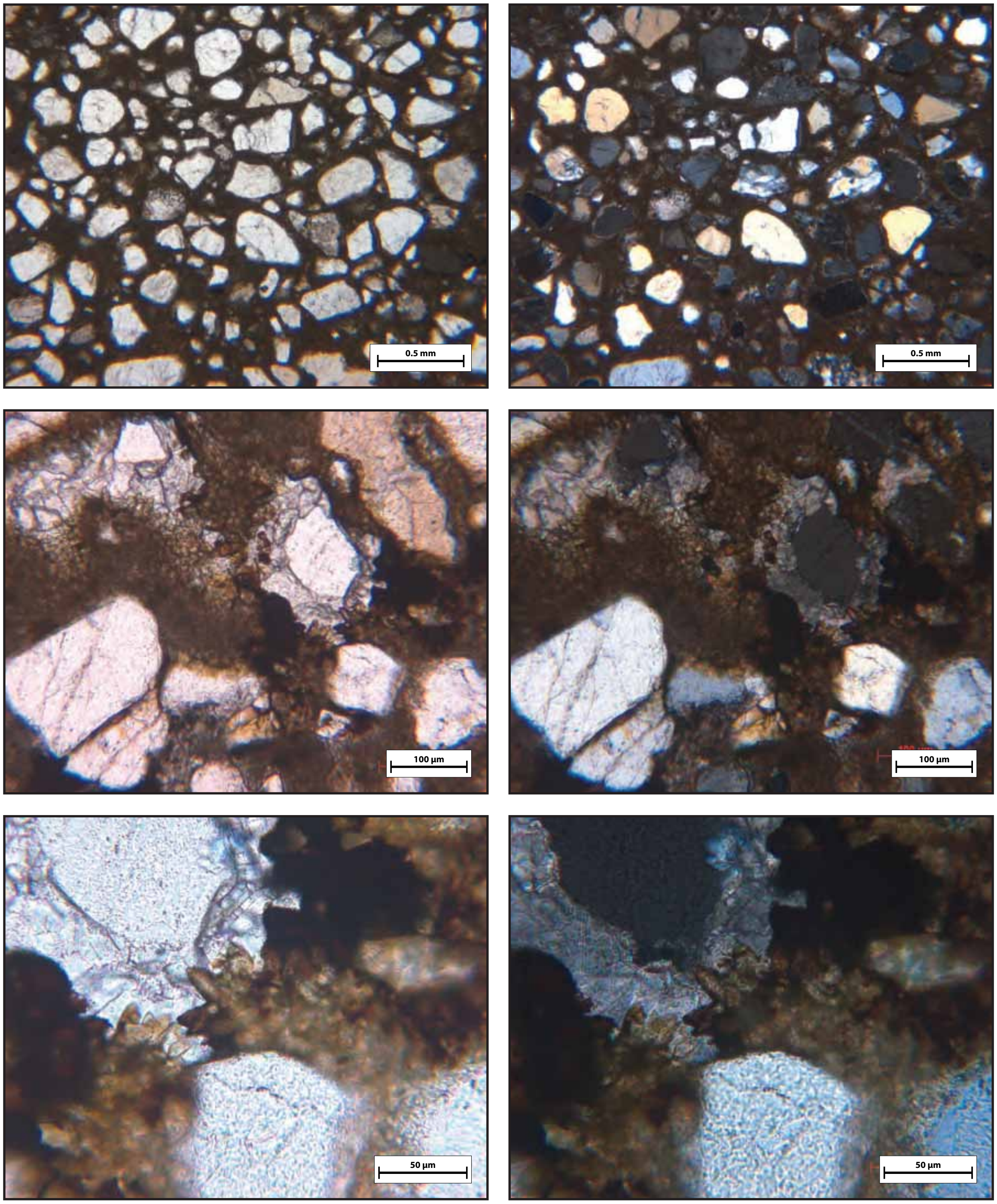

**Sample #:** 74

## Petrographic Summary

**Date:** 4/18/10

**Location Description:** Sand bridge extending off the west end of the travertine platform

**Field Trip:** ☐ April, '09 ☑ Oct., '09

**Formation:** Jms5

**Rock Type:** altered sandstone

**Grain Size:** 0.35mm

**Grain Types:** mostly quartz

**F-M-C-P:** F: M: C: P:

**Porosity (%):** Point Count: 11%

Measured: 24.35%

**Perm (mD):** 310.2 mD

**Isotopes (‰):** $\delta^{18}O$: -11.23 and -11.15 (PDB)

$\delta^{13}C$: 0.05 and 0.34 (PDB)

Other:

**Thin Section Map**

**Oriented thin section:** ☐ Yes ☑ No

**Orientation?:**

**Preparation**

☐ Thick
☑ Conventional
☐ Polished

**Stains:**
☑ Carbonate
☐ Plag ☑ Kspar

**Point Count:**

| Quartz | | | Plagioclase Feld. | | Alkali Feld. | | Lithics | | Misc. | Clay | Cement | | | | Porosity | | | | Total |
|---|---|---|---|---|---|---|---|---|---|---|---|---|---|---|---|---|---|---|---|
| mono | poly | mic/chert | intact | dissolved | intact | dissolved | opaque | sed | Grains | Matrix | spar | micrite | quartz | clay | inter | oversize | intra | micro | Points |
| 223 | 5 | 9 | 0 | 0 | 1 | 1 | 0 | 1 | 0 | 0 | 65 | 34 | 0 | 16 | 40 | 0 | 4 | 1 | 400 |
| 56% | 1% | 2% | 0% | 0% | 0% | 0% | 0% | 0% | 0% | 0% | 16% | 9% | 0% | 4% | 10% | 0% | 1% | 0% | |

**Cement:** (types, sequence)

Very obvious stained calcite -- mostly pink, some darker, closer to purple (slightly ferroan)

**Comments:**

Few kspars; Some partially dissolved plag grains, signs of clay, rotten with porosity

Appears to have opaque clay mixed with micrite

Calcite spar between plag fragments indicates early grain breakup

Lots circumgranular porosity; some recycled qtz-cemented sandstone (sed. lithics)

Some ferroan calcite (only one hit during point count)

**Sketches:**

**Sample #: 74**

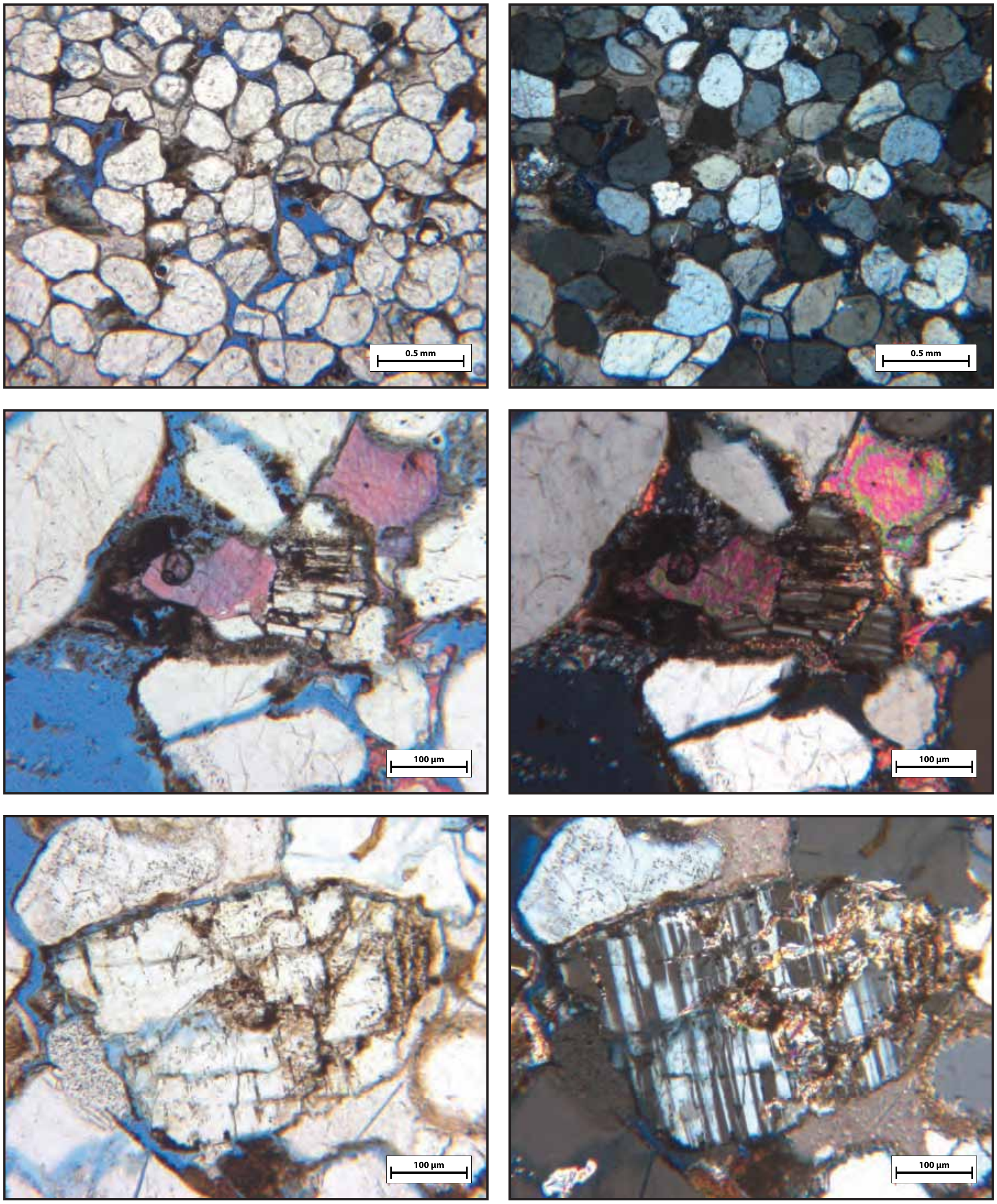

**Sample #:** 75-1

## Petrographic Summary

**Date:** 4/18/10

**Location Description:** Slope NW of travertine platform, below sand bridge coming off west end of platform

**Field Trip:** ☐ April, '09 ☑ Oct., '09

**Formation:** Jms5?

**Rock Type:** sand-in-clay-ey matrix

**Grain Size:** 0.30mm

**Grain Types:** quartz, some kspars

**F-M-C-P:** F: M: C: P:

**Porosity (%):** Point Count: 0%

Measured: --

**Perm (mD):** --

**Isotopes (‰):** $\delta^{18}$O: -9.72 (PDB)

$\delta^{13}$C: 4.56 (PDB)

Other:

### Thin Section Map

**Oriented thin section:** ☐ Yes ☑ No

**Orientation?:**

**Preparation** ☐ Thick ☑ Conventional ☐ Polished

**Stains:** ☑ Carbonate ☐ Plag ☑ Kspar

**Point Count:**

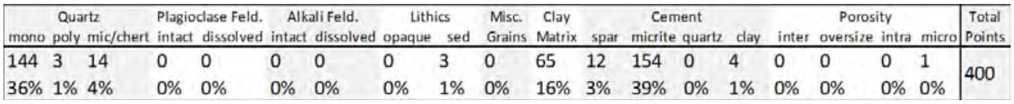

| Quartz | | | Plagioclase Feld. | | Alkali Feld. | | Lithics | | Misc. | Clay | Cement | | | | Porosity | | | | Total |
|---|---|---|---|---|---|---|---|---|---|---|---|---|---|---|---|---|---|---|---|
| mono | poly | mic/chert | intact | dissolved | intact | dissolved | opaque | sed | Grains | Matrix | spar | micrite | quartz | clay | inter | oversize | intra | micro | Points |
| 144 | 3 | 14 | 0 | 0 | 0 | 0 | 0 | 3 | 0 | 65 | 12 | 154 | 0 | 4 | 0 | 0 | 0 | 1 | 400 |
| 36% | 1% | 4% | 0% | 0% | 0% | 0% | 0% | 1% | 0% | 16% | 3% | 39% | 0% | 1% | 0% | 0% | 0% | 0% | |

**Cement:** (types, sequence)

spar-filled fracs

pervasive micrite matrix

patchy opaque clay cement, especially near dissolved grains

**Comments:**

Dense micrite matrix (stains well) w/ spar-filled fractures

Grains are matrix supported, floating in micrite, with occasional larger crystals of spar filling in a pore or fracture.

Some plag grains

Some kspar grains, slightly dissolved

**Sketches:**

**Sample #: 75-1**

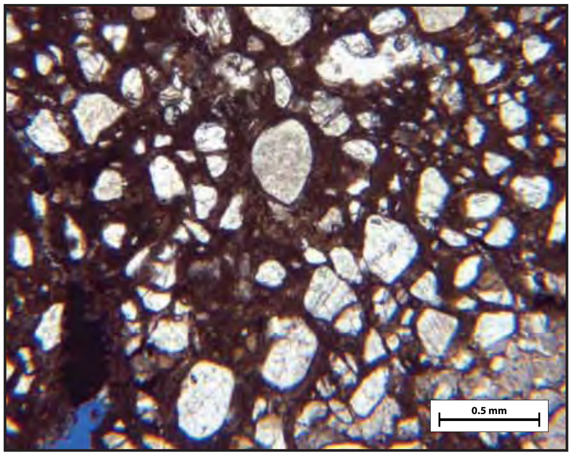

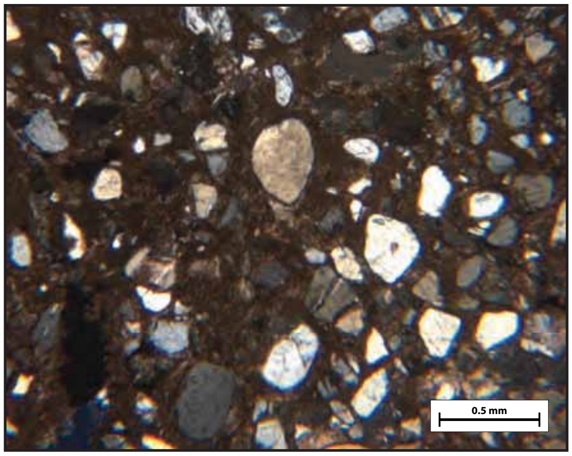

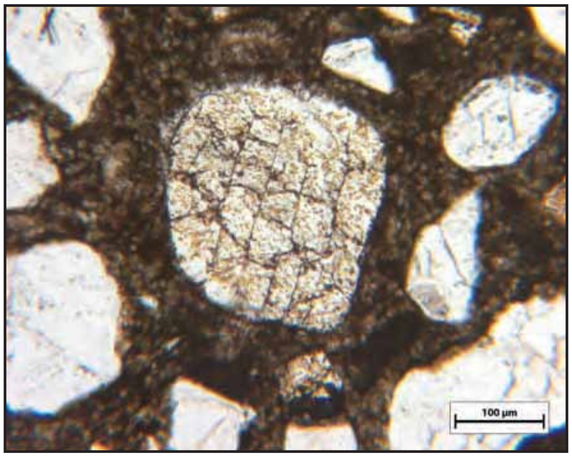

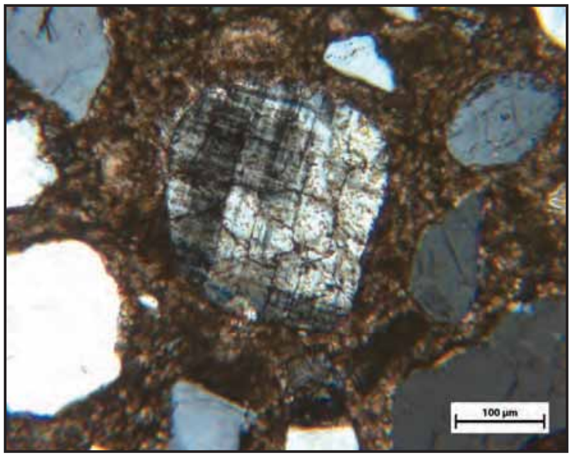

**Sample #:** 75-2

## Petrographic Summary

**Date:** 4/18/10

**Location Description:** Slope NW of travertine platform, below sand bridge coming off west end of platform

**Field Trip:** ☐ April, '09 ☑ Oct., '09

**Formation:** Jms5?

**Rock Type:** sand-in-clayey-matrix

**Grain Size:** 0.30 mm

**Grain Types:** mostly quartz

**F-M-C-P:** F: M: C: P:

**Porosity (%):** Point Count: 0%

Measured: --

**Perm (mD):** --

**Isotopes (‰ ):** $\delta^{18}$O: -9.72 (PDB)

$\delta^{13}$C: 4.56 (PDB)

Other:

**Thin Section Map**

**Oriented thin section:** ☐ Yes ☑ No

**Orientation?:**

**Preparation**

☐ Thick
☑ Conventional
☐ Polished

**Stains:**
☑ Carbonate
☐ Plag ☑ Kspar

**Point Count:**

| Quartz | | | Plagioclase Feld. | | Alkali Feld. | | Lithics | | Misc. | Clay | Cement | | | | Porosity | | | | Total |
|---|---|---|---|---|---|---|---|---|---|---|---|---|---|---|---|---|---|---|---|
| mono | poly | mic/chert | intact | dissolved | intact | dissolved | opaque | sed | Grains | Matrix | spar | micrite | quartz | clay | inter | oversize | intra | micro | Points |
| 116 | 6 | 4 | 0 | 0 | 1 | 0 | 0 | 1 | 0 | 30 | 8 | 218 | 0 | 16 | 0 | 0 | 0 | 0 | 400 |
| 29% | 2% | 1% | 0% | 0% | 0% | 0% | 0% | 0% | 0% | 8% | 2% | 55% | 0% | 4% | 0% | 0% | 0% | 0% | |

**Cement:** (types, sequence) Pervasive micrite; mixed with some clay matrix

**Comments:**
Parts of slide are rather plucked
Looks like there might be patches of microporosity
Some kspars
Pervasive matrix appears to be mixture of intergrown matrix micrite (takes stain, has high B in crossed polars) and clay cement (opaque brownish).

**Sketches:**

**Sample #: 75-2**

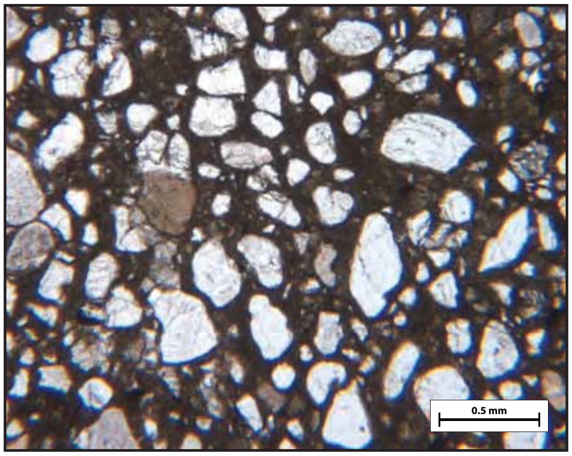

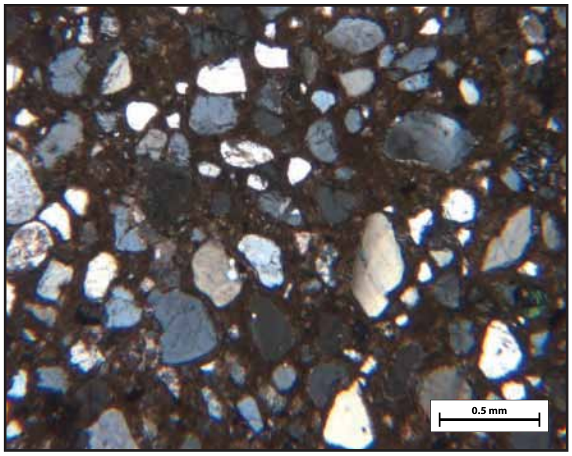

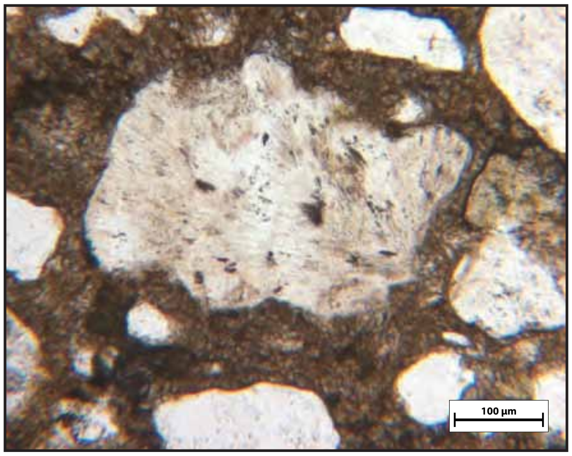

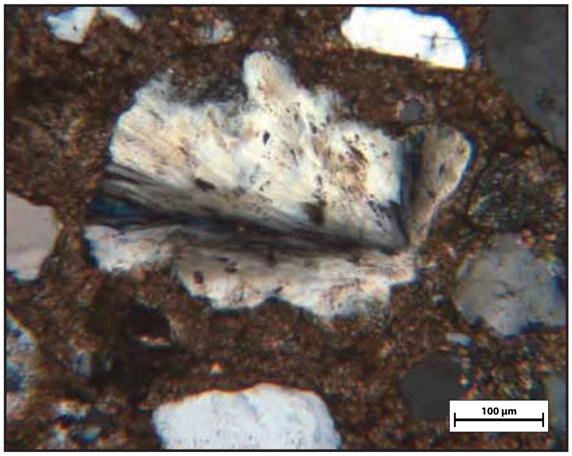

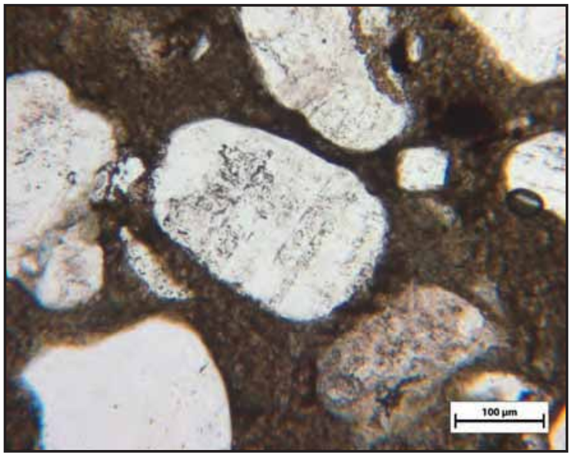

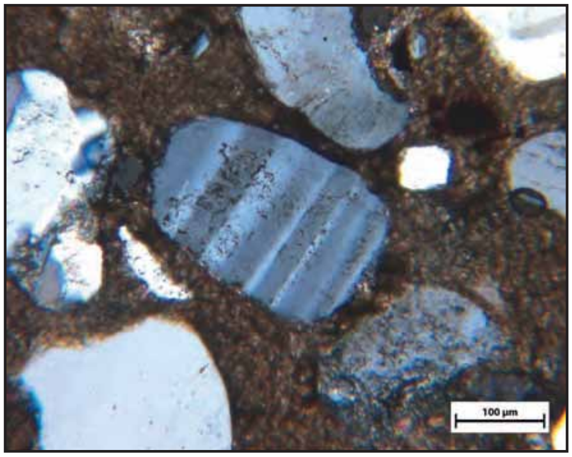

**Sample #:** 76

## Petrographic Summary

**Date:** 4/18/10

**Location Description:** Fault-overhanging ridge-y outcrop just N-NW of travertine mound, where major fault deflects north

**Field Trip:** ☐ April, '09 ☑ Oct., '09

**Formation:** Jms5

**Rock Type:** Sandstone

**Grain Size:** 0.1-0.5 mm

**Grain Types:** qtz, plag, kspar, lithics

**F-M-C-P:** F: M: C: P:

**Porosity (%):** Point Count: 1%

Measured: --

**Perm (mD):** --

**Isotopes (‰):** $\delta^{18}$O: -12.37 (PDB)

$\delta^{13}$C: -3.73 (PDB)

Other:

**Thin Section Map**

**Oriented thin section:** ☐ Yes ☑ No

**Orientation?:**

**Preparation**
☐ Thick
☑ Conventional
☐ Polished

**Stains:**
☑ Carbonate
☐ Plag ☑ Kspar

**Point Count:**

| Quartz | | | Plagioclase Feld. | | Alkali Feld. | | Lithics | | Misc. | Clay | Cement | | | | Porosity | | | | Total |
|---|---|---|---|---|---|---|---|---|---|---|---|---|---|---|---|---|---|---|---|
| mono | poly | mic/chert | intact | dissolved | intact | dissolved | opaque | sed | Grains | Matrix | spar | micrite | quartz | clay | inter | oversize | intra | micro | Points |
| 201 | 12 | 21 | 1 | 2 | 5 | 3 | 0 | 3 | 1 | 0 | 139 | 0 | 0 | 7 | 4 | 0 | 0 | 1 | 400 |
| 50% | 3% | 5% | 0% | 1% | 1% | 1% | 0% | 1% | 0% | 0% | 35% | 0% | 0% | 2% | 1% | 0% | 0% | 0% | |

**Cement:** (types, sequence)

Abundant, well-stained calcite spar (zoned pink [non-ferroan] and violet [ferroan])
Porosity completely filled with calcite

**Comments:**

Well-cemented
Rare feldspars (only saw one)... intact, not dissolved

Yellow stain taking on micro/poly-qtz? Grains don't look like kspar

"Micrite" looks like it's slide damage to the spar; added 10 points to spar count instead of micrite count

**Sketches:**

**Sample #: 76**

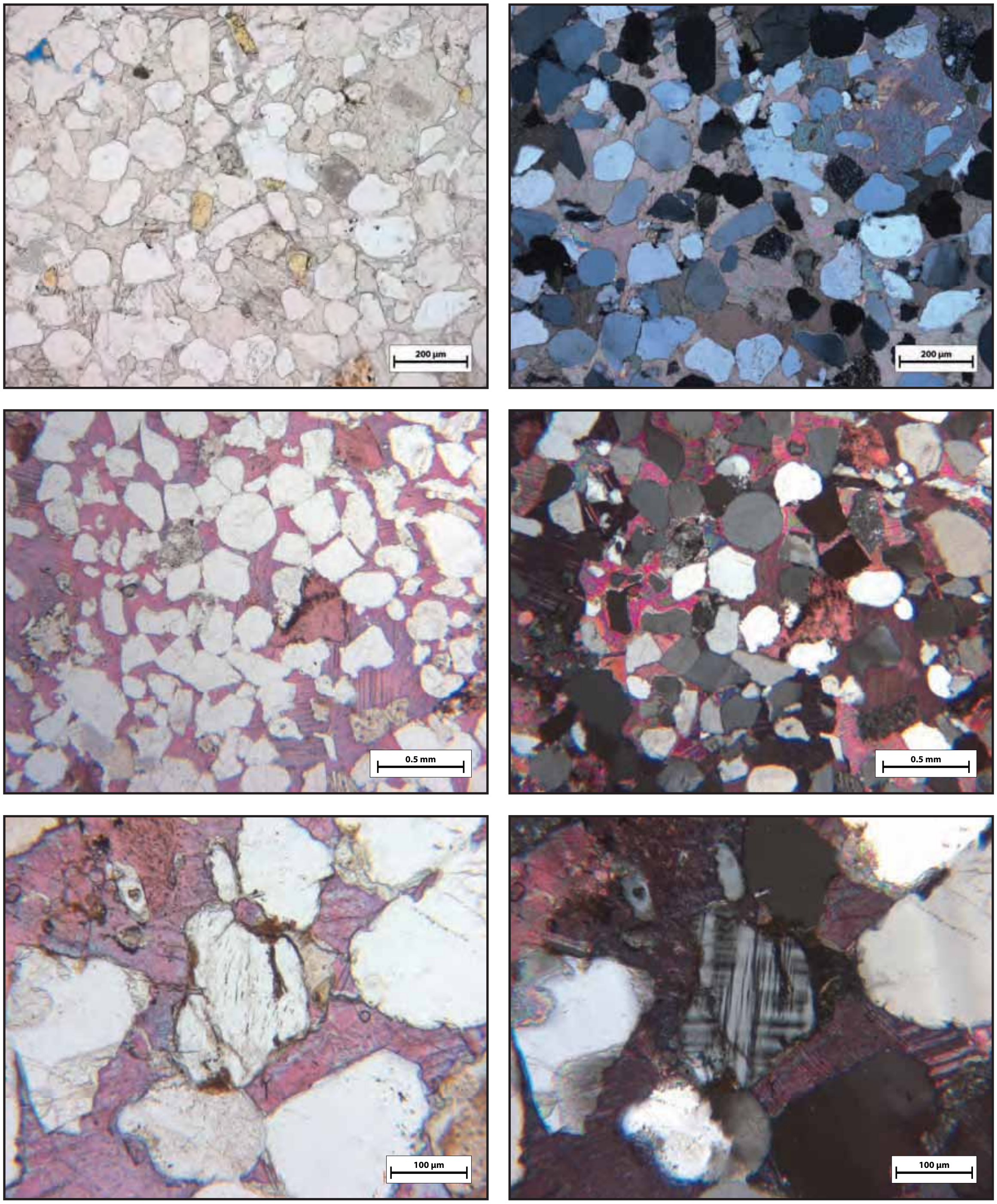

**Sample #:** 77

## Petrographic Summary

**Date:** 4/18/10

**Location Description:** Jms4 sand outcrop at the west end of main ramp

**Field Trip:** ☐ April, '09 ☑ Oct., '09

**Formation:** Jms4

**Rock Type:** Sandstone

**Grain Size:** 0.2-0.5 mm

**Grain Types:** mostly qtz, some kspars

**F-M-C-P:** F: M: C: P:

**Porosity (%):** Point Count: 25%

Measured: 33.46%

**Perm (mD):** 374.8 mD

**Isotopes (‰ ):** $\delta^{18}$O: -11.71 (PDB)

$\delta^{13}$C: -1.47 (PDB)

Other:

**Thin Section Map**

**Oriented thin section:** ☐ Yes ☑ No

**Orientation?:**

**Preparation**

☐ Thick
☑ Conventional
☐ Polished

**Stains:**
☑ Carbonate
☐ Plag ☑ Kspar

**Point Count:**

| Quartz | | | Plagioclase Feld. | | Alkali Feld. | | Lithics | | Misc. | Clay | Cement | | | | Porosity | | | | Total |
|---|---|---|---|---|---|---|---|---|---|---|---|---|---|---|---|---|---|---|---|
| mono | poly | mic/chert | intact | dissolved | intact | dissolved | opaque | sed | Grains | Matrix | spar | micrite | quartz | clay | inter | oversize | intra | micro | Points |
| 231 | 8 | 20 | 0 | 1 | 2 | 5 | 0 | 3 | 0 | 0 | 9 | 5 | 9 | 9 | 74 | 5 | 9 | 10 | 400 |
| 58% | 2% | 5% | 0% | 0% | 1% | 1% | 0% | 1% | 0% | 0% | 2% | 1% | 2% | 2% | 19% | 1% | 2% | 3% | |

**Cement:** (types, sequence)

Sparse bits of carbonate cement
Spots of clay cement where it looks like grains have been dissolving.

**Comments:**

Some very dissolved kspars
Many green grungy spongy grains
Relatively few qtz overgrowths
Lots of dissolution: oversize, intragranular and micro pores

**Sketches:**

**Sample #: 77**

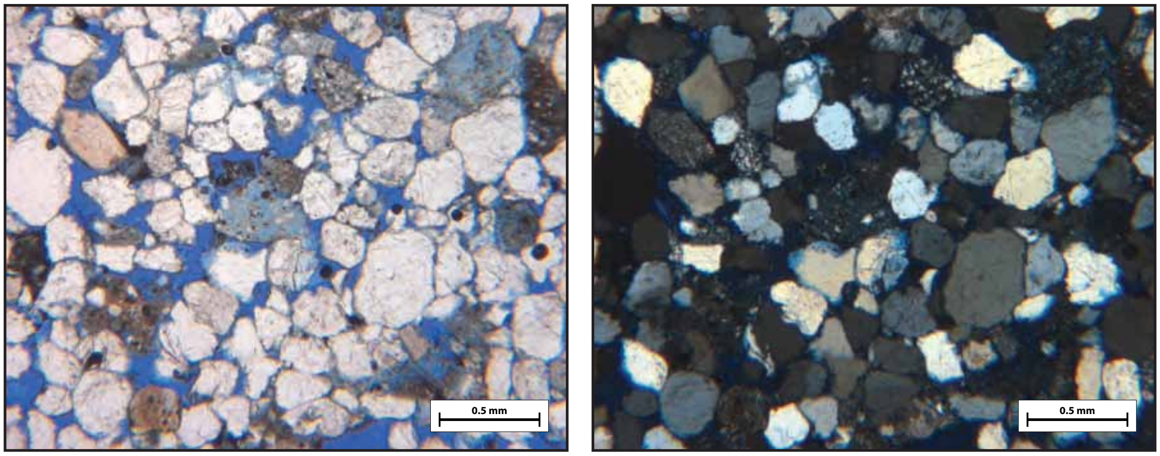

**Sample #:** 78A

## Petrographic Summary

**Date:** 4/18/10

**Location Description:** Edge of large pavement outcrop of Jms3 (at western end of ramp); very near a low-throw fault

**Field Trip:** ☐ April, '09 ☑ Oct., '09

**Formation:** Jms3

**Rock Type:** sandstone

**Grain Size:** 0.15-0.60mm

**Grain Types:** quartz, some plagioclase

**F-M-C-P:** F: M: C: P:

**Porosity (%):** Point Count: 14%

Measured: 15.10%

**Perm (mD):** 2.1 mD

**Isotopes (‰ ):** $\delta^{18}$O: -14.95 (PDB)

$\delta^{13}$C: -4.39 (PDB)

Other:

**Thin Section Map**

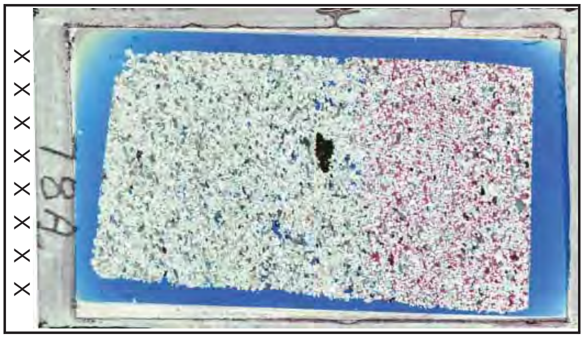

**Oriented thin section:** ☐ Yes ☑ No

**Orientation?:**

**Preparation** ☐ Thick ☑ Conventional ☐ Polished

**Stains:** ☑ Carbonate ☐ Plag ☑ Kspar

**Point Count:**

| Quartz | | | Plagioclase Feld. | | Alkali Feld. | | Lithics | | Misc. | Clay | Cement | | | | Porosity | | | | Total |
|---|---|---|---|---|---|---|---|---|---|---|---|---|---|---|---|---|---|---|---|
| mono | poly | mic/chert | intact | dissolved | intact | dissolved | opaque | sed | Grains | Matrix | spar | micrite | quartz | clay | inter | oversize | intra | micro | Points |
| 238 | 8 | 9 | 1 | 1 | 0 | 0 | 0 | 14 | 0 | 0 | 60 | 3 | 9 | 3 | 34 | 3 | 14 | 3 | 400 |
| 60% | 2% | 2% | 0% | 0% | 0% | 0% | 0% | 4% | 0% | 0% | 15% | 1% | 2% | 1% | 9% | 1% | 4% | 1% | |

**Cement:** (types, sequence) Well-stained calcite cement evident, not completely pore-occluding

**Comments:** Some qtz overgrowths

Very few feldspars

Oversize pores and intragranular porosity indicate considerable dissolution.

**Sketches:**

**Sample #: 78A**

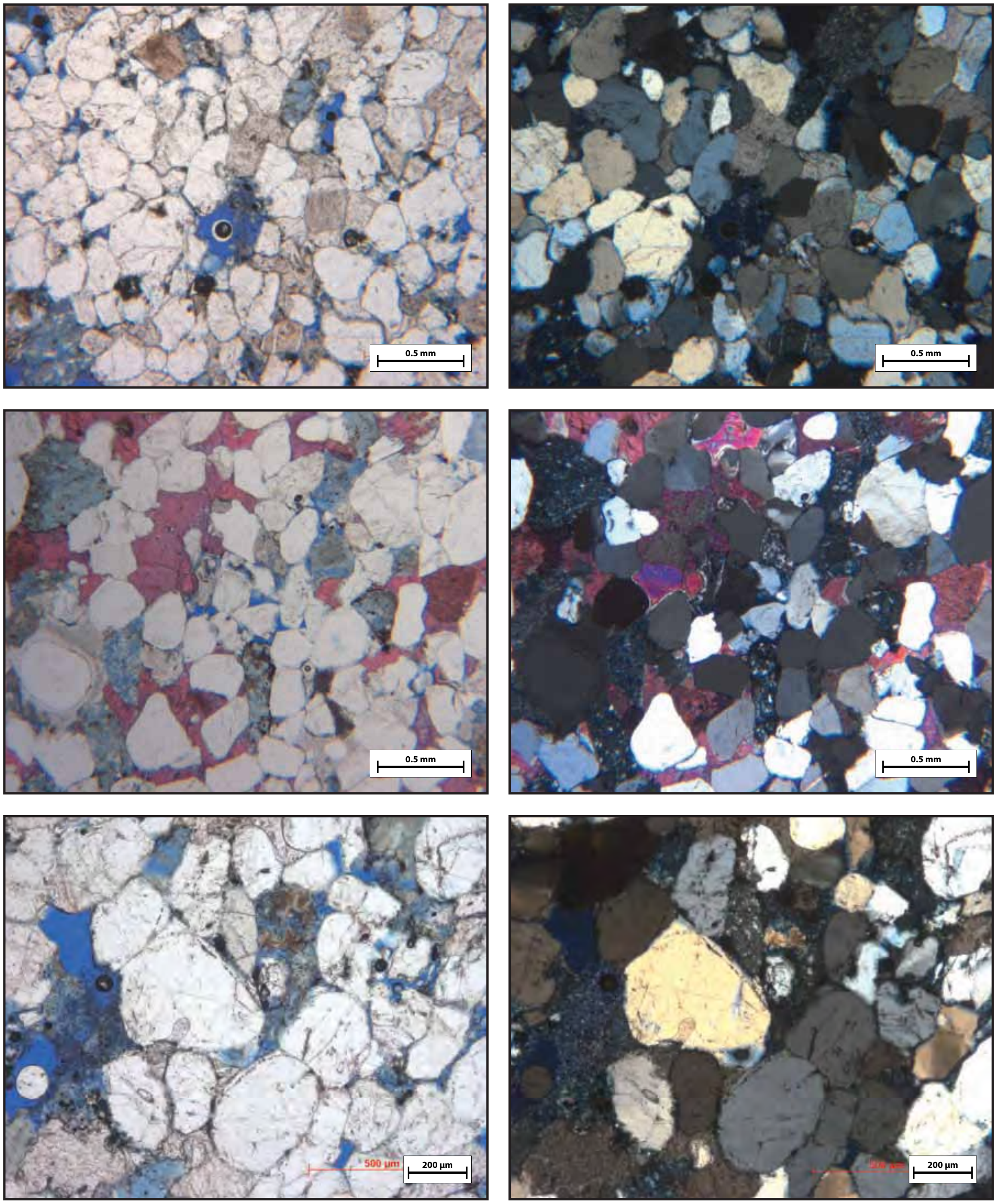

**Sample #:** 78B

## Petrographic Summary

**Date:** 4/18/10

**Location Description:** Inner part of Jms3 pavement at west end of ramp

**Field Trip:** ☐ April, '09 ☑ Oct., '09

**Formation:** Jms3

**Rock Type:** sandstone

**Grain Size:** 0.1-0.5 mm

**Grain Types:** quartz + kspars, some plag

**F-M-C-P:** F: M: C: P:

**Porosity (%):** Point Count: 19%

Measured: 23.99%

**Perm (mD):** 142.3 mD

**Isotopes (‰):** $\delta^{18}$O: -14.01 (PDB)

$\delta^{13}$C: -2.74 (PDB)

Other:

**Thin Section Map**

**Oriented thin section:** ☐ Yes ☑ No

**Orientation?:**

**Preparation**

☐ Thick
☑ Conventional
☐ Polished

**Stains:**
☑ Carbonate
☐ Plag ☑ Kspar

**Point Count:**

| Quartz | | | Plagioclase Feld. | | Alkali Feld. | | Lithics | | Misc. | Clay | Cement | | | | Porosity | | | | Total |
|---|---|---|---|---|---|---|---|---|---|---|---|---|---|---|---|---|---|---|---|
| mono | poly | mic/chert | intact | dissolved | intact | dissolved | opaque | sed | Grains | Matrix | spar | micrite | quartz | clay | inter | oversize | intra | micro | Points |
| 248 | 7 | 14 | 0 | 2 | 1 | 5 | 0 | 2 | 0 | 0 | 29 | 3 | 6 | 7 | 60 | 0 | 15 | 1 | 400 |
| 62% | 2% | 4% | 0% | 1% | 0% | 1% | 0% | 1% | 0% | 0% | 7% | 1% | 2% | 2% | 15% | 0% | 4% | 0% | |

**Cement:** (types, sequence)

Some patchy carbonate cement
Quartz overgrowths

**Comments:** High porosity; quite a few dissolved kspars; Some dissolved grains, some green/spongy greens

Some qtz overgrowths in lower-porosity zones; calcite spar, where it appears, in many cases seems to prevent quartz growth. Well quartz-cemented zones have no quartz cement where there is calcite spar; there are also bits of quartz cement with with calcite growing on top of them, though this could be synchronous or later-stage calcite.

**Sketches:**

**Sample #: 78B**

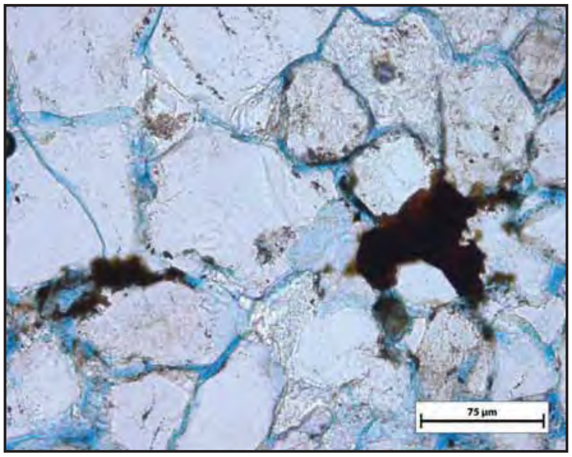

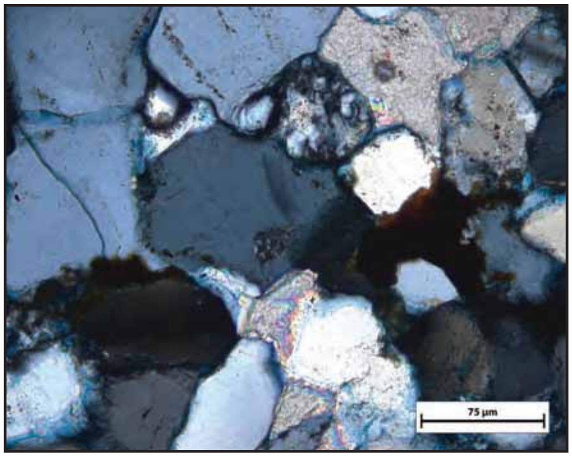

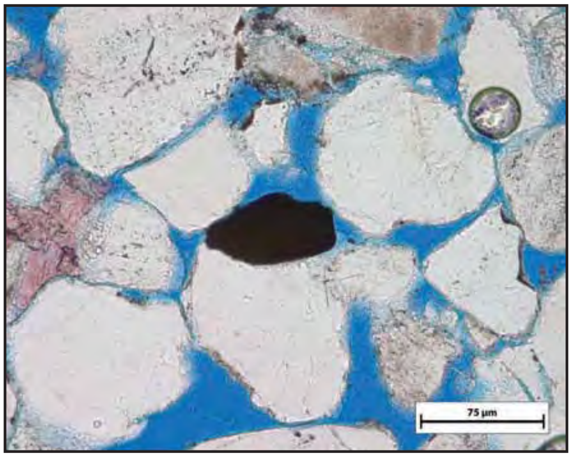

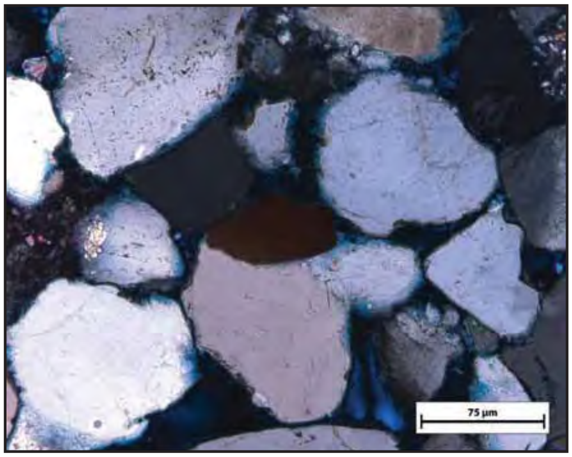

**Sample #:** 79

## Petrographic Summary

**Date:** 4/18/10

**Location Description:** Jms3 outcrop in northern field area, above big Jms2 pavement bench, in low area near Jms-Jmb contact.

**Field Trip:** ☐ April, '09 ☑ Oct., '09

**Formation:** Jms3

**Rock Type:** porous sandstone

**Grain Size:** 0.2-0.8 mm

**Grain Types:** quartz, plagioclase

**F-M-C-P:** F: M: C: P:

**Porosity (%):** Point Count: 20%

Measured: 30.77%

**Perm (mD):** 215.4 mD

**Isotopes (‰ ):** $\delta^{18}O$: -12.76, -12.91, -13.04

$\delta^{13}C$: -2.95, -2.94, -3.16 PDB

Other:

**Thin Section Map**

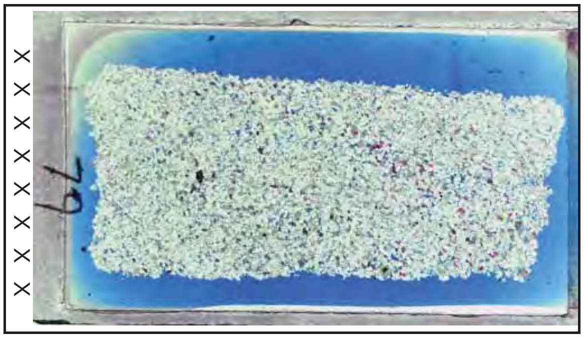

**Oriented thin section:** ☐ Yes ☑ No

**Orientation?:**

**Preparation** ☐ Thick ☑ Conventional ☐ Polished

**Stains:** ☑ Carbonate ☐ Plag ☑ Kspar

**Point Count:**

| Quartz | | | Plagioclase Feld. | | Alkali Feld. | | Lithics | | Misc. | Clay | Cement | | | | Porosity | | | | Total |
|---|---|---|---|---|---|---|---|---|---|---|---|---|---|---|---|---|---|---|---|
| mono | poly | mic/chert | intact | dissolved | intact | dissolved | opaque | sed | Grains | Matrix | spar | micrite | quartz | clay | inter | oversize | intra | micro | Points |
| 254 | 8 | 11 | 1 | 6 | 0 | 0 | 0 | 15 | 0 | 0 | 9 | 9 | 4 | 3 | 59 | 1 | 16 | 4 | 400 |
| 64% | 2% | 3% | 0% | 2% | 0% | 0% | 0% | 4% | 0% | 0% | 2% | 2% | 1% | 1% | 15% | 0% | 4% | 1% | |

**Cement:** (types, sequence)

Stain very helpful in highlighting SCANT spar

Some ferroan, some non-ferroan calcite

**Comments:**

Some qtz overgrowths

A few moderately-to-highly dissolved plagioclase grains
(lots of oversize and intragranular porosity)

**Sketches:**

**Sample #: 79**

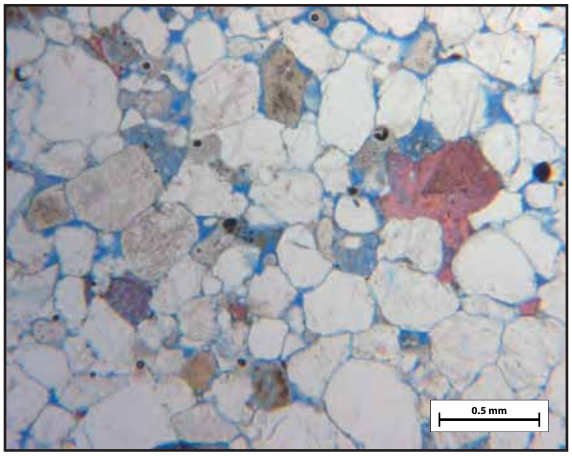

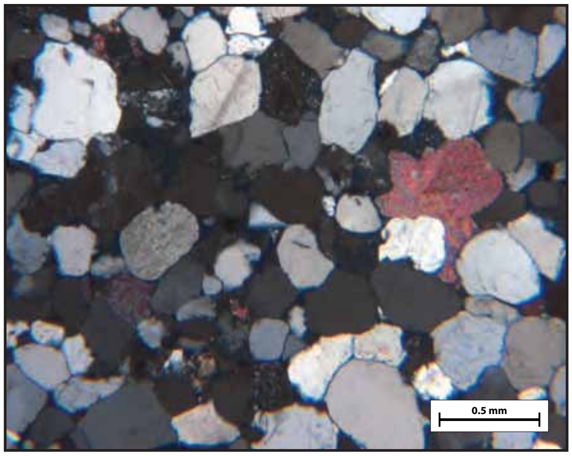

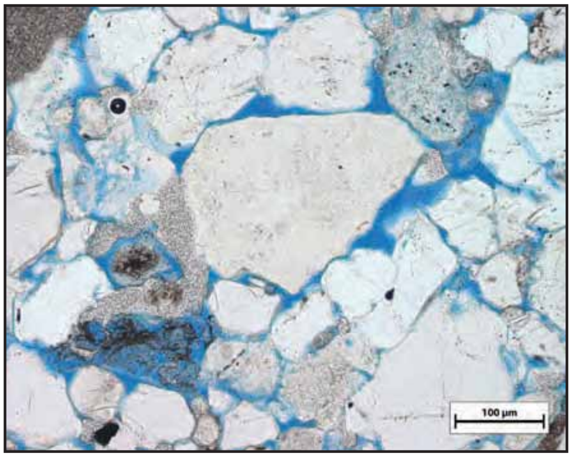

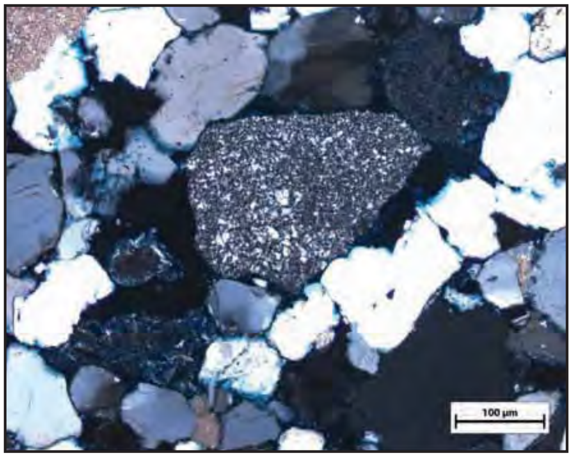

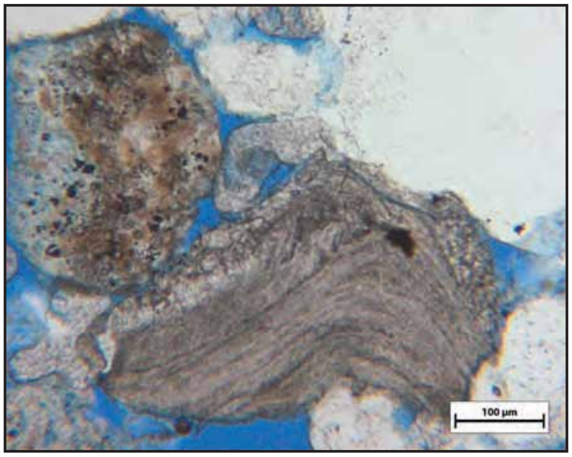

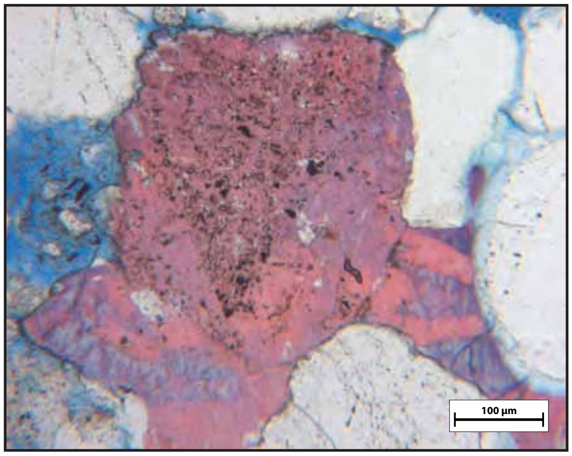

**Sample #:** 80A

## Petrographic Summary

**Date:** 4/18/10

**Location Description:** Western portion of field area; west corner of Jms2 pavement outcropping directly south of little hill

**Field Trip:** ☐ April, '09 ☑ Oct., '09

**Formation:** Jms2

**Rock Type:** sandstone

**Grain Size:** 0.1-0.6 mm

**Grain Types:** qtz, plag, kspar, lithics

**F-M-C-P:** F: M: C: P:

**Porosity (%):** Point Count: 13%

Measured: 20.64%

**Perm (mD):** 198.0 mD

**Isotopes (‰):** $\delta^{18}O$: -2.23 (PDB)

$\delta^{13}C$: 2.76 (PDB)

Other: --

**Thin Section Map**

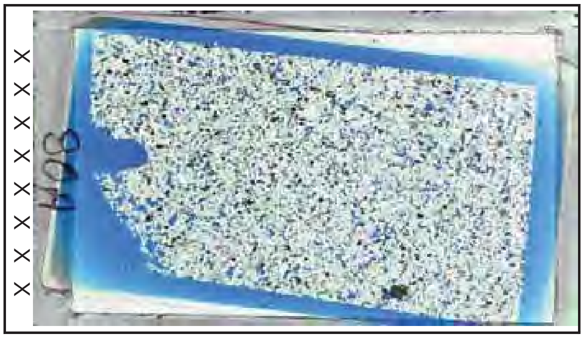

**Oriented thin section:** ☐ Yes ☑ No

**Orientation?:**

**Preparation** ☐ Thick ☑ Conventional ☐ Polished

**Stains:** ☐ Carbonate ☐ Plag ☑ Kspar

**Point Count:**

| Quartz | | | Plagioclase Feld. | | Alkali Feld. | | Lithics | | Misc. | Clay | Cement | | | | Porosity | | | | Total |
|---|---|---|---|---|---|---|---|---|---|---|---|---|---|---|---|---|---|---|---|
| mono | poly | mic/chert | intact | dissolved | intact | dissolved | opaque | sed | Grains | Matrix | spar | micrite | quartz | clay | inter | oversize | intra | micro | Points |
| 247 | 16 | 12 | 1 | 5 | 2 | 2 | 0 | 18 | 0 | 0 | 0 | 6 | 24 | 16 | 30 | 7 | 12 | 2 | 400 |
| 62% | 4% | 3% | 0% | 1% | 1% | 1% | 0% | 5% | 0% | 0% | 0% | 2% | 6% | 4% | 8% | 2% | 3% | 1% | |

**Cement:** (types, sequence) No calcite! Lots of euhedral/sub-euhedral qtz overgrowths

**Comments:** Major quartz overgrowths
At max magnificaiton thick chlorite rims visible; also possibly partially replacing some dissolved-looking grains. A few kspars; some porous grains look to have taken the kspar stain; Some rare plag grains, partially dissolved
80A is altered material from this station; 80B is unaltered material from the same station.

**Sketches:**

**Sample #: 80A**

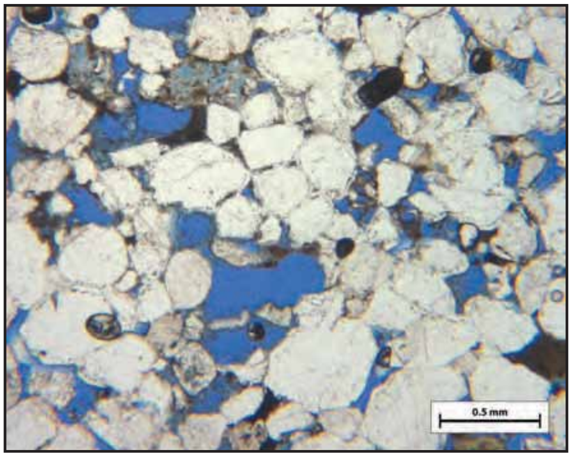

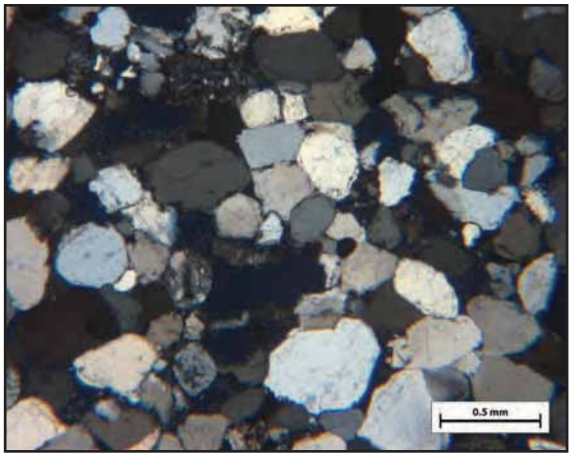

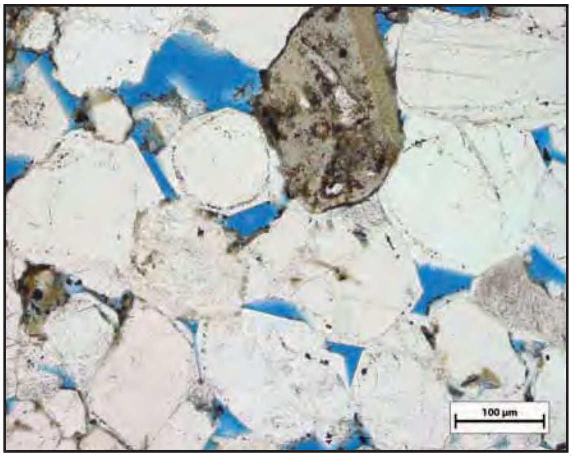

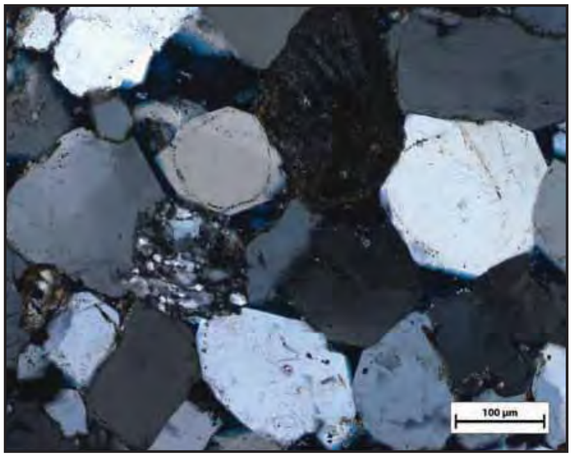

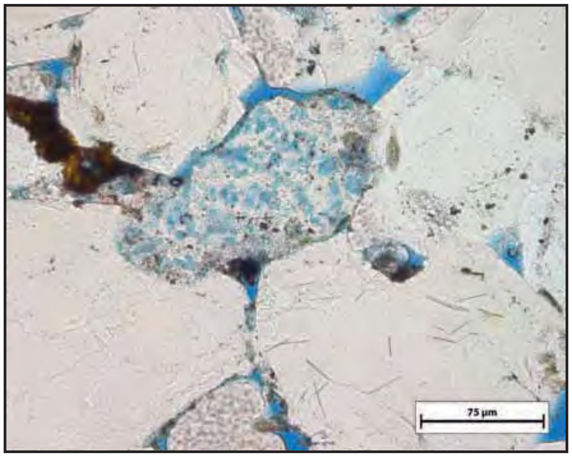

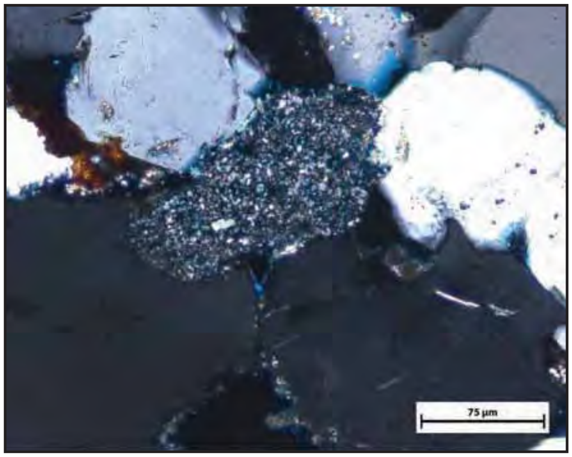

**Sample #:** 80B-1

## Petrographic Summary

**Date:** 7/22/10

**Location Description:** Far west of field area, at intersection of big ledge, Jms2 and Jms3 platforms

**Field Trip:** ☐ April, '09 ☑ Oct., '09

**Formation:** Jms2

**Rock Type:** unaltered sandstone

**Grain Size:** 0.2-0.4 mm

**Grain Types:** qtz, some plag/kspar

**F-M-C-P:** F: M: C: P:

**Porosity (%):** Point Count: 14%

Measured: 16.4% (on 80B-2)

**Perm (mD):** 69.9 mD

**Isotopes (‰ ):** $\delta^{18}O$: -13.30, -13.08 (PDB)

$\delta^{13}C$: -2.54, -2.43 (PDB)

Other: --

**Thin Section Map**

**Oriented thin section:** ☐ Yes ☑ No

**Orientation?:**

**Preparation** ☐ Thick ☑ Conventional ☐ Polished

**Stains:** ☑ Carbonate ☐ Plag ☑ Kspar

**Point Count:**

| Quartz | | | Plagioclase Feld. | | Alkali Feld. | | Lithics | | Misc. | Clay | Cement | | | | Porosity | | | | Total |
|---|---|---|---|---|---|---|---|---|---|---|---|---|---|---|---|---|---|---|---|
| mono | poly | mic/chert | intact | dissolved | intact | dissolved | opaque | sed | Grains | Matrix | spar | micrite | quartz | clay | inter | oversize | intra | micro | Points |
| 247 | 14 | 11 | 0 | 3 | 1 | 1 | 0 | 2 | 1 | 0 | 34 | 5 | 24 | 3 | 43 | 0 | 10 | 1 | 400 |
| 62% | 4% | 3% | 0% | 1% | 0% | 0% | 0% | 1% | 0% | 0% | 9% | 1% | 6% | 1% | 11% | 0% | 3% | 0% | |

**Cement:** (types, sequence)

Sparse patchy carbonate cement
Some qtz overgrowths; 12 points counted as "qtz cement"
were actually cataclastic qtz from the deformation band

**Comments:**

Big deformation band; Almost no feldspars, but 1 small plag looks very dissolved; Qtz overgrowths -- look recycled; Miscellaneous grain appears to be a zircon (very high B) Some dissolved carbonate cement; some carbonate cement INSIDE def band... how? not crushed, fully intact; 80A is altered material from this station; 80B is unaltered material from the same station; calcite does not appear to preclude quartz -- in most cases appears on top of quartz

**Sketches:**

**Sample #: 80B-1**

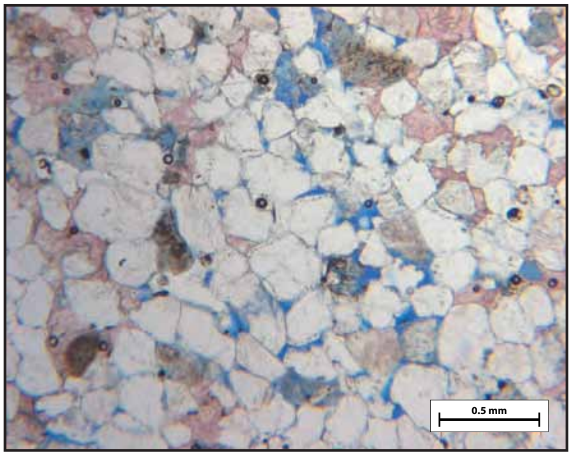
0.5 mm

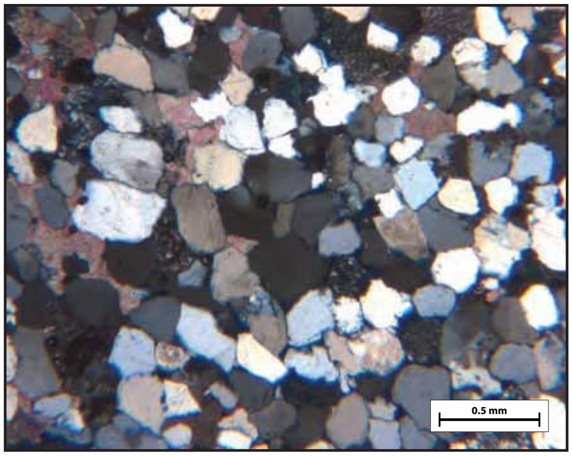
0.5 mm

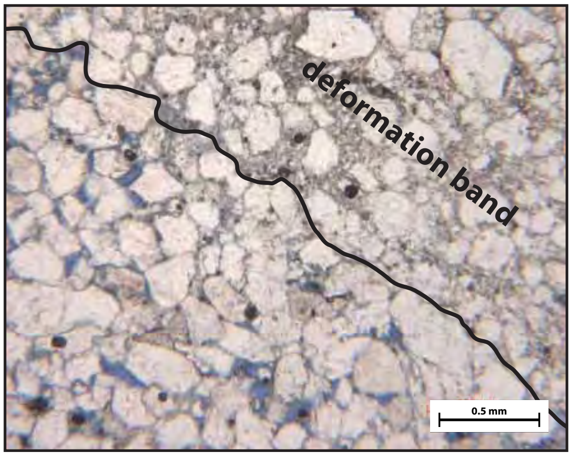
deformation band
0.5 mm

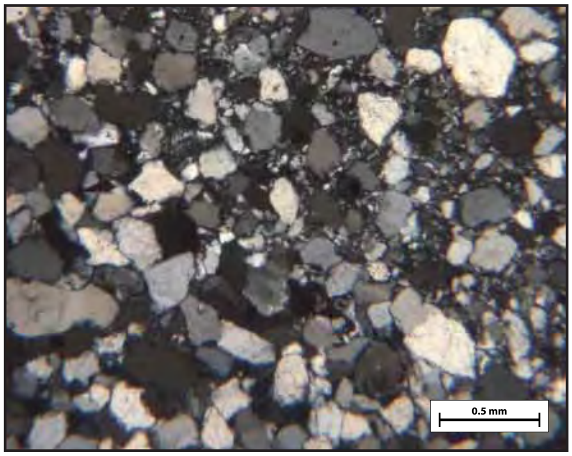
0.5 mm

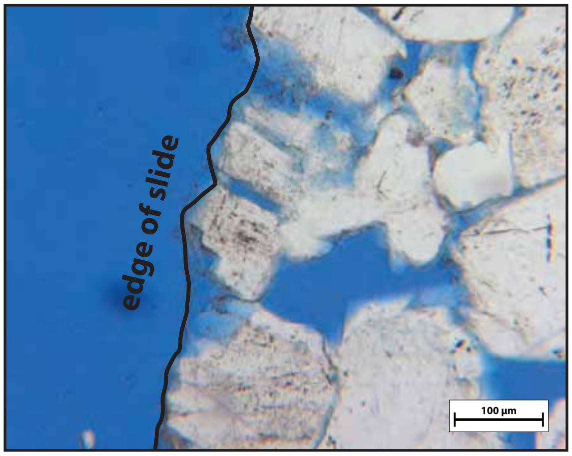
edge of slide
100 µm

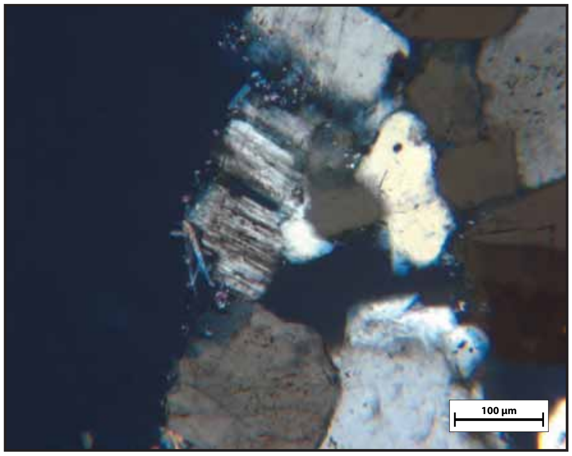
100 µm

**Sample #:** 80B-2

## Petrographic Summary

**Date:** 4/18/10

**Location Description:** Far west of field area, at intersection of big ledge, Jms2 and Jms3 platforms

**Field Trip:** ☐ April, '09 ☑ Oct., '09

**Formation:** Jms2

**Rock Type:** unaltered sandstone

**Grain Size:** 0.2-0.4 mm

**Grain Types:** qtz, some plag

**F-M-C-P:** F: M: C: P:

**Porosity (%):** Point Count: --

Measured: --

**Perm (mD):** --

**Isotopes (‰ ):** $\delta^{18}O$: --

$\delta^{13}C$: --

Other: --

### Thin Section Map

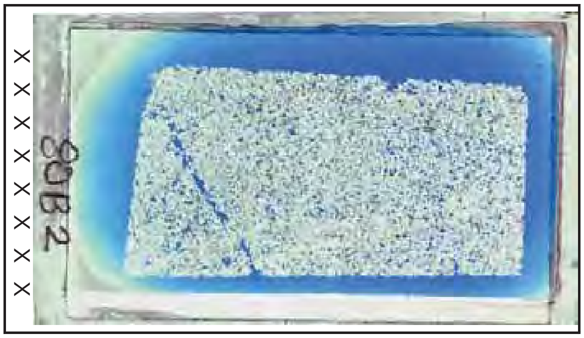

**Oriented thin section:** ☐ Yes ☑ No

**Orientation?:**

**Preparation** ☐ Thick ☑ Conventional ☐ Polished

**Stains:** ☑ Carbonate ☐ Plag ☑ Kspar

**Point Count:**

**Cement:** (types, sequence) no calcite; small quartz overgrowths on some grains; small amounts of clay cement associated with "spongy" blue-green partially dissolved grains

**Comments:** Very high porosity throughout. Even deformation bands show signs of some dissolution and associated (low-level) porosity.

No kspar

Dissolution apparent (spongy bluish grains) but not extensive.

**Sketches:**

## Sample #: **80B-2**

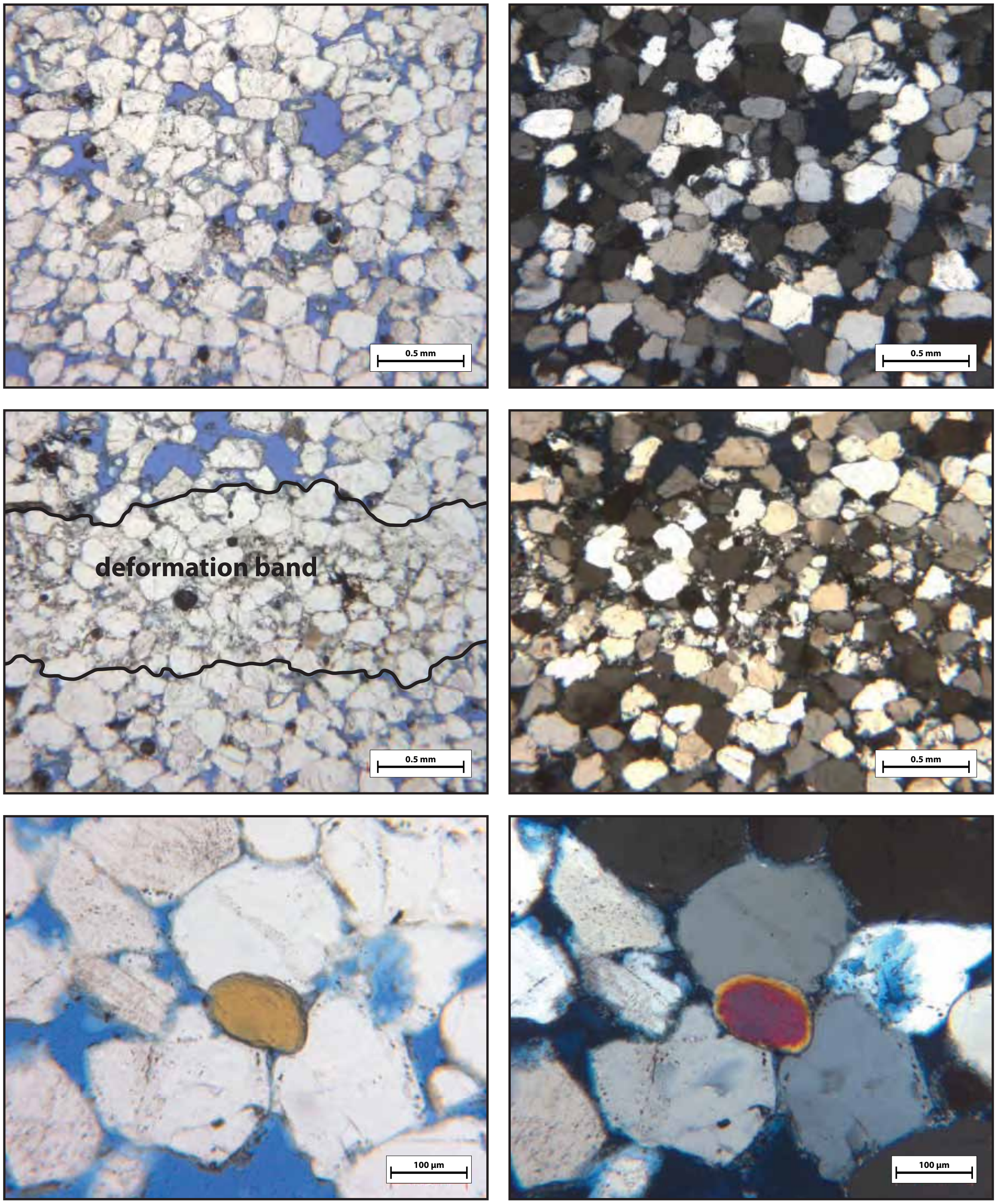

**Sample #:** 82

## Petrographic Summary

**Date:** 4/18/10

**Location Description:** Jms4 ledgy outcrop in south slope of ravine (ravine to the NW of travertine platform)

**Field Trip:** ☐ April, '09 ☑ Oct., '09

**Formation:** Jms4

**Rock Type:** sandstone

**Grain Size:** 0.10-0.30mm

**Grain Types:** qtz, kspar and plag

**F-M-C-P:** F: M: C: P:

**Porosity (%):** Point Count: 1%

Measured: 8.83%

**Perm (mD):** 8.9 mD

**Isotopes (‰):** $\delta^{18}$O: --

$\delta^{13}$C: --

Other:

**Thin Section Map**

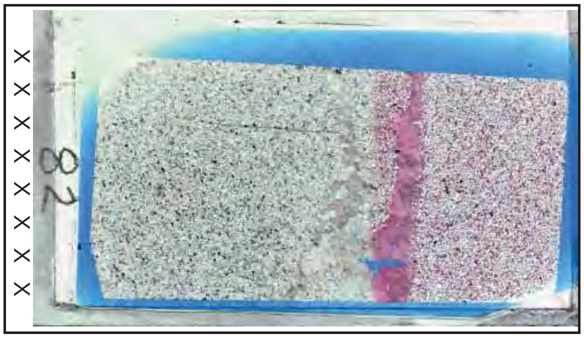

**Oriented thin section:** ☐ Yes ☑ No

**Orientation?:**

**Preparation**

☐ Thick
☑ Conventional
☐ Polished

**Stains:**
☑ Carbonate
☐ Plag ☑ Kspar

**Point Count:**

| Quartz | | | Plagioclase Feld. | | Alkali Feld. | | Lithics | | Misc. | Clay | Cement | | | | Porosity | | | | Total |
|---|---|---|---|---|---|---|---|---|---|---|---|---|---|---|---|---|---|---|---|
| mono | poly | mic/chert | intact | dissolved | intact | dissolved | opaque | sed | Grains | Matrix | spar | micrite | quartz | clay | inter | oversize | intra | micro | Points |
| 166 | 5 | 5 | 1 | 6 | 2 | 4 | 0 | 5 | 0 | 0 | 199 | 0 | 0 | 4 | 1 | 0 | 1 | 1 | 400 |
| 42% | 1% | 1% | 0% | 2% | 1% | 1% | 0% | 1% | 0% | 0% | 50% | 0% | 0% | 1% | 0% | 0% | 0% | 0% | |

**Cement:** (types, sequence)

Lots of stained calcite cement and fracture fill, fully porosity-occluding.

Some ferroan calcite

**Comments:**

Heavily spar cemented

Some micrite grains

Major spar-filled veins

Lots of grains take yellow (kspar) stain (best seen in reflected light) but most (all?) appear to be either porous lithics or micro/poly-quartz -- not obviously kspar

Relatively abundant kspars

**Sketches:**

**Sample #: 82**

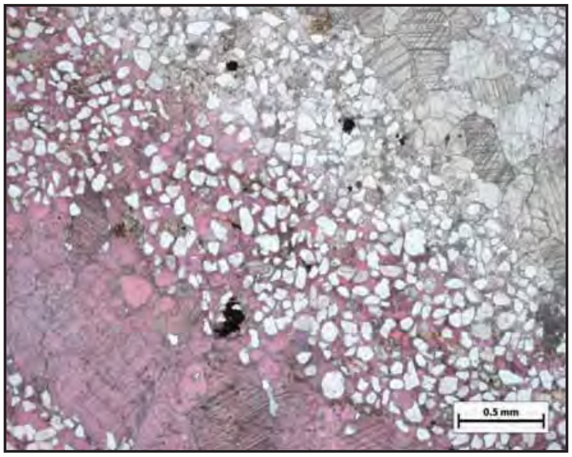

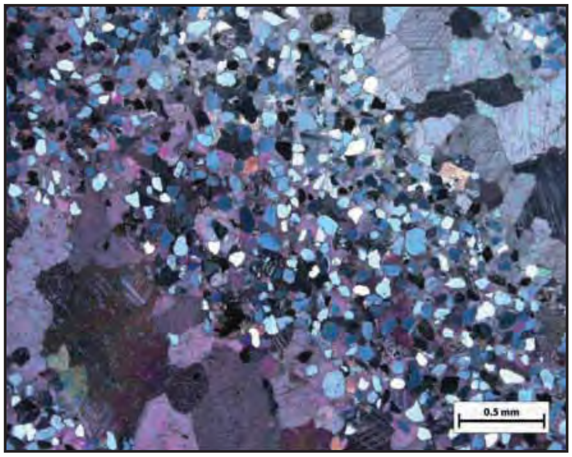

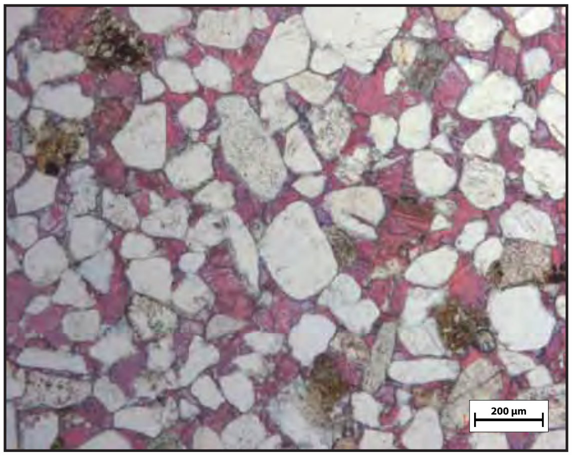

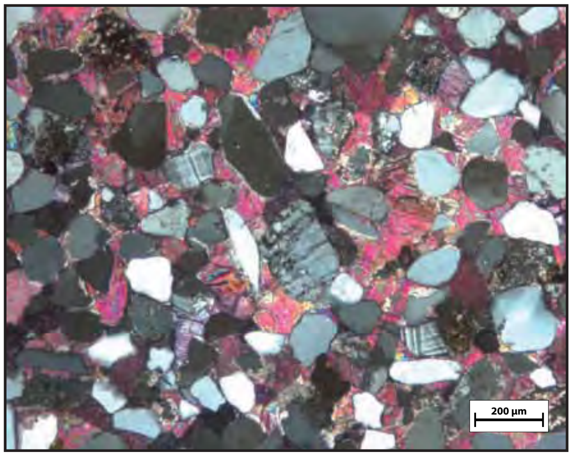

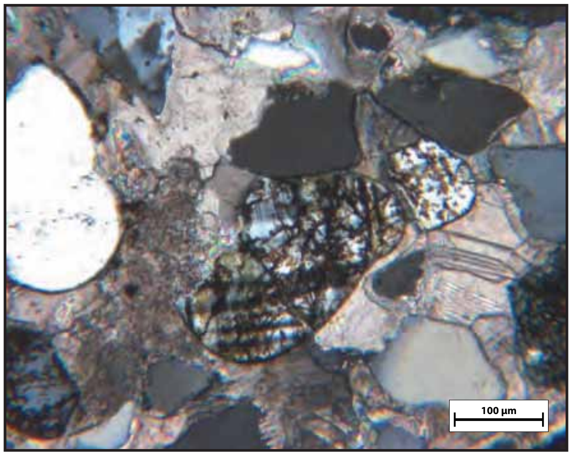

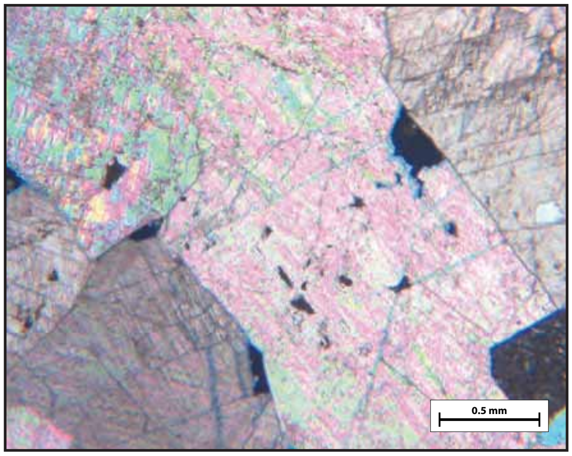

**Sample #:** 83

## Petrographic Summary

**Date:** 4/18/10

**Location Description:** Sand block across wash (to west) of west promontory of travertine mound; on fault running along north side of the ramp

**Field Trip:** ☐ April, '09 ☑ Oct., '09

**Formation:** Jms4

**Rock Type:** sandstone

**Grain Size:** 0.10-0.45 mm

**Grain Types:** quartz, sed liths, felds

**F-M-C-P:** F: M: C: P:

**Porosity (%):** Point Count: 11.75%

Measured: --

**Perm (mD):** --

**Isotopes (‰):** $\delta^{18}O$: --

$\delta^{13}C$: --

Other: --

### Thin Section Map

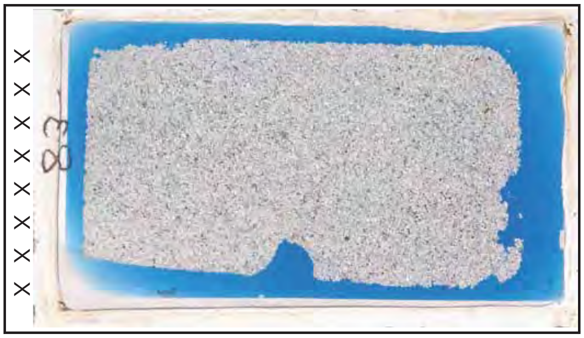

**Oriented thin section:** ☐ Yes ☑ No

**Orientation?:**

**Preparation** ☐ Thick ☑ Conventional ☐ Polished

**Stains:** ☑ Carbonate ☐ Plag ☑ Kspar

**Point Count:**

**Cement:** (types, sequence)
Calcite spar abundant, but limited by low IGV
Quartz overgrowths

**Comments:**
Low porosity due to fairly dense grain compaction and the presence of calcite spar
Some green/spongy dissolved grains
Some intact, some partially dissolved feldspars (plag and kspar)
Unusually large number of small (<0.05 mm) opaque lithics

**Sketches:**

**Sample #: 83**

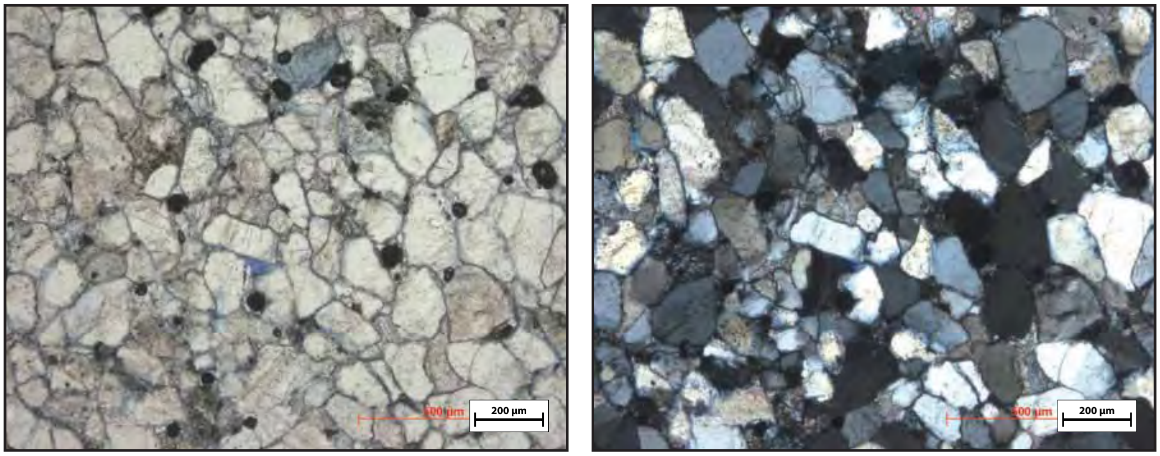

**Sample #:** 84

## Petrographic Summary

**Date:** 4/18/10

**Location Description:** Exposed sand in small basin behind (north of) travertine mound

**Field Trip:** ☐ April, '09 ☑ Oct., '09

**Formation:** Jms5

**Rock Type:** sandstone

**Grain Size:** 0.2-0.5 mm

**Grain Types:** quartz, sed liths,

**F-M-C-P:** F: M: C: P:

**Porosity (%):** Point Count: 4%

Measured: 10.02%

**Perm (mD):** 2.3 mD

**Isotopes (‰):** $\delta^{18}O$: -9.41, -9.54 (PDB)

$\delta^{13}C$: 2.63, 2.31 (PDB)

Other: --

**Thin Section Map**

**Oriented thin section:** ☐ Yes ☑ No

**Orientation?:**

**Preparation**

☐ Thick
☑ Conventional
☐ Polished

**Stains:**

☑ Carbonate
☐ Plag ☑ Kspar

**Point Count:**

| Quartz | | | Plagioclase Feld. | | Alkali Feld. | | Lithics | | Misc. | Clay | Cement | | | | Porosity | | | | Total |
|---|---|---|---|---|---|---|---|---|---|---|---|---|---|---|---|---|---|---|---|
| mono | poly | mic/chert | intact | dissolved | intact | dissolved | opaque | sed | Grains | Matrix | spar | micrite | quartz | clay | inter | oversize | intra | micro | Points |
| 252 | 7 | 3 | 0 | 0 | 0 | 1 | 0 | 0 | 0 | 0 | 18 | 73 | 31 | 1 | 6 | 0 | 4 | 4 | 400 |
| 63% | 2% | 1% | 0% | 0% | 0% | 0% | 0% | 0% | 0% | 0% | 5% | 18% | 8% | 0% | 2% | 0% | 1% | 1% | |

**Cement:** (types, sequence)

Spar and micrite cement -- patchy but significant presenceHeavy quartz overgrowths; Opaque clay fills the interstices in a few small regions, but this is uncommon

**Comments:**

Low porosity, mostly filled with carbonate cement
Quartz overgrowths cause dense zones of low porosity
Feldspars very rare
Relatively few green spongy dissolved grains (compared to stations like 22 and 26 (see low intra/microporosity count... 2% of total).

**Sketches:**

## Sample #: 84

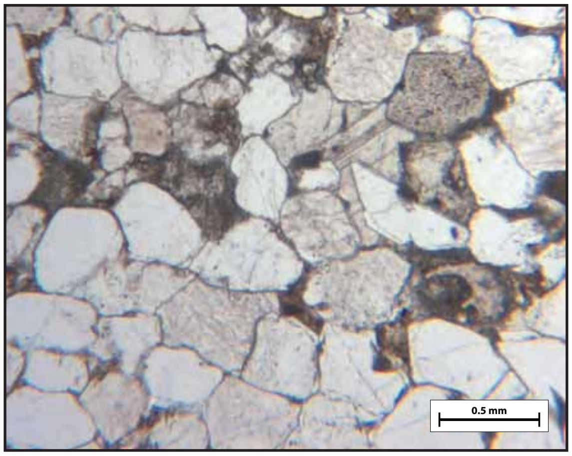

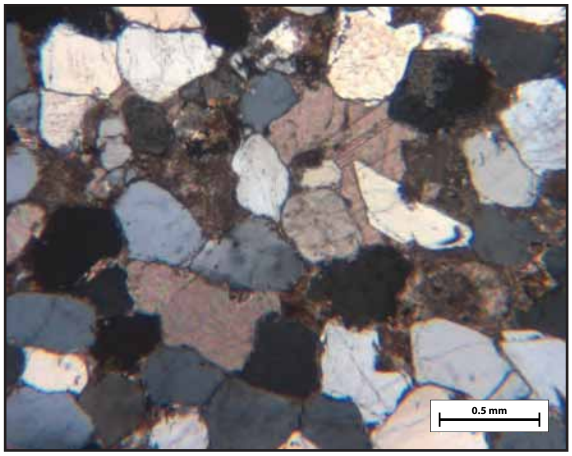

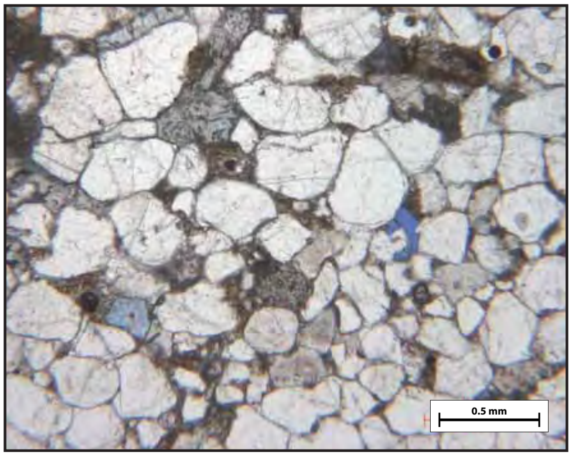

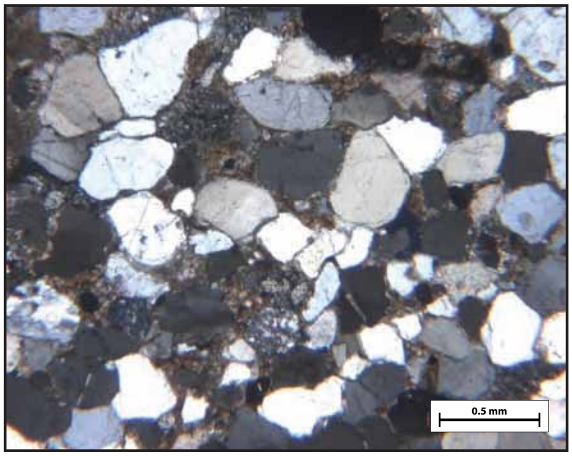

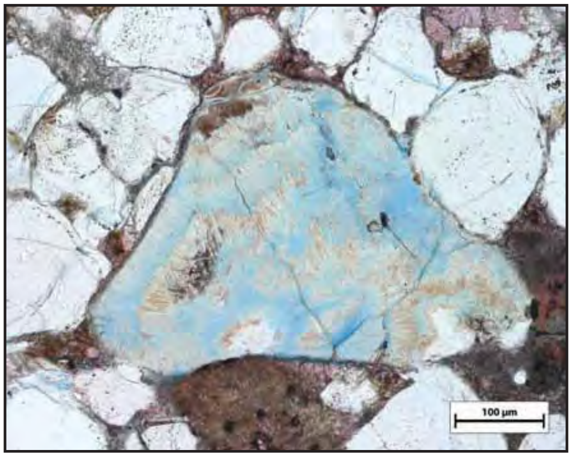

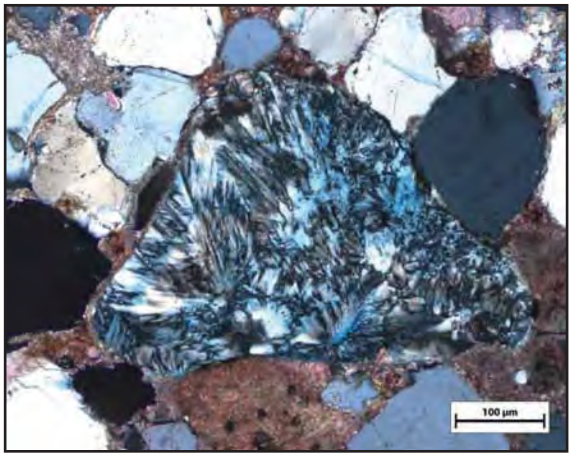

**Sample #:** 85

## Petrographic Summary

**Date:** 4/18/10

**Location Description:** Jms2 ledge above ravine directly north of travertine platform

**Field Trip:** ☐ April, '09 ☑ Oct., '09

**Formation:** Jms2

**Rock Type:** sandstone

**Grain Size:** 0.05-0.20 mm

**Grain Types:** quartz, kspars, lithics

**F-M-C-P:** F: M: C: P:

**Porosity (%):** Point Count: 18%

Measured: 20.13%

**Perm (mD):** 36.9 mD

**Isotopes (‰):** $\delta^{18}O$: -13.57 (PDB)

$\delta^{13}C$: -3.47 (PDB)

Other:

**Thin Section Map**

**Oriented thin section:** ☐ Yes ☑ No

**Orientation?:**

**Preparation** ☐ Thick ☑ Conventional ☐ Polished

**Stains:** ☑ Carbonate ☐ Plag ☑ Kspar

**Point Count:**

| Quartz | | | Plagioclase Feld. | | Alkali Feld. | | Lithics | | Misc. | Clay | Cement | | | | Porosity | | | | Total |
|---|---|---|---|---|---|---|---|---|---|---|---|---|---|---|---|---|---|---|---|
| mono | poly | mic/chert | intact | dissolved | intact | dissolved | opaque | sed | Grains | Matrix | spar | micrite | quartz | clay | inter | oversize | intra | micro | Points |
| 224 | 6 | 15 | 0 | 0 | 0 | 4 | 1 | 1 | 2 | 0 | 50 | 7 | 11 | 6 | 64 | 0 | 4 | 5 | 400 |
| 56% | 2% | 4% | 0% | 0% | 0% | 1% | 0% | 0% | 1% | 0% | 13% | 2% | 3% | 2% | 16% | 0% | 1% | 1% | |

**Cement:** (types, sequence)

Scattered slight carbonate cements

Very slight quartz overgrowths

**Comments:**

Small grains

Abundant green/spongy grains

Quite high porosity -- not enough calcite to fill porosity

"Miscellaneous" includes a zircon

Very grungy -- too much dissolution to get a good sense of whether calcite is precluding the development of quartz overgrowths.

**Sketches:**

## Sample #: 85

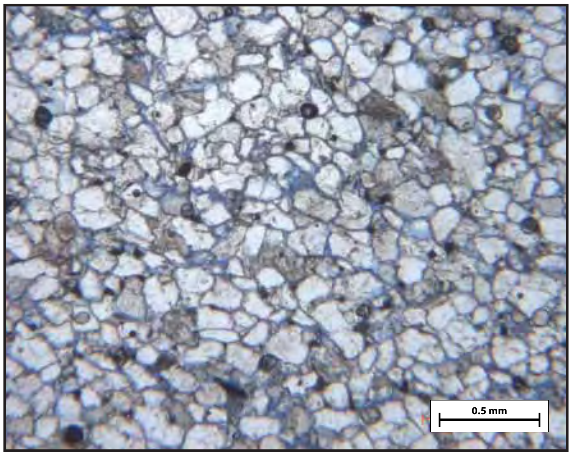

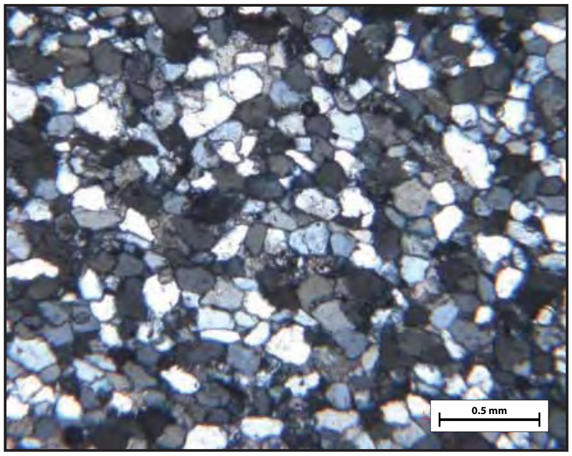

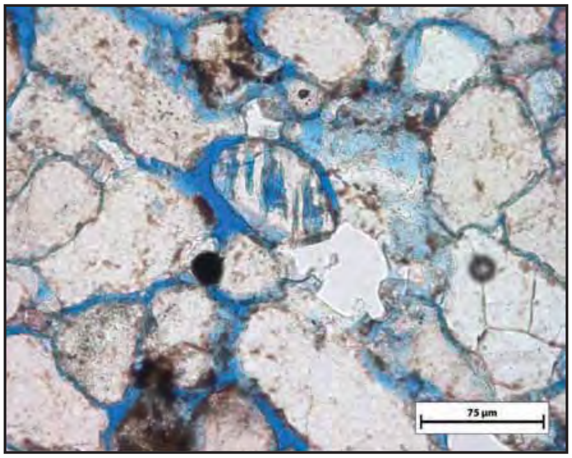

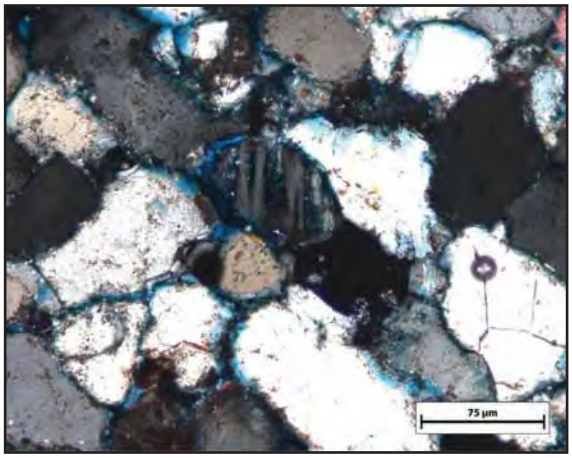

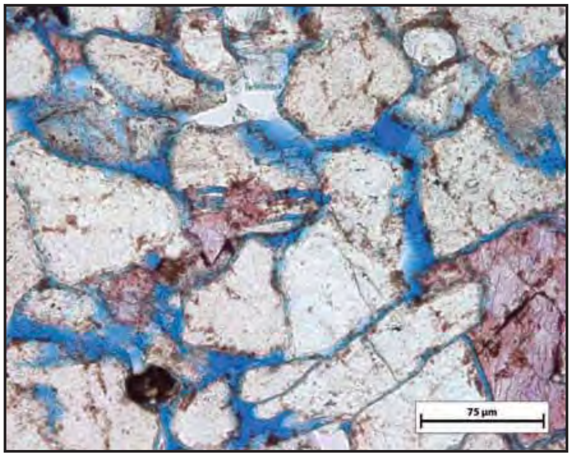

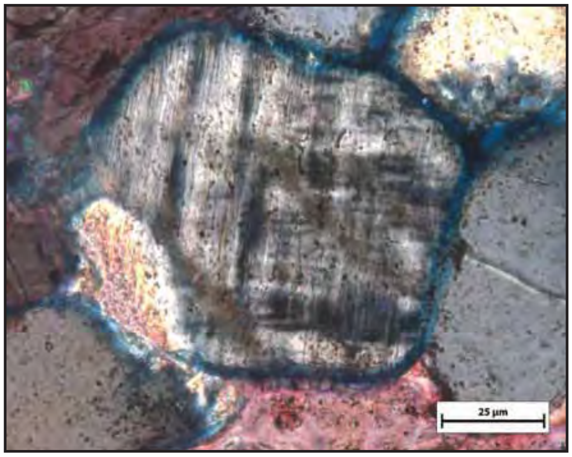

**Sample #:** 86

## Petrographic Summary

**Date:** 4/18/10

**Location Description:** Non-numbered discontinuous Jms sand above Jms2 and below Jms3, NNE of travertine mound; edge of wide bench (w/ large fracture pattern visible in aerials)

**Field Trip:** ☐ April, '09 ☑ Oct., '09

**Formation:** Jms

**Rock Type:** spar-cemented sandstone

**Grain Size:** 0.1-0.5 mm

**Grain Types:** Mostly quartz, some kspars

**F-M-C-P:** F: M: C: P:

**Porosity (%):** Point Count: 0%

Measured: 5.65%

**Perm (mD):** 2.1 mD

**Isotopes (‰):** $\delta^{18}O$: -10.39 (PDB)

$\delta^{13}C$: -4.50 (PDB)

Other:

**Thin Section Map**

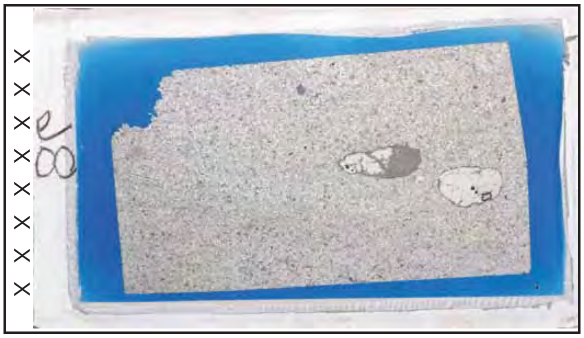

**Oriented thin section:** ☐ Yes ☑ No

**Orientation?:**

**Preparation** ☐ Thick ☑ Conventional ☐ Polished

**Stains:** ☑ Carbonate ☐ Plag ☑ Kspar

**Point Count:**

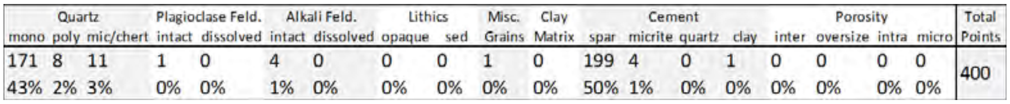

| Quartz | | | Plagioclase Feld. | | Alkali Feld. | | Lithics | | Misc. | Clay | Cement | | | | Porosity | | | | Total |
|---|---|---|---|---|---|---|---|---|---|---|---|---|---|---|---|---|---|---|---|
| mono | poly | mic/chert | intact | dissolved | intact | dissolved | opaque | sed | Grains | Matrix | spar | micrite | quartz | clay | inter | oversize | intra | micro | Points |
| 171 | 8 | 11 | 1 | 0 | 4 | 0 | 0 | 0 | 1 | 0 | 199 | 4 | 0 | 1 | 0 | 0 | 0 | 0 | 400 |
| 43% | 2% | 3% | 0% | 0% | 1% | 0% | 0% | 0% | 0% | 0% | 50% | 1% | 0% | 0% | 0% | 0% | 0% | 0% | |

**Cement:** (types, sequence) Carbonate, fully porosity-occluding

**Comments:** Large recycled-micrite grains -- maybe explains heavy cementing; other smaller (qtz-grain-sized) micrite grains
Quite a few totally undissolved kspar grains
Very low porosity -- totally filled with calcite cement

Rare green/spongy grains but some brown-freckled grains

No qtz overgrowths

**Sketches:**

**Sample #: 86**

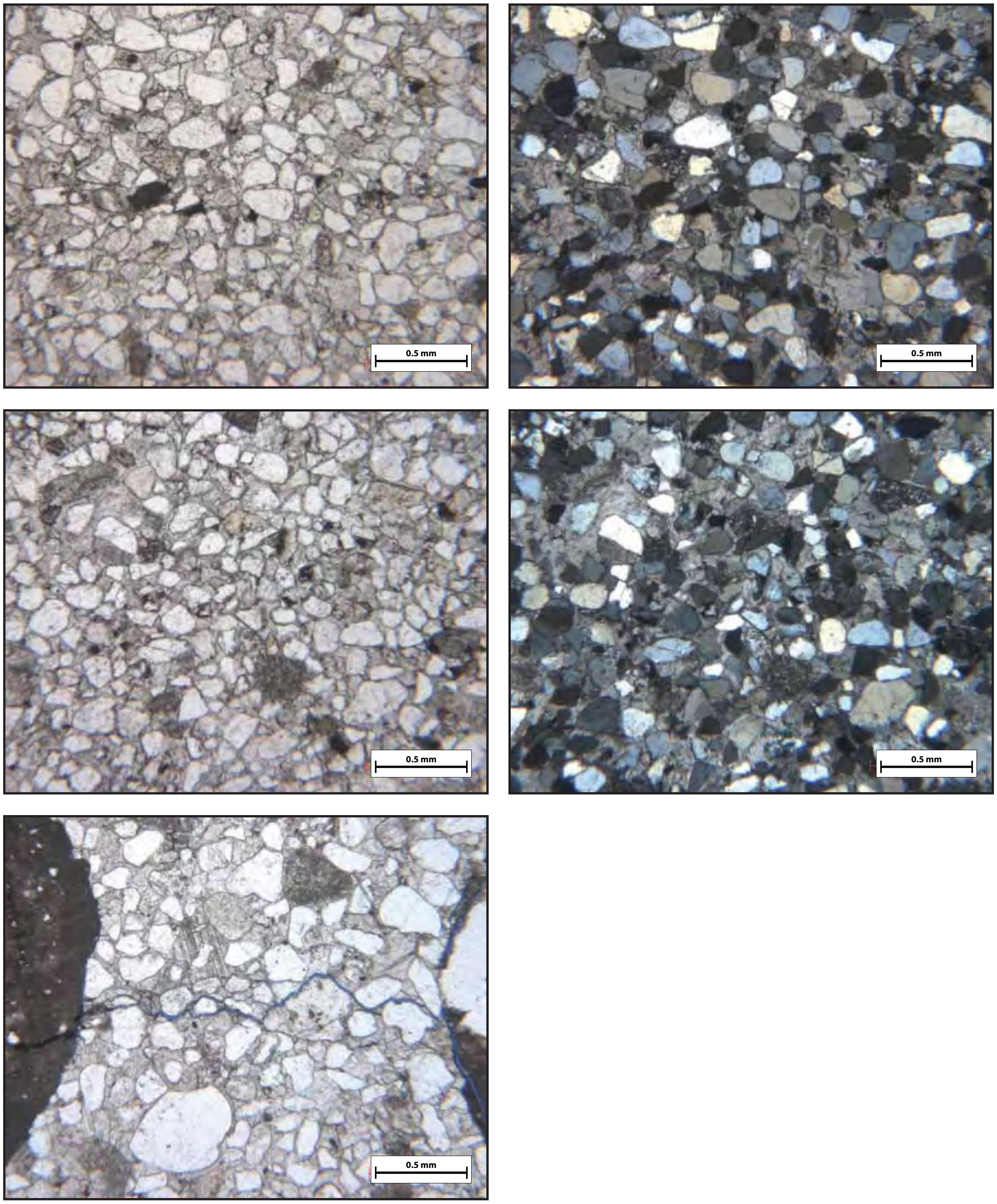

**Sample #:** 87 (polished)

**Petrographic Summary**

**Date:** 7/22/10

**Location Description:** Small outcrop to the east of travertine mound, at base of small wash between the mound and adjacent shale-y hill

**Field Trip:** ☐ April, '09 ☑ Oct., '09
**Formation:** Brushy Basin
**Rock Type:** sandstone
**Grain Size:** 0.10-0.40 mm
**Grain Types:** qtz, chert, few feldspars
**F-M-C-P:** F: M: C: P:
**Porosity (%):** Point Count: --
Measured: --
**Perm (mD):** --
**Isotopes (‰ ):** $\delta^{18}$O: --
$\delta^{13}$C: --
Other: --

**Thin Section Map**

**Oriented thin section:** ☑ Yes ☐ No
**Orientation?:** notch is top of bedding

**Preparation**
☑ Thick
☐ Conventional
☑ Polished

**Stains:**
☐ Carbonate
☐ Plag ☐ Kspar

**Point Count:**

**Cement:** (types, sequence) calcite spar, pervasive in banded zones; quartz cement; lots of clay (brown/black opaque) cement occurring patchily throughout the sample, associated with dissolution

**Comments:** Slide is zoned -- some bands have medium porosity, some have no porosity due to calcite cement filling the pores. Areas of higher porosity have many more green spongy dissolved grains than areas of low porosity. All areas have Occasional plagioclase grains. Fracture in bottom of slide appears lithologically controlled: It is bordered by microcrystalline chert grains, whereas most of the grains slightly farther away are monocrystalline quartz grains.

**Sketches:**

**Sample #: 87** (polished)

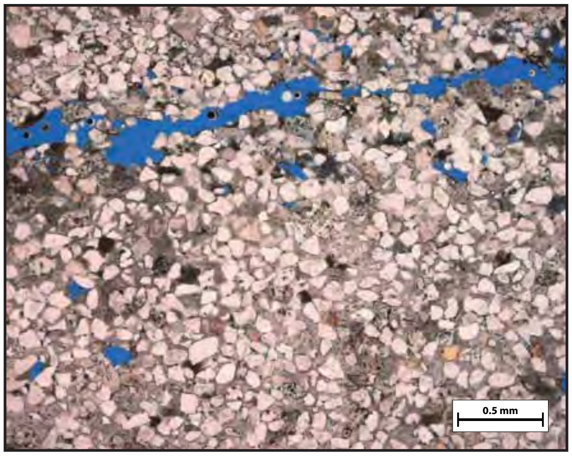

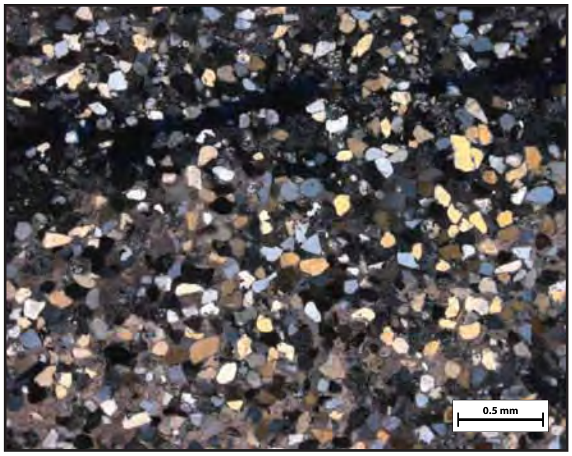

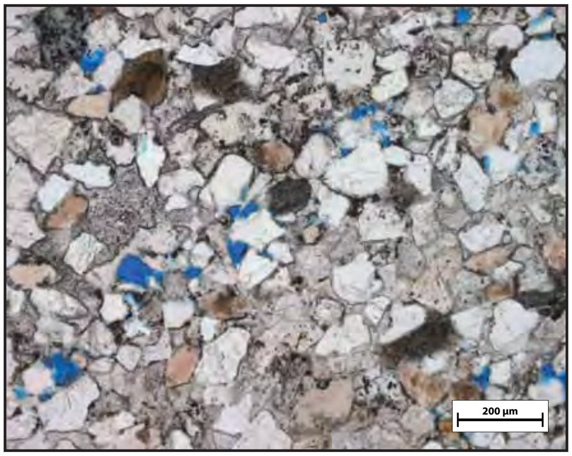

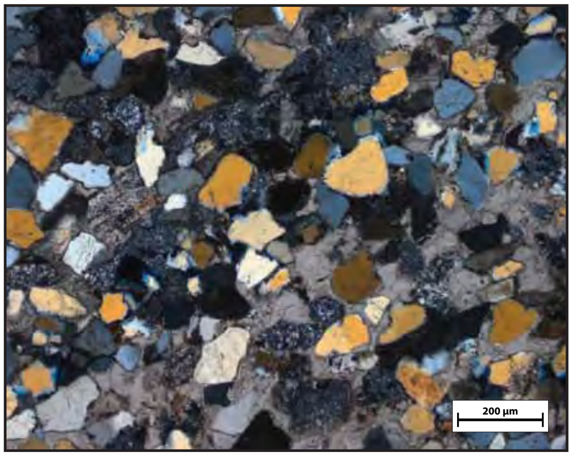

**Sample #:** 87 (stained)

## Petrographic Summary

**Date:** 7/22/10

**Location Description:** Small outcrop to the east of travertine mound, at base of small wash between the mound and adjacent shale-y hill

**Field Trip:** ☐ April, '09 ☑ Oct., '09

**Formation:** Brushy Basin

**Rock Type:** sandstone

**Grain Size:** 0.10-0.40 mm

**Grain Types:** qtz, chert, rare felspars

**F-M-C-P:** F: M: C: P:

**Porosity (%):** Point Count: --

Measured: --

**Perm (mD):** --

**Isotopes (‰ ):** $\delta^{18}O$: --

$\delta^{13}C$: --

Other: --

**Thin Section Map**

×
×
×
×
×
×
×
×

no thin section scan available

**Oriented thin section:** ☐ Yes ☑ No

**Orientation?:**

**Preparation** ☐ Thick ☑ Conventional ☐ Polished

**Stains:** ☑ Carbonate ☐ Plag ☑ Kspar

**Point Count:**

**Cement:** (types, sequence) Bands of calcite cement interfingered with bands of porous rock (a lot of green/spongy pore-filling material); small amounts of clay cement (black/brown opaque).

**Comments:** Lots of chert, lots of monocrystalline grains. Zero porosity where calcite is present; some porosity in other bands -- inter- and intragranular (green spongy dissolved grains). Porous low-cement bands seem to occur where chert is the dominant grain type. Some rare plag grains; SOME calcite appears to be ferroan (stains blue), especially in fracture fill. Adjacent qtz grains seem to be all solidly connected (no cracks or IGV between them)

**Sketches:**

**Sample #: 87** (stained)

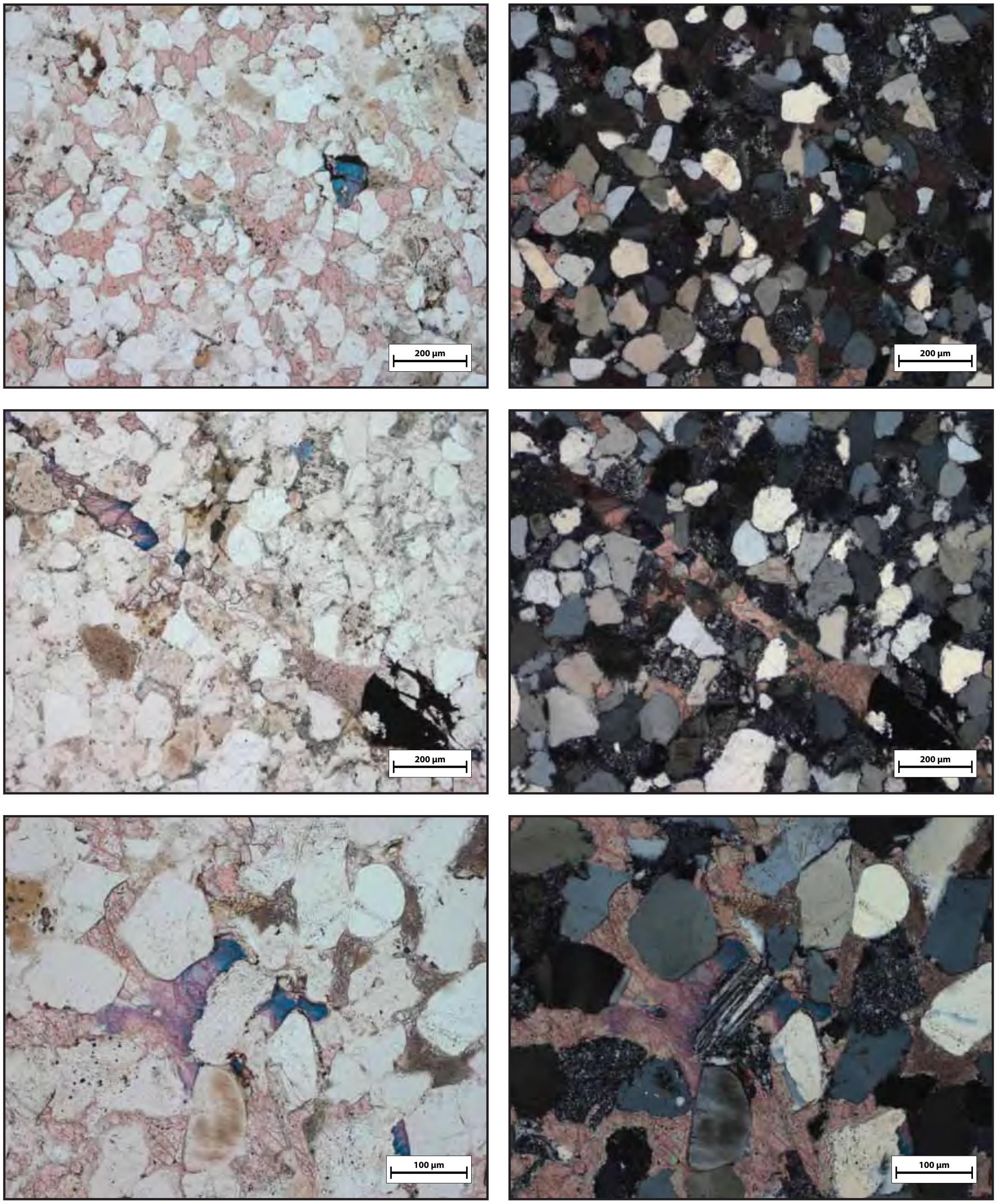

**Sample #:** 100

## Petrographic Summary

**Date:** / /

**Location Description:** Brushy Basin outcrop north of the field area; small hill rising out of shales.

**Field Trip:** ☐ April, '09 ☑ Oct., '09

**Formation:** Brushy Basin

**Rock Type:** volcanic ash

**Grain Size:** clay matrix, 2-mm xstals

**Grain Types:** volcanic ash, qtz xstals

**F-M-C-P:** F: M: C: P:

**Porosity (%):** Point Count: - -

Measured: - -

**Perm (mD):** - -

**Isotopes (‰ ):** $\delta^{18}O$: - -

$\delta^{13}C$: - -

Other: - -

**Thin Section Map**

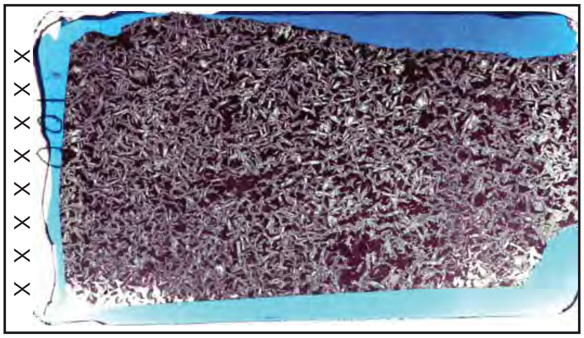

**Oriented thin section:** ☐ Yes ☑ No

**Orientation?:**

**Preparation** ☐ Thick ☐ Conventional ☑ Polished

**Stains:** ☐ Carbonate ☐ Plag ☐ Kspar

**Point Count:**

**Cement:** none

(types, sequence)

**Comments:** The red matrix material appears to be volcanic ash. The lathe-like crystals are sometimes grouped in star-shaped clusters. They appear to be quartz and are likely a result of devitrification of the glass matrix.
Lathes have very thin (<0.01 mm) rim around their border; the interior appears to be composed of larger quartz crystals.

**Sketches:**

**Sample #: 100**

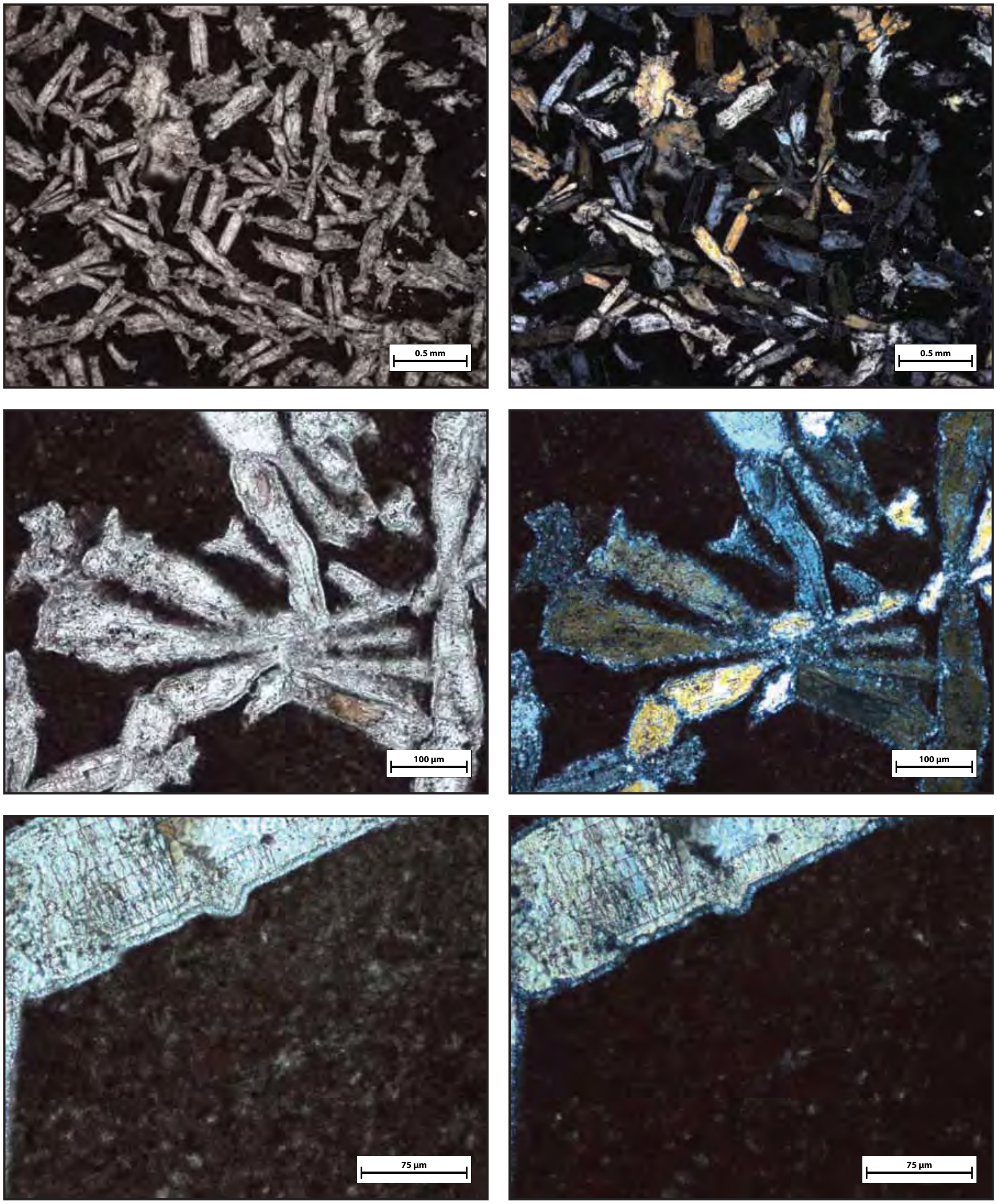

**Sample #:** X

## Petrographic Summary

**Date:** 1/ 7 /11

**Location Description:** Around Crystal Geyser itself. Sample was originally collected as a desktop curiosity, so the exact location was not recorded.

**Field Trip:** ☐ April, '09 ☑ Oct., '09

**Formation:** Quaternary precip

**Rock Type:** calcite precipitation

**Grain Size:** nuclei: 0.1 mm

**Grain Types:** ooid-like grains w/qtz nuclei

**F-M-C-P:** F: M: C: P:

**Porosity (%):** Point Count: 44%

Measured: --

**Perm (mD):** --

**Isotopes (‰ ):** $\delta^{18}O$: --

$\delta^{13}C$: --

Other: --

**Thin Section Map**

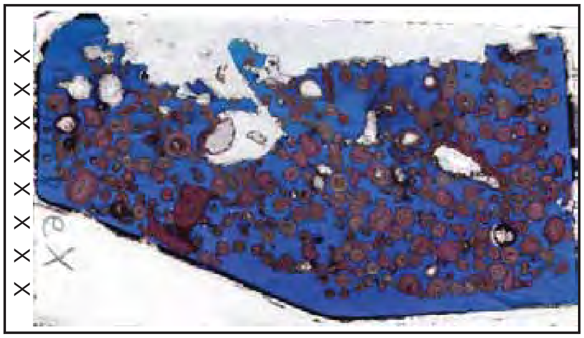

**Oriented thin section:** ☐ Yes ☑ No

**Orientation?:**

**Preparation** ☐ Thick ☑ Conventional ☐ Polished

**Stains:** ☐ Carbonate ☐ Plag ☐ Kspar

**Point Count:**

| Quartz | | | Plagioclase Feld. | | Alkali Feld. | | Lithics | | Misc. | Clay | Cement | | | | Porosity | | | | Total |
|---|---|---|---|---|---|---|---|---|---|---|---|---|---|---|---|---|---|---|---|
| mono | poly | mic/chert | intact | dissolved | intact | dissolved | opaque | sed | Grains | Matrix | spar | micrite | quartz | clay | inter | oversize | intra | micro | Points |
| 4 | 0 | 0 | 0 | 0 | 0 | 0 | 0 | 3 | 0 | 0 | 0 | 180 | 0 | 39 | 174 | 0 | 0 | 0 | 400 |
| 1% | 0% | 0% | 0% | 0% | 0% | 0% | 0% | 1% | 0% | 0% | 0% | 45% | 0% | 10% | 44% | 0% | 0% | 0% | |

**Cement:** (types, sequence) Concentric layers of calcite accreting around quartz nuclei. Some bands appear to be more clay rich.

**Comments:** "Ooids" with qtz and calcite nuclei. Concentric concretions of micrite readily apparent. Occasional rings of cuticle-like clay on the interior, as well as coating the exterior of all ooids.

Looks like an example of how some rocks (71A/B) near the travertine platform may have formed -- surface precip of carbonate around sedimentary nuclei, with periodic influxes of fine-grained seds. Less space between nuclei in 71A.

**Sketches:**

**Sample #: X**

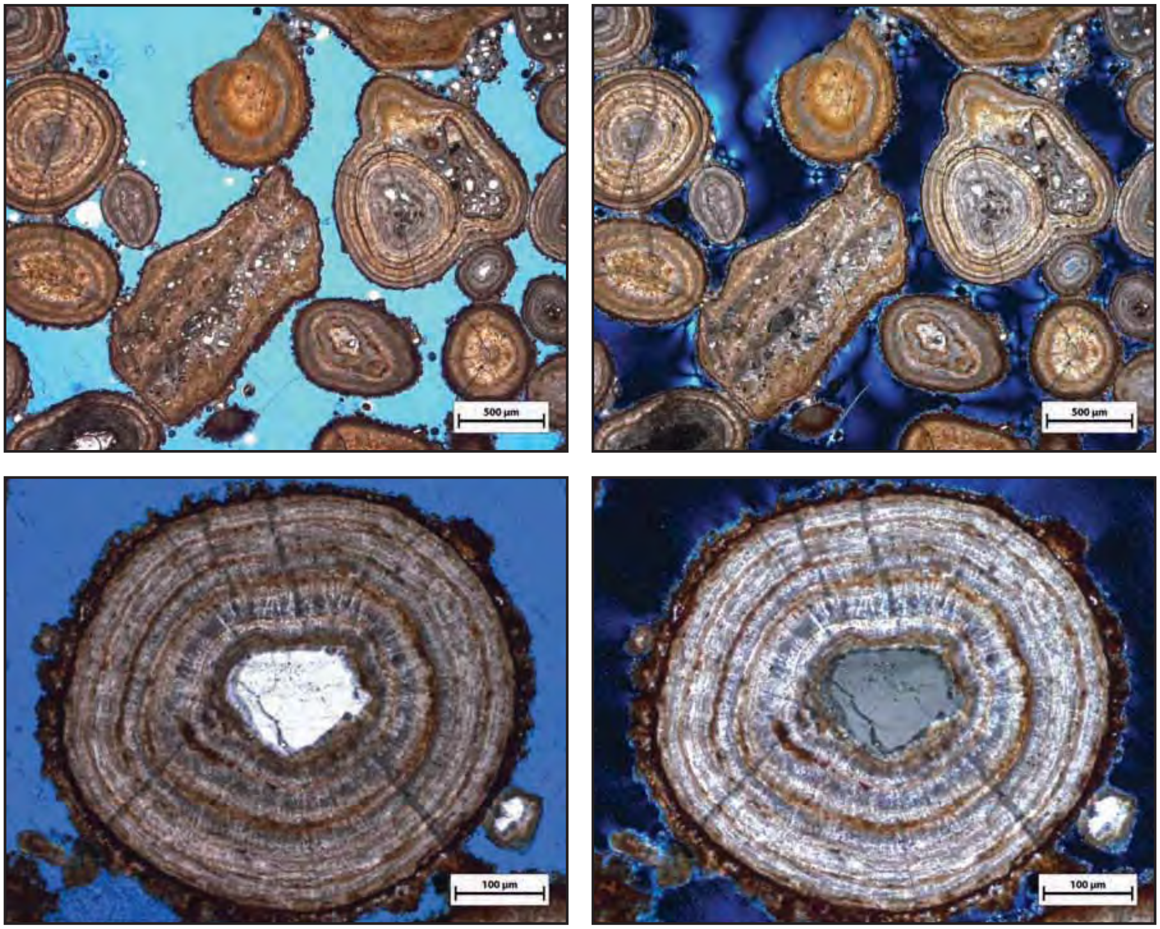

# Appendix D: Methodologies and Techniques

## FIELD WORK

During field mapping I used two-foot resolution (1:24,000 scale), natural color, non-orthorectified aerial photographs purchased from the Bureau of Land Management. The photographs are from 2001 and do not show a recently drilled gas platform on the upper east side of the map area. I drew lithology, alteration, faults and other details of a geologic map on translucent Mylar sheets on top of the aerial photographs. I used preexisting topographic maps for the basic contours of the map area (Doelling, 2002); these contours did not fit the aerial photographs, however, possibly because the aerials are not orthorectified. Contours were therefore adjusted using GPS elevation readings in the field to make a new site-specific topographic survey. All field observations were compiled into a single multilayered file in Adobe Illustrator (see enclosed CD).

## LABORATORY WORK

### Petrography

All standard and polished thin sections were prepared by Greg Thompson in the Department of Geosciences. For staining, some slides were sent to Wagner Petrographic and others I stained myself. To apply a stain to alkali feldspars I used the following method, after Houghton (1980):

> **Preparation:** Wash each slide with warm soapy water, then rinse and dry it thoroughly. In a glass beaker, dissolve 50 g of Na-cobaltinitrite in 100 ml of distilled water to create a saturated solution. Pour a quarter-inch of 55% hydrofluoric acid into a covered plastic container with a roughly thin section-sized opening cut in the lid.

**5.** Etch the thin section by placing it on the opening over the hydrofluoric acid for 30 seconds. Important: Hydrofluoric acid should be handled with extreme care. Wear eye protection, long sleeves and two pairs of nitrile exam gloves. Hold the slide with tweezers.

**6.** Remove the slide with flat tweezers and place it immediately into the beaker of Na-cobaltinitrite solution. Let it sit for about 45 seconds.

**7.** Remove the slide and rinse it twice in tap water. Dry it with compressed air.

For the carbonate stain I used a method based on work by Friedman (1959), Evamy (1963) and Lindholm et al. (1972):

**Preparation:** Mix a solution of 0.2% hydrochloric acid (2 ml of concentrated acid in 998 ml of distilled water). In a large beaker, dissolve 1.0 g of Alizarin red S in 500 ml of 0.2% hydrochloric acid. In another beaker dissolve 2.5 g of potassium ferricyanide in 500 ml of 0.2% hydrochloric acid. This solution will have a shelf life of only about four hours, so a new solution must be prepared every session. Create a separate 2% hydrochloric acid solution by adding 10 ml of concentrated acid to 490 ml of distilled water. Arrange five 400-ml beakers in an assembly line: etch, potassium ferricyanide stain, rinse, Alizarin red S stain, rinse. Do not use running water for the rinse stages, as this can remove the stains.

**1.** Etch the slide in the 2% hydrochloric acid solution for 5–10 seconds.

**2.** Submerge slide in potassium ferricyanide solution for 2–3 minutes.

**3.** Rinse

**4.** Submerge slide in Alizarin red S solution for 20–30 seconds.

**5.** Rinse

Because I did not want stains to interfere, and wanted to preserve a portion of unstained section, each slide was divided into thirds: One end was stained for alkali feldspars, the middle part was unstained, and the other end was stained for carbonates. Because the feldspar staining process required corrosive hydrofluoric acid, it was done first to avoid etching the carbonate stain.

For point counting I used a Zeiss optical microscope, generally at a magnification of 40X or 100X. Slides were held in a Hacker Instruments stage connected to a Swift Model E counter. I counted 400 points per slide; the jump from point to point was two stage intervals, or about 0.33 mm, intended to land only once on a typical grain. Descriptions defining the categorization of each point are included in Appendix E.

To gold-coat rock fragments for electron microscopy I used a Denton Vacuum Desk II gold sputter etch unit. To carbon-coat polished thin sections for electron microscopy I used a Ladd Vacuum Evaporator. (Note that a small carbon peak at 0.25 keV is typical in energy dispersive spectroscopy of all samples as a result of this carbon coating.) For electron microscopy three machines were available to me at the Jackson School of Geosciences: In the Department of Geosciences I used an FEI/Philips XL30 environmental scanning electron microscope with cathodoluminescence and EDAX XL30 energy dispersive spectrometer attachments and a JEOL JSM-6490LV scanning electron microscope with an EDAX Genesis energy dispersive spectrometer attachment; at the Bureau of Economic Geology I used an FEI Nova NanoSEM 430 with an energy dispersive spectrometer attachment used for composite element mapping.

### Porosity and permeability

Gas injection permeability and porosity measurements were done by Glen Baum in the Department of Petroleum and Geosystems Engineering at the University of Texas at Austin. Permeability measurements were made using nitrogen gas injection. The plug was placed in a Hassler type core holder and surrounded by an impermeable sleeve while gas was pumped through it. The change in pressure over the length of the core was measured at flow rates of 20%, 40%, 60%, 80% and 100% of the full scale range of a mass flow meter and the results were plugged into Darcy's equation for permeability (personal communication: Baum, 2011; Tiab and Donaldson, 2004). Porosity measurements were made using helium gas injection. A core plug of known total bulk volume was placed in a chamber (sample chamber) that was connected to a valve-separated chamber (reference chamber), both of known volume. A vacuum was pulled on the entire system. The valve was then used to isolate the sample chamber from the reference chamber while helium of a known pressure filled the reference chamber. When the valve was opened, the equilibrium pressure ($p_e$) of both chambers could be used to calculate the solid (non-pore) volume of the plug ($V_s$) using the Boyle's Law equation:

$$V_s = \frac{V_1(p_e - p_1) + V_2(p_e - p_2)}{p_e - p_1}$$

where $V_1$ is the volume of the sample chamber, $V_2$ is the volume of the reference chamber, $p_1$ is the starting pressure of the sample chamber and $p_2$ is the starting pressure of the reference chamber (Tiab and Donaldson, 2004). Knowing the volume of solids in the plug, the porosity is simply

$$\text{porosity} = \frac{1.00 - V_s}{V_{\text{plug}}}$$

where $V_{plug}$ is the total cylindrical volume of the plug. Because this method assumes the plug is a perfect cylinder, it will be slightly skewed by any imperfections in the actual plugs, which in some cases were slightly chipped or did not have perfectly parallel ends. I eschewed the more accurate mercury injection method due to its considerable expense and because core plugs submitted to this process cannot be reused and I have limited sample material.

## Mass spectrometry

For calcite stable isotope measurements, 18 samples of ground sample material were sent to Dr. Peter Blisniuk at the Stanford University School of Earth Sciences. Two of the vials (samples “98” and “99”) were duplicates (of samples 84 and 79, respectively) intended to check measurement precision. To completely homogenize the material, Dr. Blisniuk crushed it to silt-sized particles using an alumina mortar and pestle. He tested the effectiveness of homogenization by re-running four samples—71B, 74, “99” and 80B—the results of which are within the uncertainty shared by all samples. The blind duplicates similarly fall within the same uncertainty. All samples were run twice to ensure that their signal strengths fell within the range of 8–40 Vsec (the minimum signal strength in the final dataset is 9.4 Vsec; the maximum is 29.6 Vsec).

In addition to stable isotopes, Dr. Blisniuk also recorded calcite content based on the signal strength (measured by mass spectrometer) of $CO_2$ produced from the reaction of sample calcite with phosphoric acid. The measurements were made by comparing the signal produced from pure calcite standards of known mass to the signal produced by sample material of known mass but unknown calcite content. The signal relationship between sample and standard is linear (the same amount of calcite will produce the same signal). Using the signal strength of the pure standard as a calibration point, sample calcite content can be calculated by taking the signal strength produced by the sample as a percentage of the signal strength that would be expected if the sample’s entire weight were pure calcite. For example, Blisniuk (personal communication, 2011) explains: If a 200-μg calcite standard produces a 5.0-V signal, 100 μg of the same standard will produce a 2.5-V signal. If 2,000 μg of sample material produces a signal of 5 V, this would indicate about 10% calcite content (of the 2,000 μg of material, 200 μg are calcite, a portion which produces the same signal as the 200-μg standard). This method is referred to in the text as the "Signal calibration" method of measuring calcite content.

Blisniuk (personal communication, 2011) reports that these measurements should be accurate to within a few percent. This is premised on the assumption that there is only calcite present—no dolomite or other carbonates in the sample. Extensive petrographic analysis using optical and electron microscopy and X-ray diffraction shows that there are no other carbonates present in detectable amounts.

**X-ray diffraction**

To prepare randomly oriented bulk rock powders for X-ray diffraction analysis, I first crushed a portion of each sample in a SPEX SamplePrep 8000M Mixer/Mill ball mill for one minute in order to achieve a finely crushed homogeneous mixture. If, after one minute, there were any remaining grains larger than sand-sized, I milled the mixture for another minute. I then took 4.50 g of sample material and added 0.75 g of corundum powder for a ratio of 6:1. I put this material into a McCrone micronizing mill to create a finer and more uniform powder. Before milling it, 13 ml of 0.5% polyvinyl alcohol were added to give binding strength to the powder when dried, and one drop of 1-octanol, to prevent frothing in the mill (Hillier, 1999). I ran the mill for 12 minutes to reduce the material to a particle size of less than 10 μm.

To achieve random orientation, I followed the airbrush and drying chamber method described by Hillier (1999). The milled slurry was loaded into an airbrush, which was powered by compressed nitrogen at 10 psi. I used the airbrush to spray the slurry into the top of a chimney oven heated to 130°C. As the slurry descends through the chimney it dries to a fine dust of randomly oriented spherules about 50 μm in diameter (Figure D1) and falls

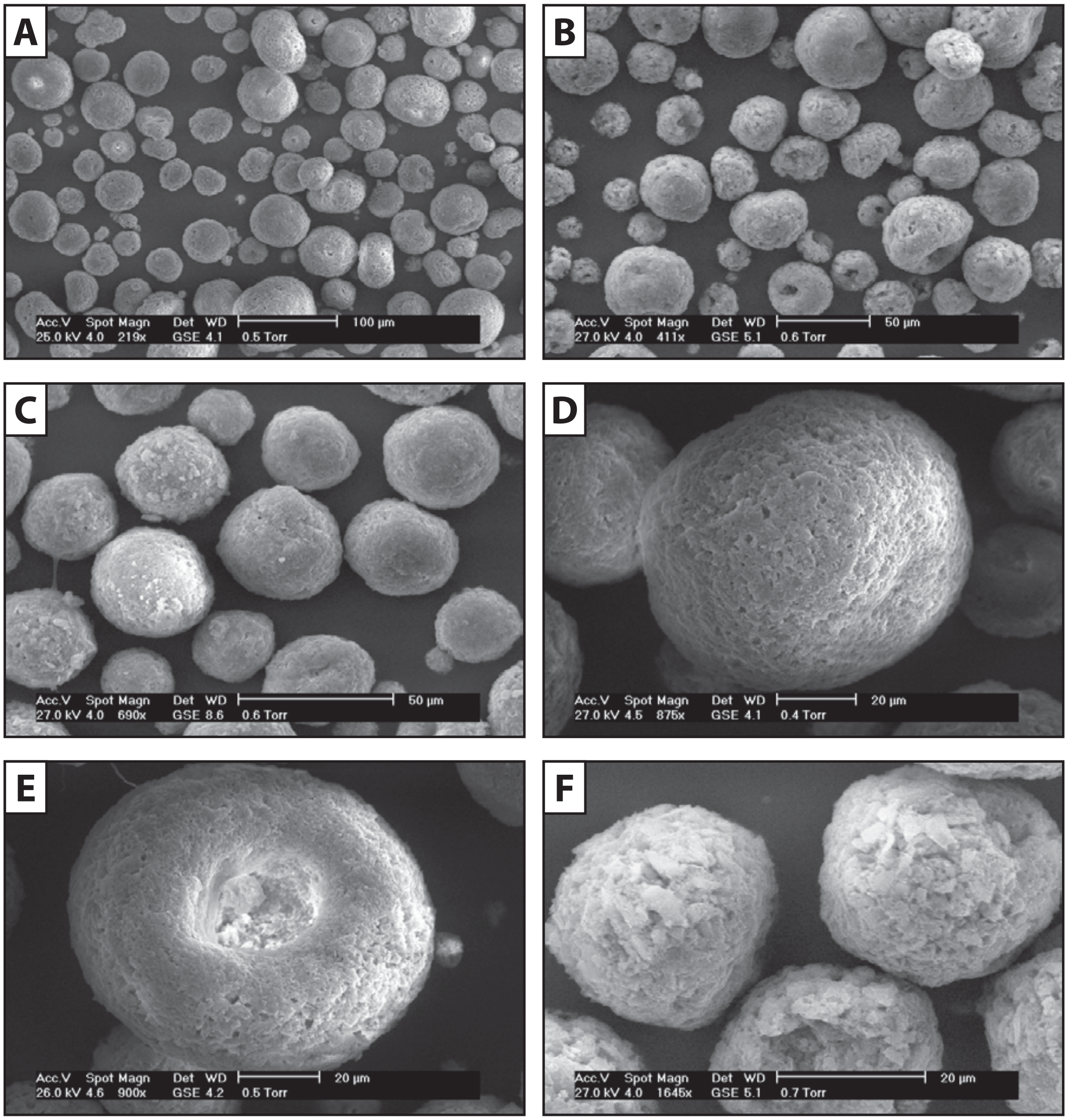

Figure D1: Secondary electron images at increasing magnification of spray-dried, randomly oriented bulk rock sample powders. (A), (D) and (E) are from sample 17C, a calcite-cemented sandstone; (B) and (F) are from sample 80A, a porous, mostly uncemented yellow sandstone; (C) is from sample 71A, a mixture of sand and muddy micritic matrix.

to a glossy collection paper at the base. This powder was collected in a glass vial and was ready for X-ray analysis.

To prepare oriented clay-size separation mounts for X-ray diffraction I followed the process described by Moore and Reynolds (1997). To separate clay-sized grains, I soaked about 10 g of sample material overnight, then placed it in a bath of 0.3 M acetic acid in order to remove much of the carbonate cement binding it together. The carbonate reacting with the acid acts as a buffer to prevent clays from being affected by the reduced pH (Ostrom, 1961), but if the carbonate material is entirely removed no such buffer will remain. Because of this risk I was conservative with the application of acid, removing and rinsing sample material before the solution had stopped effervescing (while carbonates still remained), but at a point when enough cement had been removed that sonication could be used to further disaggregate the sample. I put the sample material into a beaker of distilled water and used a Misonix horn-type ultrasonic processor (sonicator) to continue sample disaggregation and disperse fine sediment in the water. The advantage of sonication is that it does not break large grains into clay-sized grains, as would be the case if a mortar and pestle were used for disaggregation. The disaggregated sample material suspended by sonication was poured into a large collection beaker; the remaining material was repeatedly irradiated and decanted until there was a large volume of decanted material.

The decanted sample material was loaded in 10-cm-tall 250-ml bottles. To leave clay-sized (2-μm) particles in suspension and settle larger particles, according to Stokes' Law, I centrifuged the dispersions for 149 seconds at 1,000 RPM in a Sorvall Legend T+ centrifuge with a Fiber*Lite* F14–6x250 LE carbon fiber rotor. The sample material remaining in suspension after centrifugation was poured into a collection beaker. Stokes' Law was used to calculate the time for 2.1-μm particles to settle 10 cm, however, which meant that smaller particles floating at a level below 10 cm would also have settled during centrifugation. The settled portion was therefore repeatedly disbursed by sonication, centrifuged and decanted until all clay-sized material was collected—when all material settled during centrifugation, leaving the water perfectly clear. The decanted clay-sized distillation was drawn through a Millipore 0.45-μm filter, forcing sedimentation of all particles and forming a film on the filter about one millimeter thick. A glass slide pressed to the filter paper peeled off with a uniformly thick layer of oriented clay-size sediment (Figure D2). These slides were then ready for analysis.

For X-ray diffraction analyses I used a Bruker D8 Advance X-ray diffractometer. During bulk rock analysis I scanned from 4–45° 2θ and during clay-size analysis I scanned from 4–70° 2θ. The step size increment for each was 0.01° at 0.3 seconds per step. The machine was set to PSD LynxEye locked coupled continuous scan at 40 kV and 35 mA. The 2θ ranges were intended to include most clay peaks, which are at 2θ values of 40° or less (Moore and Reynolds, 1997), and to avoid an artificial high-intensity peak at 2–4° that obscures other peaks. I scanned a larger range with the clay-size separations in order to include a search for possible carbonates other than calcite and any other unexpected minerals that might be detectable in clay-size separations.

After running the air-dried scans, for all clay-size separations I also ran glycolated scans intended to swell clays such as smectite, causing an identifiable shift in peak positions. To do this I placed samples in a chamber partially filled with ethylene glycol and warmed the chamber to about 60°C using a Sargent-Welch oven. To allow sufficient time for swelling the samples were left for 8 hours, at which point I removed them one at a time to be scanned.

Lastly I heated two of the clay-size separation samples to check for clays—illite-smectite and chlorite-smectite—by dehydrating them and creating corresponding peak shifts. I baked these samples in a Thermolyne 2000 furnace one at a time for one hour at 375°C,

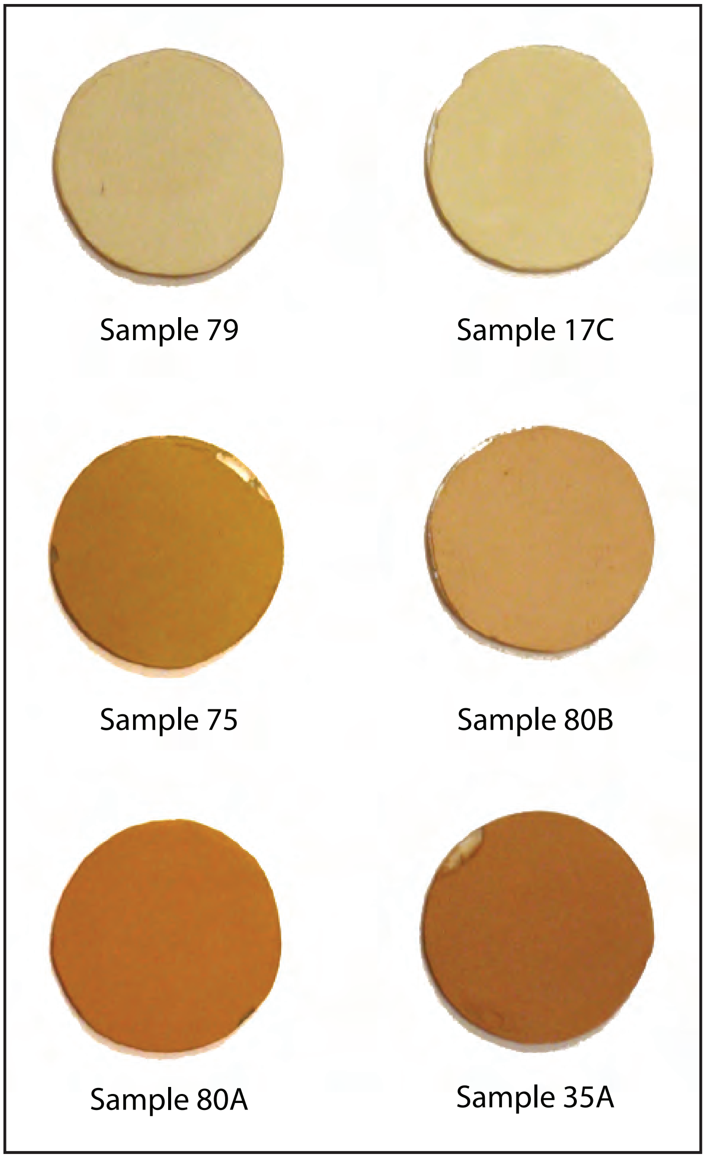

Figure D2: Oriented clay-size separation slides, ready for X-ray diffraction.

then immediately scanned them from 4–40° (the essential clay range). These scans confirmed the presence of chlorite-smectite but did not reveal any new minerals. For this reason, and because heating appeared to damage the samples (they came out of the oven with small, slightly charred-looking speckles) I did not perform heated scans on other samples.

For a preliminary analysis of X-ray diffraction data, patterns were compared against the International Center for Diffraction Data's database, the 2008 release of Powder Diffraction File 2. For more in-depth analysis I cross-referenced this database with Moore et al.'s (1997) book, *X-Ray Diffraction and the Identification and Analysis of Clay Minerals*, as well as the excellent online RRUFF X-ray diffraction database (Downs, 2006).

# Appendix E: Description of Point Count Categories

During point counting I counted whichever mineral was at the top of the thin section—if I landed on calcite overlapping the edge of a quartz grain, I counted it as calcite. If the crosshairs landed exactly on the boundary between minerals, I arbitrarily counted whichever was in the top right quadrant. The following are definitions and explanations for each point count category.

**Monocrystalline quartz** grains (Figure E1) are composed of a single large crystal of quartz. The grains may have either uniform or undulatory extinction. In the samples for this project, the birefringence color varies from very low (dark gray) to first-order yellow, depending on how thick the thin section was cut.

**Polycrystalline quartz** grains (Figure E1) are composed of multiple genetically fused quartz crystals (i.e., no grains of recycled sandstone). The discrete crystals can be identified because they tend to have different orientations and therefore different extinction angles. Each crystal must be distinct, however. If individual crystals are too small to be easily distinguished from adjacent crystals, then the grain is considered microcrystalline.

**Microcrystalline quartz and chert** (Figure E1) include any purely $SiO_2$ grain with crystals too small to distinguish at low-to-medium magnification. This includes grains composed of genetically fused crystals (similar to polycrystalline grains) that are too small to be differentiated. It also includes organically derived silica, such as chert.

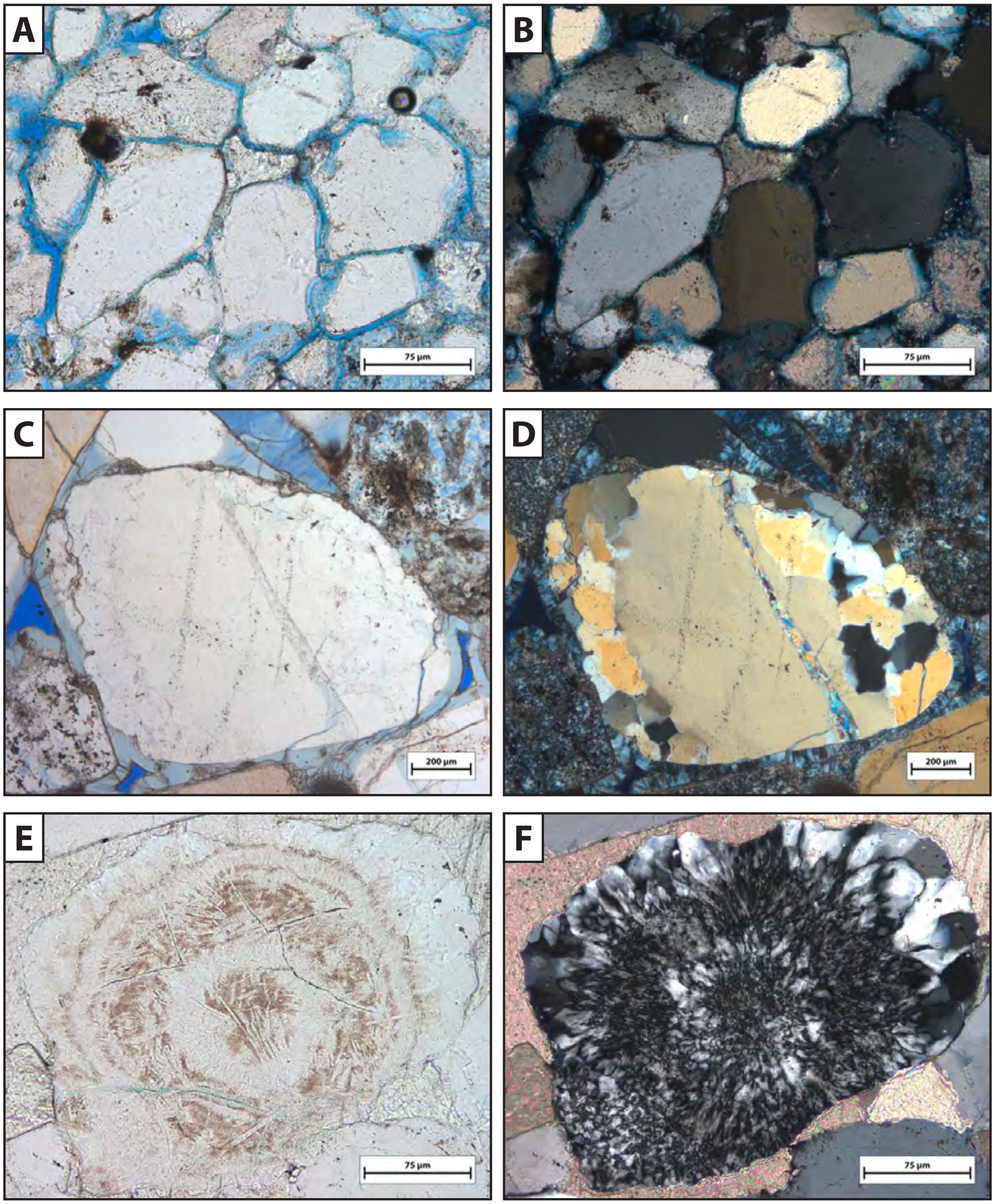

Figure E1: *Quartz grains* **A–B:** Monocrystalline quartz grains at various stages of extinction. **C–D:** Polycrystalline quartz grains must usually be viewed in crossed polars to identify discrete crystals. **E–F:** A chert grain (microcrystalline quartz) with an interesting radial pattern.

**Intact plagioclase feldspars** (Figure E2) are grains of plagioclase that are entirely undissolved. I tried staining some samples for plagioclase using the K-rhodizonate (pink) stain recommended by Houghton (1980), but this process was only moderately effective, damaged the Na-cobaltinitrite (yellow) stain used for alkali feldspars, and was absorbed by porous clays. I therefore decided not to apply the stain and did not request that it be applied by Wagner Petrographic, the company to which I sent some slides for staining. To distinguish plagioclase grains from quartz and alkali feldspar, I relied largely on the presence of polysynthetic twinning and fracture patterns resulting from cleavage planes.

**Dissolved plagioclase feldspars** (Figure E2) are grains that can be identified as plagioclase (generally by the presence of polysynthetic twinning), but which include dissolution features ranging from incipient to nearly complete. The dissolution commonly follows cleavage planes and leaves behind a pocked texture with clay-ey material in the interstices. During point counting, when the crosshairs landed on this clay material, I counted it as clay cement, not as a feldspar grain.

**Intact alkali feldspars** (Figure E3) are grains of alkali feldspar that show no signs of dissolution. I stained several thin sections with yellow Na-cobaltinitrite in order to highlight alkali feldspars. The stain was inconsistent, however, and took to porous clays and plagioclase feldspars (Figure E2) as well as the intended alkali feldspars. This makes the process somewhat confusing, and I often relied on the presence of perthitic twinning and cleavage plane fractures in order to distinguish undissolved alkali feldspars from quartz and plagioclase feldspars.

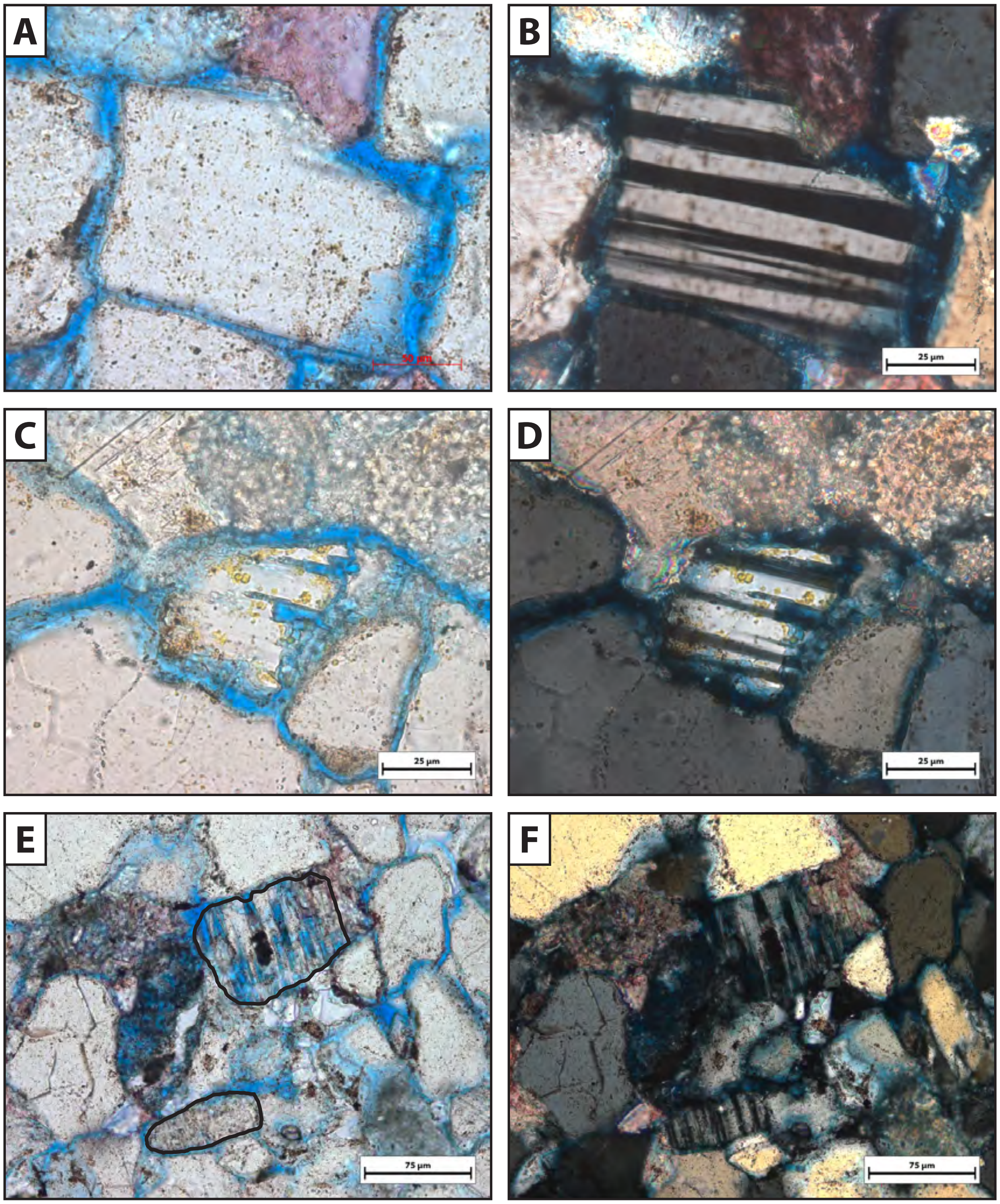

Figure E2: *Intact and dissolved plagioclase feldspars* **A–B:** Fully intact plagioclase grain displaying typical polysynthetic twinning. **C–D:** Plagioclase grain in an early stage of dissolution—large intragranular pores are following cleavage planes, but it is still recognizable as plagioclase. The yellow blots are Na-cobaltinitrite stain, which is not intended to take on plagioclase grains. **E–F:** Pair of plagioclase grains, one mostly intact and one at an advanced stage of dissolution.

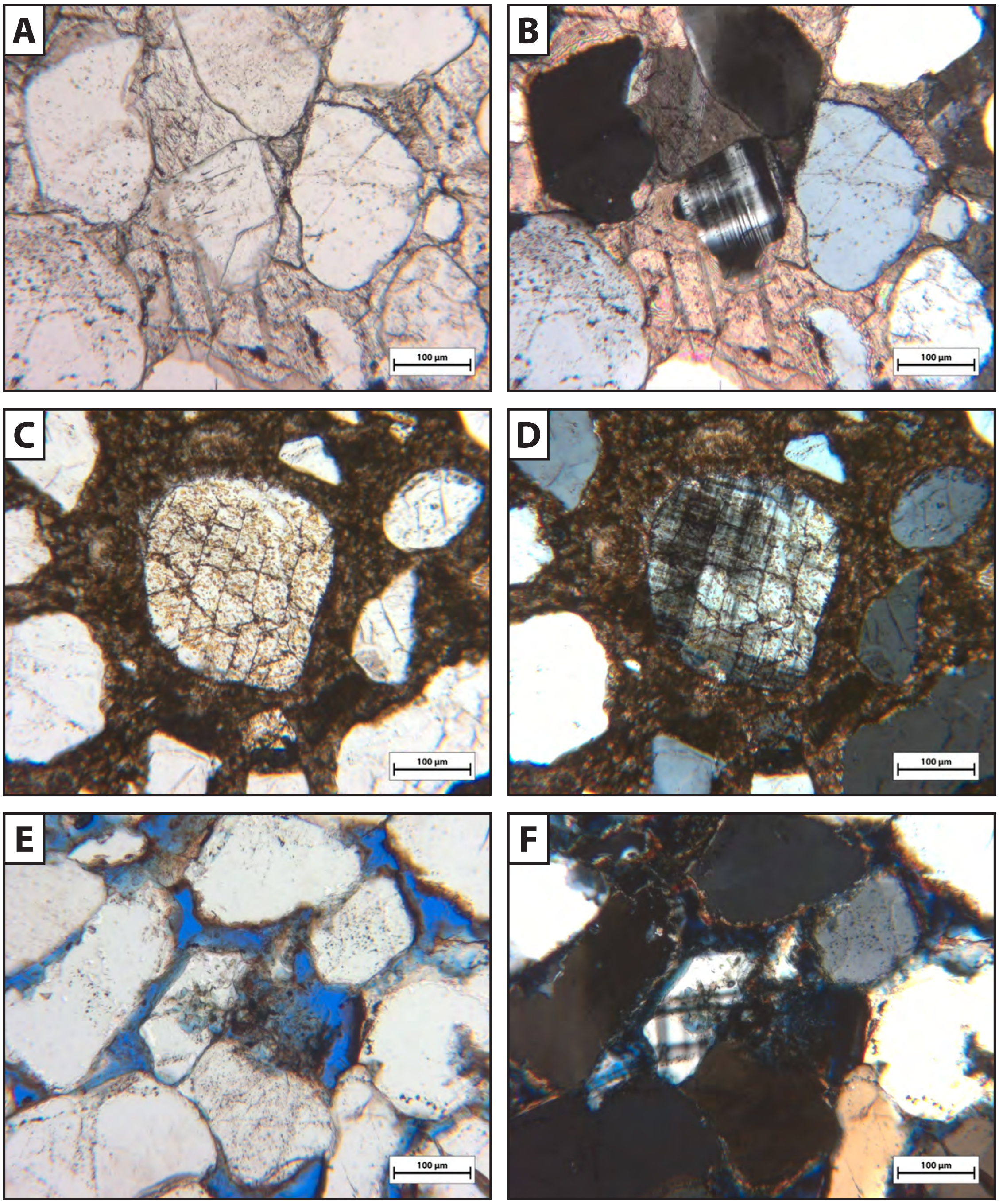

Figure E3: *Intact and dissolved alkali feldspars* **A–B:** Intact grain displaying the perthitic twinning typical of alkali feldspars. **C–D:** The yellow Na-cobaltinitrite stain was not a great success, staining minerals it was not intended for and showing up patchily at best on alkali feldspars, as seen here. **E–F:** Alkali grain in early stages of dissolution showing an incipient intragranular pore.

**Dissolved alkali feldspars** (Figure E3) are grains that can be identified as alkali feldspar (generally by the presence of perthitic twinning), but which include dissolution features ranging from incipient to nearly complete. The dissolution commonly follows cleavage planes and leaves behind a pocked texture with clay-ey material in the interstices. During point counting, when the crosshairs landed on this clay material, I counted it as clay cement, not as a feldspar grain.

**Sedimentary lithic** grains (Figure E4) include all well-defined grains that are recycled from a previous sedimentary rock: “grains” of multiple grains from an earlier sandstone, clay rip-up clasts and recycled grains of micrite are all present in samples from this project. During point counting I did not count the individual components of a grain; if the crosshairs landed on a monocrystalline quartz grain included in a larger grain of mixed clay and quartz, I counted the point as a sedimentary lithic grain. The most common types of these grains are clusters of fine- to clay-sized sediment.

**Opaque lithic** grains (Figure E4) have the polygonal or circular-to-oblong shape of a grain with well defined boundaries. I use several criteria to distinguish opaque lithic grains from clay-rich sedimentary lithic grains: Opaque lithic grains are very dark brown or black and uniformly colored, as opposed to clay-rich sedimentary lithic grains, which are usually light brown and mottled, probably due to variable grain thickness; opaque lithics show signs of large, rigid crystal structure (e.g., straight edges, corners and fractures indicating cleavage), as opposed to clay clasts, which, because they are composed of countless tiny grains, tend to be amorphous and show signs of malleable deformation.

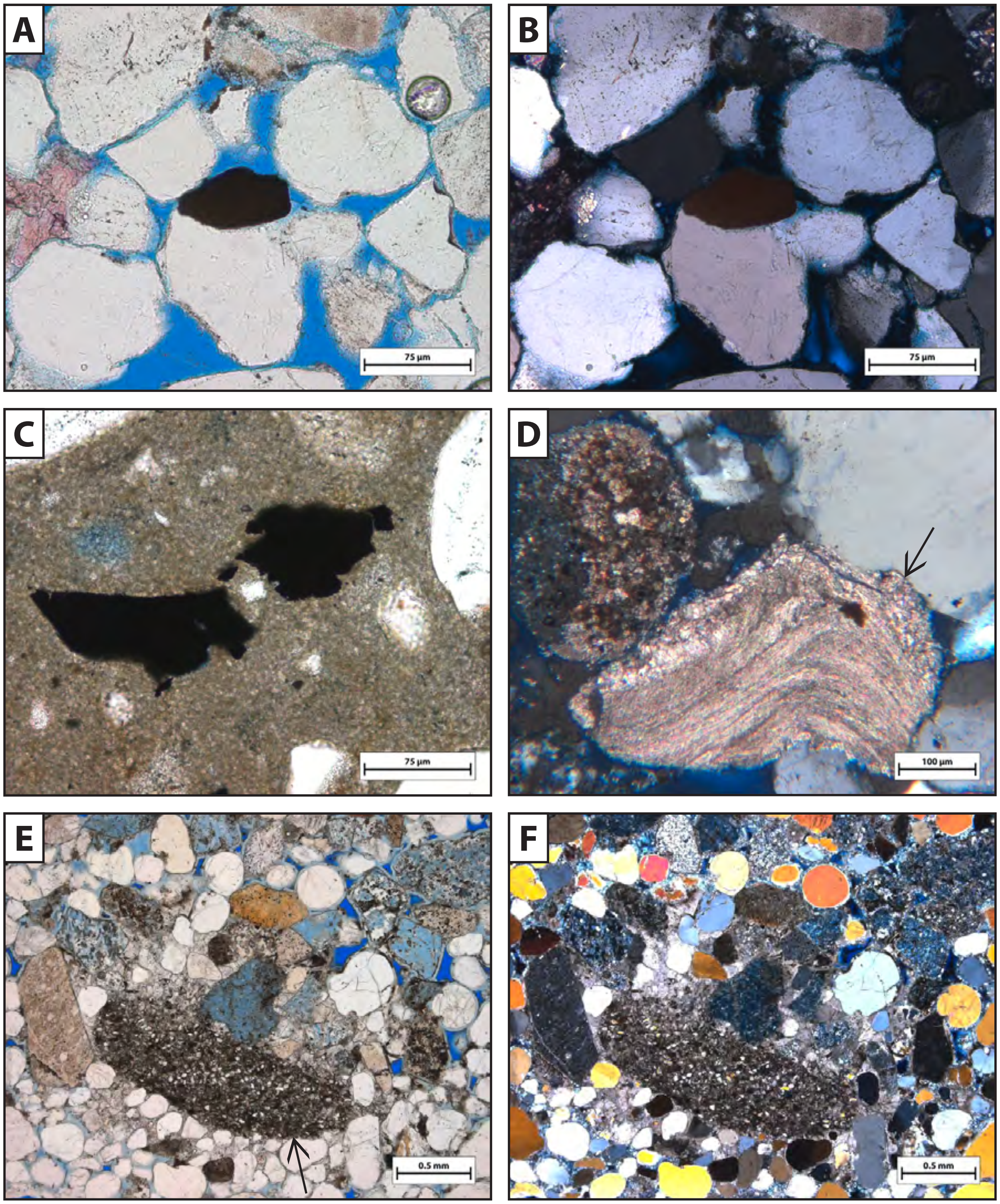

Figure E4: *Opaque and sedimentary lithic grains* **A–B:** An opaque lithic grain; note the well-defined grain boundaries and the uniformly black appearance. **C:** Opaque lithic grains showing elongate rigid edges. **D:** Sedimentary lithic recycled micrite grain. **E–F:** Silty sedimentary lithic grain.

**Miscellaneous grains** (Figure E5) are any type of grain I was unable to identify or that I could identify but which did not fit into a predefined category. One common type of identifiable grain is zircon. Zircon grains not present in great enough abundance to justify a separate category in the point-counting process. They appear as small, generally elongate, anomalously high-birefringence grains with high relief. Other miscellaneous grains include possible zeolites.

**Clay matrix** (Figure E6) is pervasive dark brown-to-opaque allogenic material. It is clay-sized sedimentary material mixed in with larger sediments during deposition, but not in great enough proportion to form shale strata. I have identified several rocks in the map area dominated by a clay-micrite matrix. The interpretation of these rocks is that significant amounts of wind-blown and water-borne clay were deposited in carbonates as they precipitated at the surface around a $CO_2$-rich spring. These fine-grained sediments are the clay matrix.

Because the clay matrix is so fine-grained and is deposited unevenly among other microcrystalline crystals (micrite), it was often difficult to determine the topmost mineral during point counting. The light passes through many layers of each mineral within the thickness of the thin section. I categorized these points by whichever mineral appeared to be most dominant—considering the immediately adjacent grains and the full thickness of the slide (30–40 μm).

**Calcite spar cement** (Figure E7) is authigenic carbonate that grows in crystals large enough to be individually identified and easily delineated at low-to-medium magnifications (25–40X). This includes pore-filling calcite as well as euhedral crystals growing along

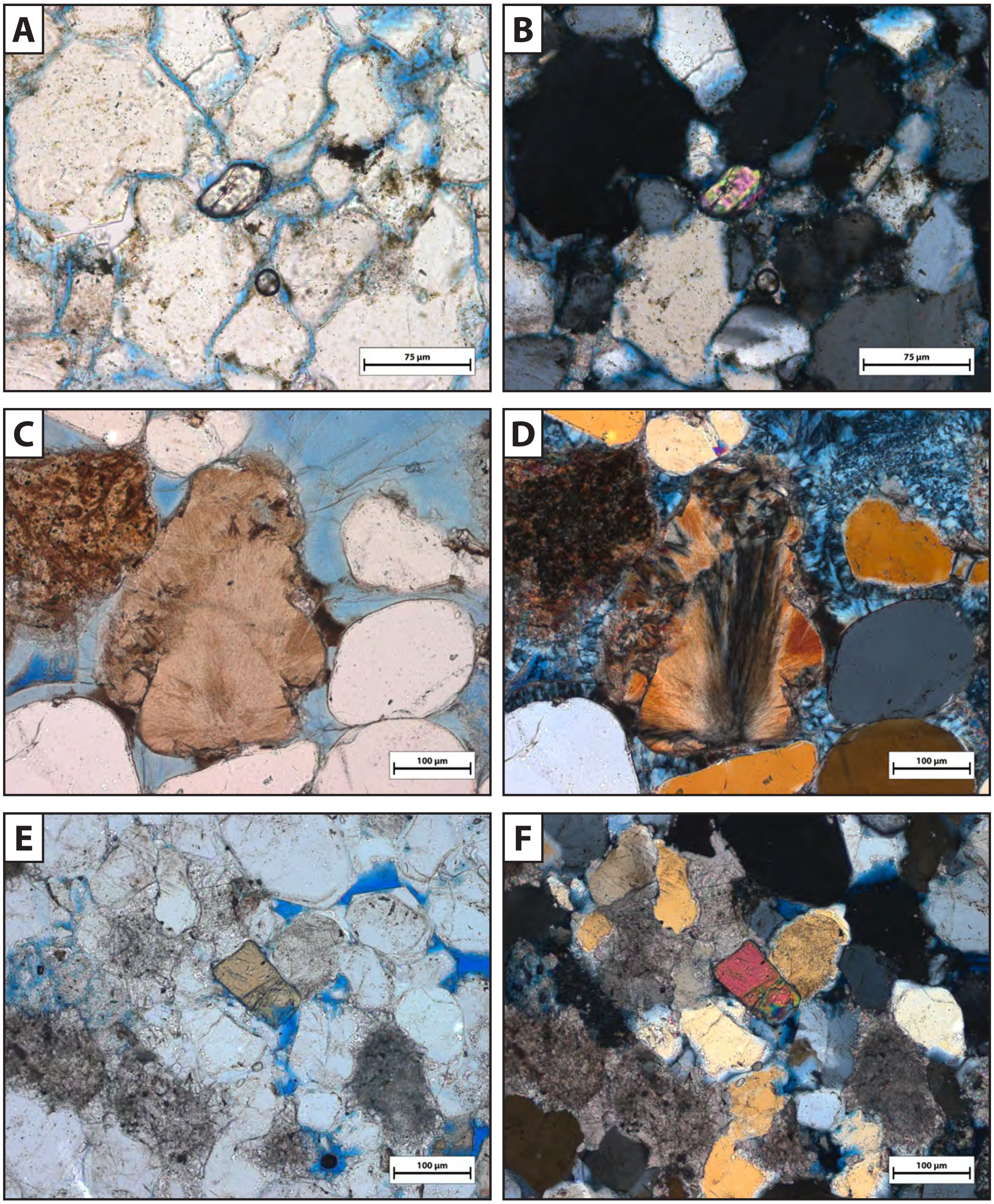

Figure E5: *Miscellaneous grains* **A–B:** A zircon grain stands out by its high relief and high birefringence. **C–D:** Possible zeolite grain—the fibrous habit and radial extinction are similar to zeolites such as natrolite. **E–F:** Unknown grain with high birefringence.

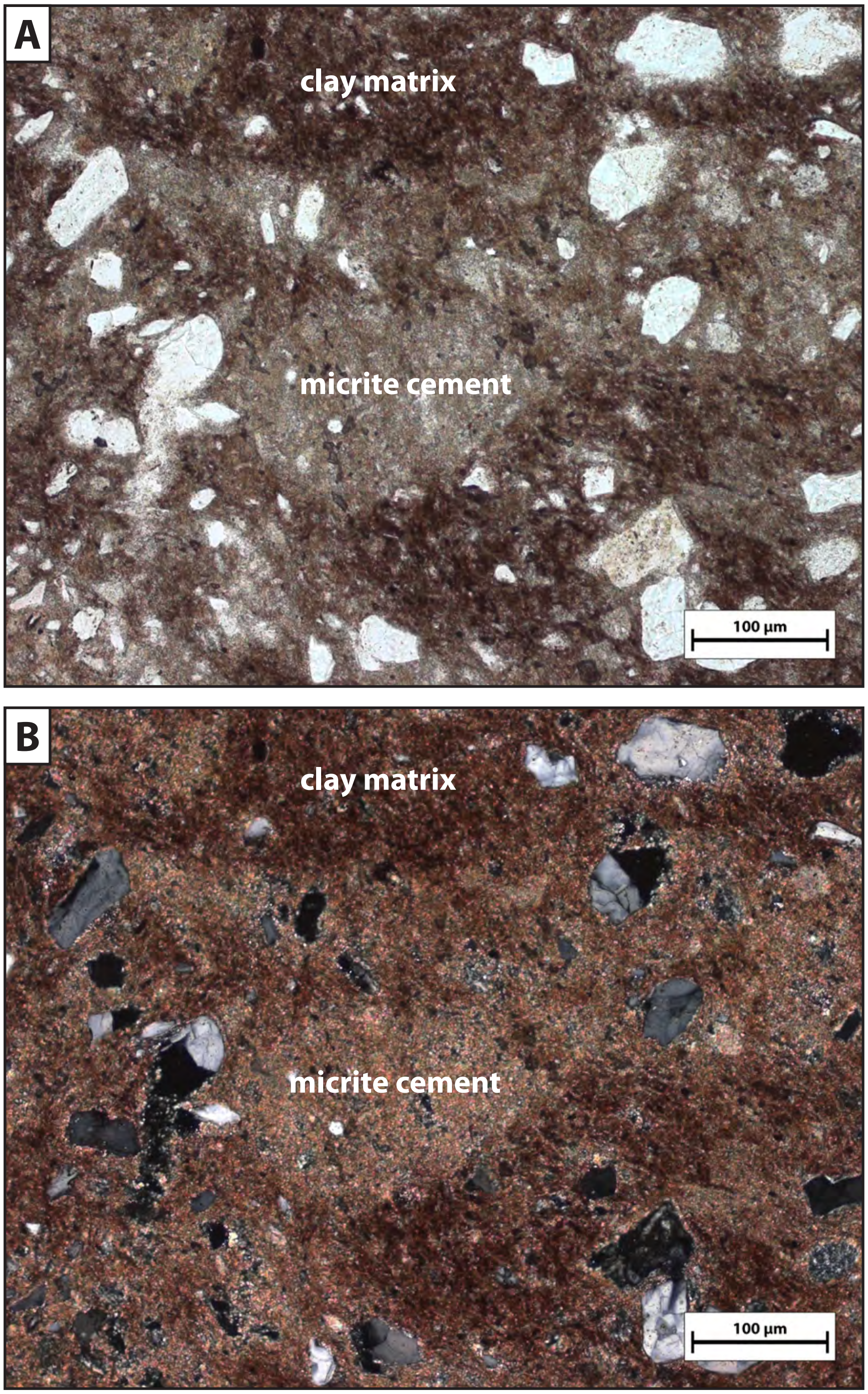

Figure E6: *Clay matrix* **A–B:** Plane light and crossed-polars views of dark red-brown clay matrix mixed with lighter-colored micrite. Clay matrix material is most often mixed pervasively with micrite cement. Clay matrix is easiest to identify in plane light, while intermixed micrite cement is easier to identify under crossed-polars due to its bright birefringence.

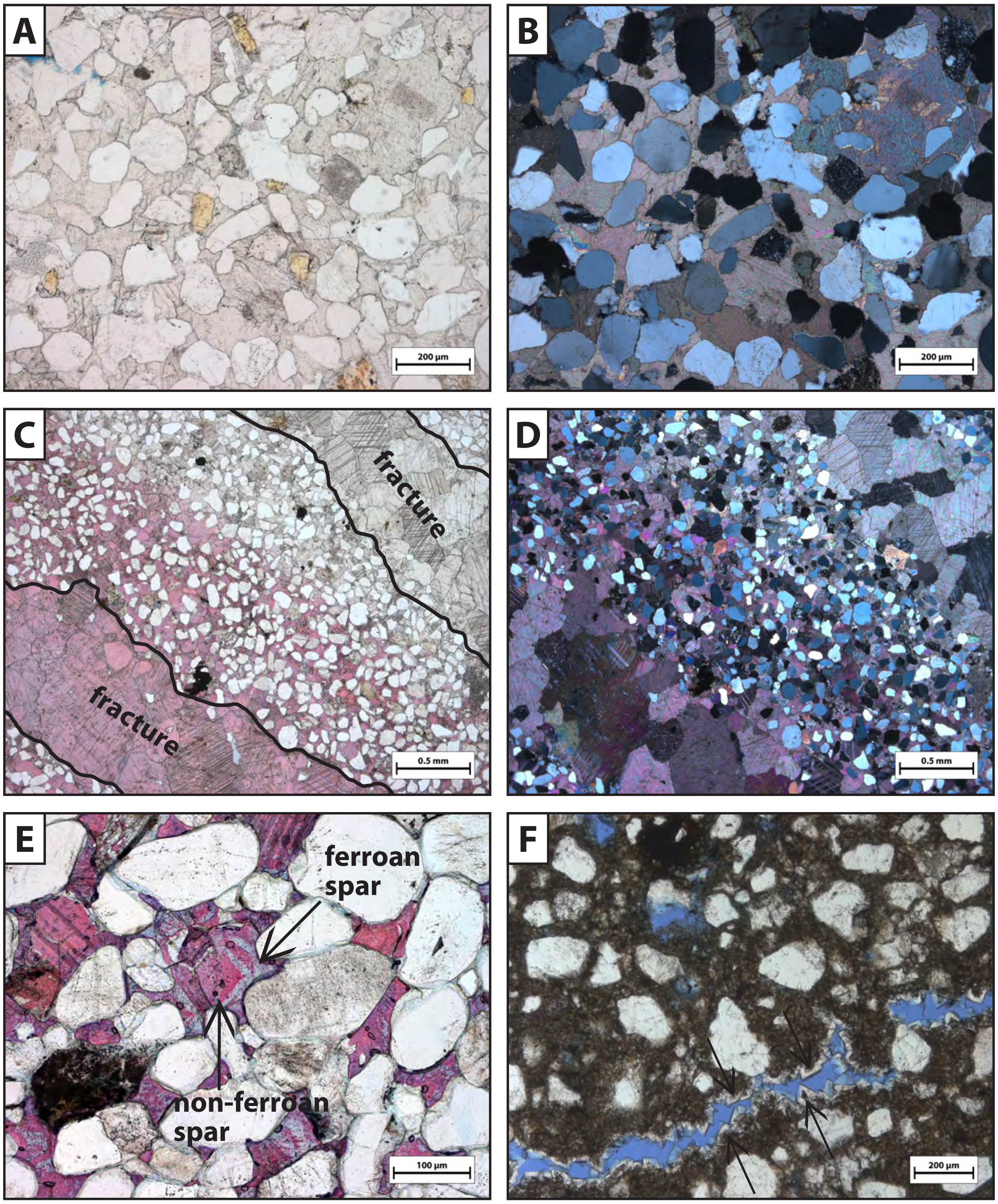

Figure E7: *Stained and unstained calcite spar cement* **A–B:** No porosity is visible in this sample because it has been fully occluded by calcite spar. **C–D:** Parallel calcite-filled fractures show the difference between stained and unstained calcite; the cross-hatching results from cleavage planes in the calcite. **E:** The stain turns blue in the presence of ferroan calcite; this may show two generations of calcite. **F:** Euhedral spar crystals growing into an open fracture.

the edges of fractures. In some spots, calcite spar appears to have been damaged during the thin section preparation process—a rounded zone of what looks like micrite is present almost like a smudge across one or many distinct spar crystals. In these cases I counted the point as spar cement, not micrite. Identification of spar (and micrite) is facilitated in some slides (see Table C1) by application of the combined potassium ferricyanide and Alizarin red S carbonate stains.

**Micrite cement** (Figure E8) is microcrystalline authigenic carbonate. It forms masses that can be clearly identified as carbonate by their habit, birefringence, and, in some cases, the carbonate stain. Individual crystals are difficult to delineate even at high magnification (100–250X). Micrite cement forms a pervasive matrix in some samples, and in these samples is often mixed with brown-to-black clay matrix. During point counting, the top layer was counted, if it could be determined. Because individual crystals of these types of mineral are so thin and virtually indistinguishable, if I could not identify a "top" mineral I categorized the point as whichever mineral appeared to be most dominant in the column of the thin section at that spot. In these cases I considered the immediately adjacent grains and the full thickness of the slide (30–40 μm).

**Quartz cement** (Figure E9) is authigenic quartz, generally in the form of quartz overgrowths that nucleate on the surface of quartz grains. Quartz cement frequently forms distinctive euhedral quartz crystals that grow into intergranular porosity. Quartz overgrowths were only tallied if they appeared to have grown in their current position. If they are relict cements from a previous rock (a recycled sandstone), I counted them as a sedimentary lithic grain.

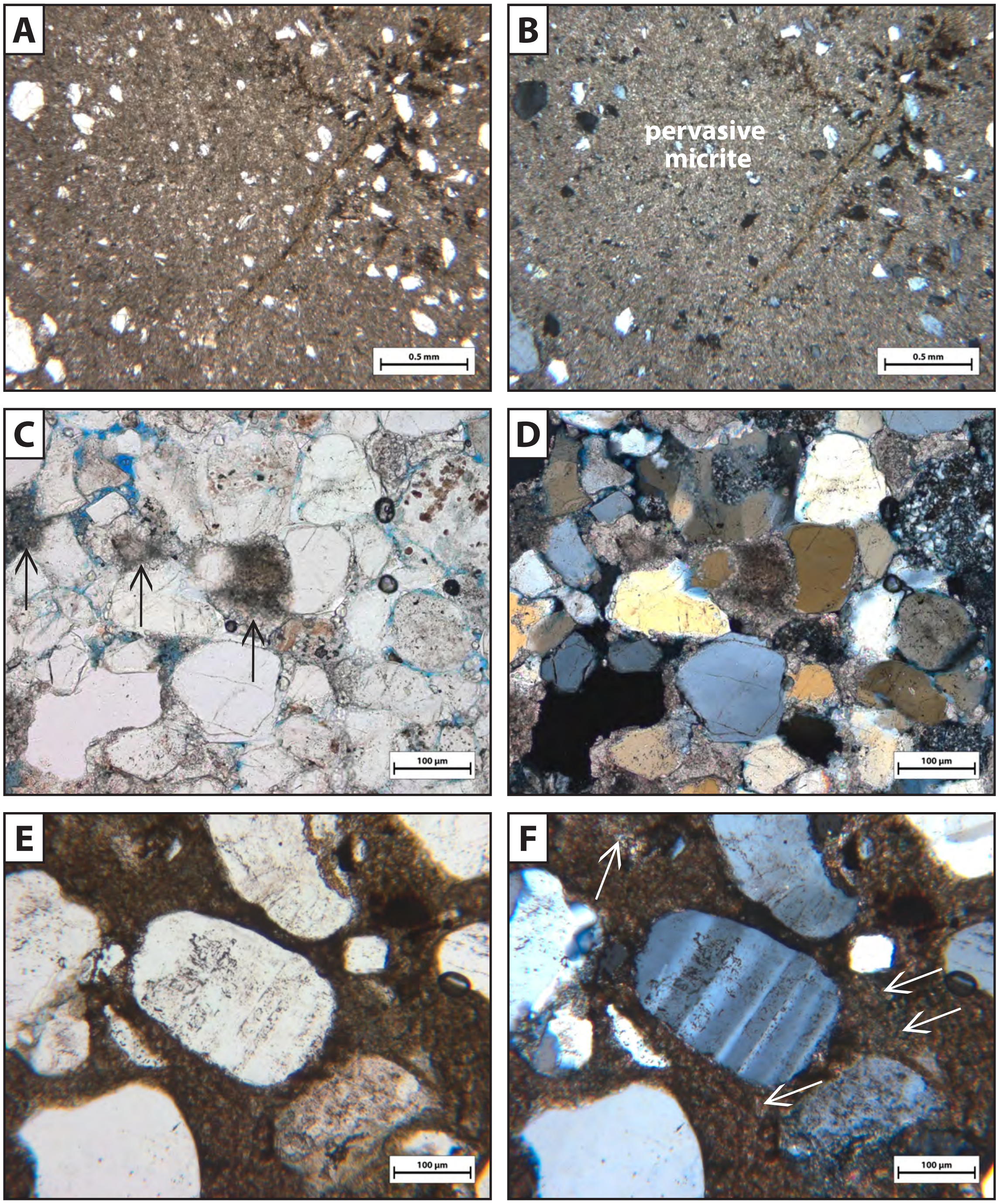

Figure E8: *Micrite cement* **A–B:** Pervasive micrite with small, silt-sized grains of quartz floating in it. It is easiest to identify it by its birefringence in crossed polars. **C–D:** Patchy micrite cement filling in a small portion of porosity in an already quartz- and spar-cemented sandstone. **E–F:** A mixture of micrite (arrows) and muddy matrix surrounding a plagioclase grain.

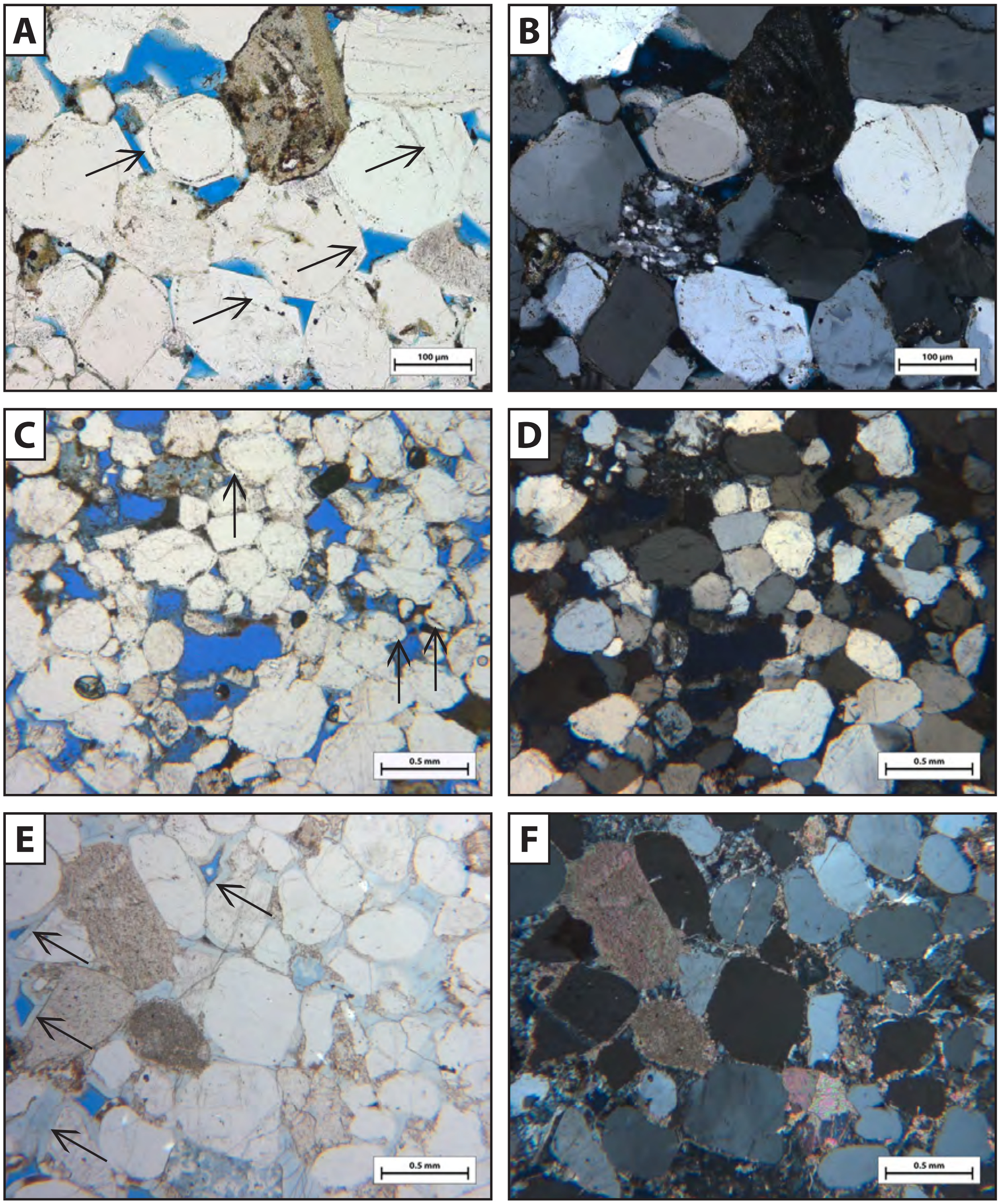

Figure E9: *Quartz cement* **A–B:** Euhedral quartz overgrowths form straight and sharply angled edges around quartz grains. They are crystallographically aligned with the grain, but can generally be distinguished by a dust rim at the edge of the grain. **C–D:** Some quartz overgrowths do not make the distinctive sharp euhedral faces, but are still axially aligned with the grain. **E–F:** Chalcedonic cement forms isopachous rims on grain surfaces in sample 35B.

One sample (35B) is pervasively cemented by chalcedony that forms isopachous, non-euhedral rims around each grain. I originally counted this as a separate category of cement ("Isopachous Quartz Cement"), but because it only appears in one sample I eventually combined this category with "Quartz Cement."

**Clay cement** (Figure E10) is defined as dark-to-opaque authigenic pore-filling material, generally brown to black. It is amorphous, lacking well-defined, grain-like boundaries. Similar to clay-rich sedimentary lithic grains, it is not always uniformly colored, but instead exhibits uneven shading where the material appears to vary from dense to wispy. It is distinct from the clay matrix that mixes with micrite in some samples in that clay cement has formed in place. Clay cement most commonly appears as cuticles around the edges of large grains, in dendritic form growing in a micritic matrix, or in the intragranular pores of dissolving feldspars.

**Intergranular porosity** (Figure E11) is primary porosity that occurs in the interstices of a rock where the sediment is not perfectly compacted. Thin sections in this project were injected with blue-stained epoxy before being cut and polished. The blue epoxy floods the pore space and is useful for quickly identifying porosity. In some rare cases, a spot that appears to be a pore is not stained by the epoxy. In these cases I could not be sure if it was the result of low permeability preventing the epoxy from reaching the pore, or if it was damage caused by plucking when the slide was polished. Because of this uncertainty, I passed over these points without counting anything.

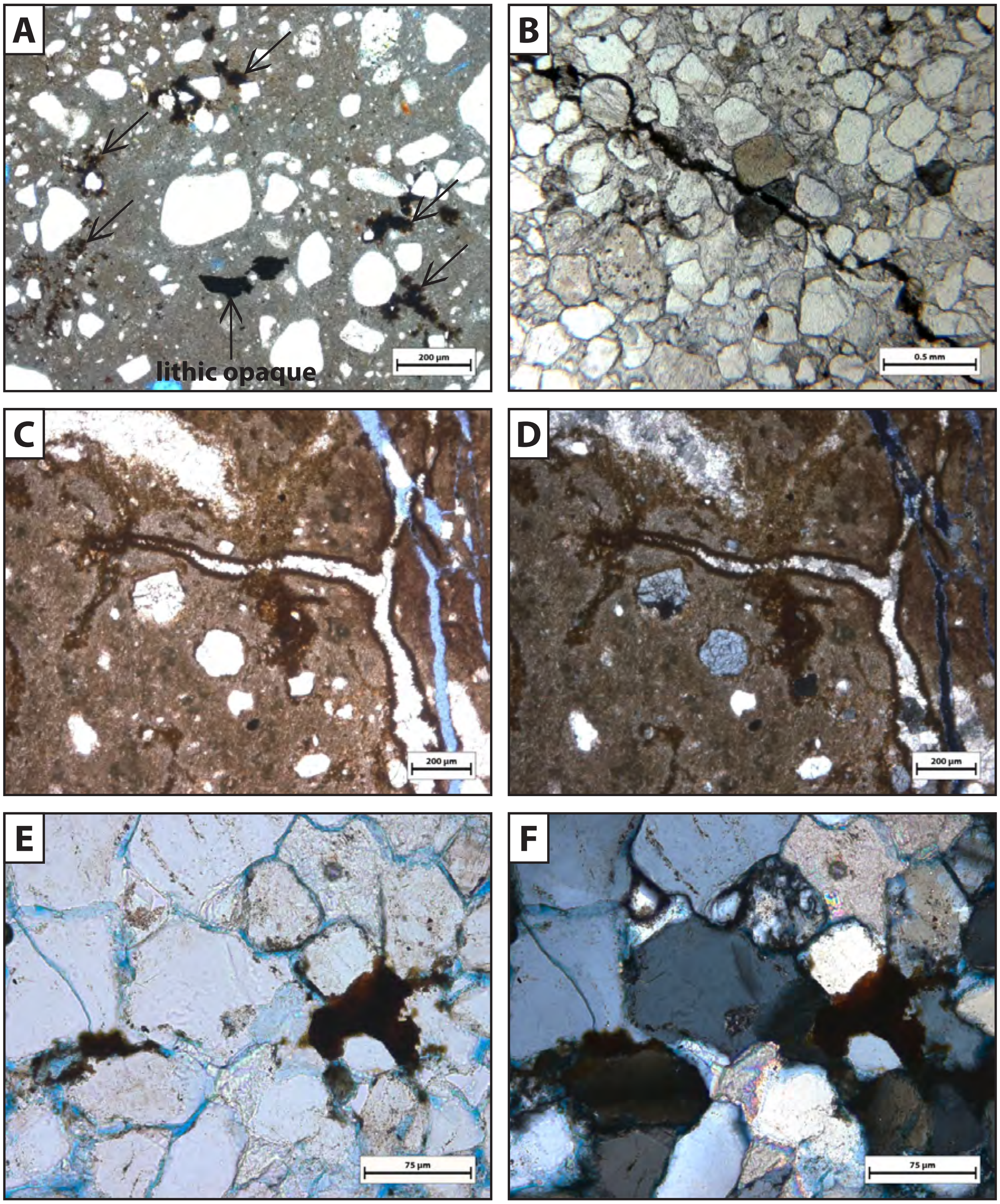

Figure E10: *Clay cement* **A:** Clay cement in a micritic matrix—note the difference between lithic opaque grains (rigid, completely opaque) and clay cement (dendritic, mottled brown). **B:** Filling a narrow fracture in calcite-cemented sandstone. **C–D:** Lining the walls of a fracture. **E–F:** Amorphous clay cement filling porosity between sand grains and calcite spar.

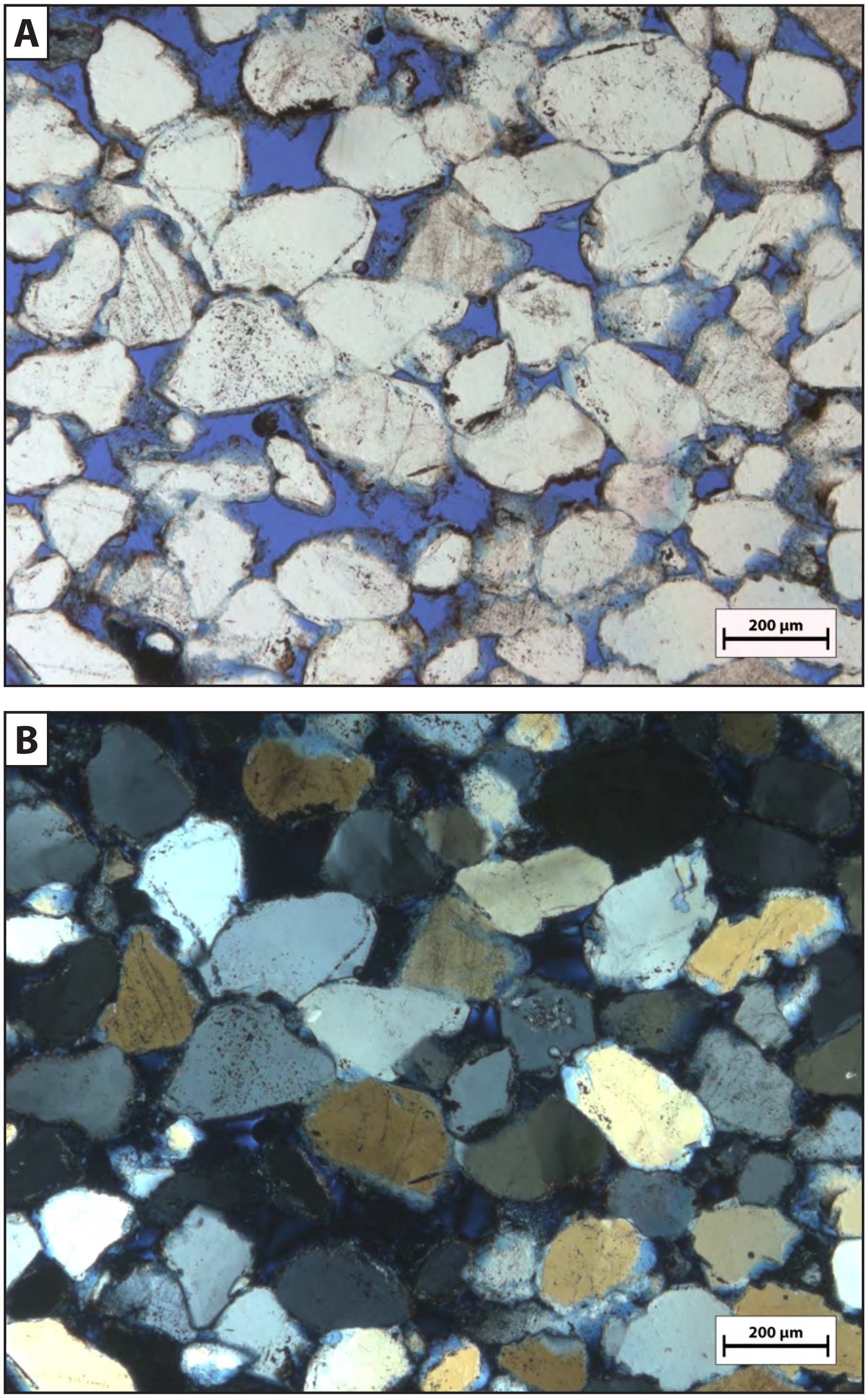

Figure E11: *Intergranular (primary) porosity* **A–B:** Blue-stained epoxy is injected into the sample during thin section preparation. This allows for easy identification of porosity.

**Oversize porosity** (Figure E12) is secondary porosity where, due to complete dissolution of a grain, a pore is created that is larger than typical surrounding grains. Oversize porosity is often found in rocks with significant intragranular porosity and microporosity, being an indication that the rock has undergone substantial dissolution. I drew a line between pervasive intragranular porosity and oversize porosity based on whether or not I could see any remnant of the original grain. If not, I counted the point as oversize porosity.

**Intragranular porosity** (Figure E12) is secondary porosity occurring on the edges of or inside a discrete grain, representing dissolution of the grain. It commonly follows cleavage planes in feldspars, or appears to have fully removed soft minerals in sedimentary lithic grains. Intragranular porosity represents essentially the same process as microporosity (grain dissolution), but is distinguished by having pores that are large enough to individually identify.

**Microporosity** (Figure E12) is a third type of secondary porosity and a subset of intragranular porosity. It is similar to intragranular porosity in that it represents the dissolution of a grain, but qualitatively different in that discrete pores cannot be identified even at very high magnification (250–500X). Although individual pores are imperceptible, a bluish tinge indicates the presence of microporosity. The tinge shows where blue-stained epoxy has penetrated the grain and filled the micropores, creating an overall effect that is easily observable. I drew the line between microporosity and intragranular porosity based on whether or not I could distinguish discrete pores. If not, I counted it as microporosity.

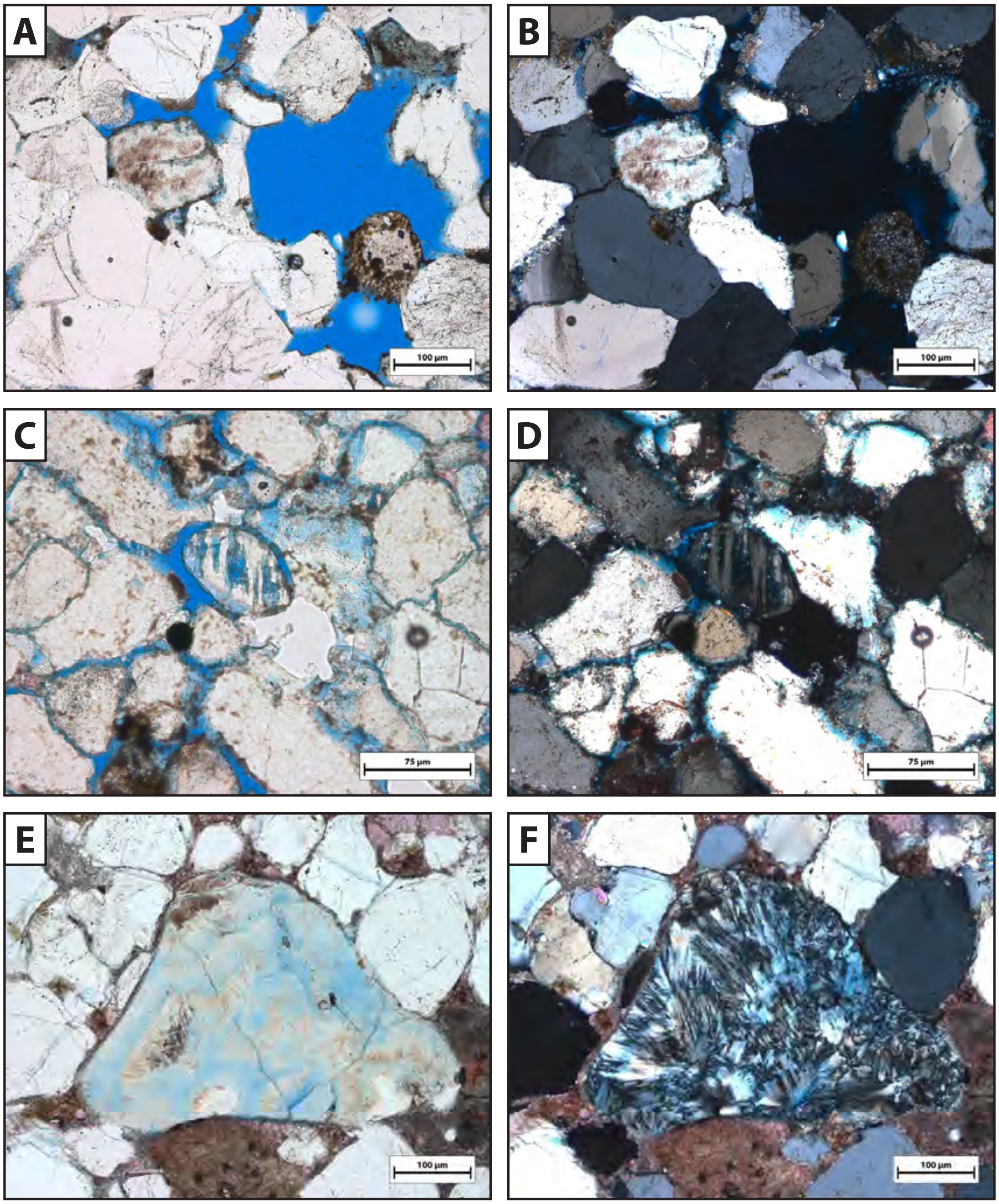

Figure E12: *Three stages of secondary porosity* **A–B:** Oversize porosity resulting from the total dissolution of a grain, which leaves behind a pore larger than normal primary porosity. **C–D:** Dissolution follows cleavage planes in a feldspar grain and results in relatively large, distinct cavities, or intragranular porosity. **E–F:** A bluish tinge indicates the presence of microporosity—tiny dissolution features tinted by the epoxy so that their cumulative presence is apparent, though individual pores are indiscernible.

# Appendix F: X-ray Diffraction Data and Interpretations

The following are the results of X-ray diffraction analysis on randomly oriented bulk rock powders (Figures F1–F12) and oriented clay-size separations (Figures F13–F14). Both sets include the same 12 samples. Two-theta ranges of particular interest are magnified.

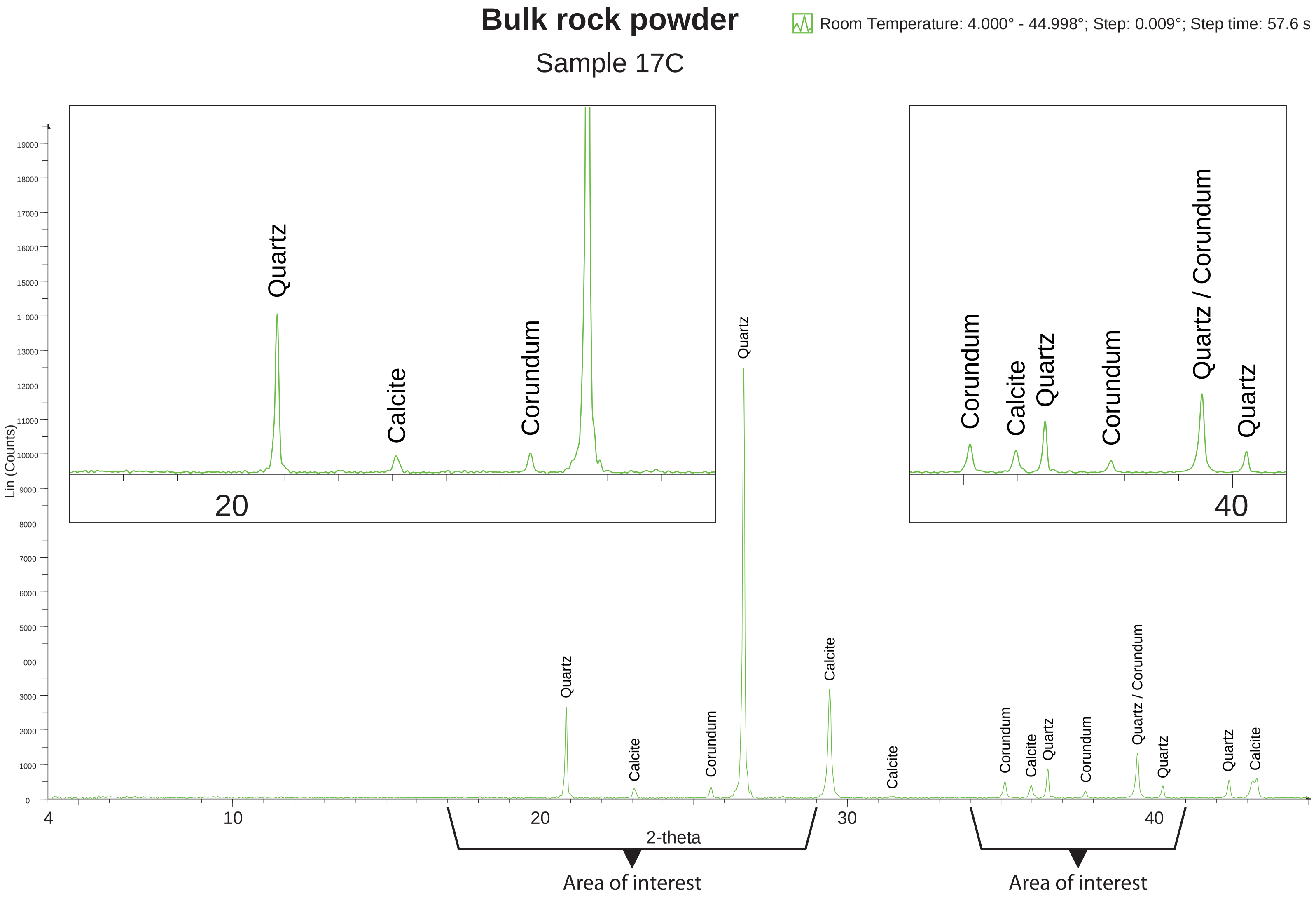

Figure F1: Bulk rock X-ray diffraction results and interpretation for sample 17C.

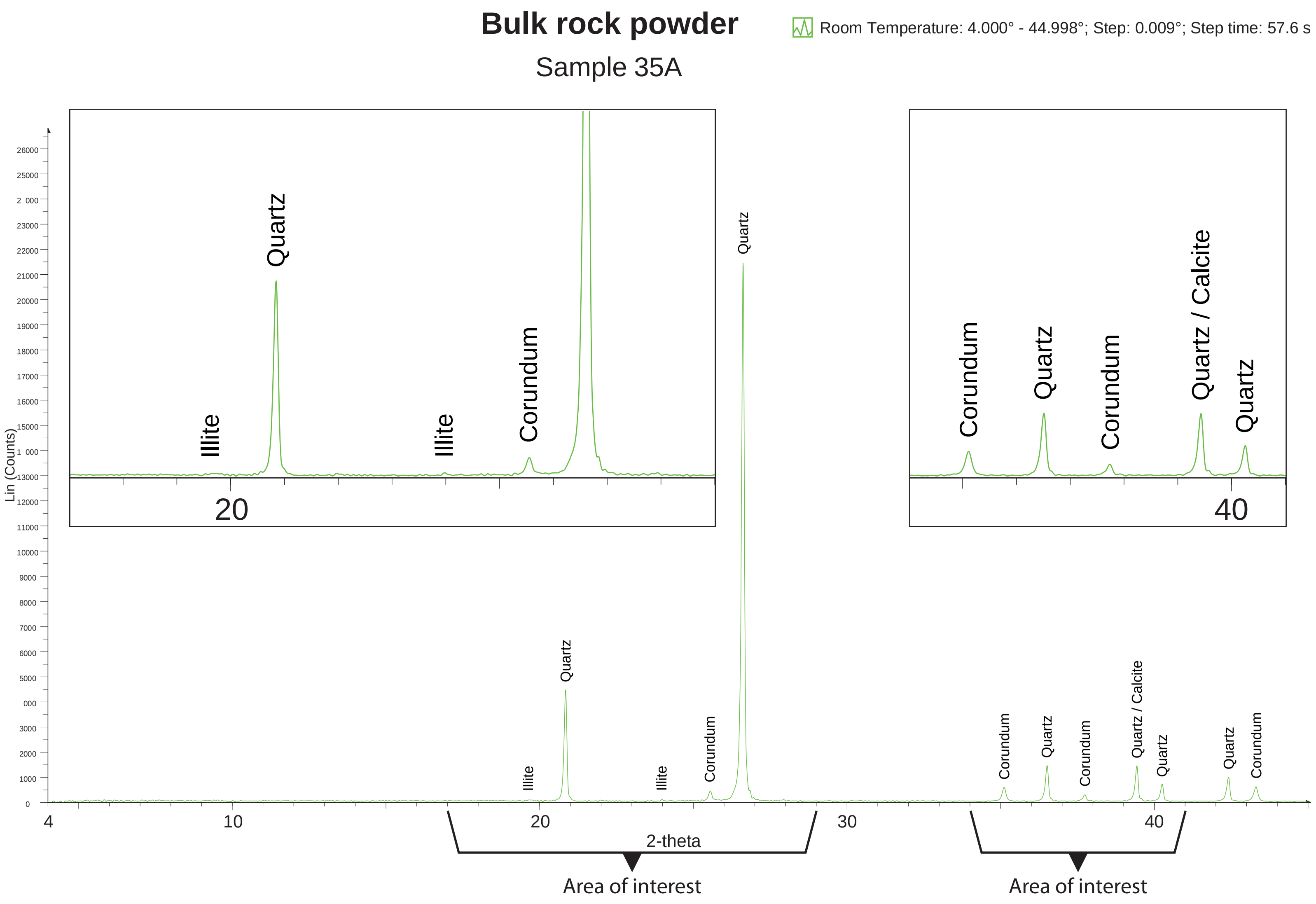

Figure F2: Bulk rock X-ray diffraction results and interpretation for sample 35A.

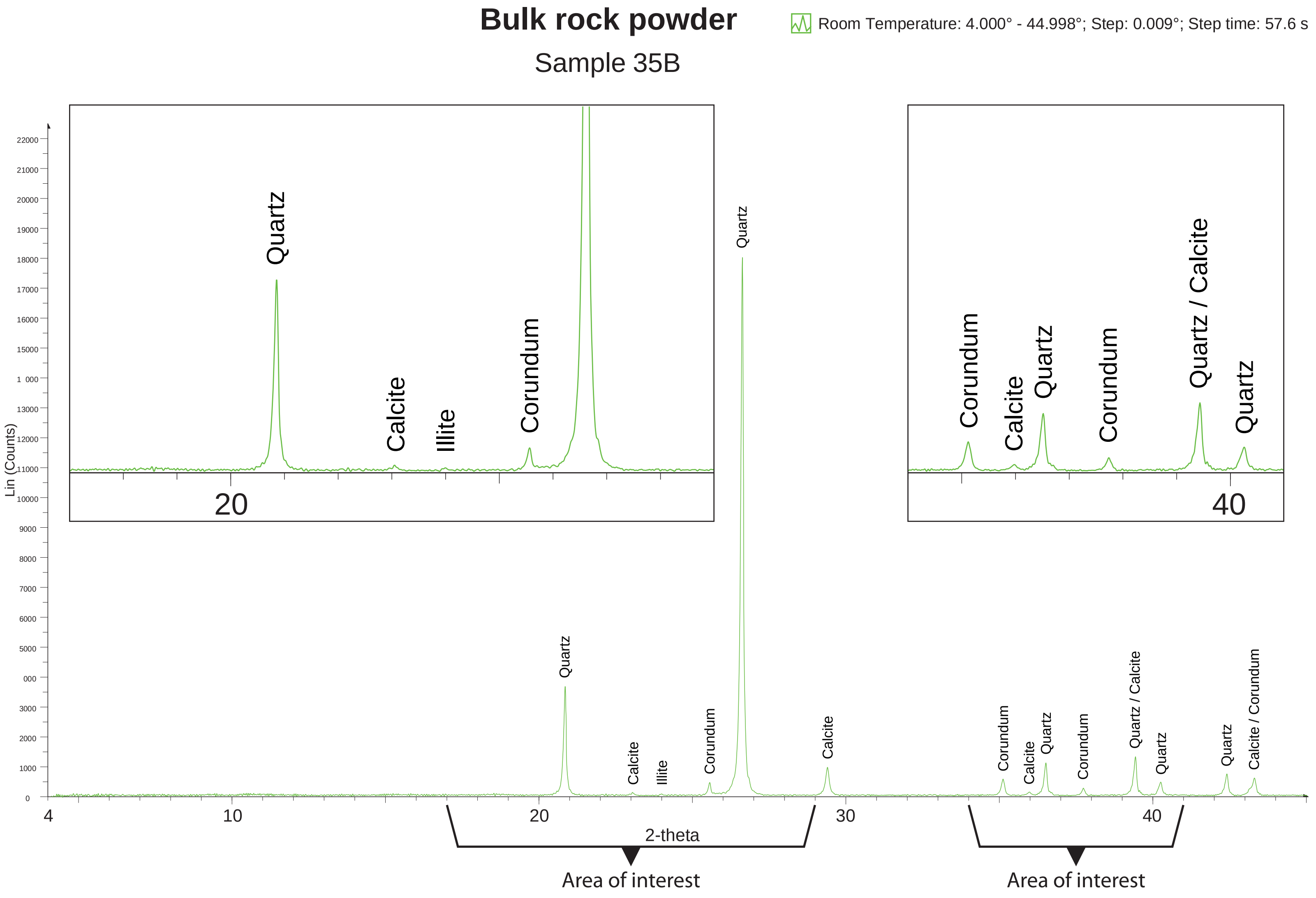

Figure F3: Bulk rock X-ray diffraction results and interpretation for sample 35B.

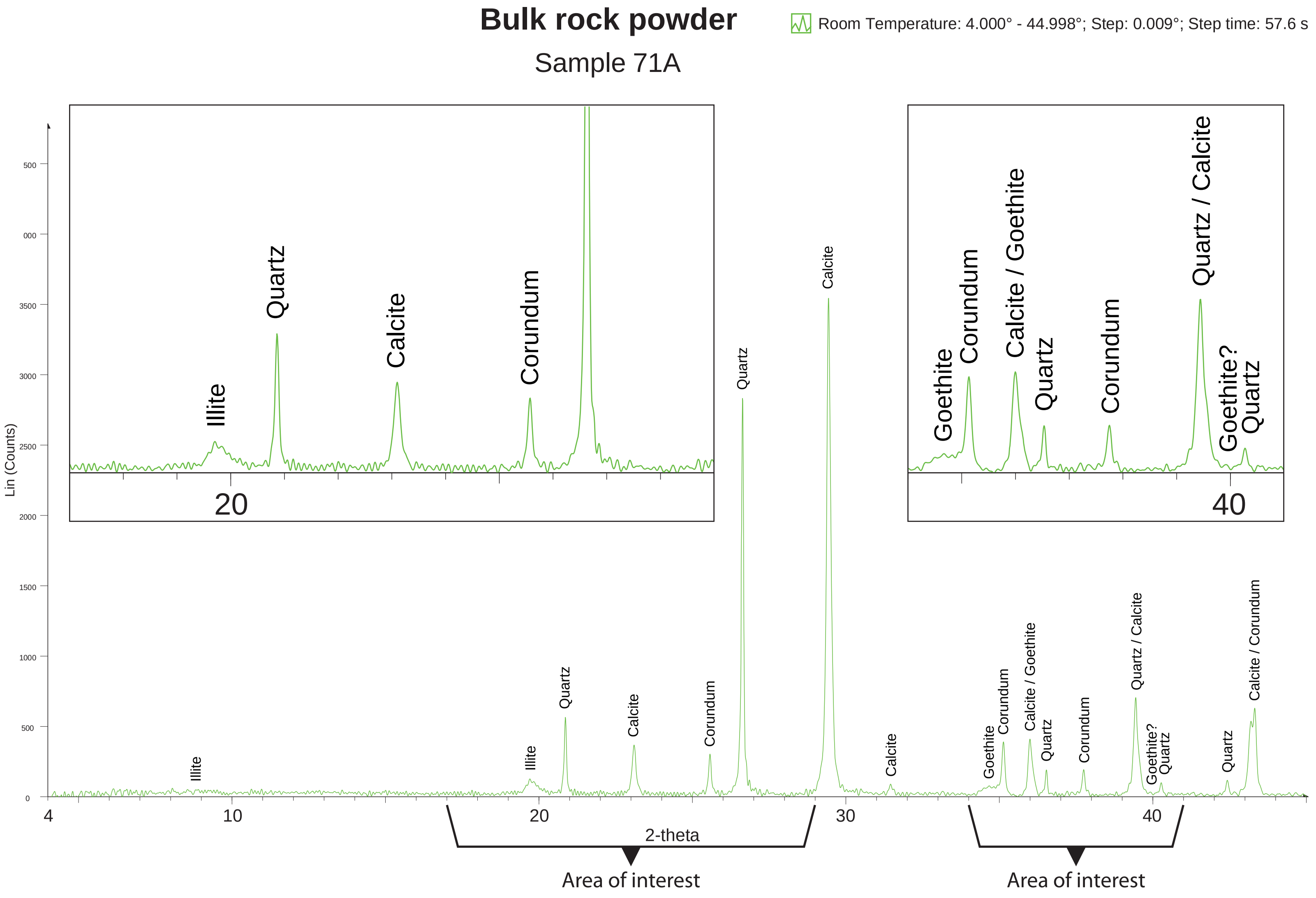

Figure F4: Bulk rock X-ray diffraction results and interpretation for sample 71A.

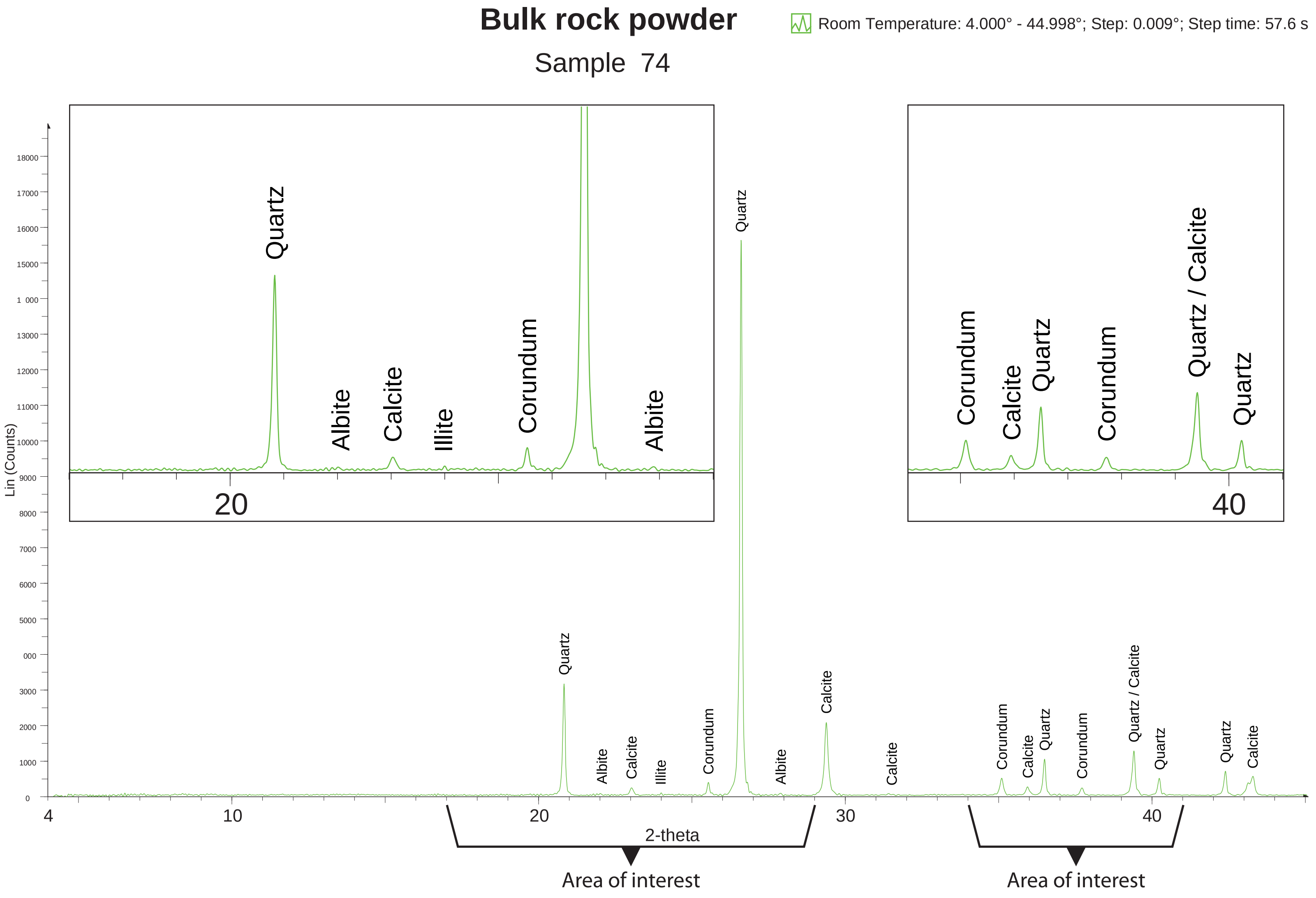

Figure F5: Bulk rock X-ray diffraction results and interpretation for sample 74.

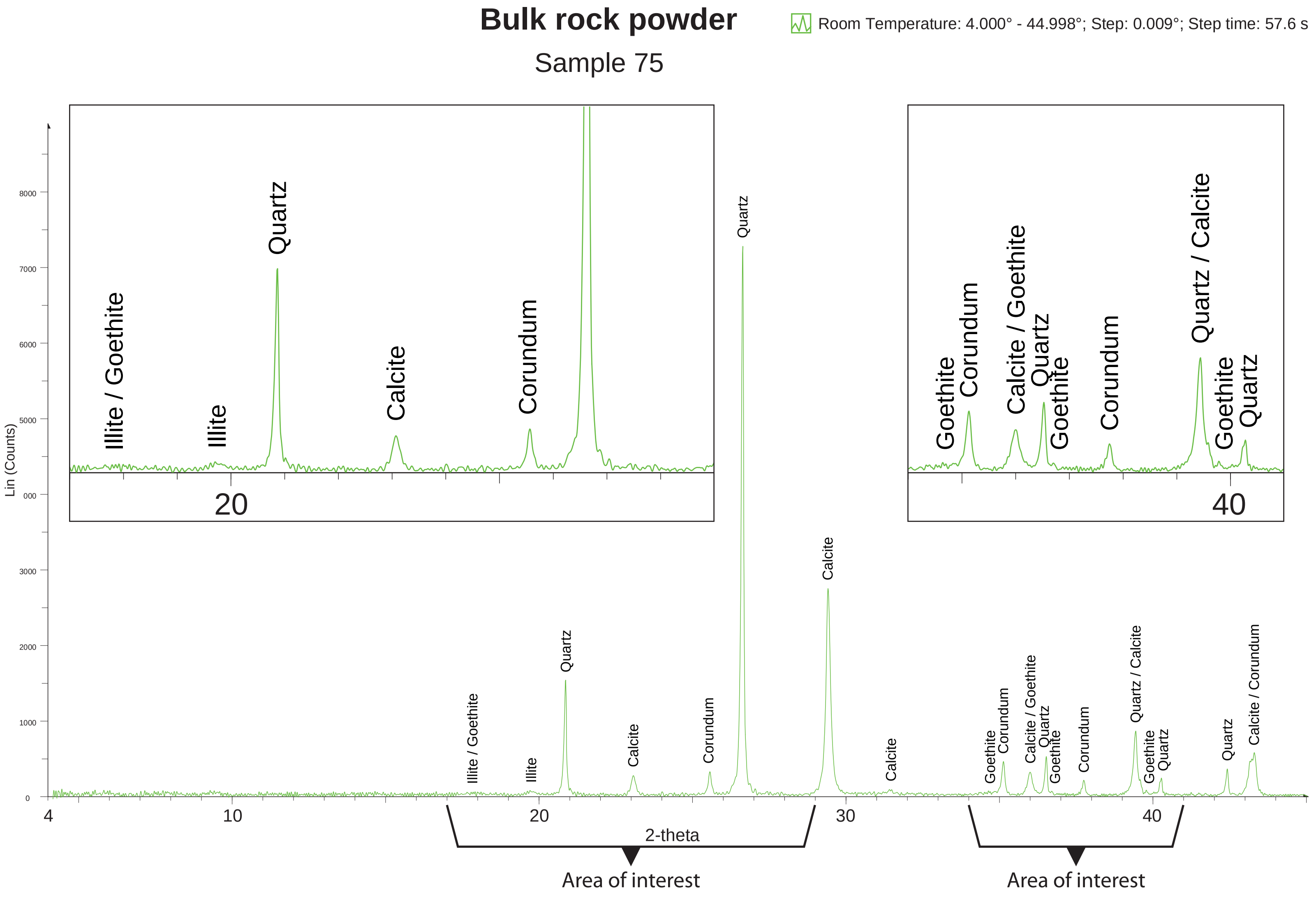

Figure F6: Bulk rock X-ray diffraction results and interpretation for sample 75.

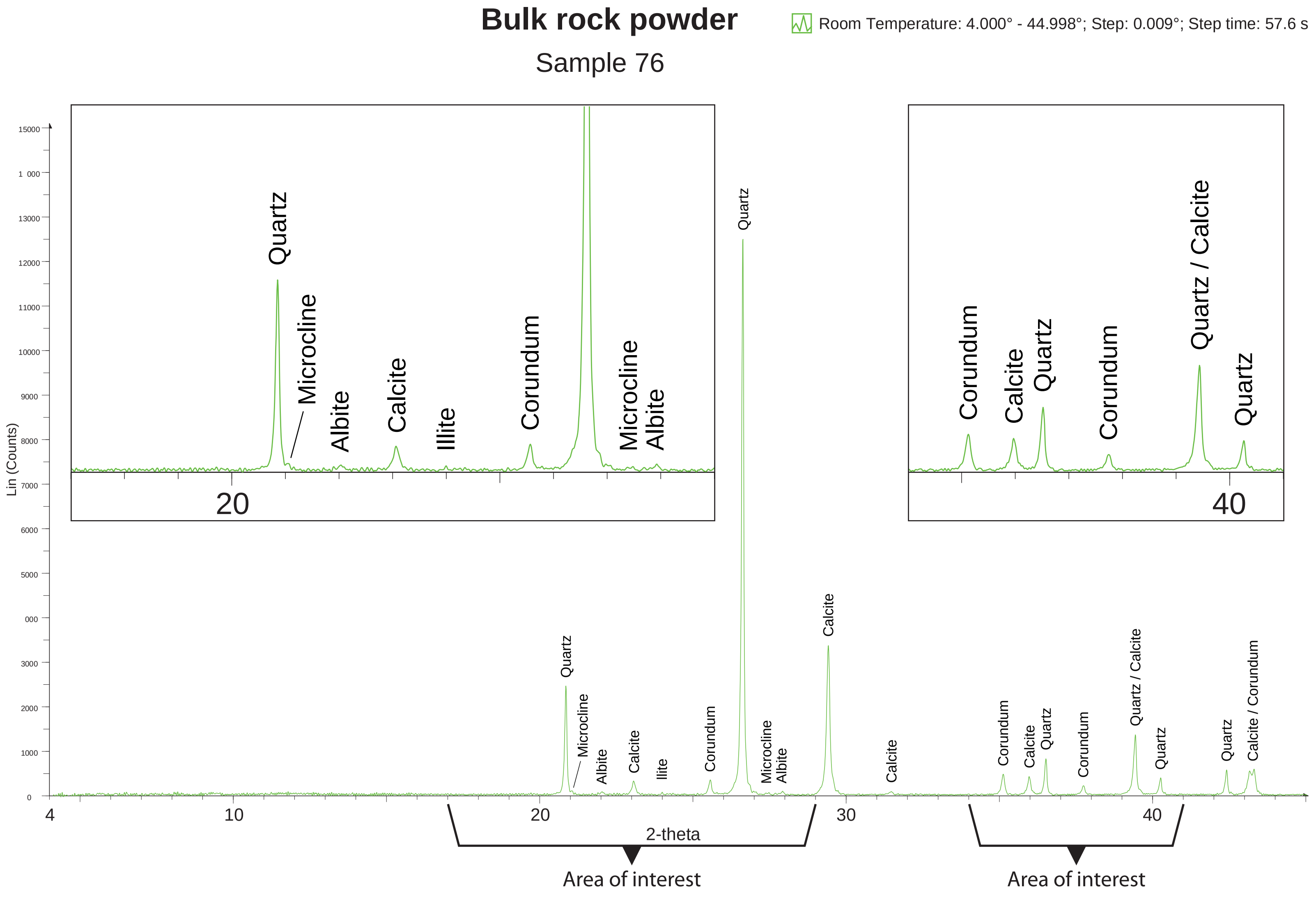

Figure F7: Bulk rock X-ray diffraction results and interpretation for sample 76.

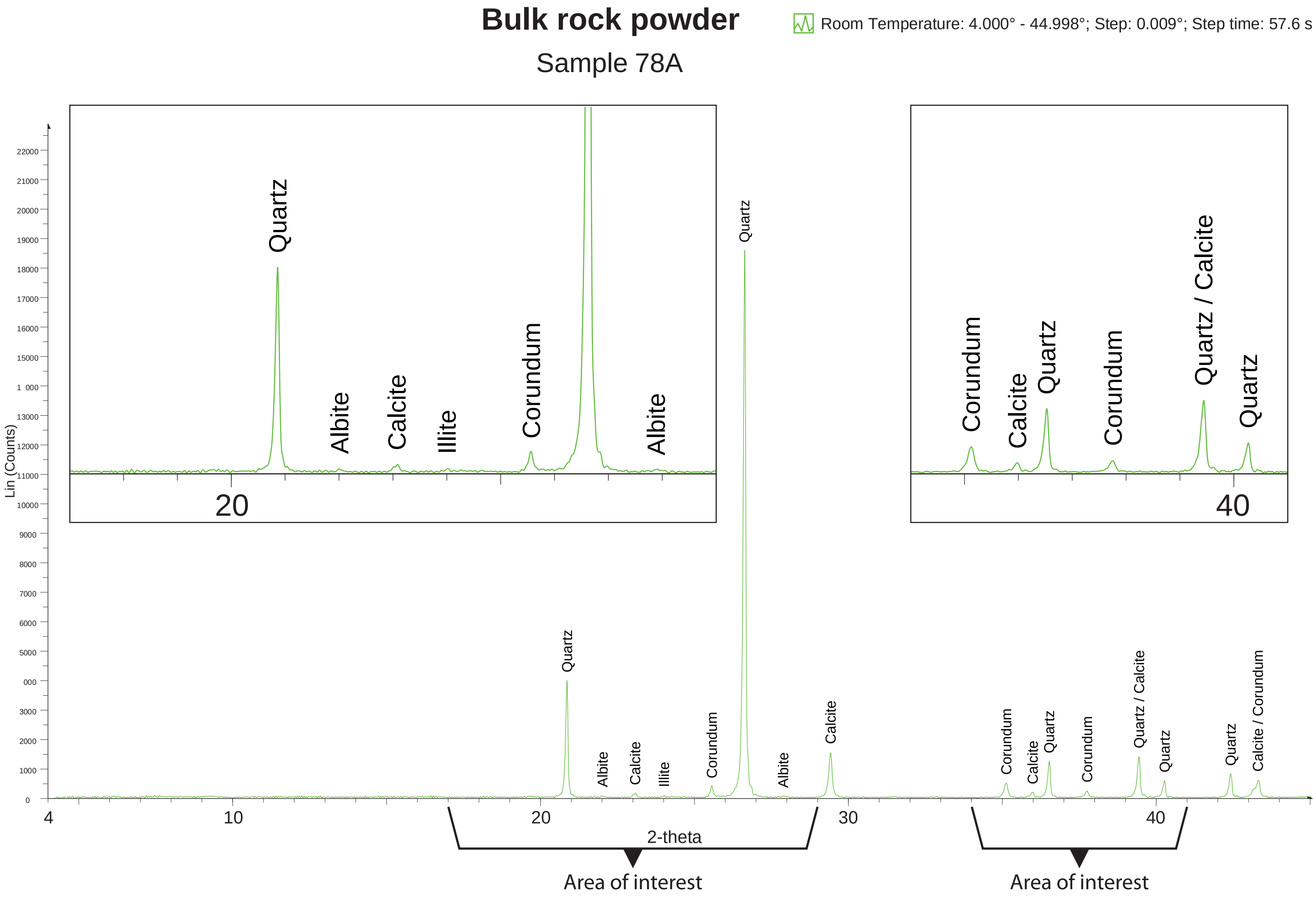

Figure F8: Bulk rock X-ray diffraction results and interpretation for sample 78A.

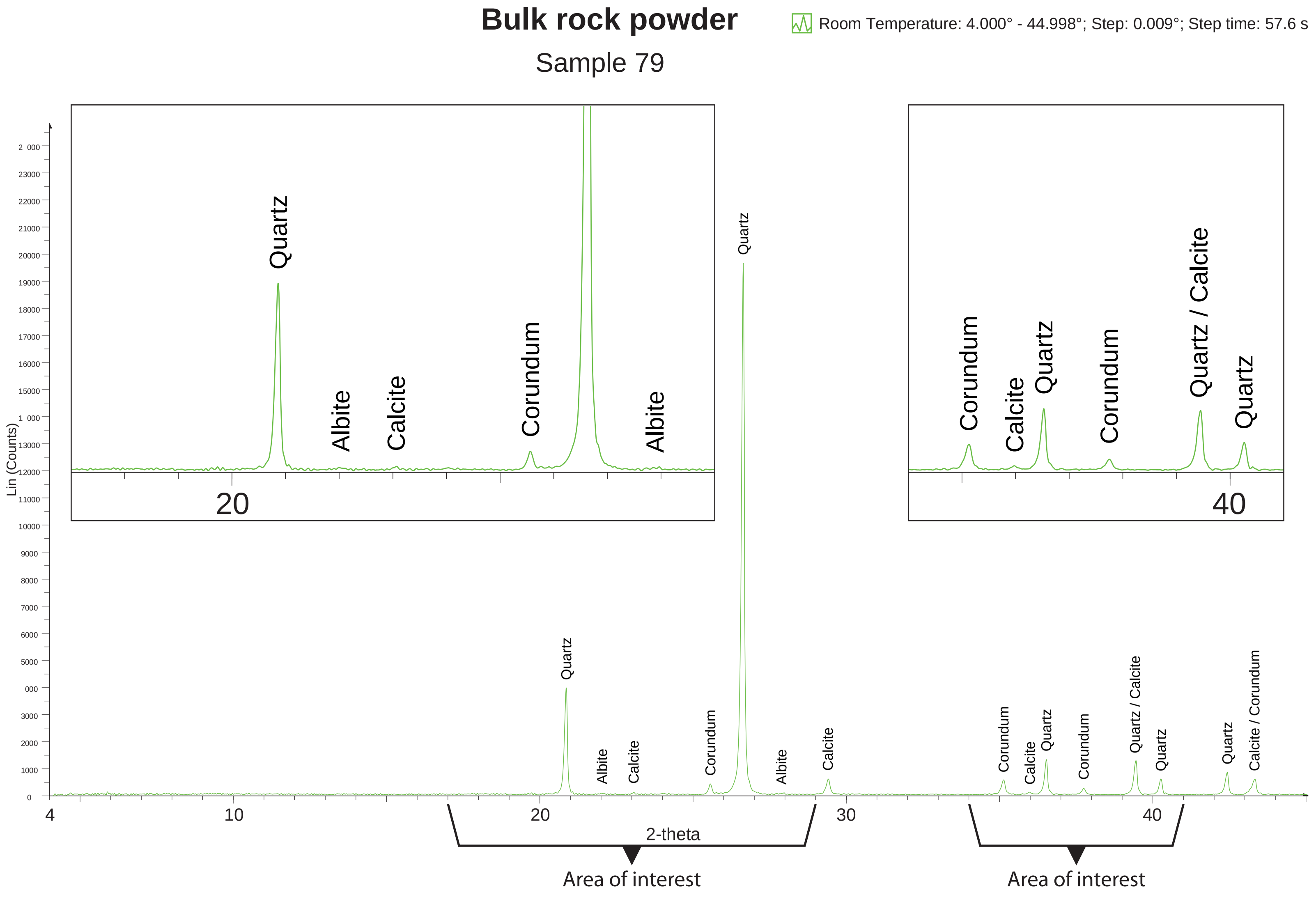

Figure F9: Bulk rock X-ray diffraction results and interpretation for sample 79.

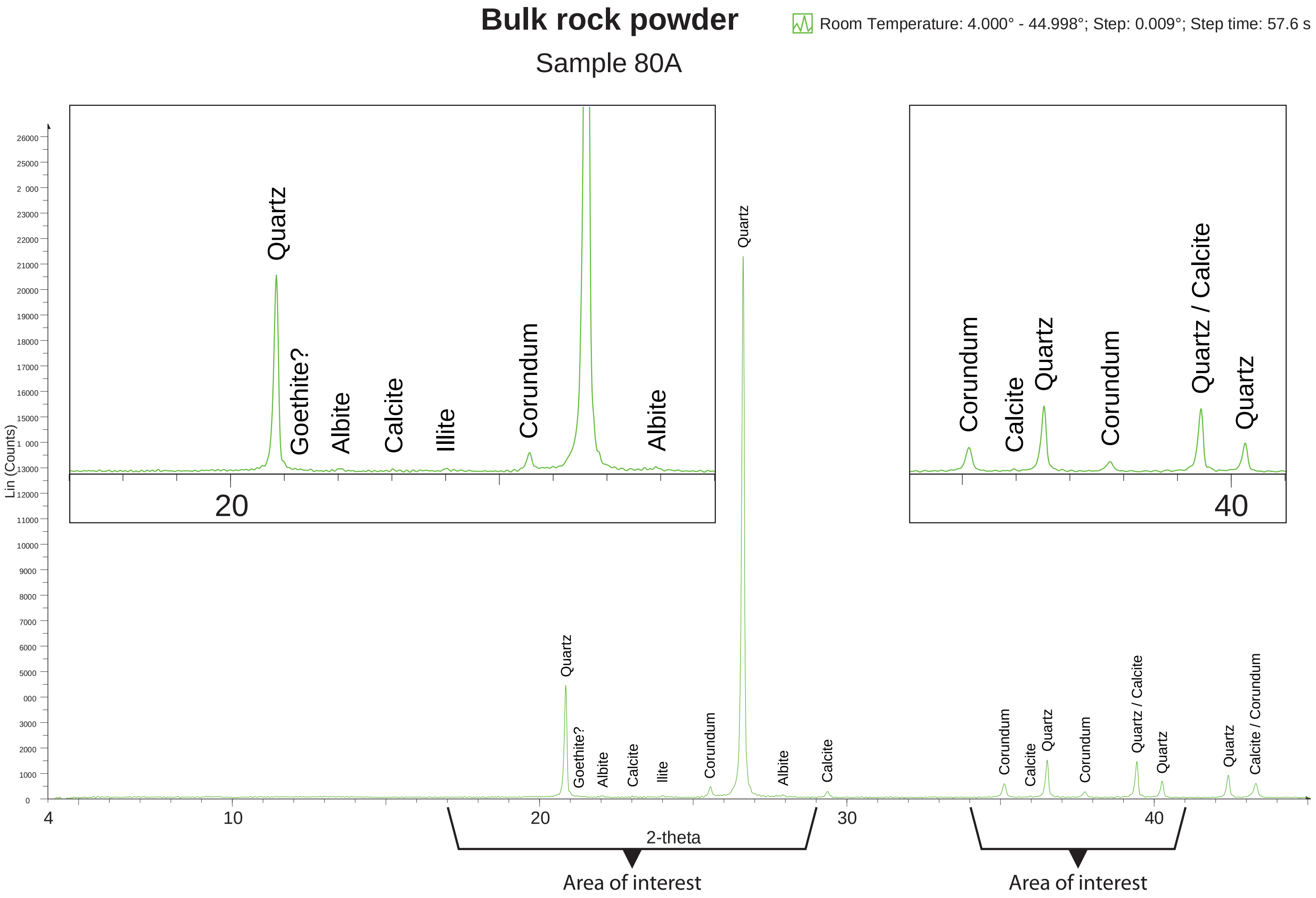

Figure F10: Bulk rock X-ray diffraction results and interpretation for sample 80A.

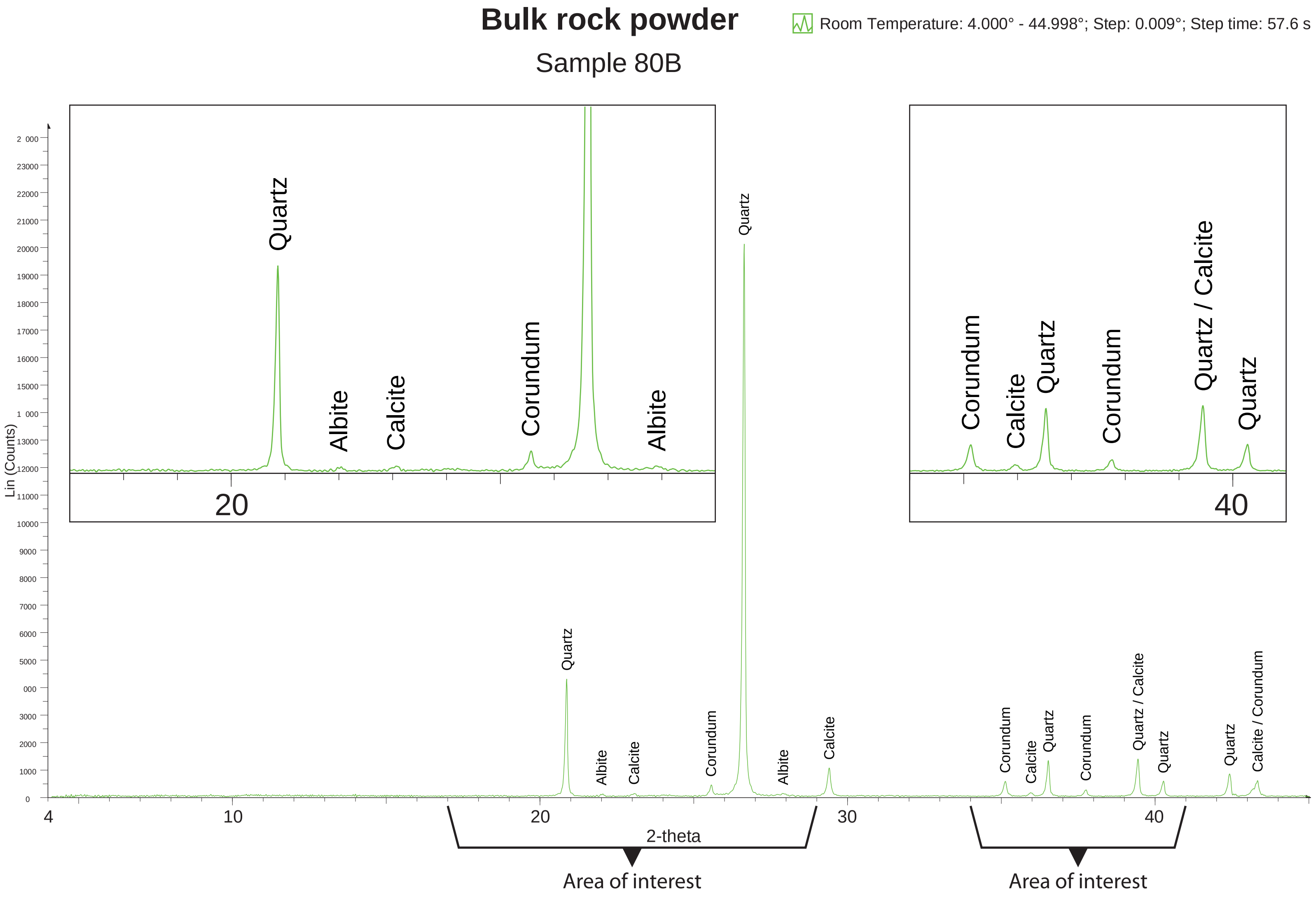

Figure F11: Bulk rock X-ray diffraction results and interpretation for sample 80B.

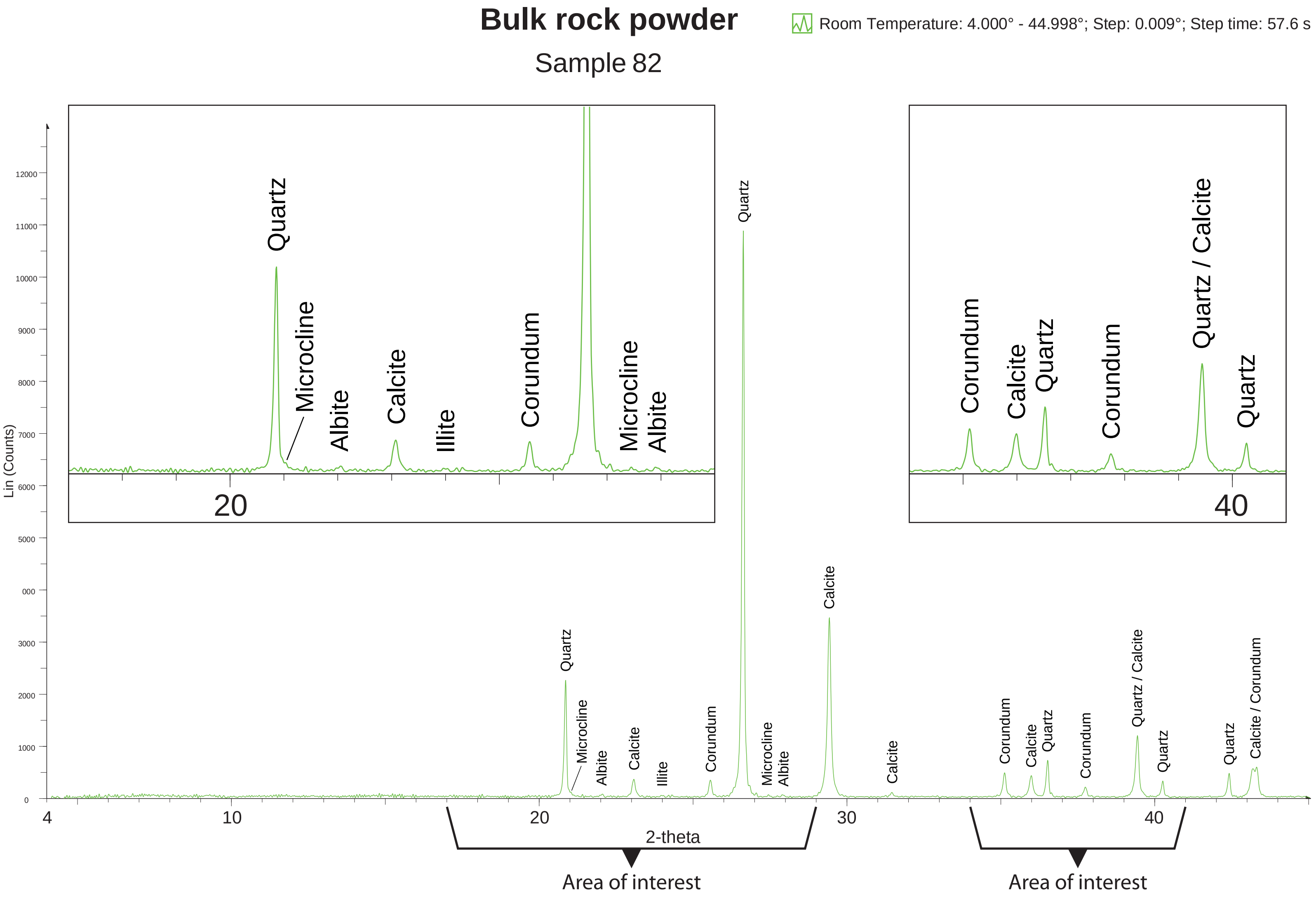

Figure F12: Bulk rock X-ray diffraction results and interpretation for sample 82.

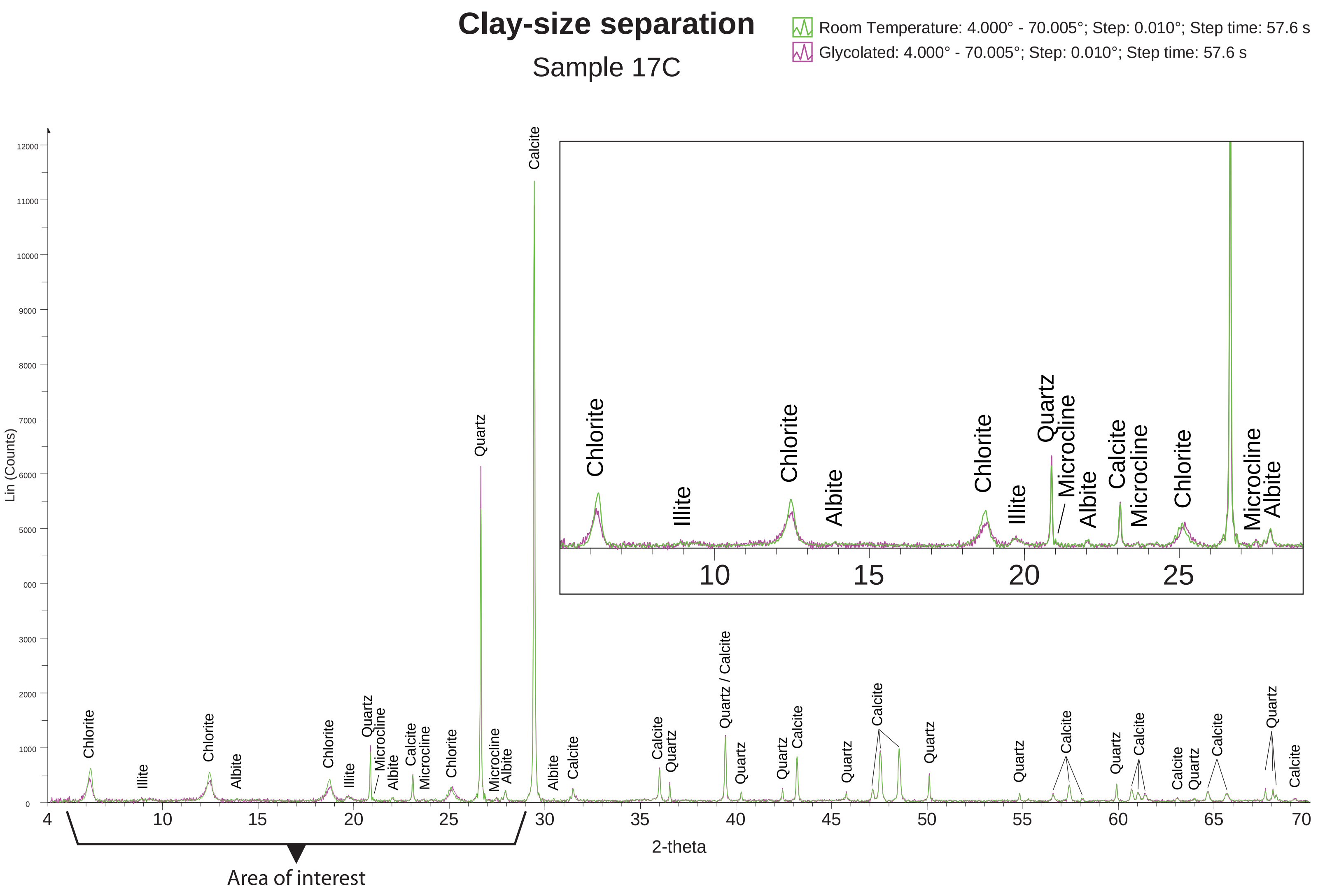

Figure F13: Clay-size separation X-ray diffraction results and interpretation for sample 17C.

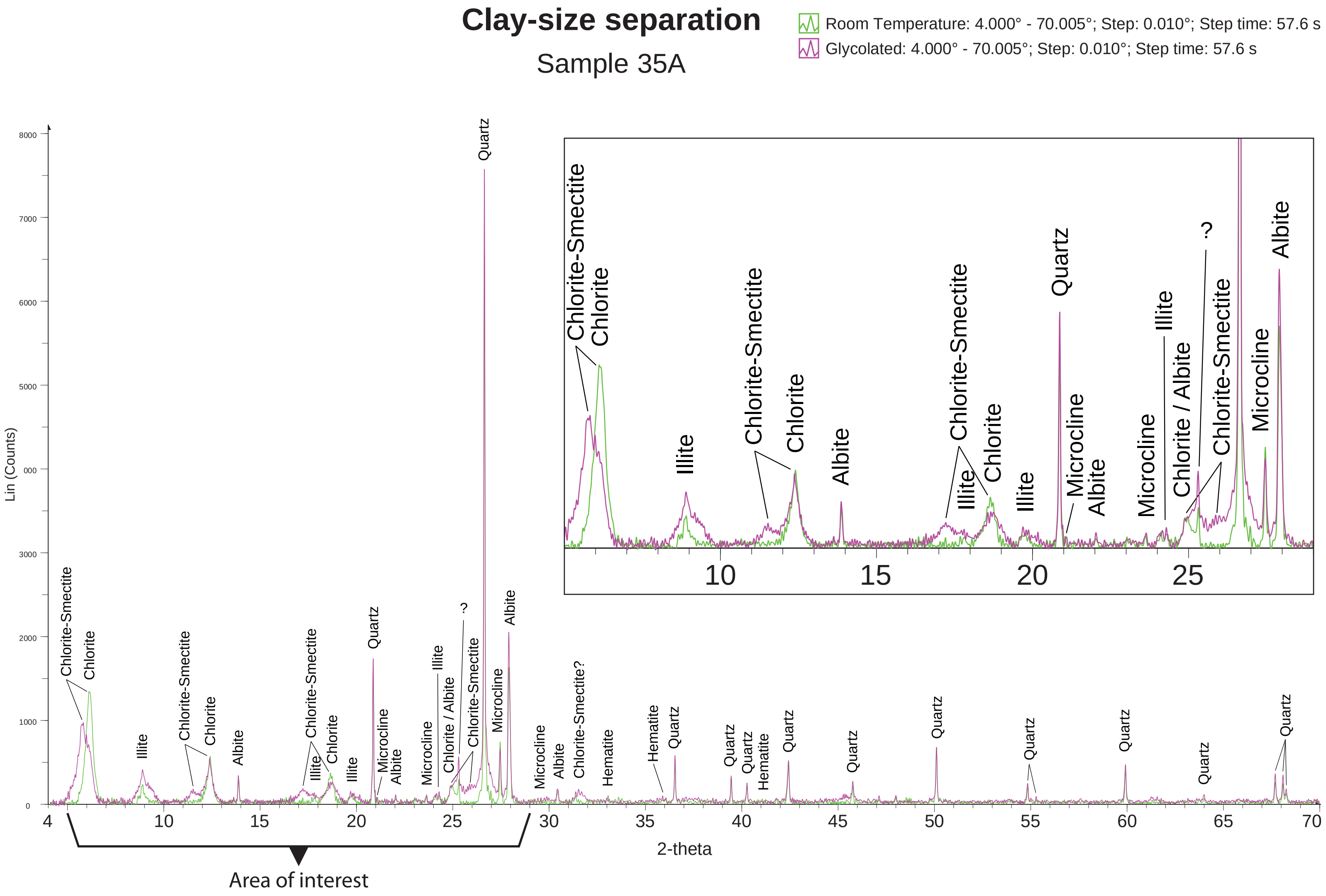

Figure F14: Clay-size separation X-ray diffraction results and interpretation for sample 35A.

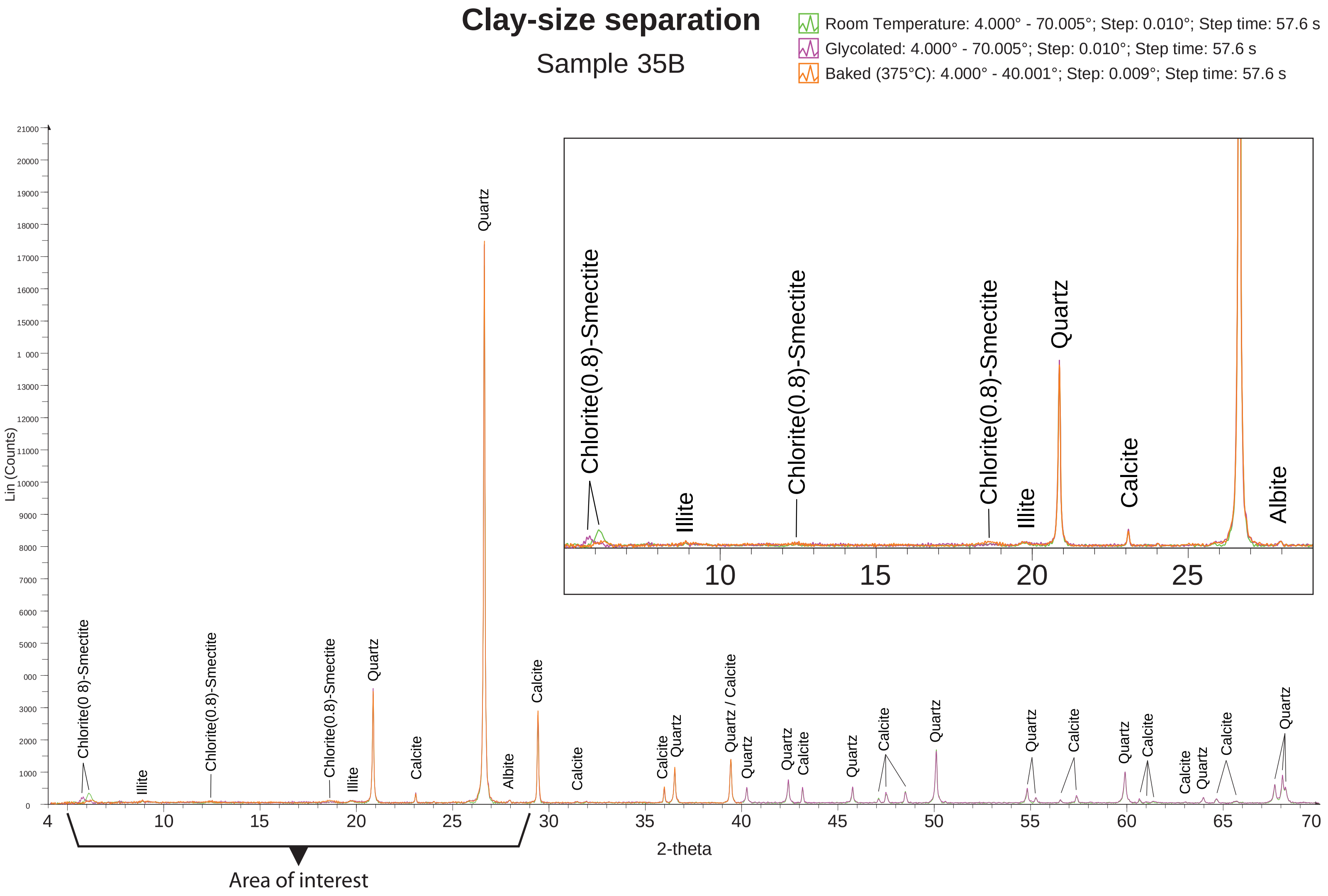
**Clay-size separation**

Sample 35B

Figure F15: Clay-size separation X-ray diffraction results and interpretation for sample 35B.

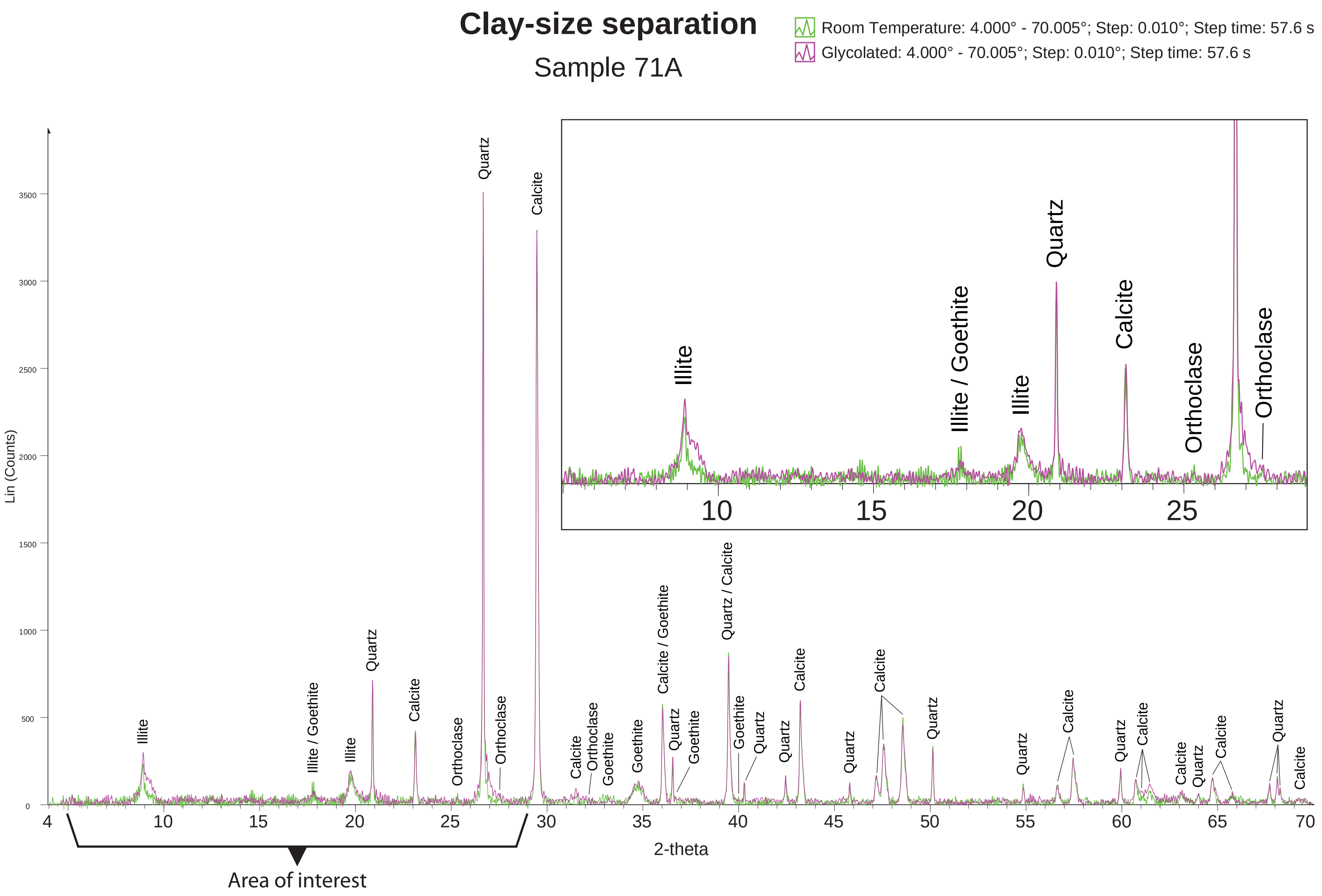

Figure F16: Clay-size separation X-ray diffraction results and interpretation for sample 71A.

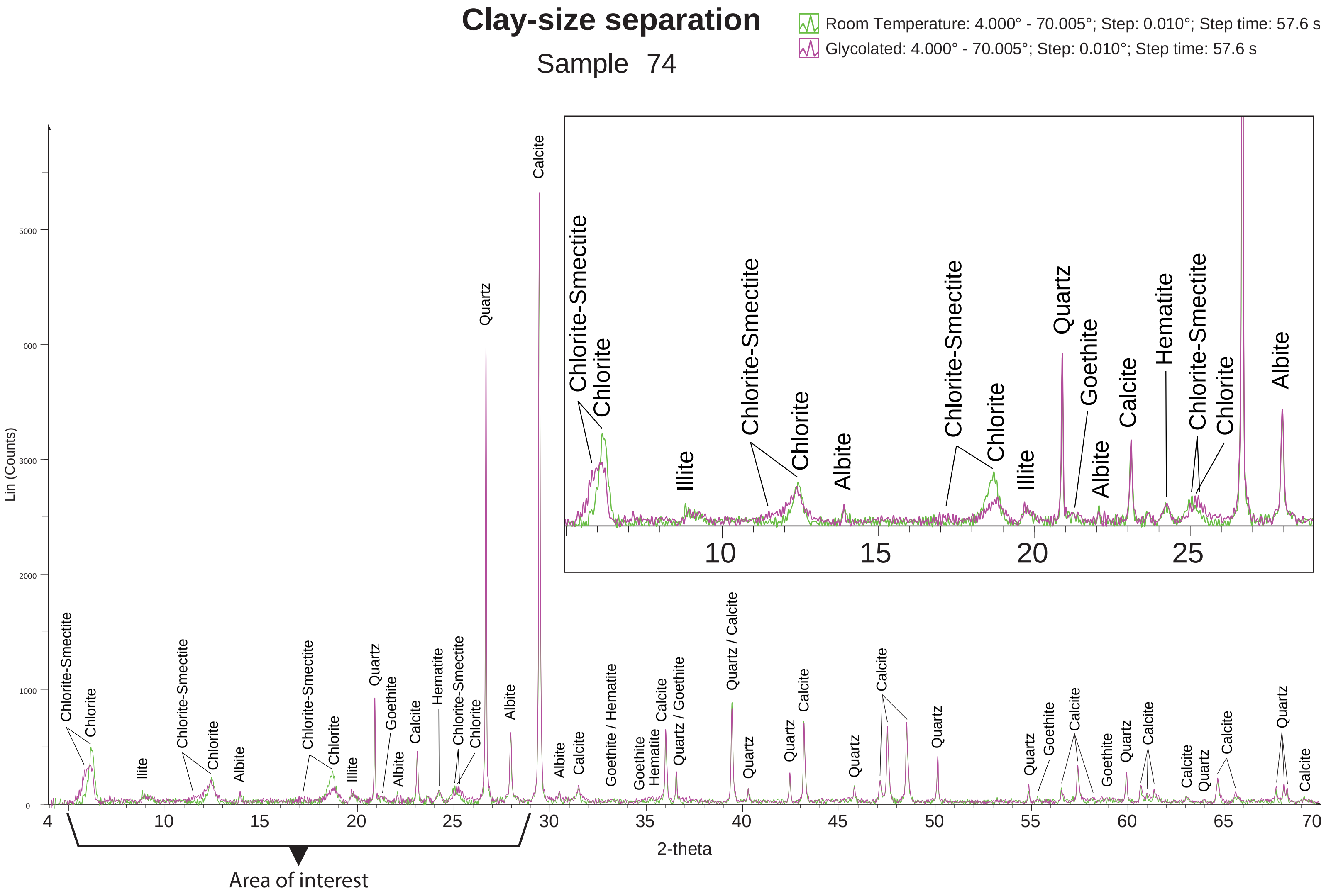

Figure F17: Clay-size separation X-ray diffraction results and interpretation for sample 74.

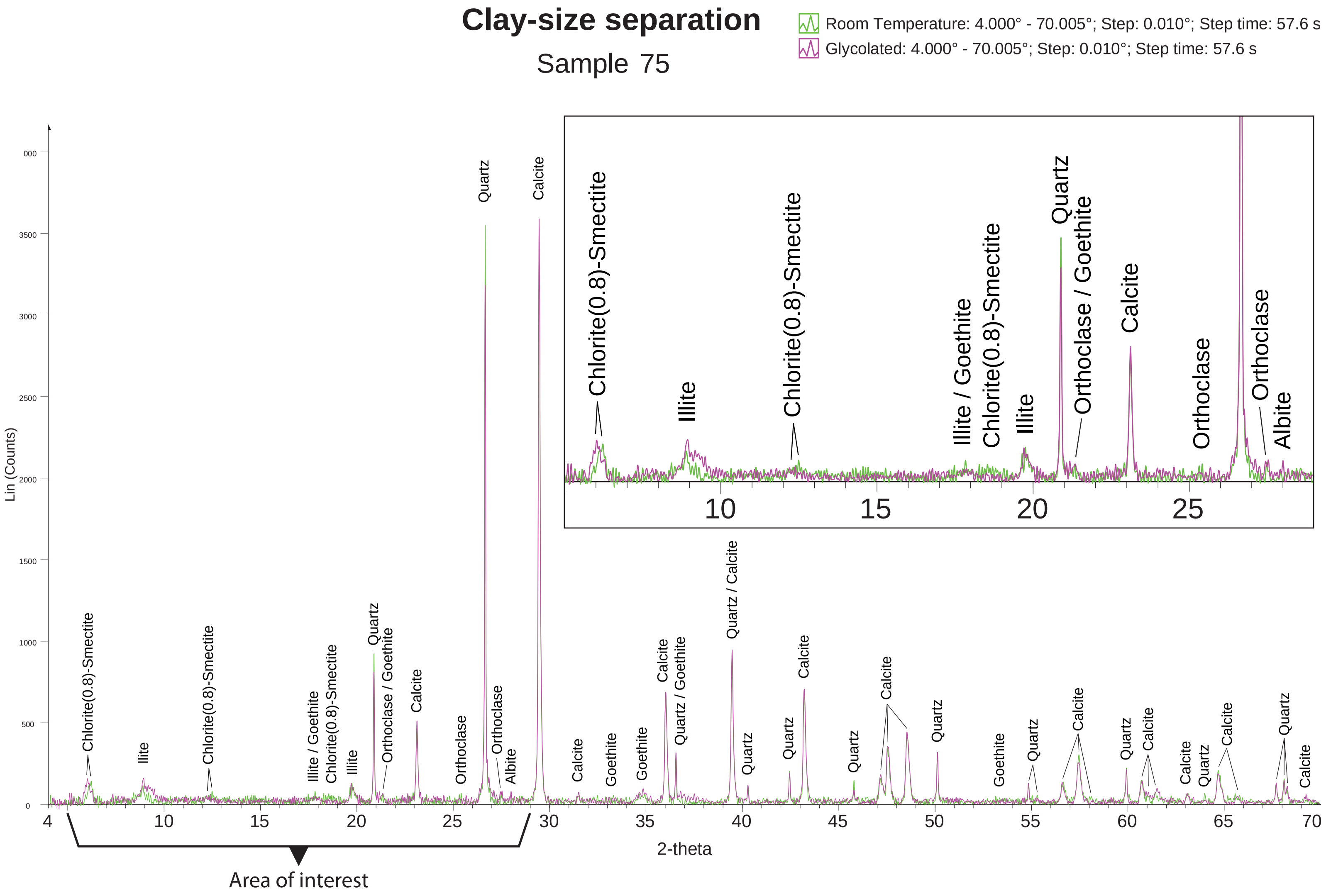

Figure F18: Clay-size separation X-ray diffraction results and interpretation for sample 75.

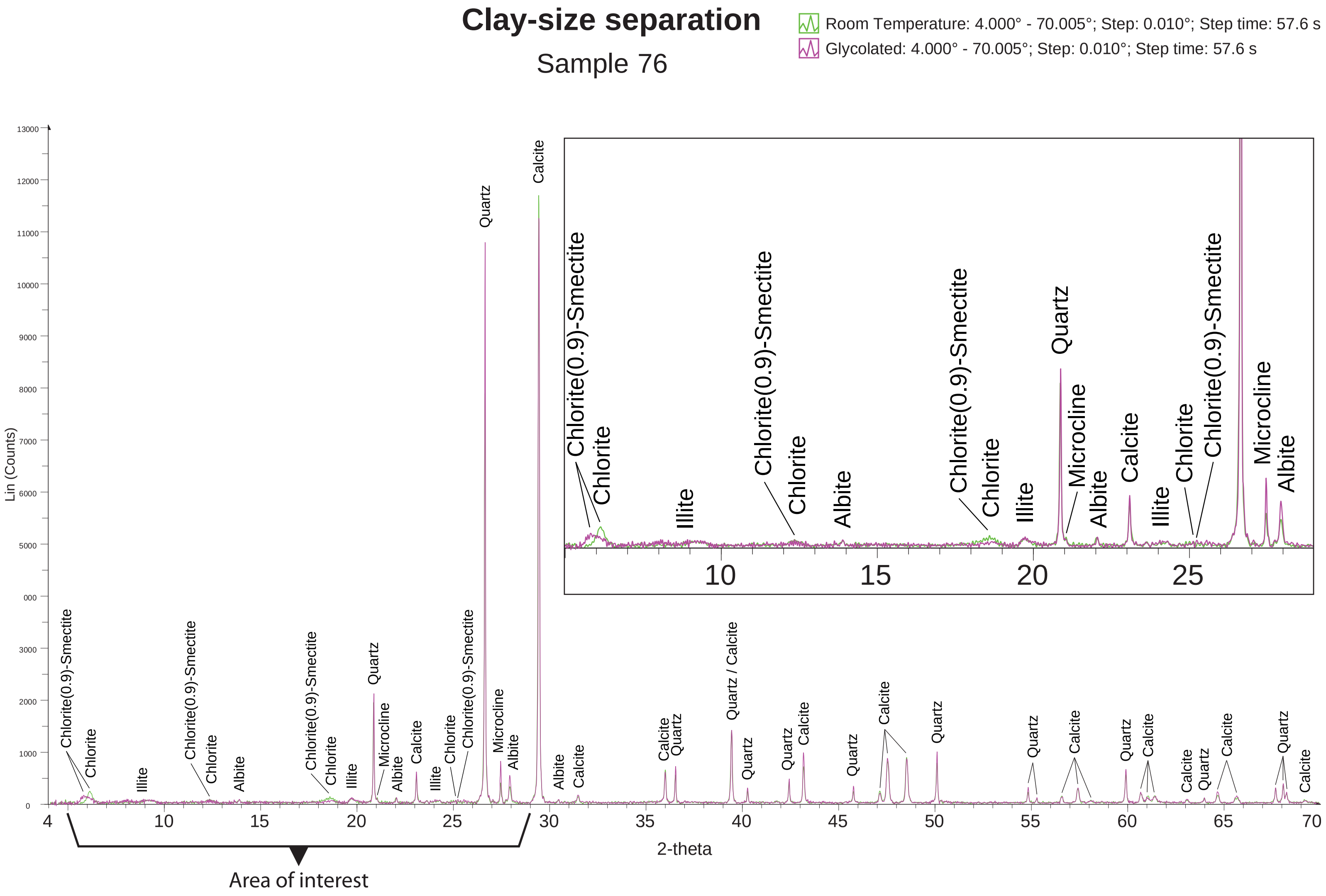

Figure F19: Clay-size separation X-ray diffraction results and interpretation for sample 76.

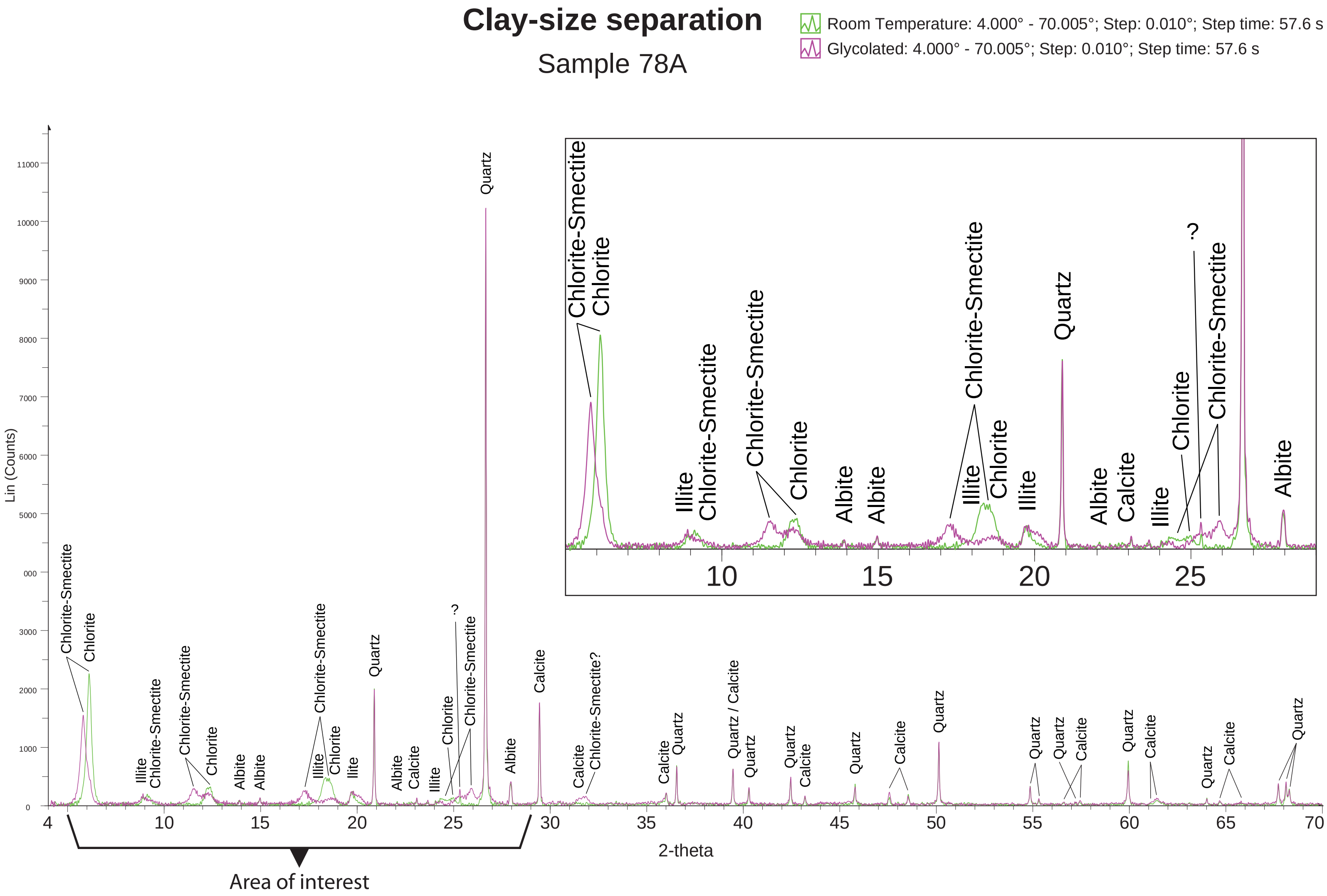

Figure F20: Clay-size separation X-ray diffraction results and interpretation for sample 78A.

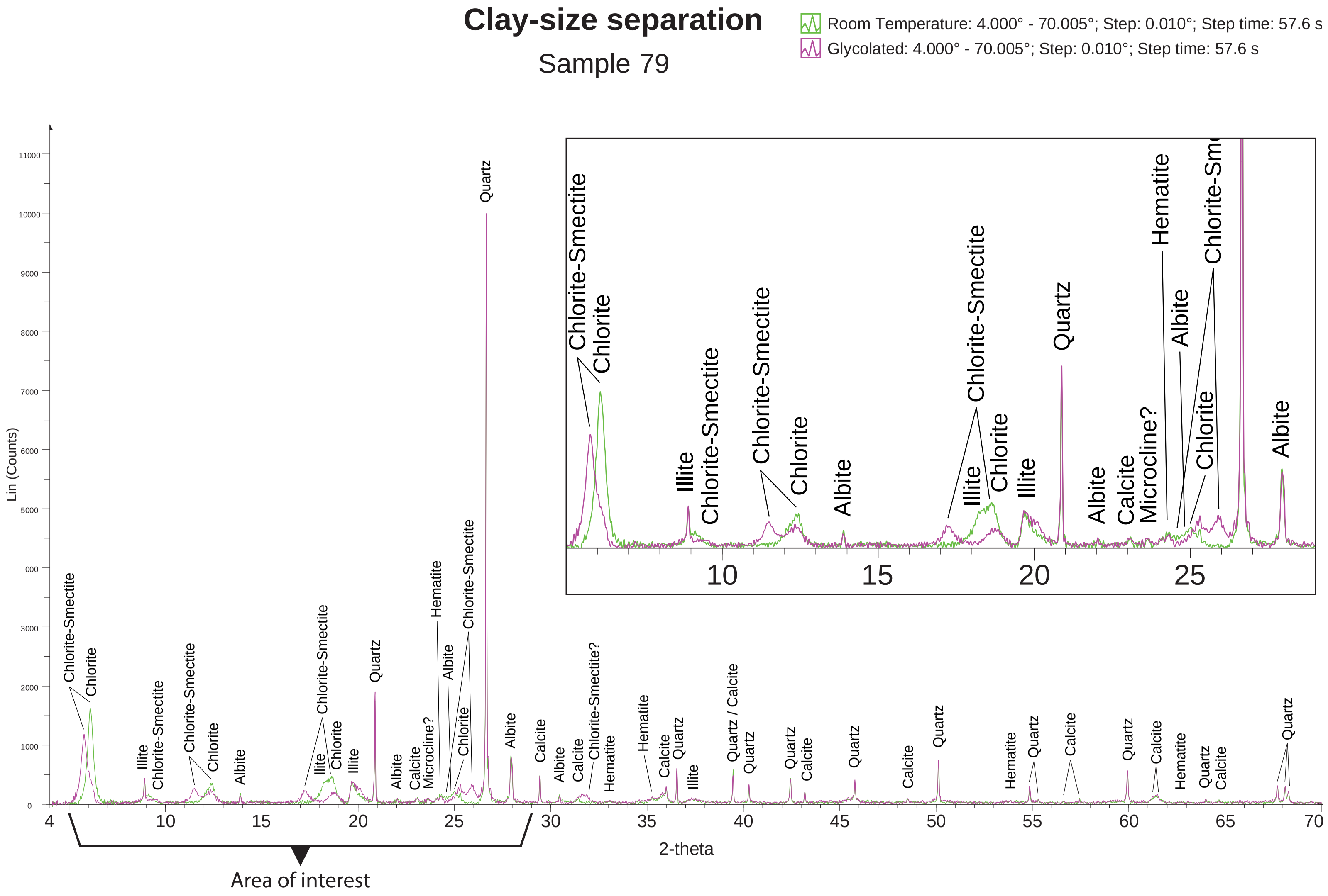

Figure F21: Clay-size separation X-ray diffraction results and interpretation for sample 79.

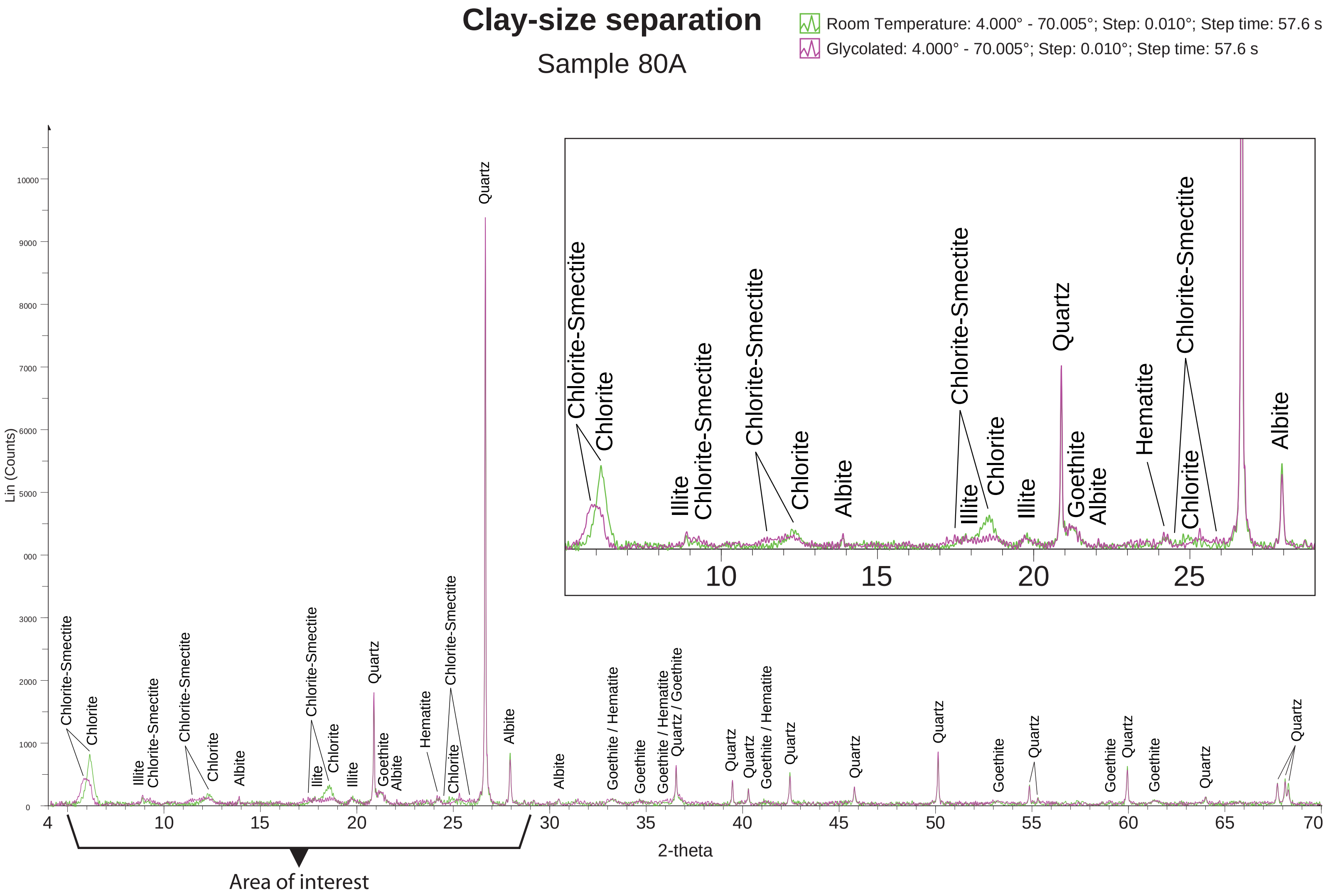

Figure F22: Clay-size separation X-ray diffraction results and interpretation for sample 80A.

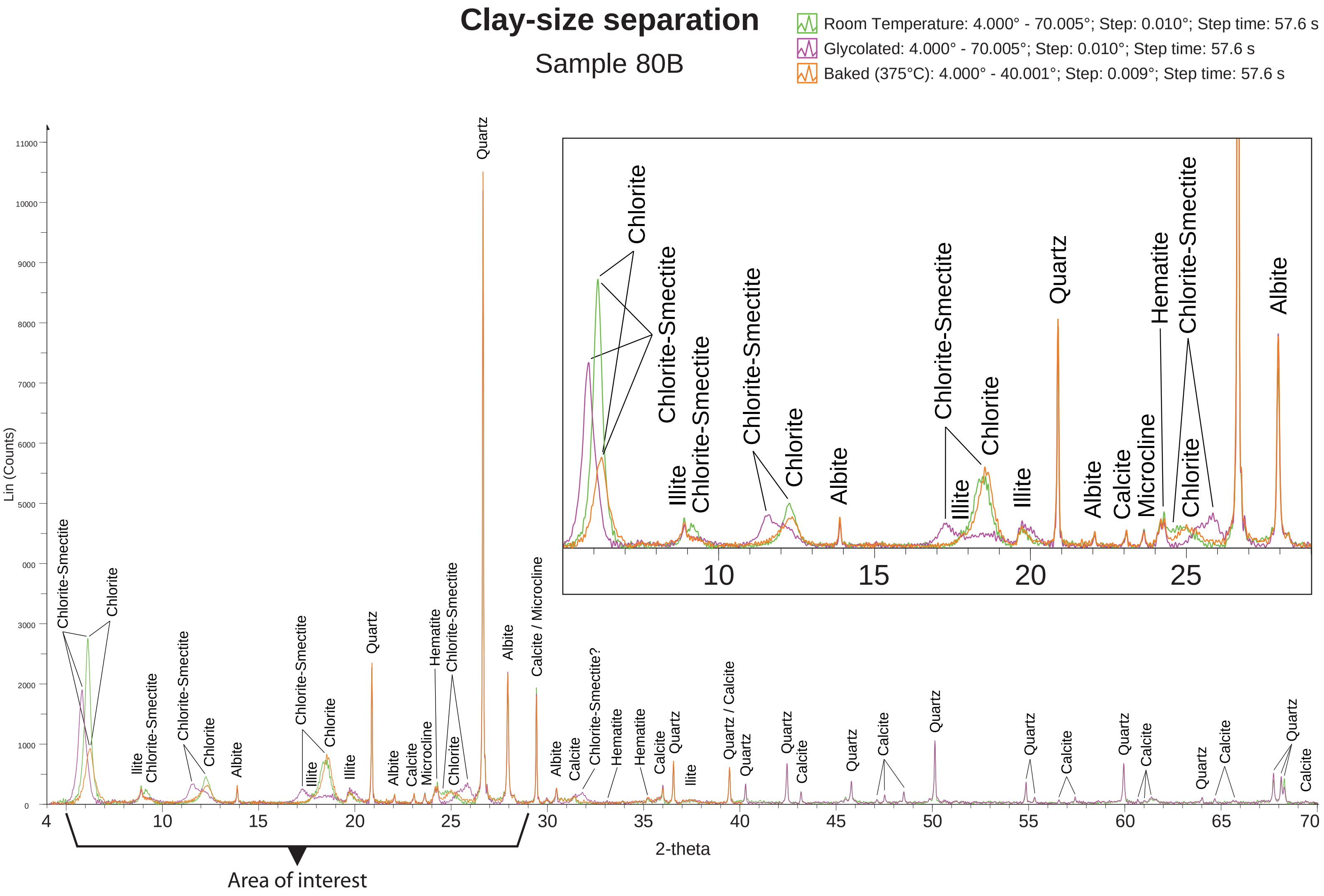

Figure F23: Clay-size separation X-ray diffraction results and interpretation for sample 80B.

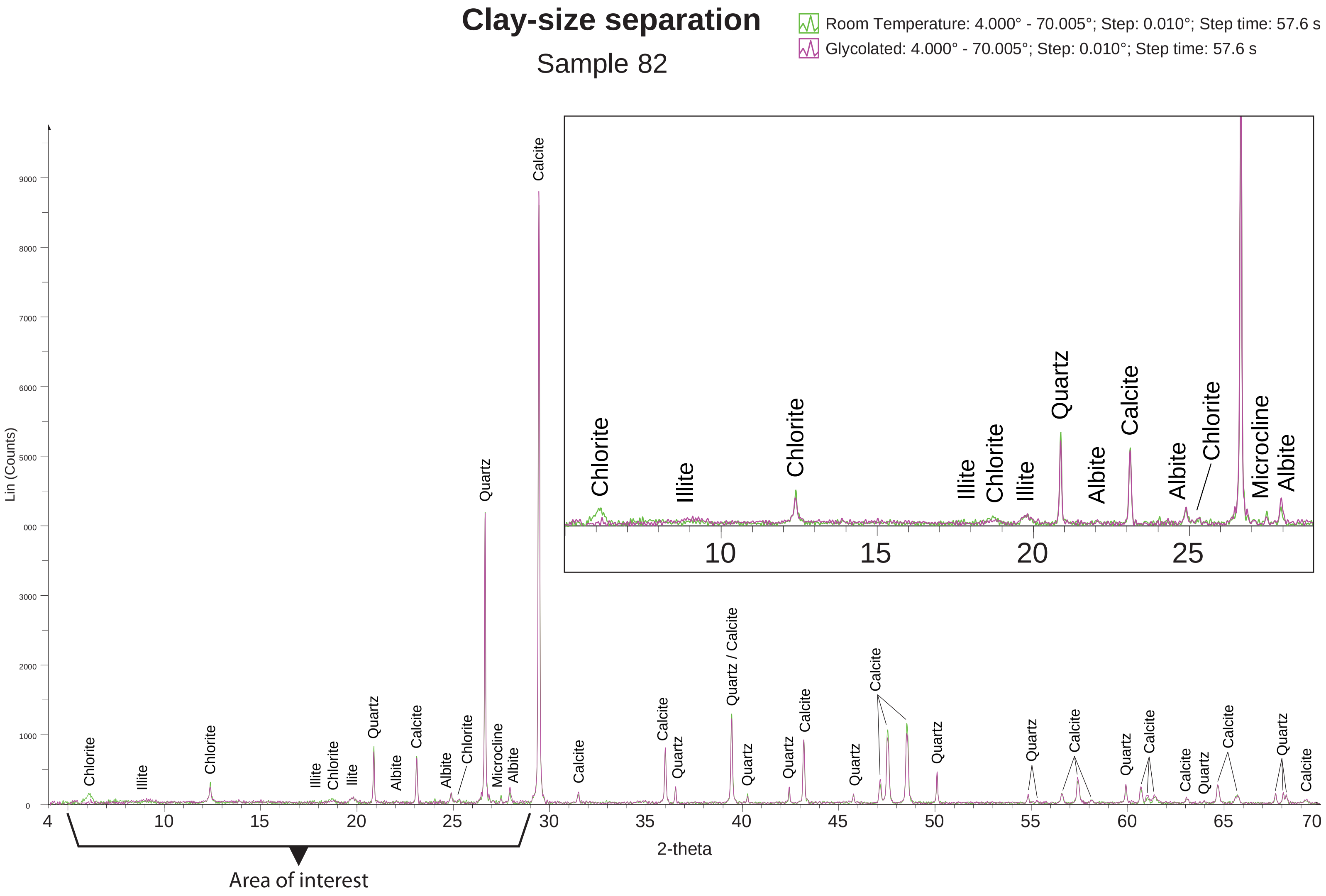

Figure F24: Clay-size separation X-ray diffraction results and interpretation for sample 82.

# Appendix G: Quantifying the Water Temperature Effect

To predict the magnitude of calcite $\delta^{18}$O fractionation in the conduit as a result of precipitation from water warmer than the surrounding surface water, I used reported water isotope data from Little Grand Wash (Mayo et al., 1991; Evans et al., 2004; Shipton et al., 2004). SMOW isotope values were converted to PDB values using this equation from Friedman et al. (1977):

$$\delta_{\mathrm{PDB}} = (0.97006 \times \delta_{\mathrm{SMOW}}) - 29.94.$$

The following equation, which uses fractionation factors from Friedman and O'Neil (1977, after Land, 1983), relates calcite $\delta^{18}$O (SMOW) to water $\delta^{18}$O (SMOW) and water temperature (°C):

$$\mathrm{T} = \sqrt{\frac{2{,}780{,}000}{2.89 + 1000\left(ln\dfrac{1{,}000 + \delta^{18}\mathrm{O}_{\mathrm{calcite}}}{1{,}000 + \delta^{18}\mathrm{O}_{\mathrm{water}}}\right)}} - 273.$$

Using 9–13°C for surface water temperatures (USGS, 2011) and 15–18°C for spring water temperatures (Baer and Rigby, 1978; Heath, 2004; Gouveia and Friedmann, 2006; Heath et al., 2009), I calculated a likely range of calcite $\delta^{18}$O (PDB) values (Table G1). The results show that calcite precipitating from seep water 2–9°C warmer than surface water is likely to have $\delta^{18}$O values reduced by no more than 0.5–2.1‰.

**Predicted values of $\delta^{18}O$ (PDB) for precipitating calcite**

| | **Water temperature** | **Water $\delta^{18}O$ (SMOW)*** | | | | |
|---|---|---|---|---|---|---|
| | | **-13.0‰** | **-14.0‰** | **-14.4‰** | **-16.0‰** | **-16.5‰** |
| Surface water | 9°C | -11.3‰ | -12.3‰ | -12.7‰ | -14.3‰ | -14.8‰ |
| | 13°C | -12.2‰ | -13.2‰ | -13.6‰ | -15.2‰ | -15.7‰ |
| Spring water | 15°C | -12.7‰ | -13.7‰ | -14.1‰ | -15.7‰ | -16.2‰ |
| | 18°C | -13.4‰ | -14.4‰ | -14.8‰ | -16.4‰ | -16.9‰ |

*Based on the maximum range of SMOW values reported in Evans et al. (2004), Heath (2004), Mayo et al. (2001) and Shipton et al. (2004)

Table G1: Predicted variability in $\delta^{18}O$ (PDB) values of calcite precipitating from the same parental water at different temperatures (i.e., reported spring and local surface water temperature ranges). The minimum difference between surface and spring water for any given $\delta^{18}O$ (SMOW) water composition is 0.5‰; the maximum difference is 2.1‰.

# Appendix H: Likely Travertine Samples

During field work I collected and interpreted samples 17B, 71A, 71B, 73 and 75, all abutting the travertine, as yellow-colored $CO_2$-altered Jurassic silt- and sandstones. These samples are pervasively cemented by the microcrystalline material characterized in Figures 42 and 43—a mixture of shale and micrite that forms a grain-supporting matrix around fine- to medium-grained sand. Detailed petrography, however, indicates that these samples are likely travertine deposits. They are discussed here separately.

Where this mud-micrite matrix is present, it dominates the fabric, as shown in Table H1, which presents the point count results from slides that contain this type of matrix. The total matrix percentage ("Clay Matrix" plus "Micrite") is as high as 91% in sample 71B, and averages 68%. Paxton et al. (2002) showed that the maximum intergranular volume for sandstones (percent intergranular porosity plus percent pore-filling cement plus percent depositional matrix) is about 42%, and this number decreases rapidly with burial. Although in the field these matrix-dominated rocks were interpreted as part of the $J_{ms}5$ sandstone, the intergranular volume is clearly too high for any sandstone, especially considering that these strata were deeply buried before being more recently exhumed.

The granular component in some of these samples is so minor that grains are entirely matrix-supported (Figure H1). To create the same rock as a product of diagenesis in sandstone would require extensive grain dissolution concurrent with the emplacement of micrite and clay cement. This process is unlikely. Quartz is inherently stable and resistant to dissolution; in addition, the quartz grains in place show no signs of dissolution, which would be expected if their neighbors had been entirely dissolved. Quartz grains could theoretically remain pristine even while other less stable grains such as feldspars or lithic fragments were entirely dissolved, but no correlatable sandstones in the map area contain a sufficient portion

| | Quartz | | | Plag | | Kspar | | Lithics | | Misc. | Clay | Cement | | | | Porosity | | | | Total | Total |
|---|---|---|---|---|---|---|---|---|---|---|---|---|---|---|---|---|---|---|---|---|---|
| **Sample** | **mono** | **poly** | **mic/ch** | **intact** | **diss** | **intact** | **diss** | **opaq** | **sed** | **Grains** | **Matrix** | **spar** | **mic** | **qtz** | **clay** | **inter** | **over** | **intra** | **micro** | **Points** | **Matrix** |
| 17B-2 | 126 | 3 | 3 | 0 | 0 | 0 | 1 | 0 | 9 | 0 | 79 | 4 | 143 | 0 | 6 | 10 | 0 | 11 | 5 | 400 | 222 |
| | 32% | 1% | 1% | 0% | 0% | 0% | 0% | 0% | 2% | 0% | 20% | 1% | 36% | 0% | 2% | 3% | 0% | 3% | 1% | | 56% |
| 71A-3 | 41 | 1 | 6 | 0 | 0 | 0 | 1 | 2 | 2 | 0 | 79 | 0 | 258 | 0 | 2 | 0 | 0 | 0 | 8 | 400 | 337 |
| | 10% | 0% | 2% | 0% | 0% | 0% | 0% | 1% | 1% | 0% | 20% | 0% | 65% | 0% | 1% | 0% | 0% | 0% | 2% | | 84% |
| 71B | 13 | 2 | 3 | 0 | 0 | 0 | 1 | 0 | 2 | 0 | 106 | 10 | 259 | 0 | 4 | 0 | 0 | 0 | 0 | 400 | 365 |
| | 3% | 1% | 1% | 0% | 0% | 0% | 0% | 0% | 1% | 0% | 27% | 3% | 65% | 0% | 1% | 0% | 0% | 0% | 0% | | 91% |
| 72B | 38 | 0 | 30 | 0 | 0 | 0 | 0 | 0 | 23 | 0 | 125 | 7 | 149 | 0 | 10 | 14 | 0 | 0 | 4 | 400 | 274 |
| | 10% | 0% | 8% | 0% | 0% | 0% | 0% | 0% | 6% | 0% | 31% | 2% | 37% | 0% | 3% | 4% | 0% | 0% | 1% | | 69% |
| 73 | 139 | 4 | 8 | 0 | 1 | 0 | 0 | 0 | 0 | 1 | 133 | 0 | 108 | 0 | 6 | 0 | 0 | 0 | 0 | 400 | 241 |
| | 35% | 1% | 2% | 0% | 0% | 0% | 0% | 0% | 0% | 0% | 33% | 0% | 27% | 0% | 2% | 0% | 0% | 0% | 0% | | 60% |
| 75-1 | 144 | 3 | 14 | 0 | 0 | 0 | 0 | 0 | 3 | 0 | 65 | 12 | 154 | 0 | 4 | 0 | 0 | 0 | 1 | 400 | 219 |
| | 36% | 1% | 4% | 0% | 0% | 0% | 0% | 0% | 1% | 0% | 16% | 3% | 39% | 0% | 1% | 0% | 0% | 0% | 0% | | 55% |
| 75-2 | 116 | 6 | 4 | 0 | 0 | 1 | 0 | 0 | 1 | 0 | 30 | 8 | 218 | 0 | 16 | 0 | 0 | 0 | 0 | 400 | 248 |
| | 29% | 2% | 1% | 0% | 0% | 0% | 0% | 0% | 0% | 0% | 8% | 2% | 55% | 0% | 4% | 0% | 0% | 0% | 0% | | 62% |
| Average | 22% | 1% | 2% | 0% | 0% | 0% | 0% | 0% | 1% | 0% | 22% | 1% | 46% | 0% | 2% | 1% | 0% | 0% | 1% | | 68% |

Table H1: Point count results for samples dominated by a mud-micrite matrix. Sample 72B is a piece of travertine from the known travertine deposit. It shows similar composition, having a high abundance of clay-ey and micritic matrix. mono = monocrystalline; poly = polycrystalline; mic/ch = microcrystalline quartz/chert; spar = calcite spar; mic = micrite; inter = intergranular; over = oversize; intra = intragranular; micro = microporosity

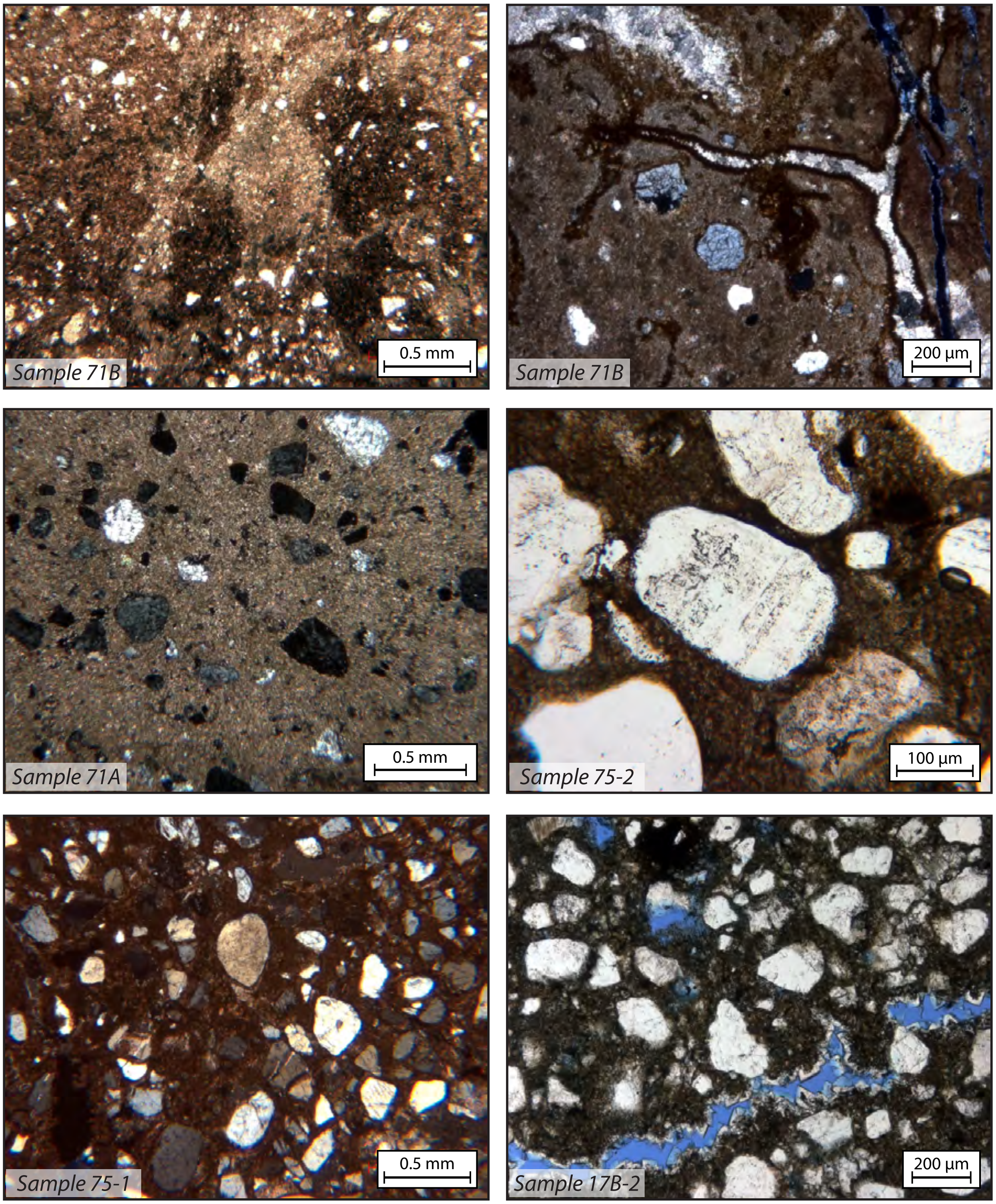

Figure H1: Samples dominated by the mud-micrite matrix are matrix-supported even where sand-sized grains are abundant.

of such soft grains to make this possible. The maximum total of lithics fragments and feldspars is (an outlier) of 11%, and this sample (35B) is a coarse-grained sandstone (0.30–1.20 mm), while the matrix-supported quartz is much more fine-grained (0.05–0.50 mm).

The lithology of these samples could be interpreted as original depositional lithology—shale material deposited with a small, fine-grained quartz component—but this interpretation is problematic. It would be peculiar for channel fill and overbank deposits in an alluvial plane to contain such an essentially homogeneous mixture of shale peppered with quartz grains. Such a lithology is seen nowhere else in the map area—it is unique to the outcrops immediately surrounding the travertine deposit. Moreover the micrite cement is not accounted for in this explanation, and would require pervasive dissolution followed by cementation. The dissolved material would be either shale, which returns to the problem of an unlikely depositional facies; or it would have been sand-sized feldspars and lithic fragments in high abundance, a lithofacies that is absent in the study area.

Although the layering characteristic of travertines is not observed, I interpret these samples as travertine deposits: As the travertine was being deposited as the surface, it would have been at a topographic low where the spring erupted. Sand grains could easily be washed onto the surface of the platform by runoff coming down the fault scarp only meters away; finer clay- and mud-sized dust in great abundance could also be washed in, or wind-transported from the expansive Mancos Shale, Cedar Mountain Formation, Brushy Basin Member and Salt Wash Member shale exposures surrounding the Little Grand Wash fault on all sides. As these Quaternary sediments were deposited on top of the platform, they were mixed with and trapped by calcite precipitating from the erupting $CO_2$-rich water. This explains both their location immediately adjacent to the travertine and their unusual composition of shale, micrite and sand. Forming concurrently and by the same processes as the travertine deposit, they are older deposits of travertine. A sample of known travertine (sample 72B) from the recognized platform is shown in Figure H2 for comparison. The similarities to the matrix-dominated samples are plain: Although it has entrapped larger grains, it is dominated by mud-micrite matrix comparable to the matrix in samples 17B, 71A, 71B, 73 and 75.

Shipton et al. (2005a) described a "carbonate-cemented sediment suggesting that colluvium surrounding the leak site was cemented by the erupting spring waters" at the base of inactive travertines. This may be a deposit similar to the one I describe, but the range of isotope values do not match the samples I describe: Shipton et al. have $\delta^{18}O$ values between -11.1‰ and -11.3‰ and $\delta^{13}C$ values from 3.3‰ to 3.9‰. My samples have $\delta^{18}O$ values between -9.3‰ and -9.8‰ and $\delta^{13}C$ values from 4.4‰ to 4.8‰. Burnside (2010) referred to a carbonate-cemented breccia composed of fine-grained clast-supported matrix formed by initial leakage of $CO_2$-rich fluids to the surface. This seems more akin to what I describe. The several meters' thickness in the map area seems to imply more than just an initial mixing of spring water with surface cover, however. While thick desiccated surface shales may be deeply infiltrated by surface outflow, this material contains too high an abundance of silt- and sand-sized particles to be simply shale exposed at the surface.

Other isotopic comparisons help confirm this interpretation. Isotope data from samples 71A, 71B, 72B (the known travertine), 73 and 75 are clustered in the same region when plotting $\delta^{18}O$ against $\delta^{13}C$ (Figure H3). Published isotope data from other travertines along Little Grand Wash (Shipton et al., 2004; Shipton et al., 2005a) lie in the same region of the plot. This shows that these samples have an isotopic signature typical of travertine. Because pore-filling conduit cement shares a similar isotopic composition (Figure H3), however, this is not definitive proof that these samples are travertine.

Compositional differences between these samples indicate that the nature of deposition has changed, incorporating at times very fine sediment and other times coarser

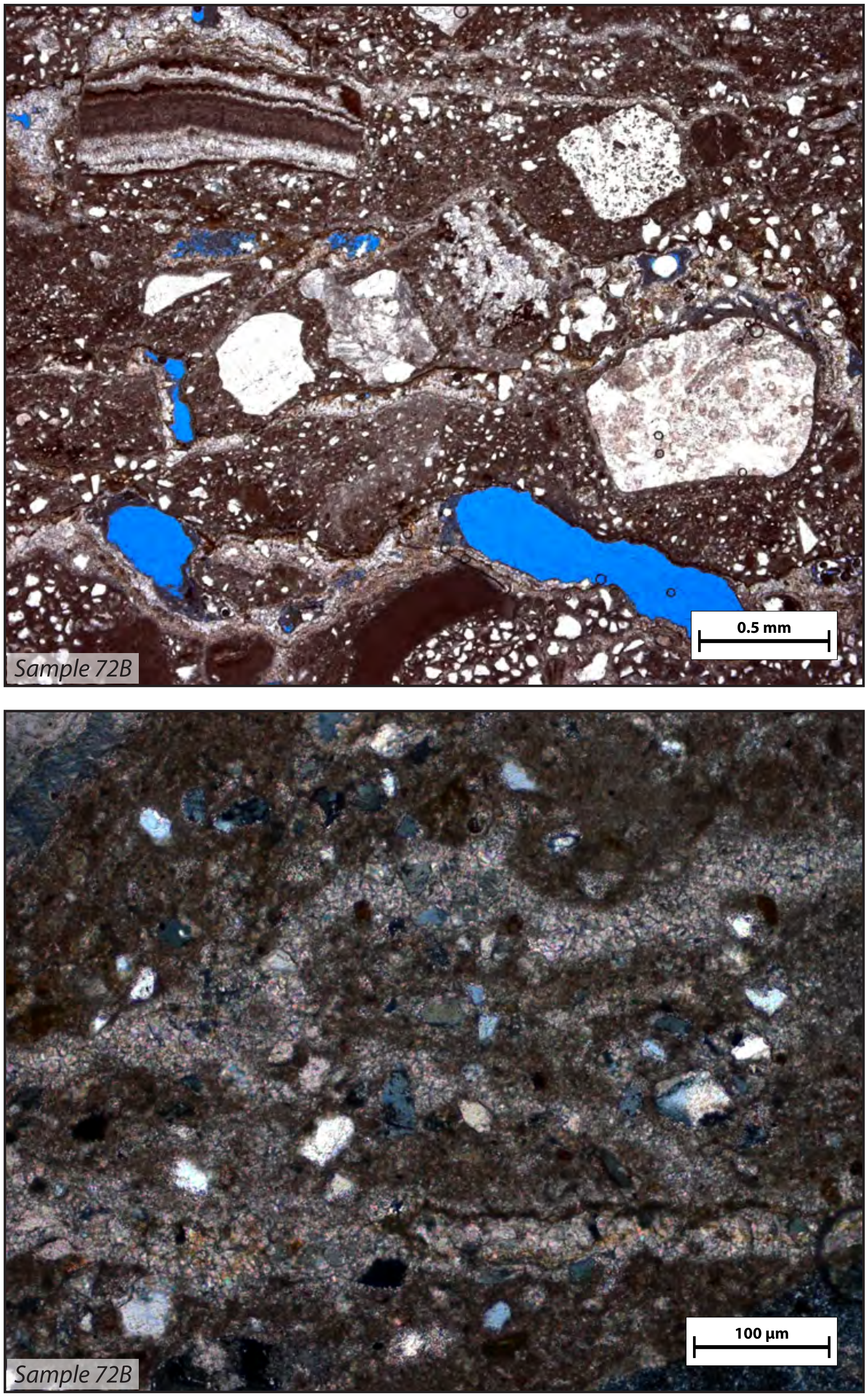

Figure H2: A sample of known travertine contains larger grains but has a matrix similar to samples 17B, 71A and 71B (compare to Figure H1).

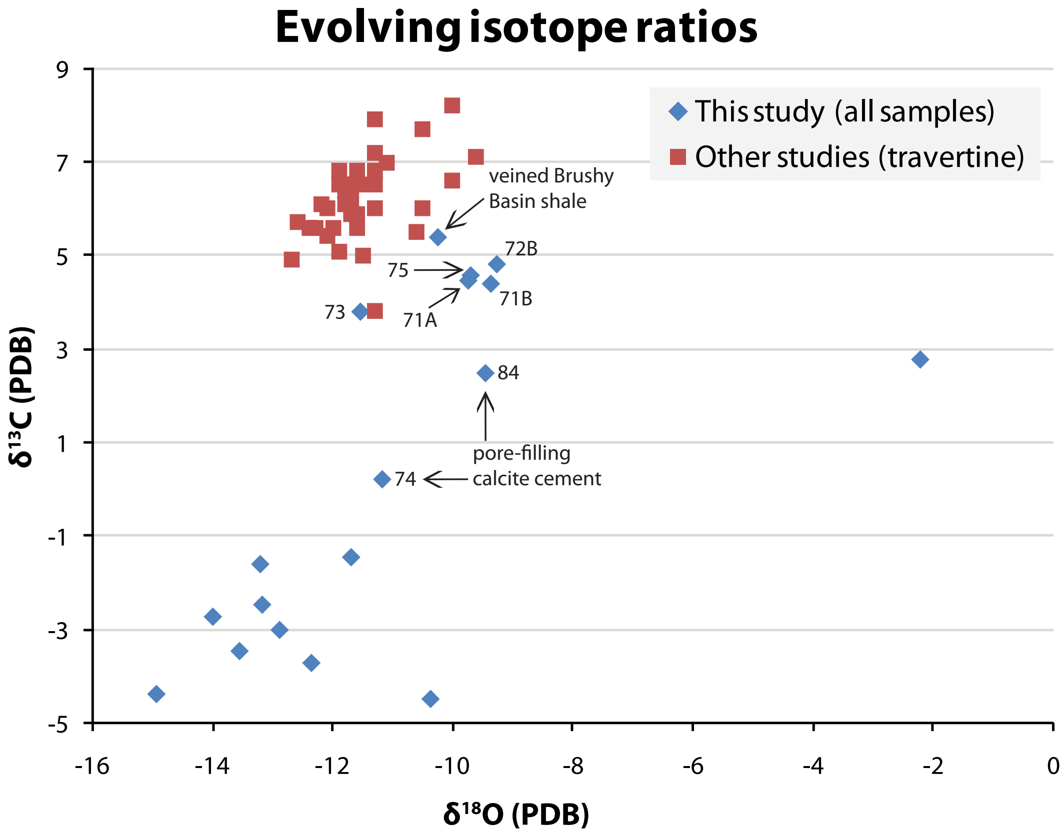

Figure H3: When $\delta^{18}$O is plotted against $\delta^{13}$C, samples with high mud-micrite content (labeled) lie in the same region, relatively heavy compared to other map area samples. Isotope data from studies of other travertines along Little Grand Wash (Shipton et al., 2005; Shipton et al., 2004) lie in the same region of the plot. Samples 74 and 84 are labeled for comparison to seep-related pore-filling calcite cement.

sand- and even pebble-sized grains. Although outcrops have an isotropic texture, lacking distinct layering, such differences in grain size could indicate discrete depositional periods when circumstances favored allochthonous input of different size. Alternately, deposition could have been continuous, with variation in grain size a result of non-systematic controls (e.g., seasonal drought, rock falls from the fault scarp). Burnside et al. (2009) did not note discrete deposits in their uranium dating analysis of this travertine, and I do not have enough data to properly address this.

# References

Allis, R., Bergfeld, D., Moore, J., McClure, K., Morgan, C., Chidsey, T., Heath, J., and McPherson, B., 2005, Implications of results from $CO_2$ flux surveys over known $CO_2$ systems for long-term monitoring. From proceedings of Fourth Annual Conference on Carbon Capture and Sequestration: May 2–5, Alexandria, VA. United States Department of Energy, National Energy Technology Laboratory, 22 p.

Allis, R., Chidsey, T., Gwynn, W., Morgan, C., White, S., Adams, M., and Moore, J., 2001, Natural $CO_2$ reservoirs on the Colorado Plateau and Southern Rocky Mountains: Candidates for $CO_2$ sequestration. From proceedings of First National Conference on Carbon Sequestration: May 14–17, Washington, DC. United States Department of Energy, National Energy Technology Laboratory, 19 p.

Anderson, T.R., and Fairley, J.P., 2008, Relating permeability to the structural setting of a fault-controlled hydrothermal system in southeast Oregon, USA: Journal of Geophysical Research, v. 113, B05402.

Annunziatellis, A., Beaubien, S.E., Bigi, S., Ciotoli, G., Coltella, M., and Lombardi, S., 2008, Gas migration along fault systems and through the vadose zone in the Latera caldera (central Italy): Implications for $CO_2$ geological storage: International Journal of Greenhouse Gas Control, v. 2, 353–372.

Antonellini, M., and Aydin, A., 1994, Effect of faulting on fluid flow in porous sandstones: Petrophyical properties: AAPG Bulletin, v. 78, 355–377.

Antonellini, M., and Aydin, A., 1995, Effect of faulting on fluid flow in porous sandstones: Geometry and spatial distribution: AAPG Bulletin, v. 79, 642–671.

Arvidson, R.S., and Mackenzie, F.T., 1999, The dolomite problem: Control of precipitation kinetics by temperature and saturation state: American Journal of Science, v. 299, 257–288.

Aydin, A., and Johnson, A.M., 1978, Development of faults as zones of deformation bands and as slip surfaces in sandstone: Pure and Applied Geophysics, v. 116, 931–942.

Baer, J.L., and Rigby, J.K., 1978, Geology of the Crystal Geyser and environmental implications of its effluent, Grand County, Utah: Utah Geology, 1978, v. 5, 6.

Baines, S.J., and Worden, R.H., 2004, The long-term fate of $CO_2$ in the subsurface: Natural analogues for $CO_2$ storage, *in* Worden, R.H., and Baines, S.J., eds., Geological Storage of Carbon Dioxide: Special Publication 233, Geological Society of London, p. 59–85.

Baker, J.C., Bai, G.P., Hamilton, P.J., Golding, S.D., and Keene, J.B., 1995, Continental-scale magmatic carbon dioxide seepage recorded by dawsonite in the Bowen-Gunnedah-Sydney Basin system, eastern Australia: Journal of Sedimentary Research, v. A65, 522–530.

Baum, G., 2010, Email correspondence about how to to interpret the results of helium injection porosity and nitrogren injection permeability: Austin, TX.

Baum, G., 2011, Revisions to description of gas injection methods of porosity and permeability measurement: Austin, TX, April 27.

Bénézeth, P., Palmer, D.A., Anovitz, L.M., and Horita, J., 2007, Dawsonite synthesis and reevaluation of its thermodynamic properties from solubility measurements: Implications for mineral trapping of $CO_2$: Geochimica et Cosmochimica Acta, v. 71, 4438–4455.

Berger, A., Gier, S., and Krois, P., 2009, Porosity-preserving chlorite cements in shallow-marine volcaniclastic sandstones: Evidence from Cretaceous sandstones of the Sawan gas field, Pakistan: AAPG Bulletin, v. 93, 595–615.

Blisniuk, P., 2011, Emails regarding the methods and accuracy of calcite content measurements.

Bogen, K.T., Homann, S.G., Gouveia, F.J., and Neher, L.A., 2006, Prototype near-field/GIS model for sequestered-$CO_2$ risk characterization and management. From proceedings of International Symposium on Site Characterization for $CO_2$ Geological Storage: March 20–22, Berkeley, CA. Lawrence Berkeley National Laboratory, 3 p.

Boggs, S., Jr., 2009, Petrology of Sedimentary Rocks: Cambridge, Cambridge University Press, 599 p.

Boyd, C., 2011, Discussion on the possible and likely species represented by fossilized bone fragments in the Morrison Brushy Basin: Austin, TX.

Brenner, R.L., 1983, Late Jurassic tectonic setting and paleogeography of Western Interior, North America, *in* Reynolds, M.W., and Dolly, E.D., eds., Mesozoic Paleogeography of the West-Central United States: Rocky Mountain Paleogeography Symposium 2: Denver, CO, Society of Economic Paleontologists and Mineralogists, Rocky Mountain Section, 119–132.

Brigatti, M.F., and Poppi, L., 1984, Crystal chemistry of corrensite: A review: Clays and Clay Minerals, v. 32, 9.

Burnside, N.M., 2010, U-Th dating of travertine on the Colorado Plateau: Implications for the leakage of geologically stored $CO_2$ [Ph.D Dissertation]: Glasgow, University of Glasgow, 290 p.

Burnside, N.M., Dockrill, B., Shipton, Z.K., and Ellam, R.M., 2009, Dating and Constraining Leakage Rates from a Natural Analogue for $CO_2$ Storage – The Little Grand Wash and Salt Wash Fault. From proceedings of 2nd International Conference on Fault and Top Seals – From Pore to Basin Scale: September 21–24, Montpellier, France, 3 p.

Burnside, N.M., Shipton, Z.K., and Ellam, R.M., 2007, Using spring deposits to track the evolution of fluid pathways through faults: Little Grand Wash Fault and Salt Wash

Graben, Utah, USA. Abstract, *in* GSA Annual Meeting Abstracts with Programs: October 28–31, Denver, CO. Geological Society of America, p. 240.

Burton, E., Myhre, R., Myer, L., and Birkinshaw, K., 2008, Geologic carbon sequestration strategies for California: Report to the legislature: Joint Report (CEC-500-2007-100-CMF). California Energy Commission, 139 p.

Caine, J.S., Evans, J.P., and Forster, C.B., 1996, Fault zone architecture and permeability structure: Geology, v. 24, 1025–1028.

Campbell, J.A., and Baer, J.L., 1978, Little Grand Wash Fault – Crystal Geyser Area, *in* Fassett, J.E., Thomaidis, N.D., and Matheny, M.L., eds., Oil and Gas Fields of the Four Corners Area, Volume 2: Durango, CO, Four Corners Geological Society, p. 666–669.

Cartwright, J.A., Mansfield, C., and Trudgill, B.D., 1996, The growth of normal faults by segment linkage, *in* Buchanan, P.G., and Nieuwland, D.A., eds., Modern Developments in Structural Interpretation, Validation and Modelling: Special Publication 99, Geological Society of London, p. 163–177.

Cecil, C.B., and Heald, M.T., 1971, Experimental investigation of the effects of grain coatings on quartz growth: Journal of Sedimentary Research, v. 41, 582–584.

Celia, M.A., and Nordbotten, J.M., 2009, Practical Modeling Approaches for Geological Storage of Carbon Dioxide: Ground Water, v. 47, 627–638.

Chan, M.A., Parry, W.T., and Bowman, J.R., 2000, Diagenetic Hematite and Manganese Oxides and Fault-Related Fluid Flow in Jurassic Sandstones, Southeastern Utah: AAPG Bulletin, v. 84, 1281–1310.

Childs, C., Watterson, J., and Walsh, J.J., 1995, Fault overlap zones within developing normal fault systems: Journal of the Geological Society of London, v. 152, 535–549.

Childs, C., Watterson, J., and Walsh, J.J., 1996, A model for the structure and development of fault zones: Journal of the Geological Society of London, v. 153, 337–340.

Clark, I.D., and Fritz, P., 1997, Environmental Isotopes in Hydrogeology: Boca Raton, FL, CRC Press, Lewis Publishers.

Cotter, E., 1975, Late Cretaceous sedimentation in a low-energy coastal zone: The Ferron Sandstone of Utah: Journal of Sedimentary Petrology, v. 45, 669–685.

Craig, L.C., Mullens, T.E., Weir, G.W., Cadigan, R.A., Freeman, V.L., and Holmes, C.N., 1955, Stratigraphy of the Morrison and related formations, Colorado Plateau region: A preliminary report [USGS Bulletin 1009-E]: Reston, VA, United States Geological Survey, 168 p.

Crider, J.G., and Peacock, D.C.P., 2004, Initiation of brittle faults in the upper crust: A review of field observations: Journal of Structural Geology, v. 26, 17.

Cruikshank, K.M., and Aydin, A., 1994, Role of fracture localization in arch formation, Arches National Park, Utah: Geological Society of America Bulletin, v. 106, 879–891.

Cruikshank, K.M., Zhao, G., and Johnson, A.M., 1991, Analysis of minor fractures associated with joints and faulted joints: Journal of Structural Geology, v. 13, 865–886.

Curewitz, D., and Karson, J.A., 1997, Structural settings of hydrothermal outflow: Fracture permeability maintained by fault propagation and interaction: Journal of Volcanology and Geothermal Research, v. 79, 149–168.

Davatzes, N.C., Eichhubl, P., and Aydin, A., 2005, Structural evolution of fault zones in sandstone by multiple deformation mechanisms: Moab fault, southeast Utah: Geological Society of America Bulletin, v. 117, 135–148.

Deer, W.A., Howie, R.A., and Zussman, J., 1966, An introduction to the rock-forming minerals: London, Longman, 528 p.

Delta Petroleum Corporation, 2009, Well Completion or Recompletion Report and Log for Greentown State 36-24H (API: 4301931519). Utah Department of Natural Resources – Division of Oil, Gas and Mining.

Dickinson, W.R., Beard, L.S., Brakenridge, G.R., Erjavec, J.L., Ferguson, R.C., Inman, K.F., Knepp, R.A., Lindberg, F.A., and Ryberg, P.T., 1983, Provenance of North American Phanerozoic sandstones in relation to tectonic setting: GSA Bulletin, v. 94, 222–235.

Dickinson, W.R., and Suczek, C.A., 1979, Plate tectonics and sandstone compositions: AAPG Bulletin, v. 63, 2164–2182.

Dixon, S.A., Summers, D.M., and Surdam, R.C., 1989, Diagenesis and preservation of porosity in Norphlet Formation (Upper Jurassic), southern Alabama: AAPG Bulletin, v. 73, 707–728.

Dockrill, B., 2006, Understanding leakage from a fault-sealed $CO_2$ reservoir in east-central Utah: A natural analogue applicable to $CO_2$ storage [Ph.D dissertation]: Dublin, Trinity College Dublin, The University of Dublin.

Dockrill, B., and Shipton, Z.K., 2009, Structural Controls on Leakage from a Natural $CO_2$ Geologic Storage Site – Central Utah, USA. From proceedings of 2nd International Conference on Fault and Top Seals – From Pore to Basin Scale: September 21–24, Montpellier, France, 3 p.

Dockrill, B., and Shipton, Z.K., 2010, Structural controls on leakage from a natural $CO_2$ geologic storage site: Central Utah, USA: Journal of Structural Geology, v. 32, 1768–1782.

Doelling, H., 1994, Tufa deposits in western Grand County: Survey Notes – Utah Geological Survey, v. 26, 4.

Doelling, H.H., 2002, Interim Geologic Map of the San Rafael Desert 30' x 60' Quadrangle, Emery and Grand Counties, Utah (Open-file Report 404). Utah Geological Survey, 21 p.

Dooley, J.J., Dahowski, R.T., Davidson, C.L., Wise, M.A., Gupta, N., Kim, S.H., and Malone, E.L., 2006, Carbon Dioxide Capture and Geologic Storage: A core element of a global energy technology strategy to address climate change. The Global Energy Technology Strategy Program, Battelle Memorial Institute, 67 p.

Dooley, J.J., and Wise, M.A., 2003a, Retention of $CO_2$ in Geologic Sequestration Formations: Desirable Levels, Economic Considerations, and the Implications for Sequestration R&D. From proceedings of The 6th International Conference on Greenhouse Gas Control Technologies: October 1–4, Kyoto, Japan. Elsevier, 6 p.

Dooley, J.J., and Wise, M.A., 2003b, Why injecting $CO_2$ into various geologic formations is not the same as climate change mitigation: The issue of leakage (B2-5). Joint Global Change Research Institute, Battelle Memorial Institute.

Dott, R.H., Jr., 1964, Wacke, graywacke and matrix: What approach to immature sandstone classification?: Journal of Sedimentary Petrology, v. 34, 625–632.

Downs, R.T., 2006, The RRUFF Project: an integrated study of the chemistry, crystallography, Raman and infrared spectroscopy of minerals. Abstract, *in* 19th General Meeting of the International Mineralogical Association – Program and Abstracts: July 23–28, Kobe, Japan. International Mineralogical Association.

Dutton, S.P., and Willis, B.J., 1998, Comparison of outcrop and subsurface sandstone permeability distribution, Lower Cretaceous Fall River Formation, South Dakota and Wyoming: Journal of Sedimentary Research, v. 68, 890–900.

Eichhubl, P., and Boles, J.R., 2000, Focused fluid flow along faults in the Monterey Formation, coastal California: Geological Society of America Bulletin, v. 112, 1667–1679.

Eichhubl, P., D'Onfro, P.S., Aydin, A., Waters, J., and McCarty, D.K., 2005, Structure, petrophysics, and diagenesis of shale entrained along a normal fault at Black Diamond Mines, California – Implications for fault seal: AAPG Bulletin, v. 89, 1113–1137.

Eichhubl, P., Davatzes, N.C., and Becker, S.P., 2009, Structural and Diagenetic Control of Fluid Migration and Cementation Along the Moab Fault, Utah: AAPG Bulletin, v. 93, 653–681.

Eichhubl, P., Taylor, W.L., Pollard, D.D., and Aydin, A., 2004, Paleo-fluid flow and deformation in the Aztec Sandstone at the Valley of Fire, Nevada: Evidence for the coupling of hydrogeologic, diagenetic, and tectonic processes: Geological Society of America Bulletin, v. 116, 1120–1136.

Ellis, A.J., 1959, The solubility of calcite in carbon dioxide solutions: American Journal of Science, v. 257, 354–365.

Ellis, M.A., and Dunlap, W.J., 1988, Displacement variation along thrust faults: implications for the development of large faults: Journal of Structural Geology, v. 10, 183–192.

Environmental Protection Agency, 2010, Underground Injection Control (UIC) Program Requirements for Geologic Sequestration of Carbon Dioxide Final Rule (Rule Number 816-F-10-073). Office of Water, 3 p.

Evamy, B.D., 1963, The application of a chemical staining technique to a study of dedolomitisation: Sedimentology, v. 2, 164–170.

Evans, J.P., Heath, J., Shipton, Z.K., Kolesar, P.T., Dockrill, B., Williams, A., Kirchner, D., Lachmar, T.E., and Nelson, S.T., 2004, Natural leaking $CO_2$-charged systems as analogs for geologic sequestration sites. From proceedings of Third Annual Conference on Carbon Capture and Sequestration: May 3–6, Alexandria, VA. United States Department of Energy, National Energy Technology Laboratory, 8 p.

Farmer, R.E., 1965, Genesis of subsurface carbon dioxide, *in* Young, A., and Galley, J.E., eds., Fluids in subsurface environments – A symposium: AAPG Memoir 4, American Association of Petroleum Geologists, p. 378–385.

Fenter, P., Zhang, Z., Park, C., Sturchio, N.C., Hu, X.M., and Higgins, S.R., 2007, Structure and reactivity of the dolomite (104)–water interface: New insights into the dolomite problem: Geochimica et Cosmochimica Acta, v. 71, 566–579.

Folk, R.L., 1980, Petrology of Sedimentary Rocks: Austin, Hemphill Publishing Company.

Forster, C., and Smith, L., 1988, Groundwater flow systems in mountainous terrain: 2. Controlling factors: Water Resources Research, v. 24, 1011–1023.

Fossen, H., Schultz, R.A., Rundhovde, E., Rotevatn, A., and Buckley, S.J., 2010, Fault linkage and graben stepovers in the Canyonlands (Utah) and the North Sea Viking Graben, with implications for hydrocarbon migration and accumulation: AAPG Bulletin, v. 94, 597–613.

Friedman, G.M., 1959, Identification of carbonate minerals by staining methods: Journal of Sedimentary Petrology, v. 29, 87–97.

Friedman, I., and O'Neil, J.R., 1977, Data of Geochemistry: Compilation of stable isotope fractionation factors of geochemical interest, *in* Fleischer, M., ed., USGS Professional Paper 440: Reston, VA, United States Geological Survey, KK1–KK12.

Frima, C., Moretti, I., Brosse, E., Quattrocchi, F., and Pizzino, L., 2005, Can Diagenetic Processes Influence the Short Term Hydraulic Behaviour Evolution of a Fault?: Oil & Gas Science and Technology - Rev. IFP, v. 60, 213–230.

Gale, J., 2004, Geological storage of $CO_2$: What do we know, where are the gaps and what more needs to be done?: Energy, v. 29, 1329–1338.

Gale, J., and Davison, J., 2004, Transmission of $CO_2$ – safety and economic considerations: Energy, v. 29, 1319–1328.

Gilfillan, S.M.V., Ballentine, C.J., Holland, G., Blagburn, D., Lollar, B.S., Stevens, S., Schoell, M., and Cassidy, M., 2008, The noble gas geochemistry of natural $CO_2$ gas reservoirs from the Colorado Plateau and Rocky Mountain provinces, USA: Geochimica et Cosmochimica Acta, v. 72, 25.

Gillette, D.D., 1999, Vertebrate paleontology in Utah, Miscellaneous Publication 99-1: Salt Lake City, UT, Utah Geological Survey, p. 554.

Gould, K., Pe-Piper, G., and Piper, D.J.W., 2010, Relationship of diagenetic chlorite rims to depositional facies in Lower Cretaceous reservoir sandstones of the Scotian Basin: Sedimentology, v. 57, 587–610.

Gouveia, F., and Friedmann, S.J., 2006, Timing and prediction of $CO_2$ eruptions from Crystal Geyser, UT (UCRL-TR-221731). Lawrence Livermore National Laboratory, 14 p.

Gouveia, F., Johnson, M., Leif, R., and Friedmann, J., 2005, Aerometric measurement and modeling of the mass of $CO_2$ emissions from Crystal Geyser, UT (UCRL-TR-211870). Lawrence Livermore National Laboratory, 57 p.

Gunter, W.D., Perkins, E.H., and McCann, T.J., 1993, Aquifer disposal of $CO_2$-rich gases: Reaction design for added capacity: Energy Conversion and Management, v. 34, 941–948.

Heath, J.E., 2004, Hydrogeochemical characterization of leaking carbon dioxide-charged fault zones in east-central Utah [Masters thesis]: Logan, UT, Utah State University, 166 p.

Heath, J.E., Lachmar, T.E., Evans, J.P., Kolesar, P.T., and Williams, A.P., 2009, Hydrogeochemical characterization of leaking, carbon dioxide-charged fault zones in east-central Utah, with implications for geological carbon storage, *in* McPherson, B.J., and Sundquist, E.T., eds., Carbon Sequestration and Its Role in the Global Carbon Cycle: Geophyiscal Monograph Series, 183: Washington, DC, American Geophysical Union, 147–158.

Heath, J.E., Lachmar, T.E., Shipton, Z.K., Nelson, S., and Evans, J.P., 2002, Hydrogeochemical analysis of leaking $CO_2$-charged fault zones: The Little Grand Wash and Salt Wash fault zones, Emery and Grand Counties, Utah. Abstract, *in* GSA Annual Meeting Abstracts with Programs: October 27–30, Denver, CO. Geological Society of America, p. 392.

Heath, J.E., Williams, A.P., and Evans, J.P., 2003, Structural and hydrogeochemical characterization of fault zones leaking $CO_2$-charged fluids: The Salt Wash and Little Grand Wash fault zones, Emery and Grand Counties, Utah. Abstract, *in* AAPG Annual Convention Abstracts with Programs: May 11–14, Salt Lake City, UT. American Association of Petroleum Geologists and Society of Economic Paleontologists and Mineralogists, p. 73.

Hecker, S., 1993, Quaternary tectonics of Utah with emphasis on earthquake-hazard characterization [Utah Geological and Mineral Survey: Bulletin 127]: Salt Lake City, UT, Utah Geological and Mineral Survey, 157 p.

Hellevang, H., Aagaard, P., Oelkers, E.H., and Kvamme, B., 2005, Can Dawsonite Permanently Trap $CO_2$?: Environmental Science & Technology, v. 39, 8281–8287.

Hepple, R.P., and Benson, S.M., 2003, Implications of Surface Seepage on the Effectiveness of Geologic Storage of Carbon Dioxide as a Climate Change Mitigation Strategy. From proceedings of The 6th International Conference on Greenhouse Gas Control Technologies: October 1–4, Kyoto, Japan. Elsevier, 6 p.

Hepple, R.P., and Benson, S.M., 2005, Geologic storage of carbon dioxide as a climate change mitigation strategy: Performance requirements and the implications of surface seepage: Environmental Geology, v. 47, 576–585.

Hillier, S., 1999, Use of an air brush to spray dry samples for X-ray powder diffraction: Clay Minerals, v. 34, 127–135.

Hintze, L.F., 1982, Marine evaporites in southwestern Utah, USGS Professional Paper: Reston, VA, United States Geological Survey, 14.

Hintze, L.F., 1988, Geologic History of Utah [Brigham Young University Geology Studies: Special Publication]: Provo, UT, Brigham Young University, 202 p.

Holloway, S., Pearce, J.M., Hards, V.L., Ohsumi, T., and Gale, J., 2007, Natural emissions of $CO_2$ from the geosphere and their bearing on the geological storage of carbon dioxide: Energy, v. 32, 1194–1201.

Hood, J.W., and Patterson, D.J., 1982, Bedrock aquifers in the northern San Rafael Swell area, Utah, with special emphasis on the Navajo Sandstone (Open-file Report 82-866). United States Geological Survey, 110 p.

Houghton, H.F., 1980, Refined techniques for staining plagioclase and alkali feldspars in thin section: Journal of Sedimentary Research, v. 50, 3.

Humphreys, B.A., Smith, S.A., and Strong, G.E., 1989, Authigenic chlorite formation in Late Triassic sandstones from the Central Graben, North Sea: Clay Minerals, v. 24, 427–444.

Hus, R., Acocella, V., Funiciello, R., and De Batist, M., 2005, Sandbox models of relay ramp structure and evolution: Journal of Structural Geology, v. 27, 459–473.

Hutcheon, I., Shevalier, M., and Abercrombie, H.J., 1993, pH buffering by metastable mineral-fluid equilibria and evolution of carbon dioxide fugacity during burial diagenesis: Geochimica et Cosmochimica Acta, v. 57, 1017–1027.

Hutchison, C.S., 1974, Laboratory handbook of petrographic techniques: New York, John Wiley & Sons, Inc., 527 p.

Intergovernmental Panel on Climate Change, 2005, Carbon Dioxide Capture and Storage. Cambridge University Press, 431 p.

International Centre for Diffraction Data, 2008, Powder Diffraction File 2.

Jamison, W.R., and Stearns, D.W., 1982, Tectonic deformation of Wingate Sandstone, Colorado National Monument: AAPG Bulletin, v. 66, 2584–2608.

Johnson, J.W., and Nitao, J.J., 2002, Enhanced Cap Rock Integrity and Self-Sealing of the Immiscible Plume through Mineral Trapping during Prograde and Retrograde $CO_2$ Sequestration in Saline Aquifers. From proceedings of AAPG Annual Meeting: March 10-13, 2002, Houston, TX. American Association of Petroleum Geologists.

Kampman, N., Bickle, M., Becker, J., Assayag, N., and Chapman, H., 2009, Feldspar dissolution kinetics and Gibbs free energy dependence in a $CO_2$-enriched groundwater system, Green River, Utah: Earth and Planetary Science Letters, v. 284, 473–488.

Karig, D.E., and Lundberg, N., 1990, Deformation Bands From the Toe of the Nankai Accretionary Prism: Journal of Geophysical Research, v. 95, 9099–9109.

Knauss, K.G., Johnson, J.W., and Steefel, C.I., 2005, Evaluation of the impact of $CO_2$, co-contaminant gas, aqueous fluid and reservoir rock interactions on the geologic sequestration of $CO_2$: Chemical Geology, v. 217, 339–350.

Knipe, R.J., 1993, The influence of fault zone processes and diagenesis on fluid flow, *in* Horbury, A.D., and Robinson, A.D., eds., Diagenesis and basin development: AAPG Studies in Geology 36, American Association of Petroleum Geologists, p. 135–151.

Land, L.S., 1983, The application of stable isotopes to studies of the origin of dolomite and to problems of diagenesis of clastic sediments, *in* Arthur, M.A., Anderson, T.F., Kaplan, I.R., Veizer, J., and Land, L.S., eds., Stable Isotopes in Sedimentary Geology: SEPM Short Course No. 10: Tulsa, OK, Society for Sedimentary Geology, p. 4-1–4-22.

Land, L.S., 1998, Failure to precipitate dolomite at 25°C from dilute solution despite 1000-fold oversaturation after 32 years: Aquatic Geochemistry, v. 4, 361–368.

Land, L.S., and Dutton, S.P., 1978, Cementation of a Pennsylvanian deltaic sandstone: Isotopic data: Journal of Sedimentary Petrology, v. 48, 1167–1176.

Lander, R.H., Larese, R.E., and Bonnell, L.M., 2008, Toward more accurate quartz cement models: The importance of euhedral versus noneuhedral growth rates: AAPG Bulletin, v. 92, 1537–1563.

Lander, R.H., and Walderhaug, O., 1999, Predicting porosity through simulating sandstone compaction and quartz cementation: AAPG Bulletin, v. 83, 433–449.

Larsen, P.-H., 1988, Relay structures in a Lower Permian basement-involved extension system, East Greenland: Journal of Structural Geology, v. 10, 3–8.

Lindholm, R.C., and Finkelman, R.B., 1972, Calcite staining: semiquantitative determination of ferrous iron: Journal of Sedimentary Petrology, v. 42, 239–242.

Lu, J., 2011, Discussion of the difficult-to-identify peaks in bulk rock and clay-size separation x-ray diffraction data: Austin, TX, March 22.

Lu, J., Wilkinson, M., Haszeldine, R., and Boyce, A., 2011, Carbonate cements in Miller field of the UK North Sea: A natural analog for mineral trapping in $CO_2$ geological storage: Environmental Earth Sciences, v. 62, 507–517.

Mannan, A., 2002, Stratigraphic evolution and geochemistry of the Neogene Surma Group, Surma Basin, Sylhet, Bangladesh [Dissertation]: Oulu, Finland, University of Oulu, 190 p.

Martel, S.J., and Boger, W.A., 1998, Geometry and mechanics of secondary fracturing around small three-dimensional faults in granitic rock: Journal of Geophysical Research, v. 103, 21299–21314.

Mayo, A.L., Morris, T.H., Peltier, S., Petersen, E.C., Payne, K., Holman, L.S., Tingey, D., Fogel, T., Black, B.J., and Gibbs, T.D., 2003, Active and inactive groundwater flow systems: Evidence from a stratified, mountainous terrain: Geological Society of America Bulletin, v. 115, 1456–1472.

Mayo, A.L., Shrum, D.B., and Chidsey, T.C., Jr., 1991, Factors contributing to exsolving carbon dioxide in ground water systems in the Colorado Plateau, Utah: Utah Geological Association Publication, v. 19, 335–341.

McKnight, E.T., 1940, Geology of the area between Green and Colorado rivers, Grand and San Juan counties, Utah [USGS Bulletin 908]: Reston, VA, United States Geological Survey, 147 p.

Miller, J.P., 1952, A portion of the system calcium carbonate-carbon dioxide-water, with geological implications: American Journal of Science, v. 250, 161–203.

Milliken, K., 2010, Discussion of when it is advisable to stain sandstone thin sections and whether stains are effective when used simultaneously: Austin, TX.

Milliken, K., 2011, Discussion on the nature of isopachous chalcedony cement, including precipitation rate and conditions: Austin, TX, April 26.

Milliken, K.L., 1979, The silicified evaporite syndrome – two aspects of silicification history of former evaporite nodules from southern Kentucky and northern Tennessee: Journal of Sedimentary Petrology, v. 49, 12.

Mook, C.C., 1916, A study of the Morrison Formation: Annals of the New York Academy of Sciences, v. 27, 39–191.

Moore, D.M., and Reynolds, R.C., 1997, X-Ray Diffraction and the Identification and Analysis of Clay Minerals: Oxford, Oxford University Press, 378 p.

Moore, J., Adams, M., Allis, R., Lutz, S., and Rauzi, S., 2005, Mineralogical and geochemical consequences of the long-term presence of $CO_2$ in natural reservoirs: An example from the Springerville-St. Johns Field, Arizona, and New Mexico, USA: Chemical Geology, v. 217, 365–385.

Mullens, T.E., and Freeman, V.L., 1957, Lithofacies of the Salt Wash member of the Morrison Formation, Colorado Plateau: Geological Society of America Bulletin, v. 68, 505–526.

National Energy Technology Laboratory, 2007, Carbon Sequestration Atlas of the United States and Canada, United States Department of Energy, 90 p.

Nightingale, M., Johnson, G., Shevalier, M., Hutcheon, I., Perkins, E., and Mayer, B., 2009, Impact of injected $CO_2$ on reservoir mineralogy during $CO_2$-EOR: Energy Procedia, v. 1, 3399–3406.

Osborne, P., 2002, Technical Program Overview: Underground injection control regulations (EPA 816-R-02-025). Environmental Protection Agency, 81 p.

Ostrom, M.E., 1961, Separation of clay minerals from carbonate rocks by using acid: Journal of Sedimentary Petrology, v. 31, 123–129.

Paxton, S.T., Szabo, J.O., Ajdukiewicz, J.M., and Klimentidis, R.E., 2002, Construction of an intergranular volume compaction curve for evaluating and predicting compaction and porosity loss in rigid-grain sandstone reservoirs: AAPG Bulletin, v. 86, 2047–2065.

Pay, M.D., Astin, T.R., and Parker, A., 2000, Clay mineral distribution in the Devonian-Carboniferous sandstones of the Clair Field, west of Shetland, and its significance for reservoir quality: Clay Minerals, v. 35, 151–162.

Peacock, D.C.P., and Sanderson, D.J., 1991, Displacements, segment linkage and relay ramps in normal fault zones: Journal of Structural Geology, v. 13, 721–733.

Peacock, D.C.P., and Sanderson, D.J., 1994, Geometry and development of relay ramps in normal fault systems: AAPG Bulletin, v. 78, 147–165.

Pearce, J.M., Holloway, S., Wacker, H., Nelis, M.K., Rochelle, C., and Bateman, K., 1996, Natural occurrences as analogues for the geological disposal of carbon dioxide: Energy Conversion and Management, v. 37, 1123–1128.

Pearson, F.J., Fisher, D.W., and Plummer, L.N., 1978, Correction of ground-water chemistry and carbon isotopic composition for effects of $CO_2$ outgassing: Geochimica et Cosmochimica Acta, v. 42, 1799–1807.

Peterson, F., 1980, Sedimentology of the uranium-bearing Salt Wash Member and Tidwell Unit of the Morrison Formation in the Henry and Kaiparowits basins, Utah: Utah Geological Association Publication, 305–322.

Peterson, F., 1987, The search for source areas of Morrison (Upper Jurassic) clastics on the Colorado Plateau. Abstract, *in* GSA Annual Meeting Abstracts with Programs: October 26–29, Phoenix, AZ. Geological Society of America, p. 804.

Peterson, F., 1994, Sand dunes, sabkhas, streams, and shallow seas: Jurassic paleogeography in the southern part of the Western Interior Basin, *in* Caputo, M.V., Peterson, J.A., and Franczyk, K.J., eds., Mesozoic Systems of the Rocky Mountain Region, USA: Denver, CO, Society for Sedimentary Geology, Rocky Mountain Section, 233–272.

Pittman, E.D., 1981, Effect of fault-related granulation on porosity and permeability of quartz sandstones, Simpson Group (Ordovician), Oklahoma: AAPG Bulletin, v. 65, 2381–2387.

Poppe, L.J., Paskevich, V.F., Hathaway, J.C., and Blackwood, D.S., 2001, A laboratory manual for X-ray powder diffraction (Open-File Report 2001-41): United States Geological Survey, http://pubs.usgs.gov/of/2001/of01-041/: Accessed 2009–2011.

Powell, J.W., 1961, The Exploration of the Colorado River and Its Canyons (formerly titled: Canyons of the Colorado): New York, Dover Publications, Inc., 400 p.

Pruess, K., García, J., Kovscek, T., Oldenburg, C., Rutqvist, J., Steefel, C., and Xu, T., 2004, Code intercomparison builds confidence in numerical simulation models for geologic disposal of $CO_2$: Energy, v. 29, 1431–1444.

Rawling, G.C., Goodwin, L.B., and Wilson, J.L., 2001, Internal architecture, permeability structure, and hydrologic significance of contrasting fault-zone types: Geology, v. 29, 43–46.

Reynolds, R.C., 1992, X-ray diffraction studies of illite/smectite from rocks, <1 μm randomly oriented powders, and <1 μm oriented powder aggregates: The absence of laboratory-induced artifacts: Clays and Clay Minerals, v. 40, 387–396.

Riggs, E.S., and Farrington, O.C., 1901, The dinosaur beds of the Grand River Valley of Colorado: Field Columbian Museum Geological Series, v. 1, 267–274.

Robinson, J.W., and McCabe, P.J., 1997, Sandstone-body and shale-body dimensions in a braided fluvial system: Salt Wash sandstone Member (Morrison Formation), Garfield County, Utah: AAPG Bulletin, v. 81, 1267–1291.

Rotevatn, A., Fossen, H., Hesthammer, J., Aas, T.E., and Howell, J.A., 2007, Are relay ramps conduits for fluid flow? Structural analysis of a relay ramp in Arches National Park, Utah, *in* Lonergan, L., Jolly, R.J.H., Rawnsley, K., and Sanderson, D.J., eds., Fractured Reservoirs: Special Publication 270, Geological Society of London, p. 55–71.

Rotevatn, A., Tveranger, J., Howell, J.A., and Fossen, H., 2009, Dynamic investigation of the effect of a relay ramp on simulated fluid flow: Geocellular modelling of the Delicate Arch Ramp, Utah: Petroleum Geoscience, v. 15, 45–58.

Rowland, J.V., and Sibson, R.H., 2004, Structural controls on hydrothermal flow in a segmented rift system, Taupo volcanic zone, New Zealand: Geofluids, v. 4, 259–283.

Shipton, Z.K., Evans, J.P., Heath, B.D.J., Williams, A., Kirschner, D., and Kolesar, P.T., 2005a, Natural leaking $CO_2$-charged systems as analogs for failed geologic storage reservoirs, *in* Benson, S.M., Oldenburg, C., Hoversten, M., and Imbus, S., eds., Carbon Dioxide Capture and Storage in Deep Geologic Formations – Results from the $CO_2$ Capture Project: Volume 2: Geologic Storage of Carbon Dioxide with Monitoring and Verification: London, Elsevier, 699–712.

Shipton, Z.K., Evans, J.P., Kirschner, D., Kolesar, P.T., Williams, A.P., and Heath, J., 2004, Analysis of $CO_2$ leakage through 'low-permeability' faults from natural reservoirs in the Colorado Plateau, east-central Utah, *in* Baines, S.J., and Worden, R.H., eds., Geological Storage of Carbon Dioxide: Special Publication 233, Geological Society of London, p. 43–58.

Shipton, Z.K., Evans, J.P., and Thompson, L.B., 2005b, The geometry and thickness of deformation-band fault core and its influence on sealing characteristics of deformation-band fault zones, *in* Sorkhabi, R., and Tsuji, Y., eds., Faults, fluid flow, and petroleum traps: AAPG Memoir 85, American Association of Petroleum Geologists, p. 181–195.

Siirila, E.R., Navarre-Sitchler, A.K., Maxwell, R.M., and McCray, J.E., 2010, A quantitative methodology to assess the risks to human health from $CO_2$ leakage into groundwater: Advances in Water Resources, In press.

Simonson, B.M., 1987, Early silica cementation and subsequent diagenesis in arenites from four early Proterozoic iron formations of North America: Journal of Sedimentary Petrology, v. 57, 494–511.

Stocker, M., 2011, Discussion of the possible and likely species represented by fossilized bone fragments in the Morrison Brushy Basin: Austin, TX.

Stokes, W.L., 1944, Morrison formation and related deposits in and adjacent to the Colorado Plateau: Geological Society of America Bulletin, v. 55, 951–992.

Tiab, D., and Donaldson, E.C., 2004, Petrophysics: Theory and practice of measuring reservoir rock and fluid transport properties.: Boston, Elsevier, 889 p.

Torrent, J., and Schwertmann, U., 1987, Influence of hematite on the color of red beds: Journal of Sedimentary Petrology, v. 57, 682–686.

Trimble, L.M., and Doelling, H.H., 1978, Geology and uranium-vanadium deposits of the San Rafael River mining area, Emery County, Utah [Utah Geological and Mineral Survey: Bulletin 113]: Salt Lake City, UT, Utah Geological and Mineral Survey, 122 p.

Trudgill, B., and Cartwright, J., 1994, Relay-ramp forms and normal-fault linkages, Canyonlands National Park, Utah: Geological Society of America Bulletin, v. 106, 1143–1157.

Tucker, M.E., and Wright, V.P., 1990, Carbonate Sedimentology: Oxford, UK, Wiley-Blackwell, 496 p.

Underhill, J.R., and Woodcock, N.H., 1987, Faulting mechanisms in high-porosity sandstones; New Red Sandstone, Arran, Scotland, *in* Jones, M.E., and Preston, R.M.F., eds., Deformation of Sediments and Sedimentary Rocks: Special Publication 29, Geological Society of London, p. 91–105.

U.S. Climate Data, no date, Climate – Green River – Utah, www.usclimatedata.com/climate.php?location=USUT0094: Accessed July, 2011.

United States Geological Survey, 1988, Topographic Map of Green River NE, Utah: Provisional Edition.

United States Geological Survey, 2011, Surface-Water Annual Statistics for the Nation: 09314500 Price River at Woodside, UT, http://waterdata.usgs.gov/nwis/annual/?referred_module=sw: Accessed April, 2011.

Van der Plas, L., and Tobi, A.C., 1965, Reliability of point counting results: Reply: American Journal of Science, v. 263, 722–724.

Vrolijk, P., Myers, R., Sweet, M.L., Shipton, Z.K., Dockrill, B., Evans, J.P., Heath, J., and Williams, A.P., 2005, Anatomy of reservoir-scale normal faults in central Utah: Stratigraphic controls and implications for fault zone evolution and fluid flow, *in* Pederson, J., and Dehler, C.M., eds., Interior Western United States: Geological Society of America Field Guide 6, 261–282.

Vrolijk, P., and van der Pluijm, B.A., 1999, Clay gouge: Journal of Structural Geology, v. 21, 1039–1048.

Walderhaug, O., 1994, Precipitation rates for quartz cement in sandstones determined by fluid-inclusion microthermometry and temperature-history modeling: Journal of Sedimentary Research, Section A: Sedimentary Petrology and Processes, v. 64, 324–333.

Walsh, J.J., and Watterson, J., 1991, Geometric and kinematic coherence and scale effects in normal fault systems, *in* Roberts, A.M., Yielding, G., and Freeman, B., eds., The Geometry of Normal Faults: Special Publication 56, Geological Society of London, p. 193–203.

Waltham, T., 2001, Crystal Geyser: Utah's cold one: Geology Today, v. 17, 22–24.

Warren, E.A., and Pulham, A.J., 2001, Anomalous porosity and permeability preservation in deeply buried Tertiary and Mesozoic sandstones in the Cusiana Field, Llanos Foothills, Colombia: Journal of Sedimentary Research, v. 71, 2–14.

Welton, J.E., 1984, SEM Petrology Atlas [AAPG Methods in Exploration], Chevron Oil Field Res. Co.

White, S.P., Allis, R.G., Moore, J., Chidsey, T., Morgan, C., Gwynn, W., and Adams, M., 2005, Simulation of reactive transport of injected $CO_2$ on the Colorado Plateau, Utah, USA: Chemical Geology, v. 217, 387–405.

Wibberley, C.A.J., Yielding, G., and Di Toro, G., 2008, Recent advances in the understanding of fault zone internal structure: A review, *in* Wibberley, C.A.J., Kurz, W., Imber, J., Holdsworth, R.E., and Collettini, C., eds., The Internal Structure of Fault Zones: Implications for Mechanical and Fluid-Flow Properties: Special Publication 299, Geological Society of London, p. 5–33.

Wilkinson, M., Gilfillan, S.M.V., Haszeldine, R.S., and Ballentine, C., 2009a, Plumbing the depths: Testing natural tracers of subsurface $CO_2$ origin and migration, Utah, *in* Grobe, M., Pashin, J.C., and Dodge, R.L., eds., Carbon dioxide sequestration in geological media – State of the science: AAPG Studies in Geology 59, American Association of Petroleum Geologists, p. 619–634.

Wilkinson, M., Haszeldine, R.S., Fallick, A.E., Odling, N., Stoker, S.J., and Gatliff, R.W., 2009b, $CO_2$-mineral reaction in a natural analogue for $CO_2$ storage – implications for modeling: Journal of Sedimentary Research, v. 79, 486–494.

Willemse, E.J.M., and Pollard, D.D., 1998, On the orientation and patterns of wing cracks and solution surfaces at the tips of a sliding flaw or fault: Journal of Geophysical Research, v. 103, 2427–2438.

Williams, H., Turner, F.J., and Gilbert, C.M., 1982, Petrography: An introduction to the study of rocks in thin section: San Francisco, W. H. Freeman and Co., 626 p.

Wilson, M.D., and Pittman, E.D., 1977, Authigenic clays in sandstones: Recognition and influence on reservoir properties and paleoenvironmental analysis: Journal of Sedimentary Petrology, v. 47, 3–31.

Woodward-Clyde Consultants, 1983, Overview of the Regional Geology of the Paradox Basin Study Region (ONWI-92). Office of Nuclear Waste Isolation, Battelle Memorial Institute, 443 p.

Xu, T., Apps, J.A., and Pruess, K., 2005, Mineral sequestration of carbon dioxide in a sandstone-shale system: Chemical Geology, v. 217, 295–318.

Yielding, G., Freeman, B., and Needham, D.T., 1997, Quantitative fault seal prediction: AAPG Bulletin, v. 81, 897–917.

Zerai, B., Saylor, B.Z., and Matisoff, G., 2006, Computer simulation of $CO_2$ trapped through mineral precipitation in the Rose Run Sandstone, Ohio: Applied Geochemistry, v. 21, 223–240.

Zhou, J., and Chafetz, H.S., 2009a, Biogenic caliches in Texas: The role of organisms and effect of climate: Sedimentary Geology, v. 222, 207–225.

Zhou, J., and Chafetz, H.S., 2009b, The genesis of late Quaternary caliche nodules in Mission Bay, Texas: Stable isotopic compositions and palaeoenvironmental interpretation: Sedimentology, v. 56, 1392–1410.

# Vita

Alexander Sebastian MacDonald Urquhart was born in Cambridge, England, and moved to the United States when he was three. He grew up in coastal Maine, where he gained an appreciation for nature and the out-of-doors. He was particularly fascinated by rocks, which he collected by the bag-full and carried home from around the world.

He joined the class of 2008 at Amherst College, in Massachusetts, where he at first took a particular interest in history and journalism and aimed for a degree in English. Taking an introductory geology class in his sophomore year, however, filled him with fond memories of his youth as he gained a greater appreciation for the chests of rocks previously collected only because they looked neat. Geology fascinated him because of the new dimension it lent to his perception of the world around him. He eventually graduated with a dual major in Geology and English.

Foregoing the many career paths available to the modern English major, he decided to pursue the geologic side of his education towards a structure-related graduate degree. On the advice of his undergraduate geology advisor, Tekla Harms, he looked into The University of Texas at Austin, and learned about the concept of carbon sequestration. After learning about the research being done on sequestration—which interested him, as a conservationist and naturalist at heart—he applied to the Jackson School of Geosciences, which was conducting much of the most advanced and exciting work in this field.

After completing his masters thesis, he hopes to continue researching carbon sequestration and reservoir geology in cooperation with the energy industry. He would like to reconcile the petroleum industry and environmentalists, both of whom, he believes, could benefit greatly from a closer and more collaborative relationship. To be determined.

Permanent address and email: 10 Winslow Road, Falmouth, ME 04105

asmurquhart@gmail.com

This thesis was typed by Alexander S. M. Urquhart.